Springer Series in Materials Science 152

Michael Nosonovsky
Pradeep K. Rohatgi

Biomimetics in Materials Science

Self-Healing, Self-Lubricating, and Self-Cleaning Materials

Springer

Springer Series in
MATERIALS SCIENCE 152

Springer Series in
MATERIALS SCIENCE

Editors: R. Hull C. Jagadish R.M. Osgood, Jr. J. Parisi Z. Wang

The Springer Series in Materials Science covers the complete spectrum of materials physics, including fundamental principles, physical properties, materials theory and design. Recognizing the increasing importance of materials science in further device technologies, the book titles in this series reflect the state-of-the-art in understanding and controlling the structure and properties of all important classes of materials.

Please view available titles in *Springer Series in Materials Science*
on series homepage http://www.springer.com/series/856

Michael Nosonovsky • Pradeep K. Rohatgi

Biomimetics in Materials Science

Self-Healing, Self-Lubricating, and Self-Cleaning Materials

Springer

Michael Nosonovsky
College of Engineering and Applied Science
University of Wisconsin-Milwaukee
Milwaukee, 53211-0413 WI, USA
nosonovs@uwm.edu

Pradeep K. Rohatgi
College of Engineering and Applied Science
University of Wisconsin-Milwaukee
Milwaukee, 53211-0413 WI, USA
prohatgi@uwm.edu

Springer Series in Materials Science ISSN 0933-033X
ISBN 978-1-4614-0925-0 e-ISBN 978-1-4614-0926-7
DOI 10.1007/978-1-4614-0926-7
Springer New York Dordrecht Heidelberg London

Library of Congress Control Number: 2011938278

To my wife Naomi and my sons Mark Mordecai and Ari.

Michael Nosonovsky

To my wife Kalpana, my children Rajat and Sonali, my grandchildren Milan, Uma, and Meera, and my parents.

Pradeep K. Rohatgi

Preface

We live in an interesting time for materials scientists and engineers, when new advanced technology gives us the ability to control structure and properties at the micro- and nanoscale, and when new experimental discoveries in biology give us the insight of how materials and tissues in living nature achieve their remarkable properties. At this interface, the new fields of advanced, nanostructured, smart, functional, and biomimetic materials have emerged. This book describes this new and expanding area of materials that have the ability for self-organization, including self-healing, self-lubricating, and self-cleaning properties. Self-healing is the ability of a material to repair damage, such as a crack or void. Most living organisms can repair minor or moderate damage in their tissues. This ability is a result of a complex hierarchical organization of biological systems. A living tissue has many mechanisms sometimes acting simultaneously and complementing each other, which implement partial or complete self-repair, and this can be a complicated process with many stages. Most artificial or engineered materials do not have the ability for self-healing and tend to deteriorate irreversibly with time due to wear, fatigue, creep, fracture, corrosion, erosion, and other modes. Degradation and wear limit the lifespan of devices, and can cause a catastrophic failure leading to economic loss and even to the loss of human lives. Therefore, deterioration is a significant problem in many areas of engineering. For this reason, creating self-healing artificial materials has always been a dream of engineers.

Recent advances in nanoscience and technology, biotechnology, and other areas have enhanced our ability to control the structure of materials at various scale levels, from the macroscale down to the nanoscale and the atomic and molecular levels. It is becoming possible to build micro- and nanostructured materials as well as to create complex hierarchical structures. Because of these advances, it is now possible to design and synthesize certain artificial self-healing materials. While the area of self-healing materials is still emerging, most progress has been made with polymeric materials, concrete, and some ceramics. The area of self-healing cracks has been around for some time, and many concepts of self-healing materials are borrowed from it; however, considerable improvement is required before these

materials can be widely used. Certain advances have been made with metallic self-healing materials, but the field remains in its infancy due to numerous problems that must be overcome to create successful self-healing composite alloys.

Strictly speaking, there are two types of self-healing: autonomous and nonautonomous. While autonomous self-healing implies no external intervention at all, nonautonomous healing implies certain human intervention, for example, heating a material to initiate the repair process. Most self-healing systems suggested so far use some kind of healing agent, often a liquid or a solid with a low melting point, embedded into the matrix of the composite material. When activated either by the deterioration process itself or by an external intervention such as heating, the agent is released and seals the void or crack by solidifying or through a chemical reaction. Another approach involves incorporation of shape memory alloy fibers in metallic matrices. The shape memory alloys stretch when subjected to tensile stress leading to cracks in the matrix. Upon heating the composite, the shape memory alloys shrink to the original length, compressing the crack and shutting the crack closed. Liquation of matrix at crack surfaces due to heating causes the compressed crack surfaces to weld to each other sealing the crack.

Since living nature often provides solutions that are superior to human technology, many scientists are trying to learn from nature and mimic its approaches to engineering problems. Mimicking nature for engineering applications is called biomimetics or bionics. While a true biomimetic approach would imply mimicking and copying the mechanisms used in living nature, a less extreme approach considers nature a source of inspiration for an engineer leading to so-called "bio-inspired" systems and materials. In most situations nature's solutions cannot be mimicked directly, so an adjustment for engineering applications is required. Several ideas have been suggested for biomimetic self-healing, including an artificial vascular system that provides circulation of a healing liquid to the damaged area or nanoparticles serving as artificial leucocytes loaded with a healing agent that stream to the crack or void.

The surface is the most vulnerable part of most engineering components. Not surprisingly, most deterioration – such as wear – occurs at the surface of a body or at the interface between contacting bodies. For this reason, in this book we pay special attention to self-healing and self-organization processes that occur at the interface. One important area of study is self-lubrication. Most technical systems with sliding parts require lubrication to reduce friction and wear. A system that provides low friction and wear without external lubrication is called a self-lubricating system, and a material that can be used in such a system is called a self-lubricating material.

The term "self-lubrication" has been used for more than two decades, and it refers to several methods and effects that reduce friction or wear. Among these methods is depositing self-lubricating coatings that are either hard (to reduce wear) or with low surface energy (to reduce adhesion and friction) or have a crystal structure, which facilitates formation of protective layers on the surface. Besides coatings, self-lubrication can mean the development of metal, polymer, or ceramic-based composite self-lubricating materials, often with a matrix that provides structural integrity and a reinforcement material that provides low friction and wear.

Many nanocomposites which exhibit very low friction and wear have become a focus of this research, as well as numerous attempts to include nanosized reinforcement, carbon nanotubes, graphene, and fullerene C_{60} molecules in a variety of matrices and with lubricants. Simple models assume that these large molecules and nanosized particles serve as "rolling bearings" that reduce friction; however, it is obvious now that the mechanism can be more complicated and sometimes may involve self-organization. For example, dynamic self-organization is thought to be responsible for self-lubrication in experiments at atomic resolution conducted with atomic force microscopy and other high-resolution techniques involving TEM. A different approach involves a layer of lubricant that is formed in situ during friction due to a chemical reaction. Such a reaction can be induced in situ by mechanical contact, such as, a copper protective layer formed at a metallic frictional interface due to the selective transfer of Cu ions from a copper-containing alloy (e.g., bronze) or from a lubricant. A protective layer can be formed with a chemical reaction of oxidation or a reaction with water vapor. For example, a self-lubricating layer of boric acid (H_3BO_3) is formed as a result of a reaction of water molecules with a B_2O_3 coating. Another type of self-lubricating material involves lubricant embedded into the matrix, or sometimes, inside microcapsules that rupture during wear and release the lubricant. Surface microtexturing provides holes and dimples that would serve as reservoirs for lubricant and can be viewed as another method of providing self-lubrication. We should mention that self-lubrication is observed in many biological systems, and that the term "self-lubrication" is also used in geophysics where it refers to abnormally low friction between tectonic plates that is observed during some earthquakes.

Friction has been traditionally viewed as a process that leads to irreversible energy dissipation and wear. Today it is clear that friction can also lead to self-organization. This is because frictional sliding is a nonequilibrium process which involves numerous nonlinear effects. In particular, due to positive feedback, even a steady frictional system can be driven away from equilibrium by various tribochemical processes as well as mechanical and thermal effects such as thermoelastic instabilities. In that case, the steady state loses its stability, and the system reaches a limiting cycle with so-called secondary structures formed that can reduce friction and wear. It was shown since the 1980s that many dynamic effects associated with frictional sliding, avalanche, landslide, and earthquake formation deal with so-called self-organized criticality.

Self-cleaning is another phenomenon related to self-organization at an interface. Leaves of many water-repellent plants, such as the lotus, have the ability to emerge clean even from dirty water. This is due to the special microstructure of their surface. Such a microstructure leads to superhydrophobicity (contact angles with water greater than 150°). The phenomenon of roughness-induced superhydrophobicity and self-cleaning is called the lotus effect. Due to advances in surface microstructuring of materials it became possible to create artificial biomimetic surfaces that use the lotus effect. There is a great need for such nonadhesive and self-cleaning materials and surfaces, especially for small devices. With the decreasing size of a device, the surface-to-volume ratio grows, and surface forces,

such as friction and adhesion, tend to dominate over volume forces. Therefore, adhesion is a challenging problem for small-scale applications, while the lotus effect provides a promising way of designing nonadhesive surfaces. In many senses superhydrophobicity is similar to self-lubrication as the former leads to the reduction of friction between water and a solid surface due to surface micro- and nanostructuring, whereas the latter leads to the reduction of friction between two solid surfaces due to microstructuring or surface modification.

While the conventional lotus effect provides the ability to repel water and contamination particles which tend to be washed away with the repelled water, it is important also to be able to repel organic liquids, such as oils. This is a much more difficult task because organic liquids have much lower surface energy than water. The ability to repel organic liquids is called oleophobicity, and significant progress has been made in achieving roughness-induced oleophobicity. Synthesis of micro- and nanocomposites with engineered structure and reinforcement presents a great opportunity for creating self-cleaning materials.

One of the most remarkable features of biological systems is the hierarchical organization of their structure. Hierarchical structure allows them to achieve flexibility and optimization of desired properties. Not surprisingly, hierarchical organization and multiscale structure play a prominent role in the area of biomimetic materials. Hierarchical structures are found at the surface of a lotus leaf, a water strider leg, bird feathers, a gecko toe, and fish scales. These structures play a prominent role in self-cleaning.

One of the main tasks of materials science and engineering is to establish structure–property–processing–performance relationships for a given system. However, currently, self-healing, self-lubricating, and self-cleaning materials are designed and produced using the trial-and-error approach since there is no general theory of these phenomena that would relate their quantitative structural characteristics to their self-organizing properties. On the other hand, it can be seen from the above that there are many common features among these phenomena. First, most of them involve macro-, micro-, and nanostructuring. Second, they often involve self-organization. Third, many of these phenomena are observed in living nature. It is, therefore very important to identify common mechanisms in all these processes, and to identify central design themes and structural parameters that control the self-healing, self-lubricating, and self-cleaning properties.

Self-organization became a topic of active theoretical and experimental research in physics and chemistry in the middle of the last century when many self-organizing systems were discovered or investigated, such as the *Bénard cells* in boiling water of the Belousov–Zhabotinsky oscillating chemical reaction. On the other hand, it was understood that self-organization in physical, chemical, biological, and even social systems has many typical features that could be described by the methods of nonequilibrium thermodynamics. Significant results were achieved in understanding self-organization and its relation to nonequilibrium (irreversible) thermodynamics. At the same time many new examples of self-organizing systems in nature and technical applications were found. However, the general principles of self-organization and nonequilibrium thermodynamics in materials have not been

applied to the study of self-healing, self-lubricating, and self-cleaning materials. One of the purposes of this book is to close this gap.

The monograph is divided into three parts. The first chapter introduces basic concepts and summarizes several fields of research that are relevant to this multi-disciplinary book, so that self-healing, self-lubricating, and self-cleaning materials are reviewed. Our purpose is to discuss very recent experimental findings and emerging design methods in these fields, and at the same time we attempt to provide a significant level of theoretical generalization. We view these three fields as special cases of self-organizing materials and surfaces, and thus we attempt to generalize by applying the methods of nonequilibrium thermodynamics. This is what makes our book different in comparison with similar books in the area. Each of the three parts follows the same logical organization of the material. First, we present currently known basic experimental facts, many of which were discovered in recent years or decades. After that, a detailed theoretical analysis is presented, and additional experimental observations are discussed in light of the theoretical analysis. Finally, practical design considerations for emerging materials and applications are formulated.

The book is intended for research scientists, graduate students, and engineers who want to familiarize themselves with the new and exciting area of self-healing, self-lubricating, and self-cleaning materials and surfaces.

Some of the work presented in Parts I and II of the book was done in support of US Army TARDEC (under TACOM contracts # W56HZV-04-C-0784 and W56HZV-08-C-0716). The material in these sections is also in part based upon work supported by the National Science Foundation under Grant No. OISE – 0710981. The research reported in Chap. 7 was partially supported by the University of Wisconsin-Malwaukee (UWM) Research Growth Initiative grant. The research reported in Chaps. 12 and 13 was partially supported by UWM Research Foundation Bradley Catalyst grant and by NSF IUCRC for Water Policy and Equipment grant. We would like to thank our colleagues from the UWM for their help in preparation and review of the manuscript of this book and very helpful and stimulating discussions: Prof. Ryoichi Amano, Drs. Benjamin Schultz, Jose Omar Martinez-Lucci, and J. B. Fergusson, as well as Messrs. Andrew Ruzek, Vahid Mortazavi, Vahid Hejazi, Mehdi Mortazavi, Anthony Macke, Gonzalo Alejandro Rocha Rivero, Dan Kongshaug, Andrew Braun, Shobhit Misra, Dean Meilicke, and Ms. Katherine Connerton for their help with text preparation.

Milwaukee, WI, USA

Michael Nosonovsky
Pradeep K. Rohatgi

Contents

Part II Self-Lubricating Materials

Abbreviations

AAO	Anodic aluminum oxide
AFM	Atomic force microscope
AKD	Alkylketen dimer
AMI	Adams–Martins instabilities
BCH	Brucite-type cobalt hydroxide
BEM	Boundary elements method
BN	Boron nitride
BP	British Petroleum
BZ	Belousov–Zhabotinsky
CA	Contact angle, cellular automata
CAH	Contact angle hysteresis
CBD	Chemical bath deposition
CFD	Computational fluid dynamics
CNT	Carbon nanotube
CRSS	Critical resolved shear stress
CTE	Coefficient of thermal expansion
CVD	Chemical vapor deposition
DLC	Diamond-like carbon
DMF	Dimethylformamide
DMT	Derjaguin–Muller–Toporov
DNA	Deoxyribonucleic acid
EDX	Energy dispersive spectroscopy
ESCA	Electron spectroscopy for chemical analysis
ESEM	Environmental scanning electron microscope
FEM	Finite elements method
FEP	Fluorinated ethylene propylene
FSM	Fluorinated silane molecules
GRW	Generalized Rayleigh wave
GW	Greenwood–Williamson
ITO	Indium tin oxide
JKR	Johnson–Kendall–Roberts

LA	Lauric acid
LBL	Layer-by-layer
LDPE	Low-density polyethylene
MC	Monte-Carlo
MD	Molecular dynamics
MEMS	Microelectromechanical systems
MMC	Metal matrix composite
MSIP	Magnetron sputter ion plating
NEMS	Nanoelectromechanical systems
NW	Nanowires
OTS	Octadecyltrichlorosilane
PAA	Polyacrylic acid
	Porous anodic alumina
PAH	Polyallylamine hydrochloride
PAS	Positron annihilation spectroscopy
PC	Polycarbonate
PCL	Poly(ε-caprolactone)
PDE	Partial differential equation
PDF	Probability density function
PDMS	Polydimethylsiloxane
PE	Polyethylene
PECVD	Plasma-enhanced chemical vapor deposition
PET	Polyethylene terephthalate
PFOS	Perfluorooctane sulfonate
PF_3	Tetrahydroperfluorodecyltrichlorosilane
PLA	Polylactide
PLD	Pulsed laser deposition
PM	Powder metallurgy
PMMA	Polymethylmethacrylate
POM	Polyoxymethylene
PP	Polypropylene
PPy	Polypyrrole
PS	Polystyrene
PTA	Plasma-transferred arc
PTFE	Polytetrafluoroethylene
PVC	Polyvinyl chloride
PVD	Physical vapor deposition
PVDF	Polyvinylidene fluoride
PVP	Polyvinylpyrrolidone
RBS	Rutherford backscattering
RD	Reaction–diffusion
RH	Relative humidity
RHF	Rice husk flour
RMS	Root mean square
RO	Reverse osmosis

SAED	Selected area electron diffraction
SAM	Self-assembled monolayer
SEM	Scanning electron microscope
SMA	Shape memory alloy
SOC	Self-organized criticality
SSPD	Semisolid powder densification
TEI	Thermoelastic instabilities
TEM	Transmission electron microscopy
TFC	Thin film composite
THF	Tetrahydrofuran
TMD	Transition metal dichalcogenides
TMS	Tetramethylsilane
UHV	Ultrahigh vacuum
UKCS	United Kingdom coastal shelf
UV	Ultraviolet
UWM	University of Wisconsin-Milwaukee
WCA	Water contact angle
XPS	X-ray photoelectron spectroscopy

Nomenclature

A	Area, Helmholtz free energy
A_r	Real area of contact
a	Crack length
B	Number of bins
B_i	Degradation coefficient
C	Molar concentration
c	Concentration
Ca	Capillary number
C_S	Composition of the liquid surrounding
C_O	Original alloy composition
$c(\tau)$	Autocorrelation function
D	Diffusion coefficient, diameter
D_0	Frequency factor
d	Distance
E	Elastic modulus
E^*	Effective modulus
E_b	Energy barrier
F	Force
F_a	Force required to shear adhesion bond
F_cap	Capillary force
F_L	Fraction of liquid phase
F_S	Composition of the solid
$f_\mathrm{SL}, f_\mathrm{LA}$	Fractions of the solid–liquid and liquid–air interfaces under the droplet, respectively
G	Modulus of torsional rigidity, Gibbs free energy
g	Gravitational acceleration
h	Planck's constant, height
H	Hardness, enthalpy, liquid–vapor interface size, Onsager coefficient
H_r	Density of the edges
H_p	Friction due to surface roughness and plowing

i	Dimensionless van't Hoff factor
J	Polar moment of inertia
J_i	Thermodynamic flow
J^{c}	Mass flow
J^{e}	Heat flow
J^{s}	Entropy flow
k	Generalized force, flow number, permeability, Boltzman's constant, spring constant, partition coefficient
Kn	Kundsen number
L	Lagrange function, Onsager coefficient
L_{ki}	Onsager coefficient
l	Characteristic length
l_0	Average distance of dislocations
l_{N}	Scale length
l_{c}	Capillary length
M	Onsager coefficient, number of microstates
m	Mean line
N	Number of particles, generalized force, Onsager coefficient, array of cells, number of contact spots
n	Amount in mole
p_j	Probability of appearance in the bin j
P	Pressure, pitch distance, generalized force
$P(h)$	Probability
$P(z)$	Probability density function
Q	Activation energy, heat
q	Liquid flow per cross-section area
q_i	Generalized coordinate
r	Average grain size
r_0	Initial grain size
R	Gas constant
R_1, R_2	Principal radii of curvature
Re	Reynolds number
R_{f}	Roughness factor
R_{c}	Critical radius
R_{k}	Asperity radius
R_{a}	Centerline average height
R_{p}	Mean asperity peak radius
S	Cross section, entropy, generalized coordinate, entropy density
S_{net}, S_{macro}, S_{micro}, S_{nano}	Net, macroscale, microscale, and nanoscale entropies, respectively
S_{f}	Nondimensional spacing factor
ΔS_{f}	Activation entropy
$\Delta S_{\mathrm{solidify}}$	Entropy of phase transition

$\Delta S_{\text{chemical}}$	Entropy of chemical reaction
T	Temperature
t	Time
U	Height of potential barrier, internal energy, generalized coordinate
$\tilde{U}$	Complimentary energy
u	Nondimensional temperature, energy density
V	Sliding velocity, volume, generalized coordinate
v	Local slip velocity
W	Load
We	Weber number
ΔW	Amount of energy dissipated per unit area
$\underline{\mathrm{w}}$	Wear rate
x	Sliding coordinate
X	Mole fraction, thermodynamic force
y	Normal coordinate
Y, Y_i	Thermodynamic force
Y^{deg}	Degradation force
Y^{heal}	Healing force
Z	Average number of atoms per unit area
z	Height
α	Slope
β	Correlation length
λ	Heat conductivity
γ	Dimensionless parameter, surface free energy
$\gamma_{\text{SA}}, \gamma_{\text{SL}}, \gamma_{\text{LA}}$	Solid–air, solid–liquid, and liquid–air interface energies, respectively
δ	Tolman's length
ε	Anisotropy coordinate
ζ	Healing parameter
Θ	Locally averaged value of $\cos\theta$
θ	Twist angle, contact angle for smooth surface, slope angle
θ_0	Contact angle for smooth surface
$\theta_{\text{adv}}, \theta_{\text{rec}}$	Advancing and receding contact angles
μ	Coefficient of friction, viscosity, generalized force
μ_{adh}	Adhesional component of the coefficient of friction
μ_{def}	Deformational component of the coefficient of friction
ξ	Degradation parameter
ρ	Density
π	Osmotic pressure
σ	Surface tension, standard deviation
σ_{Y}	Yield stress
τ	Contact line tension, torque

τ_{f}	Shear strength
φ	Material microstructure parameter
Ψ	Micro/nanostructure parameter of the material, energy dissipation rate
ψ	Plasticity index, dissipation function
Ω	Number of microstates
ω_{Σ}	Tribofatigue damage

Part I
Self-Healing Materials

There was a noise, a rattling sound, and the bones came together, bone to bone. I looked and tendons and flesh appeared on them and skin covered them

The Book of Ezekiel 37:7

Chapter 2
Thermodynamic Principles of Self-Healing Metallic Materials

In this chapter, the thermodynamics of self-healing is considered with an emphasis on metallic materials. All complex biological organisms have the ability to repair minor damage. Incorporating the self-repair function into inorganic systems is of growing interest for materials scientists. So far, most recent studies have concentrated on polymers and ceramics because it is easier to incorporate self-healing in nonmetallic materials than in metallic materials. However, metallic self-healing alloys and composites are of great practical importance. We review the design principles of self-healing materials using the nonequilibrium thermodynamics approach and the concept of hierarchical organization. The generalized thermodynamic force that leads to healing is induced by bringing the system away from thermodynamic equilibrium. We focus on the three major methods of imparting the ability for self-healing in metallic systems: precipitation-induced healing, embedding shape-memory alloys, and embedding a low-melting point alloy in the alloy matrix.

2.1 Introduction

Self-healing inorganic materials or material systems constitute a novel field of materials science that emerged relatively recently and started to rapidly expand (Files and Olson 1997; Feng et al. 2000; Zwaag 2007; Ghosh 2009). Self-healing in biological objects is a source of inspiration for this new research area. Most living tissues or organisms can heal themselves, provided the incurred damage is moderate. For example, after cutting, blood flows into the wound and clots, thus sealing the defect and allowing the skin to repair itself (Burgess 2002). A crack in bones is repaired due to regeneration of bone material. Most engineered materials; however, deteriorate with time irreversibly due to wear, brittle fracture, fatigue, creep, and other modes of degradation, which limits the life of various components and sometimes

M. Nosonovsky and P.K. Rohatgi, *Biomimetics in Materials Science: Self-Healing, Self-Lubricating, and Self-Cleaning Materials*, Springer Series in Materials Science 152, DOI 10.1007/978-1-4614-0926-7_2,

causes catastrophic damage. It would be very desirable to implement the ability of self-healing in inorganic materials, so that when these materials are cracked or damaged, a healing agent could be triggered to flow into the damaged area to "heal" the damage, essentially sealing the cracks. Whereas the inorganic system would not be able to create identical new material to replace the damaged area, the self-repair function could serve to provide new material in the damaged area, similar to the way in which an injury to the skin results in the formation of a scar.

As engineering systems become more sophisticated and mimic more characteristics of biological systems (Zhou 2000; Bruck et al. 2002), many new beneficial concepts can be realized. It is emphasized that the biological mechanisms of healing are very complex and often involve many factors acting concurrently. There is a growing understanding by materials scientists who work on the development of self-healing materials that the biological mechanisms of healing cannot be directly borrowed for artificial materials. For instance, Van Der Zwaag (2009) note that "while Nature has shown an extreme diversity in microstructures and microstructural systems, and, subsequently, has shown a wide diversity of healing mechanisms, it is unwise to try to copy these healing mechanisms in man-made engineering materials in a direct manner. Engineering materials have their own characteristics, and, in designing self-healing behavior in such materials, their intrinsic or natural character has to be taken into account." Therefore, we prefer to speak about bio-inspired, rather than biomimetic, self-healing materials.

To date self-healing has been applied most successfully in polymers, and this is because of their relatively large rates of diffusion due the presence of the cross-molecular bonds (Anderson et al. 2007; Bond et al. 2007; Zhang et al. 2009). One way to create self-healing polymers is to use thermosetting polymers that have the ability to cure (toughening or hardening by cross-linking of polymer chains), such as the thermosetting epoxy (White et al. 2001; Sarikaya and Aksay, 1995; Jones et al. 2007; Toohey et al. 2007). Epoxy is a polymer formed by a reaction of an epoxide resin with polyamine hardener. Epoxy can serve as a healing agent that is stored within thin-walled inert brittle macrocapsules embedded into the matrix along with a catalyst or hardener (also embedded in the matrix, but separate from the latter). When a crack propagates, the capsules fracture and the healing agent is released and propagates into the crack because of capillarity. Then the healing agent mixes with the catalyst embedded in the matrix, which triggers the cross-linking reaction and hardening of the epoxy that seals the crack (White et al. 2001; Trask and Bond 2006; Trask et al. 2007; Williams et al. 2007; Wool 2008). A different approach involves thermoplastic polymers, with various ways of incorporating the healing agent into the material. In this approach, heating is often required to initiate healing, since thermoplastics soften and flow with increasing temperature.

Besides the polymers, ceramic self-healing materials are being developed, with the main focus on concrete composites. For example, a concrete composite was produced with hollow glass fibers containing an air curing sealant embedded in the concrete matrix (Dry 1994; Li et al. 1998; Nakao et al. 2006). This composite exhibited the self-healing behavior but it suffered from a significant (10–40%) loss of stiffness compared with standard concrete due to the fibers. This is a typical

situation, when a compromise between self-healing and mechanical properties should be sought. In another project involving self-healing ceramics, researchers have studied the crack-healing behavior and mechanical properties of a mullite composite toughened by the inclusion of 15% (by volume) SiC whiskers (Nakao et al. 2006; Takahashi et al. 2007). Self-healing ceramic materials often use oxidative reactions, because the volume of oxide exceeds the volume of the original material, and therefore, products of these reactions, due to their higher volume, can be used to fill small cracks (Zwaag 2009). Self-healing nanocomposites constitute another area of research.

The field of self-healing metals and metal composites has received serious attention only in the last 10 years (Lumley 2007; Wang et al. 2007; Manuel 2009, 2007; Manuel et al. 2009). It is much more difficult to heal metallic materials than polymers, because metallic atoms are strongly bonded and have small volumes and low diffusion rates. Currently, there are three main directions which have been taken in the development of self-healing metallic systems. First is the formation of precipitates at the defect sites that immobilize further growth until failure. Van Der Zwaag (2009) and co-workers called this mechanism "damage prevention" because the idea is to prevent the formation of voids by the diffusion of the precipitate from an oversaturated solid–solid solution (alloy). The driving mechanism for the diffusion is the excess surface energy of the microscopic voids and cracks that serve as the nucleation centers of the precipitate that plays the role of the healing agent by filling up the voids. As a result, the newly formed void is sealed before it grows and thus minimizes the creep and fatigue.

Second, Olson (1997), Manuel (2007), and co-workers (Bender and Olson 2008) used another approach: reinforcement of an alloy matrix with microfibers or wires made of a shape-memory alloy (SMA), such as nitinol (NiTi). SMA wires have the ability to recover their original shape after some deformation has occurred if they are heated above a certain critical temperature (Wang et al. 2005; Olson and Hartman 1982; Olson et al. 2009). If the composite undergoes crack formation, heating the material will activate the shape recovery feature of the SMA wires which then shrink applying compressive force at the cracks and close the cracks.

The third approach is to use a healing agent (such as an alloy with a low-melting temperature) embedded into a metallic matrix, similarly to the way it is done with the polymers. However, encapsulation of a healing agent into a metallic material is much more difficult task than in the case of polymers. The healing agent should be encapsulated in microcapsules which serve as diffusion barriers and which fracture when a crack propagates.

Self-healing can be viewed as a self-organization process that leads to increasing orderliness of the material and thus, decreasing entropy. From the viewpoint of thermodynamics, self-healing is a nonequilibrium process. In most self-healing schemes, the self-healing material is driven away from the thermodynamic equilibrium either by the deterioration process itself or by an external intervention, such as heating. After that, the composite slowly restores thermodynamic equilibrium, and this process of equilibrium restoration drives the healing. In the following sections, we discuss the general principles of the nonequilibrium thermodynamics of

self-healing, and focus on how the self-healing function might be incorporated in metal matrices, and how various processing methods could be employed to do so, emphasizing the thermodynamic aspects of self-healing.

2.2 Thermodynamics of Self-Healing

Self-healing materials possess many features of self-organizing systems, which have been studied intensively by physicists and chemists during the past half-century (Prigogine 1961; Prigogine and Nicolis 1977), whereas net entropy grows with time in most conventional systems in accordance with the Second Law of thermodynamics. As irreversible energy dissipation occurs and deterioration accumulates, self-organizing systems may exhibit increasing orderliness and self-organization. They are thermodynamically open systems that operate far from thermodynamic equilibrium and can exchange energy, matter, and entropy with the environment.

2.2.1 Entropy of a Hierarchical System

Entropy is a measure of irreversibility and disorder. The classical thermodynamic definition of entropy, S, was introduced in 1850s by R. Clausius as

$$\mathrm{d}S = \mathrm{d}Q/T, \tag{2.1}$$

where T is temperature and Q is heat exchanged. Entropy is an additive function (the net entropy of a system is equal to the sum of entropies of its parts). When heat $\mathrm{d}Q$ is transferred from a body with temperature T_1 to a body with temperature T_2, the net entropy changes for the amount $\mathrm{d}S = -\mathrm{d}Q/T_1 + \mathrm{d}Q/T_2$. Thus, if heat is transferred from a hotter body to a colder one ($T_1 > T_2$), the net entropy grows ($\mathrm{d}S > 0$). This provides a convenient formal basis for the Second Law of thermodynamics stating that the net entropy of a closed system either remains constant (for a reversible process) or grows (for an irreversible process).

In 1877, L. Boltzmann suggested a definition of entropy using the statistical thermodynamic approach and the concept of microstates

$$S = k \ln \Omega, \tag{2.2}$$

where k is Boltzmann's constant, and Ω is the number of microstates corresponding to a given macrostate. Microstates are arrangements of energy and matter in a system that are distinguishable at the atomic or molecular level, but are indistinguishable at the macroscopic level (Craig 1992). A system tends to evolve into a less-ordered

(more random) macrostate which has a greater number of corresponding microstates, and thus the "configurational" entropy given by (2.2) grows.

Processes that lead to degradation (wear, corrosion, fatigue, fracture, creep, etc.) often involve interactions with different characteristic length scales, so that different isolated hierarchical levels (macro-, micro-, and nanoscale) can be distinguished in the system in a natural way. For example, friction and wear involve the contact of micro-, macro-, and nanoscale asperities and wear particles, capillary interactions, adhesion, and chemical molecular bonding (Nosonovsky and Bhushan 2007a; 2008d). In most cases, these interactions lead to irreversible energy dissipation and, therefore, to the production of entropy. However, in certain cases the entropy production at a particular scale level may be compensated by the entropy consumption at another level. Since the processes at different scale levels are independent and entropy is an additive function, the net entropy can be presented as the sum of entropies associated with the structures and process at corresponding scale levels

$$\Delta S_{\text{net}} = \Delta S_{\text{macro}} + \Delta S_{\text{micro}} + \Delta S_{\text{nano}}, \tag{2.3}$$

where the indices "net," "macro," "micro," and "nano" correspond to the net entropy, macroscale, microscale, and nanoscale components (Nosonovsky and Esche 2008a, b; Nosonovsky 2009, 2010a, b).

As an example, let us consider a solid homogeneous body. The micro/nanoscale level corresponds to the vibrations of atoms in the crystalline lattice and is not of interest for us at this point. The mesoscale structures, such as grains, defects, and dislocations correspond to the microscale levels. A perfect single-crystal body with no defects has lower microscale entropy ΔS_{micro} than a body with such defects. Larger scale defects such as cracks and voids contribute to the macroscale component of the entropy, ΔS_{macro}. A material or a surface with a regular microstructure (e.g., a microtextured surface) is more ordered and thus it has lower microscale configurational entropy, ΔS_{micro} than a material with an irregular microstructure or surface texture (Nosonovsky and Esche 2008b).

This can be utilized for the healing of macroscale defects. Suppose there is excess entropy, ΔS_{macro}, associated with the macroscale defects, such as cracks or voids. Healing can be triggered by affecting the mesoscale structure, e.g., by the release of microcapsules. The fracture of the microcapsules decreases the orderliness of the microstructure and thus increases the entropy for ΔS_{micro}. In the case $|\Delta S_{\text{macro}}| < -\Delta S_{\text{micro}}|$, the healing is done by decreasing the macroscale component of entropy at the expense of the mesoscale component (Nosonovsky et al. 2009). In other words, for most practical applications, the macroscale integrity and orderliness of material are of interest, and thus the expression for net entropy given by (2.3) can be truncated at the macroscale level, $\Delta S_{\text{net}} = \Delta S_{\text{macro}}$. The orderliness of the material, as observed at the macroscale, can grow (and, therefore, entropy can decrease) at the expense of excess entropy production at the lower scales. This is analogous to the crystal grain growth (e.g., in aluminum) due to thermal fluctuations; with growing grains, material structure becomes more ordered,

however, dissipation and excess entropy production occur at the nanoscale every time a grain border propagates (Nosonovsky and Esche 2008b).

2.2.2 Thermodynamic Forces that Drive Healing

In nonequilibrium thermodynamics, a thermodynamic force Y_i and a thermodynamic flow $J_i = \dot{q}_i$ are associated with every generalized coordinate q_i. In the widely accepted linear approximation, the flows are related to the forces by

$$J_{\mathrm{k}} = \sum_i L_{ki} Y_i, \tag{2.4}$$

where L_{ki} are Onsager coefficients (De Groot and Mazur 1962). The heat production per unit time is given by

$$\frac{\mathrm{d}Q}{\mathrm{d}t} = \sum_i J_i Y_i, \tag{2.5}$$

and the rate of entropy production is

$$S = \frac{\mathrm{d}Q}{T\mathrm{d}t} = \frac{1}{T}\sum_i J_i Y_i, \tag{2.6}$$

a linear function of thermodynamic flows.

In order to characterize degradation, it is convenient to introduce a so-called "degradation parameter" ξ, to represent, for example, the wear volume or the total area of the cracks. The degradation parameter is a generalized coordinate of the degradation process. Note that the dimension of ξ can be different depending on the physical meaning of the degradation parameter. Thus, it may have the dimension of volume or area. The corresponding thermodynamic flow (or the rate of degradation) is linearly related to the thermodynamic forces (2.4) and entropy rates (2.6). The physical meaning of this proportionality is that a constant fraction of the dissipated energy is spent for the deterioration in a given process and under given operating conditions. The dimensions of the flow and generalized force are dependent on the dimension of the degradation parameter. It is easy to generalize for the case of several degradation parameters that correspond to several processes; however, we concentrate on the case of a single degradation parameter.

When a self-healing mechanism is embedded in the system, another generalized coordinate, the healing parameter, ζ, can be introduced, for example, the volume of released healing agent. Again, the corresponding thermodynamic flow is linearly related to the thermodynamic forces (2.4) and entropy rates (2.6). However, the degradation and healing processes usually have characteristic scale lengths and thus

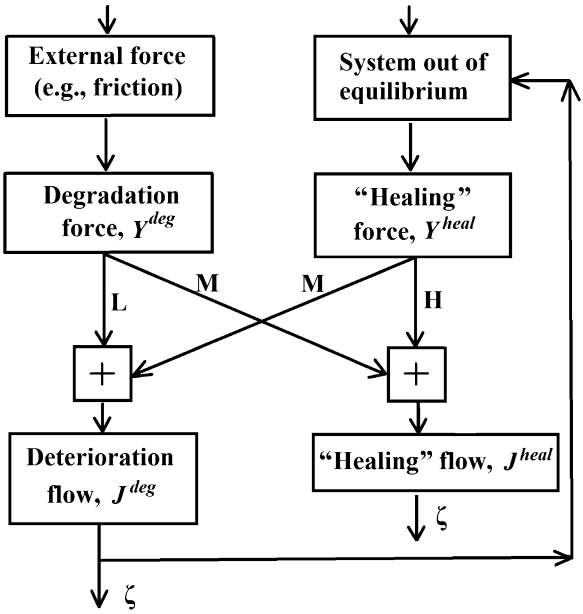

Fig. 2.1 Block diagram of the healing process. Deterioration (or degradation) is caused by an external force. The deteriorated system is brought out of equilibrium so that the restoring ("healing") force is created, which is coupled with the degradation flow through the parameter M

belong to different hierarchy levels, as was discussed above. The generalized degradation and healing forces are external forces that are applied to the system, and flows are related to the forces by the governing equations

$$\begin{aligned} J^{\text{deg}} &= LY^{\text{deg}} + MY^{\text{heal}}, \\ J^{\text{heal}} &= NY^{\text{deg}} + HY^{\text{heal}}, \end{aligned} \tag{2.7}$$

where L, M, N, H are corresponding Onsager coefficients (Fig. 2.1). It is expected that $L > 0$, $H > 0$ (degradation and healing grow when corresponding positive forces are applied), $M < 0$, $N < 0$ (degradation and healing decrease when opposite forces are applied), and $N = M$ due to the Onsager reciprocity condition (De Groot and Mazur 1962).

The degradation force Y^{deg} in (2.7) is an externally applied thermodynamic force that results in the degradation. The healing force Y^{heal} is an external thermodynamic force that is applied to the system. In most self-healing mechanisms, the system is placed out of equilibrium and the restoring force emerges, so we can identify this restoring force with Y^{heal}. Since the restoring force is coupled with the degradation parameter ξ by the negative coefficients $N = M$, it also causes a degradation decrease or healing.

The entropy rate is given, using (2.6) and (2.7), by

$$\dot{S} = \dot{S}^{\text{deg}} + \dot{S}^{\text{heal}} = \frac{L}{T}(Y^{\text{deg}})^2 + \frac{2M}{T}Y^{\text{deg}}Y^{\text{heal}} + \frac{H}{T}(Y^{\text{heal}})^2. \tag{2.8}$$

The first term in the right-hand part of (2.8) corresponds to the degradation, $\dot{S}^{\mathrm{deg}} = L(Y^{\mathrm{deg}})^2/T$, while the healing term involves positive and negative parts $\dot{S}^{heal} = 2MY^{\mathrm{deg}}Y^{heal}/T + H(Y^{heal})^2/T$. Assuming the scheme described by (2.3), when macroscale healing occurs at the expense of microscale deterioration, we postulate

$$\begin{aligned} \dot{S}_{\mathrm{macro}} &= \frac{2M}{T} Y^{\mathrm{deg}} Y^{\mathrm{heal}}, \\ \dot{S}_{\mathrm{micro}} &= \frac{H}{T} (Y^{\mathrm{heal}})^2. \end{aligned} \tag{2.9}$$

The (2.7)–(2.9) can be easily generalized for the case of several degradation and healing parameters.

2.2.3 *Friction-Induced Degradation*

Surface is the most vulnerable part of a material sample, and not surprisingly, deterioration often occurs at the surface (wear, fretting, etc.) and is induced by friction. The empirical Coulomb (or Amontons–Coulomb) law of friction states that the dry friction force F is linearly proportional to the normal load force W

$$F = \mu W, \tag{2.10}$$

where μ is the coefficient of friction, which is independent of load, sliding velocity, and the nominal area of contact. Unlike many other linear empirical laws, the Coulomb law cannot be directly deduced from the linear equations of the nonequilibrium thermodynamics, such as (2.4). Indeed, in the case of dry or lubricated friction, the sliding velocity is the thermodynamic flow, $V = J$, which, in accordance with (2.7) should be proportional to the friction force $F = Y$ (as it is the case for the viscous friction), so that the energy dissipation rate is given by the product of the thermodynamic flow and force

$$\dot{\Psi} = JY = VF. \tag{2.11}$$

However, the Coulomb friction force is independent of sliding velocity.

We discuss in the ensuing chapters how to overcome this formal difficulty. In particular, we consider the normal degree of freedom y, in addition to the sliding coordinate x (Fig. 2.2). Introducing the normal degree of freedom is a standard procedure in the study of dynamic friction, where normal vibrations are often coupled with in-plane vibrations. We further define the generalized flows as $J_1 = \dot{x}, J_2 = \dot{y}$ and forces as $Y_1 = F, Y_2 = W$ (Nosonovsky 2009).

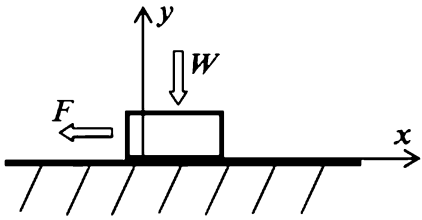

Fig. 2.2 Friction and the normal degree of freedom. The introduction of the normal degree of freedom, y, makes it possible to consider the Coulomb friction as a limiting case of the viscous friction and to include it into the linear Onsager scheme

The thermodynamic equations of motion (2.4) immediately yield the law of viscous friction in the form of

$$\begin{pmatrix} \dot{x} \\ \dot{y} \end{pmatrix} = \begin{bmatrix} L_{11} & L_{12} \\ L_{21} & L_{22} \end{bmatrix} \begin{pmatrix} F \\ W \end{pmatrix}. \tag{2.12}$$

Note that (2.12) is valid, in a general case, for the bulk of 3D deformable medium, and not necessarily for the interface between two solids.

The interface between sliding bodies has highly anisotropic properties, because a small force in the direction of the interface causes large displacements, whereas a small force in the normal direction causes only small displacements. To compensate for this anisotropy, we substitute coordinates using a small parameter ε as $(x, y) \to (\varepsilon x, y)$. The force–displacement relationships are now given by

$$\begin{pmatrix} \dot{x} \\ \dot{y} \end{pmatrix} = \begin{bmatrix} L_{11}/\varepsilon & L_{12}/\varepsilon \\ L_{21} & L_{22} \end{bmatrix} \begin{pmatrix} F \\ W \end{pmatrix}. \tag{2.13}$$

In the limit of $\varepsilon \to 0$, (2.13) yields

$$\begin{aligned} F &= -\frac{L_{12}}{L_{11}} W, \\ \dot{x} &= (L_{11}F + L_{12}W)/\varepsilon = 0/0, \\ \dot{y} &= \left(L_{22} - \frac{L_{12}L_{21}}{L_{11}} \right) W. \end{aligned} \tag{2.14}$$

According to (2.14), *any* velocity $\dot{x}$ satisfies (2.13), provided $L_{11}F + L_{12}W = 0$, which is exactly the case of Coulomb friction if $\mu = -L_{12}/L_{11}$ (Nosonovsky 2009).

Thus, we showed that the Coulomb friction law (2.10) can be deduced from the thermodynamic equations of motion (2.4) provided two assumptions are made: (1) motion in the normal degree of freedom (y) is coupled with the tangential degree of freedom (x) and (2) the change of coordinates $(x, y) \to (\varepsilon x, y)$ is introduced and the limiting case of $\varepsilon \to 0$ is investigated. The normal degree of freedom was introduced into the analysis of dynamic friction since the pioneering works of Tolstoi (1967) who discovered the existence of natural normal microvibrations coupled with the tangential vibrations, which strongly affect the magnitude of the friction force as well as the stability of sliding. The introduction of a small parameter ε and an asymptotic decomposition is the standard way of the transition from 3D to a 2D problem

(e.g., from the bulk elastic 3D body to a thin elastic plate). The Coulomb friction is an interface (2D) phenomenon and it is natural to obtain its properties using an asymptotic limit of the 3D case (Nosonovsky 2009).

For a friction-induced deterioration, such as wear, the degradation force is proportional to the frictional dissipation (Fox-Rabinovich and Totten 2006; Bryant et al. 2008)

$$Y^{\mathrm{deg}} = \alpha F\dot{x}, \tag{2.15}$$

where α is a parameter needed from dimensional considerations (note that for ξ to have the dimension of wear volume and for ξY^{deg} to have the dimension of energy, the dimension of L and α should be $\mathrm{m}^5\ \mathrm{s}^{-1}\ \mathrm{N}^{-1}$ and m^{-3} s). Taking $L\alpha = k/(\mu H)$ immediately yields the Archard's wear law, which relates the rate of wear volume $\dot{v}$ to the normal load, sliding velocity material hardness, H, and the nondimensional wear coefficient k

$$\dot{\xi} = k\frac{F\dot{x}}{\mu H}. \tag{2.16}$$

2.2.4 Optimization of Healing

Suppose that the coefficients in the governing Eq. (2.7) depend upon a micro/nanostructure parameter of the material Ψ, such as the size distribution or the concentration of microparticles embedded in a composite material, $L = L(\Psi)$, $M = M(\Psi)$, $H = H(\Psi)$. The problem of optimum design of a self-healing system can be seen as finding an optimum value of Ψ for the minimization of the degradation parameter.

For any self-healing mechanism, the following scheme is suggested. First, micro/nanostructure parameters critical for the self-healing mechanism, as well as relevant degradation and healing parameters are identified. Then thermodynamic flows and forces are related to the microstructure. The obtained system of equations is dependent upon Ψ and should be optimized by Ψ for the minimization of degradation.

For metallic materials, there are three main self-healing mechanisms that are currently being investigated by different research groups: (1) precipitation in alloys to close voids and cracks, (2) material reinforcement with embedded SMA microwires, and (3) embedding liquid healing agent into a matrix by microballoon encapsulation. In the precipitation mechanism, voids serve as nucleation centers for the diffusion of the oversaturated solute in the alloy (Fig. 1.2b). The size of the voids is the degradation parameter ξ, and the concentration of diffused solute is the healing parameter ζ, while the kinetics of the diffusion of the solute into the void is governed by a kinetic equation [similar to (2.4)]. The microstructure parameter of relevance is the concentration of the solute.

For material reinforcement with SMA microwires, the closing of the crack is achieved by heating the sample (Fig. 1.2c). The SMAs are capable of the shape memory effect due to their ability for temperature- and stress-induced reversible martensite/austenite phase transition (Perkins 1981a, b). This transition is only dependent on temperature and stress, not time (as most phase changes are), as there is no diffusion involved. The temperature of the transition is different during heating and cooling due to hysteresis. The martensitic phase can also be generated by stressing the metal in the austenitic state, and this martensite phase is capable of large strains. When the stress is released, the reversed martensite/austenite transition does not occur if the temperature remains above the transition temperature during cooling. However, when the temperature is raised above the transition temperature during heating, the martensite transforms back to the austenite phase and resumes its original shape. While the deformation of a SMA looks similar to plastic deformation, it is actually a reversible deformation. However, deformation of SMA-reinforced metal, unlike pure SMA, is not necessarily reversible, as residual stresses remain to be overcome, which can prevent the complete reoccurrence of the austenite phase. For an SMA-reinforced metal, the cross-sectional concentration of microwires can be the structural parameter Ψ, the volume of voids is the degradation parameter ξ, and the strain in SMA is the healing parameter ζ.

Encapsulation of a healing agent is used for crack damage repair. When the crack propagates, the capsule ruptures and liquid adhesive is released that can heal the crack (Fig. 1.2a). This method is especially successful with polymeric materials. Crack propagation is an irreversible process, because when intermolecular bonds are broken, the energy γ is released irreversibly, and a certain amount of entropy is produced. When a capsule ruptures and its content is released, the configurational entropy grows because mixing occurs. The macroscale entropy is reduced at the expense of the microscale entropy. For this mechanism, the total area of the cracks can be the degradation parameter ξ, the amount of released healing agent is the healing parameter ζ, and the concentration of microcapsules or microtubes is the structural parameter Ψ.

Self-healing mechanisms in metals are summarized in Table 2.1. We use the classification suggested by Van Der Zwaag (2007) and Manuel (2009). The table shows typical materials for the matrix and reinforcement, parameters that characterize microstructure, degradation, healing, characteristic length scales for the degradation and healing mechanisms, the type of phase transition involved in the healing, and what property is improved in the self-healing alloy. The nature of the healing force and details of healing mechanisms are discussed in the consequent section.

2.3 Self-Healing Metallic Systems

In this section, we review the three mechanisms of self-healing that are used for metallic materials, paying attention to thermodynamic flows and forces that act during healing. As described in the preceding section, self-healing is

Table 2.1 Self-healing mechanisms in metals

Mechanism	Precipitation	SMA reinforcement	Healing agent encapsulation
Type (according to Van Der Zwaag 2009)	Damage prevention	Damage management	
Type (according to Manuel 2009)	Solid-state	Solid-state (possibly also liquid assisted)	Liquid-assisted
Matrix material	Al–Cu, Fe–B–Ce, Fe–B–N, etc.	Sn–Bi, Mg–Zn	Al
Reinforcement materials	–	NiTi	Sn–Pb
Microstructure parameter, Ψ	Solute fraction	Concentration of microwires	Concentration of microcapsules or low-melting point alloy
Degradation measure, ξ	Volume of voids	Volume of voids	Volume of voids
Healing measure, ζ	Amount of precipitated solute	SMA strain	Amount of released healing agent
Characteristic length of degradation	Void size (microscale)	Void/crack size (macroscale)	Void/crack size (macroscale)
Characteristic length of the healing mechanism	Atomic scale (atomic diffusion)	Microwires diameter (macro or microscale)	Microcapsule size (microscale)
Phase transition involved	Solute precipitation	Martensite/austenite	Solidification of the solder
Healing temperature	Ambient	Martensite/austenite transition	Melting of the low-melting point alloy
Property improved	Creep resistance	Restored strength and toughness	Restored strength and fracture toughness

achieved by bringing the system out of thermodynamic equilibrium and coupling the restoring force with the degradation parameter.

2.3.1 Damage Prevention by Precipitation in Under-Aged Alloys

It is difficult to facilitate healing in metallic materials because atoms of metals have much lower diffusion rates compared to polymers, and they remain solid at higher temperatures. One of the techniques to provide the atomic transport of matter to voids and defects in metals is to use a supersaturated solid solution in alloys, which has a decreasing solid solubility of solute elements with decreasing

temperature (e.g., Al–Cu). Such an alloy, when quenched from high temperature, becomes supersaturated, or metastable. A typical phase diagram of an alloy capable of precipitation strengthening is presented in Fig. 2.3a (Lumley 2007). Solution treatment is conducted within a single-phase region of the phase diagram before quenching. After the heat treatment, the alloy is heated again into the $\alpha + \gamma$ phase region (γ is an intermetallic phase). However, in order to facilitate precipitation of the solute, heterogeneous nucleation sites are needed. Sites with high surface energy, such as voids, defects, grain boundaries, and free surfaces become nucleation sites and therefore an atomic flux J^{diff} due to diffusion given by Fick's law

$$\begin{aligned} J^{\text{diff}} &= -D\nabla\varsigma, \\ D &= D_0 \exp(-Q/RT), \end{aligned} \tag{2.17}$$

where $\nabla\varsigma$is the spatial gradient of the concentration, D is the diffusion coefficient, D_0 is the frequency factor, Q is the activation energy, $R = 8.31$ J K mol^{-1} is the gas constant, and T is the absolute temperature (Lumley 2007). Figure 2.3b presents a micrograph of dynamic precipitation of an under-aged Al–Cu–Mg–Ag alloy following 500 h creep at 300 MPa and 150°C (Lumley 2007). Bands of dynamically precipitated particles were formed and associated with dislocations (marked by arrows) – examples of the dynamically precipitated phase are marked "A." Lumley (2007) investigated creep behavior of the 2024 Al alloy. Creep curves for the under aged, heat treated, and artificially aged T6 alloys are shown in Fig. 2.3c (based on Lumley 2007).

The method known as age hardening or precipitation hardening is routinely used in metallurgy to increase the yield strength of an alloy by producing fine particles of an impurity phase, which impede the movement of dislocations, or defects in a crystal's lattice. Depending on the time of age hardening, an alloy can be under-aged (with many small size of precipitation particles) or over-aged (with few large particles).

An under-aged alloy can be used to provide a self-healing mechanism. When an age-hardened aluminum alloy is solution treated at high temperatures, and quenched and annealed for a relatively short period at elevated temperatures, an under-aged microstructure is produced that still retains a substantial amount of solute in the solid solution. These solute atoms can diffuse into the open-volume defects created by plastic deformation at elevated temperatures. As the degradation ξ grows, the high-energy void sites emerge, and the concentration gradient $Y^{\text{heal}} = -\nabla\varsigma$ grows, resulting in the flow of the solute, which serves as the healing agent. The solute fills the void, effectively closing it, thus decreasing the degradation – in other words; the concentration gradient is coupled with the degradation flow $\dot{\xi} = MY^{\text{heal}}$. Therefore, the (2.7) is given by

$$\begin{aligned} \dot{\xi} &= L(\Psi, \mathrm{T})Y^{\text{deg}} - M(\Psi, \mathrm{T})\nabla\varsigma, \\ \dot{\varsigma} &= M(\Psi, \mathrm{T})Y^{\text{deg}} - D(\Psi, \mathrm{T})\nabla\varsigma, \end{aligned} \tag{2.18}$$

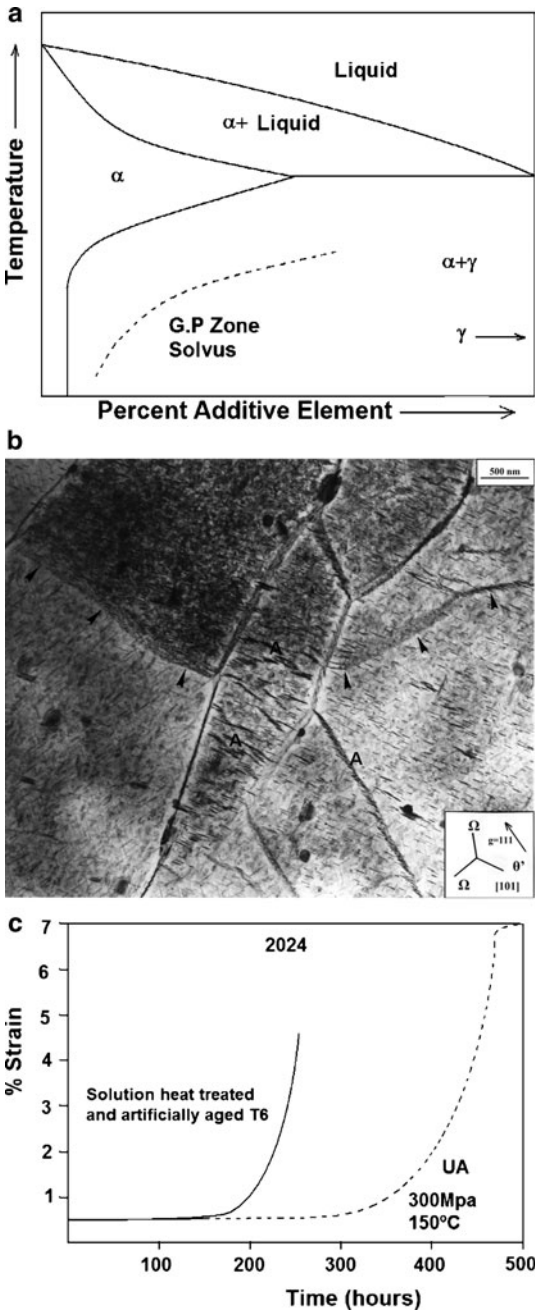

Fig. 2.3 (**a**) Model phase diagram of an alloy capable of precipitation, (**b**) dynamic precipitation of an under-aged Al–Cu–Mg–Ag alloy following 500 h creep at 300 MPa and 150°C (Lumley 2007), (**c**) creep curves (adapted from Lumley, 2007)

where Ψ is a microstructure parameter, i.e., the percentage concentration of the solute. The problem of microstructure optimization is then formulated as finding the optimum value of Ψ that provides the most efficient healing for the typical values of the degradation forces. The diffusion coefficient can have a complex dependence on Ψ and T, and so is the coefficient M, so the task of finding the optimum Ψ to minimize fatigue remains to be solved.

Self-healing alloys that employ the precipitation of the solute serving as a healing agent were successfully developed on the basis of aluminum and steel. In these alloys, the main parameter that characterizes the efficiency of healing is the creep life of the alloy. The precipitation effectively prevents creep and damage. It is difficult to observe the precipitation events directly; however, positron annihilation spectroscopy (PAS) allows quantitative measurement of solute atom/vacancy interaction and it is especially powerful when used in conjunction with a 3D atom probe field ion microscopy (Lumley 2007). PAS involves the trapping of positrons in open volume defects such as voids or vacancies, followed by annihilation with an electron into two 511 keV gamma quanta after a time period (lifetime), which is measured and is typically between 100 and 500 ps.

Van Der Zwaag and co-workers (Hautakangas et al. 2007a, b, 2008) investigated creep in under-aged Al–Cu–Mg–Ag alloys and found that dynamic precipitation, in which the movement of dislocations under load promotes the nucleation of precipitates at the defect sites, is a strong self-healing mechanism in these alloys. The initial concentration of open volume defects is larger in the under aged and deformed material than in the un-deformed material. However, after aging at room temperature, rapid diffusion of the retained copper solute atoms to the open volume defects causes the concentration of open volume defects to approach their concentration in the un-deformed material. The under-aged material is thus effectively "healed" through the room temperature aging process, due to the annihilation of the open volume defects, which can coalesce to form cracks. This is not observed in the fully aged material. This study of the effect of aging on a commercial Al2024 alloy was performed in order to investigate self-healing in metal alloys. The alloy was preheated, treated, and aged at room temperature after solutionization. Positron annihilation was performed to measure the average positron lifetime (on the order of hundreds of ps) in vacancies, and it was observed that this value has decreased. The decay of the positron lifetime is related to the dispersion of vacancy defects during the aging process where the aluminum alloy exhibited some evidence of self-healing in the process of manufacturing. Although this under aging treatment is not what would be conventionally considered a self-healing process, the authors chose to view this prevention of void coalescence as a de facto self-healing mechanism. In such a case, the self-healing is considered to be an improvement in protecting the material against any damage.

Lumley et al. (2002, 2003) and co-workers (Buha et al. 2007; Lumley and Schaffer 2006) investigated the "secondary precipitation" in an Al–Cu alloy, i.e., the process where secondary aging occurring at a low temperature ($T = 65°C$) resulted in much finer precipitates than the initial aging at a higher temperature ($T = 220°C$). They also investigated dynamic precipitation in Al–Cu–Mg–Ag

alloys that occurs in response to the generation of moving dislocations when material is under load, and found that it has potential for self-healing during fatigue and creep (Lumley et al. 2002; Hautakangas et al. 2006; 2007a, b, 2008; Zhu et al. 2000).

Laha et al. (2005, 2007a, b) studied precipitation in an austenitic stainless steel modified with boron and cerium. An improvement of creep strength coupled with creep ductility of the steel was observed and attributed to the precipitation. Similar results were observed with the steel matrix supersaturated with N, Cu, B, or Ce atoms (Shinya et al. 2006; He et al. 2009).

2.3.2 Composite Materials Reinforced with Shape-Memory Alloys

A different approach to self-healing was used by Manuel, Olson, and co-workers (2007). Their approach involves embedding SMA reinforcement microwires into the metal matrix. The SMA transforms from the martensite to the austenite phase upon heating, and back to the martensite phase upon cooling. In the martensite state, the SMA can be easily deformed. However, unlike in the case of plastic deformation that is caused by irreversible dislocation or atomic plane slip, the martensite deformation is reversible. This is because the martensite material responds to stress by "twinning," or changing the orientation of its crystal structure (Brinson 1993; Burton et al. 2006). In the martensite state, there are many variants of orientation of the crystal; however, they all correspond to only one possible austenite orientation. Therefore, when the martensite → austenite transition occurs during heating, the crystal is forced to return to its original (nondeformed) shape. The crystal keeps this nondeformed shape after the austenite → martensite transition upon cooling (Fig. 2.4). Note that during the twinning deformation of the martensite crystal, the energy is dissipated and not accumulated in the material; however, after the transition to the austenite state the energy depends on the strain.

Manuel and Olson (2007) synthesized a self-healing composite using a Sn–21Bi (wt%) alloy reinforced with 1% equiatomic NiTi SMA wires. The diameter of the wire was 190.5 μm. The temperature of transition for the wire was increased to optimize the composite self-healing by aging at 500°C. The wires were coated with gold to improve their wettability with the matrix. The reinforced alloy displayed a 73% increase in uniform ductility, compared with an unreinforced matrix. After a complete matrix fracture, the alloy was healed at 169°C for 24 h (resulting in the austenite transition of the SMA and partial melting of the matrix) and demonstrated a 95% tensile strength recovery (Fig. 2.5). The healing temperature was selected to assure that between 15 and 20% of the matrix around the crack gets liquefied to provide good welding of the crack as a result of compressive forces generated by the phase transition of the SMA. Manuel also investigated the optimum size and volume fraction of the reinforcing SMA microwires (Fig. 2.6) Manuel (2009).

Olson et al. obtained similar results with Mg-based alloys reinforced with thermally stable, precipitation-strengthened, multicomponent SMA combining

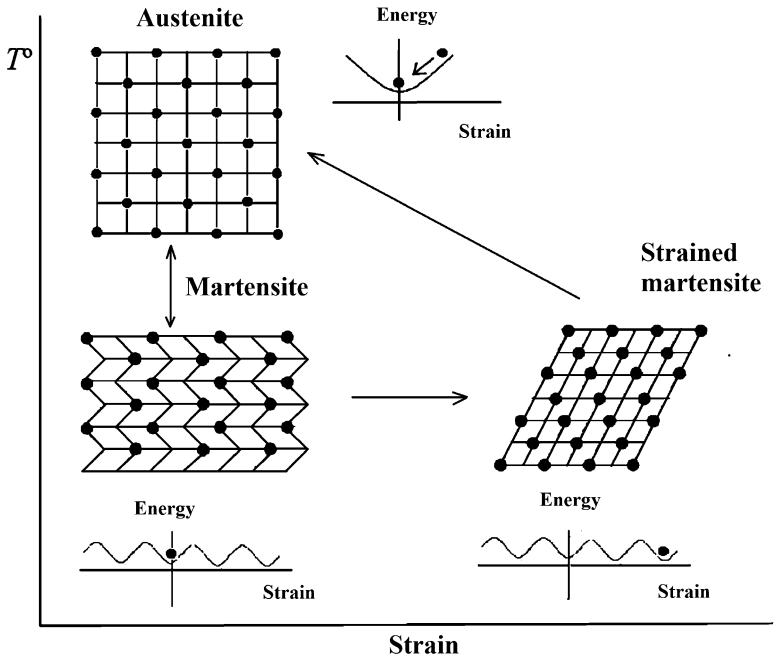

Fig. 2.4 Energy transitions in a shape-memory alloy. Dissipation occurs during the deformation in the martensite state. However, the strain energy restores when the martensite–austenite phase transition occurs

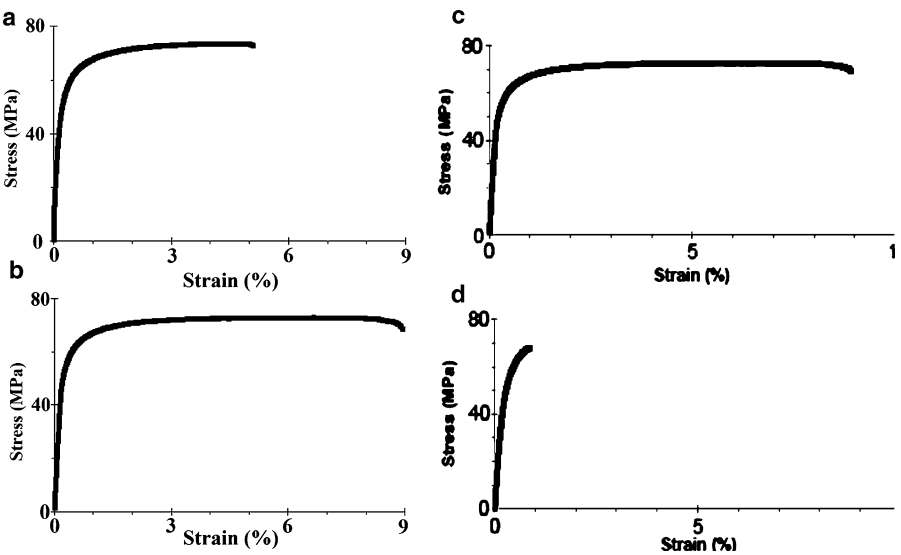

Fig. 2.5 Stress–strain diagram for heat-treated Sn – 13 at.% Bi proof-of-concept matrix and composite with 1% volume fraction of SMA wires (**a**) before and (**b**) after healing (adapted from Manuel 2009)

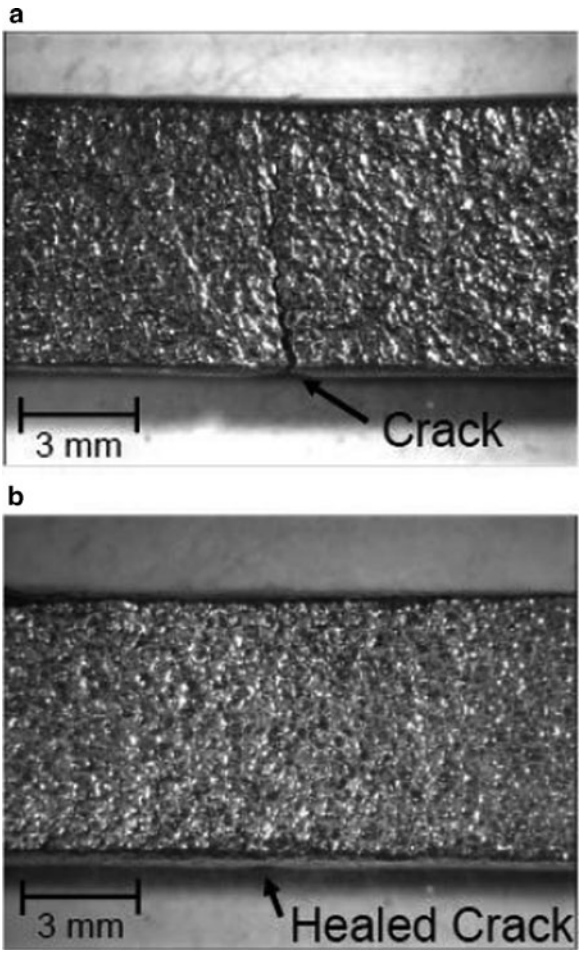

Fig. 2.6 Optical micrographs of a fractured Sn – 13 at.% Bi proof-of-concept composite (**a**) before and (**b**) after healing. It is evident that the composite was able to heal a macroscopic crack (Manuel 2009)

high-structural performance and processability (Fig. 2.7) Manuel (2009). The high-specific strength of Mg makes it an attractive option as a lightweight structural element; however, the crystal structure and microstructure of Mg causes low ductility and poor toughness. This low toughness limits the use of Mg in engineering structural applications. Nevertheless, Mg is considered a good candidate for the matrix in a self-healing alloy, provided self-healing will enhance toughness. A magnesium-based alloy was reinforced with TiNi SMA wire with a diameter of 190.5 μm. Before casting, the nitinol wires were embedded in Pyrex and annealed at 500°C for 3 h. The objective of this heat treatment is to increase the temperature of the phase transition. The limitation with Mg-based alloys is that they do not "weld" to themselves, like the Sn–Bi alloy did in the proof of concept experiment (Fig. 2.8).

It is natural to take the volume of voids and crack openings as the degradation parameter ξ, and the strain of the SMA microwires as the healing parameter ζ, while the concentration of the microwires is the microstructure parameter, Ψ. When the

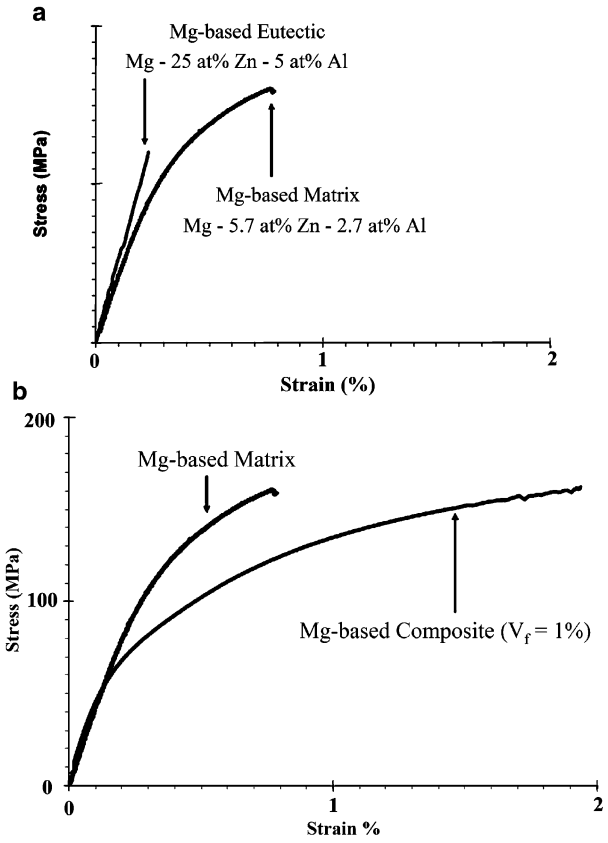

Fig. 2.7 Comparison of stress–strain curves for the heat-treated Mg-based eutectic and heat-treated Mg-based matrix alloys and Mg-based matrix and composite (1%) alloys (Manuel 2009)

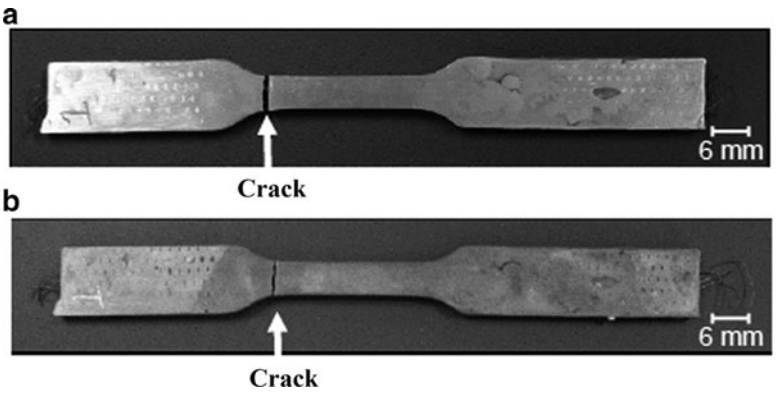

Fig. 2.8 Fractured Mg-based self-healing alloy composite (**a**) before and (**b**) after healing (Manuel 2009)

system is healed, it undergoes the martensite→austenite transition due to the elevated temperature. At this point the system is brought to a nonequilibrium state, with the amount of the excess energy dependent on ξ. We assume that the restoring thermodynamic force is approximately proportional to the strain $Y^{\text{heal}} \propto \varsigma$, and that the strain rate is proportional to the restoring force. Since the healing is achieved by the transition to the austenite phase, we take this as the healing parameter, ζ, and the fraction of the austenite state in the SMA.

$$\begin{aligned} \dot{\xi} &= L(\Psi, \mathrm{T})Y^{\text{deg}} - M(\Psi, \mathrm{T})\xi, \\ \dot{\varsigma} &= M(\Psi, \mathrm{T})Y^{\text{deg}} - H(\Psi, \mathrm{T})\varsigma. \end{aligned} \tag{2.19}$$

The problem of microstructure optimization is now reduced to the mathematical problem of finding the optimum value of Ψ that provides the best healing at the needed temperatures and degradation force levels.

To take the degradation force into consideration, a particular mechanism of degradation should be included. For friction-induced degradation (e.g., wear) the description given by (2.14)–(2.16) should apply, whereas for crack propagation the equations of fracture mechanics should be used.

2.3.3 *Composite Materials Reinforced with a Healing Agent*

A self-healing composite can also be produced by incorporating a low-melting temperature alloy that serves as a healing agent in a high-melting temperature alloy which serves as a matrix, using the methodology of metal matrix composites (Rohatgi et al. 1979, 1986; Ghosh et al. 1984; Jha et al. 1989). Lucci et al. (2008a, b, c) studied a composite consisting of an Al alloy 206 matrix reinforced with hollow ceramic tubes whose hollow spaces were infiltrated with a lower melting point (Sn60Pb40) alloy (a solder). When the low-melting point alloy encapsulated in the hollow cavities of the tubes reached the healing temperature, it became completely molten, and due to capillary pressure and surface tension, it would under certain conditions, flow out of the ceramic tube and fill in the crack. As the temperature decreased, the low-melting point healing alloy solidified and sealed the crack. The flow of the low-melting point alloy, as a liquid "healing agent," into the crack, and the sealing of the crack through solidification, can lead to the recovery of a high percentage of the original mechanical properties. A crucial property of this design is the bond between the Al matrix and the solder alloy solidified in the crack. If the bond between the solidified healing agent and the aluminum matrix is poor, the crack may continue to propagate through the aluminum matrix. An optimized model and design for this self healing material would be difficult to obtain using a trial and error approach, therefore, computational fluid analysis (CFD) could be used to obtain the parameters necessary to design the

Fig. 2.9 Front view of the self-healing composite (Nosonovsky et al. 2009)

self-healing composite (Lee et al. 2007; Xiao and Amano 2006; Chen et al. 2005; Kalra et al. 2003; Lucci et al. 2008a, b, c).

The tubes were aligned only in one direction; one purpose of using ceramic tubes is to reinforce the matrix. The tube dimensions diameters were 2.185 mm inside and 3.95 mm outside, while the length was 75 mm. A total of seven tubes were placed in a mold held by a wire mesh to prevent any misalignment during the casting. Aluminum alloy 206 was cast only slightly above the liquidus temperature for the alloy in a steel mold, which contained the alumina tubes. A relatively low pouring temperature was used to avoid precracking the alumina tubes. The mold containing the alumina tubes was preheated. A fully dense portion of the casting was used in subsequent self-healing experiments. Figure 2.9 shows the prototype of a self-healing composite. The hollow tubes were then filled with the solder alloy healing agent, by pressure infiltration. To demonstrate the concept of self-healing, the ends of the tubes were sealed with refractory cement to prevent leaking during the process of healing (Fig. 2.10).

A sample of the self-healing composite was produced and a 1-mm hole was drilled in the surface of the sample, piercing one of the tubes filled with the low-melting point alloy to simulate a crack running perpendicular to the tubes. The sample was then heated over the area of the low-melting point alloy above 300°C for 5 min and then cooled to room temperature. The solder flowed out of the microtubes and sealed the hole. A second sample was made from the matrix and a crack was created by drilling the matrix surface and cutting one of the tubes. The volume of the crack was 0.0948 cc. The external surface of the crack was then sealed with aluminum foil and both ends were refractory cemented. Gravity plays a very important role in the design of the process of self-healing; to understand this

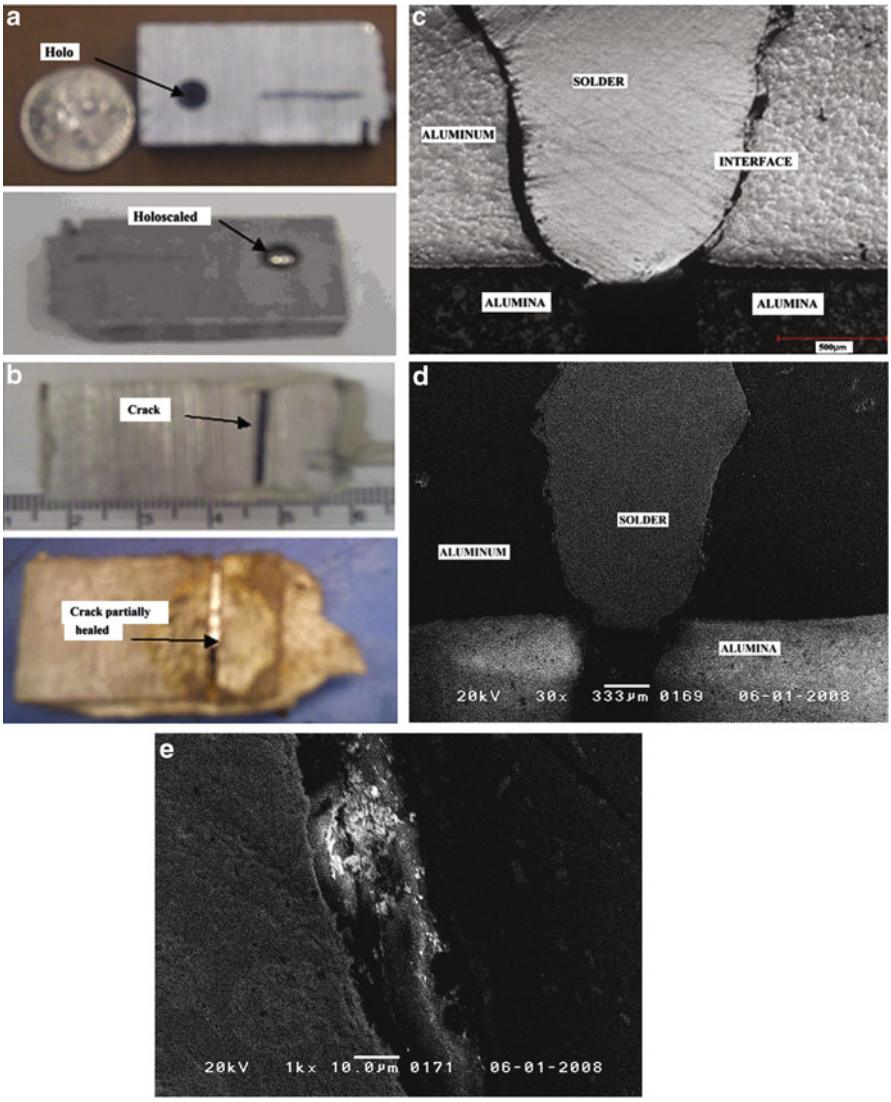

Fig. 2.10 (**a**) Self healing composite with hole (*upper*) and the sealed hole after heating (*lower*); (**b**) before and after healing the specimen; (**c**) the bond between Al206 and solder after healing; (**d**) microstructure of the healed composite (SEM); (**e**) interface between Al206 and solder after healing (SEM) (Lucci et al. 2008b)

effect the samples were placed crack face down on a plate, and then heated above the melting temperature of the solder. The composite was then cooled to ambient temperature. The healing process in this case involved sealing the damaged wall however, the damaged specimen was only partially healed by the solder (the result of this process is observed in Fig. 2.10a). One possible reason why the solder

did not fill the entire crack may be the low wettability between the matrix and solder surface, and the fluidity for infiltration into the entire length of the crack. Thus, the interface between the matrix and the self-healing molten solder and its wetting properties are crucial and require an in-depth investigation.

Figure 2.10b shows the microscopic structure of the sealed crack. The crack is only partially sealed and the bond between the aluminum and the solder has high interfacial porosity, thus the bond is likely not strong enough to stop the crack in the transversal direction of the matrix.

Figure 2.10c shows the scanning electron microscope (SEM) micrographs of the polished microstructure of the interface between a section of the "cracked" aluminum and the solder, as viewed with a Topcon SM300 SEM. Energy dispersive X-ray spectroscopy (EDS) point analysis was used to determine the elemental composition of the solder region versus the aluminum region and near the interface between the two.

The interfacial bonding between the solder within the crack and the walls of the crack is poor; the solidified solder is not in intimate contact with the aluminum matrix in the observed cross section. The porosity near the walls of the crack appears to have formed due to a lack of wetting and shrinkage as the solder solidified within the crack. No apparent reactions or bonding have occurred between the solder alloy (Sn–Pb) and the aluminum alloy (Al–Cu). Likewise there appears to be no reaction or bonding between the solder and the aluminum oxide tube. Therefore, further development in the synthesis of self-healing composites must focus on improving wetting and bonding between the healing agent (in this case the solder) and the walls of the crack in the aluminum matrix, which may even get oxidized if the crack is open to air. This is necessary to improve the properties of the healed composite (Fig. 2.10e).

Computational fluid dynamics (CFD) modeling was used to study the flow of liquids in and out of the reinforcements into cracks. The change of the phase occurring due to solidification was taken into account in the computational code. The wetting, capillarity, viscosity, and solidification will need to be tailored to achieve self-healing as a result of the flow of the low-melting point metal, its solidification in the crack, and its bonding with the crack surface. Modeling was done to select the optimum microstructure to get the most effective self-healing behavior. The simulation was done for different thicknesses of holes: 1 mm, 0.25 mm, and 10 μm with angles of 30°, 60°, and 90° relative to gravity to investigate the effect of capillarity. The simulation predicted the possibility of healing when the flow of healing liquid was toward the gravity force for a crack size between 10 μm and 1 mm. The CFD simulations conducted by Martinez Lucci (2011) showed a good agreement with the experiments.

The conclusion of this study was that wetting and capillary interactions between the molten solder and the crack/void cavity are crucial for healing. In this case, we can take the volume of voids and crack openings as the degradation parameter ξ, the amount of released solder as the healing parameter ζ, while the initial concentration of the solder as the microstructure parameter, Ψ. The diffusion of the solder into the cavity is governed by a diffusion-type equation or by a fluid flow equation,

while the healing force depends on both the amount of released solder and the volume of voids

$$\begin{aligned}\dot{\xi} &= L(\Psi, \mathrm{T})Y^{\mathrm{deg}} - M(\Psi, \mathrm{T})Y^{\mathrm{heal}}(\xi, \varsigma),\\ \dot{\varsigma} &= M(\Psi, \mathrm{T})Y^{\mathrm{deg}} - D(\Psi, \mathrm{T})Y^{\mathrm{heal}}(\xi, \varsigma).\end{aligned} \tag{2.20}$$

A quantitative analysis was suggested by Nosonovsky at al. (2009, 2010a), which found a reasonable qualitative agreement of the model with the experimental data. Again, the nature of voids and cracks was not the consideration; however it may, in principle, be included by using (2.14)–(2.16) for friction-induced degradation or similar equations for other types of degradation (e.g., fracture).

2.4 Future Approaches

In the preceding section, we described the methods that are currently used to implement self-healing in metals. These methods have a number of limitations. First, all of the methods require an input of external thermal energy. Whereas some Al alloys can age at room temperature, most of the precipitation events shown in the studies were at an elevated temperature. The SMA-reinforced and solder-in-tube/capsule composites also required elevated temperature for the phase transformation to occur to initiate healing.

Second, there is a limitation on the type of materials for which the self-healing mechanisms can be applied. Precipitation-induced healing requires that the solute remain in solution, so the method can only apply to select combinations of materials. The precipitation events will also occur over time without stress, and the formation of defects and the retained solute healing agent will be exhausted and not available for healing (Lumley et al. 2002). SMA-reinforced healing requires an alloy that can bond to itself, thus closing the crack. Otherwise additional measures (e.g., partial melting) are needed to provide the crack/void sealing. The use of an embedded healing agent does not by itself provide a mechanism to regain the volume. It is desirable to implement such a mechanism (e.g., a chemical reaction), because without it, regaining mechanical strength remains questionable. The conflicting requirements of self-healing and mechanical properties are to be balanced for an effective self-healing composite material.

Several other possible approaches have been suggested to improve self-healing in metals and to fix deficiencies in the current methods. One approach is to mimic the healing of skin, where cutting the skin triggers blood flow, coagulation and sealing of the cut due to the network of vessels and veins. The vascular network is a tree-like hierarchical structure that provides a uniform and continuous distribution of fluids throughout the material volume (Kim et al. 2006; Lee et al. 2008). Vascularization has been successfully used for polymeric composites and is expected to provide effective healing in metals as well (Therriault et al. 2003).

Material processing techniques which can incorporate a vascular network into the matrix are becoming available.

A self-healing method involving two concentric cylinders of conducting material filled with a liquid solution containing electromagnetic particles of polystyrene or silica was suggested. When damage occurs, voltage is applied between the inner pipe and outer pipe which results in the current density naturally increasing at the location of the damage. This increase in current density causes particle coagulation at the damage site, which is a way to heal the damage (Slowik 2009).

Brinker technology has developed a method to seal and locate the leakage in subsea and water pipelines. This technique is named Platelet Technology, and inspired by the method that the human body uses to seal wounds or scars on the skin. The particles are injected remotely into a pipeline, upstream of a damage site. They are carried with the flow in the pipeline and when the particles reach the leak, the fluid force exerts a pressure on the particles which holds them against the pipeline walls and seals the leak completely. In a water pipeline, the design of the particles must satisfy some requirements: the platelets must be neutrally buoyant, odorless, flavorless, nontoxic, and not promote the growth of microorganisms (Ryan 2007).

The incorporation of microballoons filled with a chemical that reacts with oxygen is another method. Thermite composites can be candidates for these materials. When the composite is damaged by a crack, the microballoons are broken as a result of the stress intensification due to the crack and the chemical will react with the oxygen in the air. This reaction increases the temperature around the crack surface to above the melting point of the metal, and the metal around the crack will melt and seal the crack. This method will only slightly deteriorate the mechanical properties with a crack closure; therefore the recovery of the mechanical properties of the composite will be high.

The incorporation of nanotubes filled with a low melting-point alloy into the metal matrix can constitute another approach to incorporate self-repair. The possibility of incorporating nanotubes into metals has been shown in the literature (Sen et al. 1997; Liu et al. 2004; Belko et al. 2007). This method will involve infiltrating a low-melting point alloy into the hollow cavities of nanotubes which will be embedded into the metal matrix. Nanotubes could be able to provide a more uniform distribution of the healing agent in the volume of the material compared to microtubes. The improvement of the mechanical properties of the metal matrix as a result of the incorporation of nanotubes is one of the advantages of using this method, compared to an incorporation of micro and macrotubes which may decrease certain mechanical properties of the matrix. Another advantage may be the possible closure of nanosize cracks.

Another more exotic approach, which has been used for polymers as well as concrete, is to incorporate bacteria into a metal matrix, so that when the composite is damaged, the bacteria will work to close a crack or repair the damage (Jonkers 2007; Jonkers and Schlangen 2009). The principle mechanism of bacterial crack healing is that the spore-forming bacteria themselves act largely as the catalyst and can transform a precursor compound into a suitable filler material.

However, it remains to be seen if bacteria-based self-healing is feasible in metallic materials, due to the high temperatures required for processing.

The field of coatings that are used to prevent or heal damage on metallic surfaces should be mentioned. Self-healing through the high temperature oxidation of Zr, Si, or Al in coating materials can be classified as a method of self-healing in metallic materials. Vitreous enamel coating for metal substrates have also been suggested in the literature (Zucchelli et al. 2009). Coatings are of special interest because, as discussed above, most degradation tends to start or occur at the interface. Sloof (2007, 2009) studied self-healing mechanisms in coatings at high temperatures. It was found that damage can be repaired by selective oxidation of the metallic alloy, if the component operates in an oxidizing environment, the alloy contains sufficient healing agent (i.e., the selectively oxidized element) and the diffusion of this element in the alloy is fast enough.

The design and synthesis of self-healing materials remain, to a large extent, as an experimental science, or even an art. In most cases, a trial-and-error approach is used to select appropriate material compositions and concentrations of components. In this situation, it may be promising to try to develop a more solid theoretical ground for self-healing. As we have shown in the above sections, most types of self-healing mechanisms are well described in terms of the nonequilibrium thermodynamics. It is expected that in principle it is possible to optimize the microstructure design using the nonequilibrium thermodynamic approach. However, to show experimental validation of these approaches remains an important future task.

2.5 Summary

Self-healing inorganic materials is a relatively new area in materials science and engineering. Inspired by living nature and modern technological opportunities, scientists are trying to implement in engineered materials, the ability for self-repair, which previously was found only in living nature. The ability to self-heal is related to the general ability of many systems for self-organization and can be described in terms of nonequilibrium thermodynamics. To provide self-organization, usually a special multiscale structure of a material is needed that allows for the maintenance of the macroscale entropy and thus maintains orderliness at the expense of the micro/nanoscale/atomic scale entropy growth.

We reviewed three main approaches to self-healing in metals and found that all of them involve multiscale organization with healing mechanisms acting at a lower scale level than the degradation mechanisms. The healing kinetics in each mechanism is described with similar nonequilibrium thermodynamics equations that relate the healing and degradation parameters and the generalized forces. The healing is achieved by coupling the degradation parameter to the generalized healing force. The healing force is induced by shifting the system away from thermodynamic equilibrium. The degradation force depends on the nature of the system and can be induced, for example, by friction.

Self-healing metals such as aluminum are potentially extremely beneficial for a wide range of industrial applications. A number of specific approaches to create self-healing metallic materials have been suggested. A number of specific obstacles should be dealt with – in particular, wetting and sufficient capillary pressure should be provided for a liquid solder to be able to infiltrate into the crack cavities. It should be kept in mind also that a self-healing requirement is often in conflict with mechanical properties (such as strength) and self-healing often cannot provide a complete recovery of undamaged material. A number of potentially useful approaches to improve performance of self-healing metallic materials have been suggested in the field. We expect that combining the fundamental thermodynamic approach of self-organization with the new advances in the synthesis of self-healing components will lead to more systematic and proactive ways of synthesizing these materials.

Chapter 3
Case Study of Self-Healing in Metallic Composite with Embedded Low Melting Temperature Solders

In the preceding chapter, we discussed the general principles of the thermodynamics of self-healing with the emphasis on metallic materials. In this chapter, we concentrate on the multiscale nature of self-healing mechanisms. To illustrate the multiscale nature of entropy production, we investigate a particular example of grain growth in metals. After that we discuss a prototype system involving an Al alloy reinforced with microtubes, filled with Sn60Pb40 solder; this is discussed as a case study.

3.1 Introduction

Wear occurs at most solid surfaces that come in contact with other solid surfaces. While biological surfaces and tissues usually have the ability to repair minor wear damage, engineered self-healing materials only started to emerge recently. An example of a smart self-healing material is the material with imbedded microcapsules or microtubes, which rupture during crack propagation and release a healing agent that repairs the crack. Self-healing mechanisms are hierarchical in the sense that they involve interactions with different characteristic scale lengths. While traditional models of self-healing require equations with many degrees of freedom, taking into account the hierarchical organization allows us to reduce the number of equations to a few degrees of freedom. We discuss the conditions under which the self-healing occurs and provide a general theoretical framework and criteria for self-healing using the concept of multiscale organization of entropy and nonequilibrium thermodynamics (Table 3.1).

Self-healing is defined as the ability of a material or surface to heal (recover or repair) damages automatically or autonomously (Ghosh 2009). Self-healing has become an object of active investigation in recent years (Balazs 2007; Zwaag 2007; Wool 2008; Ghosh 2009; Nosonovsky and Bhushan 2008a, 2009), whereas polymers have been the main focus of these studies (Chen et al. 2002; Hayes et al. 2007; Cordier et al. 2008). Self-healing materials including metals (Lumley 2007;

M. Nosonovsky and P.K. Rohatgi, *Biomimetics in Materials Science: Self-Healing, Self-Lubricating, and Self-Cleaning Materials*, Springer Series in Materials Science 152, DOI 10.1007/978-1-4614-0926-7_3,

Table 3.1 Multiscale framework for properties of metals (Nosonovsky and Esche 2008b)

Scale	Characteristic size	Entropy	Simulation method	Input	Output
Macro	Specimen	Increases	Finite Element Method	Yield strength	Deflections, stresses
Micro (meso)	Grain	Decreases	Monte Carlo Method	Parameters of (3.4)	Grain size
Molecular	Crystal lattice	Increases	Molecular Dynamics	Position of atoms	Position of atoms, parameters of (3.4)

Manuel 2009), ceramics (Nakao et al. 2009), and their composites as well as coatings (Sloof 2007; Zheludkevich 2009) are also investigated.

Several design strategies have been suggested so far for self-healing metals. These strategies include the release of a healing agent (e.g., capsules that are ruptured during crack propagation and release a liquid that "glues" the crack opening), circulation of a liquid healing agent (similar to the vascular blood circulation in humans and animals), a mixture of a low melting point solder with a high melting point alloy, reinforcement of the material with shape-memory alloys (SMA), nanoparticle migration, etc. In some cases, an external intervention such as heating is required to initiate healing (e.g., to cause melting of the healing agent or the restoration of the original shape of the SMA), while other self-healing systems are intended to act autonomously (Ghosh 2009).

There are several computational and analytical models for particular mechanisms of self-healing (Balazs 2007; Wang et al. 2007b; Lucci et al. 2008a, b, c; Manuel 2009; Remmers and de Borst 2007; Vermolen et al. 2007). Most of these models apply mechanical and hydrodynamic equations for crack propagation and propagation of the healing agent. They can be used to build a computational model such as a finite element (FE), computational fluid dynamics (CFD), or molecular dynamic (MD) analysis. However, most of these models are ad hoc and dependent on a particular shape of voids and cracks. In this chapter, the development of a general model using the physical principles of self-healing is presented.

Self-healing is, in a sense, opposite to degradation processes such as wear, fatigue, and creep. Many of these processes occur at the surface or in the subsurface layer, involving dry friction and wear and other dissipative processes that occur during sliding of two solid surfaces (Bryant et al. 2008; Nosonovsky and Bhushan 2009). The main characteristic of a dissipative process is irreversibility; or, from the thermodynamic point of view, the production of entropy. Self-healing may be viewed in the broader context of self-organization. Recent studies have shown that nonequilibrium thermodynamic processes during friction can lead to self-organization and the formation of secondary structures that result in a significant reduction of friction and wear (Fox-Rabinovich and Totten 2006; Fox-Rabinovich et al. 2007; Nosonovsky and Bhushan 2009; Nosonovsky 2010b). In this chapter,

we suggest a thermodynamic analysis of self-organization and self-healing during friction and consider a case study of void self-healing in plant leaves that serves as an inspiration for biomimetic self-healing coatings.

3.2 Modeling Self-Healing

3.2.1 Multiscale Effects of Crystal Grain Growth

It is generally accepted that physical, chemical, and mechanical properties of crystalline materials can, in principle, be deduced from their microstructure. However, in practice, it is very difficult to predict such properties as the modulus of elasticity, Poisson's ratio, yield strength, and hardness because they are a result of various, often random, factors, and interactions at different length scales, from the macroscale down to the mesoscale and molecular scale. Similarly to other dissipative systems of physical chemistry that involve interaction at various length scales, such as the wetting of rough solids (Nosonovsky and Bhushan 2007b), a multiscale method for simulating grain growth is needed. Modeling a material's mechanical behavior at the macroscale usually involves continuum solid state mechanics (elasticity and plasticity) and corresponding computational methods such as the finite element method (FEM), and the boundary element method (BEM). At the mesoscale level, the imperfections of the lattice structure, such as grains, dislocations and defects, define a characteristic length scale, and stochastic simulation methods, such as the Monte Carlo (MC) method, are used. At the molecular level, molecular dynamics (MD) simulation can be applied. Therefore, a multiscale framework is needed to analyze the mechanical properties.

In order to provide a cross-scale linkage, a material property model has to be used (Fig. 3.1a). The property model relates the mesoscale level of description with the macroscale material properties. In particular, the average grain size r is the parameter that affects the yield strength σ_Y of the material. There are several models that relate the grain size with the yield strength. The classical Hall–Petch model of grain boundary strengthening developed in 1950s states that the yield strength decreases with growing grains as

$$\sigma_Y = \sigma_{Y0} + \frac{k}{\sqrt{r}}, \tag{3.1}$$

where σ_{Y0} is the limiting value corresponding to large grains and k is a constant coefficient (Hall 1951). The reasoning behind the Hall–Petch relationship is similar to that of the linear elastic fracture theory, which states that the stress intensity factor is proportional to the square root of the crack size. In order to initiate yielding, the value of $(\sigma_Y - \sigma_{Y0})\sqrt{r}$ should reach a certain critical threshold similarly to the crack growth initiation.

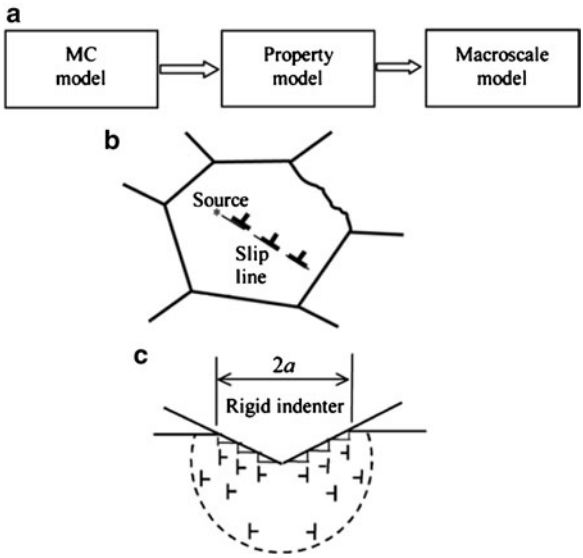

Fig. 3.1 (**a**) Multiscale modeling for material processing and properties, (**b**) scale effect in Hall–Petch theory, (**c**) strain gradient plasticity theory (Nosonovsky and Esche 2008b)

According to the Taylor model of plasticity, dislocations are emitted from Frank–Read sources and move along a slip plane that is common to many dislocations (Fig. 3.1b). Due to their interaction with each other, the dislocations may become stuck in the Taylor network, but when the externally applied stress exceeds the Peierls stress of the dislocations σ_{p}, they start to move and plastic yielding is initiated. The number of dislocations at a particular pile in a grain is proportional to the average grain size r and to the applied stress, while the total stress at the lead dislocation σ_{L} is proportional to the number of dislocations and the applied stress. Therefore, it can be easily shown that to initiate yielding $(\sigma_L > \sigma_{\mathrm{p}})$, the value of the applied stress should be proportional to $\sqrt{r}$ (Friedman and Chrzan 1998).

The Hall–Petch relationship predicts that the yield strength can increase with decreasing grain size without limit. However, very small grains with sizes comparable with that of the dislocations do not provide high strengths. In the past decade, the inverse Hall–Petch relationship has been suggested theoretically and studied experimentally for nanocrystalline materials with submicron grain sizes, and there is experimental evidence of grain boundary softening, below grain size of 10 nm.

Several models of strain gradient plasticity that emerged since the 1990s predict that the yield strength σ_{Y} is scale dependent and decreases with the decreasing characteristic size l of the system as:

$$\sigma_{\mathrm{Y}} = \sigma_{\mathrm{Y0}} \sqrt{1 + \frac{l_0}{l}}, \tag{3.2}$$

where l_0 is a material parameter that characterizes the average distance that dislocations can glide. The phenomenological explanation of the scale dependence of the yield strength is that smaller volumes of a material have fewer defects and

dislocations, which makes the material stronger. This idea is illustrated in Fig. 3.1c, which shows that dislocations are needed to accommodate for strain compatibility during the indentation deformation. Both the number of needed dislocations and the average length of dislocation loops are proportional to the contact radius l, with the volume being proportional to l^3. The density of dislocations (total length of all loops per unit volume) is thus proportional to $1/l$. According to the Taylor relation, the yield strength is proportional to the square root of the dislocation density. Thus, $\sigma_Y \sim l^{-1/2}$, which is equivalent to (3.2) for $l << l_0$ (Nix and Gao 1998; Hutchinson 2000). In other words, for an indenter of small size, the volume where the dislocations are created is not large enough to accommodate the surface deformation. This gives rise to the size-dependent strengthening predicted by the strain-gradient plasticity.

Normally, l_0 is a material parameter associated with the average distance that dislocations can glide, and it is of the order of 1 μm (Hutchinson 2000). However, for small grains, the grain size defines the distance that the dislocations can glide. Therefore, it may be assumed that $r = l_0$, and the strain gradient plasticity approach predicts grain boundary softening similarly to the inverse Hall–Petch relationship. The length scale at which the transition from the Hall–Petch to inverse Hall–Petch relationship occurs is estimated to be between dozens and hundreds of nanometers (Friedman and Chrzan 1998; Conrad and Narayan 2000).

The grain size in metals is determined by thermally activated grain growth processes and by recrystallization caused by applied stresses. Due to the misorientation of atoms in neighboring grains, there is excess energy associated with the grain boundaries, and therefore the grain growth is driven by the reduction of the energy. The grain growth is a thermally activated random process similar to diffusion, and thus the kinetics of the grain growth is dependent on the temperature (Nosonovsky and Esche 2008b).

The Monte Carlo (MC) method is widely used to simulate the grain growth. In this method, a 2D or 3D lattice is initiated by assigning a random orientation to every lattice site. An energy functional is selected to account for the misorientation of neighboring sites. Subsequently, at every MC step, an attempt is made to randomly change the orientation, and the energy of the new configuration is compared with the energy of the initial configuration. If the energy decreases as a result of the reorientation, the new orientation is accepted. A grain is defined as a group of neighboring sites with the same orientation. Since the periodicity of the MC simulation lattice is much greater than the atomic size, a scaling procedure is needed to relate the MC lattice spacing to physical size units and the MC steps to physical time units (Nosonovsky and Esche 2008b).

The MC simulation method can be applied for various phenomena such as normal grain growth in 2D or 3D and recrystallization, with varying temperature, anisotropic material, etc. The normal isotropic grain growth at constant temperature represents a convenient example because it has a theoretical solution for the average grain size, with the parabolic dependence of the average grain radius r on time t:

$$r = C\sqrt{t}, \tag{3.3}$$

Table 3.2 Hierarchy levels in the physical system and simulation (Nosonovsky and Esche 2008b)

	Physical system			Simulation		
	Objects	Driving force	Entropy	Objects	Driving force	Entropy
Macroscale	Continuum	material	–		$\Delta S_{\text{macro}} = 0$	–
–	–					
Mesoscale	Grains	Decreasing boundary energy	$\Delta S_{\text{meso}} < 0$	Cells	Decreasing energy functional	$\Delta S < 0$
Nanoscale	Atoms	Thermal fluctuations	$\Delta S_{\text{nano}} > 0$	–	–	–

where C is a proportionality constant. The constant can be determined theoretically. Then, (3.3) is given by:

$$r^2 - {r_0}^2 = \frac{4\gamma A Z {V_\text{m}}^2}{{N_\text{a}}^2 h} \exp\left(\frac{\Delta S_\text{f}}{R}\right) \exp\left(-\frac{Q}{RT}\right) t, \tag{3.4}$$

where r_0 is the initial grain size, h is Planck's constant, R is the gas constant, V_m/N_a is the atomic volume, ΔS_f is the activation entropy, Q is the activation enthalpy, γ is the grain boundary energy, A is the accommodation probability, and Z is the average number of atoms per unit area at the grain boundary. However, the uncertainty in the values of the parameters of the (3.4) (especially ΔS_f and Q, which are arguments of the exponential function) is so large that it is more practical to use (3.3) rather than (3.4). The parameters of (3.4) should be obtained from a molecular scale investigation of crystals and then supplied to the mesoscale model for the grain growth (Nosonovsky and Esche 2008b).

It is noted that the MC simulation usually takes into account only the mesoscale level of the physical system (Table 3.2). An interesting consequence of this is that the orderliness of the MC simulation lattice tends to grow, thus leading to a decreasing entropy, which represents an apparent paradoxical contradiction to the second law of thermodynamics, as it discussed in the following section. In the physical system, however, the entropy grows at the molecular level, since the grain boundary migration involves dissipation, thus providing for the overall entropy increase.

MC simulations were shown to provide very close results to those predicted by (3.4) in the case of constant temperature. However, the MC method can also be applied to more complicated phenomena, such as recrystallization, thermo-mechanical processing, and anisotropic grain growth. As the MC simulation results are confirmed by theoretical considerations in the simple case of normal grain growth, it is reasonable to extrapolate the approach for the more complicated cases (Nosonovsky and Esche 2008b).

The temperature T enters into the simulation because the atomic jump frequency that defines the time scale is dependent on T. Therefore, the normalized dependence of the average grain size r on time t has the form

$$r^2 - {r_0}^2 = Kt, \tag{3.5}$$

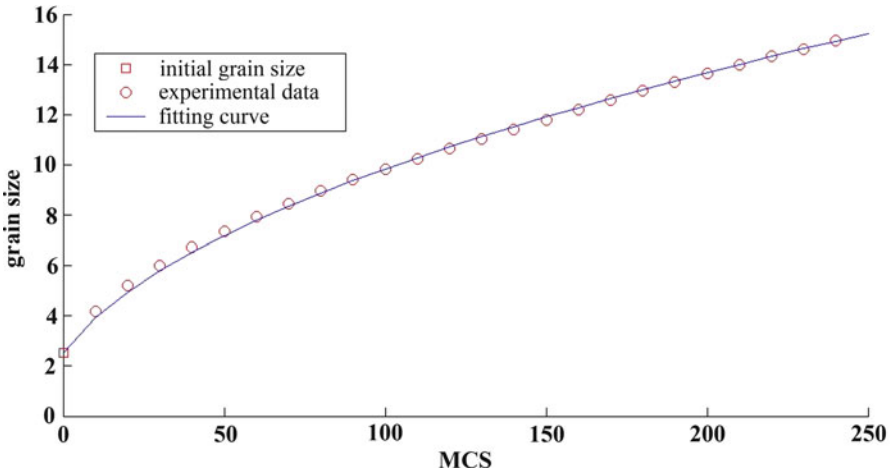

Fig. 3.2 MC simulation results for grain size as a function of time (Nosonovsky and Esche 2008b)

$$K = K_0 \exp\left(-\frac{Q}{RT}\right), \tag{3.6}$$

where K and K_0 are constants.

The MC simulations were started with an initial grain size of $r = 2.5$ and terminated after 242 MC steps when $r \approx 15$ was achieved, so that a significant number of grains were preserved in the lattice. The initial grain size was selected so as to reduce the time needed for grain growth at the initial steps compared with the case of a completely random initial configuration. Ten simulations with different seeds for random number generation were performed and their results were averaged. The microstructure was examined every 10 MC steps. Typical results for the dependence of the average grain size on the simulation time are shown in Fig. 3.2.

The multiscale approach to property simulation involves MC modeling of the grain growth under given conditions and transferring the output to a property model that allows the determination of the yield strength, which in turn is then passed on to a continuum model. In our simulation, we utilized a previously described MC simulation package and the property model based on (3.1)–(3.3). The data can then be transferred to a FEM simulation package or used for the calculation of the deformation of a structural element.

As a simple example, we consider here the twisting of an elastic–plastic rod of radius R under a constant torque τ (Fig. 3.3a). The transition from the elastic to the plastic regime is controlled by the yield strength σ_Y. Assuming that the interior of the rod up to the radius $r = R_0$ is in the elastic state while the exterior $R_0 < r \leq R$ is in the plastic state, the rod can support a torque τ of

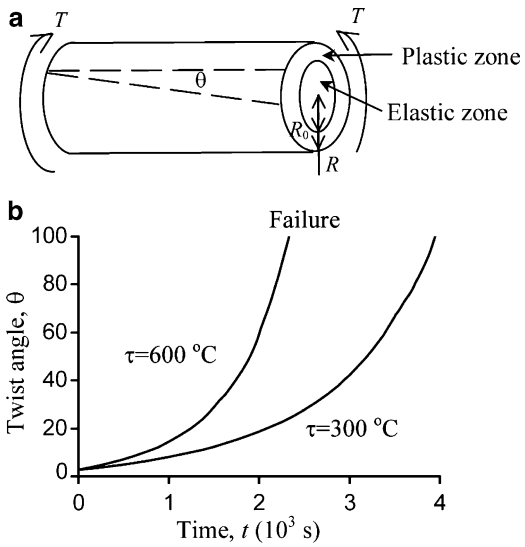

Fig. 3.3 (**a**) An elastic–plastic shaft under torsion, (**b**) twist angle dependence on time (Nosonovsky and Esche 2008b)

$$\tau = L\sigma_{\mathrm{Y}}\frac{{R_0}^2}{3} + L\sigma_{\mathrm{Y}}\frac{R^2 - {R_0}^2}{2} = L\sigma_Y\left(\frac{R^2}{2} - \frac{{R_0}^2}{6}\right). \tag{3.7}$$

From (3.7), $R_0(\tau, \sigma_{\mathrm{Y}})$ is found as

$${R_0}^2 = 3R^2 - \frac{6T}{L\sigma_{\mathrm{Y}}}, \tag{3.8}$$

the polar moment of inertia $J = 0.5\pi {R_0}^4$ is calculated, and the twist angle θ is found as

$$\theta = \frac{TL}{GJ} = \frac{2TL}{G\pi {R_0}^4} = \frac{2TL}{3G\pi\left({R_0}^2 - \frac{2T}{L\sigma_{\mathrm{Y}}}\right)^2}, \tag{3.9}$$

where G is the modulus of torsional rigidity.

The twist angle θ as a function of time t is presented in Fig. 3.3b for different annealing temperatures τ. The average grain size grows with time in accordance with (3.1), (3.5), (3.6), and (3.8), (3.9) for $K = 4.5 \times 10^6\ \mu\mathrm{m}^2\ \mathrm{s}^{-1}$ (at $T = 300^{\circ}\mathrm{C}$) and $K = 7.6 \times 10^6\ \mu\mathrm{m}^2\ \mathrm{s}^{-1}$ (at $T = 600^{\circ}\mathrm{C}$), $r_0 = 17\ \mu\mathrm{m}$, $k = 3\ \sigma_{\mathrm{Y0}}\ (\mu\mathrm{m})^{1/2}$, $2\tau L/(3\ {R_0}^4 G\pi) = 0.1$, $2\tau/({R_0}^2 L\sigma_{\mathrm{Y0}}) = 1.4$. With increasing grain size, the yield strength decreases in accordance with (3.1). As the maximum shear strength due to the twist deformation reaches the yield strength, a plastic flow zone is formed and the material is softened in accordance with (3.7)–(3.9), until static failure occurs. As expected, a higher temperature leads to the softening, while a lower temperature prevents the transition to the plastic regime.

We conclude that grain growth in metals involves interactions at three different length scales, and thus a multiscale approach is needed for studying the grain growth phenomenon in metals. Using such a multiscale approach, the simple example of the normal grain growth in a simple rod structure at constant temperature was investigated. The same methodology can be applied for more complicated situations such as the prediction of physico-chemical properties during the thermomechanical treatment of structures with complicated geometries.

3.2.2 Multiscale Nature of Degradation and Healing

While the net entropy, as defined by (2.1)–(2.2), grows in most systems in accordance with the second law of thermodynamics, some thermodynamic systems may lead to an increasing orderliness and self-organization, supporting a decrease in entropy. These are thermodynamically open systems that operate far from thermodynamic equilibrium and can exchange energy, matter, and entropy with the environment. Many of these self-organizing systems (such as the Bénard cells in boiling liquid and oscillating chemical reactions) were known a long time ago; however, the universality and generality of the processes involved in these systems was understood only with the works by Prigogine (1961). It is believed that this ability for self-organization of physical systems led to the formation of complex hierarchical chemical and biological systems.

Processes that lead to degradation (wear, corrosion, fatigue, etc) often involve interactions with different characteristic length scales. For example, friction and wear involve interactions of microscale and nanoscale asperities and wear particles, capillary interactions, adhesion, and chemical molecular bonding. In most cases, these interactions lead to irreversible energy dissipation and, therefore, to the production of entropy. However, in certain cases, the entropy production at a particular scale level may be compensated by the entropy consumption at another level.

An interesting example of a self-organizing process is the thermally activated grain growth in metals (Fig. 3.4). It is well known that metal crystals form grains, characterized by different orientations of the lattice (Humphreys and Hatherly 1995). The typical grain size is in the range between microns and millimeters. There is an additional energy associated with the grain boundaries due to the misorientation of the neighboring grains. Therefore, it is energetically profitable for larger grains to grow and to absorb smaller grains, thus reducing the total number of grains and the total boundary area. The ideal state of a perfect crystal with only one grain corresponds to the minimum energy. The grain growth is a thermally activated diffusion-like process with the Arrhenius type of kinetics. For normal isotropic grain growth, theoretical considerations predict a parabolic dependence of the average grain radius r on time

$$r^2 - {r_0}^2 = K_0 \exp\left(-\frac{Q}{RT}\right) t, \tag{3.10}$$

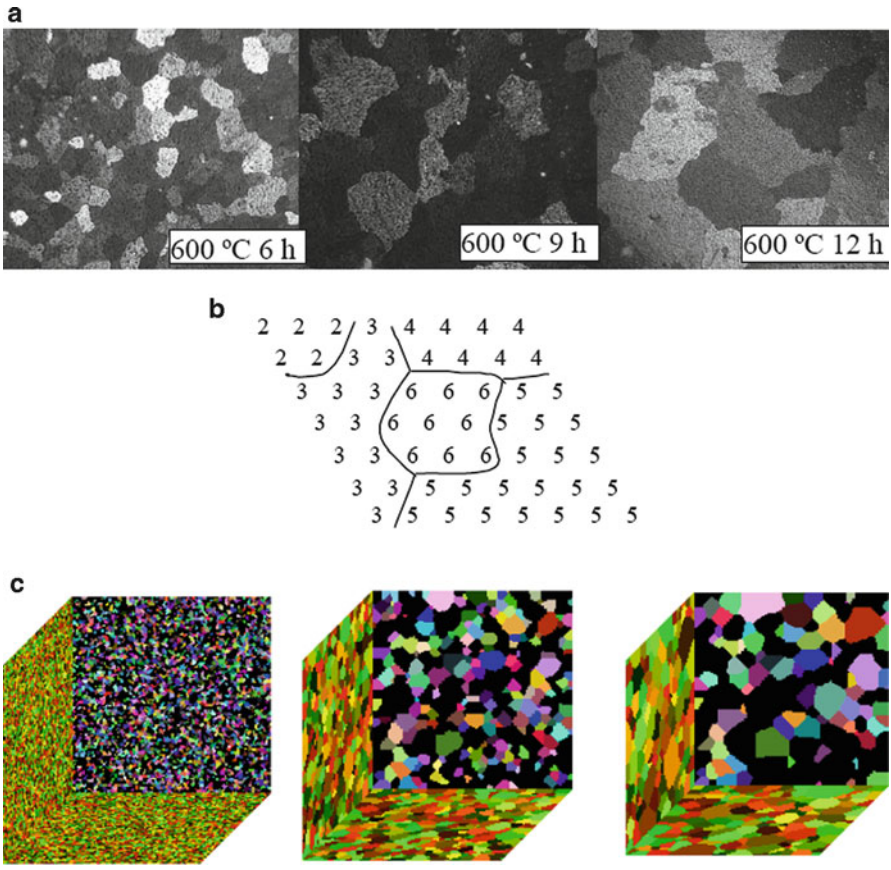

Fig. 3.4 MC simulation of grain growth (**a**) experimental observation of grains in aluminum at different time intervals, (**b**) simulation lattice, (**c**) simulation results for grain growth (Nosonovsky and Esche 2008a)

where Q is the activation enthalpy, R is the universal gas constant, K_0 is a proportionality constant, and r_0 is the initial grain size (Yu et al. 2008).

Modeling the grain growth is a challenging task. Since it is a random process, deterministic modeling is difficult. The Monte Carlo (MC) simulation and Cellular Automata (CA) approaches are often used (Raabe 2000, 2002). CA algorithms describe the spatial and temporal evolution of a complex system by applying deterministic or probabilistic local rules to the cells of a regular lattice. CA algorithms are based on finite difference formulations of local interaction laws. The MC method is based on the use of randomly generated orientation numbers. The lattice is initialized by randomly assigning to each lattice point an integer number representing its orientation. Reorientations are randomly and sequentially attempted for all lattice sites. If a new orientation is characterized by lower energy, then it is accepted (Nosonovsky and Esche 2008a).

A metal with grains represents a typical example of a partially ordered system that occupies an intermediate position between the complete disorder (a random collection of atoms) and complete order (a perfect single crystal). The grain growth is also a self-organizing system, which naturally evolves from a disordered to an ordered state being driven by random thermal fluctuations. Consider an array of N cells, representing lattice cells in the simulation method, with each cell being in one of M microstates. The total number of microstates of this system would then be:

$$\Omega = M^N. \tag{3.11}$$

When the system reaches its final state with all cells having the same orientation, the total number of microstates becomes:

$$\Omega = M. \tag{3.12}$$

Using the statistical mechanics definition of the entropy, one can find the initial entropy S_0 and the final entropy S_f of the system as:

$$S_0 = \ln(MN) = N \ln M = NS_\mathrm{f}, \tag{3.13}$$

$$S_\mathrm{f} = \ln M. \tag{3.14}$$

Based on (3.13) and (3.14), the entropy decreases between the initial and the final states by an amount of

$$\Delta S = (N - 1) \ln M. \tag{3.15}$$

This result constitutes an apparent paradox, because it seems to contradict to the second law of thermodynamics, which states that the entropy of a closed system does not decrease. Another formulation of the paradox is that the *randomness* of thermal fluctuations leads to an increased *orderliness* of the system (Nosonovsky and Esche 2008a).

To solve the paradox, we have to take into account that the system, under consideration, can be studied at different scale levels, and that it is not a closed system. At the macroscale we deal with a continuum system characterized by certain bulk mechanical properties (e.g., yield strength, hardness) dependent on the average grain size. At the macroscale, no change of entropy is expected, $\Delta S_\mathrm{macro} = 0$. At the mesoscale (or microscale) we deal with the grains that tend to grow. Hence, the mesoscale entropy is essentially the configuration entropy and with the increasing grain size it decreases due to the increased orderliness of the system, $\Delta S_\mathrm{meso} < 0$. At the molecular scale (or nanoscale) we deal with the energy barriers for grain growth and random thermal fluctuations. Every time when a lattice site is reoriented, a certain amount of energy is dissipated because the energy barrier must be overcome. However, if the system's temperature is maintained

constant, then the heat is removed from the system due to its contact with the surroundings, and thus the system is not closed. This results in an increase in the system's temperature and entropy, where $\Delta S_{\text{nano}} < 0$. In other words, the random fluctuations at the nanoscale lead to the orderliness increase at the mesoscale, which is compensated by the entropy increase at the nanoscale. The net entropy of the system can therefore be written as

$$\Delta S_{\text{net}} = \Delta S_{\text{macro}} = \Delta S_{\text{meso}} + \Delta S_{\text{nano}}. \tag{3.16}$$

Since $|\Delta S_{\text{nano}}| > |\Delta S_{\text{meso}}|$, the net entropy decreases and the second law of thermodynamics is satisfied (Table 3.2). Note that (3.16) is similar to (2.3) with the only difference that the mesoscale level is included in addition to the macro and micro/nanoscales (Nosonovsky and Esche 2008a).

Therefore, we deal with the two different systems: the physical system, characterized by the thermodynamic entropy, and the simulation system that models the physical system and is characterized by the information entropy. As far as the information entropy of the system, several interesting observations can be made with regard to the self-organizing properties of this system. The numerical CA/MC models consider only the mesoscale structure of the system, and thus only the mesoscale (configurational) entropy change, ΔS_{meso}, can be determined from the CA/MC model. This is the reason of the apparent entropy decrease. The physical system is not insulated; the heat and entropy are removed from the system, so it is not a closed system. However, the numerical CA/MC model does not take into account that aspect, because it is concentrated on the mesoscale description of the physical system. As a result, the second law of thermodynamics is apparently violated in the simulation system in a paradoxical manner. The second law is valid for closed physical systems; however, there is no reason why it cannot be violated for CA/MC models during computer simulation. It should be kept in mind that the work of a computer requires energy dissipation (that is one of the reasons why computer processor is heated and requires permanent cooling), so the decrease in entropy of the information system is compensated by an increase in the thermodynamic entropy.

Our conclusion is that there is a correspondence between the physical system (a metal crystal) and the information system, used for the simulation (for example, CA). However, the physical system is a multiscale system, with the entropy produced at the nanoscale and consumed at the mesoscale, so that the net sum of the entropy grows. The information system simulates only the mesoscale level, leading to the apparent reduction of the entropy. Thus, the second law of thermodynamics is not observed within the computer simulation network. It is noted that such a common dissipative process as the dry friction also has a hierarchical (multiscale) organization (Nosonovsky and Bhushan 2007a; Nosonovsky and Bhushan 2008d, e); therefore, the hierarchical approach to the entropy is important for a broad class of physical systems.

The issue of interest for most applications is the integrity of the macroscale structure (e.g., the absence of cracks) (Table 3.3). The integrity of the macroscale structure can

Table 3.3 Effects of interest at various scale levels for two self-healing mechanisms

	mechanisms			Embedding SMA microwires
		Microcapsule encapsulation		
Self-healing	Physical mechanisms	Interest for application	Physical mechanisms	Interest for application
Macroscale	Solid structure, cracks	Integrity of the solid structure	Solid structure, cracks	Integrity of the solid structure
Microscale	Microcapsules		Microwires	
Nanoscale	Atomic structure		Atomic structure	

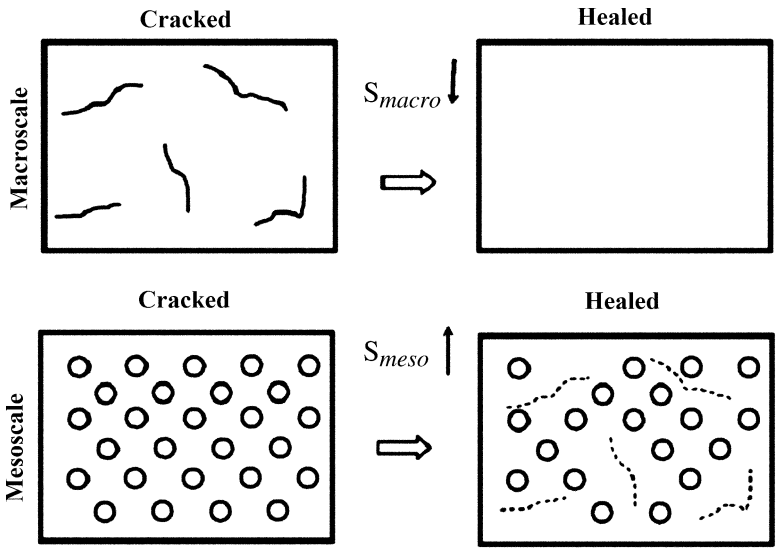

Fig. 3.5 Schematic showing crack healing by embedded capsules at the macro- and microscale levels. Crack healing decreases disorder (and entropy) as observed at the macroscale, while fracture of the microcapsules increases disorder (and entropy) when observed at the mesoscale. Macroscale healing occurs at the expense of the microscale disorder. The effectiveness of the healing mechanism should be studied by relating microstructure parameters to the entropy

be repaired at the expense of the micro- and atomic-scale structures. As an example, let us consider a solid homogeneous body. The nanoscale level corresponds to the vibrations of atoms in the crystalline lattice and is not of interest for us at this point. The mesoscale structures, such as grains, defects, and dislocations correspond to the microscale levels. A perfect single-crystal body with no defects has lower mesoscale entropy, ΔS_{meso}, than a body with such defects. Larger scale defects such as cracks and voids contribute to the macroscale component of the entropy, ΔS_{macro} (Fig. 3.5a).

A material or a surface with a regular microstructure (e.g., a microtextured surface) is more ordered, and thus it has lower mesoscale configurational entropy, ΔS_{meso}, than a material with an irregular microstructure. This can be utilized for

healing of macroscale defects. Suppose there is excess entropy, ΔS_{macro}, associated with the macroscale defects, such as cracks or voids. Healing can be triggered by affecting the mesoscale structure, e.g., by release of the healing agent from microcapsules, which decreases the orderliness of the microstructure and thus increases the entropy for ΔS_{meso}. In the case $\Delta S_{\text{macro}} < \Delta S_{\text{meso}}$, the healing is done by decreasing the macroscale component of entropy on the expense of the mesoscale component (Fig. 3.5b).

3.2.3 Healing Agent Release by Fracture

Encapsulation of a healing agent is used for crack damage repair. When the crack propagates, the capsule ruptures and liquid adhesive is released that can heal the crack. Usually, in the case of polymeric materials, a catalyst should be placed in the structure to initiate solidification of the healing agent. Crack propagation is an irreversible process, because when intermolecular bonds are broken, the energy γ is released irreversibly, so the entropy amount

$$S_{\text{crack}} = \gamma KA/T, \tag{3.17}$$

is produced to create a crack with area A. The coefficient $0 < K < 1$ is the fraction of the dissipated energy Q that is consumed for the creation of the crack, whereas the rest of the energy is dissipated (Nosonovsky et al. 2009).

Another way to introduce the entropy of cracking is to consider the configurational entropy. The ideal state without cracks corresponds to the minimum number of microstates and thus the lowest possible configurational entropy. The crack can be formed in many different ways and the cracked macrostate corresponds to many microstates and excess configurational entropy, ΔS_{macro}. In a similar manner, when a capsule ruptures and its content is released, the configurational entropy grows because mixing occurs. The configurational entropy growth of mixing of two substances is given by:

$$\Delta S_{\text{mixing}} = -R(n_1 \ln X_1 + n_2 \ln X_2) \tag{3.18}$$

where n_1 and n_2 are the amounts in moles of two pure substances, X_1 and X_2 are mole fraction in the solution, and R is the gas constant (Craig 1992). Part of this excess entropy can be consumed for healing the bonds at the crack. The net configurational entropy grows; however, the growth is not due to the cracking but due to microcapsule rupture and an irreversible decrease in the number of filled microcapsules.

If N capsules are ruptured to heal the crack with the area A, the net entropy production is given by the mesoscale entropy of mixing minus the macroscale entropy of crack healing

$$\Delta S_{\text{net}} = \Delta S_{\text{meso}} + \Delta S_{\text{macro}} + N\Delta S_{\text{mixing}} - K\frac{\gamma L}{T} > 0. \tag{3.19}$$

As it has been discussed, the macroscale entropy is reduced on the expense of the mesoscale entropy.

A different technique involves material reinforcement with a shape-memory alloy (SMA), such as NiTi. The shape-memory effect occurs due to the reversible phase transition from the martensite to the austenite phase. Tiny SMA fibers that are embedded into the matrix of the material change their shape (extend) as the crack propagates. Heated SMA fibers restore their original shape and thus close the crack. The macroscale structural integrity of the material is restored at the expense of the increase in the nanoscale entropy due to the phase transition and heat release.

It is noted that we considered a highly simplified model of crack healing. A more sophisticated model should take into account the entropy of the phase transition (in this case, the solidification of the healing agent, $\Delta S_{\text{solidify}}$) and chemical reactions $\Delta S_{\text{chemical}}$ (e.g., with the catalyst), as well as the corresponding chemical potentials. Such a model is presented in the following section.

3.2.4 Healing Agent Release by Heating and Melting

There are two types of self-healing: autonomous and nonautonomous. While autonomous healing is performed without any external intervention, an external stimulation, such as heating, is needed for the nonautonomous healing. The typical example of the nonautonomous self-healing is embedment of a low melting temperature agent that melts after heating, fills cracks and voids, and solidifies after that. The general expression of the entropy is

$$\begin{aligned}\Delta S_{\text{net}} = {} & \Delta S_{\text{heating}} + \Delta S_{\text{melting}} + \Delta S_{\text{chemical}} + \Delta S_{\text{mixing}} + \Delta S_{\text{solidify}} \\ & + \Delta S_{\text{cooling}},\end{aligned} \tag{3.20}$$

where

$$\begin{aligned}\Delta S_{\text{heating}} &= -\int \frac{\mathrm{d}Q}{T}, \\ \Delta S_{\text{cooling}} &= \int \frac{\mathrm{d}Q}{T},\end{aligned} \tag{3.21}$$

are the entropies associated with the heating and cooling process can be given as

$$\begin{aligned}\Delta S_{\text{melting}} &= -\frac{\Delta Q}{T}, \\ \Delta S_{\text{solidify}} &= \frac{\Delta Q}{T},\end{aligned} \tag{3.22}$$

are the entropies of phase transitions and ΔQ is the heat released or consumed during the phase transitions. Since usually the process is not adiabatic and the heat produced during heating and melting is irreversibly dissipated, the net entropy change is

$$\Delta S_{\text{net}} = \int \frac{\mathrm{d}Q}{T} + \frac{\Delta Q}{T_{\text{melting}}} + \Delta S_{\text{chemical}} + \Delta S_{\text{mixing}}. \tag{3.23}$$

To summarize, the self-healing mechanism restores the macroscale structure of a material at the expense of increasing the mesoscale and atomic scale entropy (Nosonovsky et al. 2009).

3.3 Entropy, Degradation, and Healing Rates During Self-Healing

Most models of self-healing use governing equations for crack propagation and for the healing agent that can be used to develop a computational scheme. These systems of equations involve many degrees of freedom (infinite number of degrees of freedom for the continuum models and very high finite number of degrees of freedom for the computational models). In this section, we suggest a different approach and develop a system of equations for degradation parameters with a low number of degrees of freedom.

3.3.1 Entropy and Degradation

Consider a process characterized by a degradation parameter ξ, for example, the wear volume or the total area of the cracks. The rate of degradation in many cases is proportional to the rate of entropy

$$\dot{\xi} = B\dot{S}, \tag{3.24}$$

where B is the degradation coefficient (Bryant et al. 2008).

Taking the degradation parameter equal to the wear volume, $\xi = w$, (3.24) yields the Archard wear law

$$\dot{w} = k\frac{WV}{H}, \tag{3.25}$$

where $k = \mu HB/T$ is the wear coefficient, and H is the hardness (Nosonovsky and Bhushan 2009). For crack propagation, (3.24) is equivalent to (3.17) if $B = T/(\gamma K)$.

Thus, the physical meaning of (3.24) is that a constant fraction of the dissipated energy at a given temperature is consumed for the degradation, and therefore the rate of degradation is proportional to the rate of entropy.

3.3.2 Degradation and Healing

Healing is characterized by a healing parameter, ζ, for example, the volume of released healing agent. The rate of healing or decrease of degradation, $\dot{\xi}_{\mathrm{h}}$, is proportional to the amount of healing material, and to a function of ξ. The rate of release of the healing agent, $\dot{\zeta}$, is a function of the rate of increase in the degradation, $g(\dot{\xi}_{\mathrm{d}})$, and the rate of consumption of the healing agent. For example, the number of fractured microcapsules is proportional to the length of newly created cracks, and thus the amount of the healing agent depends on the length of the newly created cracks minus the amount of consumed healing agent

$$\dot{\zeta} = g(\dot{\xi}_{\mathrm{d}}) - C\dot{\xi}_{\mathrm{h}}, \tag{3.26}$$

where C is a constant. Thus, the rate of crack healing depends on the amount of the healing material and available crack length. Therefore, we have the system of equations

$$\begin{aligned} \dot{\xi} &= \dot{\xi}_{\mathrm{d}} - \dot{\xi}_{\mathrm{h}}, \\ \dot{\xi}_{\mathrm{h}} &= f(\xi)\zeta, \\ \dot{\zeta} &= g(\dot{\xi}_{\mathrm{d}}) - C\dot{\xi}_{\mathrm{h}}. \end{aligned} \tag{3.27}$$

The entropy is related to the degradation rate according to (3.24). Since the degradation rate involves two components, the net entropy also involves two terms: the term responsible for the degradation and the term responsible for the healing.

$$\Delta S = \Delta S_{\mathrm{d}} - \Delta S_{\mathrm{h}}. \tag{3.28}$$

The origin of these two terms is different. While the degradation term is given by (3.24), the healing term is related to the process of repair of the damage, for example, due to an encapsulated healing agent.

According to some studies, there are five steps in the self-healing cycle: (1) the material is subjected to gradual deterioration, for example, by dynamic loading that induces microcracks; (2) the hollow microcapsule or the fiber contains self-repair fluid; (3) the fibers require a stimulus to release the repairing chemical; (4) a coating or fiber wall must be removed in response to the stimulus; and (5) the fluid must promote healing of the composite damage (Wool 2008). For a truly autonomous self-healing material, the third step may be omitted, as the damage itself serves as the stimulus (Fig. 3.6a). The scheme suggested by (3.26) scheme is intended to

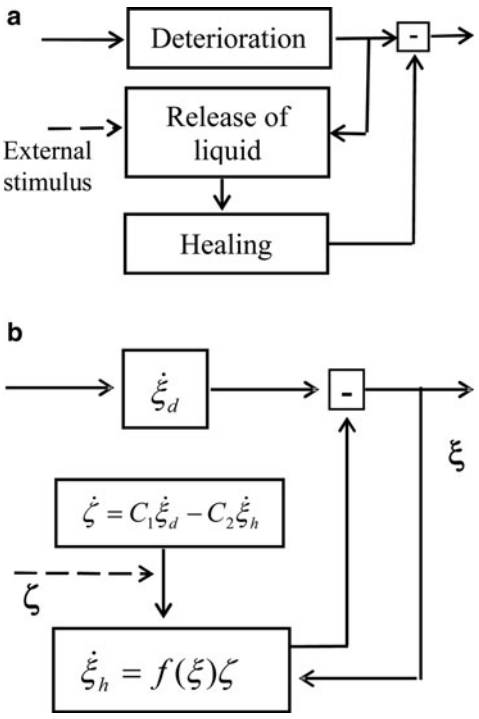

Fig. 3.6 Schematic of (**a**) the self-healing process and (**b**) its representation with (3.26)

capture this process (Fig. 3.6b). It is noted that unlike the approach that uses continuum constitutive equations with infinite degrees of freedom (Wang et al. 2007a, b, c), our method reduces the problem to only two degrees of freedom.

The criterion for self-healing is that the rate of healing is higher than the rate of degradation

$$\dot{\xi}_{\mathrm{h}} \geq \dot{\xi}_{\mathrm{d}}. \tag{3.29}$$

The function $f(\xi)$ involves the dependence of the healing rate on the total length of the cracks or other damage, because the same amount of the healing agent can result in a different rate of repairing the crack. Assuming simple constant dependencies $f(\xi) = B$, $g(\dot{\xi}_{\mathrm{d}}) = D$, and a constant degradation rate (e.g., a steady growing crack), $\dot{\xi}_{\mathrm{d}} = A$, the system of (3.27) yields

$$\begin{aligned} \dot{\xi}_{\mathrm{h}} &= a\mathrm{e}^{-BQ} + \frac{AD}{C}, \\ \dot{\xi}_{\mathrm{h}} &= B\zeta, \\ \dot{\xi} &= A\left(1 - \frac{D}{C}\right) - a\mathrm{e}^{-BQ}, \end{aligned} \tag{3.30}$$

where a is a constant of integration, and in the steady state limit ($a = 0$), the condition (3.29) yields $D/C > 1$. In other words, the crack is healed if more healing agent is released per unit length growth of the crack (constant D) than consumed per unit length of the healed crack (constant C) (Nosonovsky et al. 2009).

3.4 Validation of the Model for Self-Healing Al Alloy

Lucci et al. (a, b, c) investigated both numerically and experimentally self-healing of aluminum alloy 206 matrix reinforced with carbon fiber microtubes filled with Sn60Pb40 solder. The melting point of the solder is between 189 and 190°C. The inside and outside diameters of the tubes were 2,185 μm and 3,950 μm, respectively, their length was 75 mm, the spacing between the tubes was 3 mm on average, and a total of seven sealed tubes were placed. A hole was drilled in the specimen. This sample was then heated above 300°C for 5 min and quenched to ambient temperature. After a series of experiments, the crack was filled with the solder either completely or partially. These experiments indicated the importance of the factors that control filling of the crack by the liquid agent. These factors include the amount of available solder and the wettability of the holes with liquid solder, and the proximity of holes to healing agent as well as the diameter of holes (Fig. 3.7).

The volume of released liquid solder depends on the number of fractures microtubes and the volume of solder in every microtube. A fraction of this volume is available for healing and the healing process depends also on the size of the crack. The degradation parameter ξ in this case is the volume of the crack, while the healing parameter ζ is the volume of available liquid solder. The differential equations for the crack volume and the volume of available healing agent are given by

$$\begin{aligned} \dot{\xi} &= -f(\xi)\zeta, \\ \zeta &= g_0 + C\xi. \end{aligned} \tag{3.31}$$

The first equation states that the volume of the crack decreases with the rate proportional to the volume of available healing agent, with g_0 is the maximum volume of the healing agent. The second equation states that the volume of available healing agent decreases as the agent is consumed for healing. The system of (3.31) can be naturally derived from (3.18) with a number of natural assumptions. These assumptions include zero degradation rate, $\dot{\xi} = -\dot{\xi}_h$ (the crack does not expand after it was initially created) and $g = 0$.

In the case when all available solder is consumed, a constant dependency $f(\xi) = B$ is assumed and the system of (3.31) reduces to one simple equation

$$\dot{\xi} = -B(g_0 + C\xi), \tag{3.32}$$

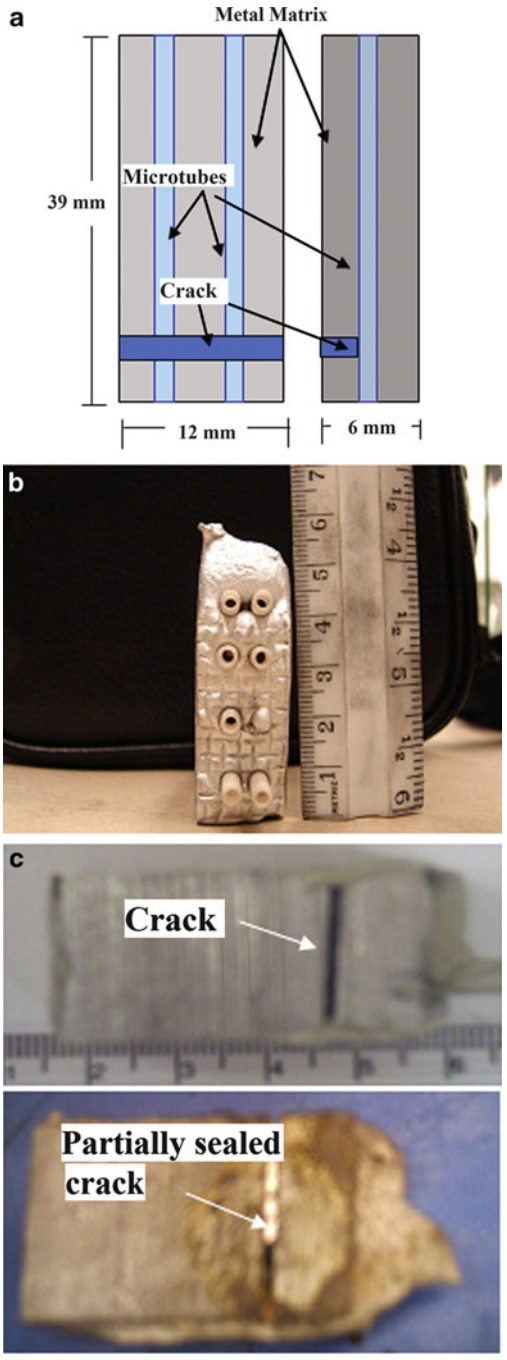

Fig. 3.7 Self-healing Al composite with microtube reinforcement (**a**) geometry of the sample, (**b**) front view, (**c**) before and after the healing (Lucci et al. 2008a, b, c)

which can be immediately solved as

$$\xi = -\frac{g_0}{C} + D\exp(-BCt). \tag{3.33}$$

The fist term is the steady-state solution corresponding to the degree of degradation after the healing is completed. The second term is the transient part of the solution. It is beneficial for the system to have a high ratio of g_0/C (maximum volume of the healing agent, g_0, over the rate of its consumption, C). We can conclude that the model is consistent with the experimental data.

3.5 Summary

Conventional engineering surfaces tend to degrade and become worn due to increasing thermodynamic entropy, which is a consequence of the dissipation during sliding contact. Most biological tissues, however, have the ability of self-healing. In order to embed the self-healing property into engineered materials, special efforts should be made. From the thermodynamic point of view, self-healing is a result of decreasing entropy. This is possible in the case of a special organization of these systems. One possibility is in the case when the system has a special multiscale structure with the dissipation occurring at one level of the system and self-organization occurring at a different hierarchy level. This can be achieved, for example, by embedding microcapsules or microtubes with a healing liquid to prevent crack propagation. We also suggested a simple system of equations that describes the degradation and healing process and provides a criterion for self-healing.

Chapter 4
Surface Healing: A Case Study

In this chapter we discuss a specific type of self-healing – surface healing – in living nature (leaves of hydrophobic and hydrophilic plants) and in artificial surfaces.

4.1 Introduction

The surface is the most vulnerable part of a material for various modes of deterioration, including wear, corrosion, fretting fatigue, etc. It is not surprising, therefore, that self-healing at the surface is a matter of especially active investigation by scientists. It is known that under certain conditions, a tribological system can enter a self-lubricating regime, with friction and wear dramatically reduced compared to the regular regime. For example, during the sliding frictional contact of steel vs. bronze in the presence of a lubricant, a protective Cu layer can form that reduces friction and almost eliminates wear (Garkunov 1985). Another example is a drastic reduction of the coefficient of friction (from 1.4 to 0.5) and wear rate (from 0.02 to 0.0001 $mm^3\ N^{-1}\ m^{-1}$) in Al–Al_2O_3 nanocomposites, which is demonstrated when the Al_2O_3 particle size reduces below 1 μm (Jun et al. 2006). The detailed mechanisms of these transitions are not well understood.

Being an opposite process to wear and surface degradation, surface healing is of interest for tribology. Dry friction and wear are dissipative processes that occur during the sliding of two solid surfaces, and they are characterized by irreversibility, or from the thermodynamic point of view, the production of entropy. Self-healing may be viewed in the broader context of self-organization during friction. In most self-healing schemes, the material is driven away from the thermodynamic equilibrium either by the deterioration process itself or by an external intervention, such as heating. After that, the composite slowly restores thermodynamic equilibrium, and this process of equilibrium restoration drives the healing serving as the thermodynamic "healing force."

The entropic description of self-healing is an integral description, as opposed to a formulation in terms of the differential equations of mass and heat transfer.

M. Nosonovsky and P.K. Rohatgi, *Biomimetics in Materials Science: Self-Healing, Self-Lubricating, and Self-Cleaning Materials*, Springer Series in Materials Science 152,
DOI 10.1007/978-1-4614-0926-7_4,

While it is extremely desirable to relate the rates of entropy production with the microstructure of the material, this has not been achieved so far. Rather than looking for direct formulation in terms of entropy rates, it may be useful to come up with another integral formulation, namely, in terms of parameters that characterize the degree of degradation and healing (Nosonovsky et al. 2009). The logic of such an approach is the following: first, the rate of entropy is related to the rate of degradation through certain degradation coefficients. Second, the rate of healing is introduced, and a general form of the relation between the rate of healing and degradation (the constitutive equations of a self-healing system) is found using the Onsager formalism of the non-equilibrium thermodynamics (Nosonovsky 2009). Third, a general criterion of whether the self-healing occurs is formulated using the constitutive equations. After that a particular form of the constitutive equation is found for the particular system, given its healing mechanism and structure. In this chapter, we suggest such an approach and investigate, as a case study, the void self-healing in plant leaves which serve as an inspiration for biomimetic self-healing coatings.

4.2 Self-Organization at the Sliding Interface

Consider two solid surfaces in sliding contact with the coefficient of friction μ. One surface has the coefficient of heat conductivity λ, while the other is made of an insulating material. Due to frictional dissipation, heat is generated at the interface

$$\mathrm{d}Q = \mu W \,\mathrm{d}x, \tag{4.1}$$

where W is the applied normal force and $\mathrm{d}x$ is the sliding distance. Using the heat conductivity equation for the temperature

$$\zeta = a\exp(-H\lambda t) + \frac{M\kappa}{H\lambda}, \tag{4.2}$$

where z is the vertical coordinate (distance from the interface) and $V = \mathrm{d}x/\mathrm{d}t$ is the sliding velocity, the temperature drop across the thin subsurface layer $\mathrm{d}z$ is $\mathrm{d}T = (\mu WV/\lambda)\mathrm{d}z$ (Fig. 4.1). Therefore, the energy released at the subsurface layer of depth $\mathrm{d}z$ is given by

$$\mathrm{d}q = \mathrm{d}Q\frac{\mu WV}{\lambda T} = \frac{(\mu WV)^2}{\lambda T}. \tag{4.3}$$

Thus the entropy production rate in the subsurface layer, $\mathrm{d}S/\mathrm{d}t = \mathrm{d}q/T$, is given by (Nosonovsky and Bhushan 2009)

$$\frac{\mathrm{d}S}{\mathrm{d}t} = \frac{(\mu WV)^2}{\lambda T^2}. \tag{4.4}$$

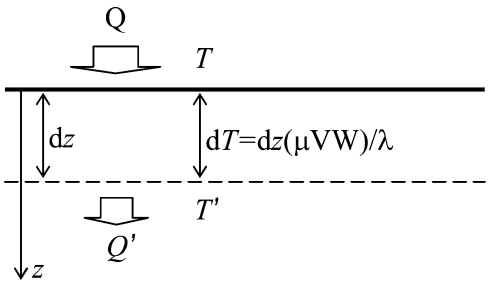

Fig. 4.1 Heat flow near the frictional interface

Simultaneously with the heat generation, there is a significant heat and entropy flow away from the interface. In some cases, the flow from the interface exceeds the rate of entropy production at the interface, causing the entropy at the interface to decrease and leading to self-organization. The stability condition for the thermodynamic system is given in variation form by

$$\frac{1}{2}\frac{\partial}{\partial t}(\delta^2 S) \geq 0, \tag{4.5}$$

where $\delta^2 S$ is the second variation of entropy. When the stability condition given by (4.5) is violated, the system is driven away from equilibrium, which creates the possibility for self-organization as a result of wear, tribochemical reactions, or other processes in the subsurface layer (Fox-Rabinovich and Totten 2006).

A simple example of an instability that drives a system away from equilibrium is when the coefficient of friction $\mu(V)$ decreases as the sliding velocity increases. For a system with zero thermal conductivity, the entropy rate is given by $\dot{S} = \mu WV/T$, and the stability condition is then violated

$$\frac{1}{2}\delta^2 \dot{S} = \frac{W}{T}\delta\mu\,\delta V = \frac{W}{T}\frac{\partial \mu}{\partial V}(\delta V)^2 < 0. \tag{4.6}$$

This is a well-known phenomenon of a dynamic frictional instability caused by "negative viscosity," which is quite common in a dry frictional contact (Nguyen 2003). The usual way of detecting frictional instability is to analyze the stability of a linear system by investigating whether the eigenvalues of a linear system have positive or negative real parts (Nosonovsky and Adams 2004). While this method provides the tool to detect the onset of instability, it does not show anything about the further evolution of the system, which is normally subjected to vibration with an exponentially growing amplitude. With growing amplitude, the system is expected to leave the linear region and enter a limiting cycle, thus exhibiting a transition to non-linear friction-induced vibration. However, neither the properties nor the parameters of this vibration can be determined from the linear model. In contrast, non-equilibrium thermodynamics suggests that the destabilized system transforms to a self-organized state with a lower rate of entropy production and lower friction and wear. The reduction of the coefficient of friction due to friction-induced

vibrations has indeed been reported for systems with dynamic frictional instability (Nosonovsky and Adams 2001).

A more complicated case is when the coefficient of friction and the thermal conductivity depend upon a material parameter, Ψ, that characterizes the microstructure of the surface (e.g., the density of a micropattern), so that

$$\mu = \mu(\psi), \tag{4.7}$$

$$\lambda = \lambda(\psi)$$

The stability condition given by (4.5) yields

$$\frac{1}{2}\delta^2\dot{S} = \frac{V^2W^2}{T^2}\frac{\partial\mu}{\partial\psi}\left(\frac{1}{\lambda}\frac{\partial\mu}{\partial\psi} - \frac{\mu}{\lambda^2}\frac{\partial\lambda}{\partial\psi}\right)(\delta\psi)^2 \geq 0. \tag{4.8}$$

The stability condition can be violated if $\partial\mu/\partial\psi<0$ while the term in the bracket is positive or vice versa. As in the previous example, when the stability condition is violated, a self-organized regime and secondary structures (such as tribofilms) can form, and the rate of entropy production decreases (Fox-Rabinovich et al. 2007). Therefore, if the stability condition given by (4.8) is not satisfied, the frictional force and wear can decrease. By selecting appropriate values of Ψ, it can be ensured that the stability condition of (4.8) is violated, and thus a low-friction, low-wear material can be obtained. This approach has been used successfully for many applications, such as ceramic and alloy hard coatings, analysis of material compatibility, and many others (Fox-Rabinovich and Totten 2006). While it is well known that a tribological process enters a steady state phase or a limiting cycle after a period of run-in and adaptation, the analysis is useful for selecting material parameters (such as the derivatives of μ and λ by V, T, and Ψ) that lead to desirable tribological behavior.

4.3 Self-Healing at the Interface

Consider now a process characterized by a degradation parameter ξ, for example, the wear volume or the total length of the cracks. Healing is characterized by a healing parameter ζ, for example, the volume of released healing agent. In the non-equilibrium thermodynamics, a thermodynamic force Y_i and a thermodynamic flow $J_i = \dot{q}_i$ are associated with every generalized coordinate q_i. In the widely accepted linear approximation, the flows are related to the forces by

$$J_k = \sum_i L_{ki}Y_i, \tag{4.9}$$

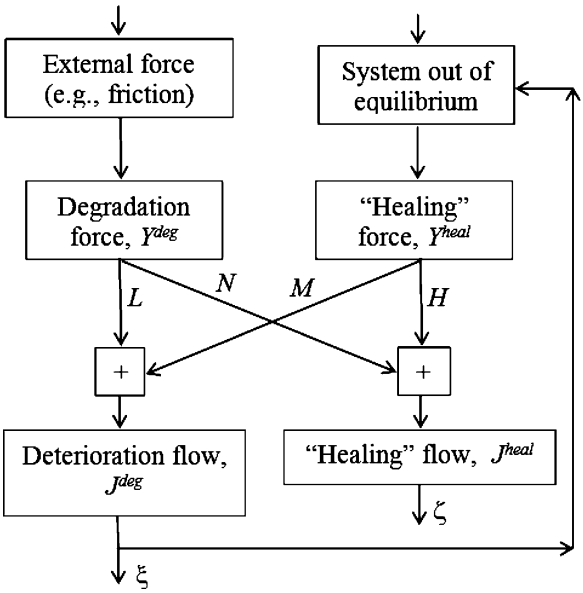

Fig. 4.2 Block diagram of the healing process. Deterioration (or degradation) is caused by an external force. The deteriorated system is brought out of equilibrium so that the restoring ("healing") force is created, which is coupled with the degradation flow through the parameter M

where L_{ki} is an Onsager coefficient; furthermore, $L_{ki} = L_{ik}$ based on the Onsager reciprocity relationships (De Groot and Mazur 1962). The rate of entropy production

$$\dot{S} = \frac{\mathrm{d}Q}{T\,\mathrm{d}t} = \frac{1}{T}\sum_i J_i Y_i \tag{4.10}$$

is a linear function of thermodynamic flows. The generalized degradation and healing forces are external forces that are applied to the system, and flows are related to the forces by the governing equations

$$\begin{aligned} J^{\mathrm{deg}} &= LY^{\mathrm{deg}} + MY^{\mathrm{heal}}, \\ J^{\mathrm{heal}} &= MY^{\mathrm{deg}} + HY^{\mathrm{heal}}, \end{aligned} \tag{4.11}$$

where L, M, and H are corresponding Onsager coefficients. It is expected that $L > 0$, $H > 0$ (degradation and healing grow when corresponding positive forces are applied), $M < 0$ (degradation and healing decrease when opposite forces are applied) (Fig. 4.2).

The degradation force Y^{deg} in (4.11) is an externally applied thermodynamic force that results in the degradation. For friction-induced degradation (Bryant et al. 2008), the degradation force is proportional to the frictional dissipation (i.e., a constant fraction of energy dissipated by friction is consumed for wear)

$$Y^{\mathrm{deg}} = k\mu WV. \tag{4.12}$$

For the wear of a material ($Y^{\text{heal}} = 0$), taking $L = 1/\mu H$, (4.12) yields the Archard wear law

$$\dot{w} = k\frac{WV}{H}, \tag{4.13}$$

where k is the wear coefficient, H is the hardness, and $w = \xi$ is the volume of worn material. When healing is introduced, the entropy rate is given, using (4.10) and (4.11), by

$$\dot{S} = \dot{S}^{\text{deg}} + \dot{S}^{\text{heal}} = \frac{L}{T}(Y^{\text{deg}})^2 + \frac{2M}{T}Y^{\text{deg}}Y^{\text{heal}} + \frac{H}{T}(Y^{\text{heal}})^2. \tag{4.14}$$

The first term in the right-hand part of (4.14) corresponds to the degradation, $\dot{S}^{\text{deg}} = L(Y^{\text{deg}})^2/T$, while the healing part involves a positive and a negative term, $\dot{S}^{\text{heal}} = 2MY^{\text{deg}}Y^{\text{heal}}/T + H(Y^{\text{heal}})^2/T$. Assuming that the macroscale healing occurs at the expense of microscale deterioration, the first term can be associated with the negentropy, observed at the macroscale, whereas the second is the microscale term.

The healing force Y^{heal} is an external thermodynamic force that is applied to the system. In most self-healing mechanisms, the system is placed out of equilibrium and the restoring force emerges, so we can identify this restoring force with Y^{heal}. Since the restoring force is coupled with the degradation parameter ξ by the negative coefficient M, it also causes degradation decrease or healing.

For example, consider the case of self-healing with the use of a healing agent encapsulated into microcapsules. When the crack propagates, the capsules rupture and the liquid adhesive is released, which comes into contact with the catalyst and solidifies to heal the crack opening. Crack propagation is an irreversible process, because when intermolecular bonds are broken, the energy γ is released irreversibly, so the entropy amount $S_{\text{crack}} = \gamma/T$ per unit length is produced. If N capsules are ruptured to heal the crack with the length L, then the total entropy production is given by

$$\Delta S_{\text{total}} = N\Delta S_{\text{conf}} - L\frac{\gamma}{T} > 0, \tag{4.15}$$

where the first term is the configurational entropy due to the mixing of two substances, given by

$$\Delta S_{\text{conf}} = R(n_1 X_1 + n_2 \ln X_2), \tag{4.16}$$

where n_1 and n_2 are the amounts in moles of two pure substances, X_1 and X_2 are mole fractions in the solution, and R is the gas constant (Craig 1992). Part of this

excess entropy can be consumed for healing the bonds at the crack. The net configurational entropy grows; however, the growth is not due to the cracking but due to microcapsule rupture and an irreversible decrease of their number. By cracking the microcapsules, the system is placed in a non-equilibrium state and the restoring thermodynamic force Y^{heal} emerges, which governs the flow and diffusion of the healing agent.

Obviously, this simplified analysis ignores many factors, such as the change of entropy due to the phase transition (solidification) of the healing agent, thermal effects, etc. However, it illustrates well the idea that entropy is consumed at the macroscale level (healed cracks) due to its excess production at the molecular level (the mixing of the healing agent with the material) (Nosonovsky and Esche 2008a).

Another approach involves the embedding of shape-memory alloy (SMA) wires. The SMAs are capable of the shape memory effect due to their ability for temperature- and stress-induced reversible martensite/austenite phase transition. The temperature of the transition is different during heating and cooling due to hysteresis. When the stress is released, the reversed martensite/austenite transition does not occur if the temperature remains above the transition temperature during cooling. However, when the temperature is raised above the transition temperature during heating, the martensite transforms back into the austenite phase and resumes its original shape. While the deformation of an SMA looks similar to plastic deformation, it is actually a reversible deformation.

It is natural to take the volume of voids and crack openings as the degradation parameter ξ, and the strain of the SMA microwires as the healing parameter ζ, while the concentration of the microwires is the microstructure parameter Ψ. When the system is healed, it undergoes the martensite $\rightarrow$ austenite transition due to the elevated temperature. At this point the system is brought to a non-equilibrium state, with the amount of the excess energy dependent on ξ. We will assume that the restoring thermodynamic force is approximately proportional to the strain $Y^{\text{heal}} \propto \varsigma$, and that the strain rate is proportional to the restoring force as it was discussed in the preceding chapters (Fig. 2.1).

To investigate a simplified model of self-healing, we will assume that the degradation force is constant $Y^{\text{deg}} = \kappa$ and the healing force is proportional to the healing parameter $Y^{\text{heal}} = f(\xi)\zeta$. The function $f(\xi)$ involves the dependence of the healing rate on the length of the cracks or other damage, because the same amount of the healing agent can result in a different rate of repairing the crack. We will further assume a simple constant dependence $f(\xi) = -\lambda$ or $Y^{\text{heal}} = -\lambda\zeta$, where λ is a constant. Then the system of (4.11) yields

$$\begin{aligned} \dot{\xi} &= L\kappa - M\lambda\zeta, \\ \dot{\zeta} &= M\kappa - H\lambda\zeta. \end{aligned} \tag{4.17}$$

And can be immediately solved as

$$\xi = \kappa\left(L - \frac{M^2}{H}\right)t + \frac{Ma}{H}\exp(-H\lambda t) + b,$$
$$\zeta = a\,\exp(-H\lambda t) + \frac{M\kappa}{H\lambda}, \tag{4.18}$$

where a and b are the constants of integration, and in the steady state limit ($a = 0$), the criterion for healing is $M^2/(HL) > 1$. In other words, the crack is healed if the absolute value of the term M that couples between healing and degradation in (4.11) is big enough compared with the terms LH that correspond to the action of the degradation and healing forces (Nosonovsky and Bhushan 2010a).

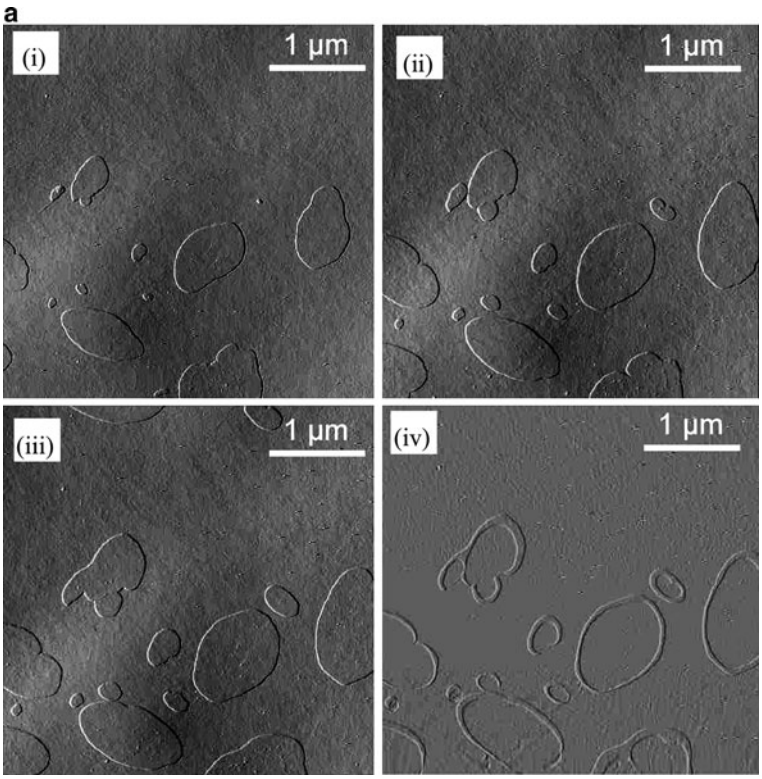

Fig. 4.3 Wax regeneration on a leaf of (**a**) *L. turbiniformis* (**i**) 20 min, (**ii**) 27 min, and (**iii**) 38 min after the wax removal, and (**iv**) the concentric wax growth between 27 and 38 min; (**b**) *Taxus baccata* (**i**) 23 min, (**ii**) 33 min, (**iii**) 70 min, and (**iv**) 138 min after the wax removal (Koch et al. 2009; Nosonovsky and Bhushan 2010a)

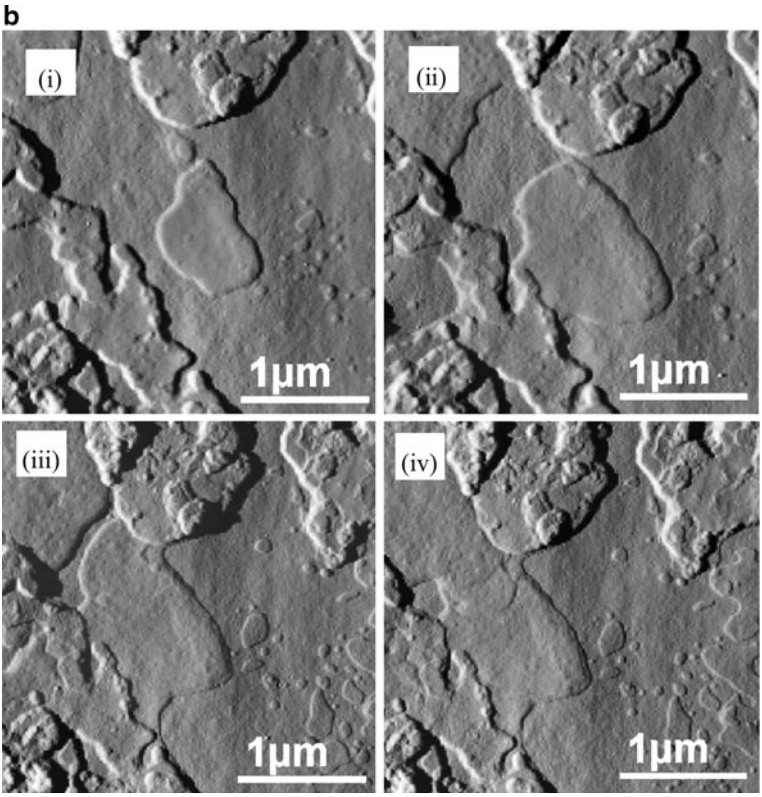

Fig. 4.3 (continued)

4.4 Self-Healing of Voids in Plant Surfaces

In this section, we will discuss the experimental observation of the self-healing of voids in the leaves of plants, such as the lotus (*Nelumba*). The lotus leaf surface is a superhydrophobic self-cleaning surface, and it serves as an example and inspiration to develop artificial superhydrophobic self-healing surfaces using the "lotus effect" (Nosonovsky and Bhushan 2005a, b; 2006a, b). The lotus effect is the result of surface roughness and a wax coating (a lotus leaf is covered by microscale bumps called papillae). Artificial superhydrophobic surfaces are either made of a moderately hydrophobic material or have a hydrophobic coating that yields superhydrophobicity in combination with roughness. While the leaf surface has the ability to regenerate the wax coating, the hydrophobic coating of an artificial surface can be quite vulnerable. It has been suggested to attach a reservoir with a hydrophobic polymer to supply the coating for a superhydrophobic surface that would produce a surface that is both superhydrophobic and self-healing (Reihs et al. 2001).

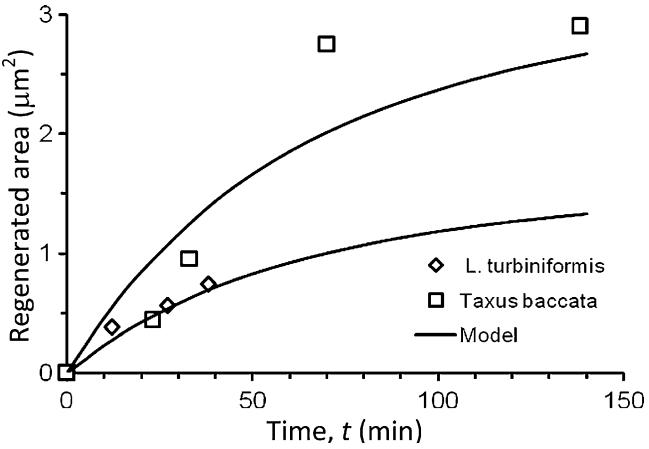

Fig. 4.4 The size of regenerated area as a function of time for two plants and the trend predicted by the model (Nosonovsky and Bhushan 2010a)

In order to build a superhydrophobic self-healing surface in a biomimetic manner, it is important to understand the self-healing mechanisms of plant leaves (Nosonovsky and Bhushan 2010a). Koch et al. (2009) investigated the self-healing of voids in the wax coating of several plant leaves after removing the layer of epicuticular wax. They found that wax is regenerated in concentric or strip-shaped modes. Figure 4.3a shows the wax regeneration on a leaf of *L. turbiniformis* 20, 27, and 38 min after wax removal. Figure 4.3b shows wax regeneration on a leaf of *Taxus baccata* 23, 33, 70, and 138 min after a partial wax removal (Koch et al. 2009). The regenerated area grew in a concentric manner, with the amount of regenerated wax proportional to the size of the healed area $f(\xi)$ and the rate of the production of wax (ζ). The size of the regenerated area as a function of time is presented in Fig. 4.4 on the basis of the data of Fig. 4.3. The data is plotted along with the theoretical curves calculated from (4.18) using $H\lambda = -0.02$ min^{-1}, $\kappa(L - M^2/H) = 0.0015$ μm^2 min^{-1}, $aM/H = -1.2$ μm^2, $b = 1.2$ μm^2 and $\kappa(L - M^2/H) = 0.003$ μm^2 min^{-1}, $aM/H = -2.4$ μm^2, and $b = 2.4$ μm^2. The non-linear growth of the regenerated area with the saturation in the case of *T. baccata* suggests a complicated dependence of $f(\xi)$ (Nosonovsky and Bhushan 2010a).

4.5 Summary

We have studied surface self-healing paying attention to the most general features that are common to different mechanisms of self-healing. Conventional engineering surfaces tend to degrade and become worn due to increasing thermodynamic entropy, which is a consequence of dissipation during sliding contact. Most biological tissues, however, have the ability to self-heal. In order to embed a self-

healing property into engineered materials, special efforts must be made. From a thermodynamic point of view, self-healing is a result of decreasing entropy. This is possible in the case of a special organization of these systems. One possibility is in the case when heat flows away from the interface and the non-equilibrium process results in self-organization during friction. Another possibility is in the case where the system has a special multi-scale structure, with dissipation occurring at one level of the system and self-organization occurring at a different level. This can be achieved, for example, by embedding microcapsules with a healing liquid to prevent crack propagation. We also suggested a simple system of equations that describes the degradation and healing process and provides a criterion for self-healing.

Chapter 5
Development of Metallic and Metal Matrix Composite Self-Healing Materials

In the preceding chapters, we discussed theoretical foundations of self-healing and surface healing. In this chapter, we will review recent developments in metallic self-healing materials with the emphasis on the work done at the University of Wisconsin-Milwaukee Center for Composites (Rohatgi et al. 1986; Nosonovsky et al. 2009a, b, c; Ruzek 2009; Martinez-Lucci 2011). This includes testing of the feasibility of various approaches to self-healing using solders, metal matrix composites (MMC), shape memory alloy (SMA) reinforcement, embedding of low melting point material as a reinforcement and other methods, including solid state precipitation of material to close off voids or cracks. Computational fluid dynamic simulation of healing in metallic materials due to the flow of liquid healing agent into cracks to help predict the types of cracks which can be healed is also included.

5.1 Self-Healing Solders

5.1.1 Composition of Solders

Solders are materials commonly used to join metallic surfaces in a process called soldering, often for a mechanical and electrical connection between electronic components and printed circuit boards. Solder is a fusible lead-based or lead-free metal alloy, with a melting point or melting range between 90°C and 450°C. Most commonly used solders melt between 180°C and 190°C. The so-called eutectic alloys melt at a single temperature, while non-eutectic alloys have markedly different *solidus* and *liquidus* temperatures. Within this temperature range, they exist as a paste of solid particles in a melt of the lower-melting phase. Lead-free solders, such as tin and its alloys, are increasingly being used due to environmental and health concerns. Long-term reliability of solders is a significant problem, and the primary concern is the effect that extended thermomechanical cycling has on the interface between the solder joint and the component. During thermal cycling, stresses develop in the solder interfaces due to differences in the coefficient of

M. Nosonovsky and P.K. Rohatgi, *Biomimetics in Materials Science: Self-Healing, Self-Lubricating, and Self-Cleaning Materials*, Springer Series in Materials Science 152, DOI 10.1007/978-1-4614-0926-7_5,

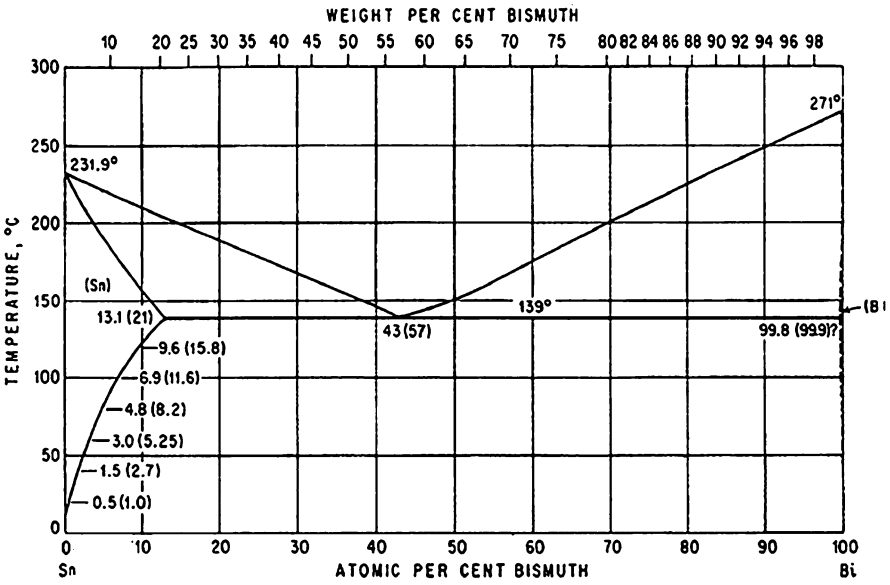

Fig. 5.1 Tin bismuth binary phase diagram (based on Handen 1958)

thermal expansion (CTE) between the solder, circuit board, and component. Eventually these stresses lead to defects, voids, and failures. Self-healing capability would be very useful in a solder joint. Since solder joints in modern electronic equipment are of the microscale size, it is desirable to develop a healing mechanism small enough to be effective at the microscale level. The key parameter of functionality in solder is the electrical conductivity, so the mechanical properties such as strength, size, and shape are less important for standard solder applications (Ruzek 2009).

One of the most common lead-free solders is the Sn–Bi alloy operating at or around the eutectic point. A eutectic alloy solidifies at a single sharp temperature corresponding to the eutectic point at a phase diagram (temperature vs. composition) of the alloy. Tin and bismuth form a binary eutectic as seen in Fig. 5.1, which allows for a eutectic composition with a low melting point of 138°C. An advantage of an Sn–Bi solder is the low CTE, which facilitates the extension of thermal fatigue life. Tin and bismuth mix very well and can be processed easily in the laboratory environment, which makes the Sn–Bi a convenient material combination. However, the low melting point reduces the maximum operating temperature of the system. If a composition that is off of the eutectic point is used, the alloy will freeze over a wide range of temperatures rather than at an exact point. This allows us to control the percentage of the system in the liquid and solid states and can be used in a wide variety of casting applications and has been extensively researched. Many alloys can exhibit this two-phase region between liquid and solid solutions; however, the width of this region can vary significantly. The Sn–Bi alloy offers a wide range of temperatures in this two-phase region, which allows for the liquid and solid percentages to be easily controlled, and this liquid can be used as a healing agent for a crack in the system.

5.1.2 Partial Melting and Solidification

The number of phases in equilibrium in the phase diagram, P, can be determined from the Gibbs' phase rule, which relates it with the number of the degrees of freedom (the number of intensive properties, such as temperature or pressure, which are independent of other intensive variables), F, and the number of components, C.

$$P + F = C + 2 \tag{5.1}$$

In a binary system ($C = 2$) such as Sn–Bi, there will exist two-phase regions ($P = 2$) with two degrees of freedom ($F = 2$) corresponding to the variation of temperature and concentration. In the Sn–Bi system there is a region between the liquid solution phase and the terminal solid solutions of both Sn and Bi. Therefore, at a given temperature and composition, the thermodynamically stable arrangement of the system can be partially liquid and partially solid over a wide range of temperatures and compositions. Given a fixed composition, an alloy will exhibit specific liquidus and solidus temperatures (Ruzek 2009).

The liquidus temperature is the highest temperature at which solid crystals are still present in a given composition. The solidus temperature is the lowest temperature at which liquid is present in a given composition. In pure metals, as well as in alloys at a eutectic point, the liquidus and solidus temperatures are identical. However, in a solid–liquid two-phase region, the liquidus temperature is higher than the solidus temperature. As an alloy is cooled from liquid into a liquid–solid two-phase region, crystals of the primary phase start to form, and its composition can be determined by using a phase diagram. In the Sn–Bi binary phase diagram shown in Fig. 5.1, there are two liquid–solid two-phase regions, one on each side of the eutectic point. At a given composition and temperature, for example 20% Bi and 150°C, the composition and amount of both the liquid and solid phases will be easily calculated.

In equilibrium, the liquid and solid portions of two-phase regions will have different compositions. Using these values we also can calculate the fraction of each phase. The fraction of liquid phase, F_L, is calculated using the lever rule (Callister 2003)

$$F_L = \frac{C_O - C_S}{C_L - C_S}, \tag{5.2}$$

where C_S and C_L are the compositions of the solid and liquid phases, C_O is the original alloy composition. This allows an alloy to be designed to have a predictable percentage of liquid at a given temperature. Precise kinetics and thermodynamics of these two-phase equilibrium states are subjects of various studies, since these processes are crucial in the solidification of castings and resulting microstructures; however, there are situations in which the calculations of fraction solid and liquid depart from equilibrium solidification.

In practice, equilibrium is not always maintained in a system due to heterogeneities and non-equilibrium processes such as diffusion. For example, when dendrites begin to solidify they protrude into the liquid. As they grow, the interdendritic liquid becomes concentrated and its composition approaches the eutectic composition. The Scheil freezing equation is the applicable theory for this effect (Flemings 1974)

$$C_S = kC_O(1 - F_s)^{k-1}, \tag{5.3}$$

where C_S is the composition of the liquid surrounding the weight fraction, C_O is the original alloy composition, k is the partition coefficient, and F_S is the composition of the solid. This equation shows that some eutectic will form between the dendrites for any original composition. This equation also predicts that there will be no effect of solidification rate on microsegregation. Observed variance from this equation is due to solid diffusion during and after solidification. Therefore, the center of a dendrite will have a composition farther from the eutectic composition than the edges of the dendrite (Ruzek 2009).

5.1.3 Shape Memory Alloy-Based Healing of a Solder

The idea to incorporate an SMA reinforcement in a solder matrix has been explored by Manuel and Olson (2007) and Dutta et al. (2006). Manuel and Olson (2007) used a tin-based alloy (Sn–13 atm.% Bi) as a proof of concept system only. They did demonstrate that long wires of shape memory alloy wires can shrink to their original shape and close an open crack in the solder tensile bar. The reversion to original length occurs as a result of increase in temperature which can also partly liquefy the matrix near the crack to help it seal when closed due to compression as a result of shrinkage of shape memory alloys. They found that long continuous fibers of an SMA are not appropriate for a self-healing solder for two main reasons. First, it would not be possible to incorporate long fibers in a solder joint that is less than a millimeter in size. Second, upon the remelting of the system to make the solder joint, the fibers could become unaligned and twisted with each other.

Dutta et al. (2006) studied the SMA-reinforced solder (95.5Sn–3.8Ag–0.7Cu) as a system, although they did not pursue the concept of self-healing. Rather, they introduced SMA particulates to improve the lifespan of solder joints due to the superelastic properties of SMA materials. They found that small particulates of SMA will easily fit into a solder joint; however a particle of SMA cannot close a crack to provide healing. The advantage of SMA particles in a matrix is the "superelastic" nature of an SMA. Superelasticity is a specific property of SMAs caused by the reversible phase transformation between the austenitic and martensitic phase induced by stress (rather than temperature). The particulates used by Dutta et al. (2006) were of superelastic NiTi and they imposed reverse shear on deformation in a system, reducing the amount of strain in the matrix, thus reducing the probability of crack formation.

Reinforcing fibers improve a composite material in several ways. One is the deflection of cracks. A crack that comes into contact with the reinforcement will be deflected along the matrix–reinforcement interface, if the matrix–fiber interface is weak. This slows the progression of the crack, and increases the energy needed for its propagation. As the crack continues to debond along the interface, the fiber bridges the crack, and continues to hold the matrix together, preventing the component from falling apart. However, at a critical bridging length, the fiber will fracture and will be pulled out of the matrix. This requires additional energy to overcome the frictional forces between the fiber and the matrix, thus slowing the crack propagation in yet another way (Ruzek 2009).

Pressure infiltration is a common method of synthesizing MMCs. The reinforcement is placed in a crucible, and a block of the matrix alloy is placed on top of it. The crucible is placed in a furnace that can be evacuated and pressurized. A vacuum is drawn and the furnace is heated above the melting point of the matrix material. The liquid matrix must form a seal above the reinforcement. Pressure, usually in the form of an inert gas, is applied and it forces the liquid matrix around the reinforcement. Since there is nothing around the fibers due to the vacuum, the pressure only has to overcome the forces resisting wetting. With pressure infiltration, the forces resisting wetting can be overcome, and a composite can be synthesized even when the reinforcement does not wet the molten metal matrix. Pressure infiltration has been successfully applied at UWM to synthesize shape memory alloy fiber reinforced composites which can exhibit self healing.

5.1.4 Eutectic-Based Healing

Another approach to healing is the use of low melting eutectic phase in an alloy system with a dendritic structure. A eutectic mixture has a composition with the melting point at a local minimum of the alloy system, so that all the constituents crystallize simultaneously at this temperature from molten liquid solution. Such a simultaneous crystallization of a eutectic mixture at a fixed temperature is known as a eutectic reaction; whereas the temperature at which crystallization takes place is referred to as the eutectic temperature or, together with the composition at which it takes place on the phase diagram, the eutectic point.

While the eutectic structure provides the lowest melting point compared to similar alloys, we cannot build our entire system out of eutectic. In order to achieve self-healing, we need to maintain the original size and shape of the part during the healing process. This self-healing concept is based on using the eutectic liquid formed with the solid itself, as a healing phase, and the solid dendritic phase to maintain the structural integrity. The best way to achieve this is to use a matrix alloy composition that is away from the eutectic composition of a system. This will cause dendrites of a phase to form at a higher temperature and eutectic to fill between these dendrites. This could be a hypoeutectic or hypereutectic system, which is off of the eutectic point.

Upon cooling, dendrites of a saturated phase will form first, since they have a higher melting point. These dendrites will change the composition of the remaining interdendritic liquid, pushing it to the eutectic point. Eventually, the eutectic will solidify between the dendrites.

To activate this system for self-healing, the temperature of the system should be elevated to a point where the eutectic will melt and act as a healing phase, while the dendrites remain solid and maintain the structural integrity of the system. The liquid eutectic is then available to flow between the dendrites and into any cracks or voids that may be present in this system. Upon the cooling of the system, this eutectic will resolidify, thus healing the system.

This method has several potential advantages. First and foremost, this method could be used in a very large number of systems. As long as the hypoeutectic or hypereutectic structure can be formed, this method of self-healing would be possible. This would allow almost any alloy system to be engineered into a self-healing system. Another advantage of using the eutectic as a healing phase is that the component can be as-cast. If the correct cooling rates are applied, a part would demonstrate healing in the as-cast state, with no modification or heat treatment necessary. This greatly improves the possible applications and lowers the cost of such a system. Finally, since the system needs no external reinforcements, and the microstructure is a simple modification, the entire system is very simple and could be synthesized by any foundry, with little or no extra cost. This will enable the concept of self-healing using interdenritic eutectic to be adopted more readily due to minimal cost increase.

Unfortunately, there are also disadvantages to using a eutectic healing system. While the system is simple in concept, the design is much more difficult than it first appears. The ratio between the volume of dendrites and eutectic has to be such that upon heating and healing there is enough liquid to not only fill a void or crack, but provide a path for the liquid to flow to the crack. This issue is similar to the design of feeding in traditional casting where shrinkage during solidification needs to be fed by promotion of flow in the interdendritic spaces to the areas where shrinkage occurs. While freezing is not a concern, since the system should be held at a static temperature, all of the liquid flow must be between the dendrites. On the other side of the same coin, the volume of the eutectic phase cannot be too high, since the system needs to maintain its structural integrity during healing. If the solid dendrite phase network is not occupying enough volume and is not sturdy enough at the healing temperature, the component would turn into mush, and lose its shape and structure. Finally, due to high liquid-to-solid ratios, we must be concerned with the possibility of interdendritic liquid leaking out of the system onto the surface during healing instead of flowing into the cracks.

Ruzek (2009) noted that since the cracks and voids that require healing occupy a given volume, the same or greater volume of eutectic healing phase is required to fill and heal them. Yet, since the system is closed, this eutectic has to come from somewhere else in the part. Therefore, the void is transferred from one area to another area of the part where it would be less harmful. One solution would be to close the void or crack before healing with the healing solution merely welding the surfaces of the void back together. One method of doing this would be to use

SMA wires. A combined system of eutectic healing and SMA wires could be very effective at self-healing. Solder only needs to maintain an electrical connection, so voids and changes in shape are allowable as long as they do not inhibit the flow of current. One last concern is that since healing takes place at elevated temperatures, Ostwald ripening would occur. The larger dendrites will grow at the expense of the smaller dendrites; since the larger dendrites have a lower surface energy, the system tries to lower its energy to the lowest possible state. As the dendrites continue to grow during healing, the effect on healing and the stability of the structure need to be studied. The coarsening, or Ostwald ripening, of dendrites may close the continuous pathways for interdendritic liquid. While any alloy with a eutectic reaction would demonstrate self-healing, it will be easier to implement it in some alloys compared to others. Alloy systems that are best suited to eutectic healing require certain traits. A large temperature range between the liquidus and solidus lines provides greater flexibility in the healing temperature. We do not want a very narrow healing temperature range ($<5^{\circ}$) as that will prove difficult to maintain. Similarly, a wide composition range between the liquidus and solidus lines at a given temperature enables one to get a wide range of liquid-to-solid ratios. As an example, Sn–Bi solder matrix is very suitable as a matrix for self-healing in this manner.

Almost any alloy with a eutectic reaction can be tailored to exhibit self-healing, and it could be done with very little modification to its microstructure. While there are challenges to overcome, the potential rewards in developing self-healing metals are great. This type of self-healing metal could be synthesized through conventional metal casting, processes including concepts of microstructure growth and composition control. The problems related to fluid flow between dendrites, and solidification shrinkage during self-healing processes could be solved using some of the feeding techniques developed for metal casting. For example, when alloys with larger freezing ranges are cast, both the liquid and solid move in the early stages of solidification to compensate for solidification shrinkage. However, if the solid is constrained by the mold, the dendrites can be pulled apart by shrinkage. This is a hot tear, and if the casting is well fed, the interdendritic liquid fills the crack essentially healing the hot tear in the hot dendritic network. This is very similar to the eutectic healing mechanism (Ruzek 2009). The major difference is that in self healing of a mechanically induced crack during the service of a component, the eutectic liquid has to flow to the crack where it is formed and this is a big challenge.

5.1.5 Low Melting Point Alloy in Hollow Reinforcement

A different method of self-healing in metals is the incorporation of the hollow reinforcements containing low-melting healing agent material in metal matrix materials. Similar to the work in polymers, this method uses a secondary healing agent that is contained in hollow reinforcements. The healing agent in this case would be a low melting point alloy, such as the Sn–Bi eutectic solder, which melts at 138°C. Upon damage, cracks in the matrix would rupture hollow reinforcements, exposing the low melting point alloy. A healing heat treatment could then be

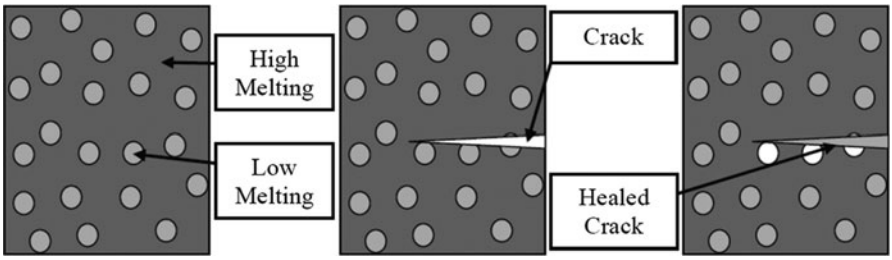

Fig. 5.2 Self-healing concept of low melting point reinforcements. (**a**) Hollow reinforcements containing a low melting point alloy are incorporated in a metal matrix. (**b**) Upon damage, the reinforcements are ruptured by cracks. (**c**) Heating to achieve self-healing will cause the low melting alloy to liquefy and flow into the cracks. Upon cooling, the healing agent would solidify, bond with the crack surface, and heal the crack (Ruzek 2009)

applied, melting the low melting point healing agent within the hollow reinforcement while the matrix remains solid. The molten healing agent could then flow out of the cracked hollow reinforcement into the cracks and voids caused by the damage. Upon cooling, the liquid that had flown into the crack would solidify, healing the cracks. This healing process is shown schematically in Fig. 5.2.

After the healing agent leaves the hollow reinforcement, the hollow reinforcement should maintain some strength, rather than just act as a void. Also, synthesis could be performed using a variety of methods, based on common techniques used for MMCs. Finally, there could be additional advantages of enhanced strength and modulus that could be achieved through the use of suitable hollow reinforcements to compensate for the hollow spaces left in the material.

However, there are pitfalls in using this method as well. Getting a pocket of a low melting point alloy into the matrix of a higher melting point alloy without mixing is difficult. Filling a hollow reinforcement with a lower melting alloy is also a challenge. Also, if the hollow reinforcement is too strong, a crack will not rupture it, but otherwise it will be destroyed in processing. The molten healing agent will require some force to push or pull it out of the hollow reinforcement. This could be capillary forces, forces due to higher expansion during melting, thermal expansion, or a preference to wet the matrix. The system will need to be designed to be functional and still get enough healing agent to fill the cracks associated with damage and bond the cracks surfaces. UWM has been successful in filling low melting healing alloys in hollow spaces of hollow microballoons and fibers, and incorporating these filled microballoons and hollow fibers in metallic matrices to form composites which have the potential to exhibit self healing.

5.2 Off-Eutectic Healing System

An off-eutectic (hypoeutectic or hypereutectic) system has the composition that allows for the formation of liquid and solid phases in equilibrium. Ruzek (2009) used a standard microstructure found in metals to provide the components needed

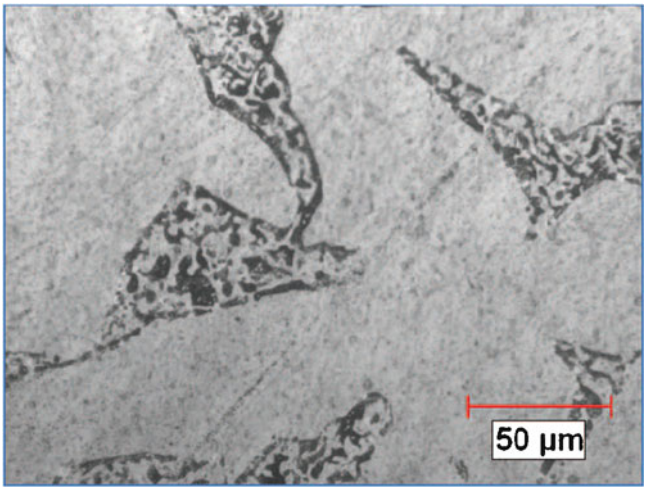

Fig. 5.3 As-cast Bi−10% Sn microstructure. The light areas are Bi, and the gray areas are of the eutectic composition of Sn and Bi. Etched. 500× (Ruzek 2009)

for a healing system. Three properties are required for materials in order to heal themselves: a structure that maintains functionality, a substance capable of transporting itself to close voids, and a trigger to activate this healing action. In an off-eutectic system, the trigger is the application of heat, dendrites act as a structural component, and the liquid eutectic phase acts as a mobile healing agent.

Two off-eutectic systems were investigated by Ruzek (2009), both using the binary Sn–Bi system, which is a simple system used in solder applications. The compositions chosen were Sn–20 wt% Bi and Bi–10% Sn, because both exhibit approximately the same percentage of liquid phase at 170°C, facilitating a comparative study. These compositions allow for the interdendritic liquid to freely flow, while maintaining some structural stability. For the Sn-20% Bi system at 170°C, the composition values are $C_O = 0.2$, $C_S = 0.14$, and $C_L = 0.42$. Using the "lever rule" (Callister 2003), one can find that the system has 21.4 wt% liquid in equilibrium providing reasonable range for healing. The Bi–10% Sn system's composition values were $C_O = 0.9$, $C_S = 0.99$, and $C_L = 0.68$. This provides a system with 29.0% liquid phases at the healing temperature of 170°C.

The alloys were synthesized by Ruzek (2009) from commercially pure Sn (99.9%) and Bi (99.9%) ingots. Melting was performed in an induction furnace under flowing Argon cover gas. After that, gravity castings were made in both graphite and steel molds. These master alloy castings were then re-melted in a small bottom pouring resistance furnace to fabricate test bars and samples. The microstructure of these castings was typical for hypereutectic or hypoeutectic systems. Figure 5.3 shows the as-cast Bi–10% Sn system, with angular Sn dendrites and a "Chinese script" eutectic between the dendrites (Ruzek 2009).

5.3 Tests of Mechanical Properties

The recovery of self-healing samples prepared by Ruzek (2009) was tested using the three-point bent test. Figure 5.4a shows an Sn–20% Bi sample which was bent significantly. This amount of bending also led to very large cracks forming on the

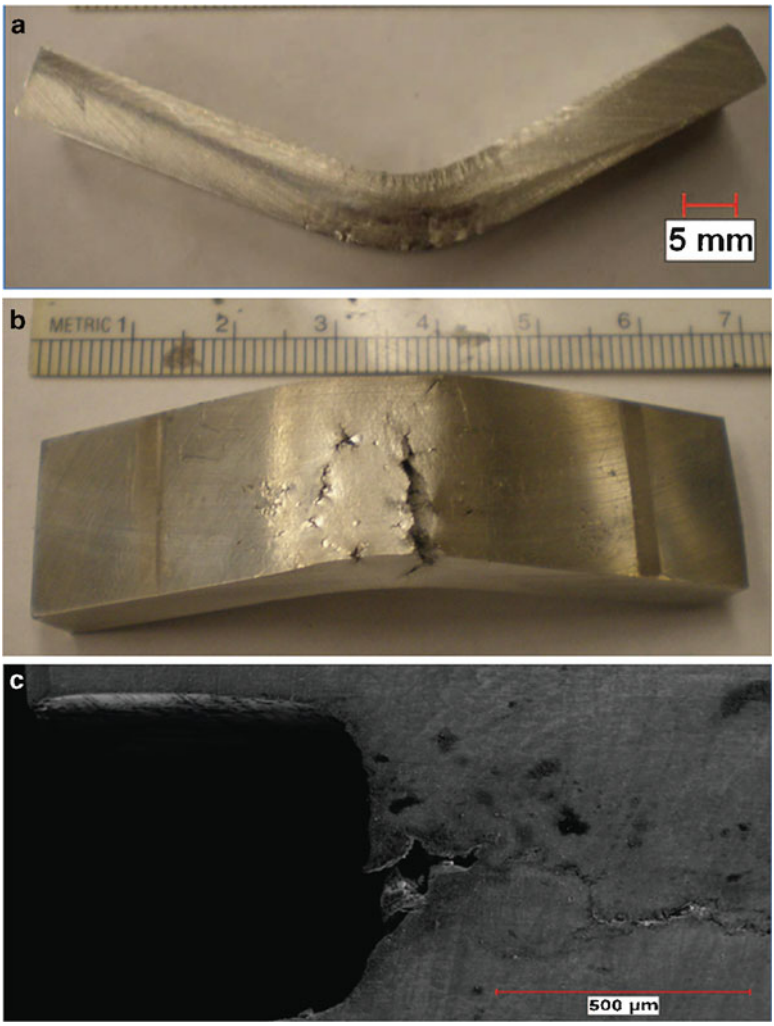

Fig. 5.4 (**a**) Sn–20% Bi three-point bend test sample. Note the amount of bending in the sample; this made healing and a rebending test difficult to execute. (**b**) Large cracks produced in Sn–20% Bi sample from three-point bend test. (**c**) Crack in Sn–20% Bi sample growing out of a notch, caused by a three-point bend test. (**d**) SEM of notch in Sn–20% Bi three point test bar. Note the crack growing from the right edge. (**e**) SEM image of partially filled notch in Bi–10% Sn three-point test bar. Note the unfilled crack continuing from the notch to the right. Note that the notch was facing down during the heat treatment (Ruzek 2009)

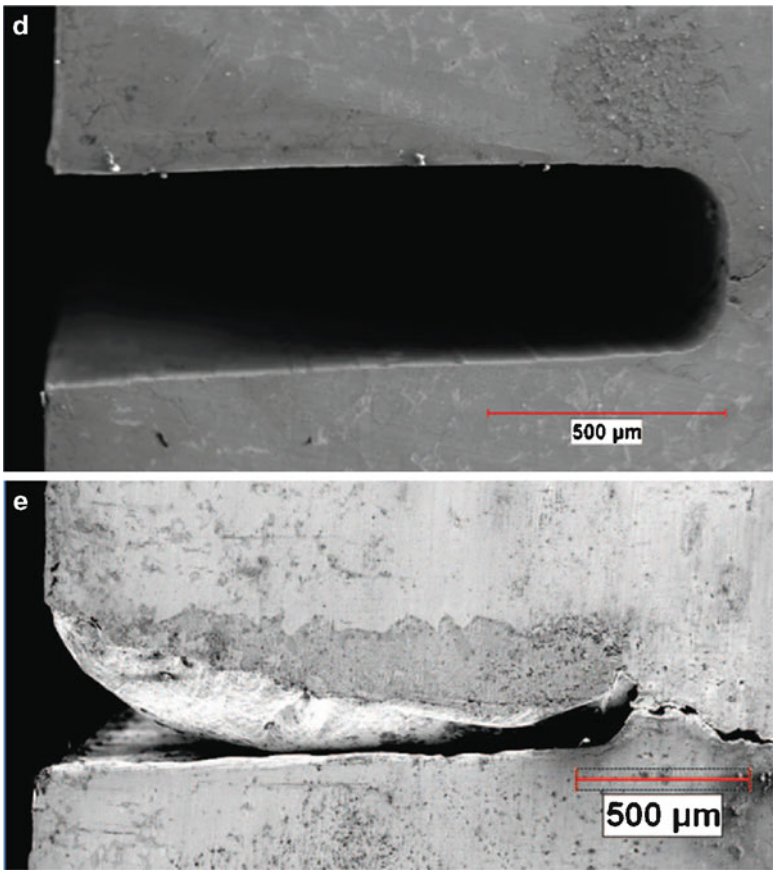

Fig. 5.4 (continued)

tension side of the samples. Such cracks, as seen in Fig. 5.4b, measured millimeters across and proved to be too wide to heal using this method.

In order to produce small, thin, hair-line cracks in the Sn–20% Bi samples, in addition to the Bi–10% Sn samples, the next set of samples were notched. By cutting a very thin notch into one face of the samples using a low-speed diamond cut-off saw, crack propagation was controlled so that only thin, hair-line cracks formed. The cuts were 350-µm wide and less than a millimeter deep as seen in Fig. 5.4c. In order to confirm the composition of the exudates present in the sample, and to observe the level of bonding between the exudates and a crack surface, scanning electron microscopy (SEM) and energy dispersive spectroscopy (EDX) were performed. Figure 5.4d shows a cross section of a Bi–10% Sn three point bend sample that was notched and cracked, while Fig. 5.4e shows a Bi–10% Sn sample after it was healed. This clearly shows an exudate of eutectic composition in the notch which appears to be well bonded to the top surface of the notch and partially fills the notched region (Ruzek 2009). Further improvement in design can lead to complete filling of the crack by eutectic healing liquid,

5.4 Shape Memory Alloy-Based Healing System

The SMA-based healing concept is similar to the eutectic-based healing with one additional feature. Reinforcements of an SMA form a composite that can close cracks before the eutectic phase melts. This means that the liquid eutectic is not needed to fill open cracks, rather, it just needs to weld cracks shut. The interface wetting is a very important issue in the development of any composite, because if the reinforcement is not bonded into the matrix, it cannot impart any improvement in properties and acts as an inclusion or void. In an Sn–NiTi system, this is especially important because NiTi tends to grow a very strong oxide layer on its surface, which is quite difficult to remove. In the past, researchers have coated the NiTi and attempted to remove the oxide layer with etchant or flux. However, there may be other ways to successfully incorporate NiTi in an Sn matrix. By using a pressure infiltration technique as described earlier in the chapter, the forces resisting the wetting of the NiTi in Sn could be overcome. Also, once the NiTi is fully incorporated, the composite could be reprocessed without the NiTi dewetting. This allows for a composite sample synthesized via pressure infiltration to be used as a master alloy to incorporate NiTi reinforcement in a larger batch of Sn. This process also allows the heavily concentrated NiTi reinforcement in pressure-infiltrated samples (~50 vol%) to be diluted down to any desired volume percentage as the application requires. This process is explained in Fig. 5.5 (Ruzek 2009).

This method is dependent on the rate of movement of the reinforcement through the melt. Since this system has NiTi reinforcement in an Sn based system, the NiTi will float to the surface due to lower density. The rate of floatation for spheres is

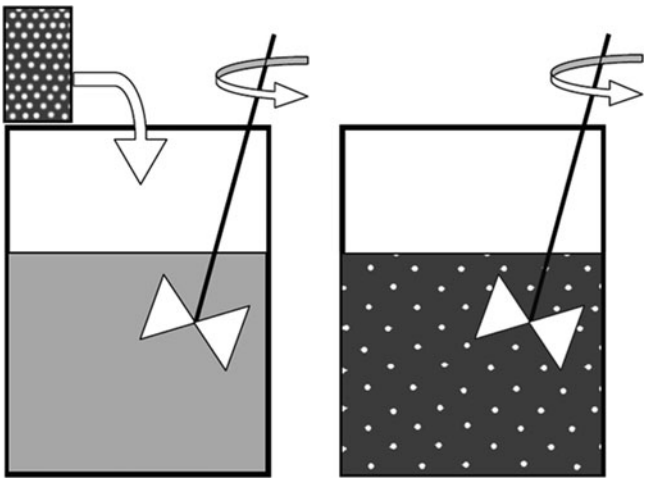

Fig. 5.5 The synthesis of a composite via a master alloy and stir mixing. By adding a master alloy composite with a high concentration of reinforcement to a melt of identical matrix composition, one can synthesis a composite of the same system, but a lower concentration of reinforcement (Ruzek 2009)

calculated using Stoke's Law. The density of the Sn–20% Bi matrix, ρ_F, is 7.6 g cc^{-1}; while the density of NiTi, ρ_P, is 6.45g cc^{-1}. The dynamic viscosity, μ, of liquid Sn for our conditions should range between 1,000 and 2,700 Pa s. The average radius, r, of the NiTi particles used was 65 μm, since that is the size of the particulate used in the experimental synthesis. Therefore, the terminal velocity (calculated as $V = 2/9(\rho_P - \rho_F)/\mu g r^2$) of the NiTi particles in liquid Sn should range from 4 to 10 nm s^{-1}. This velocity is so low that it would take hours for the NiTi reinforcement to move a single millimeter (Ruzek 2009).

By using a pressure infiltration technique, the forces resisting the wetting of the NiTi in Sn could be overcome as described earlier in the chapter. Also, once the NiTi is fully incorporated, the composite could be reprocessed without the NiTi dewetting and coming out of the system. This allows for a composite sample synthesized via pressure infiltration to be used as a master alloy to incorporate the NiTi reinforcement in a larger batch of Sn. This process also allows the heavily concentrated NiTi reinforcement in pressure-infiltrated samples (~50 vol%) to be diluted down to any desired volume percentage as the application requires.

The growth of the cracks through the composites was noted to propagate through particulate–matrix interfaces whenever possible. This would imply that the bonding between the NiTi particles, both coated and uncoated, and the Sn–20% Bi matrix, needs to be improved. Figure 5.6 shows the routes of crack propagation in the uncoated NiTi reinforced Sn-20% Bi sample. While no fibers were directly observed spanning the crack, the fracture surface seen in Fig. 5.6b shows fibers and holes, indicating that fibers did span the crack, and were pulled out. An improvement in bonding may result in short fibers being able to close cracks.

Manuel and Olson (2007) synthesized a self-healing composite using an Sn–21Bi (wt%) alloy reinforced with 1% equiatomic NiTi SMA wires. The diameter of the wires used to prove this concept was 190.5 μm. The temperature of transformation of the wires was increased by aging treatment at 500°C. The interface between wires as-received and matrix was not strong; to improve the interface, wires were coated with gold. The uniform ductility of the self-healing composite alloy was increased 73% comparing with unreinforced matrix. To test the self-repairing property, the sample was tensile tested and healed at 169°C for 24 h; where the austenite transformation of the wires occurred. After partial melting of the matrix, and removing the heat, the matrix solidified and the crack sealed. The healing temperature was selected by simulation to assure that between 15 and 20% of the matrix around the crack is liquefied to provide good welding of the crack as a result of compressive forces generated by the phase transition of the SMA (Manuel 2007; Martinez-Lucci 2011).

Mg is an attractive option as a lightweight structural element due to its high specific strength. This metal has low ductility and poor toughness, which limits the use of Mg in engineering structural applications. On the other hand, Mg is considered a good candidate for the matrix in a self-healing alloy. Manuel (2007) studied Mg-based alloy and SMA TiNi wires with diameters of 190.5 μm. To increase the austenite temperature transformation, the Nitinol wires were annealed at 500°C for 3 h. Tensile test was performed to crack the composite and healed at 358°C.

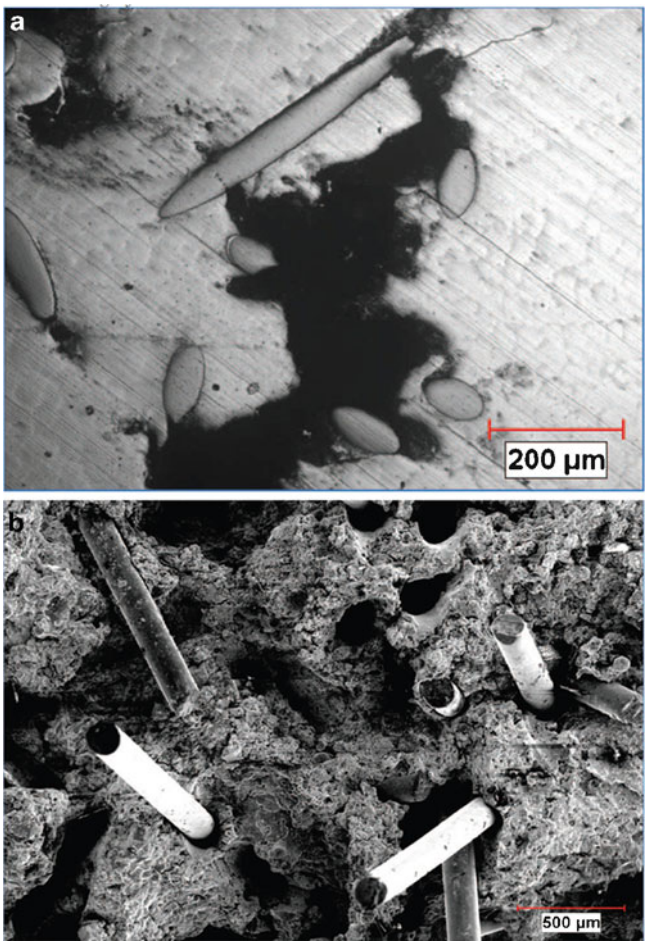

Fig. 5.6 (**a**) Optical microscopy of crack propagation in Sn–20% Bi reinforced with uncoated NiTi. Note that the path of the crack follows the interface between particles and the matrix. 50× magnification. (**b**) SEM Image of crack surface of NiTi short fiber reinforced Sn–20% Bi. Note the holes, indicating the location of fibers on the other crack surface that were pulled out (Ruzek 2009)

The research reported that the crack was partially closed and the damaged matrix Mg was not completely healed. The results from high performance alloy composites show the limitations of an Mg-based alloy not having the ability to weld to itself, and the restoring force not being sufficient to clamp the crack walls as it was displayed in the case of Sn–Bi self-healing composite alloy; which was a proof of the concept of this method. With suitable design of the composite using higher volume percentage of shape memory alloy fibers of optimum diameter, healing of the crack can be achieved in structural alloys including magnesium and aluminum.

5.5 Healing by Low Melting Point Alloy Contained in Hollow Reinforcement

The basic concept of low melting point reinforcement healing is quite similar to eutectic healing. It involves a structure that will partially melt at a given temperature, and provide a liquid healing agent that can flow into cracks to facilitate healing. However, the way that the low melting point reinforcement method accomplishes this is different. Instead of building a thermodynamically stable system that has a wide melting range, a low melting point reinforcement system contains two alloys that melt at different temperatures, including the high melting matrix and low melting healing agent contained in a hollow reinforcement. The low melting point alloy will melt first, then flow out of the hollow reinforcement which has cracked due to the crack in the matrix and then flow into any cracks or voids in the high melting point matrix. This concept was developed as a parallel in metals to the original work done in polymers by White (2001).

An advantage of a low melting point reinforcement healing is the addition of hollow reinforcement containers, which contain the low melting phase. A problem with the eutectic healing method is that any crack introduces an increase in volume so that even if healing does take place, the healing agent will leave a void where it came from, effectively forming a new void. In low melting point alloy contained in hollow reinforcement healing, these voids will be inside a hard hollow reinforcement of uniform size, and not likely to act as large stress concentrators. These hollow reinforcements could also strengthen the matrix. However, care must be taken to be sure that the hollow reinforcements will rupture to release healing agent when a crack approaches and contacts them. If the hollow reinforcement does not open to a crack, there is no way for the low melting point agent inside the hollow reinforcement to flow into the crack. Also, the low melting point healing agent must wet or react with the matrix and bond with the surface of the crack in order for healing to take place. A hollow ceramic reinforcement filled with low melting healing agent is shown in Fig. 5.7a; these were synthesized at UWM. and were then incorporated in higher melting metallic matrices to form composites (Fig. 5.7b).

Since partial melting of a single composition was not necessary for this system, commercially available solder alloys could be used. The higher temperature matrix alloy was Sn–0.7% Cu, which melts congruently at 226°C. The Sn–Bi eutectic alloy (Bi–42% Sn) was chosen as the low melting point healing agent since it has a low congruent melting temperature of 138°C. Before working with hollow reinforcements, work was done with just the high and low melting point alloys to ensure that wetting and healing would be possible. Rods of Sn–0.7% Cu were cast, and then a hole was bored down the length of the rod. This cavity was then filled with the Sn–Bi eutectic. A small notch, 350-μm wide, was cut into the side of the sample to represent a crack.

For hollow reinforcement, alumina balloons were used as containers of low melting point healing agent. For this work, bubbles with holes and cracks were used because a path was needed to fill the alumina bubbles with low melting Sn–Bi eutectic.

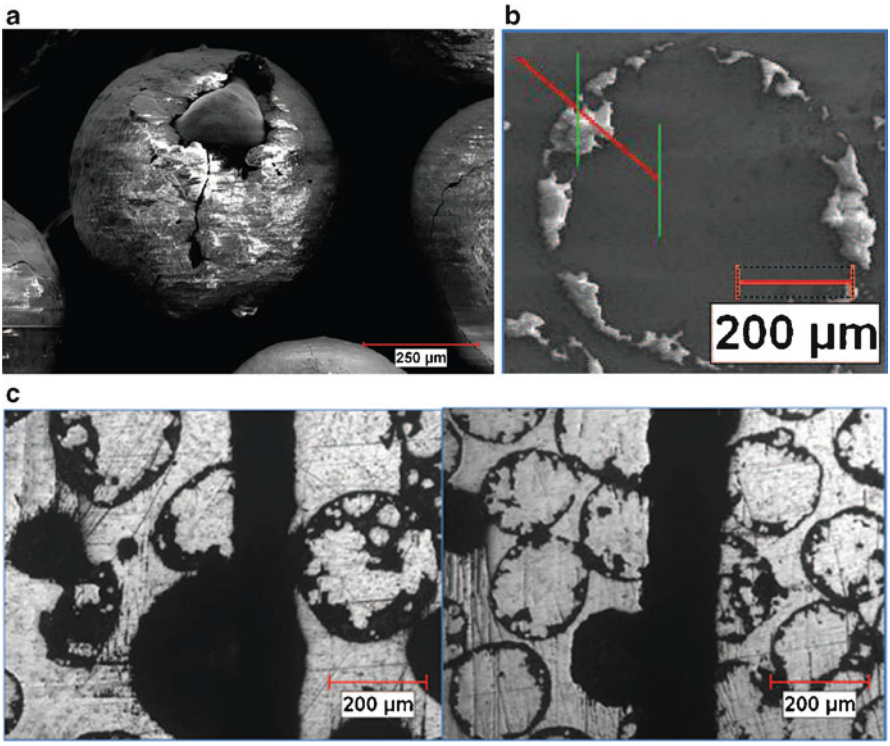

Fig. 5.7 (**a**) SEM image of an alumina balloon filled with Sn–Bi eutectic. Note the crack in the side, which allows the Sn–Bi eutectic to fill the balloon during infiltration and the Sn–Bi eutectic visible inside of the balloon. (**b**) SEM cross section of an alumina balloon filled with Sn–Bi eutectic composition in an Sn–0.7% Cu matrix. The *line* in the *upper left* is the path of the EDX line scan with two markers. (**c**) Optical microstructure of the large and small alumina balloons holding Sn–Bi eutectic in an Sn–0.7% Cu matrix after healing heat treatment. Both images are of 50× magnification (Ruzek 2009)

After the balloons had been sorted they were pressure infiltrated with Sn–Bi eutectic. Figure 5.7a shows an alumina balloon with a crack in the side to allow it to be filled with Sn–Bi eutectic (Ruzek 2009).

The alumina balloons were confirmed to be filled by measuring the bulk density. This was done by weighing a set volume of alumina balloons. The bulk density of the unfilled alumina balloons was 0.74 g cc^{-1} while the filled balloons had a density of 2.03 g cc^{-1}. These alumina balloons filled with Sn–Bi eutectic were then pressure infiltrated again with molten Sn–0.7% Cu, which entered the spaces between the balloons and solidified. This formed the final composite. The microstructure of this system was confirmed by SEM, and an EDX line scan. Figures 5.7b and 5.7c show a cross section of an alumina balloon filled with Sn–Bi eutectic in an Sn–0.7% Cu matrix. The line shows the path of the line scan. Figure 5.7 also shows a crack initiated in the composite. Optimization of these types of microstructures is needed to ensure that the healing liquid goes out of microballoons into the cracks (Fig. 5.13).

5.6 Precipitations of Supersaturated Solid Solution

The idea of this method is to use microscopic cracks or voids in the material as a nucleation point for precipitation of oversaturated, or underaged alloy. In underaged alloys solute atoms migrate to defects and voids, in effect "healing" them. This "healing" is on a nanometer scale, and is the natural process of age-hardening. Van der Zwaag and co-workers investigated this method, which provides self-healing in voids; however, this does not have the ability to heal large cracks. When an alloy is cooled from high temperature, it becomes supersaturated, or metastable. Figure 5.8 shows the model phase diagram of an alloy capable of precipitation (Lumley 2007). A micrograph of dynamic precipitation of an underaged Al–Cu–Mg–Ag alloy following 500-h creep at 300 MPa and 150°C is shown in Fig. 5.9. Bands of dynamically precipitated particles are formed and associated with dislocations, examples of the dynamically precipitated phase are marked "A." Fig. 5.10 shows an aluminum copper alloy that was first under-aged and then tested in such a way as to produce a crack. Further ageing heat treatments resulted in healing of the crack. Fig. 5.11 shows the sequence of healing that occurs with this method.

He et al. (He 2010a) have reported that creep damage can be self-healed in boron- and copper-containing austenitic stainless steels by dynamic precipitation of these elements from the supersaturated matrix. In their studies creep lifetime was significantly improved when precipitates partially filled the nanoscale open-volume defects and thereby prevented further growth. They compared the precipitation kinetics in deformed Fe-Cu and Fe-Cu-B-N alloys by positron annihilation spectroscopy in samples that were solution-treated at 850 °C for 1 h in evacuated silica tubes filled with argon gas and quenched in water to create a supersaturated state. Samples aged at 550 °C were compared with samples annealed at 700 °C for 2 h and cooled at a very slow rate of 20 °C/h in a vacuum furnace in order to deplete the

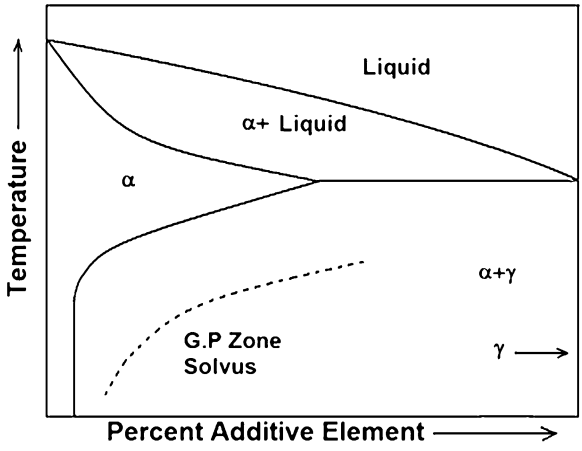

Fig. 5.8 Model phase diagram of an alloy capable for precipitation (Lumley 2007)

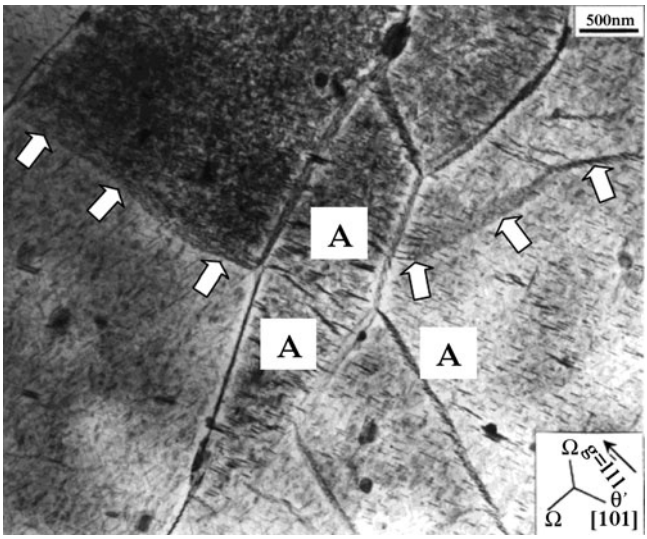

Fig. 5.9 Dynamic precipitation of an underaged Al–Cu–Mg–Ag alloy following 500-h creep at 300 MPa and 150°C (Lumley 2007)

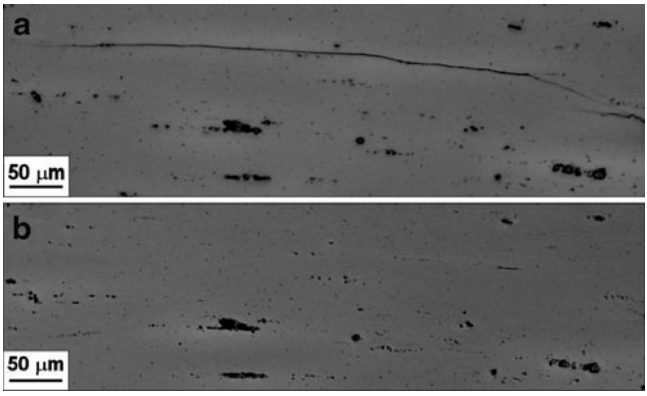

Fig. 5.10 Micrographs of an Al-Cu AA2001 alloy specimen underaged at 180°C for 5 hours and tested. **(a)** Hairline crack present **(b)** crack has been healed by ageing for an additional 10 hours. (Djugum et al. 2009)

alloys of fine precipitates. Part of the samples was subjected to tensile deformation up to a strain of 8%.

They report it is difficult to form open-volume defects in iron by thermal processes and that in all the investigated alloys predominantly dislocations were generated by tensile deformation. These results suggest that open-volume defects introduced by plastic deformation in pure Fe can be recovered almost completely by self-diffusion of Fe atoms during the aging step and that this behavior is independent

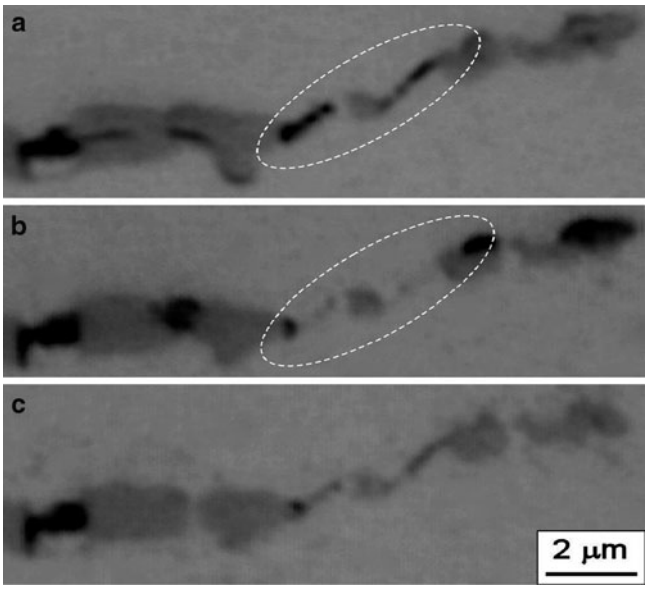

Fig. 5.11 Micrographs of an Al-Cu AA2001 alloy specimen underaged at 180°C for 4 hours and tensile tested. **(a)** cracks at the sites of two fractured Al-Cu intermatallic compounds, **(b)** crack closure after further ageing **(c)** pore fragmentation. (Djugum et al. 2009)

of the heat treatment before testing. Their tests on Fe-Cu alloys indicated that the Cu precipitation is promoted by the presence of dislocations introduced by predeformation and that the precipitation kinetics of the Fe-Cu-B-N alloy is faster than that of the Fe-Cu alloy.

In related studies (He 2010b) they suggested the mechanisms responsible for this behavior. For the Fe-Cu alloy, Cu has a tendency to segregate to open volume defects while simultaneously precipitating within the matrix, leading to a precipitation strengthening of the alloy until peak aging was reached. For the Fe-Cu-B-N alloy, the addition of boron and nitrogen accelerates the formation of spherical Cu precipitates within the matrix, but reduced the Cu precipitation at defects in the deformed samples. From these sudies they concluded that in Fe-Cu-B-N alloys self-healing will initially take place by the formation of BN precipitates, and may be assisted by copper precipitation when larger creep cavities are formed.

5.7 Experimental Studies and Simulation with Account for the Effects of Gravity and Capillarity

Among the factors affecting the efficiency of the liquid-based healing, such as reinforcement with a low melting point solder, is the ability of the healing liquid to propagate and fill the crack. This involves the capillary forces and gravity,

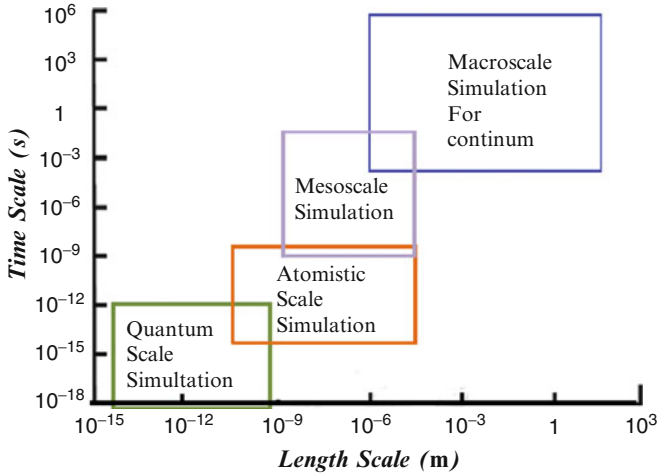

Fig. 5.12 The scales of simulations: the length scale vs. time scale (Martinez-Lucci 2011)

or weight of the liquid. In general, capillary forces prevail over gravity at the length scales smaller than the capillary length

$$l_c = \sqrt{\frac{\gamma}{\rho g}}, \tag{5.4}$$

where γ is the relevant surface tension, ρ is the density of liquid, and g is the gravity constant. If the contact angle between the liquid healing agent and a cracked solid surface is less than 90°, the liquid healing agent is said to "wet" the solid surface of the crack and it will fill the void. When the liquid healing agent does not wet the solid wall, the contact angle will be greater than 90°, and the shape of the liquid front is concave. In the absence of pressure, the healing liquid only penetrates into the crack if it wets the crack.

CFD may be used for simulation of self-healing provided certain specifications are met. Figure 5.12 shows the scale of simulation, namely, length vs. time scale. The scale of self-healing is macro and micro. The Knudsen number can be calculated to determine the applicability of continuum model. The Knudsen number is defined as the relation of the mean free path and the characteristic length of the system:

$$Kn = \frac{\lambda}{L}. \tag{5.5}$$

The Knudsen number indicates whether statistical mechanics or the continuum mechanics formulation of fluid dynamics should be used: If the Knudsen number is near or greater than one, the mean free path of a molecule is comparable to a length scale of the problem, and the continuum assumption of fluid mechanics is no longer

a good approximation, and therefore, statistical methods must be used. For an ideal gas at temperature T and pressure P

$$Kn = \frac{kT}{\sqrt{2}\pi d^2 PL}, \tag{5.6}$$

where k is the Boltzmann constant and d is the molecular diameter. For example, if the crack size is $L = 10$ μm and $\lambda = 68$ nm and, the Knudsen number is calculated for air and the value is $Kn = 0.0068$, Navier–Stoke equation with no-slip condition is valid in the domain, thus CFD simulations may be used. Martinez-Lucci (2011) performed computational fluid dynamics (CFD) simulations of the healing process with a low melting point reinforcement. His observations are summarized below; his simulations try to predict if healing fluid will flow from reservoirs into the cracks for different crack orientations and crack dimensions. In some cases the simulations have been validated by simple model experiments suggesting that CFD can be a useful tool in designing microstructures which can exhibit healing.

The following materials were synthesized at the University of Wisconsin-Milwaukee, with their properties summarized in Table 5.1.

1. 99.3Sn0.7Cu matrix and 42Sn58Bi healing agent encapsulated in hollow alumina microballoons. Alumina microballoons filled with 42Sn58Bi low melting temperature solder were embedded in high melting temperature 99.3Sn0.7Cu solder. Before the low melting alloy could be injected into the balloons, the balloons were first separated by the same size using a sifter. Then the balloons were sunk under water to separate the cracked from the sealed balloons. The cracked balloons were then infiltrated with low melting temperature eutectic Sn–Bi healing agent by pressure infiltration. Figure 5.13 shows the result of a model self-healing experiment in comparison with the simulation. Both experimental and simulation results show that the crack was not completely healed; this indicates that CFD based simulation can help predict the configuration of cracks which will not heal and require optimization of microstructure.
2. Pure Al matrix and Al–Zn healing alloy. Figure 5.14a shows that liquid healing agent can flow from the reservoir to the crack cavity, when temperature was equal to the melting temperature of the healing agent for crack orientated at 90°; CFD shows that this event occurs at 162 s after the initiation of the healing process. Figure 5.14b shows comparison of the experimental and simulation results. The simulation predicted the ability of Zn to flow into the crack when crack is oriented at 90°. The experimental result validates this prediction, since the liquid flowed and filled the crack. Figure 5.14c shows the comparison of experimental and simulation results for Zn/Al healing agent–matrix combination, when the crack was oriented at 180° (against gravity) and the crack-diameter was 10% of the container diameter. The numerical simulation predicted that the crack was not filled and the matrix was not healed, and the experimental result validates the simulations; healing

Table 5.1 Properties of healing agent used in simulations with different matrices (Martinez-Lucci 2011)

Healing agent	42Sn–58Bi	Zn	Sn	Bi	In	Dicyclopentadiene
Contact angle between healing agent and matrix	80	50	30	45	70	54.7
Surface tension healing agent and matrix, ($N\ m^{-1}$)	0.574	0.755	0.680	0.477	0.440	0.0004187
Density healing agent	960	Temperature dependent				980
Solidus temperature of healing agent (K)	411	692	505	544	429	–
Liquidus temperature of healing agent (K)	411	692	505	544	429	–
Viscosity of healing agent ($kg\ ms^{-1}$)	0.001052	0.000385	0.000128	0.000165	0.000180	0.000878
Coefficient of thermal expansion of healing agent ($\mu m\ mK^{-1}$)	20	37.9	40	13	33	–
Molecular weight of healing agent ($g\ mol^{-1}$)	–	30	50	83	49	132.2

was not displayed. Figure 5.14d shows the experimental and simulation results for Zn/Al composite when the crack is oriented at 0° (toward gravity) and its diameter is 10% of the container diameter. Both results show that liquid healing agent flowed inside the crack and matrix was healed. The experimental results validate the simulations; healing was not displayed. At the healing temperature, the experimental result showed that there is no visible reaction at the interface between the matrix and healing agent. The hair line gap is observed at the interface (Fig. 5.14d). Healing temperature is an important parameter to heal the composites as well as promote a reaction between the liquid healing agent and the solid matrix.

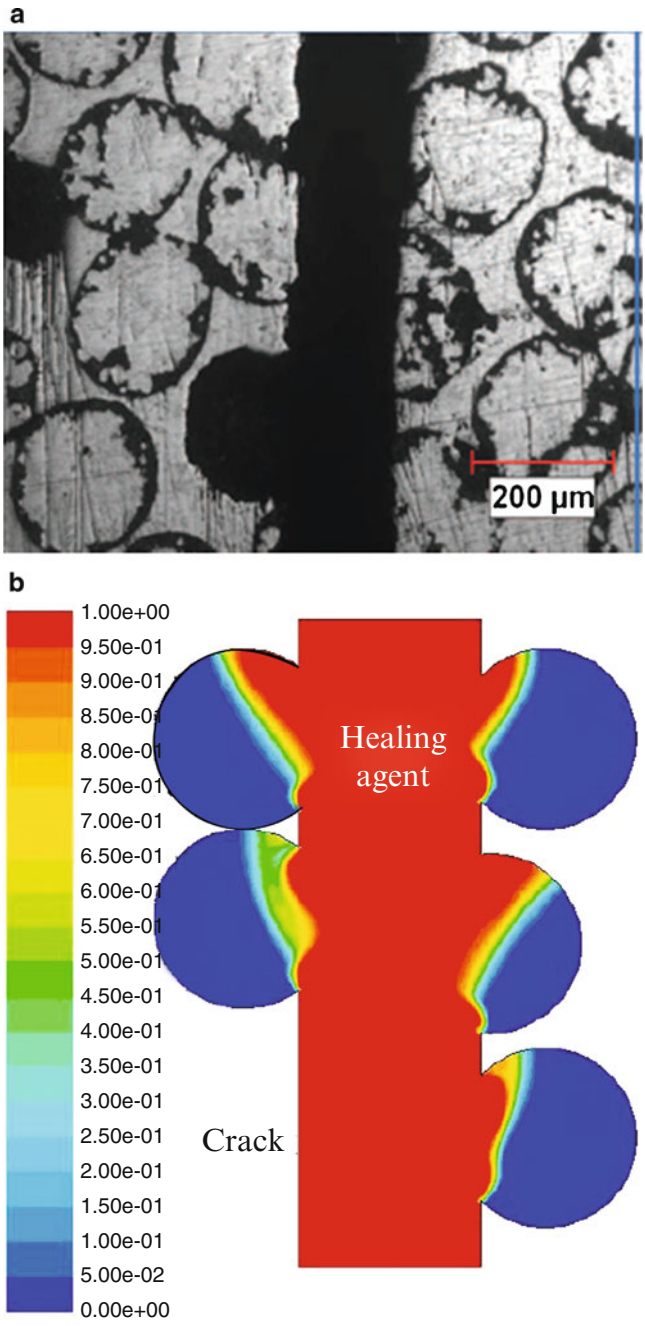

Fig. 5.13 (**a**) Self-healing Sn0.7Cu solder composite reinforced with alumina microspheres containing Sn58Bi. (**b**) Simulation results after the healing event (Martinez-Lucci 2011)

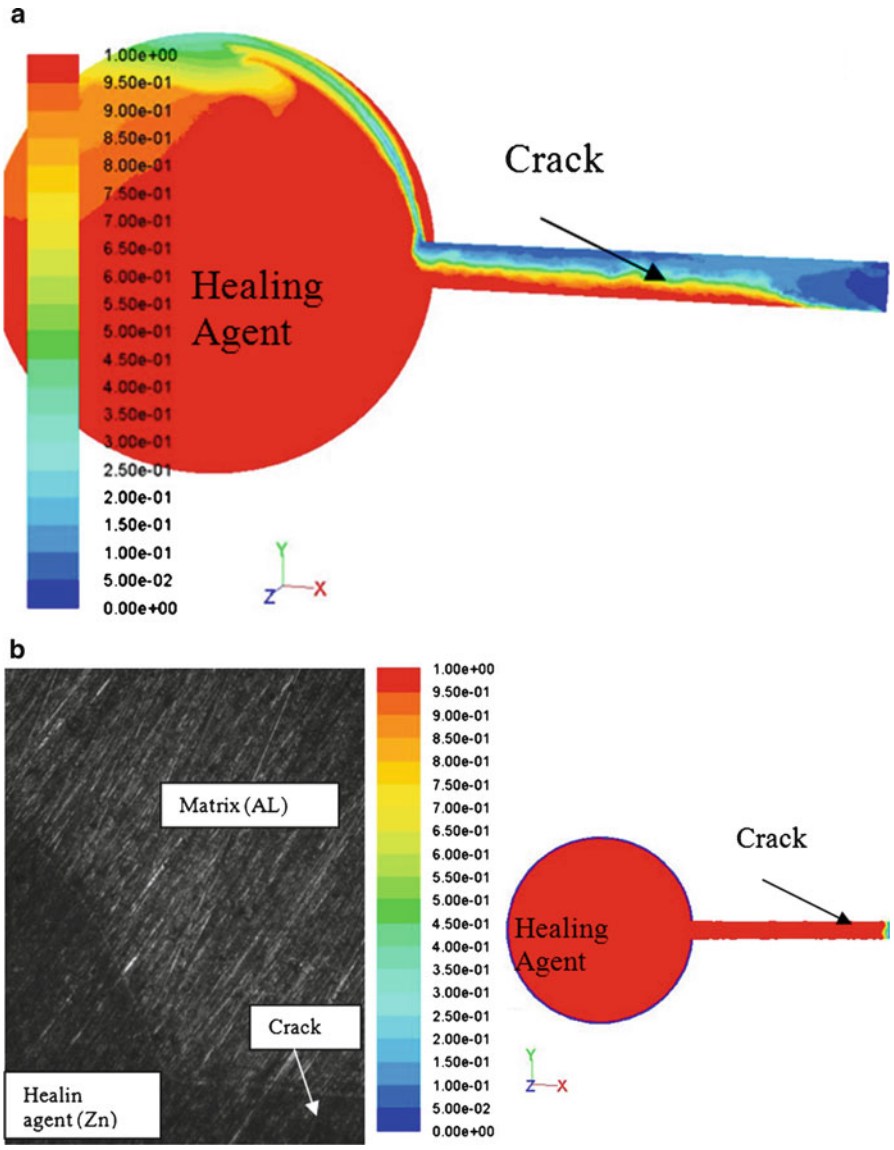

Fig. 5.14 (**a**) Liquid healing agent for the crack oriented at 90°. (**b**) Experimental and simulation results, Zn/Al healing alloy for the crack at 90°. (**c**) The crack orientation against gravity. (**d**) Crack orientation at 0° (Martinez-Lucci 2011)

3. Aluminum Matrix-Tin healing agent: For crack of 10% of the diameter at 180°. The tin healing agent volume expansion is about 6% percent of its original volume. Figure 5.15 shows the comparison of the experimental and simulation results. The contact angle of liquid tin on aluminum substrate is 30°; this is a

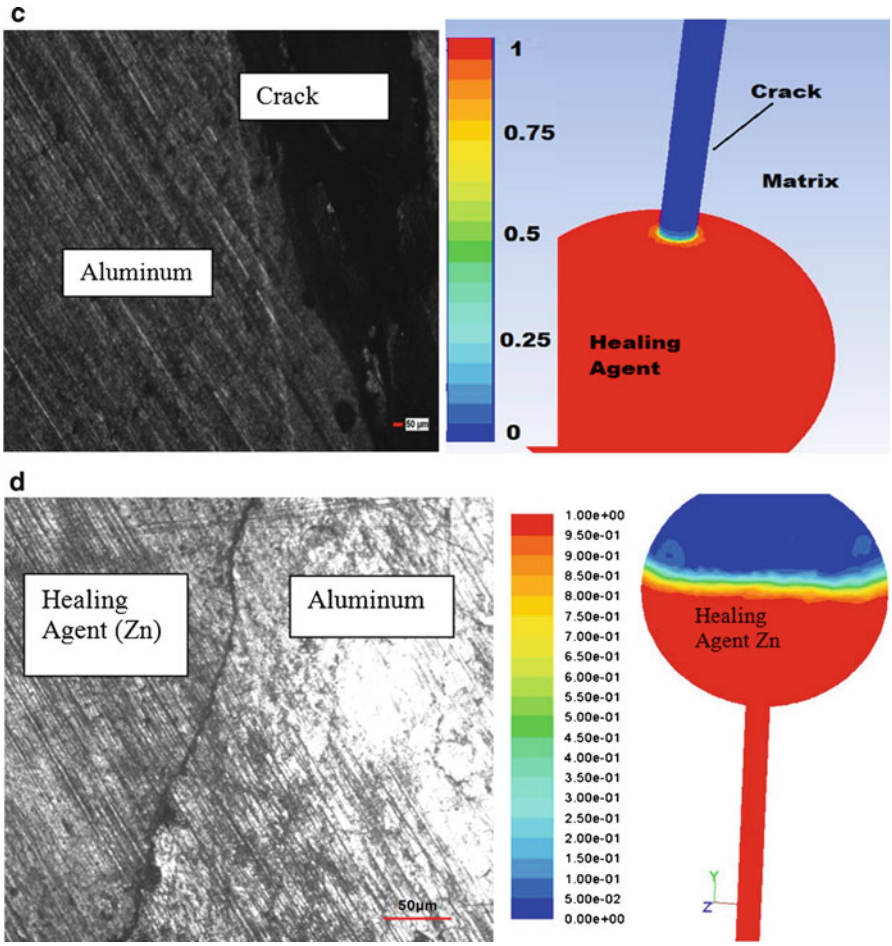

Fig. 5.14 (continued)

wetting system with low surface energy. The healing agent partially filled the crack; however, the interface between these two metals was weak. There was no bond and apparently no reaction occurred. Matrix was not healed and the capillary force was insufficient to transport the healing liquid metal from the reservoir to the entire length of the crack cavity.

4. Aluminum Matrix-Tin healing alloy: For crack diameter of 20% of the container diameter and oriented at 90°. The results are shown in Fig. 5.16a. The healing temperature was set up at 611 K for both the experiment and the simulation to compare the results. The process was conducted for 30 min, after which the sample was cooled down to the room temperature inside the furnace. Both experimental and numerical results exhibited that healing occurred in the matrix and the healing liquid completely filled the crack.

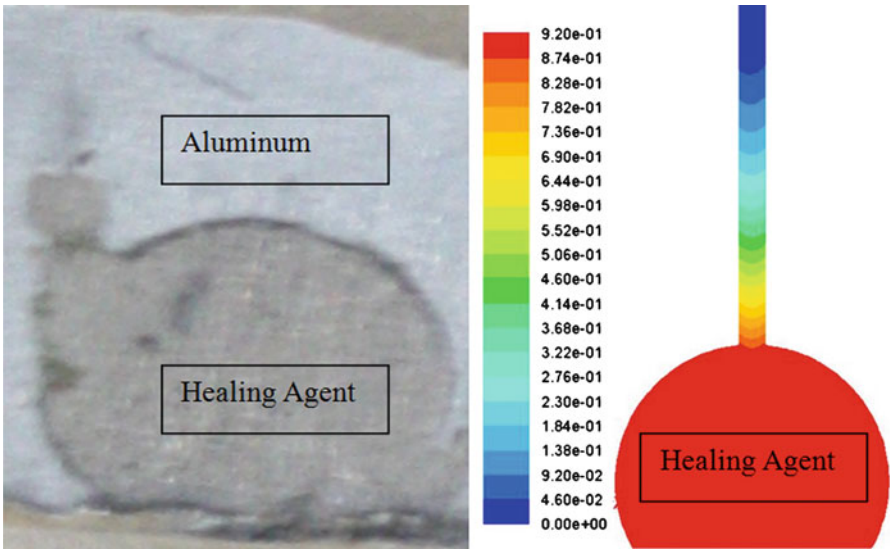

Fig. 5.15 Results from the experiment and numerical simulation of Sn/Al self-healing composite when crack was oriented against gravity and its diameter is 10% of reinforcement diameter (Martinez-Lucci 2011)

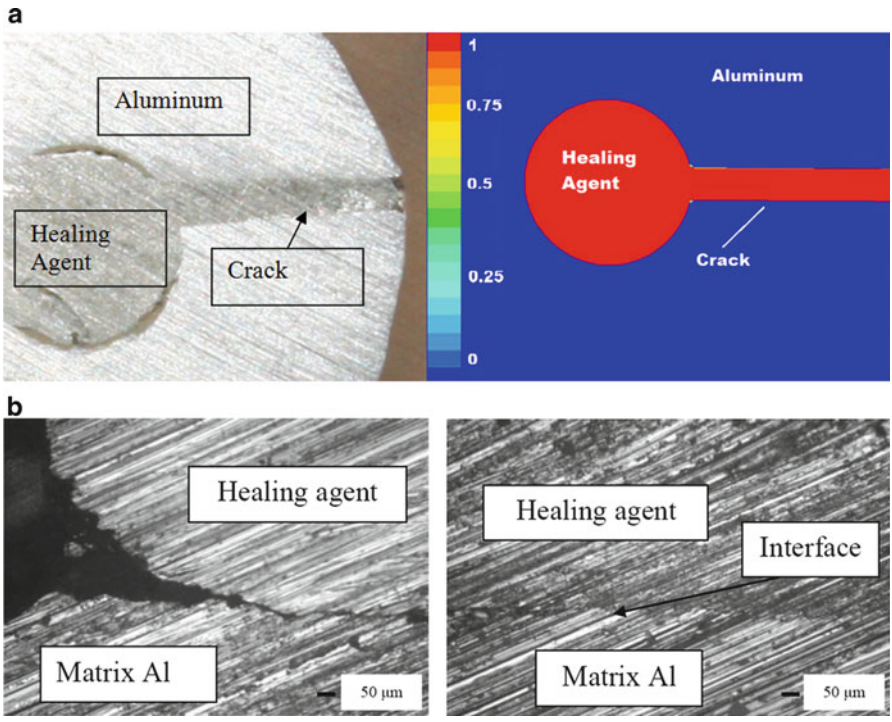

Fig. 5.16 (**a**) Experiment and simulation results for Sn/Al system for the crack orientation at 90° and diameter of 20% of container diameter. (**b**) The interface between the Al matrix and Sn healing agent (Martinez-Lucci 2011)

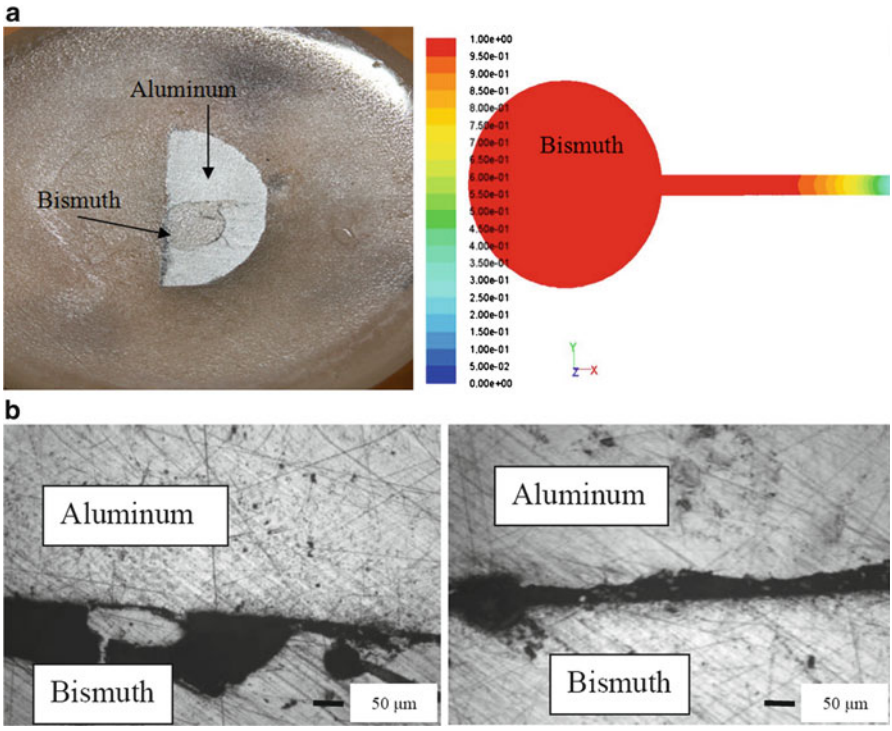

Fig. 5.17 (**a**) Experimental and simulation results after healing. (**b**) SEM images showing a weak interface between the matrix and the healing agent

The experimental result showed that the matrix and healing agent interface is weak and a metallurgical bond has not formed, and a dissolution reaction is not observed. Figure 5.16b shows the optical macrostructure of the interface between matrix and healing agent after the process of healing the composite. Note that the bonding was poor and the crack could propagate through the matrix.

5. Aluminum Matrix-Bismuth healing alloy. This is a strongly wetting system with the contact angle of 45°. The Bismuth coefficient of shrinkage is negative 3.32%; this means that bismuth's volume expands about 3.32% when it solidifies. Figure 5.17a displays the aluminum matrix with bismuth as healing agent after the process of healing. Experimental and simulation results showed that the liquid metal flowed through the crack and filled, for crack was oriented at 90° and a crack with the dimension of 10% of the container's diameter. Both experimental and simulation results showed that the matrix was healed; however the interface between aluminum and bismuth is weak and reaction is not displayed in experimental results. The optical microstructure of the interface between matrix (Al) and healing agent (Bi) is displayed in Fig. 5.17b.

6. Tin matrix-Indium healing agent. This system is not strongly wetting with the contact angle of 70°. Another parameter needed to simulate the healing process of the composite is the contact angle between healing agent and capsule, which was assumed to be 125°. Liquid metal must sufficiently expand to overcome the contact resistance of the container walls in order to penetrate into the crack cavity. Pressure infiltration was performed to infiltrate pure In inside a microtube. Figure 5.18a shows the self-healing composite. The liquid indium infiltrated the entire length of the microtube. To validate the simulations, the sample was cracked by drilling a hole on the surface of the composite then heat was applied above the melting temperature of indium to analyze the fluidity of indium in crack walls and validate the simulations results.

   Figure 5.18b shows the comparison and validation of simulation results when the crack diameter is 20% of diameter container, and crack orientation is at 90°. The simulation has predicted that the healing agent can fill the crack; this is validated by the experimental results, both have shown that the liquid was filled and matrix healed. Figure 5.18c shows the result from experiment and simulation when a crack diameter is 20% of the diameter of the container and oriented at 180°. It is observed that in both cases, the liquid remained inside the container and the crack was not filled, this implies that the matrix was not healed, and self-healing was not displayed.

   Figure 5.18d shows the comparison of experiment and simulations results, for a crack diameter 20% of the container diameter and oriented toward gravity. The result from simulation agrees with that of the experiment. In the results, the

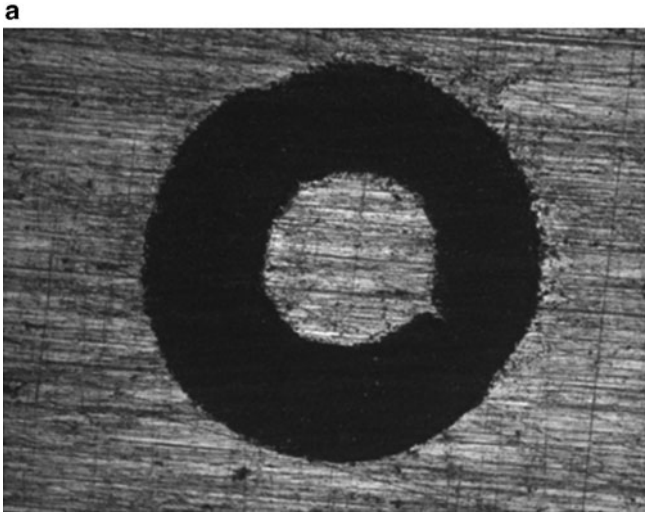

Fig. 5.18 (**a**) Optical microstructure of the microtube infiltrated with indium embedded into the tin matrix. (**b**) Experimental result and simulation for the crack orientation at 90°; simulation result agrees with the result from experiment; (**c**) against gravity, healing is not displayed; (**d**) toward gravity, healing was displayed (Martinez-Lucci 2011)

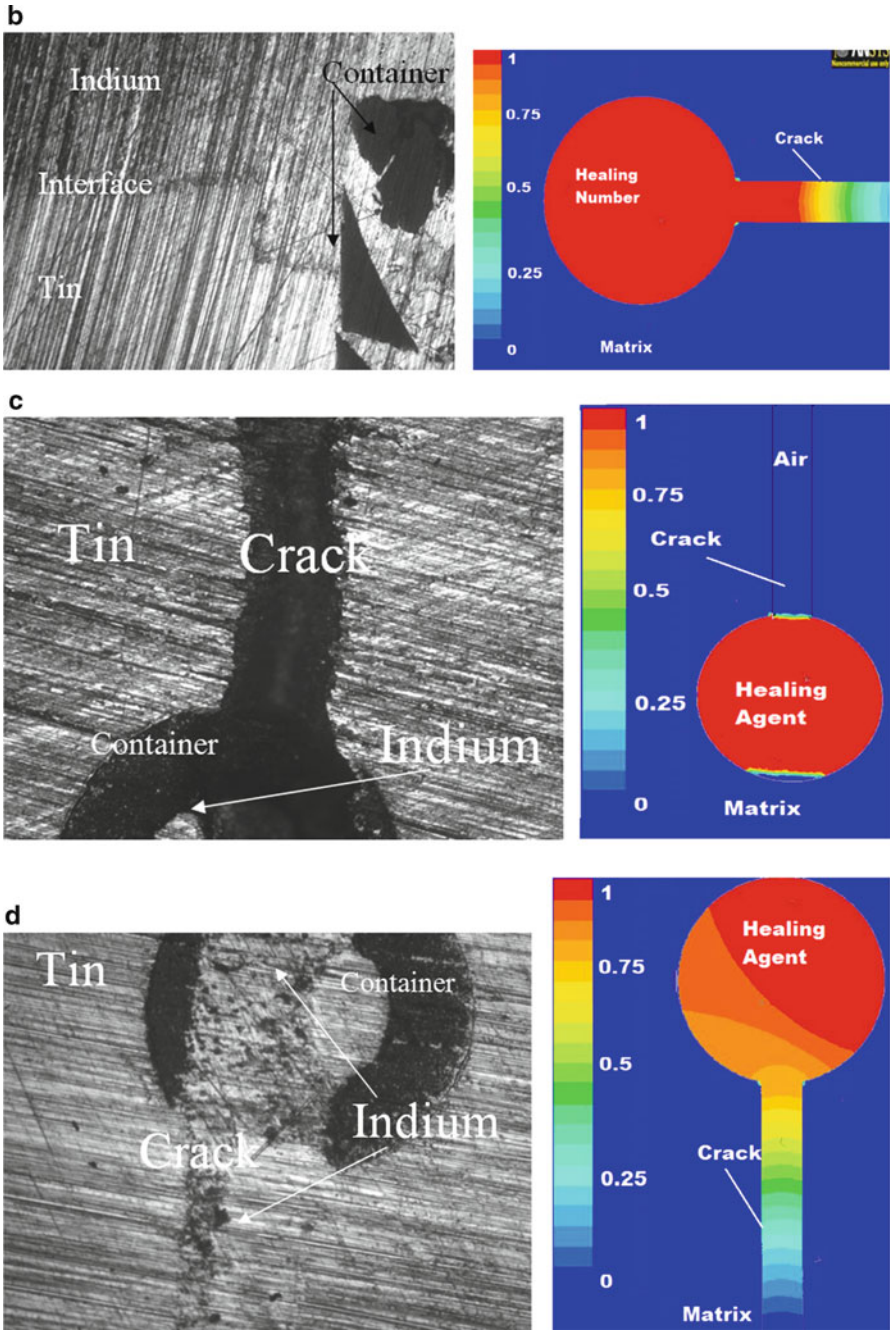

Fig. 5.18 (continued)

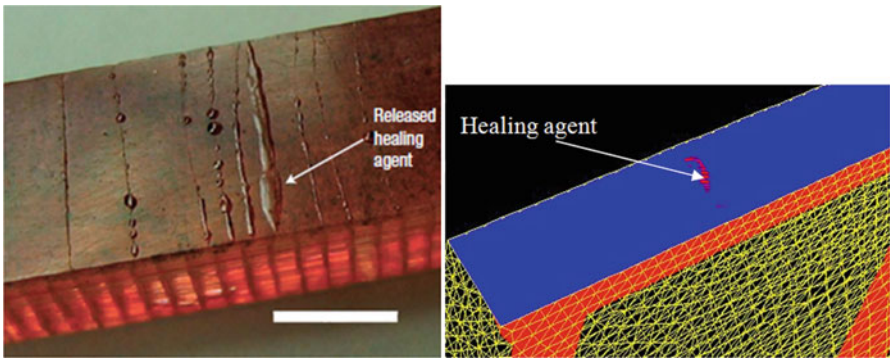

Fig. 5.19 Self-healing polymer vascular network result, healing is observed (Martinez-Lucci 2011)

Table 5.2 Effect of crack orientation on healing (Martinez-Lucci 2011)

Matrix/healing agent	Healing temperature (K)	Crack orientation (°)	Healing observed
Al/Zn	811	0	Yes
		90	yes
		180	No
Al/Sn	611	0	Yes
		90	Yes
		180	Possible
Al/Bi	600	0	Yes
		90	Yes
		180	No
Sn/In	480	0	Yes
		90	yes
		180	No
Sn0.7Cu/Sn38Bi	480	0	Possible
Epoxy/DCPD	300	180	Yes

liquid healing agent has flowed out from the container and filled the crack cavity; both simulation and experiment have displayed healing of the matrix.

7. Epoxy matrix–dicyclopentadiene healing agent composite. This material was studied for comparison with metallic healing agents. The composite consists of epoxy matrix and dicyclopentadiene healing agent. Figure 5.19 shows result from experiment when the 200-μm diameter crack was against gravity. Healing was observed in this case. In general, the results of these tests showed that whether healing takes place or not depends on the orientation of the crack (Table 5.2).
8. Several additional specimens were studied, and in particular, a composite made of an aluminum alloy matrix with ceramic microtubes as reinforcements that encapsulated a lower melting point alloy solder (the healing agent) (Fig. 5.20).

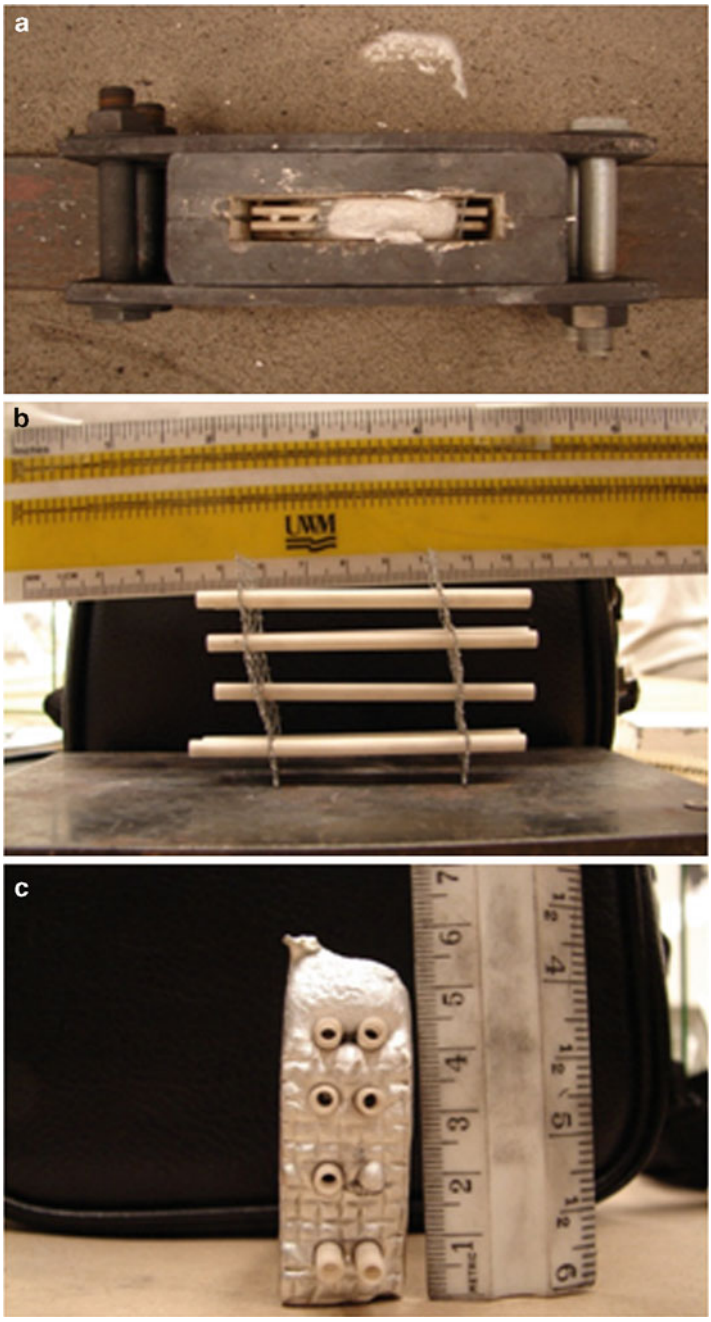

Fig. 5.20 (**a**) Mold and casting. (**b**) Side view of the tubes placed in the mesh before infiltration of matrix. (**c**) Front view of the healing composite after casting aluminum alloy around microtubes.

A specimen containing a single empty tube in its cross-section was removed from the casting and the hollow tube embedded in the aluminum alloy matrix was then filled with solder. A crack was then made and the specimen was heated above the melting temperature of the solder. Figure 5.21a shows a poor bond between the aluminum and the solder; however, it was observed that the contact and bond between the aluminum matrix and the alumina microtube reinforcement was quite good with the absence of shrinkage, and there are no micro-cracks at the boundary between the tube and the matrix 5.21b. Figure 5.21c and d show the partial filling of the crack in this sample.

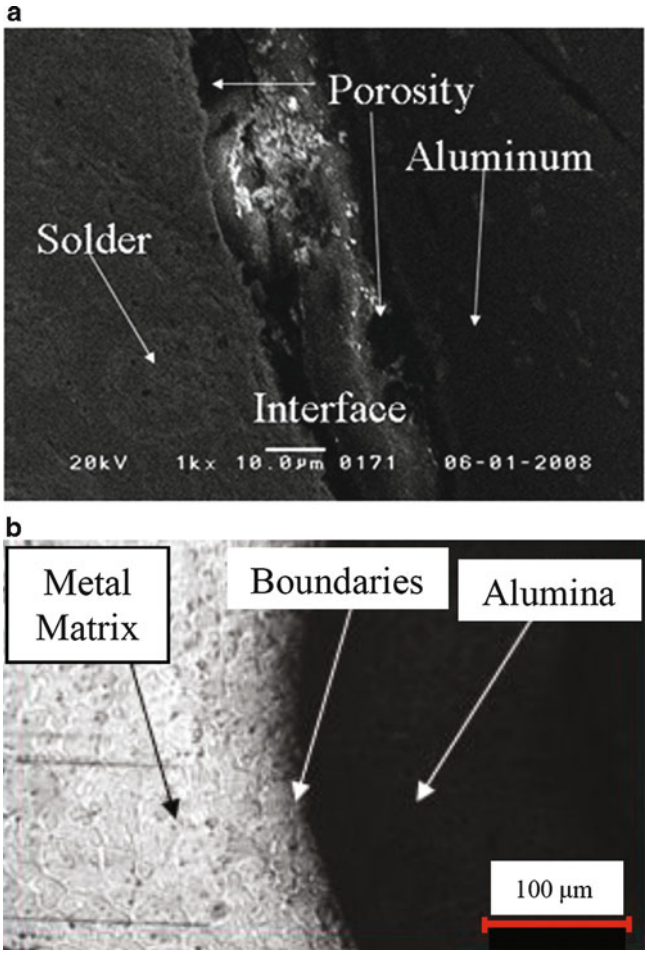

Fig. 5.21 (**a**) Scanning electron microscope image of the interface healing agent and metal matrix alloy, porosity and poor bond are shown, (**b**) Microstructure of the interface between aluminum and alumina microtube and (**c**) after healing sample; crack was partially sealed due to non-wetting system. (**d**) Scanning electron microscope image of aluminum and solder interface and aluminum and alumina interface (Martinez-Lucci 2011)

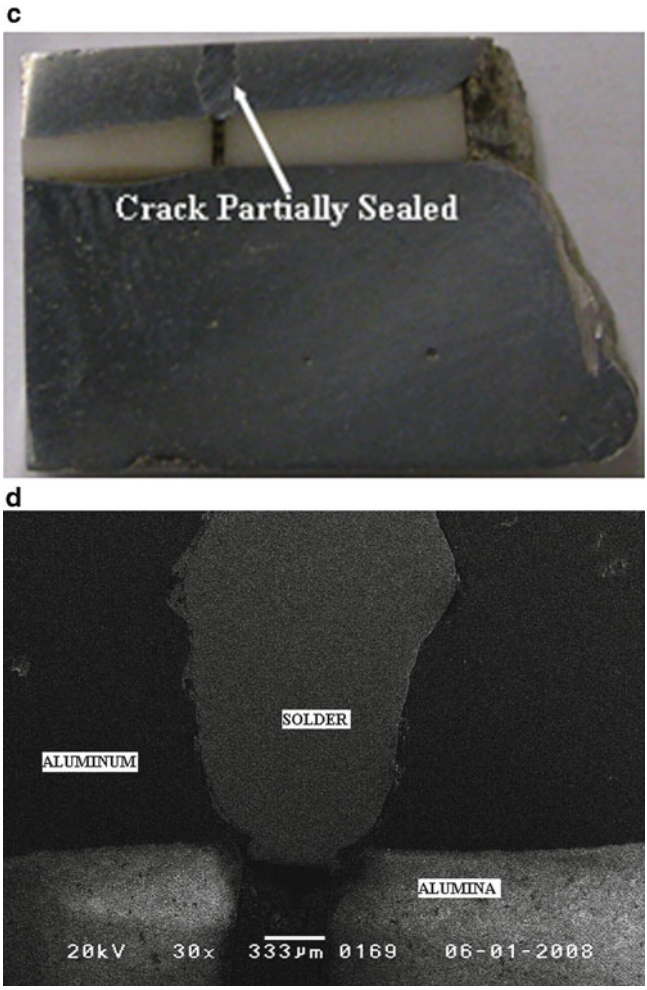

Fig. 5.21 (continued)

9. Aluminum Al206 as a matrix, hollow quartz tubes as the reinforcement filled with aluminum brazing alloy Al802 (Fig. 5.22). The melting point of the brazing alloy Al802 is almost half of that of the matrix, which facilitates selection of healing temperature. The quartz tubes were placed into a mold. The mold was preheated using a torch, and the aluminum alloy Al206 was then poured into the mold around the quartz tube. A self-healing composite sample was obtained as is shown in Fig. 5.22a, b. After that, the crack was drilled on the aluminum surface as is observed in Fig. 5.22c, then the composite was placed inside furnace and the temperature was set to 425°C, the temperature was gradually decreased until 25°C. The result after healing the aluminum-brazing aluminum alloy system is shown in Figs. 5.23 and 5.24. The healing

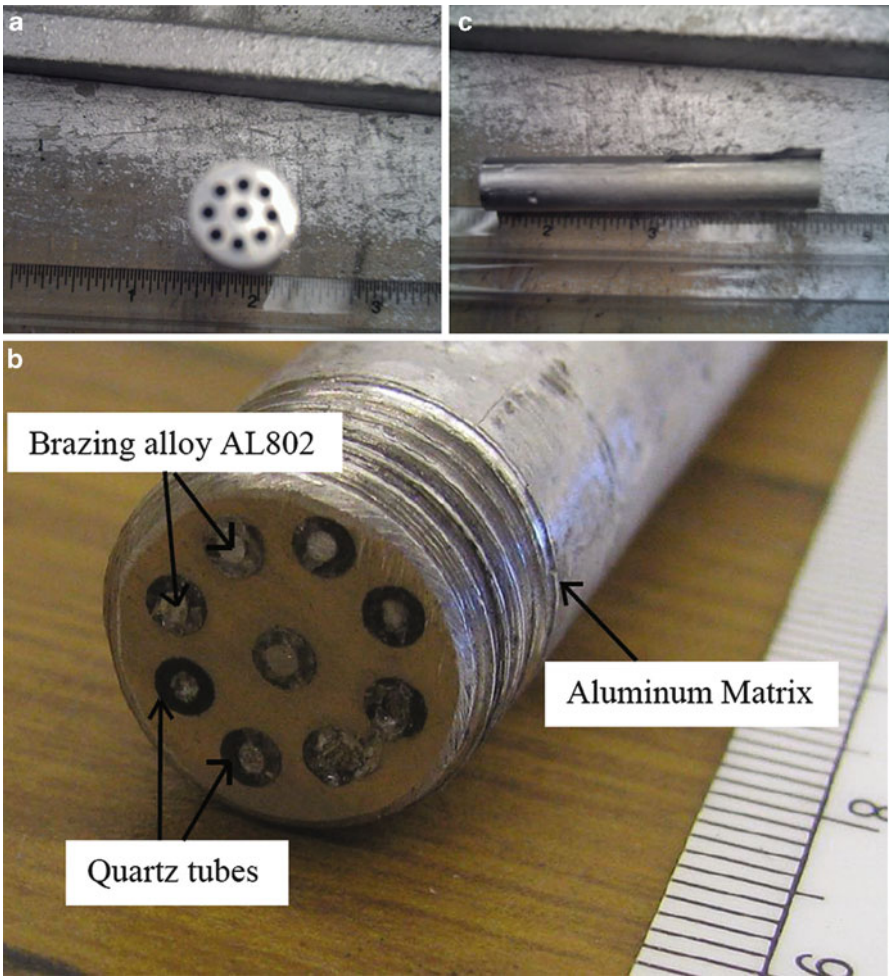

Fig. 5.22 (**a**) Aluminum matrix composite front view. (**b**) Aluminum composite with quartz tubes infiltrated with brazing alloy. (**c**) Damaged aluminum matrix composite side view (Martinez-Lucci 2011)

agent flowed inside the crack and it appears that there has been a reaction between aluminum and healing agent creating a strong bond at the interface. This makes the brazing alloy a potential candidate to heal aluminum matrix.

10. Sn0.7Cu/Sn58Bi System. The matrix solder was 99.3% Sn–0.7% Cu, which melts at 499 K. A cylinder of this solder was cast and a 4-mm hole was machined down the length of this cylinder and was filled in its cavities with a low melting point solder, 42% Sn–58% Bi, which melts at 411 K. By raising the sample temperature to a point between 411 and 499 K, the inner solder would melt, whereas the outer solder would remain solid. Then the sample was cut

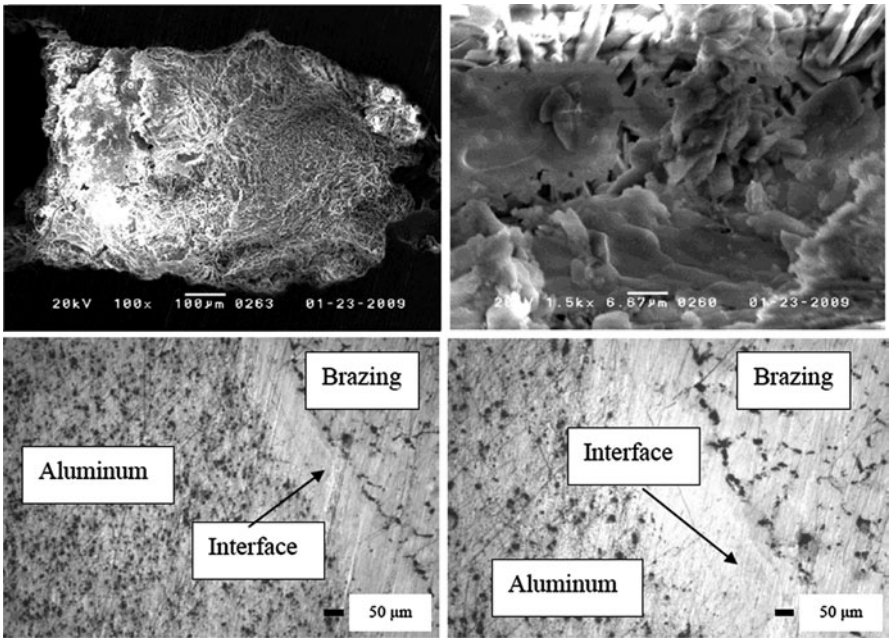

Fig. 5.23 Interface between aluminum and brazing alloy when crack was oriented at 90° (Martinez-Lucci 2011)

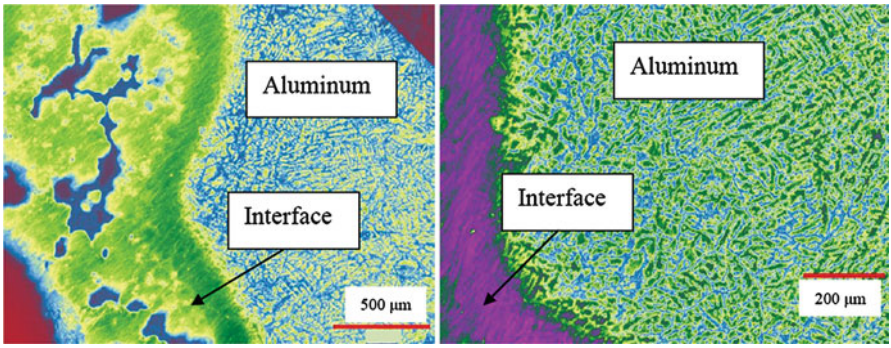

Fig. 5.24 The interface between aluminum and brazing alloy when crack was oriented toward gravity

into two test bars. The purpose of the experiment was to study the effect of gravity on the flow of the liquid healing agent into a crack. One test bar had a 1-mm hole drilled from the top, the other had a hole from the bottom; both holes pierced the internal area of Sn–Bi alloy. In this case, the Sn-Bi flowed into the hole and sealed it only when the hole was oriented toward gravity.

5.8 Summary

To summarize, experiments and simulations with metallic self-healing materials, can use various principles of healing, such as precipitation from supersaturated solid solution, embedding of low-melting temperature alloy or solder in the matrix within hollow reinforcements or in eutectic pockets, and incorporation of SMA fibers and particles in the matrix. Current results show that these methods are feasible; however, numerous obstacles must be overcome before robust self-healing metallic material can be synthesized with at least the same extent of healing as that demonstrated by polymer-based materials. Among these obstacles are surface tension, capillarity, and viscous resistance to flow of the healing liquid, which prevent the healing agent from entering the crack, bonding between healing SMA wires and matrices, affect the adequacy of clamping forces exerted by SMA wires, and affect the availability of liquid alloy to seal the crack.

Chapter 1
Introduction

In the introduction we provide an overview of scientific disciplines and research areas that are relevant to the multidisciplinary topic of the book: self-healing materials, surface science and tribology, nonequilibrium thermodynamics, self-organization during friction, nonlinear effects in friction, composite materials, and biomimetics. We introduce basic concepts and definitions that are used throughout this book.

1.1 Self-Healing in Materials Science and Engineering

Engineering materials are usually divided into several classes according to their chemical structure and properties, such as metals, polymers, ceramics, and their composites. The physical properties of metals are determined by strong nondirectional metallic bonds between their atoms, which give them a combination of strength and formability by plastic deformation as well as a constant value of stiffness. The properties of ceramic materials are determined by strong directional ionic–covalent bonds that result in high stiffness, temperature-resistance, and brittleness. The properties of polymers are determined by two types of bonds: strong covalent bonds in the polymer chain, and weak sacrificial bonds between different chains or different parts of the same chain (Zwaag 2009). In composite materials, at least two materials from different classes are used to obtain a set of properties which is difficult to obtain when only one class of materials is used. One material usually serves as a matrix that holds the material together, and the other is a reinforcement that gives special desired properties to the composite.

The common feature of most engineering materials is that they tend to irreversibly deteriorate with time due to tear and wear, fatigue, creep, brittle fracture and formation of cracks, corrosion, erosion, change of chemical structure, and so on. On the other hand, biological tissues and materials in living nature often have the ability to repair minor and moderate damage due to their ability for healing and regeneration. The biological mechanisms of healing and regeneration are complex

M. Nosonovsky and P.K. Rohatgi, *Biomimetics in Materials Science: Self-Healing, Self-Lubricating, and Self-Cleaning Materials*, Springer Series in Materials Science 152,
DOI 10.1007/978-1-4614-0926-7_1,

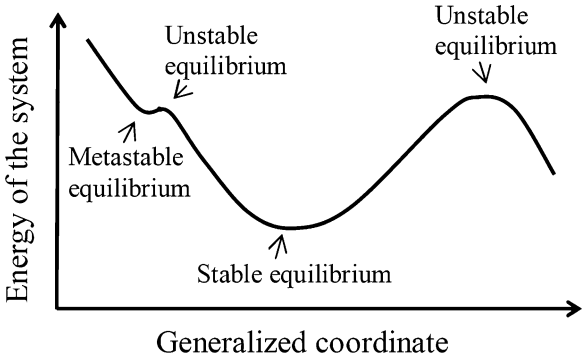

Fig. 1.1 A fragile metastable equilibrium is separated by a small energy barrier. When deterioration (e.g., cracking) occurs, the system leaves the metastable state

and lie beyond the scope of this book. However, in the 1990s a new field of artificial self-healing materials has emerged. These materials, inspired by the ability for self-healing in biological objects, are designed in such a way that they include mechanisms that can at least partially repair damage, such as voids and cracks, and partially or completely restore macroscopic material properties. Usually, a healing agent (often a liquid) is stored in the matrix of the material and when a cavity (a crack or void) is formed, it fills the cavity and closes it due to a chemical reaction or a phase transition (e.g., solidification). The healing can be autonomous (without human intervention) and nonautonomous. The latter require some external intervention, such as heating the material to trigger the repair process (Ghosh 2009; Zwaag 2007).

From the thermodynamic point of view, healing is achieved by shifting the system away from the thermodynamic equilibrium, which causes a restoring thermodynamic force (e.g., diffusion) to drive the system back to equilibrium. The restoring force also drives the healing process that is characterized by a local decrease of entropy (Nosonovsky and Bhushan 2009; Nosonovsky et al. 2009; Nosonovsky 2010a, b). Shifting the system away from equilibrium can be achieved by placing it in a metastable state (e.g., creating an oversaturated solution), so that the rupture breaks the fragile metastable equilibrium, and the system drives to the new most stable state (Fig. 1.1). The metastability can also be achieved by heating that causes a phase transition (e.g., melting, the martensite–austenite transition in metals).

Several strategies of embedding the self-healing properties into engineering materials have been suggested so far (Fig. 1.2). The most successful class of self-healing materials is the polymers, and this is because of their relatively large rates of diffusion and plasticity due to the presence of the cross-molecular bonds. One way to create self-healing polymers is to use thermosetting polymers that have the ability to cure (toughening or hardening by cross-linking of polymer chains), such as the thermosetting epoxy. Epoxy is a polymer formed by a reaction of an epoxide resin with a polyamine hardener. Epoxy can serve as a healing agent that is stored within thin-walled inert brittle macrocapsules embedded into the matrix along with a catalyst or hardener (but separately from the latter). When a crack propagates, the

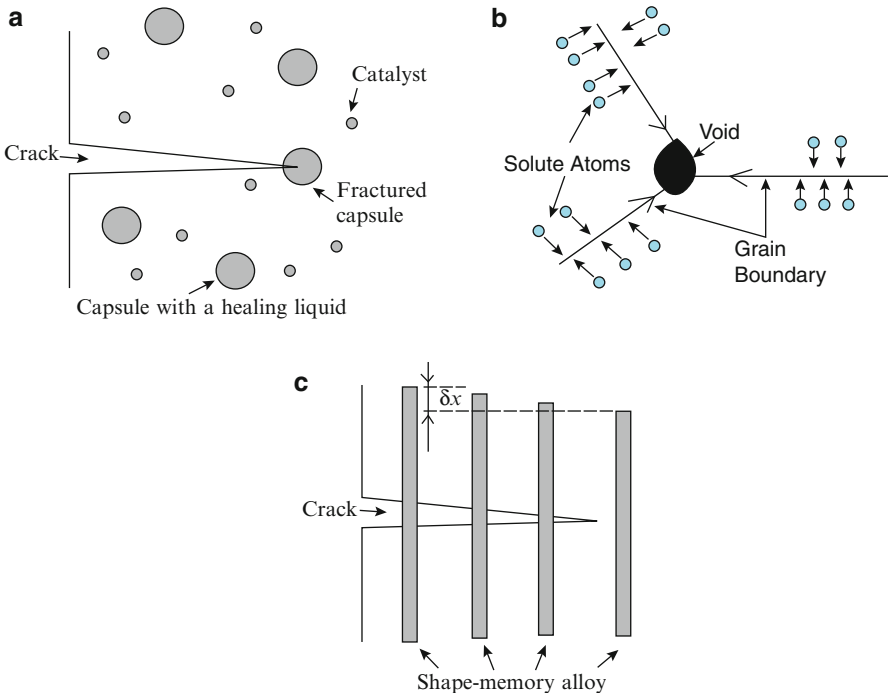

Fig. 1.2 Self-healing in metallic materials by (**a**) encapsulation of a healing agent, (**b**) precipitation in an over-saturated alloy, (**c**) embedding of shape-memory alloy microwires

capsules fracture, the healing agent is released and propagates into the crack due to capillarity. Then the healing agent mixes with the catalyst in the matrix, which triggers the cross-linking reaction and hardening of the epoxy that seals the crack (Fig. 1.2a). A different approach involves thermoplastic polymers with various ways of incorporating the healing agent into the material. In this approach, heating is often required to initiate healing. Self-healing ceramic materials often use oxidative reactions, because products of these reactions, including oxides, can be used to fill small cracks (Zwaag 2009).

It is much more difficult to heal metallic materials than polymers, because metallic atoms are strongly bonded and have small volumes and low diffusion rates. Currently, there are three main directions in the development of self-healing metallic systems. First is the formation of precipitates at the defect sites that immobilize further growth until failure. Van der Zwaag (2009) and co-workers called this mechanisms “damage prevention” because the idea is to prevent the formation of voids by the diffusion of the atoms to form precipitate from an oversaturated but under aged solid–solid solution (alloy). The driving mechanism for the diffusion is the excess surface energy of microscopic voids and cracks that serve as nucleation centers of the precipitate which plays the role of the healing agent (Fig. 1.2b). As a result, the newly formed void is sealed by the deposit of

atoms in the form of precipitates before it grows and thus minimizes the creep and fatigue. Manuel and Olson (2007) and co-workers used another approach: reinforcement of an alloy matrix with a microfiber or wires made of a shape-memory alloy (SME), such as nitinol (NiTi). SMA wires have the ability to recover their original shape after some deformation has occurred if they are heated above the phase transformation temperature. If the composite undergoes crack formation, heating from the surface will activate the shape recovery effect of the SMA wires, and close the cracks (Fig. 1.2c). The third approach is to use a healing agent (such as an alloy with a low melting temperature) embedded into a metallic solder matrix, similarly to the way it is done with the polymers. However, encapsulation of a healing agent into a metallic material is a much more difficult task than in the case of polymers. The healing agent should be encapsulated in microcapsules which serve as diffusion barriers and which fracture when a crack propagates.

1.2 Surface Science and Tribology

Surface science is the study of physical and chemical phenomena that occur at the interface of two phases (solid–liquid, solid–gas, and solid–vacuum) or of different substances of the same phase (solid–solid, liquid–liquid) (Adamson 1990). Since properties of matter can change rapidly at the interface, it is convenient to assume that the interface is a 2D surface in a sense that every point at the interface can be characterized by only two parameters. In reality, every interface has nonzero thickness and the bulk properties change gradually at the interface; however, the thickness is so small compared to the two other dimensions, it can often be neglected.

An important characteristic of every surface or interface is the surface free energy, γ. In the bulk of the body, chemical bonds exist between the molecules or atoms. To break these bonds, certain energy is required. The molecules or atoms that do not form the bonds have higher potential energy than those that form the bonds. Molecules or atoms at the surface do not form bonds on the side of the surface and thus they have higher energy (Fig. 1.3). This additional energy is called surface or interface free energy and is measured in energy per area; in the SI system, $\mathrm{J\ m^{-2}}$ or $\mathrm{N\ m^{-1}}$. In order to create an interface (e.g., to form a vapor bubble inside boiling water), the energy should be supplied, which is equal to the area of the interface multiplied by the interface free energy (Nosonovsky and Bhushan 2008a).

Any system tends to achieve a position that corresponds to its minimum energy. For the stable existence of the interface, it is required that the free energy of formation of the interface be positive, so that accidental fluctuations would not result in the dispersion of one material into the other. This is the case for most solid–solid, solid–liquid, solid–gas, and liquid–gas interfaces. However, an interface between two gases or between miscible liquids does not offer opposition to the dispersion (Adamson 1990).

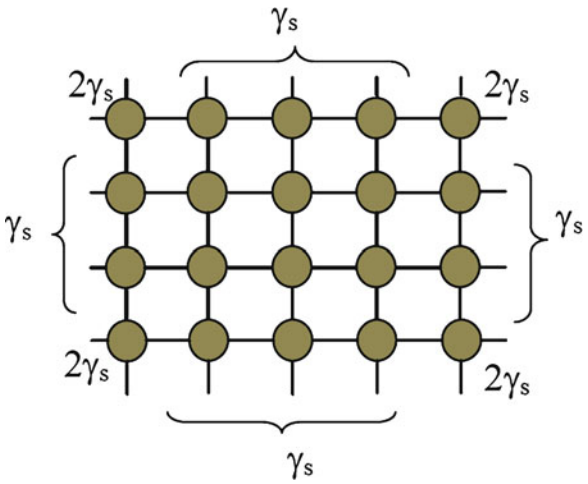

Fig. 1.3 Molecules at the surface have fewer bonds with neighboring molecules than molecules in the bulk. Therefore, surface molecules have higher energy. Edge molecules have even fewer bonds and higher energy, than surface molecules

The surface tension force is the force which should be applied to the solid–liquid–air contact line (the triple line) to expand the solid–liquid interface. The surface tension is measured in N m^{-1} and in many senses it is equivalent to surface free energy. The concept of the surface tension was introduced in 1805 by Thomas Young (1773–1829) and almost simultaneously by Pierre-Simon Laplace (1749–1827), while the idea of free surface energy was suggested by Josiah W. Gibbs (1839–1903) in about 1870. The accurate thermodynamic definition of the surface free energy involves a distinction between the concepts of the Gibbs free energy (the useful work obtainable from an isothermal isobaric thermodynamic system) and Helmholtz free energy (the useful work obtainable from a closed thermodynamic system).

The obvious manifestation of the free surface energy is found in the capillarity effect (Fig. 1.4), defined as the ability of a substance to draw another substance into it (Adamson 1990; Rowlinson and Widem 1982). When the size of a liquid droplet or a channel is much smaller than the so-called capillary length, given by $l_c = (\gamma/\rho g)^{1/2}$, where $g = 9.81$ m s^{-2} is the gravitational acceleration, γ is the free surface energy, and ρ is the density of liquid, the surface energy dominates over the gravity potential energy and the corresponding capillary forces dominate over the weight. For water at room temperature, $\gamma \approx 72$ mN m^{-1}, $\rho \approx 1{,}000$ kg m^{-3}, and $l_c \approx 2.7$ mm.

Interest in the surface phenomena is stimulated by current advances in nanoscience and nanotechnology. While the volume of a body is proportional to the third power of its linear size, the surface area is proportional to the second power of the linear size. With decreasing size of an object, the surface-to-volume ratio grows and surface effects dominate over the volume effects. This is why all surface phenomena, such as capillarity, adhesion, friction etc., become increasingly important for small objects (Nosonovsky and Bhushan 2008a), and the behavior changes below a certain size scale.

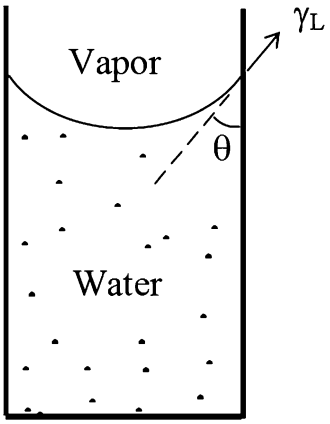

Fig. 1.4 The rise of water in a capillary tube due to the surface tension

Tribology is a technical discipline that studies contacting surfaces in relative motion, including adhesion, friction, lubrication, and wear. As opposed to the surface science, tribology is an application-oriented multidisciplinary area, which involves mechanics, physics, chemistry, materials science, fluid dynamics, heat transfer, biology, and other related areas. The word "tribophysics" (from the Greek word *tribos* "to rub") was coined in the 1940s by David Tabor (1913–2005), who was working in Australia (Dowson 1998). The intention of Bowden and Tabor was to alleviate the status of the friction, lubrication, and wear science and to attract public attention to the importance of these subjects for technology. The first official use of the term "tribology" was in 1966, in the "Jost report," when the British government reported on research in this area.

Although the word "tribology" appeared only about 40 years ago, people paid attention to friction and lubrication from ancient times. There is evidence that water lubrication may have been used in ancient Egypt as early as 2300 BC or 1800 BC, as shown in two examples (Nosonovsky 2007a). Oil lubrication is mentioned in the Bible in the King Saul story (1020 BC), animal fat may have been used as a lubricant for ancient Egyptian and Chinese chariots, and there is a list of lubricants in the treatise of Roman author Pliny the Elder (first century BC) (Dowson 1998; Nosonovsky 2007a). The emergence of the modern study of friction and lubrication is related to the activity of Leonardo da Vinci (1452–1519), Guillaume Amontons (1663–1705), and Charles August Coulomb (1736–1806), who formulated the empirical rules of friction.

It should be emphasized that despite the decades of intensive tribological studies in the twentieth century and the hundreds of years of investigation of friction, there is no general or axiomatic theory of friction. It is still viewed as a complex phenomenon dependent on different and unrelated mechanisms of dissipation, and governed by empirical laws, such as the Coulomb–Amontons law. Despite that, the Coulomb friction force plays a fundamental role in theoretical and applied mechanics, where frictional boundary conditions or constitutive laws are common

(e.g., for the granular flow when the interaction between the grains of the material is governed by the dry friction law). The case of wear is different; although wear is almost as universal as friction, it is rarely considered an inherent part of models of mechanical contact. Instead, there are several phenomenological models of wear, the most popular of which is the Archard's law, which states that the volume of the worn material is proportional to the sliding distance, normal load, and a coefficient called "the wear coefficient," divided by hardness of a softer material in contact. Despite numerous models developed in the past 50 years that attempt to correlate tribological properties with material microstructure, there is no reliable way to always predict quantitatively the coefficient of friction or the wear coefficient from any microstructural material parameters. The reason for this is that most relevant interactions occur at the mesoscale, rather than at the atomic scale, and it is very difficult to take these mesoscale interactions into consideration.

The community of researchers who call themselves tribologists includes both practical engineers, chemists, and surface scientists who work on various aspects of surface characterization and modification, lubrication, etc., as well as mechanical engineers and mathematicians who work on contact mechanics. The boom of tribology occurred in the last third of the twentieth century stimulated by the space and arms race of the two superpowers (the USA and the Soviet Union). However, despite the fact that today many scientists, especially in the USA, consider the field of tribology (or at least the use of the term "tribology") shrinking, there are still many researchers who identify themselves as "tribologists." Modern tribology concentrates on such issues as rough surface topography, contact mechanics, adhesion, mechanisms of dry and lubricated friction, hydrodynamic (thick film) and boundary (thin film) lubrication, bearings, lubricant chemistry and additives, wear, surface texturing, and medical and biotribology.

Since the 1990s the new field of nanotribology has emerged due to the advances in nanotechnology. The idea of nanotechnology was suggested in 1960 by physicist Richard Feynman (1912–1985) who pointed out that no laws of physics prohibit manufacturing of very small devices, which would be able to perform many tasks considered earlier impossible. It took more than 40 years until Feynman's vision began to materialize, when the field of nanotechnology emerged in 1990s, stimulated by the discoveries of carbon nanotubes, C_{60} molecules (fullerenes), graphene (graphite monolayer), and quantum dots (Poole and Owens 2003; Nosonovsky and Bhushan 2008a).

Since the importance of surface effects is inversely proportional to the size of the investigated object, it is not surprising that tribological studies became an important area in nanotechnology. Nanotribology is concentrated on the study of the adhesion, friction, lubrication (in particular, by self-assembled molecular monolayers) and wear at the nanoscale (Nosonovsky and Bhushan 2008a). The main instrument currently used in nanotribological research is the atomic force microscope (AFM) and its variations such as the friction force microscope and various other scanning probe microscopes. In the AFM, a small cantilever (typical length is 100 μm or less) with a very sharp tip (typical radius is 10–30 nm) can scan the surface of a sample, the position of which is controlled with a great accuracy by a piezoelectric tube (Fig. 1.5).

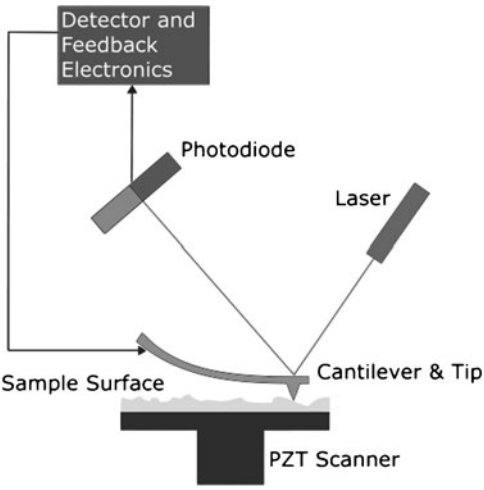

Fig. 1.5 The principle of the atomic force microscopy

The cantilever bends when in contact with the surface or under effect of forces (such as the adhesion and friction force) and its deflection is measured with a reflected laser beam. If the stiffness of the cantilever is known, it can be converted into the force acting upon the tip and thus small adhesion and friction forces can be measured with high accuracy.

1.3 Nonequilibrium Thermodynamics and Self-Organization

1.3.1 Classical Thermodynamic Potentials

Many physical processes result in irreversible energy dissipation. Examples include plastic deformation, friction, and viscosity. The energy during the dissipative process is converted into heat. According to the Second law of thermodynamics, formulated by Rudolf Clausius (1822–1888), heat, Q, cannot of itself pass from a colder to a hotter body. The mathematical formulation is the entropy S, defined as $dS = \delta Q/T$, can only increase (in an irreversible process) or remain constant (in reversible processes). When heat δQ is transformed from a body at temperature T_1 to that at T_2, the change of entropy is $\delta Q(1/T_2 - 1/T_1)$, so the entropy grows when heat is transmitted from a hot to a cold body. The second law has a statistical nature and states that a system tends to transfer from a more ordered state to a less ordered state, which is more probable statistically. The state of thermodynamic equilibrium, at which the temperatures of the contacting bodies are equal ($T_1 = T_2$), corresponds to the less ordered, most probable state and to the highest entropy. At the nanoscale, when the typical energy of the system is comparable with kT, the second law can be violated due to small fluctuations, which can lead to local reductions of the entropy of the system (Anisimov 2004).

Ludwig Boltzmann (1844–1906) suggested in 1877 a definition of entropy using the statistical thermodynamics approach and the concept of microstates, so that entropy is proportional to the integral of the number of microstates $S = k \ln \boldsymbol{\Omega}$, where k is Boltzmann's constant and Ω is the number of microstates that correspond to a given macrostate. Microstates are arrangements of energy and matter in the system, which are distinguishable at the atomic or molecular level, but are indistinguishable at the macroscopic level (Craig 1992). Lower entropy corresponds to a more ordered state, and a system tends to evolve into a less-ordered (more random) macrostate that has a greater number of corresponding microstates, and thus the "configurational" entropy grows.

Heat transfer and material transfer (diffusion) play a central role in many processes. Entropy is a thermodynamic potential that characterizes heat transfer while the mass transfer is characterized by the chemical potential, μ. The chemical potential is defined in such a way that particles tend to move from regions of high chemical potential to regions of low chemical potential.

For a rigorous definition of thermodynamic quantities, the concept of a thermodynamic system is the key. The system is considered isolated if there is no exchange of heat and mass with the environment and no work is done. The state of a thermodynamic system at any moment of time is characterized by several variables, so that the energy of a system depends on these variables. The total internal energy $U(S, V, N)$ is a function of the number of particles N, volume V, and entropy S. The temperature, pressure, and chemical potential are given by partial derivatives of U as

$$T = \frac{\partial U}{\partial S}, \quad P = -\frac{\partial U}{\partial V}, \quad \mu = \frac{\partial U}{\partial N}. \tag{1.1}$$

The change of the total energy is the given by

$$\mathrm{d}U = T\mathrm{d}S - P\mathrm{d}V + \mu\mathrm{d}N. \tag{1.2}$$

The quantities S, V, and N are generalized coordinates that characterize the state of the system in a unique way, while T, P, and μ are corresponding generalized forces, namely, the temperature, pressure, and chemical potential. When atoms or molecules of more than one type are present in the system, $N_1, N_2, \ldots, N_k$, several corresponding chemical potentials, $\mu_1, \mu_2, \ldots, \mu_k$, should be introduced as well.

Several laws of thermodynamics can be formulated now. The law of mass conservation states that in an isolated system the number of particles remains constant, or

$$\mathrm{d}N = 0. \tag{1.3}$$

The First law of thermodynamic is the law of energy conservation, and it states that in an isolated system the internal energy does not change,

$$\mathrm{d}U = -P\mathrm{d}V + T\mathrm{d}S + \mu\mathrm{d}N = 0. \tag{1.4}$$

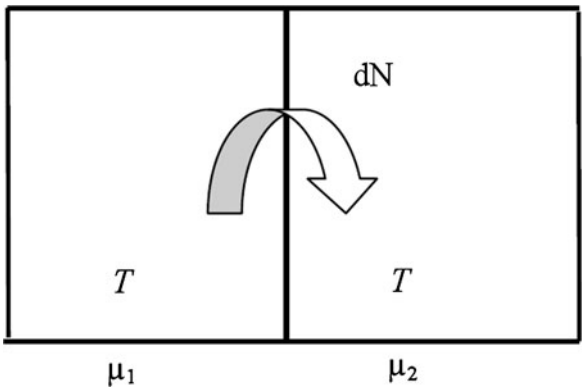

Fig. 1.6 Mass transfer between two systems at the same temperature T but different chemical potentials, $\mu_1 > \mu_2$

The Second law of thermodynamics states that entropy of an isolated system can only increase (in the case of an irreversible process) or remain constant (in the case of a reversible process) so that

$$\mathrm{d}S = \frac{P}{T}\mathrm{d}V - \frac{\mu}{T}\mathrm{d}N + \frac{1}{T}\mathrm{d}U \geq 0. \tag{1.5}$$

Suppose that a thermodynamic system is divided into two parts (subsystems) with the temperatures T_1 and T_2, so that the subsystem can exchange heat between themselves but not with the surrounding environment. The immediate consequence of Second law, as it was stated above, is that heat flows from the hotter to the colder system, since $\mathrm{d}S = \left(\frac{1}{T_2} - \frac{T}{T_2}\right)\mathrm{d}U > 0$, and, therefore, $T_2 > T_2$. In a similar manner, one can show that matter flows from the subsystem with a higher chemical potential to that with a lower one, assuming $T_1 = T_2 = T$, since $\mathrm{d}S = \left(\frac{\mu_2}{T} - \frac{\mu_2}{T}\right)\mathrm{d}N > 0$, and thus $\mu_1 > \mu_2$ (Fig. 1.6).

The volume, entropy, and the number of particles are called extensive thermodynamic properties of a system, since they are proportional to the mass of the system or the amount of substance. On the other hand, the pressure, temperature, and chemical potential are called intensive properties, since they are not dependent on the mass of the system or the amount of substance. Furthermore, the pairs P and V, T and S, μ and N are called "conjugate variables." In many cases, it is more convenient to present the state of a thermodynamic system as a function of pressure and temperature. For that, the thermodynamic potentials called Helmholtz free energy $A(V, T, N) = U - TS$ and Gibbs free energy $G(P, T, N) = U + PV - TS$ can be used instead of the internal energy. The differentials of A and G are defined as

$$\begin{aligned} \mathrm{d}A &= -S\mathrm{d}T - P\mathrm{d}V + \mu\mathrm{d}N, \\ \mathrm{d}G &= -S\mathrm{d}T - V\mathrm{d}P + \mu\mathrm{d}N. \end{aligned} \tag{1.6}$$

Note that the transformation from $U(S, V, N)$ to $A(V, T, N)$ and to $G(P, T, N)$ for a thermodynamic system is analogous to the transition from strain energy to the stress (or "complimentary") energy of a mechanical system. Indeed, for a system

consisting of a mass M on a spring with the spring constant of k, the potential energy as a function of displacement from the state of equilibrium, x, is $U(x) = kx^2/2$ while the complimentary energy as a function of spring force F, is given as $\tilde{U}(F) = FX - U(x)$. Of course, for a linear system ($F = kx$) the values of U and $\tilde{U}$ coincide $\tilde{U}(F) = F_2/2k$. The force F and displacement x are the conjugate variables of a mechanical system.

The state of a thermodynamic system is called homogeneous if its properties, such as temperature, pressure, and chemical potential, do not depend on the spatial coordinates. The state is called stationary if the properties do not depend on time. If the properties do not depend on both time and spatial coordinates and no entropy is produced, the state of the system is called equilibrium. Throughout this book we deal with both thermodynamic and mechanical processes and with two types of equilibriums: thermodynamic and mechanical equilibrium. Mechanical processes are usually slower than thermodynamic processes and thus in most cases we assume that the system has enough time to achieve a thermodynamic equilibrium with a constant temperature, pressure, and chemical potential.

1.3.2 Nonequilibrium Thermodynamics

While classical thermodynamics studies systems at equilibrium, nonequilibrium thermodynamics received a lot of attention in the twentieth century. For a nonequilibrium thermodynamic system, the dependencies of thermodynamic parameters on time and spatial coordinated should be investigated. For that end, all intensive parameters can depend on time and coordinates $T(x, y, z, t)$, $P(x, y, z, t)$, and $\mu(x, y, z, t)$. For extensive parameters, their volume densities are considered $u(x, y, z, t)$, $s(x, y, z, t)$, and $c(x, y, z, t)$, where u is the energy density, s is the entropy density, and c is the concentration (number of particles per unit volume). Furthermore, flow vectors of thermodynamic quantities are introduced, so that the law of mass conservation is now given by

$$\frac{\partial c}{\partial t} + \nabla J^{\mathrm{c}} = 0, \tag{1.7}$$

where J^{c} is the mass flow. The First law of thermodynamics is given by

$$\frac{\partial u}{\partial t} + \nabla J^{\mathrm{e}} = 0, \tag{1.8}$$

where $J^{\mathrm{e}} = q$ is the heat flow q. Finally, the Second law of thermodynamics is given by

$$\frac{\partial s}{\partial t} + \nabla J^{\mathrm{S}} \geq 0, \tag{1.9}$$

where J^{S} is the entropy flow.

In the approach developed by Lars Onsager (1903–1976), generalized thermodynamic forces Y_i and thermodynamic flows J_i are associated with every generalized coordinate q_i, so that the rate of entropy density production is given by

$$\frac{\mathrm{d}s}{\mathrm{d}t} = \frac{1}{T}\sum Y_i J_i. \tag{1.10}$$

For example, for the heat flow the force is $Y_T = \nabla\frac{1}{T} = -\frac{1}{T^2}\nabla T$ (here used $\frac{\partial}{\partial x}\frac{1}{f(x)} = -\frac{1}{f(x)^2}\frac{\partial f(x)}{\partial x}$), for the mass flow is $Y_i = -\nabla\frac{\mu_i}{T}$, thus when entropy is produced due to heat and matter flow, using (1.7)–(1.8) we find

$$\frac{\mathrm{d}s}{\mathrm{d}t} = -\frac{q}{T^2}\nabla T + \frac{J^C}{\left(\frac{T}{\mu_i}\right)^2}\nabla\left(\frac{T}{\mu_i}\right) = \frac{K}{T}(\nabla T)^2 + D\frac{\mu}{T}\left(\nabla\frac{T}{\mu_i}\right)^2, \tag{1.11}$$

where $q = -K\nabla T$ (Fourier law of heat transfer) and $J^{\mathrm{C}} = -D\nabla\left(\frac{T}{\mu i}\right)^2$ (Fick's law of diffusion). Note that entropy rate is always positive. The generalized forces must have the same tensor rank as the flows, e.g., both should be vectors (or scalars, or tensors of the 2nd rank, etc).

In general, flows can be complicated functions of the generalized forces, $J_i = J_i(Y_1, Y_2, \ldots, Y_n)$; however, in the linear approximation, the flows are related to the forces by a linear equation

$$J_{\mathrm{k}} = \sum_i L_{ki} Y_i, \tag{1.12}$$

where L_{ki} is called the Onsager (phenomenological) coefficient (de Groot and Mazur 1962). Many physical linear empirical laws, such as the Ohm's law of electrical resistance, the Fourier law of heat conduction, and Fick's law of diffusion can be interpreted as linear relationships between generalized forces and flows.

Note that (1.12) provides the possibility of coupling of various irreversible processes inside the system, or their interaction with each other in the case when nondiagonal Onsager coefficients are different from zero. Due to coupling, a process can occur without its primary driving force or it may move the process in a direction opposite to the one imposed by its own driving force. For example, in thermodiffusion a species diffuses not because of a concentration gradient but because of a temperature gradient. When a species flows from a low to a high-concentration region, it must be coupled with a compensating process. The principles of thermodynamics allow the progress of a process without or against its primary driving force only if it is coupled with another process. However, one cannot simply assume that any two phenomena are coupled. Phenomenological coupling, if it exists, must be observed in nature. In this book, we interpret self-healing, which is observed in specially prepared materials with an embedded healing mechanism, as a result of coupling between deterioration and a force which affects healing.

1.3.3 Self-Organization

Ilya Prigogine (1917–2003) and his co-workers used the methods of nonequilibrium thermodynamics to investigate self-healing. They showed that so-called dissipative systems may lead to increasing orderliness and self-organization (Prigogine 1961). These systems are thermodynamically open and they operate far from thermodynamic equilibrium and can exchange energy, matter, and entropy with the environment. The dissipative systems are characterized by spontaneous symmetry breaking and formation of complex structures, where interacting particles exhibit long-range correlations. Examples of such systems are the Bénard cells in boiling liquid and oscillating chemical reactions. Many of these systems were known a long time ago; however, the universality and generality of the processes involved in these systems was understood only with the works by Prigogine. In 1945 Prigogine suggested that a nonequilibrium system tries to minimize its rate of entropy production and chooses the state accordingly. This condition was criticized by Landauer (1975), who argued that minimum entropy production is not in general a necessary condition for the steady state, and that the most favorable state of the system cannot be determined based on the behavior in the vicinity of the steady state, but one must consider the global nonequilibrium dynamics. Prigogine was awarded the Nobel Prize in chemistry in 1977 for his contribution to the theory of dissipative structures. Later studies have developed new techniques for analyzing pattern selection (Leppänen 2004).

It is believed that this ability for self-organization of physical systems led to the formation of complex hierarchical chemical and biological systems. Nonequilibrium dissipative systems may lead to the hierarchy, and their investigation involves the study of instability and loss of symmetry. Self-organization is related to an enormous reduction of degrees of freedom and entropy of the macroscopic system, consisting of many nonlinearly interacting subsystems, which macroscopically reveals an increase of order.

The related broad field is sometimes called complexity science, and the systems that are studied are between perfect order and complete randomness. Synergetics is an interdisciplinary science which explains the formation and self-organization of patterns and structures in systems far from thermodynamic equilibrium. These disciplines employ theoretical concepts similar to those of mesoscale physics, e.g., the Landau–Ginzburg functional and the order parameter (Haken 1993).

Even prior to the work of Prigogine, famous mathematician Alan Turing (1912–1954) investigated self-organization in the form of pattern-formation in the reaction-diffusion systems. He showed that a simple mathematical model describing spontaneously spreading and reacting chemicals could give rise to stationary spatial concentration patterns of fixed characteristic length from a random initial configuration. Turing (1952) proved rigorously that a chemical state, which is stable against perturbations in the absence of diffusion, may become unstable to perturbations in the presence of diffusion. The diffusion-driven instability is initiated by arbitrary random deviations of the stationary state and results in

stationary spatially periodic variations in the chemical potentials, i.e., chemical patterns. His intention was to explain, at least qualitatively, the formation of biological patterns such as the stripes of a zebra or spots of a cheetah. Turing patterns were first observed in chemical experiments as late as 1990. Although the biological relevance of Turing's work is controversial even today, it had a significant impact on the development of nonlinear dynamics and nonequilibrium physics. Turing gave the first detailed description of a mechanism that can generate order in a nonequilibrium system. The self-oscillating chemical reactions were discovered in the 1950s–1960s by Belousov and Zhabotinsky (BZ) in Russia. They studied a mix of several ingredients, in which the ratio of concentration of the cerium (IV) and cerium (III) ions oscillated, causing the color of the solution to oscillate between a yellow solution and a colorless solution. It is remarkable that Belousov was not able to publish his discovery for a long time, because it was believed that such reactions are not possible; the BZ reactions became known in the West only in the 1970s. Unlike the patterns in the BZ oscillating chemical reactions, Turing patterns are stationary in time (Leppänen 2004).

An important example of self-organization that has been studied extensively by P. Bak (1996) is "self-organized criticality," which implies that a system tends to spontaneously achieve a critical point-like behavior. Self-organized criticality is typical for many systems where energy is accumulated for a long time, and the catastrophic release of energy is triggered by a random event, such as earthquakes, landslides, snow avalanches, or collapses of piles of granular materials. The classic example is the "sand pile model," representing a pile of sand where adding a single grain of sand can have no effect, or it can trigger a catastrophic avalanche. Self-organized critical behavior has certain characteristic quantitative features (such as the power law of amplitude distribution of the avalanches and "one-over-frequency noise"), which can be indicative of the presence of the self-organized critical behavior without a detailed analysis of the dynamics of the system. Apparently, self-organized criticality plays a role in such effects as stick–slip dry frictional motion and wetting of rough solid surfaces.

1.4 Self-Organization During Friction

Sliding friction is a nonequilibrium process that results in the dissipation of large amounts of energy and the flow of heat, entropy, and material move away from the frictional interface. Therefore, sliding friction does not always lead to wear and deterioration, but has potential for self-organization. It is well known that when the sliding is initiated, friction and wear are usually high during the initial "running-in" period. However, with time, the surfaces "adjust" to each other due to wear, relaxation, and other processes, so friction and wear decrease. This is perhaps the simplest example of frictional self-organization, which also shows why the system that underwent the transition to a self-organized state has a lower friction and wear rate.

This self-organization can occur in the form of so-called "selective transfer" which was investigated by Russian tribologists Kragelsky and Garkunov. In the 1950s, they studied the technical state of airplane chassis which included a bronze-steel lubricated frictional system, and found that a protective copper film can form, which reduces the wear to very small values. The copper film is formed by the anodic dissolution of bronze (an alloy of copper and tin with additive elements). The additives, such as iron, zinc, aluminum, and tin, dissolved in the lubricant, while the copper formed a film on the surfaces of the contacting materials. The film is in a dynamic equilibrium, while the contacting layers are worn and destroyed, new layers of copper are formed, resulting in the virtual absence of wear and the friction force reduced by an order of magnitude. A similar effect can be achieved through the diffusion of a copper ion dissolved in a lubricant. The authors called this effect the "selective transfer" of copper ions, and the protective effect, "servovit film" (Garkunov 2004). More common terms in modern literature are the "in situ formation of self-lubricating films" and "the third body effect," indicating that film is formed in situ and becomes the "third body" trapped between the two contacting bodies.

Thermodynamically, the system is driven away from equilibrium by frictional sliding. The system reacts producing a generalized thermodynamic force that acts to restore the equilibrium, which causes a diffusion (precipitation) of copper ions.

A different approach to using the concept of entropy was developed since the 1980s by a group of Russian tribologists, including N. Bushe, L. Bershadsky, Kostetsky, I. Gershman, and others, who applied nonequilibrium thermodynamics to the frictional contact (Fox-Rabinovich and Totten 2006). The stability condition for the thermodynamic system is given in the variation form by Fox-Rabinovich et al. 2007

$$\delta^2 S > 0, \tag{1.13}$$

where $\delta^2 S$ is the second variation of entropy. When (1.13) is satisfied, the system is at equilibrium. However, when this condition is violated, the system is driven away from equilibrium, which creates the possibility for self-organization and therefore, to reduce friction and wear. In the self-organized state, friction and wear can be significantly reduced. If the coefficient of friction and the thermal conductivity depend upon a material's microstructure, it may be convenient to introduce a parameter ψ that characterizes the microstructure of the surface (e.g., the density of a micropattern), so that $\mu(\psi)$, $\lambda(\psi)$. These dependencies are substituted into the stability condition (1.13) in order to determine whether the self-organization is possible. For example, in nanocrystalline AlTiN coatings for sever operating conditions (e.g., hard coatings for cutting tools) both the thermal conductivity and the coefficient of friction decrease with decreasing size of grains, which leads to self-organized regime with low friction and wear (Fox-Rabinovich et al. 2007). We understand such a self-organized regime as one of the modes of self-lubrication.

The term "self-lubrication" implies the ability of parts and components to operate without lubrication, and refers to several methods and effects, in addition to the reduced friction or wear mentioned above of. Among these methods are

the use of self-lubricating coatings that are either hard (to reduce wear) or with low surface energy (to reduce adhesion and friction). Besides coatings, self-lubrication refers to the development of metal-, polymer-, or ceramic-based self-lubricating composite materials, often with a matrix that provides structural integrity and a reinforcement material that provides low friction and wear. The nanocomposites have become a focus of this research, as well as numerous attempts to include carbon nanotubes and fullerene C_{60} molecules.

Simple models assume that these large molecules and nanosized particles serve as "rolling bearings" that reduce friction; however, it is obvious now that the mechanism can be more complicated and involve self-organization. Dynamic self-organization is thought to be responsible for self-lubrication in atomic force microscopy experiments with the atomic resolution. A protective layer can be formed through the chemical reaction of oxidation or a reaction with water vapor. For example, a self-lubricating layer of boric acid (H_3BO_3) is formed as a result of a reaction of water molecules with a B_2O_3 coating (Erdemir et al. 1990). Another type of self-lubricating material involves lubricant embedded into the matrix, e.g., inside microcapsules that rupture during wear, and release the lubricant. Surface microtexturing provides holes and dimples that can serve as reservoirs for lubricant is another method of providing self-lubrication. In addition, we should mention that self-lubrication is observed in many biological systems (e.g., human joints), and that the term "self-lubrication" is used also in geophysics where it refers to the abnormally low friction between tectonic plates that is observed during some earthquakes.

1.4.1 Frictional Dynamic Effects

Another type of self-organizing behavior during friction is related to dynamic frictional effects, such as vibrations and waves induced by frictional sliding. Two types of elastic waves can propagate in an elastic medium: shear and dilatational waves. In addition, surface elastic waves may exist, and their amplitude decreases exponentially with the distance from the surface. For two slightly dissimilar elastic materials in contact, the interface waves (Rayleigh waves) may propagate at the interface zone. Their amplitude decreases exponentially with the distance from the interface. Whereas the interface waves occur for slightly dissimilar (in the sense of their elastic properties) materials; or very dissimilar materials, waves would be radiated along the interfaces, providing a different mechanism of pumping energy away from the interface (Nosonovsky and Adams 2001). Self-excited oscillations, such as Rayleigh waves, are confined to a region near the sliding interface and can eventually lead to either partial loss of contact, or to the propagation of regions of stick–slip motion (slip waves). In a slip wave, a region of slip propagates along the interface, which is otherwise at the stick state. When a train of slip pulses propagates, two bodies shift relative to each other in a caterpillar or carpet-like motion. This microslip can lead to a significant reduction of the observed

coefficient of friction, as the slip is initiated at a shear load, which is much smaller than the coefficient of friction times the normal load (Nosonovsky and Adams 2001; Bhushan and Nosonovsky 2003; Nosonovsky and Bhushan 2005a, b).

A linear model (e.g., one based on the linear elasticity) can be used to analyze the stability and onset of nonlinear vibrations; however, in order to find the resulting regime a complicated nonlinear analysis is needed. The train of stick–slip propagating regions can be viewed as a self-organized structure that reduces frictional dissipation.

When discussing the nonlinear model of friction, it is noted that despite the apparent simplicity of the Coulomb friction law, incorporating it with fundamental theories of mechanics, such as dynamic elasticity, causes a number of difficulties. This is in part due to the intrinsic nonlinearity of the Coulombs law with respect to the sliding velocity (the friction force jumps from zero at zero velocity to a finite value at a nonzero velocity). There are a number of paradoxes related to the combining of the Coulomb friction with the mechanics of an absolutely rigid or deformable body. These include the Painlevé paradoxes and other types of paradoxes that lead to the nonuniqueness or nonexistence of a solution. In a strict mathematical sense, the Coulomb friction is inconsistent not only with rigid body dynamics, but also with the dynamics of elastically deformable bodies (Nosonovsky and Bhushan 2008a).

One of the manifestations of that inconsistency is frictional dynamic instability, in the form of self-excited vibrations where the amplitude grows with time (Adams 1995). These instabilities exist due to a positive feedback (coupling) of friction with thermal expansion, wear, or negative velocity depending on friction. However, such instabilities can exist even when there is no velocity-dependence of friction, no thermal expansion, and wear is present. These instabilities are a consequence of energy being pumped into the interface as a result of the positive work of the driving force. As a result, the amplitude of the interface waves grows with time, with the unlimited rate of growth of short wavelength (the ill-posedness). In a real system, of course, the growth is limited by the limits of applicability of the linear elasticity and linear vibration theory. In order to regularize the ill-posedness, it has been suggested to use a dynamic friction law instead of the Coulomb friction law (Ranjith and Rice 2001). One example of such a dynamic friction law is the state-and-rate friction law, according to which the coefficient of friction at first grows every time the load changes, and then decreases to the steady-state value (which by itself decreases with increasing sliding velocity). Dynamic friction laws have a high potential for self-organization dynamics.

1.5 Composite Materials for Tribological Applications

Composite materials are often used when the production of materials with desired tribological properties, such as low friction and wear, is needed. Composite materials usually consist of two or more components, with one material serving

as a matrix and others as reinforcements that provide special properties, such as high strength, to the matrix.

An important class of composite materials is the metal matrix composites (MMCs). An MMC is a composite with at least two constituent parts, one of which (the matrix) is a metal whereas the other (the reinforcement) is either a different metal or another material, such as a ceramic. When more than two different materials are incorporated simultaneously into the matrix, the composite is called a *hybrid composite*. The reverse structure to an MMC composite, a ceramic matrix with a metallic reinforcement and a high percentage of the ceramic phase, is called a *cermet*.

MMCs are created by dispersing a reinforcing material into a metal matrix. More than two components can be required, for example, when the need arises to coat the surface of the reinforcement material to prevent a chemical reaction with the matrix. Thus, carbon fibers are commonly used in an aluminum matrix to synthesize composites with low density and high strength. However, a chemical reaction of carbon with aluminum generates a brittle and water-soluble compound, Al_4C_3, at the interface between the matrix and the fiber. To prevent this reaction, the carbon fibers are coated with nickel or TiB_2.

The matrix is the monolithic material into which the reinforcement is embedded, and the matrix is generally a continuous phase. This means that there is a path through the matrix to any point in the material, unlike two materials sandwiched together. In structural applications, the matrix is made of a lighter metal such as aluminum, magnesium, or titanium, since it provides a compliant support for the reinforcement. For high-temperature applications, cobalt and cobalt–nickel alloy matrices are common.

The reinforcement material is embedded into the matrix. The reinforcement does not always serve a purely structural task (reinforcing the compound), but is also used to change physical properties such as wear resistance, friction coefficient, or thermal conductivity. The reinforcement can be either continuous or discontinuous.

1.6 Biomimetics

Biomimetics (or biomimicry) means mimicking biological objects in order to design artificial objects with desirable properties (Bar-Cohen 2005). The word is attributed to biophysicist Otto Schmitt (1913–1998) who was a polymath and, among other problems, attempted to produce a physical device that explicitly mimicked the electrical action of a nerve. Since the late 1950s the term "biomimetics" (Vincent et al. 2006) became popular. Another term that is frequently used, "bionics," was coined in 1960 by Jack Steele of the USA air force. The term "biomimetic" has replaced, to a certain extent, the term "bionics" in scientific literature. The latter became quite popular in science fiction. The word biomimetics first appeared in Webster's dictionary in 1974 and is defined as "the study of the formation, structure or function of biologically produced substances and materials

(as enzymes or silk) and biological mechanisms and processes (as protein synthesis or photosynthesis) especially for the purpose of synthesizing similar products by artificial mechanisms which mimic natural ones". The idea of creating artificial devices mimicking living nature has inspired humankind since its very early days. Leonardo da Vinci studied birds' flight and designed machines, but never made any (Vincent et al. 2006). The motif is found in the Greek myth of Daedalus and Icarus, who mimicked bird wings to create an artificial flying device. Mechanical birds, animals, and even humans are found in many ancient legends, for example, the Talmud speaks about mechanical golden animals and peacocks in the throne of King Solomon, as well as an artificial human-like dummy (later called Golem) created by Cabbalistic magic.

Biological objects have been studied actively by physicists and chemists before the emergence of biomimetics. However, biomimetics goes further than just biophysics and bioengineering, which only study biological objects, since its objective is to imitate the objects with desirable properties. There is a growing interest toward biomimetics and growing public awareness of the field, which is stimulated in part by a general interest in "green" (environmentally friendly) manufacturing. An example of such growing interest is the database of biomimetic solutions for various engineering problems that can be found at the Web site www.AskNature.org.

The idea behind biomimetics is that nature's technical solutions, achieved by thousands of years of evolution, are perfect or at least better than those which contemporary engineering technology can suggest. This concept may be applied to various areas of engineering, for example, the artificial intelligence and neural networks in information technology are inspired by the desire to mimic the human brain. The existence of biocells and deoxyribonucleic acid (DNA) serves a source of inspiration for nanotechnologists who hope to 1-day build self-assembled molecular scale devices. In the field of biomimetic materials, there is also a whole area of bio-inspired ceramics based on seashells and other materials.

It is important to distinguish between simple *similarity* in the functionality of a biological and an engineered object (e.g., a plane is similar to a bird because it flies and has wings and a tail, a tank is similar to a turtle because the tank has armor and the turtle has a shell) and a true borrowing of *principles* and approaches used by nature in the design of artificial devices.

The best-known and most practically successful biomimetic effect related to surface science is the lotus effect. The term was coined in recognition of the fact that lotus plant leaves are water-repellent, and have the ability to emerge clean from dirty water due to a special structure of their surface. The term refers to the superhydrophobicity and self-cleaning abilities of the plant due to surface roughness. Although an accurate definition of superhydrophobicity still remains a matter of argument in the literature, the consensus is that a superhydrophobic surface should have a high contact angle with water (higher than 150°) and low contact angle hysteresis, so that a water droplet placed on a superhydrophobic surface can easily flow upon it.

Besides the lotus effect, a number of ideas have been suggested so far in the field of biomimetic surfaces (Gorb 2005; Bar-Cohen 2005; Favret and Fuentas 2010). These include the gecko foot, which has a very high and adaptive adhesion, the moth eye that does not reflect light, the sharkskin which can flow underwater suppressing turbulence, the water strider leg that can stay dry, the darkling beetle that can collect dew using hydrophilic microspots, and the sand skink that can reduce friction using nanothresholds. The common feature found among many of these surfaces is that they have hierarchical roughnesses, with rough details ranging from nanometers to millimeters. This observation inspired our earlier study of multiscale frictional dissipative mechanisms in combination with hierarchical surfaces (Nosonovsky and Bhushan 2008a).

The field of self-healing materials is often considered a biomimetic study, because a number of ideas to mimic the biological mechanisms of healing have been suggested. This includes, for example, creating a vascular system for the circulation of a healing agent, or using nanoparticles as artificial leucocytes that can deliver and unload a healing agent to a damaged zone (Balazs 2007; Gebeshuber et al. 2008). However, biological mechanisms of healing are very complex and often involve many factors acting in parallel. There is a growing understanding in the community of materials scientists who work on the development of self-healing materials that biological mechanisms of healing cannot be directly borrowed for artificial materials. For instance, the review by Van der Zwaag (2009) with the symptomatic title "Self-healing behavior in man-made engineering materials: bioinspired but taking into account their intrinsic character" ends with the conclusion "while Nature has shown an extreme diversity in microstructures and microstructural systems, and, subsequently, has shown a wide diversity of healing mechanisms, it is unwise to try to copy these healing mechanisms in man-made engineering materials in a direct manner. As shown in this chapter, engineering materials have their own characteristics, and, in designing self-healing behavior in such materials, their intrinsic or natural character has to be taken into account."

Biological materials and surfaces are known to have remarkable properties. For example, the silk fiber of the spider web has specific strength comparable with or even exceeding steel. In order to produce such strong materials as steel, humans need to use large facilities with high temperatures and pressures. A spider produces its silk at ambient temperature and pressure, while the length of a continuous fiber exceeds the size of the spider thousands of times. Such remarkable properties are achieved due to a hierarchical organization of tissues produced by living organisms. The hierarchy provides flexibility and the ability to adapt to changing environments. Biological tissues are created in accordance with certain recursive algorithms contained in their DNA, and not with final design specifications or blueprints as is the case in the conventional engineering design paradigm. These recursive algorithms lead to hierarchical organization. In the case of functional surfaces, hierarchical organization is manifested in the presence of structures with different characteristic length scales. These structures usually provide the ability to simultaneously protect the surface from

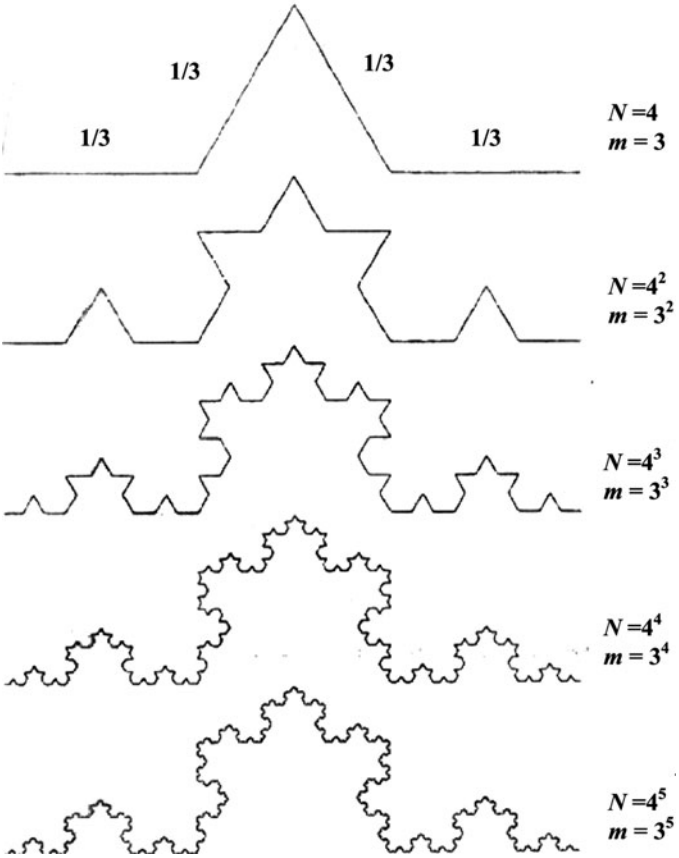

Fig. 1.7 The fractal curve (so-called Koch curve) with a fractal dimension $D = \ln 4/\ln 3 = 1.26$. The curve is built by an iterative procedure so that at every step its length l is increased by the factor of 4/3. If the curve is zoomed by three times, it length is increased by $4 = 3^D$ times

several undesirable factors having different characteristic length scales. Hierarchical structures play important roles in both the lotus effect and the gecko effect.

Not surprisingly, hierarchical structures are of great importance for biomimetic engineering. The concept of hierarchy is different from the concept of scale in a sense that hierarchy implies a complicated structure and organization. Hierarchical surfaces are built from elements of different characteristic lengths, organized in a certain manner (Fig. 1.7). This organization leads to certain functionality. Many examples of these surfaces are found in biology and will be considered in this book. An important class of hierarchical systems is the fractal objects. Self-similar, or fractal structures, can be divided by parts, each of which is a reduced-size copy of the whole. Unusual properties of the self-similar curves and surfaces, including their noninteger dimensions, were studied by mathematicians in the 1930s. The word *fractal* was coined in 1975 by Benoit Mandelbrot, who popularized the

concept of self-similarity, and showed that fractal geometry is universal in nature and engineering applications (Mandelbrot 1983). The fractal concepts were applied to rough surfaces. In the late 1980s to early 1990s, the fractal geometry approach was introduced in the study of the engineering of rough surfaces.

1.7 Summary

In the introductory chapter, we discussed some fundamental concepts related to self-organization and surface science. In the following chapters, we review self-healing, self-lubricating, and self-cleaning materials.

Part II
Self-Lubricating Materials

His substance is smoother than oil

Psalms 55:22

Chapter 6
Friction, Wear, and Self-Lubrication

The second part of this book covers self-lubrication and various issues related to the reduction of friction. Friction and wear during sliding or rolling of solid surfaces are universal phenomena and they reflect the tendencies of energy to dissipate and material to deteriorate, which are consequences of the Second law of thermodynamics. In general, solid surfaces in relative motion require lubrication, which dramatically reduces the extent of friction and wear. The situation when no external lubrication is required is called self-lubrication. There are many mechanisms of self-lubrication ranging from coatings to embedding lubricant into the matrix of a composite material, to self-organized in situ tribofilms, and to biological surfaces.

The study of friction, wear, and lubrication, as well as other phenomena related to the contact of solid surfaces in relative motion is referred to as Tribology. In this chapter, we introduce the general concepts of Tribology including the principles mechanical contact of rough surfaces, friction, wear, and lubrication. After that we discuss current advances in self-lubricating materials. Friction-induced self-organization and tribology of metal matrix composites are discussed in the consequent chapters.

6.1 Friction and Wear as Manifestations of the Second Law of Thermodynamics

Friction is resistance to the relative lateral motion of solid surfaces, fluid layers, or material elements in contact. Friction is a universal phenomenon and it reflects the general trend of energy to dissipate. In the ideal case of the contact of absolutely rigid bodies and conservative forces acting among them, there would be no energy dissipation. However, any nonideality, such as surface roughness and deformation tends to lead to dissipation. Therefore, friction has a fundamental nature and reflects the general trend of energy to be dissipated, as expressed in the Second law

M. Nosonovsky and P.K. Rohatgi, *Biomimetics in Materials Science: Self-Healing, Self-Lubricating, and Self-Cleaning Materials*, Springer Series in Materials Science 152,
DOI 10.1007/978-1-4614-0926-7_6,

Table 6.1 Dissipation and friction mechanisms corresponding to different hierarchy levels (based on Nosonovsky and Bhushan 2008a)

Ideal situation (reversible process)	Real situation (irreversible process)	Mechanism of dissipation leading to friction	Friction mechanism	Hierarchy level
Nonadhesive surfaces	Chemical interaction between surfaces is possible	Breaking chemical adhesive bonds	Adhesion	Molecule
Conservative adhesive forces	Conservative (van der Waals) forces and nonconservative (chemical) bonds	Breaking chemical adhesive bonds	Adhesion	Molecule
Rigid material	Deformable (elastic and plastic) material	Radiation of elastic waves (phonons)	Adhesion	Surface
Smooth surface	Rough surface	Plowing, ratchet mechanism, cobblestone mechanism	Deformation, ratchet, cobblestone mechanisms	Asperity
Homogeneous surface	Inhomogeneous surface	Energy dissipation due to inhomogeneity	Adhesion	Surface

of thermodynamics. Despites the apparent simplicity of the dry friction and its relation to the Second law of thermodynamics, there is no simple thermodynamic theory of friction. The reason is that there are many mechanisms of dry friction, and these mechanisms have to be considered separately. Instead, there are so-called empirical laws or rules of dry friction, which were formulated several hundred years ago by Leonardo da Vinci (1452–1519), Guillaume Amontons (1663–1705), and Charles-Augustin de Coulomb (1736–1806) and are commonly referred to as the "Amontons–Coulomb laws" or just "the Coulomb law" (sometimes also "the Amontons law"). Frictional mechanisms are summarized in Table 6.1.

Similarly to friction, wear reflects the tendency of matter to deteriorate irreversibly, which is another consequence of the Second law of thermodynamics. Again, there is no single quantitative "law" of wear, since there are several physical and chemical processes which lead to the surface deterioration. Instead, there are empirical laws or rules, which relate the wear rate (the volume of worn material per second) with the normal load at the interface. Most models of friction and wear are based on the models of mechanical contact of rough surfaces.

The third big area of Tribology, in addition to the friction and wear, is the lubrication. Lubrication is applied to the interface in order to reduce friction and wear and thus the lubrication cannot be studied separately from friction and wear. Since our interest is in self-lubrication or the ability of the interface to achieve low friction and wear without the external supply of lubrication, in this chapter, we will have to discuss first theories of contact of rough surfaces, then modern theories of friction and wear, and only after that we will be able to review modern approaches to self-lubrication.

6.2 Contact of Rough Solid Surfaces

All natural and artificial solid surfaces contain irregularities irrespective of the method of their formation. No machining method can produce a molecularly smooth surface using conventional materials. Even the smoothest surfaces, obtained by cleavage of some crystals (such as graphite or mica), contain irregularities, heights of which exceed interatomic distances.

Engineered surfaces typically have several types of deviation from the prescribed form: the waviness, random roughness, and flow. The waviness may result from machine vibration or chatter during machining as well as the heat treatment or warping strains. It includes irregularities with a relatively long (many microns) wavelength. Roughness is formed by fluctuation of the surface of short wavelengths, characterized by asperities (local maxima of the surface height) and valleys (local minima of the surface height). Flows are unintentional, unexpected, and unwanted interruptions in the texture.

In addition to surface irregularities, the engineering solid surface itself consists of several zones or layers, such as the chemisorbed layer (0.3 nm), physisorbed layer (0.3–3 nm), chemically reacted layer (10–100 nm), etc. In the chemisorbed layer, the solid surface bonds to the adsorption species through covalent bonds with an actual sharing of electrons. In the physisorbed layer, there are no chemical bonds between the substrate and the adsorbent, and only van der Waals force is involved. The van der Waals force is relatively weak (under 10 kJ mol^{-1}) and long range (nanometers) as opposed to the strong (40–400 kJ mol^{-1}) and short-range (comparable with the interatomic distance of about 0.3 nm) chemical bonding. Typical adsorbents are oxygen, water vapor, or hydrocarbons from the environment, which can condense at the surface. While chemisorbed layer is usually a monolayer, the physisorbed layer may include several layers of the molecules. The chemically reacted is significantly thicker and involves many layers of molecules. The typical example of the chemically reacted layer is the oxide layer at the surface of a metallic substrate (Bhushan 2002; Nosonovsky and Bhushan 2008a).

When two rough solid surfaces come into a mechanical contact, the real (or "true") area of contact is usually small in comparison with the nominal (or "apparent") area of contact, because the contact takes place only at the tops of the asperities. In most cases, only the highest asperities participate in the contact. This makes the dependency of the real area of contact, A_r, and the total number of contact spots, N, upon the roughness parameters during the elastic contact, an almost linear function.

There are several quantitative parameters, which are commonly used to characterize random solid surface roughness, that is, a random derivation from the nominal (prescribed) shape. These are the amplitude (or height) parameters and the spatial (related to the length of asperities) parameters (Thomas 1982; Bhushan 2002). The most commonly used amplitude parameter is the root mean square (RMS) or the standard deviation from the center-line average. For a 2D roughness

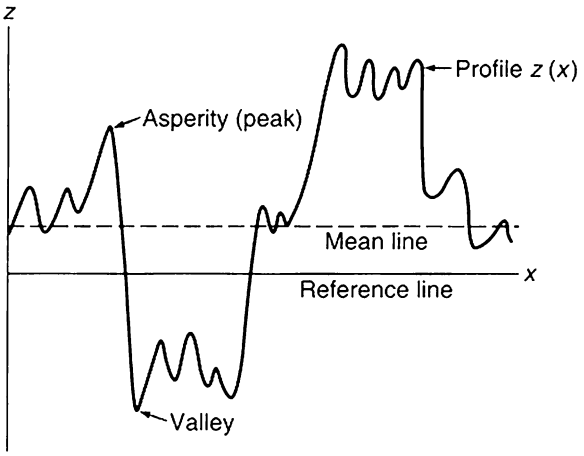

Fig. 6.1 Schematics of a rough surface profile (based on Nosonovsky and Bhushan 2008a)

profile $z(x)$, the center-line average is defined as the arithmetic mean of the absolute value of the vertical deviation from the mean line of the profile (Fig. 6.1).

$$R_{\mathrm{a}} = \frac{1}{L}\int_0^L |z - m| \mathrm{d}x, \tag{6.1}$$

where L is the sampling length and m is the mean.

$$m = \frac{1}{L}\int_0^L z \, \mathrm{d}x. \tag{6.2}$$

The square RMS is given by

$$\sigma^2 = \frac{1}{L}\int_0^L (z - m)^2 \mathrm{d}x. \tag{6.3}$$

Since different rough surface profiles can have same RMS, additional parameters are required to characterize details of surface profile. The cumulative probability distribution function, $P(h)$ associated with the random variable $z(h)$, is defined as the probability of the event that $z(x) < h$, and is written as

$$P(h) = \mathrm{Probability}(z < h). \tag{6.4}$$

It is common to describe the probability structure of random data in terms of the slope of the distribution function, known as the probability density function (PDF) and given by the derivative

$$p(z) = \frac{\mathrm{d}P(z)}{\mathrm{d}z}. \tag{6.5}$$

The integral of the PDF is equal to $P(z)$ and the total area under the PDF must be unity (Bhushan 2002).

In many practical cases, the random data tend to have the so-called Gaussian or normal distribution with the PDF given by

$$p(z) = \frac{1}{\sigma\sqrt{2\pi}} \exp\left(-\frac{(z-m)^2}{2\sigma^2}\right), \tag{6.6}$$

where m is the mean and σ is the standard deviation. For convenience, the Gaussian function is often plotted in terms of the normalized variable $z^* = (z - m)/\sigma$ as

$$p(z^*) = \frac{1}{\sqrt{2\pi}} \exp\left(-\frac{z^{*2}}{2}\right) \tag{6.7}$$

(Bhushan 2002). The Gaussian distribution is found in nature and technical applications when the random quantity is a sum of many random factors acting independently of each other. When an engineering surface is formed, many random factors contribute into the roughness, and thus in many cases roughness height is governed by the Gaussian distribution. Such surfaces are called Gaussian surfaces (Nosonovsky and Bhushan 2008a).

In order to represent spatial distribution of random roughness, the autocorrelation function, which is defined as

$$C(\tau) = \lim_{L\to\infty} \frac{1}{\sigma^2 L} \int_0^L [z(x) - m][z(x+\tau) - m]\,\mathrm{d}x. \tag{6.8}$$

The autocorrelation function characterizes the correlation between two measurements taken at the distance τ apart, $z(x)$, and $z(x + \tau)$. It is obtained by comparing the function $z(x)$ with a replica of itself shifted for the distance τ. The function $C(\tau)$ approaches zero if there is no statistical correlation between values of z separated by the distance τ; in the opposite case $C(\tau)$ is different from zero. Many engineering surfaces are found to have an exponential autocorrelation function

$$C(\tau) = \exp\left(\frac{-\tau}{\beta}\right), \tag{6.9}$$

where β is the parameter called the correlation length or the length over which the autocorrelation function drops to a small fraction of its original value. At the distance β, the autocorrelation function falls to the $1/e$. In many cases, the value $\beta^* = 2.3\beta$ is used for the correlation length, at which the function falls to 10% of its original value (Bhushan 2002).

For a Gaussian surface with the exponential autocorrelation function, σ and β^* are two parameters of the length dimension which conveniently characterize the roughness. While σ is the height parameter, which characterizes the height of a typical roughness detail (asperity), β^* is the length parameter, which characterizes the length of the detail. The average absolute value of the slope is proportional to the ratio σ/β^*, whereas the average curvature is proportional to β^*/σ^2. For a Gaussian surface, σ is related to the RMS as $\sigma = \left(\sqrt{\pi/2}\right)R_a$ (Bhushan 2002). These two parameters, σ and β^*, are convenient for characterization of many random surfaces. Note that a Gaussian surface has only one inherent length scale parameter, β^*, and one vertical length scale parameter, σ, and thus it cannot describe the multiscale roughness.

When two rough surfaces come into a mechanical contact, the real area of contact is small in comparison with the nominal area of contact, because the contact takes place only at the tops of the asperities. For two rough surfaces in contact, an equivalent rough surface can be defined of which the values of the local heights, slopes, and local curvature are added to each other. The composite standard deviation of profile heights is related to those of the two rough surfaces, σ_1 and σ_2 as

$$\sigma^2 = {\sigma_1}^2 + {\sigma_2}^2. \tag{6.10}$$

The composite correlation length is related to those of the two rough surfaces, β_1^* and β_2^* as

$$\frac{1}{\beta^*} = \frac{1}{\beta_1^*} + \frac{1}{\beta_2^*}. \tag{6.11}$$

Using the composite rough parameters allows to effectively reduce the contact problem of two rough surfaces to the contact of a composite rough surface with a flat surface (Bhushan 1999, 2002).

Two parameters of interest during the elastic and plastic contact of two rough surfaces are the real area of contact, A_r, and the total number of contact spots, N. In most cases, only the highest asperities participate in the contact. This allows to linearize the dependence of A_r and N upon the roughness parameters during the elastic contact as

$$A_r \propto \frac{W\beta^*}{\sigma E}, \tag{6.12}$$

$$N \propto \frac{W}{\sigma\beta^*}, \tag{6.13}$$

where W is the normal load force and E is the composite elastic modulus. Qualitatively, the higher the asperities, the larger is σ and smaller is A_r, the wider the asperities, the larger is β^* and smaller is A_r. The larger and wider the asperities, the smaller is A_r

(Bhushan and Nosonovsky 2003, 2004a, b). For plastic contact, N, which depends upon the contact topography and thus is independent on whether the contact is elastic or plastic, is still given by (6.13) for a given separation between the surfaces (Bhushan and Nosonovsky 2004a), whereas the real contact area is found by dividing the load by the hardness

$$A_{\mathrm{r}} \propto \frac{W}{H}. \tag{6.14}$$

Note that for elastic contact, the linear dependence of A_{r} on W (6.12) is the consequence of the fact the load W is moderate and therefore only highest asperities participate in the contact. For very high loads (or elastic materials such as rubber), the real area of contact can become comparable with the nominal area of contact and thus (6.12) and (6.13) will not stand (Nosonovsky and Bhushan 2008a). The linear dependence of the real area of contact (for both elastic and plastic contact) on the normal load is the factor responsible for the linear proportionality of the friction force to the normal load, as it will be explained below.

6.3 Dry Friction and Its Laws

Empirical observations of dry friction between solid surfaces have resulted in the laws of friction. These laws are sometimes attributed to Leonardo da Vinci. However, they became known in the scientific community after they were formulated by Guillaume Amontons and Charles-Augustin Coulomb. The three Amontons (or Amontons–Coulomb) laws state the following:

1. The friction force, F, is directly proportional to the applied normal load, W.

$$F = \mu W \tag{6.15}$$

   where μ is a constant coefficient referred to as the coefficient of dry friction. In an alternative formulation, the coefficient of friction is independent of the normal load, W.
2. The friction force, F, is independent of the nominal (or apparent) area of contact, or, μ is independent of A.
3. The friction force, F, is independent of the sliding velocity V, or μ is independent of V.

Thus, the there laws state that the coefficient of friction is independent of W, A, and V. Sometimes the first two laws are attributed to Amontons, whereas the third one is attributed to Coulomb. In the original formulation, the authors of the laws admitted that the friction force can slightly depend on the sliding velocity; in particular, it tends to increase for small but increasing velocities, remain constant for higher velocities, and decrease for even higher velocities. Summarizing the

three laws, the coefficient of friction is independent of the normal load, nominal area of contact, and sliding velocity.

The three Amontons–Coulomb laws of friction should not be viewed as logically independent "axioms." Quite oppositely, the first and the second laws can be treated as a logical consequence of each other. If the friction force F is independent of the nominal area of contact A, dividing the contact region into two halves (each having the area of $A/2$) will result in the normal load $W/2$ supported by each half. Since the total force is equal to sum of forces acting at each part of the contact region, one concludes that the friction force $F/2$ act at each half and thus the friction force is proportional to the normal load.

Speaking more formally, suppose that the friction force depends on the normal load and nominal area of contact as $F = f(W, A)$, so that changing the scale of W and A by a and b times results in the change on friction with the power exponents of n and m correspondingly

$$f(\alpha W, \beta A) = \alpha^n \beta^m f(W, A). \tag{6.16}$$

Since force is an additive function, we have also

$$f(\alpha W, \alpha A) = \alpha f(W, A). \tag{6.17}$$

Setting $\alpha = \beta$ and combining (6.16) and (6.17) yields $n + m = 1$. Therefore, the validity of the first law ($n = 1$) implies also the validity of the second law ($m = 0$) and vice versa (Nosonovsky and Bhushan 2008a).

The third empirical law of friction, which states that the friction force does not depend on the real area of contact, is logically independent of the first two laws. Despite that, it is possible to show, however, that velocity-dependence of dry friction is also related to the dependence on the size of contact. Consider the contact of a plastic rough surface with a rigid flat. An important characteristic of such contact is the average size of individual asperity contacts, a, which depends upon the separation distance between the two bodies. The simplified models of contact predict that a is independent of the normal load and the size of contact. For example, assuming that the contact shape is circular, the average area of individual asperity contact is πa^2. On the other hand, the individual contact area is given by the ratio of the real area of contact to the number of contact $\pi a^2 = A_r/N$. From (6.13) and (6.14), a is independent of W. The reasoning behind that is that when the load is increased, and the separation between the contacting surfaces increases, the size of individual asperity contacts grows; however, more new small contacts are created, so the average contact size does not change. However, in reality, the average size of contact depends on the separation between two bodies, for large separation the contact size is small (Fig. 6.2). The separation can change due to the change of the load, nominal area of contact, and sliding velocity (longer existing contacts tend to provide lower separation due to the creep and visco-plastic deformation), which makes the load-, contact size-, and velocity-dependence of friction.

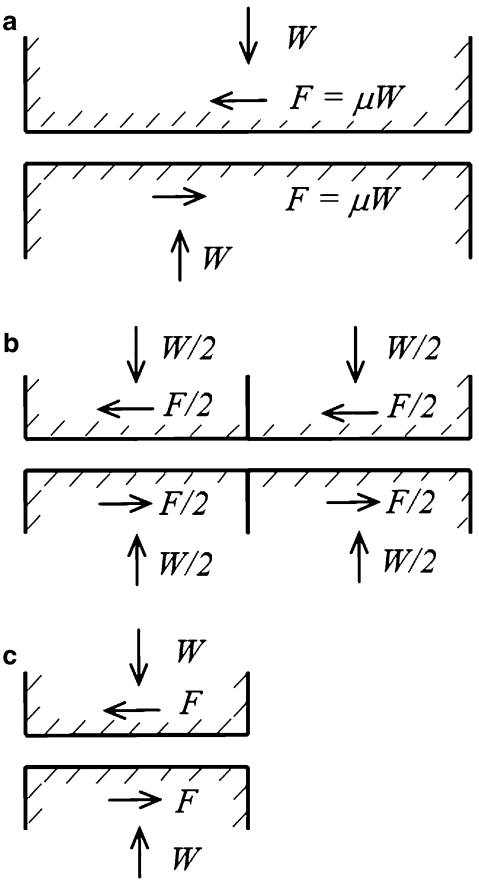

Fig. 6.2 Illustration of coupling of the laws, which state that the coefficient of friction is independent of the normal load and apparent area of contact. (**a**) The nominal area of contact A_a between two bodies supports the normal load of W and results in friction force $F = \mu W$. (**b**) Parts of the nominal area of contact, A_a/c (shown for $c = 2$) support the normal load of W/c and results in the friction force $F/c = \mu W/c$. (**c**) For friction force linearly dependent on the normal load, an increase of the load at the small contact area up to W, results in the friction force equal to F and thus independent of the area of contact (Nosonovsky 2007c)

It is usually stressed in the tribological literature that the three Amontins–Coulomb empirical laws of friction are only approximations and there are many situations when these laws are not valid. For this reason, some tribologists prefer to speak about the "rules of friction" rather than laws, reserving the word "law" for fundamental laws of nature, such as the Newton's laws of mechanics. On the other hand, the Amontins–Coulomb laws are valid for an amazingly broad range of material combinations, friction mechanisms, and loads ranging from nanonewtons to thousands of tons.

6.4 Theories Explaining Dry Friction

Despite the simplicity of its empirical laws, friction is a very complex phenomenon and it can involve various mechanisms of different physical nature, apparently unrelated, acting independently or simultaneously.

6.4.1 Adhesive Friction

Adhesion is the most common and best studied mechanism of dry friction, which occurs at a wide range of length scales and conditions. When two surfaces are brought into contact, adhesion or bonding across the interface can occur, and a normal force, called the adhesion force, is required to pull apart the two solids (Bowden and Tabor 1950). The word "adhesion" is a general term for such a force of any physical nature, which may include chemical covalent forces, electrical van der Waals interactions, electrostatic forces, and capillary forces. Since the typical range of the adhesion force (with the exception of the capillary force) is in nanometers, the role of the adhesion is important at the nanoscale. For chemically nonactive surfaces, there are two types of interatomic adhesive forces: the strong (chemical) forces, such as covalent, ionic, metallic bonds, whose rupture corresponds to large absorption of energy (around 400 kJ mol^{-1}), and weak forces, such as hydrogen bonds, van der Waals forces (few kJ mol^{-1}) (Maugis 1999). Weak conservative forces act at larger ranges of distance, whereas strong bonds act at short distances.

For macrofriction of nonadhesive surfaces, Bowden and Tabor (1950) suggested that the friction force F is directly proportional to the real area of contact A_r and shear strength at the interface τ_f

$$F = \tau_f A_r. \tag{6.18}$$

Every nominally flat surface in reality has roughness. The real area of contact is only a small fraction of the nominal area of contact because the contacts take place only at the summits of the asperities (Fig. 6.3a). Various statistical models of contact of rough surfaces show that A_r is almost directly proportional to the applied normal load W, for elastic and plastic surfaces, which explains the empirically observed linear proportionality of F and W (the so-called Coulomb–Amontons' rule), assuming constant τ_f (Greenwood and Williamson 1966). The physical nature of the surface shear strength τ_f, however, remains a subject of discussion. For the pure interfacial friction, τ_f may be viewed as the shear component of the adhesive force, which is required to move surfaces relative to each other. Note that the van der Waals adhesion force is conservative and by itself it does not provide a mechanism needed for energy dissipation. It was suggested recently (Maeda et al. 2002; Szoszkiewicz et al. 2005; Zeng et al. 2006; Ruths and Israelachvili 2007) that nanofriction is not related to the adhesion per se, but to the adhesion *hysteresis*. The energy needed to separate two surfaces is always greater than the energy gained by bringing them together (Fig. 6.4). As a result, the energy is dissipated during the separation process. The adhesion hysteresis or surface energy hysteresis can arise even between perfectly smooth and chemically homogeneous surfaces supported by perfectly elastic materials. The adhesion hysteresis exists due to surface roughness and inhomogeneity (Maeda et al. 2002). The van der Waals force itself is conservative and does not provide a mechanism of energy dissipation. However, the

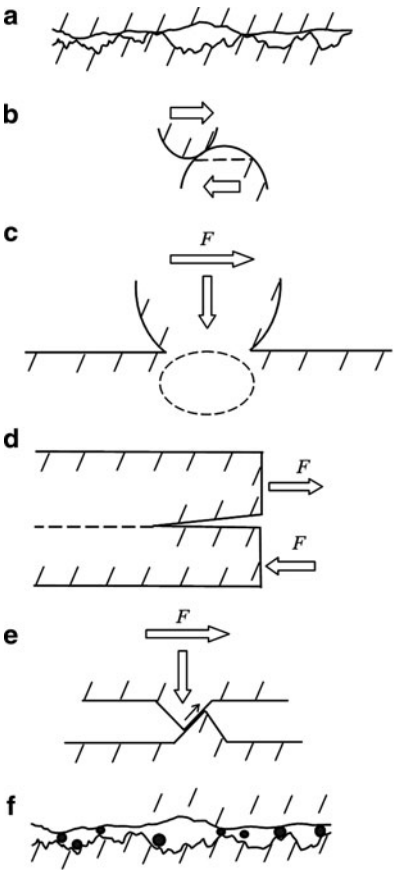

Fig. 6.3 Fundamental mechanisms of friction (**a**) adhesion between rough surfaces, (**b**) plowing, (**c**) the plastic yield, (**d**) the similarity of a mode II crack propagation and friction, (**e**) the ratchet mechanism, (**f**) the third-body mechanism (Nosonovsky and Bhushan 2008a)

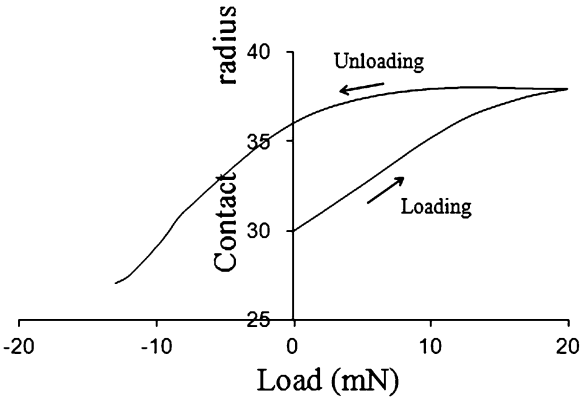

Fig. 6.4 Adhesion hysteresis. Adhesion force is different when surfaces are approaching contact and when separating for polystyrene (based on Maeda et al. 2002)

adhesion hysteresis due to surface heterogeneity and chemical reactions leads to dissipation (Maeda et al. 2002; Szoszkiewicz et al. 2005; Zeng et al. 2006; Ruths and Israelachvili 2007). Both sliding and rolling friction involve the creation and consequent destruction of the solid–solid interface. During such a loading–unloading cycle, the amount of energy ΔW is dissipated per unit area.

Since the underlying physical reason of the adhesion hysteresis is in surface roughness and chemical heterogeneity, there is a natural way to obtain the hysteresis of a conservative van der Waals force by assuming that the surface is not perfectly rigid, that is, deformable. There are a number of contact models which combine the elastic deformation and adhesion (Johnson 1998), however, these theories do not address the issue of adhesion hysteresis.

Consider a rigid cylinder of radius R and length L rolling along a solid surface with the van der Waals attractive adhesion force between them. From the energy balance, when the cylinder passes the distance d, the amount of dissipated energy $\Delta W A_\mathrm{r}$ is equal to the work of the friction force F at the distance d, and therefore, the friction force is given by (Nosonovsky 2007b)

$$F = \frac{A_\mathrm{r} \Delta W}{d}. \tag{6.19}$$

For a multiasperity contact, the real area of contact, A_r, is only a small fraction of the nominal contact area, which is equal to the surface area covered by the cylinder, Ld. During frictional sliding of a solid cylinder against a flat surface, the solid–solid interface is created and destroyed in a similar manner to rolling. Based on the adhesion hysteresis approach, the frictional force during sliding is also given by (6.19) and all considerations presented in the preceding section are valid also for the sliding friction.

Summarizing, the adhesive friction provides the mechanism of energy dissipation due to breaking strong adhesive bonds between the contacting surfaces and due to the adhesion hysteresis. In order for adhesive friction to exist, either irreversible adhesion bonds should form, or the contacting bodies should be deformable and thus nonideally rigid. Adhesive friction mechanism involves weak short-range adhesive force and strong long-range bulk forces.

6.4.2 Deformation of Asperities

Another important mechanism of friction is the deformation of interlocking asperities (Fig. 6.3b). Like adhesion, which may be reversible (weak) and irreversible (strong), deformation may be elastic (i.e., reversible) and plastic (irreversible plowing of asperities). For elastic deformation, certain amount of energy is dissipated during the loading–unloading cycle due to radiation of elastic waves and viscoelasticity, so an elastic deformation hysteresis exists, similar to the adhesion hysteresis. The value of deformational friction force is usually higher

than that of adhesive friction and depends on the yield strength and hardness, which trigger a transition to the plastic deformation and plowing. The transition from adhesive to deformational fiction mechanism depends on load and yield strength of materials and usually results in a significant increase of the friction force.

We discuss in the preceding section the effect of adhesion hysteresis on friction of a cylinder sliding upon a flat surface. We found that the contribution of adhesion hysteresis into the sliding friction is equal to that of rolling friction. However, it is well known from the experiments that sliding friction is usually greater than the rolling friction. This is because plowing of asperities takes place during sliding. Even smooth surfaces have nanoasperities, and their interlocking can result in plowing and plastic deformation of the material. Usually, asperities of softer material are deformed by asperities of a harder material. The shear strength during plowing is often assumed to be proportional to the average absolute value of the surface slope (Bhushan 1999, 2002). It is therefore assumed that in addition to the adhesion hysteresis term, there is another component, H_p, which is responsible for friction due to surface roughness and plowing (Nosonovsky 2007b).

$$F = A_r\left(\frac{\Delta W}{d + H_p}\right). \tag{6.20}$$

The plowing term may be assumed to be proportional to the average absolute value of the surface slope. Note that the normal load is not included into (6.20) directly; however, A_r depends upon the normal load. The right-hand side of (6.20) involves two terms: a term that is proportional to adhesion hysteresis and a term that is proportional to roughness. Nosonovsky (2007b) pointed out that Eq. 6.20, which governs energy dissipation during the solid–solid friction, is similar to the equations that govern energy dissipation during solid–liquid friction.

Due to the surface roughness, deformation occurs only at small parts of the nominal contact area, and the friction force is proportional to the real area of contact involving plowing, as given by (3.2). Due to the small size of the real area of contact compared with the nominal area of contact, the plastically deformed regions constitute only a small part of the bulk volume of the contacting bodies.

6.4.3 Plastic Yield

Chang et al. (1987) proposed a model of friction based upon plastic yield, which was later modified by Kogut and Etzion (2004). They considered a single-asperity contact of a rigid asperity with an elastic–plastic material. With an increasing normal load, the maximum shear strength grows and the onset of yielding is possible. The maximum shear strength occurs at a certain depth in the bulk of the body (Fig. 6.3c). When the load is further increased and the tangential load is applied,

the plastic zone grows and reaches the interface. This corresponds to the onset of sliding. Kogut and Etzion (2004) calculated the tangential load at the onset of sliding as a function of the normal load using the finite elements analysis and found a nonlinear dependence between the shear and tangential forces. This mechanism involves plasticity and implies structural vulnerability of the interface compared to the bulk of the contacting bodies.

6.4.4 *Fracture*

For a brittle material, asperities can break forming wear debris. Therefore, fracture also can contribute into friction. There is also an analogy between mode II crack propagation and sliding of an asperity (Rice 1991; Gerde and Marder 2001; Kessler 2001, Fig. 6.3d). When an asperity slides, the bonds are breaking at the rear, while new bonds are being created at the front end. Thus, the rear edge of asperity can be viewed as a tip of a propagating mode II crack, while the front edge can be viewed as a closing crack. Gliding dislocations, emitted from the crack tip, can also lead to the microslip or local relative motion of the two bodies (Bhushan and Nosonovsky 2003; Nosonovsky and Bhushan 2005a, b). Calculations have been conducted to relate the stress intensity factors with friction parameters (Rice 1991; Gerde and Marder 2001; Kessler 2001). Crack and dislocation propagation along the interface implies that the interface is weak compared to the bulk of the body.

6.4.5 *Ratchet and Cobblestone Mechanisms*

Interlocking of asperities may result in one asperity climbing upon the other, leading to the so-called ratchet mechanism (Bhushan 1999, 2002). In this case, in order to maintain sliding, a horizontal force should be applied, which is proportional to the slope of the asperity (Fig. 6.3e). At the atomic scale, a similar situation exists when an asperity slides upon a molecularly smooth surface and passes through the tops of molecules and valleys between them. This sliding mechanism is called "cobblestone mechanism" (Israelachvili 1992). This mechanism implies that the strong bonds are acting in the bulk of the body, whereas interface bonds are weak.

6.4.6 *"Third-Body" Mechanism*

During the contact of two solid bodies, wear and contamination particles can be trapped at the interface between the bodies (Fig. 6.3f). Along with liquid which condensates at the interface, they form the so-called "third body" which plays a significant role in friction. The trapped particles can significantly increase the

coefficient of friction due to plowing. Some particles can also roll and thus serve as rolling bearings, leading to reduced coefficient of friction. However, in most engineering situations, only 10% of the particles roll (Bhushan 2002) and thus the third-body mechanism leads to an increase of the coefficient of friction. At the atomic scale, adsorbed mobile molecules can constitute the "third body" and lead to significant friction increase (He et al. 2003). The third body has much weaker bonds to the surface, than those in the bulk of the body.

In summary, there are several mechanisms of dry friction. They all are associated with a certain type of heterogeneity or nonideality, including surface roughness, chemical heterogeneity, contamination, and irreversible forces. All these mechanisms are also characterized by the interface forces being small compared to the bulk force. In the consequent chapters, we discuss linearity of friction as a result of presence of a small parameter, nonlinearity of friction, related to heterogeneity and hierarchical structure and multiscale nature of the frictional mechanisms.

6.4.7 Origins of the Linearity of Friction

Empirical observations regarding dry friction are summarized in the so-called Coulomb–Amontons' rule, which states that the friction force F is linearly proportional to the normal load W

$$F = \mu W, \tag{6.21}$$

where μ is a constant for any pair of contacting materials, called the coefficient of friction. The coefficient of friction is almost independent of the normal load, nominal size of contact, and sliding velocity. Although there is no underlying physical principle, which would require the friction force to be linearly proportional to the normal load, (6.21) is valid for a remarkably large range of conditions and regimes of friction, from macro- to nanoscale, for loads ranging from meganewtons to nanonewtons and for various material combinations. Two main physical explanations of the linearity of friction have been suggested, based on the friction force proportionality to the real area of contact between the two bodies and to the average slope of a rough surface.

As it has been explained above, the real area of contact usually constitutes a small fraction of the nominal area of contact. Thus, for metals at loads typical for technical applications, the real area of contact constitutes less than 1% of the nominal area of contact. Various statistical models of contacting rough surfaces have been proposed, following the first publication by Greenwood and Williamson (1966). These models conclude, using the numerical computations, that for typical roughness distributions, such as the Gaussian roughness, for both elastic and plastic materials, the real area of contact is almost linearly proportional to the load (Adams and Nosonovsky 2000).

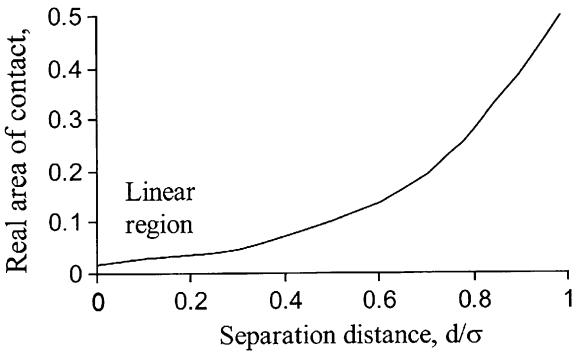

Fig. 6.5 The number of contacts and contact area as a function of separation between the contacting bodies (based on Onions and Archard 1973)

For the elastic contact of a smooth surface and a rough surface with the correlation length β^* and standard deviation of profile height σ, the real area of contact is given by (6.12). Note that σ is the vertical and β^* is the horizontal roughness parameters with the dimension of length. The smoother is the surface (higher the ratio β^*/σ), the larger is A_r. Physically, the almost linear dependence of the real area of contact upon the normal load in this case is a result of the small extent of contact, in other words, it is the consequence of the fact that the real area of contact is a small fraction of the nominal area of contact. With increasing load, as the fraction of the real area of contact grows, or for very elastic materials, such as the rubber, the dependence is significantly nonlinear. However, for small real area of contact, with increasing load the area of contact for every individual asperity grows, but the number of asperity contacts also grows, so the average contact area per asperity remains almost constant (Fig. 6.5).

For plastic contact, the real area of contact is independent of roughness parameters and given by the ratio of the normal load to the hardness of a softer material H_s (6.14). Hardness is usually defined in indentation experiments as force divided by the indentation area, so (3.11) naturally follows from this definition. In many cases, it may be assumed that the hardness is proportional to the yield strength. Whether the contact is elastic or plastic may depends upon the roughness parameters, elastic modulus, and hardness. Interestingly, Greenwood and Williamson (1966) showed whether the contact is elastic or plastic does not depend upon the load, but solely upon the so-called plasticity index $\psi = \left(\sqrt{\sigma/R_p}\right)E^*/H$, where σ is the standard deviation of peak heights and R_p is mean asperity peak radius. Combining the Bowden and Tabor's model (6.18) with the conclusions of the statistical models of contact of rough surface ((6.12)–(6.14)), the friction force due to adhesion is proportional to the real area of contact and adhesive shear strength τ_a which yields a linear dependence of F upon W.

A different explanation of the linear dependence of A_r on W is given by so-called fractal models of rough surfaces. These models assume that a rough surface or profile possesses the mathematical properties of self-similar, or fractal, surfaces and curves. When the resolution of a measuring equipment is magnified, more and more further details are observed, which are similar to the details observed at higher scale of resolution. Such a curve or surface, which reproduces all its properties at

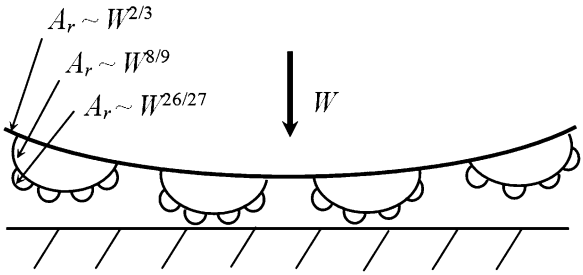

Fig. 6.6 A multiscale rough elastic surface in contact with a flat surface (Nosonovsky and Bhushan 2008a)

different length scales, is called self-similar. If some properties are reproduced, it is called a self-affine curve or surface. Self-similar and self-affine objects were introduced into the mathematics yet in 1930s; however, their application to various physical and engineering problems became popular in the consequent decades after they were popularized in the 1970s by B. Mandelbrot who actually coined the term "fractals."

Long before the term "fractal" was invented by mathematicians, Archard (1957) studied multiscale roughness with small asperities on top of bigger asperities, with even smaller asperities on top of those, and so on (Fig. 6.6). According to the Hertzian model, for the contact of an elastic sphere of radius R with an elastic flat with the contact radius a, and the contact area $A = \pi a^2$ are related the normal load as

$$A_{\mathrm{r}} = \pi\left(\frac{3RW}{4E^*}\right)^{2/3}. \tag{6.22}$$

The pressure distribution as the function of the distance from the center of the contact spot, r, is given by

$$p = \left(\frac{6WE^{*2}}{\pi^3 R^2}\right)^{1/3}\left(\sqrt{1-\left(\frac{r}{a}\right)^2}\right). \tag{6.23}$$

Let us now assume that the big spherical asperity is covered uniformly by many asperities with a much smaller radius, and these asperities form the contact. For an asperity located at the distance r from the center, the load is proportional to the stress given by (6.24). The area of contact of this small asperity is still given by (6.22) with using the corresponding load. The dependence of total contact area upon W is then given by integration of the individual contact areas by r as (Archard 1957)

$$\begin{aligned} A_{\mathrm{r}} &\propto \int_0^a \left[W^{(1/3)}\left(\sqrt{1-\frac{r^2}{a^2}}\right)\right]^{2/3} 2\pi r\,\mathrm{d}r, \\ &\propto \int_0^{\pi} \left[W^{(1/3)}\cos\phi\right] \propto^{2/3} 2\pi(a\sin\phi)a\cos\phi\,\mathrm{d}\phi, \\ &\propto W^{(2/9)}a^2 \propto W^{(2/9)}W^{(2/3)} \propto W^{(8/9)}. \end{aligned} \tag{6.24}$$

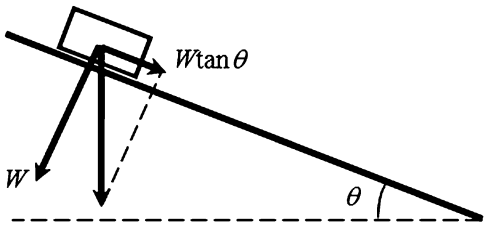

Fig. 6.7 Slope-controlled friction. For a body moving without acceleration upon an inclined surface with slope θ, the shear force, $W \tan \theta$, is proportional to the normal load, W (Nosonovsky and Bhushan 2008a)

In the above derivation, the variable change $r = a \sin \phi$ and (3.6) were used. The integral of the trigonometric functions can be easily calculated, however, its value is not important for us, because it is independent of a and W.

If the small asperities are covered by the "third-order" asperities of even smaller radius, the total area of contact can be calculated in a similar way as

$$A_r \propto \int_0^a \left[W^{(1/3)} \left(\sqrt{1 - \frac{r^2}{a^2}} \right) \right]^{2/3} 2\pi r dr \propto W^{(8/9)} a^2 \propto W^{(26/27)}. \tag{6.25}$$

Continuing this iterative procedure of building small asperities on top of larger asperities, we find that

$$A_r \propto \lim_{n \to \infty} \left(W^{\frac{3^n - 1}{3^n}} \right) = W, \tag{6.26}$$

where n is the number of orders of asperities, leading to an almost linear dependence of A_r upon W with increasing n. Later more sophisticated fractal surface models were introduced, which lead to similar results (Majumdar and Bhushan 1991).

Thus, both statistical and fractal roughness, for elastic and plastic contact, combined with the adhesive friction law (6.18) results in an almost linear dependence of the friction force upon the normal load.

A completely different explanation of the linearity of friction is based on the assumption that during sliding asperities climb upon each other (the ratchet mechanism) (Fig. 6.7). From the balance of forces, the horizontal force, which is required to initiate motion, is given by the normal load multiplied by the slope of the asperities.

$$F = W \tan \theta, \tag{6.27}$$

where θ is the slope angle of the asperities. Comparing (6.21) and (6.26), it may be concluded that for a rough surface, the coefficient of fiction is equal to the average absolute value of its slope, $\mu = |\tan \theta|$. The sign of the absolute value is required because asperities can climb only if the slope is positive. Similar to the ratchet mechanism is the cobblestone mechanism, which is typical for the atomic friction.

Among other attempts to explain the linearity of the friction force with respect to the load, two modeling approaches are worth to mention. Sokoloff (2006) suggested that the origin of the friction force is in the hardcore atomic repulsion. The vertical

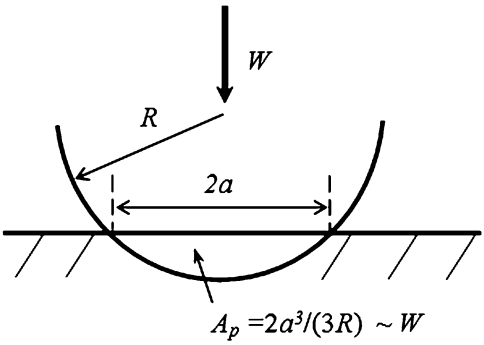

Fig. 6.8 "Elastic plowing": the transsectional area of the asperity is linearly proportional to the Hertzian normal load (Nosonovsky and Bhushan 2008a)

component of the vector of the repulsion force, which contributes to the normal load, is proportional to the horizontal component of the same vector, which contributes into friction, because the vector has a certain average orientation. In a sense, this is still the same slope-controlled mechanism, however, considered at the atomic level.

Ying and Hsu (2005) suggested another interesting macroscale explanation of the linearity of friction. They noticed that using the Herzt theory (6.22) for a spherical asperity of radius R, slightly indented into a substrate, the contact radius, a, is proportional to the power 1/3 of the penetration h (Fig. 6.8).

$$a \propto W^{1/3}. \tag{6.28}$$

When such an asperity plows the substrate, the cross-sectional plowing area (or projection of the indented part of the sphere upon a vertical plane) A_p is given by a cubic function of a and thus is proportional to the normal load

$$A_\mathrm{p} = \frac{2a^3}{3R} \propto W. \tag{6.29}$$

Thus, in the case of "elastic plowing," the plowing force, which is proportional to A_p, is linearly proportional to the normal load.

We have found that the mechanisms of friction are quite divers and apparently unrelated to each other (Table 6.2). Several physical mechanisms result in a linear dependence of the friction force upon the normal load. Mathematically, a linear dependence between the two parameters usually exists, when the domain of a changing parameter is small, and thus a more complicated dependency can be approximated within this domain as a linear function. For example, if the dependency of the friction force upon the normal load is given by

$$F = f(W) \approx f(0) + f'(0)W + \frac{f''(0)}{2}W^2 = \mu W + \frac{f''(0)}{2}W^2, \tag{6.30}$$

Table 6.2 Mechanisms of friction and linear dependence of the friction force upon the normal load (Nosonovsky and Bhushan 2008a)

	Mechanism	Friction force and real area of contact as functions of the normal load
Area-controlled	Elastic hierarchical (Archard)	$F = \tau_a A_r \propto W^{(3^n-1)/3^n}$
	Elastic statistical	$F = \tau_a A_r \propto \frac{\beta^*}{E^* \sigma} W$
	Plastic	$F = \tau_a A_r = \frac{W}{H_s}$
Slope-controlled	Ratchet	$F = W \tan \theta$
Other	Elastic plowing	$F = \tau_a A_p = \frac{2a^3}{3R} \propto W$

The dependency can be linearized as $F = \mu W$ if $W \ll 2\mu/f''(0)$. In other words, the ratio of the load W to a corresponding parameter of the system, given by (3.22) (with the dimension of force), is small. That parameter may correspond to the bulk strength of the body (Nosonovsky and Bhushan 2008a).

6.5 Wear

Wear is defined as material removal and deterioration during the contact of solid surfaces in relative motion. There are several mechanisms which lead to wear. First is the adhesive wear due to the adhesion between the contacting surfaces which can lead to the removal and transfer of particles of a material and displacement of wear debris from one surface to the other. Adhesive wear occurs when two bodies slide over or pressed into each other, which promote material transfer. This involves the plastic deformation of very small fragments within the surface layers.

Second is the abrasive wear due to plowing, cutting, and fragmentation of asperities. Abrasive wear is the loss of material due to hard particles or hard protuberances that are forced against and move along a solid surface. It occurs when a hard rough surface slides across a softer surface. Plowing is the displacement of the material to the side, away from the wear particles, resulting in the formation of grooves that do not involve direct material removal. The displaced material forms ridges adjacent to grooves, which may be removed by subsequent passage of abrasive particles. Cutting is material separated from the surface in the form of primary debris, or microchips, with little or no material displaced to the sides of the grooves. This mechanism closely resembles conventional machining. Fragmentation is material separation from a surface by a cutting process and the indenting abrasive causes localized fracture of the wear material.

Other types of wear are surface fatigue, fretting wear, erosive wear, and cavitation wear. Surface fatigue is weakening of the surface due to cyclic loading. Fretting or fretting fatigue is a repeated cyclical rubbing of the surface. Erosive wear is caused by the impact of solid particles or fluid on the surface. Cavitation wear is due to the contact with fluid.

Fracture can be another mode of wear. During the contact of two asperities with friction and shear loading, the maximum shear strength is usually achieved beneath the surface, rather than at the surface. As a result, plastic yield and flow starts at the subsurface zone and, due to repeated loading, a thin "skin-like" layer of material delaminates.

The quantitative characteristic of wear is the wear volume or volume of worn material, w. The rate of wear is measured in wear volume per unit time. The so-called empirical Archard wear law (or rule) relates the wear rate with the sliding velocity, V, the applied normal load, W, and the hardness, H, of a softer material among the two contacting materials

$$\dot{w} = k\frac{WV}{H}. \tag{6.31}$$

This empirical law of wear was formulated by Archard for the abrasive wear and it states that the wear rate is linearly proportional to the sliding velocity (or the wear volume is linearly proportional to the sliding distance), the ratio of the normal load to the hardness of the softer material, and the coefficient k referred to as "the wear coefficient," which is a characteristic of tribological system somewhat similar to the coefficient of friction.

6.6 Lubrication

Lubrication is interposing a substance called lubricant between the surfaces to carry or to help carry the load between the sliding surfaces. It is employed to reduce friction and wear. The lubricant can be a solid (e.g., graphite, MoS_2), a solid–liquid dispersion, a liquid, a liquid–liquid dispersion, or a gas. In the most common case, the lubricant is fluid capable of bearing the pressure between the surfaces. Adequate lubrication allows smooth continuous operation of equipment, with only mild wear, and without excessive stresses or seizures at bearings.

As the load increases on the contacting surfaces, three lubrication regimes can be observed:

1. Fluid film lubrication regime in which the load is fully supported by the lubricant within the space or gap between the parts in motion relative to one another (the lubricated conjunction), and solid–solid contact is avoided. Two types of the fluid film lubrication are the hydrostatic lubrication, when an external pressure is applied to the lubricant in the bearing, and the hydrodynamic lubrication, when the motion of the contacting surfaces is used to pump lubricant to maintain the lubricating film.
2. Elastohydrodynamic lubrication regime in which the contacting surfaces are separated in general, however the interaction between the asperities can occur and an elastic deformation on the contacting surface enlarges the load-bearing

area whereby the viscous resistance of the lubricant becomes capable of supporting the load.
3. Boundary lubrication is the regime in which the bodies come into closer contact at their asperities and the load is carried by the surface asperities rather than by the lubricant.

Lubricant may also cool the contact areas and remove wear products. While carrying out this function, the lubricant is constantly replaced from the contact areas either by the relative movement (hydrodynamics) or by externally induced forces.

6.7 Self-Lubrication

The term "self-lubrication" has been used for more than two decades and it refers to several methods and effects that reduce friction or wear. Among these methods are the deposition of self-lubricating coatings that are either hard (to reduce wear) or with low surface energy (to reduce adhesion and friction). Besides coatings, self-lubrication can imply the development of metal-, polymer-, or ceramic-based composite self-lubricating materials, often with a matrix that provides structural integrity and reinforcement material that provides low friction and wear. The nanocomposites have become a focus of this research, as well as numerous attempts to include nanosized reinforcement, carbon nanotubes (CNT), and fullerene C_{60} molecules. Simple models assume that these large molecules and nanosized particles serve as "rolling bearings" that reduce friction; however, it is obvious now that the mechanism can be more complicated and involve self-organization. Dynamic self-organization is thought to be responsible for self-lubrication in the atomic force microscopy experiments with the atomic resolution. A different approach involves a layer of lubricant that is being formed in situ during friction due to a chemical reaction. Such a reaction can be induced in situ by mechanical contact, for example, a copper protective layer formed at a metallic frictional interface due to the selective transfer of Cu ions from a copper-containing alloy (e.g., bronze) or from a lubricant. A protective layer can be formed also due to a chemical reaction of oxidation or a reaction with water vapor. For example, a self-lubricating layer of the boric acid (H_3BO_3) is formed as a result of a reaction of water molecules with B_2O_3 coating. Another type of self-lubricating material involves lubricant embedded into the matrix, e.g., inside microcapsules that rupture during wear and release the lubricant. Surface microtexturing that provides holes and dimples which serve as reservoirs for lubricant can be viewed as another method of providing self-lubrication. In addition, we should mention that self-lubrication is observed also in many biological systems and that the term "self-lubrication" is used also in geophysics where it refers to animally low friction between tectonic plates that is observed during some earthquakes.

The design of coatings with hard and lubricious diamond-like carbon (DLC) surfaces requires a study of transitions between adhesive metal, load supporting

carbide, and wear-resistant DLC materials. Voevodin et al. (1997) investigated these transitions were investigated on the Ti–C system prepared by a hybrid of magnetron sputtering and pulsed laser deposition (PLD). Crystalline alpha-Ti, TiC, and amorphous DLC films were formed at 100°C substrate temperature by varying film chemical composition. A gradual replacement of alpha-Ti with TiC, and a two-phase region consisting of crystalline TIC and amorphous carbon (a-C) in transitions from Ti to TiC and from TiC to DLC were found. These transitions were reflected in mechanical properties investigated with nanoindentation. This provided a hard coating with a low friction surface, which also resisted brittle failure in tests with high contact loads.

Neerinck et al. (1998) used PLD to produce superhard (60–70 GPa) self-lubricating DLC with low friction and low wear rate. They obtained thin (2–3 μm) DLC-based coatings for steel substrates, which could maintain friction coefficients of about 0.1 for several million cycles of unlubricated sliding at contact pressures above 1 GPa. Their scratch resistance exeeded that of conventional ceramic (TiN, TiC) coatings.

Vilar (1999) used laser cladding for the protection of materials against wear, corrosion, and oxidation, for the deposition of self-lubricating coatings and thermal barriers, and for the refurbishing of high-cost industrial components. Laser cladding is a hard-facing process that uses a high-powered laser beam to melt the coating material and a thin layer of the substrate to form a pore- and crack-free coating 50 μm to 2 mm thick with low dilution that is perfectly bonded to the substrate. The process may be used for large area coverage by overlapping individual tracks, but it is the ability to protect smaller, localized areas that makes it unique.

Erdemir et al. (1990, 1991, 1996a, b) investigated boric-acid (H_3BO_3)-based applications for the formation and self-lubrication mechanisms of boric acid films on boric oxide coatings prepared by vacuum evaporation. In particular, they measured the coefficients of friction of a steel ball sliding on a boric-oxide-coated steel disk and a sapphire ball sliding on a boric-oxide-coated alumina disk were 0.025–0.05 at steady state, depending on load and substrate material. This low friction was correlated with the formation of a lubricious boric acid film on boric oxide coatings exposed to open air. For the mechanism of self-lubrication, the layered triclinic crystal structure of boric acid was proposed. The atoms constituting each boric acid molecule are arrayed in closely packed and strongly bonded layers that are 0.318 nm apart and held together by weak forces, such as van der Waals. The authors hypothesized that, during sliding, these layers can align themselves parallel to the direction of relative motion and, once so aligned, can slide over one another with relative ease to provide low friction.

Boric oxide tends to react with water vapor present in air to form a boric acid protective coating

$$B_2O_3 + 3H_2O \rightarrow 2H_3BO_3. \tag{6.32}$$

The protective coating, in turn, leads to reduced friction and wear. With its layered crystal structure, boric acid resembles those other solids known for their

good lubrication capabilities (e.g., MoS_2, graphite, and hexagonal boron nitride) (Erdemir et al. 1996a, b).

Many composite and nanocomposite materials were suggested for self-lubricating coatings. This includes TiC/a-C:H nanocomposite coatings (Pei et al. 2005), Ti–B–N, Ti–B–N–C, and TiN/h-BN/TiB2 multilayer coatings (Mollart et al. 1996), various MMC materials (Kerr et al. 2000), titanium nitride (TiN) coating (Akhadejdamrong et al. 2003), aluminum/SiC/graphite hybrid composites with various amount of graphite addition synthesized by the semisolid powder densification (SSPD) (Guo and Tsao 2000), plasma-sprayed cast iron splats on an aluminum alloy substrate (Morks et al. 2003), TZP-graphite self-lubricating ceramics (Liu and Xue 1996), CuO-doped yttria-stabilized tetragonal zirconia ceramics (Tocha et al. 2008), carbon–carbon composites (Chen and Ju 1995), nitride compounds (Zheng and Sun 2006), CrN–Ag self-lubricating hard coatings (Mulligan and Gall 2005), super hard self-lubricating Ti–Si–C–N nanocomposite coatings (Ma et al. 2007), microplasma oxidation on aluminum alloys in the solution of aluminate–graphite (Wu et al. 2008).

Zhang et al. (2008) fabricated porous aluminum anodic oxide films by anodizing in phosphoric acid electrolyte containing organic acid. By controlling its microstructure, a macroporous and thick alumina template were obtained. Surface self-lubricating composites were prepared by taking ultra-sonic impregnation in polytetrafluoroethylene (PTFE) latex and the relative subsequent heat treatment technology. Polcar et al. (2009) argued that transition metal dichalcogenides (TMD) have been one of the best alternatives as low friction coatings for tribological applications, particularly in dry and vacuum environments, however, they have low load-bearing capacities. To increase the load-bearing capacity of these materials, the alloying with C should be considered. They studied self-lubricating W–S–C and Mo–Se–C sputtered coatings and found self-lubricating behavior. Skarvelis and Papadimitriou (2009) used plasma transferred arc (PTA) technique to produce composite coatings based on co-melting of MoS_2, TiC, and iron ingredients, in an attempt to obtain wear-resistant layers with self-lubricating properties. Graphite and glassy carbon composites were investigated by Hokao et al. (2000). Strnad et al. (2009) developed self-lubricated MoS_2 doped Ti–Al–Cr–N coatings developed in multilayer structure.

Various ceramics are also used for self-lubricating effect. Suh et al. (2008) studied self-lubricating behavior of structural ceramic balls (ZrO_2, Al_2O_3, and SiC) sliding against the ZrO_2 disk. Blau et al. (1999) investigated self-lubricating properties of ceramic-matrix graphite composites. Lugscheider et al. (1999) studied self-lubricating properties of tungsten and vanadium oxides deposited by MSIP-PVD process. Bae et al. (1996) studied self-lubricating TiN–MoS_2 composite coatings. Mulligan and Gall (2005) studied CrN–Ag self-lubricating hard coatings.

Powder metallurgy is another area of interest. Li and Xiong (2008) prepared Nickel-based self-lubricating composites with graphite and molybdenum disulfide, as lubricant were prepared by powder metallurgy (PM) method, powder metallurgy composites (Dellacorte and Sliney 1991), and MoS_2 precursor films on aluminum (Skeldon et al. 1997).

Polymers and polymer composites and nanocomposites are also used for the self-lubricating effect. Li et al (2008) prepared polyoxymethylene (POM) composites filled with low-density polyethylene (LDPE) and rice husk flour (RHF) were prepared by injection molding. Quintelier et al. (2009) used polymer composite to develop self-lubricating coatings. Blanchet and Peng (1998) prepared self-lubricating fluorinated ethylene propylene (FEP) and PTFE composites.

With the advent of new carbon-based nanomaterials, such as the fullerene and CNT, new opportunities for tribologists emerged. Thus, fullerene C_{60} (Bhushan et al 1993) and fullerene-like WS_2 nanoparticles (Rapoport et al. 2003), Ni-based CNT (Wang et al. 2003; Scharf et al. 2009), CNT on Al_2O_3 (Tu et al. 2004), CNT-reinforced Al composites (Zhou et al. 2007) and Mg composites (Umeda et al. 2009), boric acid nanotubes, nanotips, nanorods (Li et al. 2003), composite coatings of Co plus fullerene-like WS_2 nanoparticles on stainless steel substrate (Friedman et al. 2007), Ni-based alloy matrix submicron WS_2 self-lubricant composite coatings (Wang et al. 2008), and other materials were found to demonstrate self-lubricating effect.

Alexandridou et al. (1995) developed wear-resistant MMC composite coatings and oil-containing self-lubricating metallic coatings. The latter have been produced by electrolytic codeposition of oil-containing microcapsules from Watts nickel plating baths. For this purpose, oil-containing polyterephthalamide microcapsules were synthesized based on the interfacial polymerization of an oil-soluble monomer (terephthaloyl dichloride) and a mixture of two water-soluble monomers (diethylenetriamine and 1,6-hexamethylenediamine). The influence of several synthesis parameters (e.g., type of encapsulated organic phase, monomer concentration(s), and concentration ratio of the two amine monomers) on the size distribution and morphology of the oil-containing polyamide microcapsules as well as on their electrolytic codeposition behavior is discussed. The morphological characteristics of the microcapsules were affected to a great extent by the functionality of the water-soluble amine monomer. The composition of the core material of the microcapsules showed a marked influence on their stability upon aging in the Watts nickel plating bath. The level of codeposition was influenced by the presence of additives in the nickel electrolyte and was strongly dependent on the polymerization conditions employed in the microcapsule synthesis.

Sui et al. (2009) decided to use the superhydrophobicity to combine it with self-lubrication. They synthesized carbon coating on Ti_3SiC_2 with combined superhydrophobic and self-lubricating properties by chlorination at 1,000°C followed by modification of the $CF_3(CF_2)(5)CH_2CH_2SiCl_3$ film. The porous structure as well as organic film on carbon coating endowed the surface with super-hydrophobic property. Because of chemical inertia of the carbon coating and the modifier, the super-hydrophobic surface was very stable under various environments. Carbon coating was a good solid lubricant and greatly reduced friction coefficient of Ti_3SiC_2 sliding against Si_3N_4, which was important for Ti(3)SiC(2) used as engineering material.

Materials capable for the formation of in situ tribofilms are another big class of self-lubricating materials. Al_2O_3/TiC ceramic composites with the additions of CaF_2 solid lubricants showed reduced friction and wear due to an in situ formed

self-lubricating tribofilm between the ring-block sliding couple. Deng and Cao (2007) found that two types of tribofilms are formed on the wear surface depending on the CaF_2 content. A dense tribofilm with a smooth surface associated with small friction coefficient and low wear rate was formed by the releasing and smearing of CaF_2 solid lubricants on the wear surface when with 10 vol% CaF_2 content. This dense tribofilm acted as solid lubricant film between the sliding couple, and thus significantly reduced the friction coefficient and the wear rate. Breakdown of the tribofilm on the surface associated with a large wear rate was observed on samples with 15 vol% CaF_2 content. This is due to the large degradation of mechanical properties of the composite with higher CaF_2 contents.

Aizawa et al. (2005) studied self-lubrication mechanism via the in situ formed lubricious oxide tribofilms. They note that while TiN and TiC ceramic coating films are frequently utilized as a protective coating for dies and cutting tools, these films often suffer from severe, adhesive wearing in dry forming and machining. Chlorine ion implantation assists lubricious oxide film to be in situ formed during wearing. At the presence of chlorine atoms in the inside of TiN or TiC films, in situ formation of lubricous intermediate titanium oxides with TiO and Ti_nO_{2n-1} is sustained to preserve low frictional and wearing state. The self-lubrication process works well in dry machining in order to reduce the flank wear of cutting tools even in the higher cutting speed range up to 500 m min^{-1}.

Alexeev and Jahanmir (1993) studied self-lubricating composite material as a two-phase system with the plastic deformation of self-lubricating composite materials that contain soft second-phase particles. The soft phase flows toward the sliding surface. So the properties of both the hard matrix and the soft second-phase particles, as well as the shape and size of the particles, control the processes of deformation and flow of the soft phase. The results may be used to optimize the microstructure of self-lubricating composites to obtain the best tribological performance.

Self-lubrication was found also in the atomic friction. Livshits and Shluger (1997) presented a theoretical model and conducted molecular dynamics (MD) simulation of the interaction between a crystalline sample and an AFM tip nanoasperity, combined with a semiempirical treatment of the mesoscopic van der Waals attraction between tip and surface. They demonstrated that the adsorbed cluster can adjust itself to conditions of scanning by exchanging atoms with the surface and changing its structure and argued that this dynamic "self-organization" of the surface material on the tip during scanning could be a general effect which may explain why periodic surface images are often obtained using a variety of tips and large tip loads.

Another effect closely related to atomic scale self-lubrication is the superlubricity, or the regime of motion in which friction vanishes or very nearly vanishes. Superlubricity may occur when two crystalline surfaces slide over each other in dry incommensurate contact (Dienwiebel et al. 2004). Thus, the atoms in graphite are oriented in a hexagonal manner and form an atomic asperity-and-valley landscape, which looks like an egg-crate. When the two graphite surfaces are in registry (every 60°), the friction force is high. When the two surfaces are rotated

out of registry, the friction is largely reduced. A state of ultralow friction can also be achieved when a sharp tip slides over a flat surface and the applied load is below a certain threshold.

Thermolubricity is another atomic-scale phenomenon. The thermal excitations of atoms can assist sliding by overcoming energy barriers. Jinesh et al. (2008) argued that friction at low velocities and low surface corrugations is much lower than the weak logarithmic velocity-dependence predicted by thermally activated kinetic models of atomic friction. Furthermore, friction is zero in the zero-velocity limit. The effect was also demonstrated experimentally.

Two areas other than materials science where the term "self-lubrication" is used are geophysics and biology. In geophysics, scientists suggested that self-lubricating rheological mechanisms are most capable of generating plate-like motion out of fluid flows. The basic paradigm of self-lubrication is nominally derived from the feedback between viscous heating and temperature-dependent viscosity. Bercovici (1998) proposed an idealized self-lubrication mechanism based on void (such as pore and microcrack) generation and volatile (e.g., water) ingestion. The term self-lubrication is also used in certain biomedical applications. It has been argued by Bejan and Marden (2009) that the tendency of the system to reduce lubrication is a common feature of geophysical and biological systems reflecting the tendency for self-organization.

6.8 Summary

Friction and wear are fundamental phenomena of nature reflecting the tendency of energy to dissipate and material to deteriorate as a consequence of the Second law of thermodynamics. While there are many seemingly unrelated mechanisms of friction (adhesion, deformation, ratcheting, the "third body," etc.) and wear (abrasion, adhesion, fracture, etc.), in many situations friction and wear can be described by remarkably simple linear empirical laws, such as the Coulomb's law of friction and Archard's law of wear. These laws can be seen as a linearization of some more complex bulk material constitutive dependencies due to their asymptotic expansion at the 2D frictional interface.

Lubrication is required to reduce friction and wear for most interfaces. Those materials and surfaces which do not require external lubrication are called self-lubricating. Self-lubrication can often be viewed as a self-organized process. There are several approaches to the development of self-lubricating materials. These approaches include hard coatings, e.g., with DLC, the boric acid, development of friction and wear-resistant composite and nanocomposite materials on the basis of metals, polymers, and ceramics, as well as materials capable of forming in situ protective tribofilms and other self-organized structures. In the consequent chapter, we investigate in more detail the phenomenon of friction-induces self-organization and thermodynamic conditions leading to that phenomenon.

Chapter 7
Thermodynamic Methods in Tribology and Friction-Induced Self-Organization

In the preceding chapter, we discussed the basic principles of mechanical contact of rough surfaces, friction, wear, and self-lubrication. Physically, friction and wear are related to the Second law of thermodynamics, since they are the result of the tendencies of energy to dissipate and material to deteriorate. Friction and wear are complex phenomena which do not have single mechanisms, but rather involve physical and chemical process of a different nature. However, there are certain general rules of friction and wear, such as the linearized Coulomb–Amontons and Archard laws, which apply universally to various mechanisms. This makes it attractive to try to deduce common empirical laws of tribology directly from thermodynamic principles, such as the Second law and concepts of nonequilibrium (irreversible) thermodynamics.

While friction and wear are irreversible processes which normally lead to material deterioration, under certain circumstances friction can lead to self-organization or increased orderliness when various "secondary structures" (e.g., in situ formed tribofilms) are formed at the frictional interface. Self-lubrication is an example of such friction-induced self-organization. Nonequilibrium thermodynamics offer some insights on self-organized processes. Two concepts of nonequilibrium thermodynamics are of particular importance in tribology. First, the idea of linear (Onsager) relationships between thermodynamic forces and flows near the state of equilibrium results in linear kinetic equations for heat flow, mass flow, and other variables. These can be linked to the linear empirical laws of tribology. Second is the hypothesis of minimum entropy production, which states that a system tends to tune itself to the dynamic state when energy dissipation (or entropy production) is minimized, similarly to how a system tunes itself to the most stable static state of minimum potential energy. This can be linked to the tendency of tribosystem to tune themselves to the state of minimized friction and wear (self-lubrication). The challenge is to use this approach for the establishment of appropriate structure–property relationships, i.e., to find optimized microstructure of a composite material capable for self-lubrication.

M. Nosonovsky and P.K. Rohatgi, *Biomimetics in Materials Science: Self-Healing, Self-Lubricating, and Self-Cleaning Materials*, Springer Series in Materials Science 152,
DOI 10.1007/978-1-4614-0926-7_7,

In this chapter, we discuss the thermodynamic approach to friction, wear, and friction-induced self-organization, with the emphasis on the entropic methods, and some examples of various types of friction-induced self-organization with the potential to be used for self-lubrication.

7.1 Introduction

Friction and wear are usually viewed as irreversible processes, which lead to energy dissipation (friction) and material deterioration (wear). On the other hand, it is known that under certain circumstances frictional sliding can result in the formation (self-organization) of spatial and temporal patterns. Friction-induced self-organization has a significant potential for the development of self-lubricating, self-healing, and self-cleaning materials, which can reduce environmental contamination, and thus it is relevant to green tribology.

The idea that friction and wear can lead not only to deterioration, but, in some cases, to self-organization was at first suggested and investigated in the 1970–1980s. As we have already discussed in the introduction, this was under the clear influence of the "Synergetics" and philosophical ideas of Haken and Prigogine. The earlier work on self-organization is characterized by qualitative, rather than quantitative analysis of self-organization mechanisms. For example, it is noted in many of these publications that typical tribosystems possess the qualities which, according to Prigogine, are required (but not sufficient) for the self-organization, for example, that the system should be thermodynamically open, nonlinear, and it should operate far from the equilibrium.

Historically, first attempts to investigate friction-induced self-organization were made in Russia in the starting of 1970s. Several groups can be mentioned. First, Bershadsky (1992, 1993) in Kiev investigated the formation of the so-called self-organized "secondary structures." According to Bershadsky, friction and wear are two sides of the same phenomenon and they represent the tendency of energy and matter to achieve the most disordered state. However, the synergy of various mechanisms can lead to the self-organization of the secondary structures, which are "nonstoichiometric and metastable phases," whereas "the friction force is also a reaction on the informational (entropic) excitations, analogous to the elastic properties of a polymer, which are related mostly to the change of entropy and have the magnitude of the order of the elasticity of a gas" (Bershadsky 1993).

These ideas were influenced by the theory of self-organization developed by Ilya Prigogine, a Belgian physical chemist with Russian origin and the winner of the 1977 Nobel Prize in Chemistry. Prigogine used the ideas of the nonequilibrium thermodynamics to describe the processes of self-organization (Nicolis and Prigogine 1977). Later, Prigogine wrote several popular books about the scientific and philosophical importance of self-organization (Prigogine 1980; Prigogine and Stengers 1984). At the same time, in the end of the 1970s, the concept of "Synergetics" was suggested by Haken (1983) as an interdisciplinary science

investigating the formation and self-organization of patterns and structures in open systems, which are far from thermodynamic equilibrium. The word "synergetics" was apparently coined by the architect and philosopher R.B. Fuller (the same person, after whom the C_{60} molecule was later called "fullerene"). The books by Prigogine and Haken were published in the USSR in Russian translations and became very popular in the 1980s.

The second group to mention is the group headed by N. Bushe and then I. Gershman in Moscow. Their results were summarized in the edited book by Fox-Rabinovich and Totten (2006). In 2002, N. Bushe won the most prestigious tribology award, the Tribology Gold Medal, for his studies of tribological compatibility and other related effects. The third group is Garkunov (2004) and co-workers, who claimed the discovery of the synergetic "nondeterioration effect" also called the "selective transfer." Garkunov's mostly experimental research also received an international recognition when he was awarded the 2005 Tribology Gold Medal "for his achievements in tribology, especially in the fields of selective transfer."

In the English language literature, the works by Klamecki (1980a, b, 1982, 1984) were the first to use the concepts of the nonequilibrium thermodynamics, including the minimum entropy production principle by Prigogine, to describe friction and wear. His work was extended by Zmitrowicz (1987), Dai et al. (2000), Doelling et al. (2000), and others. Abdel-Aal (2006) developed a model to predict and explain the role of wear as a self-organizing occurrence in tribosystems. Tross and Fleischer in Germany related wear and damage in rail brakes to a so-called critical energy density, Fleischer in Magdeburg, Germany won the tribology Gold medal for developing this concept. His student Sadowski (1990, 1995) from Poland contributed several important ideas to the thermodynamic theory of wear.

Later work by Ling, Doelling, Bryant, and Khonsari relates wear to the transport of entropy (and not to the generation of entropy), which is a different approach. An important entropic study of the thermodynamics of wear was conducted by Bryant et al. (2008), who introduced a degradation function and formulated the degradation–entropy generation theorem in their approach intended to study the friction and wear in complex. They note that friction and wear, which are often treated as unrelated processes, are in fact manifestations of the same dissipative physical processes occurring at sliding interfaces. The possibility of the reduction of friction between two elastic bodies due to a pattern of propagating slip waves was investigated by Adams (1998) and Nosonovsky and Adams (2001), who used the approach of the theory of elasticity.

The endeavors to use thermodynamic methods to develop a general theory of wear have been taken by many researchers; however, most of these attempts had limited success due to the complexity of the equations involved and the difficulty of their solution (Klamecki 1980a, b; Zmitrowicz 1987; Bryant 2009). Doelling et al. (2000) experimentally correlated wear with entropy flow, dS/dt, at a wearing surface and found that wear was roughly proportional to the entropy produced for the steady sliding of copper on steel under boundary lubricated conditions. Bryant et al. (2008) conducted an interesting entropic study of wear. They started from the assumption that friction and wear are manifestations of the

Table 7.1 Entropy change during various dissipative processes (based on Bryant 2009)

Process	Entropy change
Adhesion	$\mathrm{d}S = \frac{\gamma \mathrm{d}A}{T}$, where γ is the surface energy, A is the area
Plastic deformation	$\mathrm{d}S = \frac{U_p \mathrm{d}V}{T}$, where U_p is the work per volume, V is the volume
Fracture	$\mathrm{d}S = \frac{(\partial U/\partial a - 2\gamma)\mathrm{d}a}{T}$, where $\frac{\partial U}{\partial a}$ is the energy release rate and a is the crack length
Phase transition	$\mathrm{d}S = \frac{\mathrm{d}H}{T}$, where H is the enthalpy
Chemical reaction	$\mathrm{d}S = \frac{\sum_{\text{react}} \mu_i \mathrm{d}N_i - \sum_{\text{products}} \mu_i \mathrm{d}N_i}{T}$, where N_i are numbers of molecules and μ_i are chemical potentials for reactants and products
Mixing	$\Delta S = -R \sum_i^n \frac{N_i}{N} \ln \frac{N_i}{N}$, where N_i are numbers of molecules and R is the universal gas constant
Heat transfer	$\mathrm{d}S = \left(\frac{1}{T_1} - \frac{1}{T_2}\right)\mathrm{d}Q$, where T_1 and T_2 are temperatures of the two bodies

same dissipative physical processes occurring at sliding interfaces. The production of irreversible entropy by interfacial dissipative processes is associated with both friction and wear. Friction force dissipates power and generates entropy, whereas wear irreversibly changes the structure and morphology of the material often accompained by the loss of material. Bryant (2009) identified entropy production mechanisms during various dissipative processes relevant to friction and wear, which are summarized in Table 7.1. It is observed that the change of entropy has the general form of $\mathrm{d}S = Y\mathrm{d}\xi$, that is, a thermodynamic force Y times the change of the generalized coordinate $\mathrm{d}\xi$.

Bryant et al. (2008) also formulated the so-called "degradation–entropy generation theorem," which states that for N dissipative processes, characterized by energies $p_i = p_i(\zeta^i{}_1, \zeta^i{}_2, \ldots \zeta^i{}_\mathrm{n},)$, where ζ_j are generalized coordinates (or "phenomenological variables") associated with the processes, and for a degradation measure $w(p_1, p_2, \ldots, p_n)$, which is nonnegative and monotonic function of the process energies p_i, the rate of degradation $\dot{w} = \sum_i^n B_i \dot{S}_i$ is a linear function of the components of entropy production $\dot{S}_i = \sum_j^n X_i^j J_i^j$ of the dissipative processes (where X and J are generalized forces and flows of the processes). Degradation components $\dot{w}_i = \sum_j^n Y_i^j J_{ii}^j$ proceed at rates J_i^j determined by entropy production, whereas the generalized "degradation forces" $Y_i^j = B_i Y_i^j$ are linear functions of $Y_i = B_i X_i$, and degradation coefficients B_i are partial derivatives of w by entropy.

A completely different approach to friction-induced self-organization is related to the theory of dynamical systems and involves the investigation of friction test results as time-series. Since the 1980s, it has been suggested that a specific type of self-organization, called "self-organized criticality (SOC)," plays a role in diverse "avalanche-like" processes, such as the stick–slip phenomenon during dry friction. The researches Zypman (2003), Ferrante (Adler et al. 2004; Buldyrev et al. 2006; Fleurquin et al. 2010), and others deal with this topic.

A different approach to describe some mechanisms resulting in self-organization was based on the reaction–diffusion systems and their important class the "Turing systems" (Kagan 2010). Mortazavi and Nosonovsky (2011a, b) investigated whether reaction–diffusion systems can describe certain types of friction-induced

pattern formation involving heat transfer and diffusion-like mass transfer due to wear. In somehow similar trend, Nosonovsky and Bhushan (2009, 2010a, b) and Nosonovsky et al. (2009) suggested treating self-lubrication and surface-healing as a manifestation of self-organization. They noted that the orderliness at the interface can increase (and, therefore, the entropy is decreased) at the expense of the entropy either in the bulk of the body or at the microscale. They also suggested that self-organized spatial patterns (such as interface slip waves) can be studied by the methods of the theory of self-organization.

The reduction of friction and wear due to the self-organization at the sliding frictional interface can lead to self-lubrication, i.e., the ability to sustain low friction and wear without the external supply of a lubricant. Since lubricants constitute environmental hazards, while friction and wear often lead to heat and chemical contamination of environment, self-lubrication has the potential for green tribology. Self-lubrication is also common in the living nature, and therefore, it is of interest for the scientists and engineers who are looking for biomimetic approach, which also has the potential for green tribology. In this chapter, we review some different researches which has been done on self-organization including modeling of formation of self-organized patterns during friction through destabilization of the steady state, the methods of investigating of such patterns and their relation to self-lubrication, and environment-friendly tribology.

7.2 Entropic Methods of Study of Self-Organized Tribological Systems

Tribology is defined as the science and technology of interacting surfaces in relative motion, or, in other words, the study of friction, wear, and lubrication. The concept of entropy often seems difficult and confusing for nonphysicists. The reason is that, unlike in the case of temperature and energy, there is no direct way of measuring entropy, so our everyday intuition does not work well when we have to deal with entropy. This is apparently the main reason why entropy, being the most important quantitative measure of disorder and dissipation, has not yet become the major tool for analyzing such dissipative processes as friction and wear.

While the net entropy grows in most systems in accordance with the Second law of thermodynamics, some thermodynamic systems may lead to an increasing orderliness and self-organization (Prigogine 1968). These are thermodynamically open systems that operate far from thermodynamic equilibrium and can exchange energy, matter, and entropy with the environment. Many of these self-organizing systems (such as the Bénard cells in boiling liquid and oscillating chemical reactions) were known a long time ago; however, as described in previous section, the universality and generality of the processes involved in these systems was understood only with the works by Prigogine (1968, 1980) and Haken (1983). It is believed that this ability for self-organization of physical systems led to the formation of complex hierarchical chemical and biological systems.

The flow of heat, entropy, and material away from the interface during the dry friction and wear can lead to self-organization when so-called "secondary structures" form. The secondary structures are either patterns that form at the interface (e.g., stick and slip zones) or those formed as a result of mutual adjustment of the bodies in contact. The entropy production rate reaches its minimum in the self-organized state. Therefore, the self-organization is usually beneficial for the tribolological system, as it leads to the reduction of friction and wear (Nosonovsky and Bhushan 2009).

7.2.1 Qualitative Studies

The earlier works on self-organization are characterized by qualitative, rather than quantitative analysis of self-organization mechanisms. For example, it is noted in many of publications that typical tribosystems possess the qualities which, according to Prigogine, are required (but not sufficient) for the self-organization, for example, the system should be thermodynamically open, nonlinear, and it should operate far from the equilibrium.

Bershadsky (1992) suggested a classification of various friction-induced self-organization effects. In search of self-organization during friction, he investigates quite a diverse range of processes and phenomena – auto-hydrodynamic effects, the evolution of microtopography, the formation of chemical and convective patterns, the oscillation of various parameters measured experimentally during friction. Some of these phenomena had well-investigated principles and mechanisms, while others were studied in a phenomenological manner, so it was not possible to approach them all in uniform manner. He, therefore, suggested that the state and evolution of a self-organized tribosystem might be described using different methods, including the equations of motion, statistical description, measurement of a certain parameter, etc. Depending on the method of description, different features of self-organization ("synergism") were observed, but in most situations a self-regulated parameter existed and governing principle or target function could be identified. Table 7.2 summarizes the features of "synergism" in various tribological phenomena and corresponding governing principles and by target function, based on Bershadsky (1992).

Nosonovsky (2010a, b), Nosonovsky and Bhushan (2009), Nosonovsky et al. (2009), and Mortazavi and Nosonovsky (2011a, b) suggested entropic criteria for friction-induced self-organization on the basis of the multiscale structure of the material (when self-organization at the macroscale occurs at the expense of the deterioration at the microscale) and coupling of the healing and degradation thermodynamic forces. Table 7.3 summarizes their interpretation of various tribological phenomena, which can be interpreted as self-organization. In addition, self-organization is often a consequence of coupling of friction and wear with other processes, which creates a feedback in the tribosystem.

In addition, self-organization is often a consequence of coupling of friction and wear with other processes, which create a feedback in the tribosystem. These

Table 7.2 Self-organization effects in tribosystems (Nosonovsky 2010b)

Effect	Description of the state or evolution	Features of synergism	Self-regulated parameter	Target function and/or governing principle
Auto-hydrodynamic effects (wedges, gaps, canyons)	Equations of motion, competing processes for entropy, and negentropy production	Bifurcation; self-excited vibrations and waves; feedback and target functions	Gap thickness, temperature, and microtopography distributions	Minimum friction
Self-reproducing microtopography, waviness	Equations of motion or kinetics	Bifurcations; self-excited vibrations and waves	Rough surface microtopography	Minimum energy dissipation; pressure or heat flow distribution
Steady-state microtopography of worn surfaces ("natural wear shape")	Competing processes for entropy and negentropy (information) production	Feedback and target function	Shape of the profile	Minimum energy dissipation
Self-excited vibrations of wear, electric resistance, stresses, etc.	Measurements of a parameter of the system (friction force, electrical resistance, wear rate, etc.)	Instabilities and self-excited oscillations of the measured parameter	Corresponding parameter	Minimum entropy production
Spatial or periodic chemical pattern	Molecular, atomic, or dislocation structure	Large-scale ordered structures	Secondary heterogeneity at the surface	Dissipative principles
Periodic or concentric structures, such as Bénard cells	Molecular, atomic, or dislocation structure; Entropy is measured	Large-scale order structures; a sudden decrease in entropy production	–	Minimum entropy production
Decrease in macrofluctuation of temperature, particle size and other parameters	Order-parameter dependent on generalized coordinate, measurements of a parameter of the system	Microfluctuations; phase transitions; instabilities and self-excited vibrations of the measured parameter	–	Subminimal friction

Table 7.3 Tribological phenomena which can be interpreted as self-organization effects in tribosystems (Nosonovsky 2010a)

Effect	Mechanism/ driving force	Condition to initiate	Final configuration
Stationary microtopography distribution after running-in	Feedback due to coupling of friction and wear	Wear affects microtopography until it reaches the stationary value	Minimum friction and wear at the stationary microtopography
In situ tribofilm formation	Chemical reaction leads to the film growth	Wear decreases with increasing film thickness	Minimum friction and wear at the stationary film thickness
Slip waves	Dynamic instability	Unstable sliding	Reduced friction
Self-lubrication	Embedded self-lubrication mechanism	Thermodynamic criteria	Reduced friction and wear
Surface-healing	Embedded self-healing mechanism	Proper coupling of degradation and healing	Reduced wear

"other processes" may include radiation, electricity, ultrasound, electric field, etc. Following Haken and Prigogine, Bershadsky considered self-organization as a general property of matter, which is complimentary to wear and degradation. These ideas, while interesting from the philosophical point of view, caused the criticism of the synergetics as not being a sufficiently "scientific" field in terms of quantitative analysis. It took several decades until the investigation of spatial and temporal pattern formation during friction found a foundation in the thermodynamics and the theory of dynamical systems.

7.2.2 Entropy During Friction and Dissipation

Before going through quantitative investigation of self-organization phenomena, we discuss entropic methods of the description of friction and wear. Consider a rigid body sliding upon a flat solid surface with the sliding velocity $V = \mathrm{d}x/\mathrm{d}t$ (Fig. 7.1). The normal load W is applied to the body and the friction force $F = \mu W$ is generated (Nosonovsky and Bhushan 2009). The work of the friction force is equal to the dissipated energy, and, therefore, we will assume for now that all dissipated energy is converted into heat

$$\mathrm{d}Q = \mu W \, \mathrm{d}x. \tag{7.1}$$

The rate of entropy generation during friction is given by

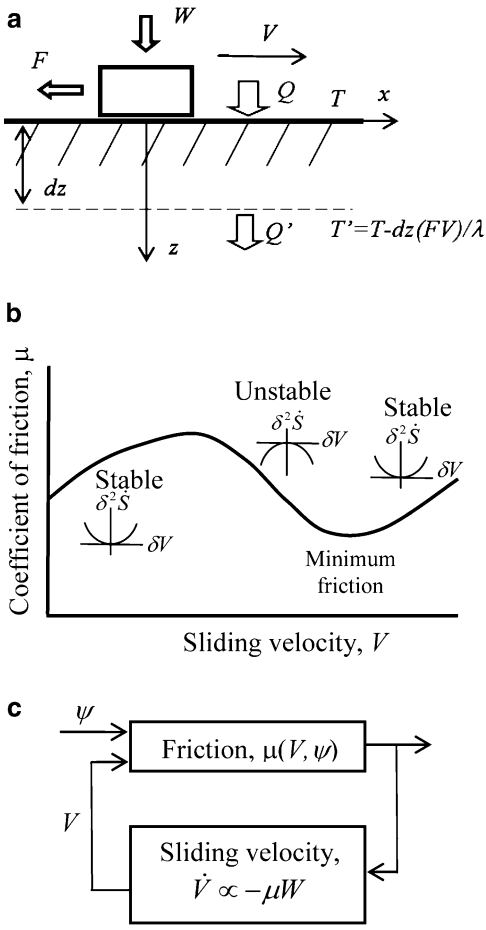

Fig. 7.1 (**a**) Heat flow away from the frictional interface. Temperature T' at the distance dz from the interface depends on the thermal conductivity λ. (**b**) Decreasing coefficient of friction with velocity results in the instability of sliding, since it forms (**c**) a positive feedback in the system

$$\frac{\mathrm{d}S}{\mathrm{d}t} = \frac{\mu W V}{T}. \tag{7.2}$$

It is noted that friction is a nonequilibrium process. When a nonequilibrium process, which can be characterized by a parameter q (a so-called generalized coordinate), occurs, a generalized thermodynamic force X that drives the process can be introduced in such a manner that the work of the force is equal to $\mathrm{d}Q = X\mathrm{d}q$. The flux (or flow rate) $J = \dot{q}$ is associated with the generalized coordinate. For many linear processes, the flow rate is linearly proportional to Y. For sliding friction, the flow rate $J = V$, and the thermodynamic force $X = \mu W/T$. Note that, for the Coulombian friction, J is not proportional to Y, which is the case for the viscous friction. Nosonovsky (2009, 2010b) discussed in detail the problem of bringing the linear friction in compliance with the linear thermodynamics.

The net entropy growth rate for frictional sliding of rigid bodies is given by (7.2). However, if instead of the net entropy, the entropy per surface area at the frictional

interface is considered, the rate equation becomes more complicated. We consider the 1D flow of entropy near the infinite interface in the steady-state situation, and suppose the flow is equal to entropy generation. Heat dQ is generated at the interface in accordance with (7.1). For simplicity, we assume that all generated heat is dissipated in one of the two contacting bodies and ignore the division of heat between the two bodies. The heat is flown away from the interface in accordance with the heat conduction equation

$$\lambda \frac{\partial T}{\partial z} = \mu WV. \tag{7.3}$$

where z is the vertical coordinate (distance from the interface), and λ is the heat conductivity. Consider a thin layer near the interface with the thickness dz. The temperature drop across the layer is $dT = (\mu WV/\lambda)dz$. The ratio of the heat released at the interface, dQ, to that radiated at the bottom of the layer, dQ', is equal to the ratio of the temperatures at the top and at the bottom of the layers

$$\frac{dQ'}{dQ} = \frac{T - \mu WV dz/\lambda}{T}. \tag{7.4}$$

Therefore, the energy released at the subsurface layer of depth dz is given by (Nosonovsky and Bhushan 2009)

$$dq = \frac{dQ - dQ'}{dz} = dQ \frac{\mu WV}{\lambda T} = \frac{(\mu WV)^2}{\lambda T}. \tag{7.5}$$

Thus, the entropy in the subsurface layer, $dS/dt = dq/T$, is given by

$$\frac{dS}{dt} = \frac{(\mu WV)^2}{\lambda T^2}. \tag{7.6}$$

Note that S in (7.6) is entropy per unit surface area and thus it is measured in J K^{-1} m^{-2}, unlike the total entropy is (7.2), which is measured in J K^{-1} (Nosonovsky 2010a, b).

The difference between (7.2) and (7.6) is that the latter takes into account the thermal conductivity and that in (7.2) gives the net entropy rate, while (7.6) gives the rate of entropy in the subsurface layer. Note the form for the thermodynamic flow is now $J = \mu WV$, and the thermodynamic force is $X = \mu WV/(\lambda T^2)$.

7.2.3 Thermally Activated Self-Organization

With describing the total entropy rates and surface entropy rate during friction [i.e., (7.2) and (7.6)], their application to the tribosystems is discussed in this section. Frictional sliding and wear are irreversible processes, since they are inhomogeneous and often nonstationary. The transition from the steady-state (stationary) sliding regime to the regime with self-organized structures occurs

through the destabilization of the steady-state regime. At the steady state, the rate of entropy production is at minimum. The stability condition for the thermodynamic system is given in the variational form by:

$$\frac{1}{2}\delta^2\dot{S} = \sum_k \delta X_k \delta J_k \ \geq \ 0, \tag{7.7}$$

where $\delta^2\dot{S}$ is the second variation of entropy production rate (Nosonovsky and Bhushan 2009) and k is the number of the generalized forces and flows. Equation (7.7) states that the energy dissipation per unit time at the steady state should be at its minimum, or the variations of the flow and the force should be of the same sign. Otherwise, the steady-state regime becomes unstable and the transition to the self-organized regime with patterns can occur. Equation (7.7) is valid for a wide range of interactions, including mechanical, thermal, and chemical, however, corresponding terms in the entropy production rate should be considered. When (7.7) is not satisfied, the system is driven away from the equilibrium, which creates the possibility for self-organization.

In the situation when only mechanical interactions are significant, and the change of temperature T has a negligible effect on friction, the entropy is proportional to the dissipated energy divided by the temperature $\mathrm{d}S = \mathrm{d}Q/T$. Consider first the situation when the production of entropy depends on the sliding velocity V. Considering that the rate of entropy production is given by (7.2), The stability condition (7.7) now yields

$$\frac{1}{2}\delta^2\dot{S} = \delta\left(\frac{\mu W}{T}\right)\delta(V) = \frac{W}{T}\frac{\partial\mu}{\partial V}(\delta V)^2 \ \geq \ 0. \tag{7.8}$$

If the slope of the $\mu(V)$ curve (the partial derivative $\mu'_V \equiv \partial\mu/\partial V$) is negative, then the steady-state sliding becomes unstable. And understandable so, since decreasing friction leads to increasing sliding velocity and to further increasing friction, and thus to the positive feedback loop.

Suppose that one contacting material has microstructure characterized by a certain parameter Ψ, such as, for example, the size of reinforcement particles in a composite material. Such values of Ψ that $\mu'_V(\psi) > 0$ correspond to steady-state sliding. However, $\mu'_V(\psi) = 0$ corresponds to the destabilization of the steady-state solution. As a result, new equilibrium position will be found with a lower value of μ. Suppose now that the coefficient of friction depends also on a microstructure parameter ϕ, such as the thickness of the interface film (Fig. 7.2). The difference between Ψ and ϕ is that the parameter Ψ is constant (the composition of the material does not change during the friction), whereas the parameter ϕ can change during friction (the film can grow or decrease due to a friction-induced chemical reaction or wear). The stability condition is now given by:

$$\frac{1}{2}\delta^2\dot{S} = \delta\left(\frac{\mu W}{T}\right)\delta(V) = \frac{W}{T}\frac{\partial\mu}{\partial\varphi}\frac{\partial V}{\partial\varphi}(\delta\varphi)^2 \ \geq \ 0. \tag{7.9}$$

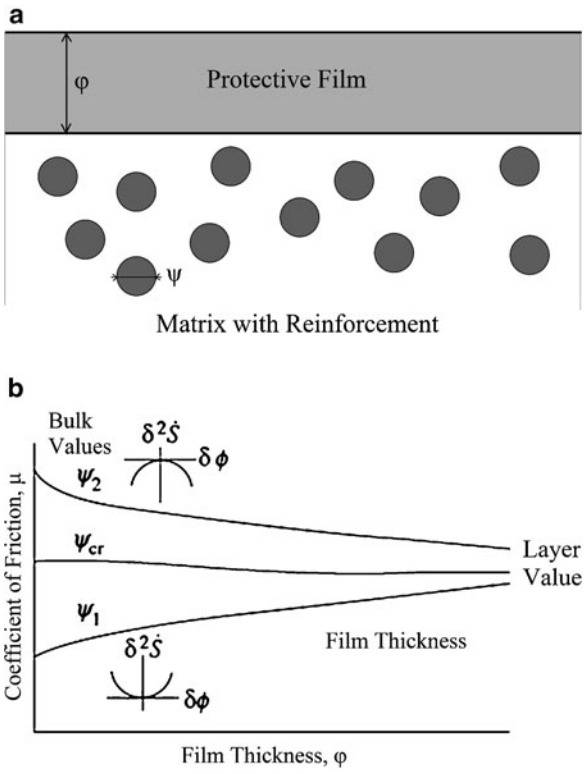

Fig. 7.2 (**a**) Self-organized protective film at the interface of a composite material. (**b**) The coefficient of friction as a function of film thickness for various values of the microstructure parameter Ψ. Subcritical values of $\Psi < \Psi_{cr}$ result in the positive slope (no layer formed), whereas $\Psi > \Psi_{cr}$ results in the instability and self-organization of the protective layer. The slope depends on the ratio of the bulk and layer values of μ, which allows to find composite microstructure providing the self-organization of the layer (Nosonovsky 2010b)

If the stability condition is violated for a certain value of ϕ, then further growth of the film will result in decreasing friction and wear, which will facilitate the further growth of the film. The destabilization occurs at $\mu'_{\varphi}(\psi, \varphi) = 0$. Note that (7.9) becomes (7.8) if $\phi = V$. At this point, we are not discussing the question of which particular thermodynamic force is responsible for the growth of the film.

Since we are interested in the conditions of the formation of such a protective film, consider now the limit of the thin film ($\varphi \to 0$). With increasing film thickness, the value of μ changes from that for the bulk composite material to that of the film material. On the other hand, the value for the bulk composite material depends also on its microstructure Ψ (Fig. 7.2) the volume percent of particles, and their shape. The critical value, Ψ_{cr}, corresponds to $\mu'_{\varphi}(\psi, 0) = 0$. For the size of reinforcement particles finer than Ψ_{cr}, the bulk (no film, $\phi = 0$) values of the coefficient of friction are lower than the values of the film. That can lead to a sudden destabilization (formation of the film with thickness ϕ_0) and reduction of friction to the value of $\mu(\Psi, \phi_0)$ as well as wear reduction. Here, we do not investigate the question why the film would form and how its material is related to the material of the contacting bodies. However, it is known that such reaction occurs in a number of situations when a soft phase is present in a hard matrix, including Al–Sn and Cu–Sn-based alloys (Bushe and Gershman 2006).

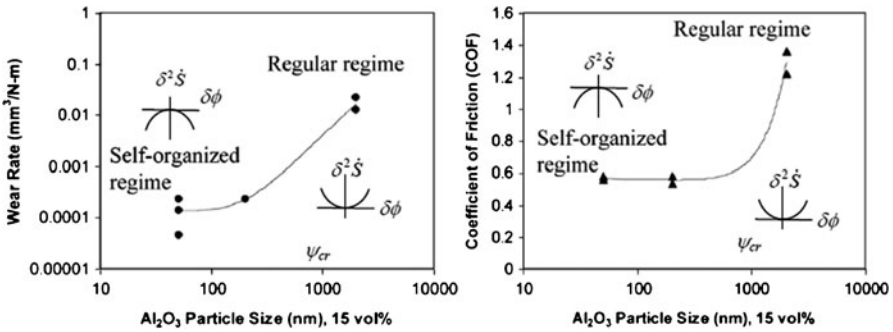

Fig. 7.3 A significant wear and friction reduction with decreasing particle size in Al–Al_2O_3 nanocomposite (based on Jun et al. 2006) can be attributed to surface self-organization

An experimental example of such sudden decrease of friction and wear with a gradual decrease of the size of reinforcement particles, which could be attributed to the destabilization, is presented in Fig. 7.3 for Al_2O_3-reinforced Al matrix nanocomposite friction and wear tests (steel ball-on-disk in ambient air) based on Jun et al. (2006). The abrupt decrease of friction and wear occurs for reinforcement particles smaller than $\Psi_{\text{cr}} = 1$ μm in size and can be attributed to the changing sign of the derivative $\mu'_{\varphi}(\psi_{\text{cr}}, 0) = 0$. The decrease is sudden and dramatic, so it can be explained by the loss of stability [cf. (7.7)] rather than by a gradual change of properties; although additional study is required to prove it.

For the entropy production governed by (7.6), the stability condition of (7.7) yields

$$\frac{\partial}{2\partial t}(\delta^2 S) = \frac{1}{2}\delta^2\left(\frac{(\mu WV)^2}{\lambda T^2}\right) = \delta X \delta J = \delta(\mu WV)\delta\left(\frac{\mu WV}{\lambda T^2}\right) \geq 0. \tag{7.10}$$

The coefficient of friction and the thermal conductivity depend upon material's microstructure, ϕ, so that

$$\begin{aligned} \mu &= \mu(\psi, \phi), \\ \lambda &= \lambda(\psi, \phi). \end{aligned} \tag{7.11}$$

The stability condition given by (7.10) takes the form of

$$\frac{1}{2}\delta^2\dot{S} = \frac{V^2W^2}{T^2}\frac{\partial\mu}{\partial\varphi}\left(\frac{1}{\lambda}\frac{\partial\mu}{\partial\varphi} - \frac{\mu}{\lambda^2}\frac{\partial\lambda}{\partial\varphi}\right)(\delta\varphi)^2 \geq 0. \tag{7.12}$$

The stability condition can be violated if

$$\frac{\partial\mu}{\partial\varphi}\frac{\partial\lambda}{\partial\varphi} < 0. \tag{7.13}$$

It is known from nonequilibrium thermodynamics that when the secondary structure is formed, the rate of entropy production reduces (Fox-Rabinovich et al. 2007). Therefore, if (7.13) is satisfied, the frictional force and wear can reduce. By selecting appropriate values of Ψ (e.g., the density of a micropattern), the condition of (7.13) can be satisfied. Note, that the wear rate is related to the rate of surface entropy production

$$\frac{\mathrm{d}w}{\mathrm{d}t} = B\frac{\mathrm{d}S}{\mathrm{d}t} = YJ, \tag{7.14}$$

It is suggested to use the theory presented in this section to optimize the microstructure of a composite material in order to ensure that the self-organized regime occurs. For that end, the dependencies (7.11) should be investigated experimentally and their derivatives obtained. Selected experimental studies are summarized in chapter 8. Following that the value of Ψ should be selected, which provides the best chances for the transition to the self-organized regime (Nosonovsky 2010a).

A particular field where this approach has been applied is the electrical contact, involving the current collection (e.g., for a railroad locomotive). It is noted that when Tribology, which is today considered the science and technology of friction, wear, and lubrication, emerged in the 1960s, it was meant to include the fourth component, namely, the electrical contact. The electrical current is important in many applications involving the mechanical contact, such as the microelectromechanical systems (MEMS). Besides that, electromechanical contact is a typical example of a system, where two coupled processes (friction and electrical current) take place simultaneously which creates a potential for feedback, destabilization, and pattern formation. Frictional self-organization during electromechanical contact was investigated by Gershman (2006). Other areas where this approach has been successfully applied include cutting tools, and the theory of "tribological compatibility" of materials (Bushe and Gershman 2006).

7.2.4 The Concept of "Selective Transfer"

The concept of the "selective transfer" or the "nondeterioration effect" was developed by Garkunov (2000). According to his definition, the selective transfer is a type of friction which is characterized by the formation at the contact interface of a thin nonoxidized metallic film with a low shear resistance which is not able to accumulate dislocations. According to the selective transfer scheme, a selective dissolution of a component of a copper alloy occurs, followed by the transfer of the component to a contacting body (a steel shaft). The standard example of the selective transfer is the formation of a copper layer in a bronze-steel system lubricated by glycerin.

Kragelsky and Garkunov studied in the 1950s the state of airplane chassis which included a bronze-steel lubricated frictional system and found that a protective copper film can form, which reduces the wear to very small values. The copper

film is formed due to the anodic dissolution of bronze (an alloy of copper and tin with additive elements). The additives, such as iron, zinc, and aluminum, as well as tin, dissolved in the lubricant, while copper forms a film on the surfaces of the of contacting materials. The film is in a dynamic equilibrium, while contacting layers are worn and destroyed, new layers of copper are formed, resulting in virtual absence of wear and the friction force reduction by an order of magnitude. A similar effect can be achieved by the diffusion of copper ion dissolved in a lubricant. The authors called the effect the "selective transfer" of copper ions, and the protective effect "servovite films" (or "serfing-films") (Garkunov 2004), although a more common term in modern literature is "in situ formation of self-lubricating films."

While the "nondeterioration" effect was presented as a unique and universal type of self-organization in tribosystems and as a very promising way of wear reduction, the concept also caused criticism of scientist who did not see any generality in the suggested effect. For example, Bershadsky (1992) wrote: "Selective transfer shows neither new mechanisms nor new phenomena that change our concepts. The concept of self-organization is used here in an artificial manner without any convincing proof."

7.2.5 The Concept of "Tribofatigue"

The concept of tribofatigue (or "tribofatika") was suggested and developed since the early 1990s by Dr. L. Sosnovsky from Gomel, Byelorussia. The concept implies the coupling between the wear damage and fatigue damage. It stresses the fact that in engineering calculations of lifetime of components it may not be sufficient to consider the two modes separately. Sosnovskiy and Sherbakov (2009) provide several examples when "the normative documents and methods of calculation" could not predict a catastrophic failure in a machine, such as a gigantic turbine of the 1.2 GW power plant, which he calls a ticking "tribofatigue bomb." Apparently, the phenomenon is a manifestation (or even just another mane) of the fretting fatigue.

The concepts of entropy and information play a certain role in the "tribofatogue" analysis. For the tribofatigue damage, ω_Σ, the change of energy in the volume W_p, where degradation occurs, the effective energy and the tribofatigue entropy production are given by

$$\begin{aligned} \mathrm{d}U_\Sigma &= \gamma_1 \omega_\Sigma \, \mathrm{d}W_p, \\ \mathrm{d}S_{\mathrm{TF}} &= \frac{\gamma_1 \omega_\Sigma}{T} \, \mathrm{d}W_p, \end{aligned} \tag{7.15}$$

where γ_1 is a coefficient characterizing the proportionality.

Sosnovskiy and Sherbakov (2009) further consider the rate of change of the damaged volume $\mathrm{d}W_p/\mathrm{d}t$ as the generalized flux and $\gamma_1\omega_\Sigma/T$ as the corresponding generalized force. The authors claim that, on the basis of Prigogine's approach,

Table 7.4 Application of entropic description of various friction-related phenomena (Nosonovsky 2010a)

Phenomena	Principle	Application
Wear (friction-induced)	Proportionality of the wear rate and entropy flow	Wear reduction for various applications (Bryant et al. 2008)
Running-in	Microtopography adjustment observed as Shannon entropy and roughness reduction	Friction and wear reduction in the stationary regime (Fleurquin et al. 2010; Nosonovsky 2010b)
Formation of in situ tribofilms	Friction-induced diffusion of the film material to the interface due to the destabilization of the stationary state	Friction and wear reduction due to protective tribofilm (Fox-Rabinovich and Totten 2006; Garkunov 2000; Nosonovsky and Bhushan 2009)
Slip waves	Elastic waves at the interface which can result in friction reduction. Can result in self-organized critical behavior and stick–slip	Novel ways of ultrasonic motors, etc. (Adams 1995); new theories of dislocation-assisted sliding (Bhushan and Nosonovsky 2003, 2004a, b); geomechanical applications (Buldyrev et al. 2006)
Friction-induced instabilities	Coupling of friction with wear, thermal expansion, etc. Usually leads to the "negative viscosity" and similar types of frictional instabilities	Eliminating friction-induced vibrations and noise (Kincaid et al. 2003; Adams 1995; Nosonovsky and Adams 2001, 2004).
Self-healing by embedding microstructures	A mechanism, which provides the coupling of healing with another relevant thermodynamic force, is embedded into material. Healing can occur due to the deterioration of embedded microstructure (e.g., microcapsules)	Self-healing materials and surfaces (van der Zwaag 2009; Nosonovsky 2010b)
Damage prevention	A mechanism to heal voids as they appear is embedded into material (e.g., nucleation of a solute at void points in supersaturated solid solution)	Wear-resistant and self-healing materials and surfaces (Manuel 2009)
Self-lubrication	Various mechanisms, including embedded microstructure, to reduce friction and wear	Self-lubricating materials (Nosonovsky 2010b)

the state of thermodynamic equilibrium is characterized either by the minimum entropy generation (in the self-organized state) or by the maximum entropy. They also distinguish several states of objects depending on the value of the tribofatigue damage parameter: (a) $\omega_\Sigma = 0$ (undamaged), (b) $0 < \omega_\Sigma < 1$ (damaged) (c) $\omega_\Sigma = 1$ (critical), (d) $1 < \omega_\Sigma < \infty$ (supercritical), (e) $\omega_\Sigma = \infty$ (decomposition). Further investigation of structure–property relationship on the basis of this model can be promising.

The entropic approach to different phenomena related to friction, which were discussed in the preceding sections, is summarized in Table 7.4, and their potential applications are discussed.

There are several areas of tribology where nonequilibrium thermodynamics can be successfully used. First are various situations when friction is coupled with another process. The obvious example is the electrical contact. Tribology emerged as a new scientific discipline in the 1960s, following the so-called "Jost report" for the UK government on the importance of this area (although the term "tribophysics" was used in the 1940s by D. Tabor, who worked then in Australia). According to some founders of tribology, the original concept was to combine the study of friction, wear, lubrication, and electrical contact (Greenwood 2009). Despite the fact that the electrical contact dropped from the list later, many situations that involve electrical contact have also relevance to tribology, since the contact of rough surfaces in relative motion is involved. These are both macroscale systems (such as the devices for the collection of the electrical current) as well as micro/nanoelectromechanical systems, for which microswitches constitute one of the main elements.

7.3 Friction-Induced Self-Organization

The entropic methods are especially promising for the analysis of friction-induced self-organization, especially self-lubrication, surface-healing, and self-cleaning. According to the preliminary studies, there are two key features in these processes. First, the hierarchical (multiscale) organization of the material, which allows implementing healing (as observed at the macroscale) at the expense of microscale deterioration. Second is the presence of positive and/or negative feedbacks that lead to dynamic destabilization and friction-induced vibrations. Hierarchical organization is the key feature of biological systems, which have the capacity for self-organization, self-healing, and self-lubrication, so it is not surprising that hierarchy plays a central role also in artificial materials capable for self-organization. In most cases, the self-organization is induced by bringing the system out of thermodynamic equilibrium, so that the restoring force is coupled with the degradation in such a manner that healing (decreasing degradation) occurs during the return to the thermodynamic equilibrium. In this section, we discuss phenomenological observations of friction-induced self-organization and review several examples.

7.3.1 Running-In

When sliding between two contacting, solid bodies is initiated, friction and wear often remain high during a certain initial transient period, referred to as the running-in period (Blau 1989). After running-in, friction and wear tend to decrease to their steady-state values. Numerous phenomenological explanations of the running-in phenomenon deal with various mechanisms, such as creep and viscoplastic deformation of asperities. However, a general thermodynamic description of the running-in, which would explain its underlying physical principles, is missing.

Table 7.5 Entropic description of the surface roughness, friction, and wear

	Information	Energy	Mass
	Surface roughness	Friction (dissipation)	Wear (mass flow)
Entropic description	Shannon entropy and entropy rate for a stochastic process $S = -\sum_{j=1}^{B} p_j \ln(p_j)$	Thermodynamic entropy $dS = \frac{dQ}{T}$	Entropy of mixing (configurational) $\Delta S = -R \sum_{i}^{n} \frac{N_i}{N} \ln \frac{N_i}{N}$

During running-in, the surface topography evolves until it reaches a certain stationary state referred to as the equilibrium roughness distribution (Blau 1989). The surfaces adjust to each other, leading to a more ordered state, resulting in lower energy dissipation rates, demonstrating friction-induced self-organization (Fox-Rabinovich and Totten 2006). Friction and wear are two sides of the same irreversible process leading to energy dissipation and material deterioration. It is therefore natural to use entropy as a measure of irreversibility to describe them.

Consider a two-dimensional surface height profile $y_n = y(x_n)$, (where $n = 1, N$) measured with some resolution so that every value of y_n belongs to a certain "bin." The Shannon entropy S of a rough surface profile is a measure of its randomness (Fleurquin et al. 2010), where

$$S = -\sum_{j=1}^{B} p_j \ln(p_j), \tag{7.16}$$

and $p_j = N_j/N$ is the probability of appearance of some height in the bin j, N_j is the number of appearances in the bin j, and B is the total number of bins. A surface profile having a lower Shannon entropy is considered to be "more ordered" (or "less random") than one with a higher Shannon entropy. Thus, a decrease in Shannon entropy during the transient process is an indication of self-organization.

The interplay between the three types of entropy during the frictional contact is of great interest, namely, (1) the Shannon entropy of the rough surface, (2) the thermodynamic entropy of frictional dissipation, and (3) the entropy of mixing during wear (Table 7.5). The lowest value of the surface entropy (following the running-in regime) can correspond to the lowest rates of friction and wear and corresponding types of entropy production.

The following scheme can be suggested. A surface is micropatterned to achieve certain functionality, e.g., to decrease friction and wear. The micropattern corresponds to a (negative) component of the Shannon entropy rate. Due to the presence of the micropattern, the rates of the frictional and wear entropy production decrease; however, the micropattern can deteriorate. Thus, friction and wear are reduced at the expense of the entropy growth (deterioration) of the micropattern. A more detailed example is discussed in the following section, where "self-healing" materials are introduced, i.e., materials with embedded capability to heal cracks.

Healing can be achieved, for example, due to release of the healing agent ("glue") from microbaloons embedded into the matrix of the material, while the balloons themselves are fractured.

Note that the profile entropy as a measure of randomness is not the same as the surface roughness in a more traditional sense, such as the root-mean-square (RMS) roughness. Two profiles can have the same degree of randomness at different values of the RMS roughness and conversely, different RMS roughness for the same level of randomness.

Two types of event can occur during the evolution of the surface profile: (1) a smoothening event, which is typical of deformation-driven friction and wear; high asperities fracture due to deformation (abrasive wear) resulting in a smoothening of the profile; and (2) a roughening event, which is typical for the adhesive-driven friction and wear, which is higher for smoother surfaces.

When a particle is removed from the interface due to abrasive or adhesive wear, a data point $y(x)$ is driven from a higher bin j into a lower bin i, so the Shannon entropy would change by:

$$\Delta S = \frac{N_j - 1}{N} \ln \frac{N_j - 1}{N} - \frac{N_j}{N} \ln \frac{N_j}{N} + \frac{N_{j-1} + 1}{N} \ln \frac{N_{j-1} + 1}{N} - \frac{N_{j-1}}{N} \ln \frac{N_{j-1}}{N}. \quad (7.17)$$

Using $\ln(x + \Delta x) - \ln(x) \approx \Delta x / x$ yields

$$\Delta S = \frac{1}{N} \ln \frac{N_i}{N_j}. \quad (7.18)$$

Smoothening occurs when a particle moves from a less populated bin j into a more populated bin i. Here, the change in entropy is negative, whereas in the opposite case of roughening, the change of entropy is positive. Furthermore, for a very rough surface, smoothening is significant, whereas for a very smooth surface roughening is significant, so that a certain value of equilibrium roughness can exist, corresponding to $S = S_0$. Therefore, the rate of entropy change is given by

$$\dot{S} = f(S) = f_S(S) + f_R(S), \quad (7.19)$$

where $f_S(S)$, designating the rate due to smoothening, is a negative monotonically decreasing function such that $f_S(0) = 0$, and $f_R(S)$, designating the rate due to roughening, is a positive monotonically decreasing function. The value S_0 corresponds to the stationary state at $f(S_0) = 0$, which is stable if the derivative is negative, $f'(S_0) < 0$.

Sliding friction is associated with a number of phenomena. The intensity of some of these phenomena (such as the deformation of asperities) grows with roughness, whereas the intensity of others (such as adhesion) decreases, so that the coefficient of friction μ is given by

$$\mu = \mu_{\text{def}}(S) + \mu_{\text{adh}}(S),$$

where $\mu_{\text{def}}(S)$ is a positive increasing function and $\mu_{\text{adh}}(S)$ is a positive decreasing function. The minimum value of $\mu = \mu(S_{\text{m}})$ is obtained from $(S_{\text{m}}) + (S_{\text{m}}) = 0$. The coefficient of friction will always decrease with decreasing roughness only if $S_0 = S_{\text{m}}$. This occurs when $f_{\text{S}}(S) \propto \mu_{\text{def}}(S)$ and $f_{\text{R}}(S) \propto \mu_{\text{adh}}(S)$. Physically, such proportionality implies that the mechanisms affecting surface roughness (e.g., abrasive and adhesive wear) are proportional to friction mechanisms (e.g., asperity deformation and adhesion).

To investigate these observations, Mortazavi and Nosonovsky (2011b) conducted an experiment. The coefficient of friction between a tungsten carbide (WC) pin sliding over a copper (Cu) substrate was measured experimentally in an ultrahigh vacuum (UHV) tribometer, operating at the pressure ~3.5×10^{-10} Torr. A pure 99.99% Cu sample (about $20 \times 10 \times 1$ mm) was vacuum cleaned, and mounted to a sample manipulator, which was oriented horizontally and on the opposite side of the chamber to the tribometer. A WC tribopin, mounted to the end of an arm, was brought into contact with the sample and rubbed its surface during each scan. The tribometer was under computer control, so that the normal loads, scan speed, scan area, and scan pattern could be selected. More details of the apparatus are presented by Wu et al. (2002).

The aim was to produce wear scars after different numbers of passes of the tribopin over the surface, each one representing different period of the transient running-in process. Measurements were made using a single pass in the same direction with the sliding speed of 4 mm s^{-1} using a normal load of 0.9 N. The experiment was conducted at room temperature, and five different wear scars were created, each with a length of 4 mm collected for different rubbing time. The experiment was carried out by increasing the number of scans of the tribopin on the surface of sample from 1, 4, 8, 16, and 32 scans. Two series of wear scars were produced.

The coefficient of friction during the running-in process was calculated as the ratio of the lateral to the normal forces, and is plotted in Fig. 7.4. The coefficient of friction decreases monotonically during run-in until it reached a steady-state value of $\mu = 0.43 \pm 0.02$.

Images of surface topography of the sample at different positions for each of the wear tracks were obtained using a Pacific Nanotechnology Nano-R™ Atomic Force Microscope (AFM) operating in contact mode. The images were collected using a conical Si cantilever coated with Si_3N_4 with the tip radius of about 10 nm. Scans (512×215 pixels) were collected at a minimum of three different locations on each wear track. The images were processed using a standard software package (SPIP from Image Metrology) to obtain statistical roughness parameters such as the RMS, skewness (SK) and kurtosis (K), as shown in Fig. 7.5.

Both the RMS roughness and surface skewness decreased during the running-in process since the surfaces were smoothened steadily during the running-in period until an equilibrium roughness was achieved. However, the kurtosis increases from $K = 4.39 \pm 0.05$ to 6.52 ± 0.05 as the number of scans increases. Increasing kurtosis implies an increasing degree of pointedness of surface profile.

To compute the Shannon entropy during running-in stage, we proceeded as follows. We obtained the height probability distribution for each location using

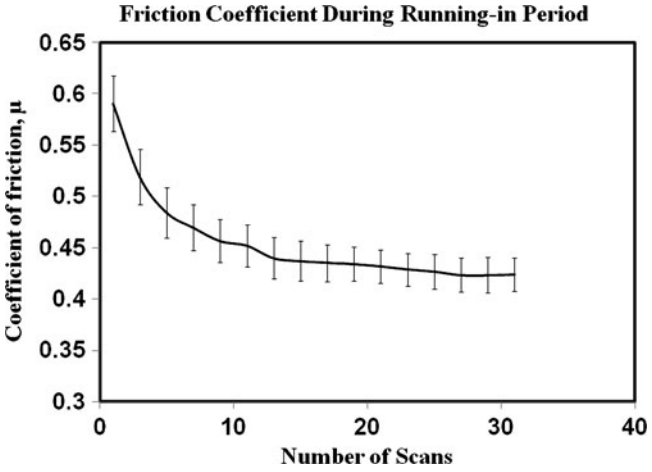

Fig. 7.4 Evolution of the coefficient of friction μ plotted as a function of the number of scans during the running-in process (Mortazavi and Nosonovsky 2011b)

the above mentioned software. We took a fixed range of heights in this profile and divide this interval in B bins. We numerically found that for the number of bins more than 1,000 the amount of error in calculation of Shannon entropy was less than 1%; thus, we subsequently chose $B = 1{,}000$. Then using (7.16), the results were plotted as shown in Fig. 7.6. It is observed that the entropy tended to decrease indicating that self-organization had occurred during the run-in period.

This indicates that self-organization occurred during the transient running-in process due to mutual adjustment of surface roughness topography. The corresponding decrease in the friction force can be explained by postulating that the same mechanisms (deformation and adhesion) affect both the roughness evolution and the change in friction, which therefore have stationary values at close values of roughness.

7.3.2 Feedback Loop Model for the Running-In

Let us consider such transient process of running-in, when sliding that causes friction and wear is initiated. Since we are looking for very general, qualitative conclusions about the running-in, we will investigate a simplified model, which, however, is intended to capture the main qualitative features of the running-in. We assume that both friction and wear depend on two different mechanisms, namely, the deformation (plastic plowing and fracture of asperities) and the adhesion mechanisms. It is recognized that other mechanisms of friction can be present as well. However, we assume that their action, in terms of the formation of the

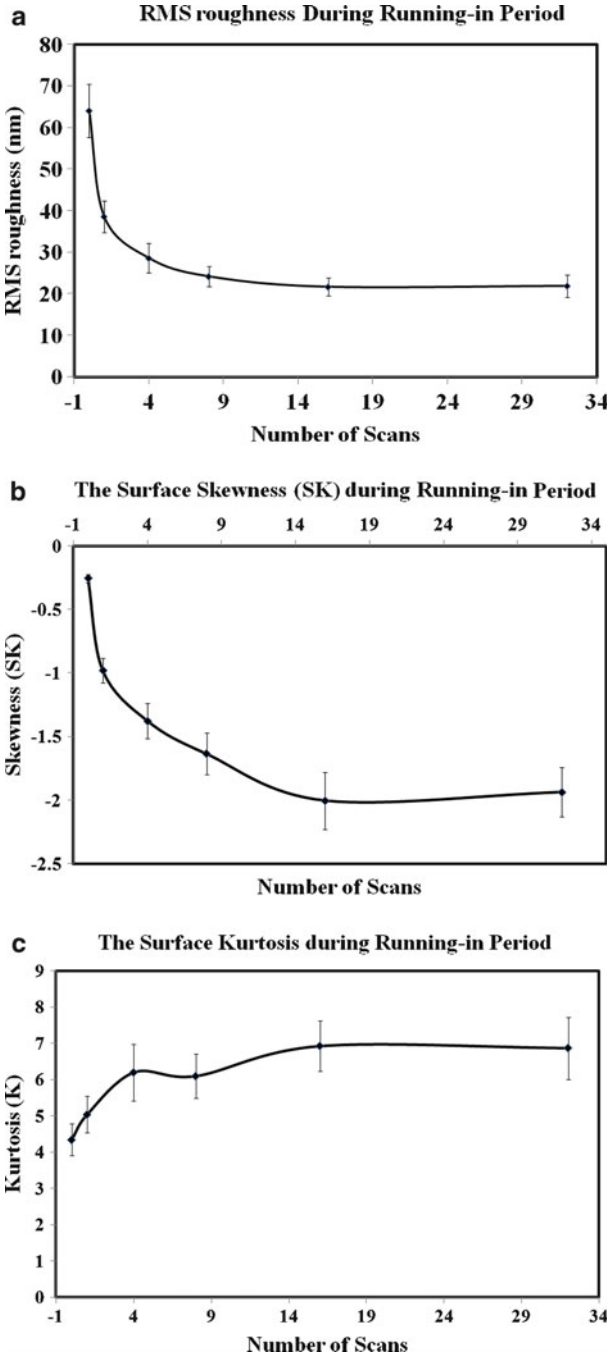

Fig. 7.5 Evolution of (**a**) the root-mean square roughness, (**b**) skewness, and (**c**) kurtosis measured within the wear track as a function of the number of scans during running-in (Mortazavi and Nosonovsky 2011b)

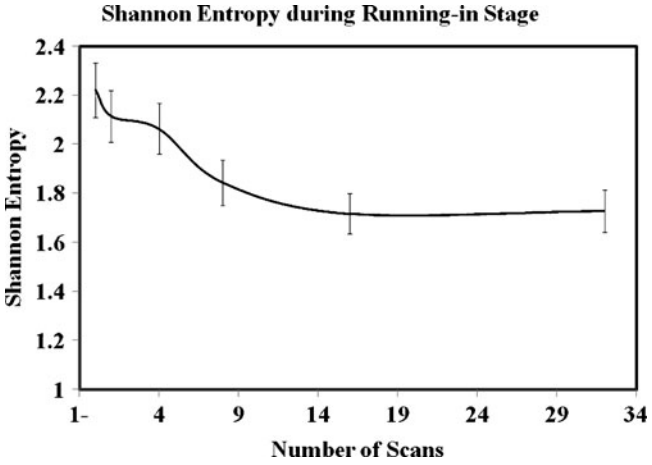

Fig. 7.6 Evolution of Shannon entropy during running-in (Mortazavi and Nosonovsky 2011b)

feedback loop, is similar to the adhesive and deformational mechanisms of friction and wear.

One of the surfaces in contact is harder than the other, so most wear occurs on the softer surface. The surface roughness of the softer surface at any moment of time is characterized by a certain distribution of microtopography parameters. For simplicity, we assume that the surface roughness is sufficiently characterized by only one parameter, R, for example, the RMS of the rough profile of the softer material.

For the deformational mechanism, higher asperities results in higher wear rates and higher friction coefficients. For the adhesion mechanism, quite oppositely, smother surface results in higher adhesion force, and, therefore, in higher friction and higher wear rates. We assume a simple linear dependence of the friction and wear coefficients on R for the deformational mechanism, and on $1/R$ for the adhesional mechanism.

$$\begin{aligned} \mu_{\text{def}} &= C_{\text{def}} R, \\ k_{\text{def}} &= K_{\text{def}} R, \\ \mu_{\text{adh}} &= \frac{C_{\text{adh}}}{R}, \\ k_{\text{adh}} &= \frac{K_{\text{adh}}}{R}, \end{aligned} \tag{7.20}$$

where μ_{def} and μ_{adh} are the deformational and adhesional components of the coefficient of friction, k_{def} and k_{adh} are the deformational and adhesional components of the wear coefficient, and C_{def}, K_{def}, C_{adh}, and K_{adh} are corresponding proportionality constants.

There is a feedback between wear and surface roughness since, for the deformational mechanism, higher asperities tend to fracture due to wear and make the surfaces smoother. For the adhesional mechanism, quite oppositely, wear tends to make the surface rougher. Again, we assume a linear dependency of the rate of change of roughness on the wear coefficient; however, the sign of the corresponding proportionality constants, A and B, will be opposite

$$\dot{R} = -Ak_{\text{def}} + Bk_{\text{adh}} = -AK_{\text{def}}R + \frac{BK_{\text{adh}}}{R}. \tag{7.21}$$

The total friction and wear are given by the sum of the deformational and adhesional components

$$\mu = C_{\text{def}}R + \frac{C_{\text{adh}}}{R}, \tag{7.22}$$

$$k = K_{\text{def}}R + \frac{K_{\text{adh}}}{R}.$$

The solution of (7.21) has a stationary point that corresponds to $\dot{R} = 0$, and it is given by

$$R = \sqrt{\frac{BK_{\text{adh}}}{AK_{\text{def}}}}. \tag{7.23}$$

The stationary point is stable, since the slope of the curve $\dot{R}$ vs. R is negative. The coefficient of friction and wear that correspond to the stationary state are given by

$$\begin{aligned} \mu &= C_{\text{def}}\sqrt{\frac{BK_{\text{adh}}}{AK_{\text{def}}}} + \frac{C_{\text{adh}}}{\sqrt{BK_{\text{adh}}/AK_{\text{def}}}}, \\ k &= K_{\text{def}}\sqrt{\frac{BK_{\text{adh}}}{AK_{\text{def}}}} + \frac{K_{\text{adh}}}{\sqrt{BK_{\text{adh}}/AK_{\text{def}}}}. \end{aligned} \tag{7.24}$$

Note that the minimum wear occurs at the minimum point of k, that is, $R = \sqrt{K_{\text{adh}}/K_{\text{def}}}$, whereas minimum friction occurs at $R = \sqrt{C_{\text{adh}}/C_{\text{def}}}$. The stationary point given by (7.23) corresponds to the minimum wear only if $A = B$, and it further corresponds to minimum friction if $K_{\text{adh}}/K_{\text{def}} = C_{\text{adh}}/C_{\text{def}}$. The assumption of $A = B$ is justified if the rate of change of roughness is proportional to the wear rate. The assumption $K_{\text{adh}}/K_{\text{def}} = C_{\text{adh}}/C_{\text{def}}$ is justified if wear is proportional to friction.

The above derivation remains valid in the case of a more complicated (e.g., nonlinear) dependencies instead of the linear dependencies of (7.24). The only requirement is that the function $\dot{R}$ vs. R is decreasing and crosses zero.

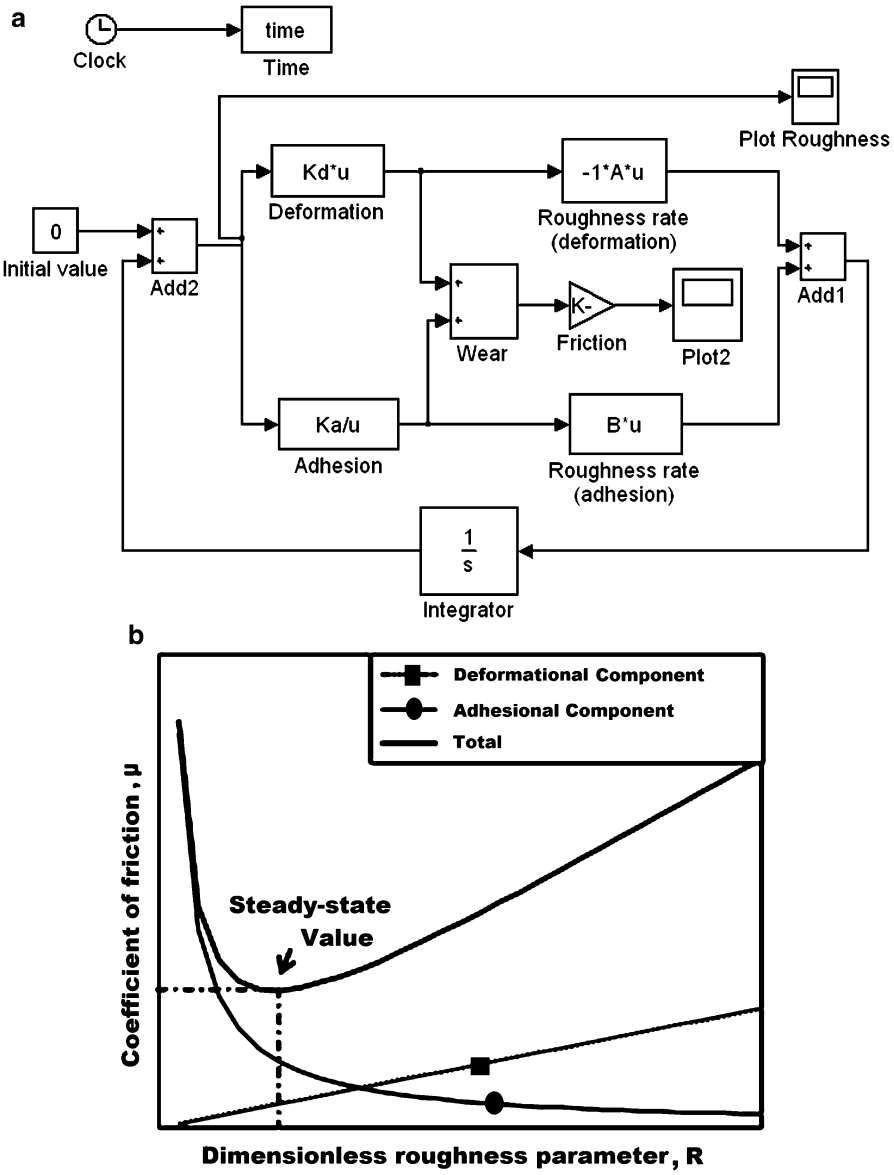

Fig. 7.7 (**a**) A feedback loop to model two simultaneous processes (adhesion and deformation) during the running-in period. (**b**) Total friction is the sum of the deformational and adhesional components and the equilibrium value of roughness (R) corresponds to the minimum value of friction (Mortazavi and Nosonovsky 2011a)

For that end, essentially two mechanisms of friction/wear are needed: one that tends to decrease the magnitude of roughness for a rough surface, and one that tends to increase roughness for a smooth surface. A control model, using the concept specified above, was developed with Matlab/Simulink software (Fig. 7.7).

We can conclude that two (or more) of such mechanisms are present, there is a stationary (steady state) value of surface roughness, which corresponds to the minimum friction and wear.

The time-dependence of the coefficient of friction and roughness parameter during the running-in simulated with Simulink for $A = B$ and $A \neq B$ (Fig. 7.8). For $A = B$, while roughness reaches its equilibrium value (which may be higher or lower than the initial value of R), the coefficient of friction always decreases. Therefore, self-organization of the rough interface results in the decrease of friction and wear. This is due to the fact that the two concurrent processes (wear due to adhesion and deformation) have opposite effect on roughness in accordance to (7.27): deformation makes the surface smoother, whereas adhesion can make a smooth surface rougher.

In the preceding sections, we discussed the growth of a tribofilm, when a growth of the film thickness due to a random fluctuation results in the decrease of wear and therefore causes a further growth of the film, until the thickness reaches an equilibrium value. In a similar manner, the decrease of the roughness results in the decrease of the deformational wear and, therefore, causes a further decrease of the roughness, until another process – the adhesion – starts to play a significant role and thus the equilibrium value of roughness is achieved. The values presented in Fig. 7.8 were obtained with MATLAB and Simulink modeling and they correspond to the equilibrium roughness $R = 1$ (and corresponding coefficient of friction $\mu = 2$), and initial values of roughness lower and higher than $R = 1$.

For $A \neq B$, the coefficient of friction can decrease or increase depending on the initial value of roughness. For most practical situations, the initial roughness state of surface is rougher than the equilibrium steady-state roughness, so both the roughness and the coefficient of friction decrease during the running-in transient period.

7.3.3 Self-Organized Elastic Structures

In the preceding sections, we discussed the self-organization of interface films and microtopography evolution. Another type of self-organized microstructures is elastic slip waves. The mathematical formulation of quasi-static sliding of two elastic bodies (half-spaces) with a flat surface and a frictional interface is a classical contact mechanics problem. Interestingly, the stability of such sliding has not been investigated until the 1990s, when, separately, Adams (1995) and Martins et al. (1995) showed that the steady sliding of two elastic half-spaces is dynamically unstable, even at low sliding speeds. Steady-state sliding was shown to give rise to a dynamic instability [Adams–Martins instabilities (AMI)] in the form of self-excited oscillations with exponentially growing amplitudes. These oscillations confined to a region near the sliding interface and can eventually lead to either partial loss of contact or to propagating regions of stick–slip motion (slip waves). The existence of AMI instabilities depends upon the elastic properties of the surfaces, however, it does not depend upon the friction coefficient, nor does it require a nonlinear

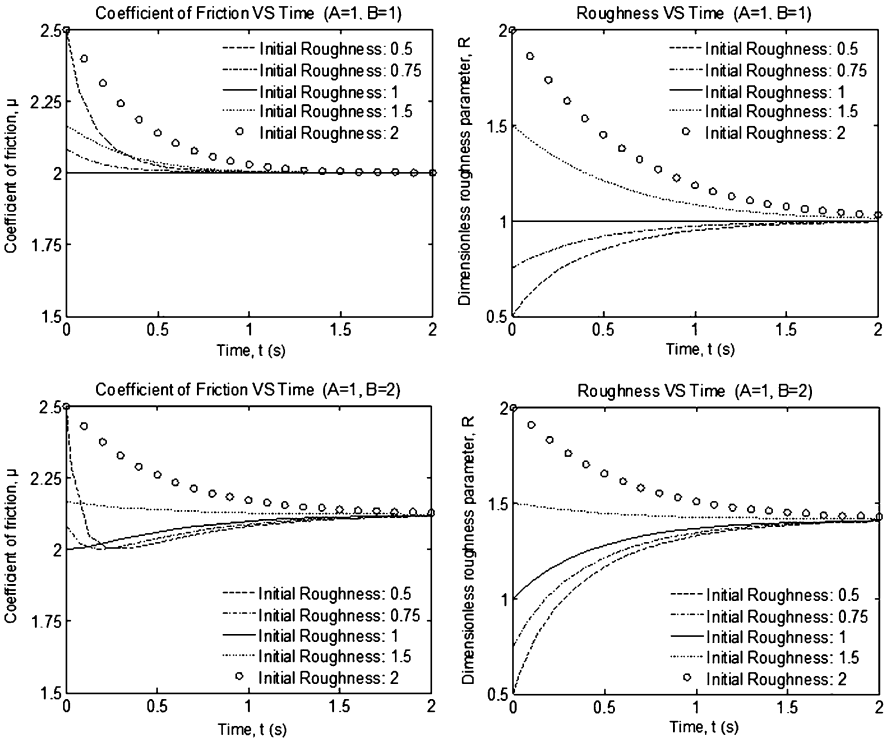

Fig. 7.8 The time-dependence of the coefficient of friction and roughness parameter during the running-in period simulated with Simulink for $A = B$ and $A \neq B$. For $A = B$, while roughness reaches its equilibrium value, the coefficient of friction always decreases. Therefore, self-organization of the rough interface results in the decrease of friction and wear. For $A = B$, the coefficient of friction can decrease or increase depending on the initial value of roughness

contact model. The same effect was predicted theoretically by Nosonovsky and Adams (2004) for the contact of rough periodic elastic surfaces.

It is well known that two types of elastic waves can propagate in an elastic medium: the shear and dilatational waves. In addition, surface elastic waves (Rayleigh waves) may exist, and their amplitude decreases exponentially with the distance from the surface. For two slightly dissimilar elastic materials in contact, the generalized Rayleigh waves (GRW) may exist at the interface zone. The instability mechanism described above is essentially one of GRW destabilization, that is, when friction is introduced, the amplitude of the GRW is not constant anymore, but it exponentially grows with time.

The stability analysis involves the following scheme. First, a steady-state solution should be obtained. Second, a small arbitrary perturbation of the steady-state solution is considered. Third, the small arbitrary perturbation is presented as a superposition of modes, which correspond to certain eigenvalues (frequencies). Fourth, the equations of the elasticity (Navier equations) with the boundary conditions are formulated for the modes, and solved for the eigenvalues. Positive real parts of the eigenvalues show that the solution is unstable.

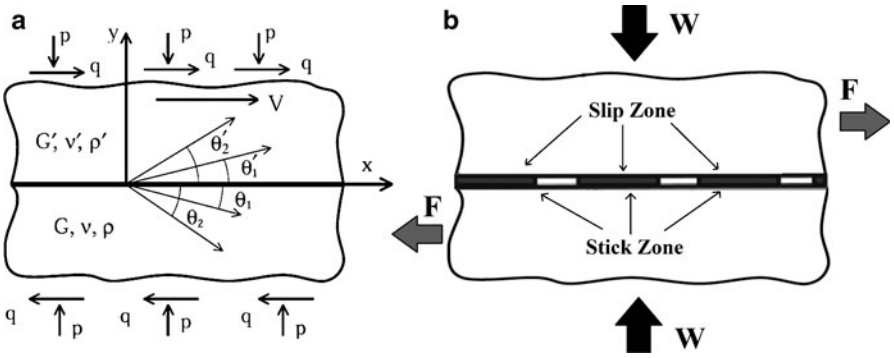

Fig. 7.9 (**a**) Elastic waves radiated from the frictional interface, (**b**) friction reduction due to propagating stick–slip zones (Nosonovsky and Adams 2001)

For the GRW, the 2D displacement field at the interface is given by

$$\begin{aligned} u &= \sum_k u_k(x,y,t), \\ v &= \sum_k v_k(x,y,t), \\ u_k(x,0,t) &= \mathrm{Re}\left[A_k \mathrm{e}^{ikx/l}\mathrm{e}^{\Lambda t}\right], \\ v_k(x,0,t) &= \mathrm{Re}\left[B_k \mathrm{e}^{ikx/l}\mathrm{e}^{\Lambda t}\right], \end{aligned} \tag{7.25}$$

where k stands for the x- or y-component of the displacement field at the interface ($y = 0$), A_k is the complex amplitude, k/l is the wavenumber, l is the wavelength of the lowest wavenumber, and Λ is the complex frequency. It can be shown that for the frictionless case $\Lambda = \pm i\lambda$ is purely imaginary and thus, for real A_k, the displacement is a propagating GRW, $u_k(x,0,t) = A_k \cos(kx \pm \lambda t)$. It can be shown also that if small friction with the coefficient μ is present, then $\Lambda = \pm(i\lambda + \alpha\mu)$, where α is a real number, and thus one root of Λ always has a positive real component, leading to the instability (Adams 1995; Ranjith and Rice 2001). As a result, the amplitude of the interface waves grows with time. In a real system, of course, the growth is limited by the limits of applicability of the linear elasticity and linear vibration theory. This type of friction-induced vibration may be, at least partially, responsible for noise (such as car brake squeal) and other effects during friction, which are often undesirable (Nosonovsky and Adams 2004).

Although the GRW occur for slightly dissimilar (in the sense of their elastics properties) materials, for very dissimilar materials, the waves would be radiated along the interfaces, providing a different mechanism of pumping the energy away from the interface (Nosonovsky and Adams 2001). These waves can form a rectangular train of propagation of slip pulses, two bodies shift relative to each other in a "caterpillar" or "carpet-like" motion (Fig. 7.9). This microslip can lead to

Table 7.6 Types of elastic waves and instabilities at the interface

System	Single half-space	Two half-spaces, no friction	Two welded half-spaces	Two half-spaces, finite friction	
				Slightly dissimilar	Significantly dissimilar
Waves	Surface (Rayleigh) waves	Interface (generalized Rayleigh) waves (GRW)	Stoneley waves	Instabilities confined at the interface (GRW with growing amplitude)	Radiated waves
Derivative waves				Nonlinear stick–slip waves	Linear slip waves

a significant reduction of the observed coefficient of friction, as the slip is initiated at a shear load much smaller than μW (Nosonovsky and Adams 2001; Bhushan and Nosonovsky 2003, 2004a, b; Nosonovsky and Bhushan 2005a, b).

The motion is observed as the reduction of the coefficient of friction (in comparison with the physical coefficient of friction μ) to the apparent value of $\mu_{app} = q/p$, where q is applied shear force per unit area and p is the normal pressure. The slip pulses can be treated as "secondary structures" self-organized at the interface, which result in the reduction of the observed coefficient of friction. Note that the analysis in this case remains linear and it just shows that the equations of elasticity with friction are consistent with the existence of such waves. The amplitude of the slip waves cannot be determined from this analysis, since they are dependent of the initial and boundary conditions. In order to investigate whether the slip waves will actually occur, it is important to ask the question whether it is energetically profitable for them to exist. For that end, the energy balance should be calculated of the work of the friction force and the energy dissipated at the interface and radiated away from the interface. A stability criterion based on (7.8) can be used.

Various types of elastic waves at the interface are summarized in Table 7.6. It shows the Rayleigh and GRW, Stoneley waves (which exist in the case of welded elastic surfaces with no slip or infinite friction), and frictional elastic instabilities. For the latter, the basic instabilities are shown and liner or nonlinear slip waves that can form due to these instabilities.

7.3.4 The Problems of Combining Friction with Dynamics and Linear Elasticity

Despite the simplicity of the Coulomb friction law, combining friction with other areas of mechanics, such as dynamics and the elasticity, encounters numerous difficulties. First, there are several paradoxes of friction due to the nonexistence

or nonuniqueness of static and dynamic solutions of the equations of elasticity, combined with friction. Second, many dynamic problems of elasticity that involve friction result in unstable solutions and, in some cases, in ill-posedness (a situation when small wavelength perturbations has unlimited rate of growth). Together, these two observations lead us to the conclusion that (1) frictional dynamic instabilities should be investigated, since they can lead to self-organized patterns and structures, and (2) additional efforts should be made to consistently combine friction laws with other areas of mechanics.

Despite the linear dependence of the friction force upon the normal load, Amontons-Coulomb's rule is inherently nonlinear. The direction of the friction force depends upon the direction of motion, so that in the vector form the friction force is given by $\vec{F} = -(\vec{V}/|\vec{V}|)\mu|\vec{W}|$, where $\vec{V}$ is sliding velocity. The ratio $\vec{V}/|\vec{V}|$ is nonlinear. This nonlinearity results in some static frictional problems having no solution or nonunique solution, e.g., the so-called Painlevé (1895) paradox. These paradoxes show that the rigid-body dynamics is inconsistent with the Coulombian friction. To resolve these problems, the dynamic friction and elastic deformation should be considered (Stewart 2001). Note also, that the coefficient of static friction (for $\vec{V} = 0$) is usually greater than the coefficient of the kinetic friction (for $\vec{V} \neq 0$), which can also be viewed as a manifestation of nonlinearity.

Adams et al. (2005) also demonstrated that dynamic effects lead to new types of frictional paradoxes, in the sense that the assumed direction of sliding used for Coulomb friction is opposite that of the resulting slip velocity. In a strict mathematical sense, the Coulomb friction is inconsistent not only with the rigid-body dynamics (the Painlevé paradoxes), but also with the dynamics of elastically deformable bodies.

What is the reason for the inconsistency? In order to investigate it, the very nature and foundation of the Coulomb friction should be examined. Urbakh et al. (2004) viewed friction as a nonlinear phenomenon which is characterized by the reduction of a very large number of collective degrees of freedom (molecular vibrations) to one or several degrees of freedom of a tribosystem. It is clear that the Coulomb friction law does not always adequately describe such a radical reduction, which constitutes an over-simplification in many situations. Bershadski (1993) suggested that since the Coulomb law leads to paradoxes due to the incompatibility of mechanical links, the coefficient of friction should be treated not as a coefficient, but as an operator that performs an orthogonal transformation of forces. According to his approach, the friction force is the reaction of the tribosystem on the dissipative flux, and this reaction is delayed.

7.3.5 SOC and Avalanche Dynamics

The methods in the preceding sections of this paper describe the onset of the instability, which can lead to the self-organization of spatial and temporal structures. The linear stability analysis is independent of the amplitudes of small

vibrations and in the case of the instability it predicts an exponential growth of the amplitudes until they become so large that the linear analysis cannot apply anymore. It is much more difficult to perform the nonlinear analysis to find the amplitudes and actual finite motion. Several approaches have been suggested.

One is that a specific type of self-organization, known as self-organized criticality (SOC), plays a role in frictional systems. SOC is a concept in the theory of dynamic systems that was introduced in the 1980s (Bak 1996). The best studied example of SOC is the "sandpile model," representing grains of sand randomly placed into a pile until the slope exceeds a threshold value, transferring sand into the adjacent sites and increasing their slope in turn. There are typical external signs of a SOC system, such as the power-law behavior (the magnitude distribution of the avalanches) and the "one-over-frequency" noise distribution. The concept has been applied to such diverse fields as physics, cellular automata theory, biology, economics, sociology, linguistics, and others (Bak 1996).

The term "criticality" originates in the physics of phase transitions, which provides another way of viewing SOC. Many physical systems have a critical point, that is, a point at which a distinction between two phases vanishes. Typical length of fluctuations (referred to as the correlation length) tends to grow up to infinity near the critical point. Simple scaling relationships between various parameters of the system in the vicinity of the critical point can usually be established. These relationships are governed by power laws with certain critical exponents. For example, the critical point of water is at $T_c = 374°C$ and $P_c = 218$ atm, and the distinction between liquid and gas water at these conditions disappears, so that no energy is needed to convert liquid water into vapor. At the critical point, the energy barrier vanishes. The systems with SOC have a critical point as an attractor, so that they spontaneously reach the vicinity of the critical point and exhibit power law scaling behavior. Since SOC allows a system to reach criticality spontaneously and without tuning the controlling parameter, it was suggested that it plays a major role in the spontaneous creation of complexity and hierarchical structures in various natural and social systems (Bak 1996). SOC was suggested to be responsible for landslides and earthquakes, because it is known that the number of earthquakes and their amplitude are related by a power law. In other words, a number of earthquakes with the amplitude greater than a certain level in a given area during a given period are related to that level by a power law. During earthquakes, the stress between two plates is accumulated for a long time and released suddenly in a catastrophic event, which is similar to the sandpile avalanche (Turcotte 1999; Nosonovsky 2010a).

In the case of dry frictional sliding, it has been suggested that a transition between the stick and slip phases during dry friction may be associated with the SOC, since the slip is triggered in a similar manner to the sandpile avalanches and earthquake slides. Zypman et al. (2003) showed that in a traditional pin-on-disk experiment, the probability distribution of slip zone sizes follows the power law. In a later work, the same group found nanoscale SOC-like behavior during AFM studies of at least some materials (Buldyrev et al. 2006; Zypman et al. 2003). Thus, "stick" and "slip" are two phases, and the system tends to achieve the critical state between them: in the stick state, elastic energy is accumulated until slip is initiated,

whereas energy release during slip leads, again, to the stick state. The entropic methods of analysis of frictional the systems with SOC were used by Zypman and co-workers (Fleurquin et al. 2010), who calculated Shannon entropy of the surface profile and showed that the entropy of the profile decreased indicating the self-organization.

7.3.6 Pattern Formation and Turing systems

As discussed in previous sections, under certain circumstances friction can also result in self-organization or formation of patterns and structures at the frictional interface. These self-organized patterns or "secondary structures" (Fox-Rabinovich and Totten 2006) can include a broad range of phenomena, such as in situ formed tribofilms (Aizawa et al. 2005), patterns of surface topography, and other interfacial patterns including propagating trains of stick and slip zones formed due to dynamic sliding instabilities (Maegawa and Nakano 2010; Nosonovsky and Adams 2001). Moreover, experimental observations demonstrate various structures formed by friction and wear, such as the Schallamach (Maegawa and Nakano 2010) and slip waves (Zypman et al. 2003), wave-like topography patterns (Menezes et al. 2006), honeycomb-like and other structures (Lin and Chu 2009).

Frictional sliding generates heat, and heat tends to lead to the thermal expansion of materials. This can result in so-called thermoelastic instabilities (TEI), which have been studied extensively in the past 30 years (Barber 1969). The effect of TEI on sliding is similar to that of AMI discussed in Sect. 7.3.2. Besides heat generation, friction can be coupled with other effects, such as wear, which can lead to similar instabilities. In addition, the coefficient of friction can depend upon the sliding velocity, load, and interface temperature, which can also lead to complex dynamic behavior (Nosonovsky 2010b).

Another mechanism that may provide instability is the coupling between friction and wear. As friction increases, so does the wear, which may result in an increase of the real area of contact between the bodies and in further increase of friction. The sliding bodies adjust to each other, and the process is known as the frictional self-organization. On the other hand, wear produces smoothening of the surface distorted by the TEI mechanism, and thus the wear and thermal expansion are competing factors, with the wear leading to stabilization of sliding and the thermal expansion leading to destabilization (Fig. 7.10).

The so-called reaction–diffusion systems and their important class called the "Turing systems" constitute a different type of self-organization mechanism (Kagan 2010; Mortazavi and Nosonovsky 2011a). These systems can describe certain types of friction-induced pattern formation involving heat transfer and diffusion-like mass transfer due to wear. While AMI and TEI involve wave propagation (hyperbolic) partial differential equations (PDEs), which describes dynamic behavior of elastic media, the reaction–diffusion (RD) system involves parabolic PDE, typical for diffusion and heat propagation problems. The RD systems describe evolution of

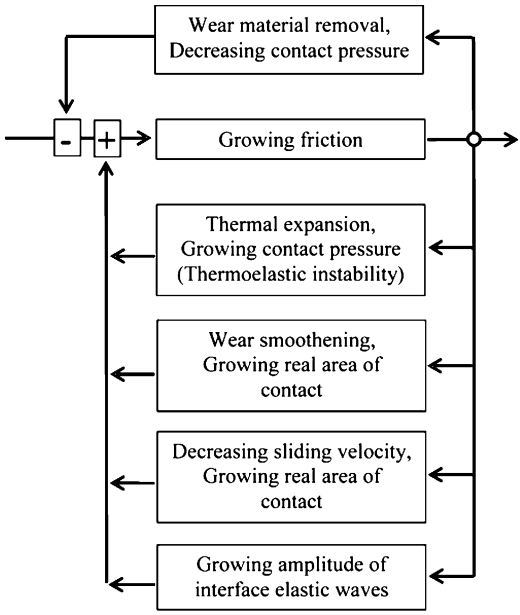

Fig. 7.10 Various mechanisms which can lead to a positive feedback loop and friction-induced instabilities (Nosonovsky 2010b)

concentrations of reagents in space and time due to local chemical reactions and the diffusion of the product of reactions (Leppänen 2004). The RD system of PDEs is given by

$$\frac{\partial w_j}{\partial t} = f_i(w_j) + d_{ij}\Delta w_j, \tag{7.26}$$

where w_j is the vector of concentrations, f_i represent the reaction kinetics, and d_{ij} and Δ are a diagonal matrix of diffusion coefficients and Laplace operator, respectively. Turing (1952) showed that a state that is stable in the local system can become unstable in the presence of diffusion, which is counter-intuitive, since diffusion is commonly associated with a stabilizing effect. The solutions of RD equations demonstrate a wide range of behaviors including the traveling waves and self-organized patterns, such as stripes, hexagons, spirals, etc.

While parabolic RD equations cannot describe elastic deformation, they may be appropriate for other processes, such as viscoplastic deformation and interface film growth. For a system of two components, u and v, (7.21) has the following form:

$$\frac{\partial u}{\partial t} = f(u,v) + d_u\left(\frac{\partial^2 u}{\partial x^2} + \frac{\partial^2 u}{\partial y^2}\right), \tag{7.27}$$

$$\frac{\partial v}{\partial t} = g(u,v) + d_v\left(\frac{\partial^2 v}{\partial x^2} + \frac{\partial^2 v}{\partial y^2}\right), \tag{7.28}$$

where f and g are the reaction kinetics functions and d_{ij} is a diagonal matrix ($d_{11} = d_u$ and $d_{22} = d_v$). Suppose that u represents the nondimensional temperature at the sliding interface and v is the local slip velocity, also nondimensional. The nondimensional values of u, v, x, t, and other parameters are obtained from the dimensional values by division of the latter by corresponding scale parameters. Then (7.27) is interpreted as the description of heat transfer along the interface, and (7.28) describes the flow of viscous material along the interface. In the present chapter, we discuss several types of kinetic functions which can lead to the formation of periodic patterns.

One of the standard forms for functions $f(u, v)$ and $g(u, v)$ based on transferring original reaction–diffusion equations and proper scaling was proposed to be (Dufiet and Boissonade 1991; 1992):

$$f(u, v) = \gamma(a - u + u^2 v), \tag{7.29}$$

$$g(u, v) = \gamma(b - u^2 v). \tag{7.30}$$

In order to investigate the possibility of pattern formation in a Turing system, a stability analysis should be performed (Mortazavi and Nosonovsky 2011a). A reaction–diffusion system exhibits diffusion-driven instability or Turing instability if the homogeneous steady state is stable to small perturbations in the absence of diffusion; however, it is unstable to small spatial perturbations when diffusion is introduced (Murray 1989). Diffusion results in the spatially inhomogeneous instability and determines the spatial patterns that evolve.

From the linear stability analysis, one can show that a solution with pattern formation (Turing pattern) can exist (Dufiet and Boissonade 1991; Murray 1989; Mortazavi and Nosonovsky 2011a). The results of the stability analysis were shown that depends on parameters of (7.27) and (7.28) (i.e., d_v, d_u, a, b, and γ) three regions of stability could be identified. In the region 1, the steady state is stable to any perturbation. In the region 2, the steady state exhibits an oscillating instability. In the region 3, the steady state is destabilized by inhomogeneous perturbations, which is "Turing space."

In this section, we discuss several exemplary cases of parameter values and initial conditions which can lead to patterns. The cases 1 and 2 are the classical examples of the Turing systems, whereas the case 3 is justified by the frictional mechanism of heat generation and mass transfer.

Examples of Turing patterns for two different cases with following values of the parameters in (7.27) and (7.28) are shown in Figs. 7.11 and 7.12. For case 1:

$$\gamma = 10,000, d_v = 20, d_u = 1, a = 0.02, \text{ and } b = 1.77, \tag{7.31}$$

and considering a random distribution function as the initial conditions for both values of u and v. For case 2:

$$\gamma = 10,000, d_v = 20, d_u = 1, a = 0.07, b = 1.61. \tag{7.32}$$

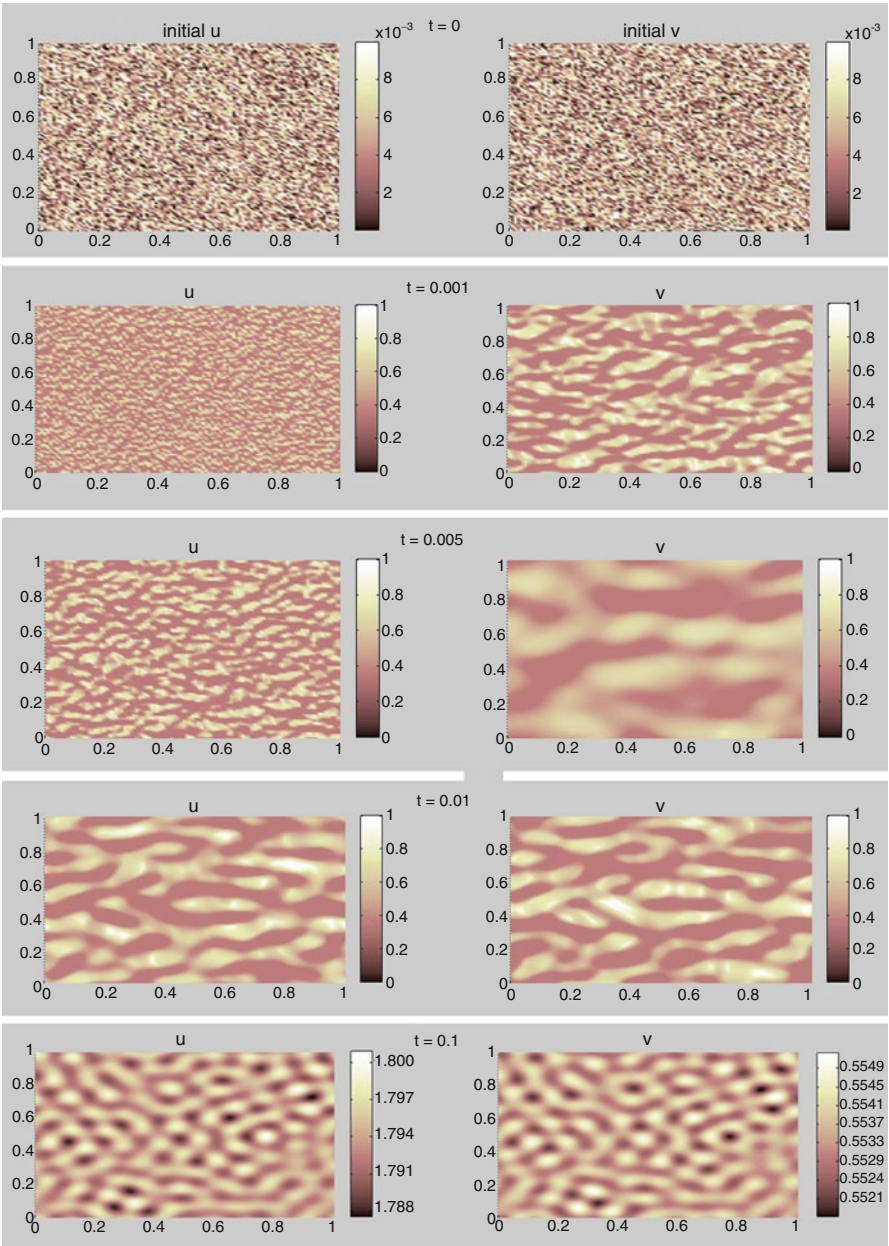

Fig. 7.11 Time evolution of amounts of u and v in different time steps, at $t = 0$, 0.001, 0.005, 0.01, and 0.1 (first case) (Mortazavi and Nosonovsky 2011a)

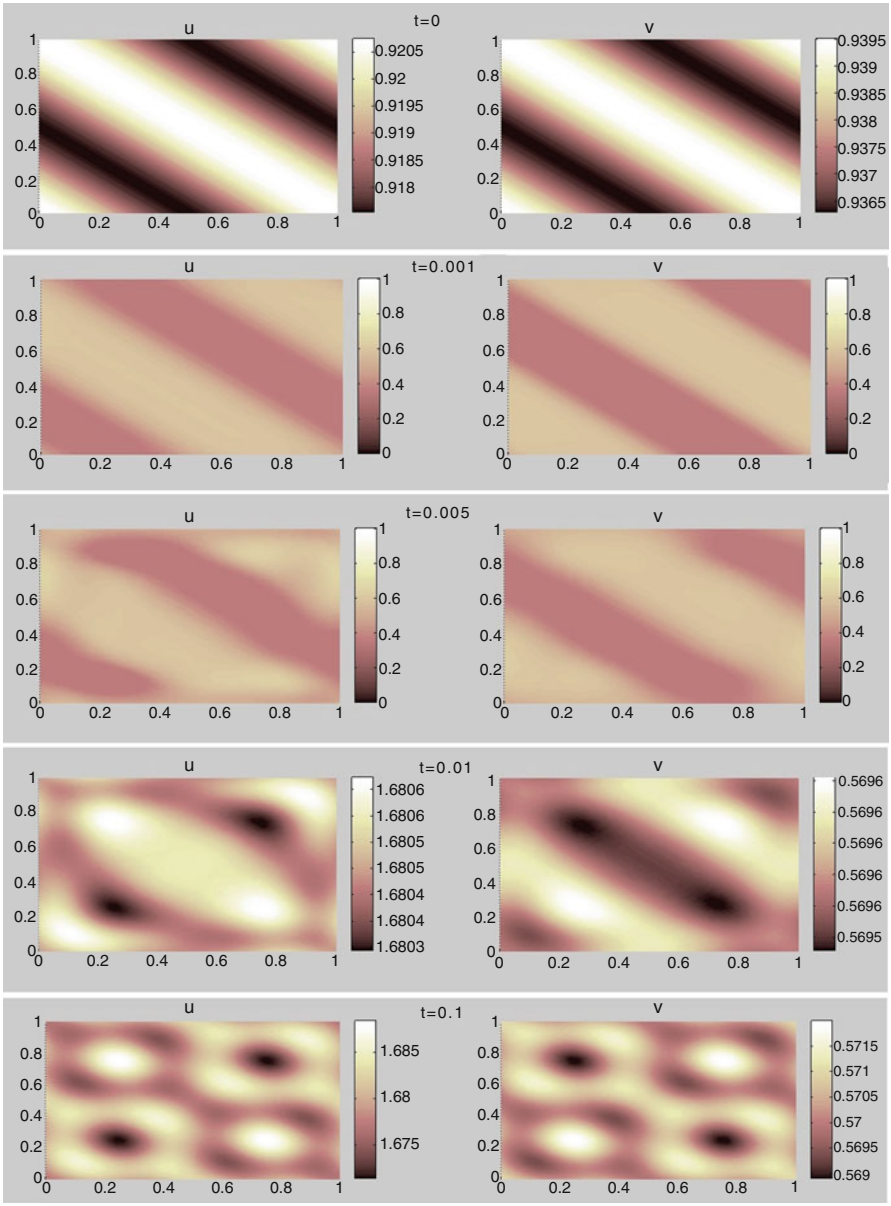

Fig. 7.12 Time evolution of u and v values in different time steps, $t = 0, 0.001, 0.005, 0.01, 0.05,$ and 0.1 (second case) (Mortazavi and Nosonovsky 2011a)

For initial conditions, we considered the following harmonic functions

$$u(x, y) = 0.919145 + 0.0016\ \cos(2\pi(x + y)), \tag{7.33}$$

$$v(x, y) = 0.937903 + 0.0016\ \cos(2\pi(x + y)). \tag{7.34}$$

The results in Figs. 7.11 and 7.12 present five consecutive snapshots of system presented by (7.27) and (7.28) corresponding to different time steps ($t = 0$, 0.001, 0.005, 0.01, and 0.1). It is observed in both cases that the initially random pattern ($t = 0$) evolves finally into a so-called hexagonal-like (or honeycomb) pattern ($t = 0.1$), which indicates that the pattern formation occurs.

Although the two first cases showed that the model is capable of capturing the self-organized patterns in Turing systems, in the third case Mortazavi and Nosonovsky (2011a) tried to use more specific functions of reaction kinetics, which were expected to characterize friction-induced reaction mechanisms. They assumed that functions $f(u, v)$ and $g(u, v)$ to be in the following forms

$$f(u, v) = w_0(\mu_0 + \alpha_1 u + \beta_1 v)u, \tag{7.35}$$

$$g(u, v) = (\alpha_2 u + \beta_2 v), \tag{7.36}$$

or:

$$g(u, v) = (\alpha_2 u + \beta_2 v)u, \tag{7.37}$$

where $\mu_0 + \alpha_1 u + \beta_1 v$ is the coefficient of friction dependent on the temperature u and local slip velocity v, and the nondimensional coefficients α_1 and β_1 and w_0 are constant. The function $g(u, v)$ characterizes rheological properties of the material and depends on its viscous and plastic properties.

Such interpretation of (7.27)–(7.28) can be used if the growth of a tribofilm (a thin interfacial layer activated by friction) is considered. Whereas u still represents the interfacial temperature, v can be interpreted as the nondimensional thickness of the tribofilm formed at the interface. The tribofilm can grow due to the material transfer to the interface via diffusion activated by friction, due to precipitation of a certain component (e.g., a softer one) in an alloy or composite material, due to a chemical reaction, temperature gradient, etc. For example, during the contact of bronze vs. steel, a protective Cu tribofilm can form at the interface, which significantly reduces the wear. Such in situ tribofilm has protective properties for the interface since it is formed dynamically and compensates the effect of wear. Furthermore, if wear is a decreasing function of the tribofilm thickness, it is energetically profitable for the film to grow, since growing film reduces wear and further stimulates its growth forming a feedback loop, until a certain equilibrium thickness is attained. Therefore, such tribofilms can be used for machine tool protection and other applications, as discussed in the literature (Aizawa et al. 2005). The growth of the film is governed by interfacial diffusion and by a local kinetic function $g(u, v)$ dependent upon the temperature and local film thickness.

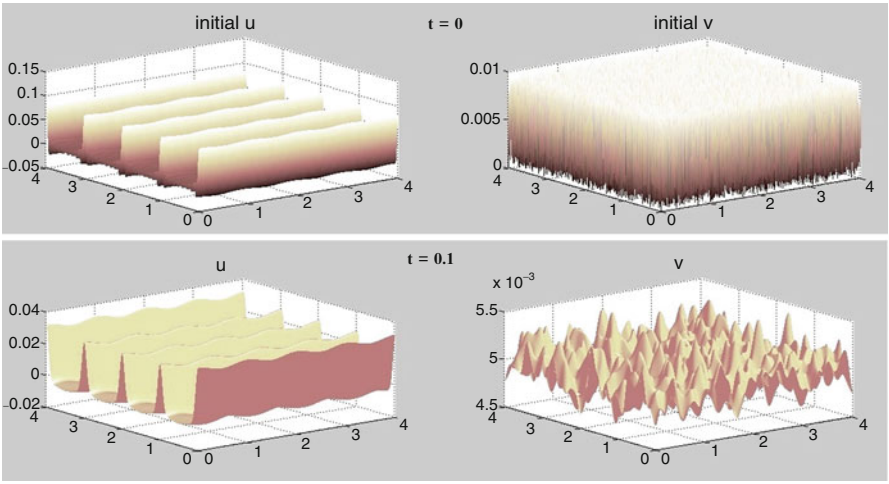

Fig. 7.13 Time evolution of u and v values in two different time steps [third case, using (7.30) and (7.31)] (Mortazavi and Nosonovsky 2011a)

Using following equation as a temperature distribution for initial conditions

$$u(x,y) = 0.002\cos\left(2\pi(x,y)\right) + 0.01\sum_{j=1}^{a}\cos\left(2\pi jx\right), \tag{7.38}$$

and random distribution function as a initial roughness for $v(x, y)$ and, moreover, considering following values for the parameters of (7.27) and (7.28)

$$w_0 = 10^2, \alpha_1 = 10^{-4}, \beta_1 = 10^{-4}, \mu_0 = 5\times 10^{-1}, \alpha_2 = 10^{-4}, \beta_2 = 10^{-4}. \tag{7.39}$$

The obtained results for different time steps are shown in Figs. 7.13 and 7.14 considering (7.36) and (7.37) and as $g(u, v)$, respectively. While patterns found in Figs. 7.13 and 7.14 are not the same as the patterns found in the two previous cases, similar trends in the evolution of tribofilm thickness (v) from an initially random distribution of roughness to a more organized and more patterned distribution could be observed. However, the investigation of pattern formation based on solving complete three-dimensional heat and mass transfer equations in tribofilm is needed to show more realistic picture of how and under what conditions such patterns could occur**.**

The modeling analysis in the preceding sections shows that properly selected functions $f(u, v)$ and $g(u, v)$ can lead to pattern formation. The question remains on whether any experimental data can be interpreted as friction-induced patterns formed by the RD mechanism? It would be appropriate to look for this type of self-organization in processes involving viscoplastic contact or diffusion-dominated effects, e.g., in situ tribofilms. There are several effects which can be interpreted in this way. The so-called "secondary structures" can form at the frictional interface

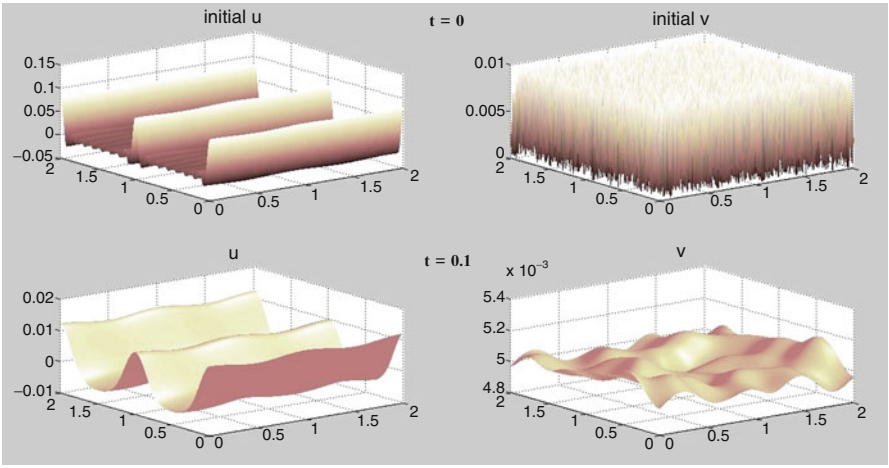

Fig. 7.14 Time evolution of u and v values in different time steps [the third case, using (7.30) and (7.32)] (Mortazavi and Nosonovsky 2011a)

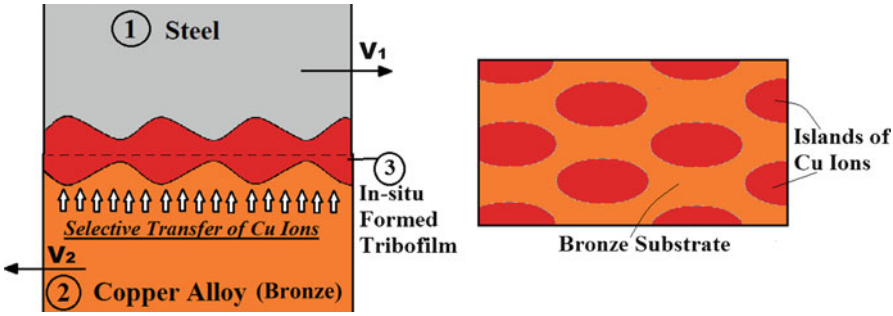

Fig. 7.15 Schematic presentation of the selective layer obtained by friction between a surface of steel and a surface of copper alloy (bronze) (Mortazavi and Nosonovsky 2011a)

due to the self-organization (Fox-Rabinovich and Totten 2006), and some of these structures can have a spatial pattern. The so-called "selective transfer" discussed in Sect. 7.2.4 could be another example.

The selective layer (an in situ tribofilm due to the selective transfer) formed during friction between steel and a copper alloy (bronze) was investigated experimentally by Ilie and Tita (2007). In the presence of glycerin or a similar lubricant, the ions of copper were selectively transferred from bronze to the frictional interface forming the copper tribofilm. This copper was different in its structure from the copper that falls out through normal electrolytic procedures. Ilia and Tita (2007) investigated the selective layer using the AFM and found that the layer formed micro-island pattern with the size on the order of 1 μm, rather than a uniform film of constant thickness. Schematic figure of such layer could be seen in Fig. 7.15.

Another important example of pattern formation reported in the literature is related to the self-adaptive mechanisms improving the frictional properties of hard coatings, e.g., during dry cutting, by tailoring their oxidation behavior (Erdemir et al. 1991, 1996a, b; Lovell et al. 2010). Thus, boric acid formation on boron carbide is a potential mechanism for reaching ultra-low friction. Such mechanism uses the reaction of the boric oxide (B_2O_3) with ambient humidity (H_2O) to form a thin boric acid (H_3BO_4) film. The low friction coefficient of boric acid is associated with its layered triclinic crystal structure (Erdemir 2001; Singer et al. 2003). The layers consist of closely packed and strongly bonded boron, oxygen, and hydrogen atoms, but the layers are widely separated and attracted by van der Waals forces only. During sliding, these atomic layers can align themselves parallel to the direction of relative motion and slide easily over one another (Erdemir et al. 1996a, b).

The tribological behavior of protective coatings formed by both ex situ and in situ transfer films were studied by Singer et al. (2003). Coatings that exhibit long life in sliding contact often do so because the so-called "third body" forms and resides in the sliding interface. The concept of the "third body" as a separate entity, different from the two contacting bodies, is very similar to the concept of the tribofilm. Ex situ surface analytical studies identified the composition and structure of third bodies and provided possible scenarios for their role in accommodating sliding and controlling friction. In situ Raman spectroscopy clearly identified the third bodies controlling frictional behavior during sliding contact between a transparent hemisphere and three solid lubricants: the amorphous Pb–Mo–S coating was lubricated by an MoS_2 transfer film; the diamond-like carbon/nanocomposite (DLC/DLN) coating by a graphite-like transfer film; and the annealed boron carbide by H_3BO_3 and/or carbon couples. In situ optical investigations identified third body processes with certain patterns responsible for the frictional behavior (Singer et al. 2003).

TiB_2 thin films are well known for their high hardness which makes them useful for wear-resistant applications. Mayrhofer et al. (2005) showed that overstoichiometric $TiB_{2.4}$ layers have a complex self-organized columnar nanostructure pre-cursor. Selected area electron diffraction (SAED) pattern from a $TiB_{2.4}$ layer showed a texture near the film–substrate interface with increased preferred orientation near the film surface (Mayrhofer et al. 2005). The film has a dense columnar structure with an average column diameter of ~20 nm and a smooth surface with an average RMS roughness essentially equal to that of the polished substrate surface, ~15 nm.

Aizawa et al. (2005) investigated in situ TiN and TiC ceramic coating films utilized as a protective coating for dies and cutting tools. They found that chlorine ion implantation assists these lubricious oxide (TiO and Ti_nO_{2n-1}) film to be in situ formed during wearing. They also performed the microscopic analysis and observed worn surfaces and wear debris and found microscale patterns.

Lin and Chu (2009) described Bénard cell-like surface structures found from the observation of the transmission electron microscopy (TEM) images of the scuffed worn surface as a result of lubricated steel vs. steel contact. They attributed the cells

Table 7.7 Summary of different experimental pattern formation evidences discussed in the literature

	Materials in contact	Tribofilm material	Mechanism	Pattern	Reference
1.	Steel vs. copper alloy (bronze)	Copper	The selective transfer	Cu islands (~1 μm)	Ilie and Tita (2007)
2.	Boric oxide (B_2O_3)	Thin boric acid (H_3BO_4) film	Oxidation	Layered pattern	Erdemir et al. (1991, 1996a, b) and Lovell et al. (2010)
3.	Glass vs. Pb–Mo–S	MoS_2 films	Transfer film	MoS_2 islands (nanoscale)	Singer et al. (2003)
4.	Sapphire against a DLC/DLN coating	Silicone-formed DLC/DLN coating	Transfer film	Silicone islands (nanoscale)	Singer et al. (2003)
5.	TiN vs. AlN	TiB_2 thin films	Oxidation	Columnar structure (~20 nm)	Mayrhofer et al. (2005)
6.	Steel vs. steel	TiN or TiC films of 1 μm	Oxidation	Microscale patterns	Aizawa et al. (2005)
7.	Steel vs. steel	α-Fe inside the substrate of the unscuffed surface	Wear	Bénard cell-like patterns	Lin and Chu (2009)

to high temperatures (800°C) and very strong fluid convection or even evaporation occurring inside the scuffed surface. However, the possibility of diffusion-driven based pattern formation should not be ruled out.

The experimental evidences of pattern formation, which can, at least theoretically attributed to the reaction–diffusion mechanism, are summarized in Table 7.7. Further evidence is needed to rule out alternative explanations.

7.4 Summary

Despite the fact that self-organization during friction has received relatively little attention in the tribological community so far, it has a potential for the creation of self-healing and self-lubricating materials, which are of importance for the green or environment-friendly tribology. The principles of the thermodynamics of irreversible processes and of the nonlinear theory of dynamical systems are used to investigate the formation of spatial and temporal structures during friction. These structures lead to friction and wear reduction (self-lubrication). The self-organization of these

structures occurs through the destabilization of the stationary sliding. The stability criteria involve minimum entropy production. Some evidences of friction-induced self-organization like running-in stage, elastic structures, and Turing pattern formation were studied. A self-healing mechanism, which provides the coupling of the degradation and healing, can be embedded into material. Structure–property relationships were formulated and can be used for optimized design of self-lubricating and self-healing materials and surfaces for various ecologically friendly applications and green tribology.

Chapter 8
Tribological Properties of Metal Matrix Composites

Metal matrix composite (MMC) materials constitute an important class of materials for tribological applications. In this chapter, we review tribological properties of some MMC with emphasis on the graphite-reinforced materials.

8.1 Introduction

Composite materials are engineered or naturally occurring materials made from two or more constituent components with significantly different physical or chemical properties which remain separate and distinct at the macroscopic or microscopic scale within the finished structure. In the case of two constituent components, one with the highest volume fraction is considered the "matrix," whereas the other is the "reinforcement" modifying the properties of the matrix. A metal matrix composite (MMC) is composite material with at least two constituent parts, one (the matrix) being a metal. The other material may be a different metal or another material, such as a ceramic or organic compound. When at least three materials are present, it is called a hybrid composite. MMCs are synthesized by dispersing a reinforcing material into a metal matrix. The reinforcement surface can be coated to prevent a chemical reaction with the matrix.

The matrix is the monolithic material into which the reinforcement is embedded, and is completely continuous. This means that there is a path through the matrix to any point in the material, unlike two materials sandwiched together. In typical structural applications, the matrix is usually a lighter metal such as aluminum, magnesium, or titanium, and provides a compliant support for the reinforcement. In high-temperature applications, cobalt and cobalt–nickel alloy matrices are common.

The reinforcement material is embedded into the matrix, usually in the form of particles, fibers, whiskers, or wires. The reinforcement does not always serve a

M. Nosonovsky and P.K. Rohatgi, *Biomimetics in Materials Science: Self-Healing, Self-Lubricating, and Self-Cleaning Materials*, Springer Series in Materials Science 152, DOI 10.1007/978-1-4614-0926-7_8,

purely structural task (reinforcing the compound), but is also used to change physical properties such as wear resistance, friction coefficient, or thermal conductivity. The reinforcement can be either continuous, or discontinuous. Discontinuous MMCs can be isotropic, and can be worked with standard metalworking techniques, such as extrusion, forging, or rolling.

Continuous reinforcement uses monofilament wires or fibers such as carbon fiber or silicon carbide. Because the fibers are embedded into the matrix in a certain direction, the result is an anisotropic structure in which the alignment of the material affects its strength. Discontinuous reinforcement uses "whiskers," short fibers, or particles. The most common reinforcing materials in this category are alumina and silicon carbide.

There are several methods to synthesize MMCs, which can be classified as solid, liquid, and vapor deposition. Solid state methods include powder blending and consolidation (powder metallurgy) and foil diffusion bonding: Liquid state methods include electroplating, stir casting, squeeze casting, spray deposition, and reactive processing (in the latter, a chemical reaction occurs, with one of the reactants forming the matrix and the other reinforcement).

Carbon-reinforced MMC are widely used for tribological applications. When lamellar solids such as graphite or molybdenum disulphide are applied to sliding surfaces, friction and wear are observed to decrease. The crystal structure of a lamellar solid has sheets or layers weakly bonded with each other but the bonding within the sheet is quite strong These solids are thus strong in compression but weak in shear, and act as solid lubricants as discussed by Bragg (1928) explaining the origin of lubricity in graphite. Graphite, which consists of carbon atoms arranged in a layer-like structure, displays a very low coefficient of friction ranging from 0.1 to 0.2 while sliding on another clean surface, thus suggesting that it can be used as a solid lubricant. In Bragg's view the layered structure imparts graphite with an inherent quality of lubricity. However, a fourfold increase in friction of graphite and three orders of magnitude increase in wear under vacuum over that in air clearly indicates that the lubricity of graphite is not inherently derived from its structure alone. The environment appears to play a significant role in the lubrication behavior of graphite. In fact, graphite has been found to require the presence of absorbed vapors such as water or hydrocarbons to develop good lubrication properties (Rohatgi et al. 1992).

One of the main difficulties in using graphite as a solid lubricant lies in maintaining a continuous supply of graphite which acts as a solid lubricant between two sliding surfaces; such a continuous supply is more easily maintained in the case of fluid lubricants. An interesting innovation to ensure a supply of graphite between sliding surfaces is to incorporate graphite into the matrix of one of the sliding components forming a composite. Under optimum conditions the metal–graphite composite becomes self-lubricating because of the transfer of the graphite embedded in its matrix to the tribosurfaces and its formation into a thin film which prevents direct contact between the mating surfaces. The success of metal matrix–graphite particle composites depends on the ability of the graphite particles

to come out of their embedded state in the matrix and spread evenly in the form of a solid lubricating film over the tribological surface to provide lubrication.

In recent years, considerable work has been done on the metal matrix–graphite particle composites which exhibit low friction, low wear rate, and excellent antiseizing properties. In these composites, graphite presumably imparts improved tribological properties to the composite through the formation of a graphite-rich film on the tribosurface which provides solid lubrication. The formation of the solid lubricating film depends on the matrix characteristics, for example, its deformability helping the process of transfer of graphite to the tribosurface, adhesion of graphite film to the matrix, and the presence of an environment which permits graphite to spread in the form of a film and act as a solid lubricant. In metal matrix–graphite composites, graphite particles are embedded in the matrix, and the formation of a graphite film will take place by transfer of the graphite from the particles embedded in the matrix on to the tribosurfaces during initial periods of sliding. The observed friction and wear behavior will, therefore, have two distinct stages: (a) transient state, while a graphite film is being established, and (b) steady state, when a stable graphite film (in the dynamical sense of being continuously replenished to make up for the wear loss) has formed.

It should be noted that there is a growing family of composites where graphite is present in fiber form. While much of the discussion is on synthetically prepared graphite particle composites, for example, copper–graphite, iron–graphite, silver–graphite, and aluminum–graphite, discussion on tribological properties of cast irons has been included even though they represent iron–graphite mixtures which form during solidification of molten carbon-rich irons and are not generally classified as modern composites. They have been used extensively in antifriction applications and illustrate the mechanism of solid lubrication by graphite. In the second section, the processes for fabrication of composites containing graphite particles are outlined and in the third section the theoretical framework for understanding the tribological behavior of these composites is described. The influence of the matrix alloy composition, the graphite content and its shape and size, and test variables such as contact pressure and sliding velocity on the tribological behavior of MMCs are discussed in the fourth section. The effects of chemical, electrical, and thermal environmental factors on the friction and wear behavior of metal matrix–graphite particle composites are presented in the fifth section. In the sixth section, the process of graphite-rich film formation on the tribosurfaces of these composites is described; this has been critically examined since the superior tribological properties of metal matrix–graphite composites are strongly dependent on the formation of graphite-rich film on tribosurfaces. In the seventh section, selected applications of metal matrix–graphite particle composites and their industrial potential are described. In the eighth section, an attempt is made to give an integrated picture of current understanding of the overall tribological behavior of these composites, highlighting the gaps in knowledge.

Typical microstructures of selected metal matrix–graphite particle composites are shown in Fig. 8.1. The microstructures generally exhibit dark particles of

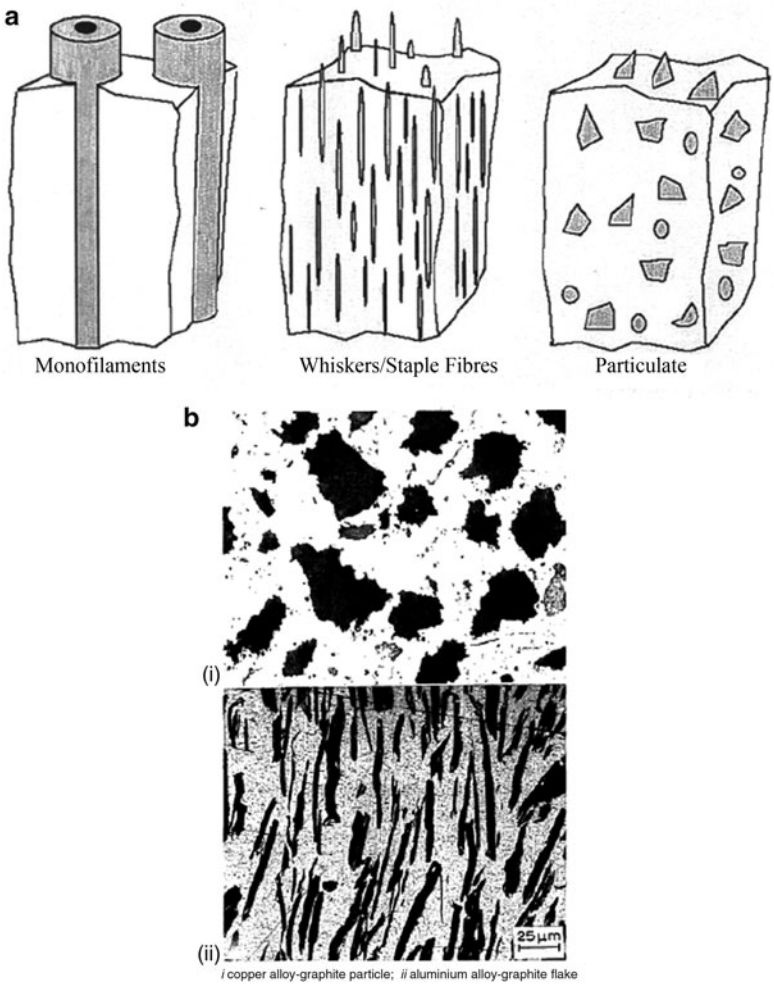

Fig. 8.1 (**a**) Monofilament, whiskers, and particulate reinforcement in composite materials. (**b**) Typical microstructure of MMCs (Al–Si/20 vol% Gr_p (i) and Al-alloy graphite flake (ii))

graphite dispersed in the matrix of light etching matrix phase which is generally the continuous phase. The microstructure of the matrix phase depends on the technique used for processing the composite.

Generally, the processes for synthesis of MMCs containing graphite can be divided into three main categories depending on techniques employed: (a) powder metallurgy, (b) casting metallurgy, and (c) spray deposition. The process used to synthesize the composite appears to have an effect on its tribological properties, because of its influence on matrix microstructures, the distribution of graphite particles, and the bonding between the matrix and the graphite.

8.2 Manufacturing Methods of MMC

8.2.1 Powder Metallurgy

The basic manufacturing in powder metallurgy (PM) includes mixing, compacting, and sintering of mixtures of powders of metals constituting the matrix and graphite powders. The initial process of mixing raw materials is an important first step, since it controls the distribution of particles and porosity in composites both of which influence the tribological behavior. Segregation or clustering of particles is thus a common problem with the present state-of-the-art mixing technology. The reason for segregation is the different flow characteristics of different powders during mixing and the tendency of agglomeration of particles to minimize surface energy (Rack 1988). It has been reported that generally the larger the size of the powders, the better the degree of their distribution. Spherical particles mix better than irregular particles. Density differences also affect the results of mixing. During mixing, light particles tend to stay on the top, while the heavy particles primarily segregate to the bottom.

After the mixing operations, mixtures of powders are pressed in a die at pressures that make the mixtures adhere at contacting points. This process is called compacting. Sintering is closer to the final step in manufacturing and the primary control parameters during this stage are the temperature and atmosphere. The primary problems in fabrication of metal–graphite composites by PM are the presence of oxide films on powder, imperfect distribution of graphite in metal matrices, sweating during liquid phase sintering, and poor strength in solid phase sintering. The tendency of liquid metals to sweat out results from the frequent poor wettability of graphite powders by liquid metal.

The inadequate bonding between the graphite and the matrix at sintering temperatures below the melting point of the metal results in poor strength in the composite. The problem of sweating has been solved by adding a small amount of calcium in the form of calcium–silicon alloy to the powder mixture in iron–graphite systems and the volume fraction of graphite can then be increased to values as high as 90%. The techniques developed to overcome lower strengths include mechanical alloying and hot pressing processes. The mechanical alloying involves repeated fracturing and partial melting of mixtures of constituent powders by high energy compressive impact forces. It has been reported that by sintering the compacts under pressure, the density of composite materials may be increased up to 98% of theoretical density (Rack 1988). Various metals and alloys have been used as matrix material for the synthesis of metal matrix–graphite particle composites, using PM techniques. These include copper and silver. The cost of synthesis of metal matrix–graphite particle composites by powder processes is an order of magnitude higher than the liquid metallurgy processes, and the sizes and shapes which can be produced by PM methods are limited.

8.2.2 Casting

The advantage of casting processes for the synthesis of metal matrix–graphite particle composites is their relatively low cost compared with PM techniques, and the ability to produce large complex shapes. In the casting process, one can either produce graphite particles in situ by precipitation from liquid, according to the equilibrium phase diagram, or one can introduce graphite particles from the outside into the liquid without the restraints of the phase diagram. An example of the phase equilibrium generated composite is cast iron, where graphite precipitates from the molten iron during the solidification of cast iron. Currently, two types of casting methods are employed for synthesizing the nonequilibrium synthetic type of MMCs: (a) impregnation methods whereby a bed of dispersoids is impregnated by liquid metal flowing under a pressure differential, as in squeeze casting and pressure infiltration, and (b) dispersion methods such as stircasting or compocasting where the dispersoids such as the particles or fibers are dispersed in liquid or semisolid alloys by stirring and the resulting slurry is cast. In squeeze casting, liquid metal is forced under high pressure (70–100 MPa) into a bed or a preform of particles or fibers (Cornie et al. 1990). In pressure infiltration, molten alloy is usually forced in under low pressures (<15 MPa) (Cornie et al. 1990). A typical method in this category is pressure infiltration, in which pressurized gas is used to apply pressure on liquid metals and the particles, compacted into a preform or a bed in a tube. The preform or the bed is penetrated by the liquid metal to form a composite. By using this method, the composites can be produced with high volume fraction of dispersoids. The pressure required for infiltration can also be applied by a hydraulic ram in a die casting machine (Heine 1988).

In dispersion processes such as stircasting or compocasting, dispersoid particles are stirred into alloys in molten or semisolid state and the resulting slurry is cast by gravity or pressure die casting. The main advantage of dispersion processes is that the methods can be used to manufacture composite components using conventional foundry type casting processes. The different processes for fabricating cast composites have been reviewed recently by Ray (1990), Zhang (1988), Cornie et al. (1990), and Rohatgi et al. (1986).

8.2.3 Spray Deposition

In this method, liquid metal and dispersoid powders are co-sprayed through an atomizer on a substrate to form billet, disc, tube, strip, or laminated structures. Particles of sizes 5–500 μm have been used with metal flow rates of 0.25–2.5 kg s^{-1} to produce composites with 5–35 vol% particles (Lavernia 1989). Aluminum, iron, nickel, titanium, copper, and cobalt base alloys have been used to produce MMCs by this method (Lavernia 1989; Momoun 1975).

8.3 Theoretical Basis for Understanding Friction and Wear Behavior in Composites

It is well known that even the most carefully prepared real surface is gently undulating and consists of many microscopic and macroscopic asperities. The friction between two mutually contacting solid surfaces arises from the interaction at these discrete points of asperities where actual contact occurs. The basic processes involved in these interactions are (a) adhesion at the contacting points and (b) deformation (either elastic or plastic) of the asperities by the load. The force required to overcome friction will consist of the force required to shear the adhesion bond F_a, and the force F_d required to deform elastically or plastically the obstructing asperities of the relatively softer material in the path of the asperities of the relatively harder material. If N is the applied normal load on the contacting surface, the coefficient of friction f is given by Bowden et al. (1945)

$$f = \frac{F_a + F_d}{N} = \frac{F_a}{N} + \frac{F_d}{N} = f_a + f_d, \tag{8.1}$$

where f_a and f_d are, respectively, the coefficients of friction due to adhesion and deformation. The adhesion strength and the resulting friction f_a are strongly influenced by the presence of surface films and contaminants. The presence of oxides, absorbed films, and grease prevents intimate contact between the mating surfaces and inhibits the growth of a strong adhesional bond. When a surface consisting of solid lubricants like graphite dispersed in a metallic matrix comes into contact with another surface, a thin film of solid lubricant graphite-rich layer covers the mating surface, reducing the adhesional friction. The nature of this film then governs the adhesional component of friction in graphite-containing MMCs. However, the contribution of deformation to the coefficient of friction is still determined by the mechanical properties of the underlying composites.

8.3.1 Friction and Thin Film Lubrication in Metal Matrix–Graphite Particle Composites

In 1945, Bowden and Tabor (1945), developed a theory for thin film lubrication and the coefficient of friction f was expressed as

$$f = \frac{S_f}{H_g} \tag{8.2}$$

A low shear strength of the film S_f on the sliding surface and a relatively high substrate hardness H_s, results in a low coefficient of friction compared with that of either the substrate or bulk of film material alone. However, this simple picture

cannot explain the detailed friction behavior of a combination of a film and a substrate. Further, the plastic deformation of the film begins to influence the contact area. The shear strength of the lubricating film S_f has to be replaced by S_p, the shear strength of the film under pressure as proposed by Bridgman (1936)

$$S_p = S_f + \alpha P, \tag{8.3}$$

where α is a constant of the film material and P is the applied normal pressure. The friction coefficient under these conditions becomes

$$f = \frac{S_f + \alpha P}{P} = \frac{S_f}{P} + \alpha. \tag{8.4}$$

At low pressures P, the indentation of the asperities of the mating surface may be confined within the film layer if the film is thick and the load will be supported by the film, resulting in $P = H_f$, the hardness of the film. If the film is soft, then the coefficient of friction will be higher because of the higher contribution of the first term in (8.4). However, for thin films, the indentation load will be supported by relatively hard substrate material and $P = H_s$ resulting in a lower value of coefficient of friction. As the normal load increases, the real area of contact will also increase; but, after it becomes equal to the geometrical area of contact, there will be no further increase in this variable. As pressure will increase above this value, the contribution of the first term in 8.4 will reduce, and in the limiting case of very high pressure the coefficient of friction will approach the value of α, a characteristic of the film material. In the case of MMCs before any sliding, the area fraction of tribosurface occupied by graphite is close to the original volume fraction of graphite in the composite if the distribution of graphite particles is uniform, and the planar surface is representative of the volume distributions. However, as the tribosurface is subjected to deformation during sliding, the graphite is squeezed out of the graphite particles in the embedded state, and these are spread during sliding on the tribosurface in the form of a film of solid lubricant. The film of graphite may not cover the entire tribosurface and the coefficient of friction of the composite may be roughly correlated with the extent of film formation on the interface by the rule of mixture

$$f = (1 - A_g) f_m + A_g f_g, \tag{8.5}$$

where f_m and f_g are, respectively, the coefficients of friction in the matrix and in the areas covered by graphite film and A_g the fraction of the interface covered by graphite film. Following (8.1) and (8.4), one may write

$$f_m = f_{am} + f_{dm} \tag{8.6}$$

and

$$f_g = \frac{S_g}{P} + \alpha, \tag{8.7}$$

where f_{am} and f_{dm} are contributions to the coefficients of friction of the matrix f_m due to the process of adhesion and deformation, respectively. S_g is the shear strength of graphite and $P = H_m$ the hardness of the matrix. Thus, the coefficient of friction may vary from f_m to f_g depending on the composition of the composite, and the ability of the solid lubricant phase to spread over the given matrix and counterface.

The formation of a film of solid lubricating graphite takes place during the initial period of sliding of the solid lubricant bearing composites against a counterface. During this period the solid lubricant emerges from the embedded graphite particles and, as wear proceeds, spreads over the sliding surface of the composite and is transferred to the counterface. These processes progress along with continued wear of the film and the matrix. After a given time, the rate of formation of the film in terms of its area and thickness balances the rate of its wear, giving rise to a dynamic steady state characterized by a steady value of friction. The evolution of the graphite film on the tribosurface from its initial transient stage to its dynamical steady state can be characterized by the changing coefficient of friction. During the transient period there will be greater metal–metal asperity interaction; during later stages the film formation will intervene and prevent such metal to metal contact. In the presence of lubricating oil there will be fluid film lubrication preventing direct metal to metal contact, until the running conditions change into a boundary lubrication when the solid lubricant film of graphite will intervene.

8.3.2 Wear in Composites Containing Solid Lubricants

In elastic–plastic materials like composites, wear particles are generated by the following mechanisms (Suh 1977; Suh 1986; Jahanmir et al. 1975; Rigney et al. 1984): (a) adhesion, deformation, and fracture of asperities resulting from repeated single or multiasperity interaction during sliding, (b) ploughing by hard entrapped particles or hard asperities at the sliding surface, and (c) delamination caused by subsurface crack nucleation and propagation. The wear debris generated by these mechanisms forms loose particles, or sometimes transfers to the countersurface by mechanical interlocking or by adhesion on the counterface. In the dynamic steady state of wear, the asperities are continuously reformed, and are removed by asperity deformation and fracture. Ploughing also will contribute to the process of wear and formation and reformation of asperities. When a sample of a given roughness is put to wear, the extent of material removal depends on the size of the asperities. Abrahamson et al. (1975) have shown that the higher is the initial roughness, the more is the material removed in the initial transient period before steady state wear characterized by a wear rate independent of initial roughness sets in. It is therefore obvious that the often omitted data on the initial surface roughness of the samples are very important when reporting results on bulk wear averaging over a period including that of transient state. The initial roughness of the composite will have an important influence on the process of film formation in the transient state.

Wear arising out of the three basic mechanisms (Bowden et al. 1950; Rabinowicz 1966; Sasada 1985) of adhesion, delamination, and abrasion is found to be proportional to the applied normal load W, the sliding distance S, and inversely proportional to the hardness of the wearing body H

$$w = k\frac{WS}{CH}, \tag{8.8}$$

where w is the abraded volume, k the wear constant, and C a geometrical factor equal to 1 for abrasion and 3 for adhesion. The reciprocal of wear constant K is often taken as a measure of the wear resistance of a material. Since both the hardness and the wear constant of a material depend on its microstructure, (8.8) can be simplified as

$$w = kWs, \tag{8.9}$$

where k is called the wear factor and depends on the material and microstructure. The surfaces of pure metals and alloys are often contaminated with oxides and absorbed gases. During sliding at very small loads, the oxide or absorbed layer may not be disturbed and the wear behavior will correspond to that of the contaminated layer. At a still larger load the oxide or absorbed layer may wear out, exposing fresh metallic surface, but the fresh layer may become contaminated again before its next contact with the counterface in some test configuration used in practice. The process of re-forming the oxide or absorbed layer is promoted by higher local temperatures at contact spots. When the conditions of load and sliding velocity are such that the oxide layer wears out during contact and fails to form again before the next contact because the time between successive contacts is insufficient for contaminating the surface again, the wear behavior changes. From mild oxidative wear, the wear becomes severe and metallic. However, this transition will also depend on the test configuration which determines the time between successive contacts.

In mild wear, the worn out particles are very fine (1–10 μm) and the subsurface is not heavily deformed. The coefficient of friction does fluctuate in mild wear. In severe wear, the worn particles are large (~10–100 μm) and metallic, and subsurface is heavily distorted. The coefficient of friction is relatively stable. For a given load the transition from mild to severe wear takes place at a specific sliding velocity; for a given sliding velocity, the transition takes place at a specific load. This transition is quite distinct from time-dependent transition at constant load.

In metal matrix–graphite particle composites, if the composition is such that the tribosurface is partly covered by the graphite film, the change in the nature of wear of the metallic part of the tribosurface will be reflected in the overall wear of the composite. Thus, for low graphite bearing composites one may observe a transition in wear behavior, but this effect will be obliterated when a large part of the tribosurface is covered by graphite films, as is the case in composites containing higher amounts of graphite.

The wear in the graphite film may take place primarily by delamination within the film when the thickness of the film exceeds a critical value. Accumulation of dislocations below the tribosurface may lead to subsurface cracking resulting in delamination (Suh 1986). The softer asperities on graphite are fractured by repeated loading due to asperity interaction and a smooth surface is generated. The nature of the contact changes from asperity–asperity type to asperity–plane contact. The harder asperity induces plastic deformation on the softer surface under repeated loading. This accumulated plastic deformation results in void nucleation below the surface. Any dislocation generated near the surface will move out to the surface because of the image force, leaving a thin surface layer free of dislocations. During sliding there will be two types of stress: (a) tri-axial compressive stress, and (b) shear stress. The former is greater at the surface and opposes nucleation of voids. Thus, the nucleation of voids does not take place on the surface. Below the surface, the compressive stress diminishes and below a certain critical depth it is possible for the shear stress to nucleate voids. If there are second phase particles below the surface, the void nucleation takes place preferentially at the interface of the second phase and the soft material; such voids have been observed even at the interface between the matrix and the graphite particles in the subsurface region in aluminum–graphite particle composites. The voids so nucleated extend and coalesce to form crack exceeding a critical length. This crack is unstable and propagates to the surface generating a thin sheet of soft material as debris of this wear process. This wear process continues to erode the thickness of the soft graphite layer unless its thickness is so small that it is totally free from dislocations and tri-axial compressive stress prevents any void nucleation or resulting delamination in the layer.

8.4 Friction, Wear, and Seizure Behavior of Graphite Bearing Composites

8.4.1 Friction Characteristics

The particulate composites of graphite and a matrix alloy are characterized by (a) the composition and microstructure of the matrix alloy, (b) the size, volume fraction, and distribution of particles, and (c) the nature of the interface between the matrix and the dispersed graphite. In addition, the composites may have defects such as voids and porosity which, unless accounted for, will result in an erroneous estimate of area of contact and thereby influence wear and friction. In addition, the strength of the composite will reduce with increased porosity content, enhancing wear. An insufficient characterization of composites, particularly in respects of particle size, distribution, and defects, often lead to variations in observed friction as shown in Fig. 8.2, where the friction coefficients of two cast Al–Si alloy–graphite composites, with some variation in matrix composition, are shown (Gibson et al. 1984; Tokisue et al. 1978). The difference in matrix composition cannot explain the doubling of the friction coefficient in one set of alloys compared

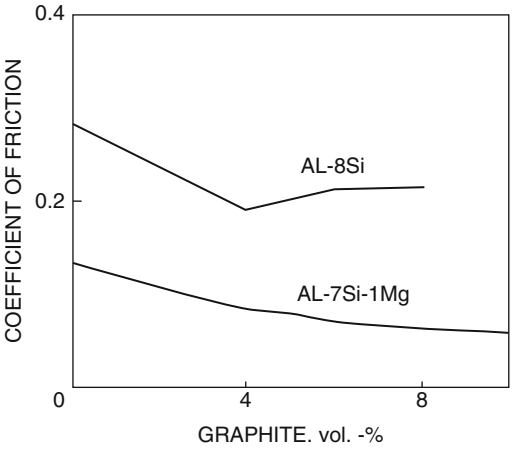

Fig. 8.2 Variation of coefficient of friction with graphite content for composites of similar base composition

Ref.	27 ■	33 △	35 □	36 ▲	37 ● ×	38 ▽	39 ○	40 ▼
Materials	Al–Si	Al–Si	Al	Ag	Fe and Ni	Cast iron	Cu	Cu
Normal pressure, MPa	1	1.6–0.12	0.2	0.3	...	0.6	0.5–0.05	0.5–2
Sliding speed, ms^{-1}	1	0.1–0.2	0.5–1	13–26	1.2–2.3	5	...	0.6

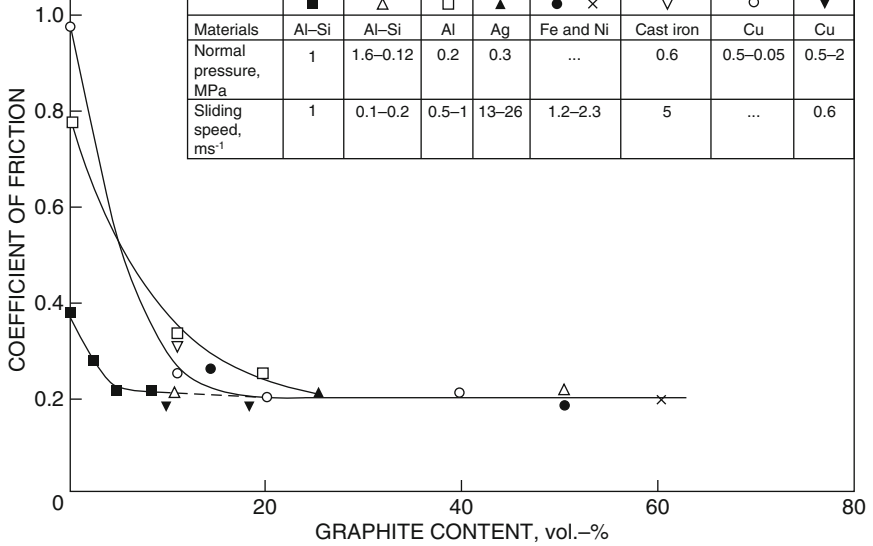

Fig. 8.3 Variation of coefficient of friction with graphite content for composites with different base alloys

with the coefficient in the other. It is suspected that other contributing factors might have been responsible for this variation but could not be identified during the analysis of this data because of insufficient characterization of the samples; this type of large scatter in the data is endemic to this field of study.

Figure 8.3 shows the coefficient of friction observed in a number of particulate graphite composites with aluminum, copper, iron, nickel, and silver as the matrix (Gibson et al. 1984; Lancaster 1983; Pardee 1967; Dillich et al. 1983; Rybakova et al. 1985; Rohatgi et al. 1990a, b, c, d; Rohatgi et al. 1991; Yuasa et al. 1986;

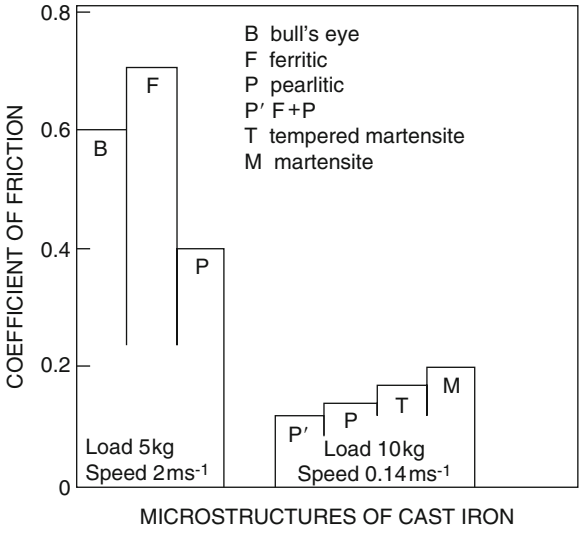

Fig. 8.4 Influence of matrix microstructure on coefficient of friction of gray cast iron

Johnson and Kuhlmann-Wilsdorf 1983a, b; Bowen 1963; Kawamoto et al. 1980; Tsuya 1985; Owen et al. 1987). Results for the coefficient of friction of pearlitic gray cast iron and aluminum–silicon alloy–graphite particle composites have also been included in this figure. The tests were carried out with different loads and sliding velocities. All the composites, with the exception of the silver matrix, were tested against steel, for the conditions indicated in Fig. 8.3. The variation in friction coefficient with graphite content shows that when the graphite content in the composites exceeds 20 vol%, the friction coefficients observed in different composites are virtually independent of the matrix and the graphite content, and appear to attain a constant value close to 0.2. The elemental graphite has a friction coefficient of 0.18 and this increases with the desorption of adsorbed vapors. Thus, it appears that both the mating surfaces, including the graphitic composite and the counterfaces like steel, become completely smeared with graphite, and a friction coefficient close to that of pure graphite against itself is observed, regardless of the matrix. The contribution of the first term in (8.4) and (8.7) to the coefficient of friction f is dependent on the hardness of the substrate or matrix alloy, but it does not appear to make a significant difference in the friction coefficient observed in these composites (Fig. 8.3) containing more than 20 vol% graphite.

The influence of the microstructure and the resulting hardness of gray cast iron on its coefficient of friction as determined by Sugishita and Fujiyoshi (1981a, b) is given in Fig. 8.4. Similar values of coefficients of friction have been reported by Kawamoto et al. (1978) as shown in Fig. 8.5: the increase in friction with hardness of the matrix is contrary to what is expected from (8.4) probably because the cast iron surface will have very little graphite film. A study by Barry and Binkelman (1966) on the friction observed in different substrates covered with a thin film of MoS_2 reveals that for substrates softer than the film material, there is a sharp increase in the coefficient of friction with a decrease in hardness of the substrate; however, for harder substrates the friction becomes independent of the hardness of

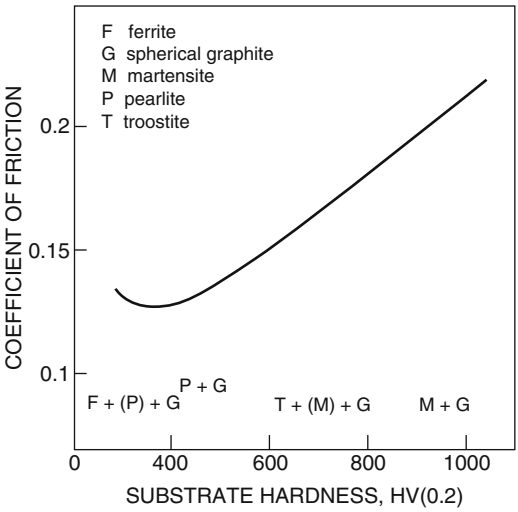

Fig. 8.5 Variation of coefficient of friction with matrix hardness in gray cast iron

the substrate. It appears that the trend of variation of coefficient of friction as given in Fig. 8.4 may have resulted from the process of film formation on the sliding surface. Microscopic examination of the gray cast iron samples shows that a softer matrix leads to a larger area of the sliding surface being covered by graphite films. If there is a supply of graphite on the covered surface, the plastic flow of the surface layer of the matrix appears to help in spreading of graphite into a film. This layer is capable of deforming continuously without much work hardening or fracture because of the absence of dislocations and voids as explained above. The graphite film in gray cast iron is not likely to cover the entire sliding surface because of lower volume fraction of graphite, so the overall coefficient of friction should reflect the friction of the matrix as well. It has been observed that the pearlite matrix results in a lower coefficient of friction than that for ferrite matrix as shown in Fig. 8.5 because of relatively poor adhesion and the higher strength of pearlite. However, the pearlite matrix contains part of the carbon as carbide, thus affecting the amount of graphite available for the process of film formation. Thus, a mixed ferrite–pearlite matrix shows lower friction compared with that in either a ferrite or pearlite matrix alone. The relatively higher friction in martensite or troostite matrix over that in pearlite, indicates that the increase in matrix strength was more than offset by the lowering of the amount of graphite due to carbon in solid solution in iron; in addition, the spreading of graphite with the flow of the surface layer was adversely affected because of the higher hardness of the matrix.

The variation of friction in composites with load was discussed above in the section "Theoretical basis for understanding friction and wear behavior in composites," on the basis of (8.4) and (8.5). If the steady state has been achieved, the contribution of the uncovered matrix on the tribosurface to the overall friction should be governed by (8.5), and f_m would be reasonably constant. However, the contribution from the regions of tribosurface which are covered by graphite film

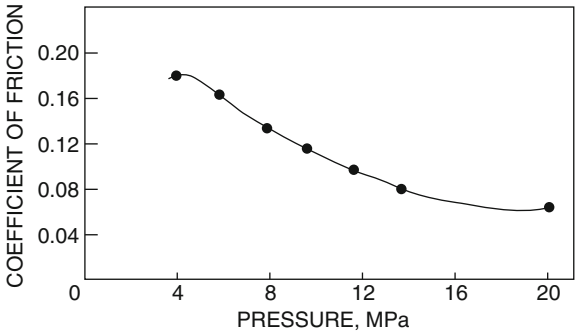

Fig. 8.6 Variation of coefficient of friction with normal pressure for Al–1.5 vol% graphite composite tested at sliding velocity of 1.5 m s^{-1}

may vary with pressure. For lower contact pressures, P in (8.7) is equal to the hardness of the film and thus, f_g should be constant. However, as the pressure increases beyond the point of total contact, P increases till the asperities indent the matrix below, and P is equal to the hardness of the matrix. The friction should thus be constant at lower load, and then reduce with a further increase in pressure. A similar behavior has been observed by Muran and Srnanek (1985) in Al–1.5 vol% graphite composite tested at a sliding velocity of 1.5 m s^{-1} as shown in Fig. 8.6. The agreement between the predicted and the experimentally observed variation of friction with load in the steady state is apparent. But, the absolute values of friction coefficients observed are very low.

8.4.2 Wear Characteristics

The dry wear in composites containing solid lubricant graphite is governed by the nature, thickness, and the spread of the lubricating film on the tribosurface as discussed above in the section.

Figure 8.7 shows the wear volume with sliding distance for different Al alloys, and that for the same alloys containing different amounts of graphite (Kawamoto et al. 1978; Barry et al. 1966; Muran et al. 1985; Suwa et al. 1976; Biswas et al. 1981; Choo et al. 1979; Jha et al. 1989). All investigators, apart from Biswas and Pramila Bai (1981) find that wear decreases when the alloy contains dispersed particles of graphite. However, the absolute values cannot be compared because of different test conditions and poor characterization of the composites. The porosity content and particle size distributions are known to affect wear; however, these microstructural parameters are inadequately reported while describing the wear behavior. This problem becomes more apparent when one considers the variation of wear rate with pressure in Al–Si alloys as shown in Fig. 8.8 (Gibson et al. 1984; Suwa et al. 1976; Choo et al. 1979; Das et al. 1989). The wear rates of the

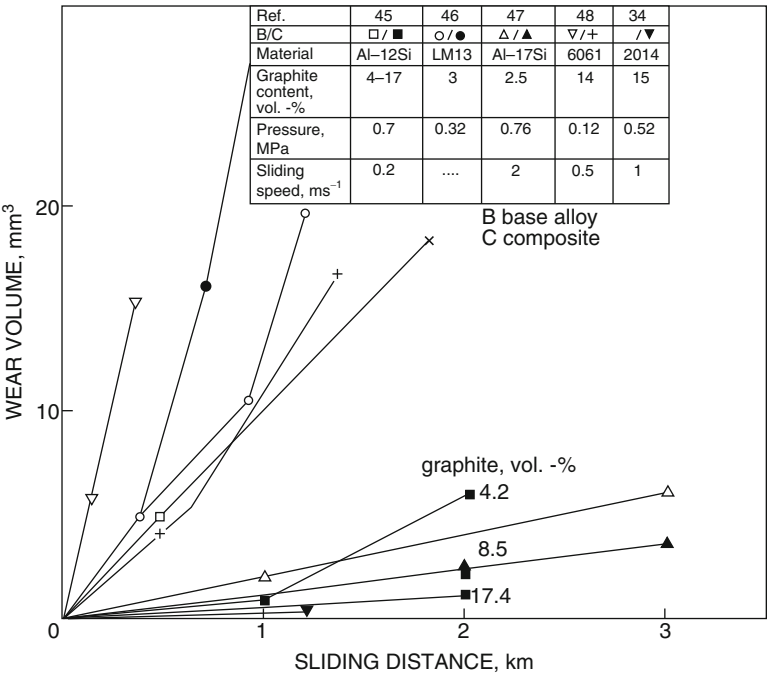

Fig. 8.7 Variation of wear volume with sliding distance for different aluminum alloy–graphite particle composites and corresponding base alloys

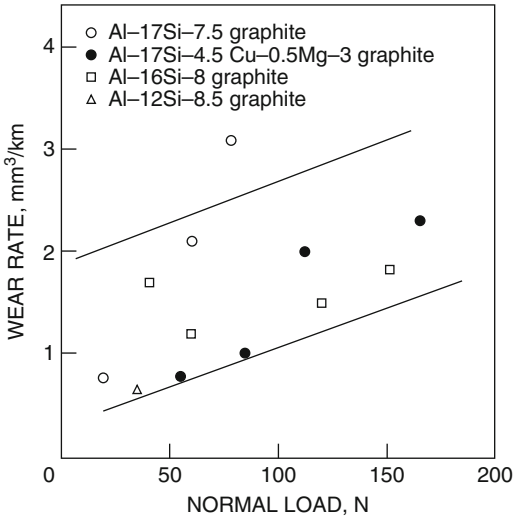

Fig. 8.8 Variation of wear rate with normal load for Al–Si alloy–graphite particle composites

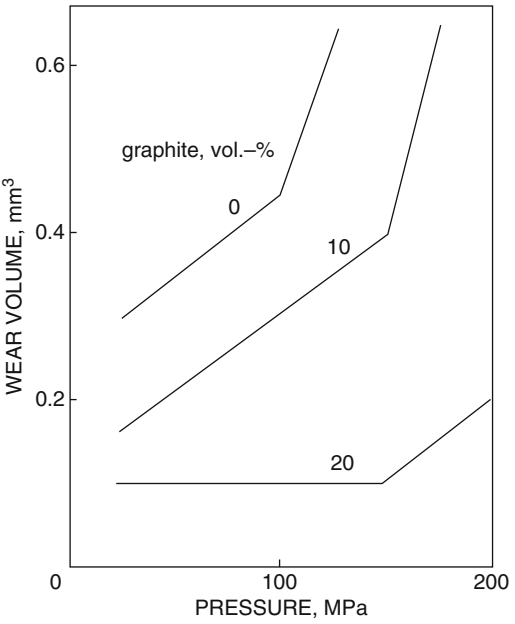

Fig. 8.9 Variation of wear volume with pressure (normal) for copper–graphite particle composites containing 0–20 vol% graphite

composites investigated by various investigators do not fall on a single curve, but are scattered (within limits) as the normal load increases, even though the base alloys and the graphite contents are similar.

Figure 8.9 shows the variation of wear in copper–graphite composite with contact pressure (Suwa 1986). The critical load for transition from "mild" to "severe" wear increases with increase in the graphite content from 0 to 10%. In addition, the wear both before and after transition is lower the higher the graphite content in the composite. Since the wear rate in Cu–20 vol% graphite composite is so low after transition, compared with the rate of severe wear in the matrix alloy, it is possible that this may merely correspond to instability of the film and not represent severe wear in its true sense. That is the reason for using the terms mild or severe within quotes in the context of composites. If the experiments could have been carried out using greater applied pressures, it is possible that another transition might have occurred.

Figure 8.10 shows the variation of wear with sliding velocity in graphitic composites of Al–Si alloys, and compares it with that of the respective matrix alloys without any graphite (Choo et al. 1979; Yuasa et al. 1986). As the sliding speed increases, the interface temperature also increases resulting in (a) the formation of oxides on the sliding surface, and (b) decrease in flow stress. In addition, there may be microstructural changes such as dissolution of precipitates, which will also be reflected in the wear behavior. In Fig. 8.10, one observes that the composite with only 5 vol% graphite retains more or less the same trend of wear rate with sliding speed as that of the matrix. However, the composite with 15 vol% graphite

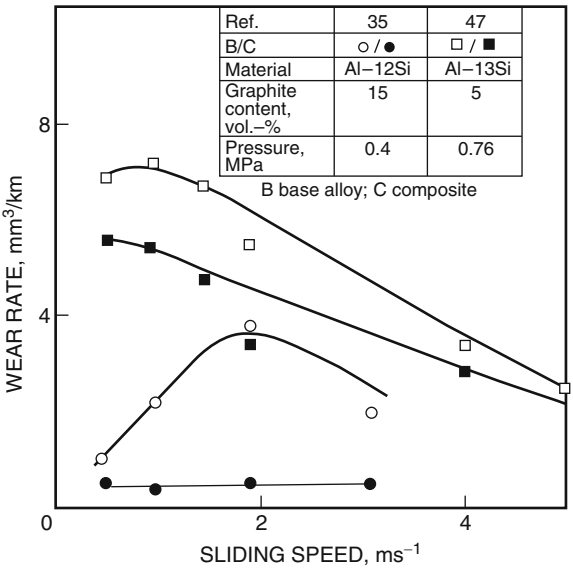

Fig. 8.10 Variation of wear rate with sliding speed for Al–Si alloy–graphite particle composites and corresponding base alloys

shows a completely different trend to that of the matrix; this is an indication that the sliding surface might have been largely covered by graphite film so that the wear rate becomes almost unaffected by changes in sliding speed under the given test conditions. When the graphite content is low, the sliding interface is, for the most part, not covered by the graphite-rich film, and the wear characteristics.

Figure 8.11, which shows that the wear rate decreases with increasing graphite content, and levels off once the film of graphite completely covers the sliding surface (Gibson et al. 1984; Suwa et al. 1976; Choo et al. 1979; Das et al. 1989). However, Jha et al. (1989) observed a different trend where wear rate increases with graphite content; their anomalous results may have been caused by porosity as the composite used by them had been prepared by powder techniques.

It is likely that the wear rate may increase when graphite content in the matrix reaches very high values, because of the decrease in strength of the matrix at very high graphite levels and the formation of thick graphite film of thickness exceeding the critical value, which itself can wear by delamination within the film in a manner similar to that of bulk graphite. The reciprocal of the wear constant in (8.8) may be taken as a measure of wear resistance, and it increases with an increase of graphite content for both Al and Cu-base alloys, as shown in Fig. 8.12.

The effect of particle size of graphite on the wear behavior of composites of bronze containing graphite particles is illustrated in Fig. 8.13, where one observes that, for the same sliding distance, wear volume is higher in composites containing finer graphite particles. This effect has been attributed to the plastic flow of matrix alloy to cover the smaller graphite particles effectively so that the sliding surface has very little graphite. The smaller the particle, and the more ductile the matrix, the greater will be the extent to which the particles are covered. If the ductility of the

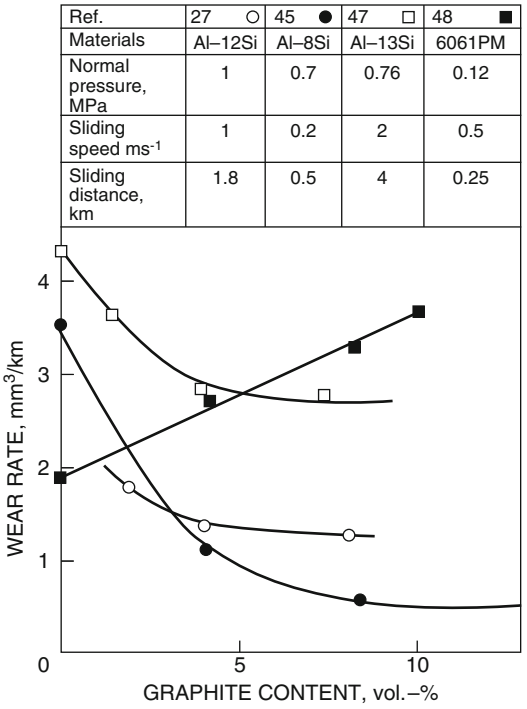

Fig. 8.11 variation of wear rate with graphite content and Al alloy matrix

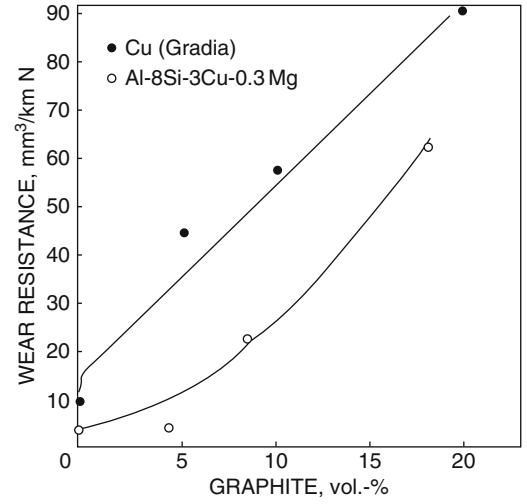

Fig. 8.12 Improvement in wear resistance with graphite content in Al alloy and Cu alloy base composites

matrix is reduced by the addition of phosphorus, the wear reduces because of a decrease in the extent of plastic flow of the matrix on the top of the embedded graphite particles. Sugishita and Fujiyoshi (Sugishita and Fujiyoshi 1981a, b) have observed the same effect in nodular cast iron, where the larger nodule size results in lower wear.

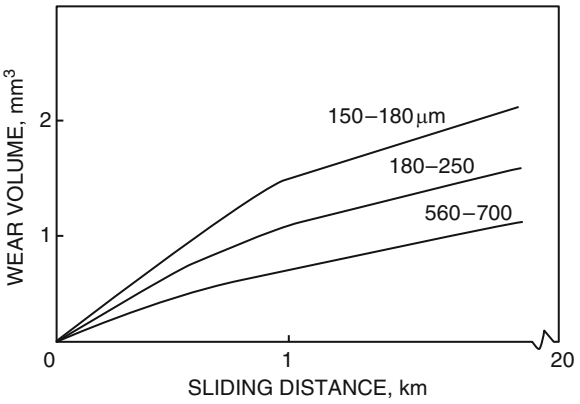

Fig. 8.13 Effect of graphite particle size on variation of wear volume with sliding distance for bronze matrix composites; 4.9 MPa, 0.2 m s^{-1}

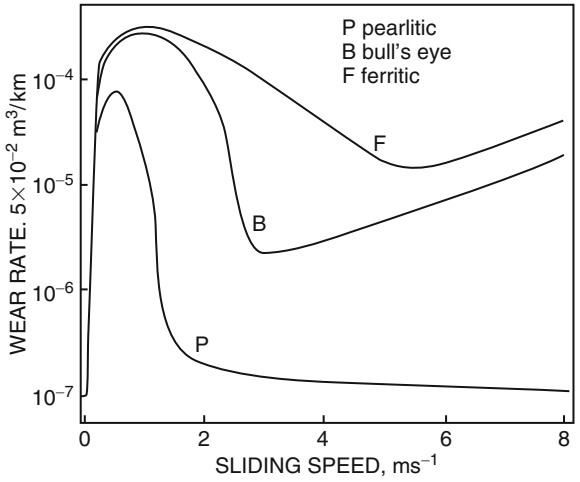

Fig. 8.14 Influence of matrix microstructure on variation of wear rate with sliding speed for spheroidal gray cast iron

Also, a softer matrix over the graphite undergoes larger deformation and results in enhanced removal of metal by fatigue. Kawamoto and Okabayashi have investigated extensively the effect of the matrix on the wear of spheroidal gray cast iron under dry sliding condition as shown in Fig. 8.14. Fully pearlitic matrix shows the lowest wear when compared with that of fully ferritic, and bull's eye structure with free ferrite and pearlite in the ratio of 1:1. Okumoto et al. (1974) have observed that the wear is also dependent on the shape of graphite. Gray cast iron with flake graphite's has inferior wear resistance compared with spheroidal gray cast iron. This may be due to lower matrix strength in gray cast iron containing flake graphite and also, the small transverse dimension of the flake makes it easier for matrix to cover it by plastic flow. Wear rate becomes dependent on the relative orientation of the flakes, the sliding direction, and the flake size.

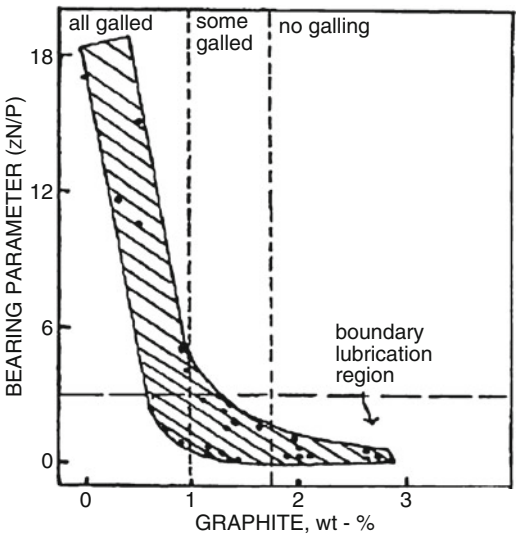

Fig. 8.15 Variation of bearing parameter with graphite content for Al–Si alloy base composites

8.4.3 Seizure Characteristics

The seizure resistance of a material can be defined as its resistance to welding under pressure during sliding contact (Rohatgi et al. 1980). The seizure of aluminum on aluminum is particularly severe under boundary lubrication, and it sometimes occurs even under full film lubrication because of instabilities in the film (Rohatgi et al. 1980; Smith et al. 1959; Prasad et al. 1987; Rohatgi et al. 1979). Investigations of Badia and Rohatgi (1969) have shown that the seizure resistance of aluminum alloys can be improved significantly by dispersing graphite particles in the matrix of these alloys. Figure 8.15 shows that the minimum bearing parameter *(zN/P)* corresponding to seizure, reduces significantly with graphite content; z is the viscosity of the lubricant, N the rotational speed of shaft, and P the contact pressure. The improvement in seizure resistance could be due to the following factors (Badia 1989): (a) lubrication provided by the graphite film between the mating surfaces, (b) dispersion of fine graphite particles in the debris in lubricating oil and resulting in improved lubrication, and (c) the voids left in the matrix after transfer of graphite to tribosurface, acting as reservoir of lubricant. Rohatgi et al. (1979, 1987) suggest that the improvement in gall resistance is primarily due to the formation of graphite film and that there is an observed minimum graphite content of about 2 wt% required to prevent galling in Al–Si–Ni alloys.

Pai and Rohatgi (1974) have pointed out only 2 wt% graphite can considerably improve the seizure resistance of aluminum base alloys against the same alloy under boundary lubrication conditions. Das and Prasad (1989) have concluded that 3 wt% of graphite in Al–Si–Cu alloys (LM 30) increases the seizure pressure by 2 MPa over that for the base alloy under boundary lubrication, as shown in Fig. 8.16. Rohatgi et al. (1990a, b, c, d) have summarized the results of the seizure behavior in aluminum–graphite composites by using normalized velocity and pressure as shown in Fig. 8.17. It is evident that the seizure resistance of Al alloys

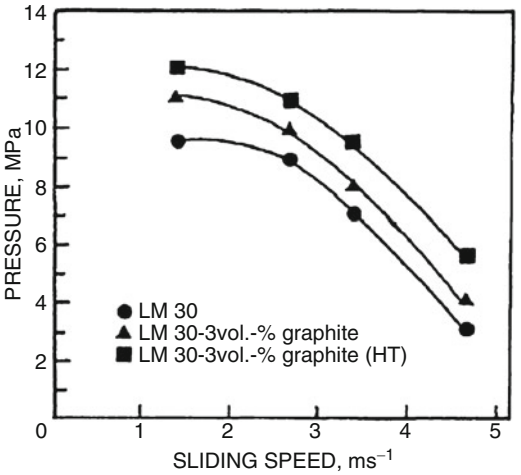

Fig. 8.16 Influence of graphite on pressure variation corresponding to seizure at different sliding speed in Al–17Si–4Cu matrix composites

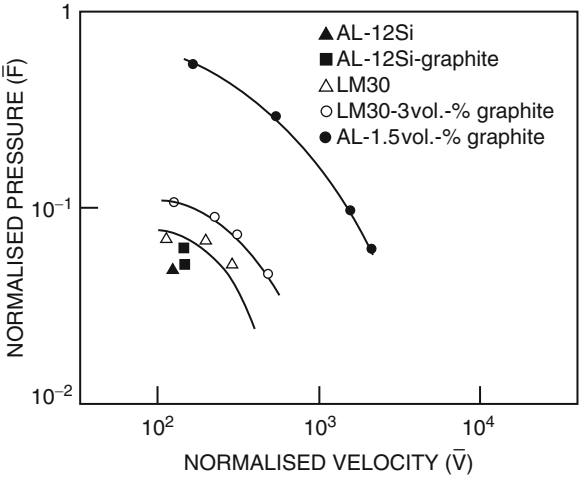

Fig. 8.17 Displacement of seizure boundary by graphite in Al alloy base composites

can be improved by adding graphite particles. This is evidence of graphite interfering with asperity interactions and cold welding. Microstructural studies have revealed that the increase in seizure resistance of aluminum alloys was primarily due to the formation of a graphite film on the tribosurface.

8.5 Effect of Environmental Factors on Friction and Wear

8.5.1 Environmental Conditions and Lubrication

One of the most important factors affecting the tribological properties of metal matrix–graphite particle composites is lubrication provided by the graphite film on

Table 8.1 Effect of environment gas [a]

Gas[b]	Contact drop (V)	Friction coefficient	Energy loss ($J\ cm^{-2}\ m^{-1}$)	Wear in brush ($mm^3\ Mm^{-1}$)
Air	0.00	0.34	2.3	23.3
CO_2	0.03	0.18	1.6	3.2
SF_6	0.18	0.10	1.9	2.2
N_2	0.17	0.06	1.6	1.5
He	0.26	0.06	2.1	1.3
Ar	0.17	0.06	1.5	0.7

Copper ring surface velocity 13 m s^{-1}
Brush loads: 78 A cm^{-2}, 8 N cm^{-2}
Brush bulk temperature range: 67–80°C
[a] SG2 silver–graphite brushes, 75 wt% Ag: 1 cm^2/brush.
[b] ~10^5 Pa total pressure. Moisture partial pressure 600 Pa

the tribosurface. However, some environmental factors significantly affect the lubrication behavior of graphite. Graphite has a layered structure which allows the material to smear out on both the rubbing surfaces by interlayer slippage (Bryant et al. 1964; Deacon and Goodman 1958). However, Savage (1948) has pointed out that easy slip of one layer of graphite over another occurs readily only in the presence of water vapor or some volatile organic solvents. The importance of environmental condition on the lubrication behavior of MMCs containing graphite have been stressed by Kuhlmann-Wilsdorf et al. (1988a, b), Johnson et al. (1967, 1970, 1982), Tsuya (1985), Casstevens et al. (1978a, b, c), and others (Baker and Hewitt 1936; Johnson and Kuhlmann-Wilsdorf 1983a, b; Lee and Johnson 1978). Lee and Johnson (1978) have investigated the effect of environmental gas on the friction and wear of Ag–25 wt% graphite composite and the results are given in Table 8.1. Brush performance, in terms of desired low energy loss and low wear, is significantly improved in different moist nonoxidizing gas environments compared with that in moist air. A low level of moisture (partial pressure of 600 Pa in 10^5 Pa total pressure) significantly improves the performance of electrical brushes.

The effect of operating temperature on friction has been reported separately for different metal matrices (Bowen 1963). The increase in temperature from 38°C to 540°C increases the value of friction coefficient by about 0.05 only for iron–graphite composites. It is apparent that the lubricity of graphite is largely retained up to about 540°C if the presence of graphite is ensured by preventing oxidation through suitable environmental control. But the easy plastic flow of the matrix material at an elevated temperature may result in a greater coverage of small graphite particles reducing its supply on the tribosurface for film formation and an increase in the coefficient of friction may result.

The effect of lubricant on the wear behavior of composites containing graphite particles is illustrated in Fig. 8.18, where the variation of wear volume with sliding distance is compared for composites based on an Al–Si alloy with different graphite contents under dry sliding and under lubrication with turbine oil (Suwa et al. 1976). The load for lubricated sliding had to be considerably increased (to 10 MPa) before getting a significant amount of wear. Rohatgi et al. (1980, Biswas and Rohatgi

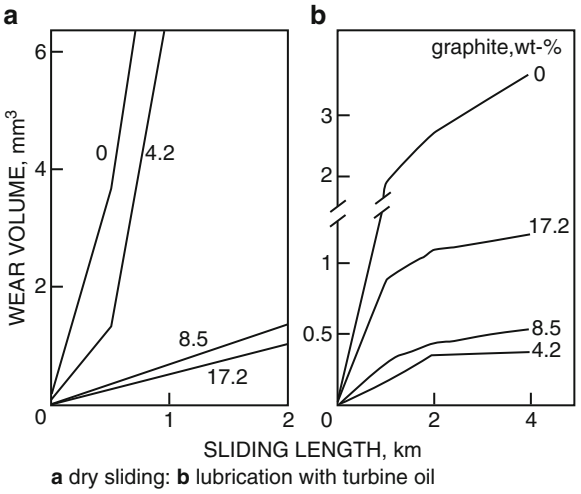

Fig. 8.18 Variation of wear volume with sliding distance for Al–8Si–3Cu–0.3Mg–graphite composites

1983) have observed that the graphite film formed on the tribosurface of the composites helps to spread the lubricant oil much more rapidly than that observed in alloys without graphite, resulting in better tribological behavior of the former. It is observed that only a small amount of graphite (~4.2 vol%) reduces the wear volume drastically in the presence of lubricant, but an increase in graphite content above this level results in enhanced wear. This may be a result of higher amounts of graphite in debris getting mixed with the lubricant and contributing to lowering of its mobility which may counteract the contribution of graphite toward lubrication.

The effect of atmospheric pressure on the coefficient of friction of copper–graphite composites is shown in Fig. 8.19. A marked increase in coefficient of friction is observed in the composite when the atmospheric pressure is reduced from 100 to 0.01 Pa. A similar increase in coefficient of friction is observed in graphite itself presumably because of desorption of gases from graphite resulting in loss of its lubricity. Desorption of gases from the surface of matrix alloy will also contribute to a change in coefficient of friction of a composite under reduced pressure.

8.5.2 Wear in Electrical Contacts

Several composites have been designed for use in electrical contacts by combining constituents which impart excellent wear resistance with constituents which have high electrical conductivity (Clauss 1972; Pardee 1967; Dillich and Kuhlmann-Wilsdorf 1983; Johnson and Kuhlmann-Wilsdorf 1983a, b; Kuhlmann-Wilsdorf et al. 1988a, b; Johnson and Schreurs 1982; Johnson and Moberly 1967; Johnson and Mckinney 1970; Casstevens et al. 1978a, b, c; Baker and Hewitt 1936; Lee and Johnson 1978; Johnson and Taylor 1980; Jones 1957; Teraoka 1983) and ability to

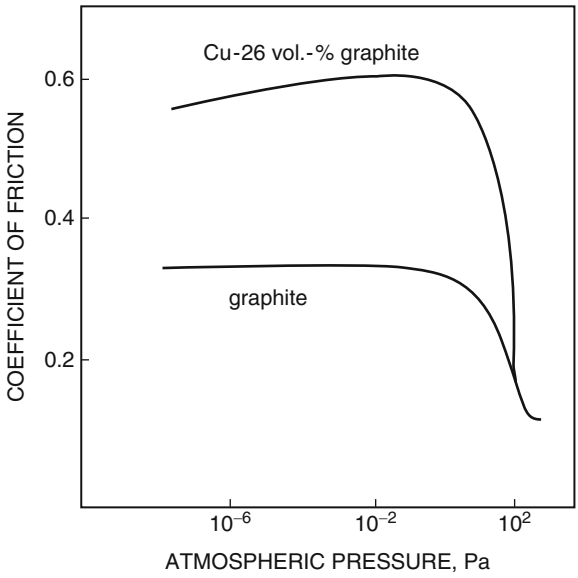

Fig. 8.19 Effect of reduced atmospheric pressure on coefficient of friction of graphite and copper–graphite composite

suppress arc erosion. The most widely used composites in this field include copper base–graphite composites (considered to be inexpensive) and silver base–graphite composites with very low bulk and contact resistance (Kuhlmann-Wilsdorf et al. 1988a, b). The electrical contacts wear under sliding during flow of current, which complicates the friction and wear behavior compared with that under purely mechanical sliding conditions. The amount of materials removed under sliding electrical contact is the sum of contributions from purely mechanical wear in the absence of current arc erosion and an increment of mechanical wear resulting from softening of the matrix by local heating as a result of arcing (Jones 1957).

Various workers have reported (Kuhlmann-Wilsdorf et al. 1988a, b; Johnson and Schreurs 1982; Lee and Johnson 1978) that in silver–graphite systems, the wear rate of composites increased with an increase of current density at both low and high temperatures, as shown in Fig. 8.20. The figure shows that when there is a transition in the mode of sliding wear with temperature the current density for the same wear is considerably higher while sliding at higher temperatures, compared with that observed during sliding at ambient temperature. The coefficient of friction decreases with the current density, as shown in Fig. 8.21, both in air and in a CO_2 atmosphere.

The effect of sliding velocity on wear seems a little complex. Teraoka (1983) has reported that for pantographs with contact strips made of copper–graphite composites, the wear rate decreases as the sliding velocity is increased from 6.9 to 27 m s^{-1}. The opposite result has been reported by Casstevens et al. (1978a, b, c) for copper–lead–graphite composites under high sliding speeds of 750 m s^{-1} and by Johnson and Kuhlmann-Wilsdorf (1983a, b) for silver–graphite composites tested under speeds of 13 and 26 m s^{-1}.

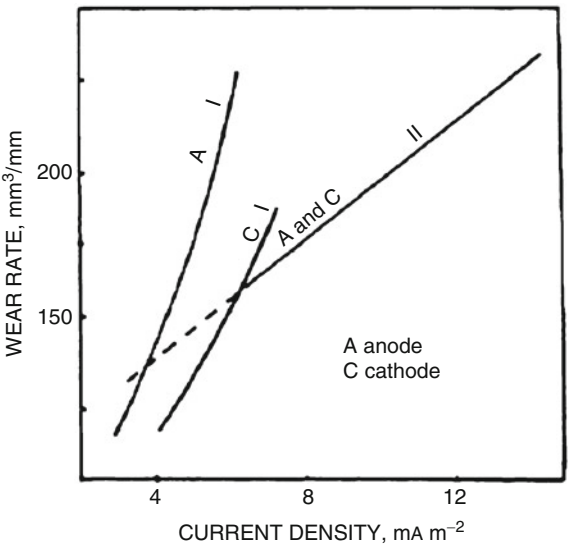

Fig. 8.20 Variation of wear rate with current density at ambient and elevated temperatures; I is observed below 100°C, but II is observed at elevated temperatures, above 100°C

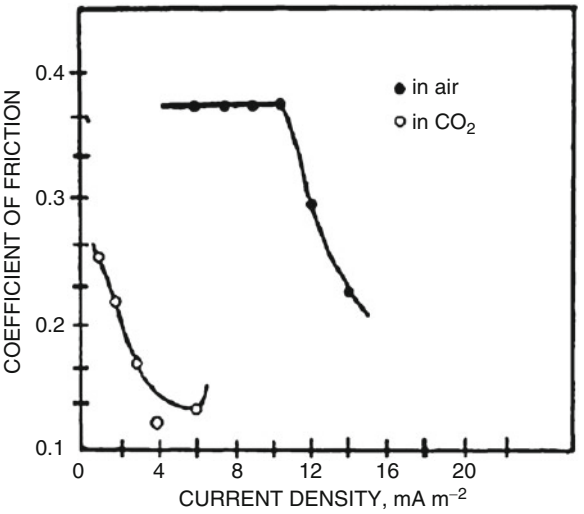

Fig. 8.21 Reduction in coefficient of friction of Ag–25 vol% graphite composite with current density in air and CO_2 atmosphere

The arc erosion tests carried out in copper–graphite composites (Jones 1957) indicate an increase in erosion with arc current. The erosion rate of the copper–graphite composite is also higher than that of the base alloy, as shown in Fig. 8.22. However, Marshall (1966) has suggested that the wear of the brush resulted mainly from mechanical factors rather than the electrical current.

Different contact pairs also affect the results, and Teraoka (1983) has reported that the different rail car bases affected the wear results of pantograph contact strips. Similar results have been reported by Lee and Johnson (1978).

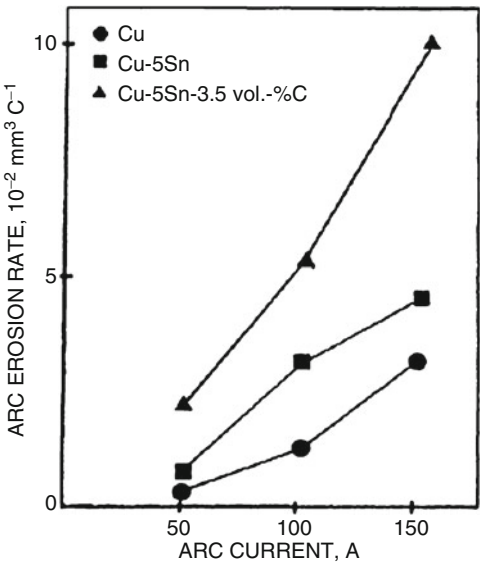

Fig. 8.22 Variation of rate of arc erosion with arc current for bronze–graphite composite, bronze, and copper

The wear mechanism in electrical contacts of composites is complex and depends on the composition of the composites, the contact pairs, the current and voltage levels, the sliding speed, the testing environments, and the contact pressure. Some insights into mechanisms have been provided by Kuhlmann-Wilsdorf and co-workers (Kuhlmann-Wilsdorf et al. 1988a, b; Johnson and Schreurs 1982; Lee and Johnson 1978; Kuhlmann-Wilsdorf 1987) and these are discussed in the next section.

8.5.3 Film Formation

During sliding contact of various materials with graphite particle composites, it has been observed that graphite film forms on the sliding surfaces reducing the extent of direct metal–metal contact as observed from the microstructure of aluminum–-graphite composites, before and after tribodeformation, as shown in Fig. 8.23. When the surface of a graphite particle composite is polished, there is plastic flow of the metal at the surface layer that tends to mask the graphite particles, restricting their transfer to the tribosurface. The friction coefficient and wear rates of such surfaces are high until the metallic layer masking the graphite particles partially wears away and the normal load squeezes out the graphite on the sliding surface. These graphite particles sheared on the sliding surface and eventually joined to form a continuous layer or a film. The process of masking of the graphite particles by the plastic flow in the surface layer of matrix alloy as shown in Fig. 8.23 for aluminum–graphite composites (Rohatgi et al. 1990a, b, c, d) is particularly effective in cases of fine particles of graphite. This process interferes very effectively with film formation by restricting the supply of graphite to the tribosurface,

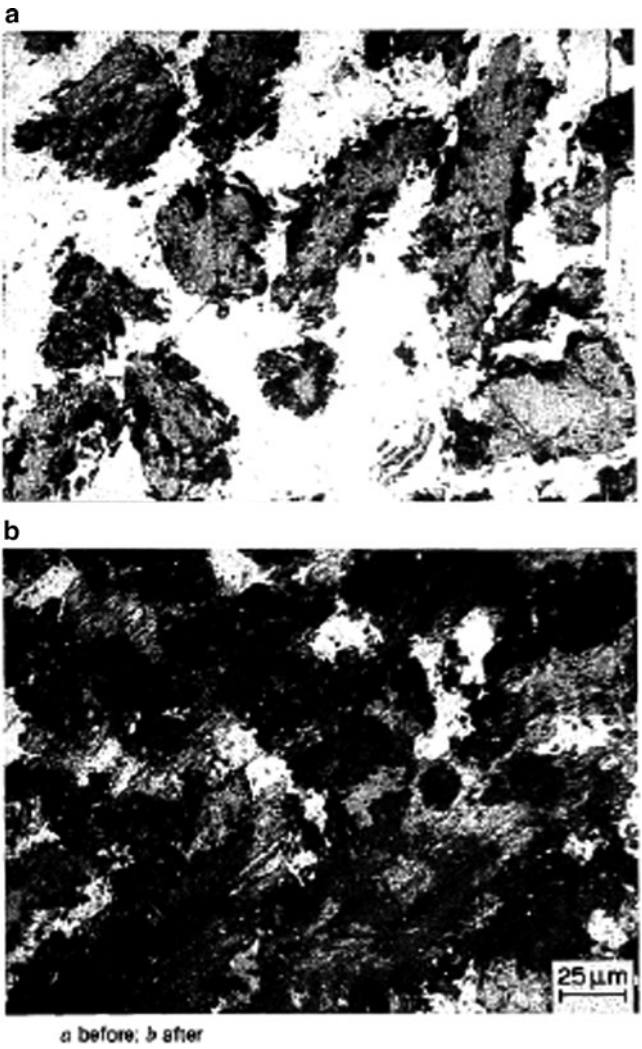

Fig. 8.23 Effect of sliding of microstructure of aluminum–graphite composite (**a**) before; (**b**) after

resulting in higher wear as shown in Fig. 8.13. However, if there is partial metal coverage over the graphite particles the graphite can still be squeezed out, as observed by Sugishita and Fujiyoshi (1981a, b) for nodular gray cast iron.

Rohatgi et al. (1990a, b, c, d) have analyzed the sliding surface of Al–10 vol% graphite by Auger spectroscopy, and established that the major elements on the tribosurface are carbon, oxygen, and aluminum as shown in Fig. 8.24. The surface is covered by graphite to the extent of 30%, which is a clear indication of smearing. However, the thickness of the film is not uniform as seen from the three-dimensional carbon distribution map shown in Fig. 8.25 (Rohatgi et al. 1990a, b, c, d).

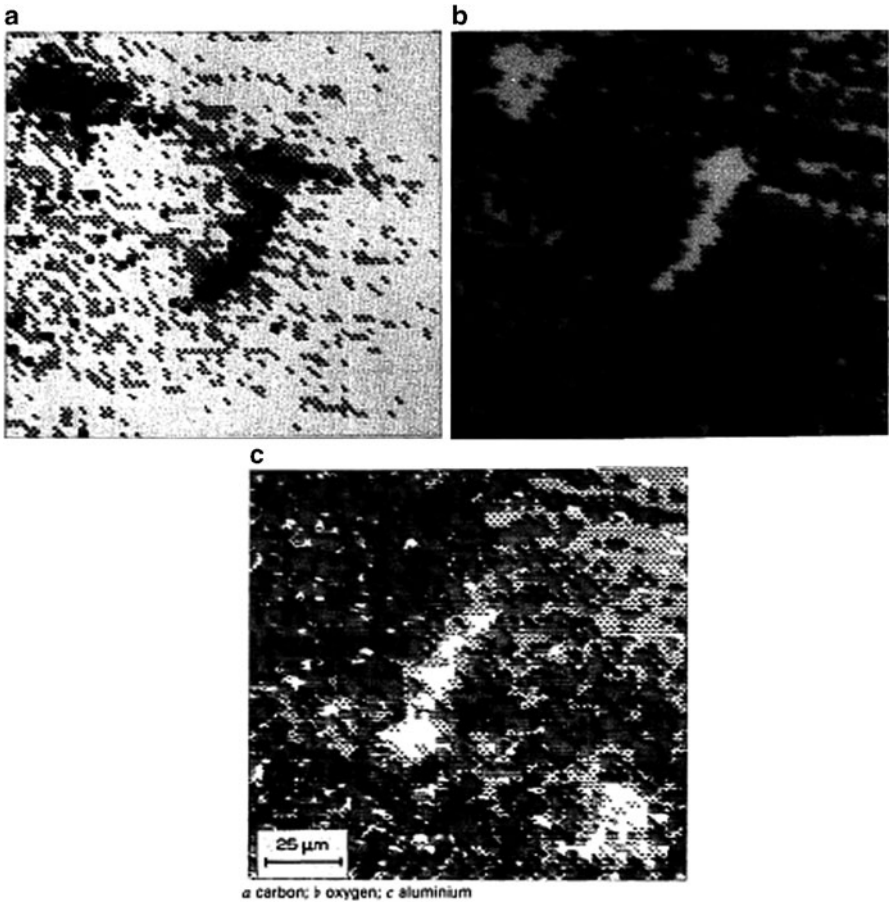

Fig. 8.24 Distribution of (**a**) C, (**b**) O, and (**c**) Al on tribosurface of Al–10 vol% graphite composite as determined by Auger spectroscopy

The film is generally 10–20-nm thick, but there are places where the thickness is relatively large. The phenomenon of film formation has also been reported in other composites containing solid lubricants such as MoS_2 (Tsuya and Takagi 1964) and Pb (Mohan et al. 1990).

Ruff and Peterson (1990) have observed similar film formation in copper-intercalated ($NiCl_2$)-graphite composites both on the wear test pins and on the counterface of steel. The films are patchy in distribution and nonuniform in thickness. Surface profilometry indicates an average thickness of about 1.1 μm but some film patches are as thick as 10 μm. However, the film distribution on the tribosurface and the thickness would depend on test conditions as well as the matrix characteristics. Ruff and Peterson (1990) have also observed that the wear debris is preferentially collected at the entrance edge of the recessed graphite region and the

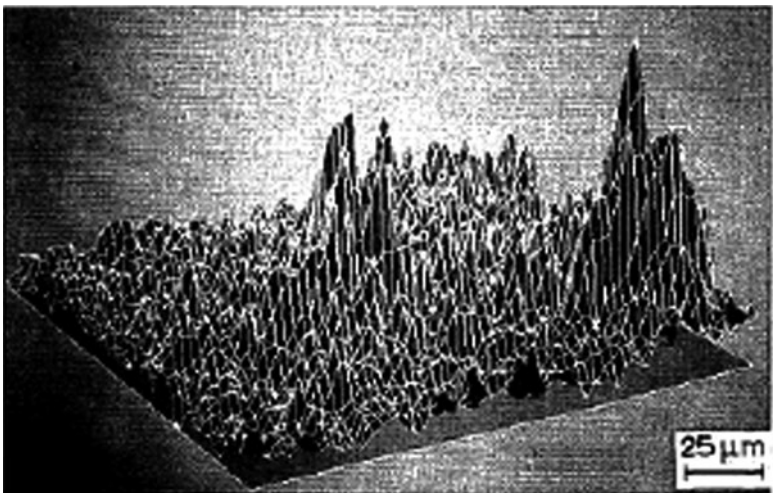

Fig. 8.25 Intensity distribution of carbon in an area on tribosurface

graphite film is formed at the exit edge. Various workers (Bryant et al. 1964; Deacon and Goodman 1958; Baker and Hewitt 1936; Kuhlmann-Wilsdorf 1987; Kuhlmann-Wilsdorf et al. 1988a, b) have observed a change in the mechanism of wear with temperature in silver–graphite and copper–graphite particle composites. At relatively lower temperatures of below 100°C, they assume a layer of moisture in graphite which permits easy shear on the basal plane of graphite. However, at higher temperatures, the moisture is desorbed resulting in the rise of critical resolved shear stress of graphite to a level above that of the matrix alloy or counterface. The graphite will not spread in the form of films because shear will take place in the softer material and the mechanism of wear will be predominantly that for metal–metal sliding.

8.6 Industrial Applications

Metal matrix–graphite particle composites combines the strength, hardness, and abrasion resistance of the matrix alloy with the natural lubricity and machinability of graphite. The matrix alloy may also be chosen to impart good electrical and thermal conductivity to the composite. The dry coefficient of friction of the composites against polished steel shafts is in the range 0.2–0.25 when the graphite content of the composite exceeds about 20 vol%; when submerged in water, petrol, and most other liquids the coefficient of friction drops to a fraction of the value for running dry (Clauss 1972; Kauffman 1980). Table 8.2 summarizes a few important applications of metal matrix–graphite composites.

Table 8.2 Tribological application of metal matrix–graphite composites

Composite	Applications
Copper–graphite	Plane bearing for trucks, cranes, bulldozers, and automotives: drive shafts, bearings, stoker chain, screw conveyor, roller conveyor and roller bearings; spherical bushings for automotive transmission; slider for electric cars, overhead railways, dams and flood gates; slide bushing for discharge valves in hydraulic turbines; electrical contacts and brushes
Al–Si alloy–graphite (Silgraph)	Piston and liner in two stroke and four stroke engines in passenger and racing cars tested by Ferrari, Alfa Romeo, and Hiromotors
Al alloy–graphite	Cylinder block, journal bearings, connecting rods and pins, fan bushings, and internal combustion engines
Mg alloy–graphite	Pistons, structural applications in space
Silver–graphite	Electrical contacts and brushes, bushing in chemical solutions that attack other lubricants and metallic bushings
Babbitt metal–graphite	Medium load and medium speed application in pump and stoker bushings, thrust washers, rotating seal rings
Cadmium–graphite	Current carrying bushings and electrical contacts

Copper–graphite composites can be used up to a temperature of 370°C in oxidizing atmosphere and a temperature of 925°C in submerged conditions or under nonoxidizing atmospheres. These composites are quite suitable for high load and slow speed applications such as in stoker bushings, drying oven conveyor bushings, high temperature stirring shafts and agitators, and current carrying bushings. A number of other applications have been conceived by Hitachi Ltd particularly for cast copper–graphite composites called Gradia (Suwa 1986). It has been suggested that a slider made of Cu–10–20 vol% graphite composite can result in very low wear if used for trolley wire contact (Suwa et al. 1976). A slider made of cast copper–graphite has resulted in lower wear compared with that made of sintered copper–graphite composite as shown in Fig. 8.26. Copper–graphite composite electrical brushes are distinguished from carbon electrical brushes by their very low resistivity and high current carrying capacity, and are therefore suitable for applications such as automotive starter brushes which require low and stable resistance and ability to carry high current instantaneously as the starter commences. Graphite when dispersed in copper base alloys imparts excellent machinability by breaking the chips and providing lubrication at chip/tool interface. Graphite has, therefore, the potential to act as a substitute for lead which is a potential health hazard in copper base alloys particularly when applied for plumbing, and bearings.

Silver–graphite composite brushes are marked by very low noise level, low and stable contact resistance, low friction, and high conductivity. In modern inertial energy storage devices (homopolar motor generators), a large amount of energy is stored and the energy is delivered in the form of low voltage, high current pulses. Silver–graphite or copper–graphite brushes are suitable for such systems. Silver–graphite brushes suppress radio interference noise level and are useful for slip rings, segmented rings, and other applications where special requirements justify the high cost.

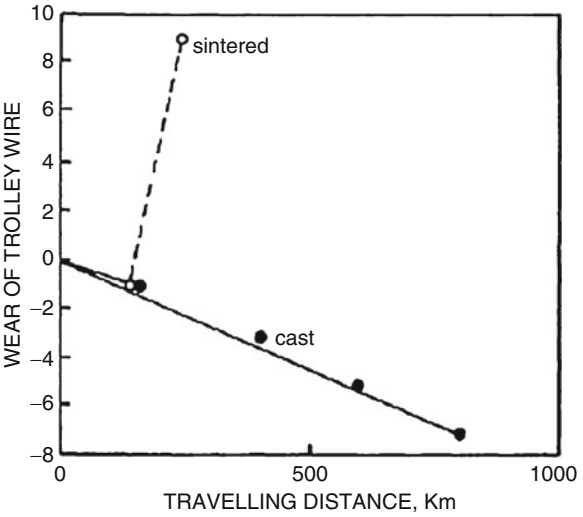

Fig. 8.26 Comparison of wear by trolley wire of sliders made of sintered copper–graphite and cast copper–graphite composite

Much of the early work on metal matrix–graphite particles composites was done using powder metallurgy which is expensive and limited in the sizes that can be produced. Cast aluminum–graphite composites for antifriction applications were developed beginning in 1966. The cast aluminum–graphite alloys have a unique structure, in which graphite particles are in the interdendrite regions and the alloys have been reported to have superior tribological properties compared with similar alloys prepared by PM techniques (Hitachi). These alloys have been cast into tribological components using sand casting, gravity die casting, centrifugal casting, and pressure die casting.

Cast aluminum–graphite particle composites exhibited lower friction coefficients and wear rates and ability to run under boundary lubrication conditions when tests were run with samples submerged in oil in a Hohman wear tester. The composites with over 2 vo1% graphite were able to attain bearing parameters and friction coefficients characteristic of boundary lubrication without galling when they were either self-mated or were running against other aluminum alloys without any graphite (Badia and Rohatgi 1969; Badia 1989).

Microscopic and ESCA examination showed that a graphite film had formed on the sample containing over 2 vo1% graphite particles. In addition, the subsurface had deformed extensively under shear and contributed to the formation of the film of graphite which apparently imparted the antiseizing properties.

Composites were tested as cylindrical sleeve bearings against steel shafts in lubricated conditions and they exhibited a performance superior to that of copper alloy bearings, including phosphor bronze. The bearings of aluminum–graphite were successfully tried out as a replacement for bronze bearings in machine tools, electric fans, water pumps, and in diesel engines at the small end of the connecting rod. Gorbunov et al. (1974) have reported successful use of aluminum– graphite bearings as a replacement for copper alloy bearings in marine diesel engines.

Pistons of aluminum–graphite particle composites when tested in a 3.7-kW diesel engine resulted in reduced wear of the piston and the rings, reduced loss of frictional horsepower, and freedom from seizing under adverse lubrication conditions. The specific fuel consumption decreased. The use of pistons and liners of Al–Si eutectic alloy–graphite particle composite alloys lead to similar results in 0.4 kW petrol engines (Kirshnan et al. 1983; Kirshnan et al. 1981).

Associated Engineering Co., in Italy dispersed 4 vo1% graphite particles in Al–18Si alloy. This composite was wear tested against Al–11.48Si alloy in heated oil in a wear testing rig and it was shown that graphite improved scuffing resistance by a factor of two (Bruni and Iguera 1978; Rohatgi 1991). Further evaluation was made of liners of these alloys in two stroke and four stroke engines for Ferrari, Hiromotors, and Alfa Romeo for passenger and racing car applications. They found that the power generated was improved by 10%, there was no scuffing well beyond the 5-min limit along with no friction marks, and negligible wear was observed. When the tests were run in a four-stroke engine (Alfa Romeo 1300 cc), no liner wear was found and the pistons were in good conditions with no signs of scuffing.

8.7 Development of New Graphite Reinforced MMC Materials

The friction and wear behavior of composites containing graphite particles depend critically on the ability of the graphite to leave its embedded state and smear out in the form of a self-lubricating film separating the matrix and the counterface. The tentative mechanism of film formation as it is understood at present is shown schematically in Fig. 8.27. When a composite surface makes the initial sliding contact with the counterface, the graphite particles are in the embedded state, and the matrix interacts directly with the counterface, resulting in plastic flow of the matrix at the tribosurface and in the subsurface region. The cavities containing graphite particles in the subsurface region deform, and the graphite particles are squeezed out. However, the concurrent plastic flow of matrix alloy tries to smear the matrix alloy over graphite particles. The former process transfers graphite to the tribosurface whereas the latter restricts it. The relative magnitudes of these two processes will depend on the strength, ductility, deformation behavior, and the stress state of the matrix, the smallest dimension of the particle, and its orientation with respect to the sliding direction. The importance of these processes accompanying particle transfer is manifested in the observed effects of particle size and orientation of flake particles on the friction and wear of composites containing graphite. However, no systematic investigation has been directed as yet to understand these two processes and identify the important variables. Nonetheless, it is established that it is the persistence of the self-lubricating graphite-rich layer on the tribosurfaces of metal matrix–graphite particle composites which results in lower coefficient of friction, lower wear rate, and increased seizure resistance.

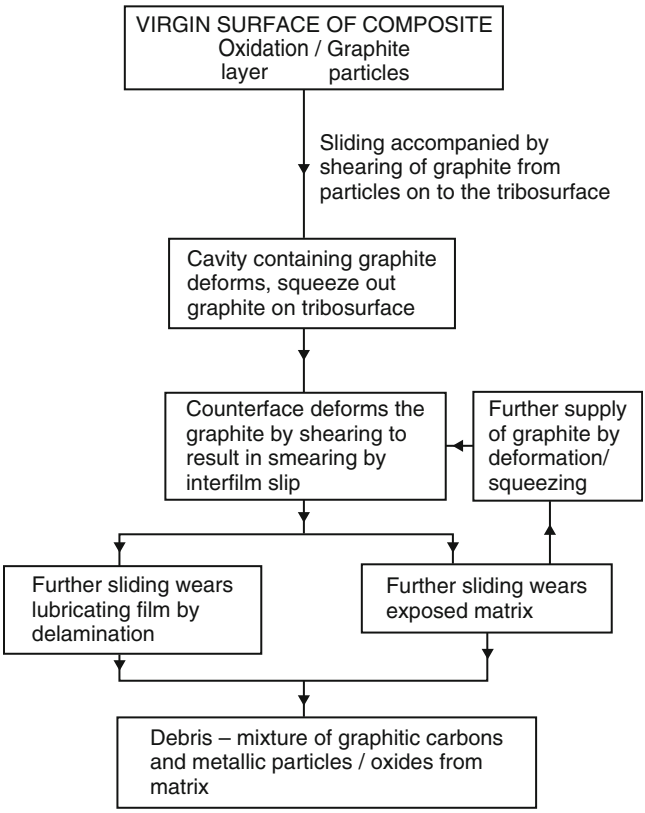

Fig. 8.27 Stage in wear process in metal matrix–graphite particle composites

Once the graphite particles are on the tribosurface, the shear stresses induced by sliding cause slip on the basal plane of graphite if its critical resolved shear stress (CRSS) is lower than those of the matrix and counterface. In addition, one of the interfaces between the graphite and matrix, or the counterface, should be so strong that it does not shear on sliding, and basal slip of graphite takes place in preference to debonding of graphite. It is well known that the CRSS of graphite is lowered by adsorbed moisture and gases. If the temperature is above the desorption temperature, the CRSS of graphite will be very high and the mechanism of wear may change depending on the matrix and the counterface. For a given matrix and counterface, the CRSS of graphite can be varied with appropriate intercalations and its impact on friction and wear behavior should be systematically investigated in the future.

The extent of film formation will depend on the supply of graphite on the tribosurface and the test conditions of load and sliding velocity. The supply of graphite will also depend on the nature of the matrix and its composition.

It is observed that above 20 vol% of graphite in a composite, the friction coefficient is more or less independent of the matrix. This is probably indicative of near complete elimination of direct matrix–counterface interaction. While the variation of wear with sliding velocity is similar to matrix alloy in Al-base composites containing 5 vol% graphite, the trend is completely changed in composites with 15 vol% graphite; this needs further investigation. There has been no investigation as yet on the variation in the extent of film formation with composition in a given composite system. The extent of film formation can be characterized by profilometry as it has been done by Ruff and Peterson (1990) or by sputter etching and XPS as employed by Rohatgi et al. (1990a, b, c, d). The influence of test parameters on the film formation should also be investigated in selected metal matrix graphite particle composites with a given graphite content, to illustrate the effect of matrix composition.

The friction behavior of a composite will clearly have two distinct stages from the time the sliding starts (Rohatgi et al. 1990a, b, c, d) (a) the transient stage during which film formation is taking place (this could include films on composite component as well as on the counterface), and (b) steady state (dynamical) when the extent of coverage by graphite film on both the rubbing surfaces has become more or less constant and the amount of wear in the film is being replenished by new graphite supplied to the tribosurface. These characteristics of friction behavior have been broadly reflected in high initial values of friction, and its reduction to a steady value during sliding; however, detailed investigations are required to correlate test parameters to the process of evolution of film to steady states. The study of the transient state is important, since during this period high friction coefficients can occur and seizing and galling can also take place.

The wear of a composite will be high in the transient state, but will decrease considerably in the steady state depending on the composition of the alloy. There may be several transitions in the wear mechanisms when the test parameters are varied. If the composite has a lower graphite content, there will be direct interaction between the metallic matrix and the counterface in the steady state, and a transition from oxidative mild wear to metallic severe wear should be observed. In addition, if the supply of graphite on the tribosurface becomes large because of composition or test conditions, the thickness of built up graphite film will take it beyond the critical thickness for the initiation of extensive delamination wear within the graphite film itself. These different regimes of wear in metal matrix–graphite composites should be identified by careful analysis of the debris and may be represented in a wear map similar to that proposed by Ashby and co-workers for metals and alloys (Rohatgi et al. 1990a, b, c, d). It is also necessary to make long-term wear tests to determine the overall life of the graphite rich film and its ability to be replenished by graphite in the matrix. There are very limited data available on the P–V limits of metal matrix–graphite particle composites and these need to be studied at higher speeds/loads. Table 8.3 summarizes the present state of knowledge and suggests some directions for future investigation on the tribological behavior of composites containing graphite.

Table 8.3 Present state of knowledge and suggested future work on tribocharacteristics of metal matrix–graphite particle composites

Broad aspect	Indicator variables	Characteristic behavior	Present state of knowledge	Suggested future work
1. *Intrinsic characteristics*				
Tribological behavior	Coefficient of friction, wear, and bulk wear	Variation with pressure, sliding speed, and volume % and size of graphite	Limited scattered data available for very few systems including Al, Cu, Fe, Ag base	Establish minimum amount of graphite significantly to change the friction and wear; and optimum amount of graphite for minimum friction and wear
Mechanism of transfer of embedded lubricant to the tribosurface and mechanism of film formation	Graphite distribution (area and thickness) on tribosurfaces; graphite content of debris	Variation with composition volume % of graphite, pressure, and sliding speed	Limited microscopic observations on tribosurfaces after film formation available for very few systems	Establish total mass balance involving transfer, delamination process (slip/shear), and compacting; role of counterface, recycling process
Nature of film	Composition, structure, orientation, particle size, adhesion, and microhardness of film, chemical nature of debris	Variation with pressure, sliding speed, matrix structure	Limited recent data available on very few systems	Determine: film composition (NMR, EMP, EDAX), film structure (XRD, LEED, SR), film orientation (XRD, LEED), film microhardness, film thickness (ESCA, Auger profile, RBS) for selected systems
Effect of matrix on film formation	Graphite distribution on the sliding interface; nature and deformation of subsurface	Variation with different matrix alloys for given experimental conditions	No systematic information available	Establish relation between the film and plastically deforming layer of matrix. Examine film matrix interface using ESCA profile, laser Raman, and RBS. Examine subsurface area using sections vertical to tribosurface
Development of models to explain observed tribological behavior	Graphite distribution	Variation of friction and wear	Very scanty evidence of some of the mechanisms proposed	Schematic description of process of film formation and failure, development of models and equations

(continued)

Table 8.3 (continued)

Broad aspect	Indicator variables	Characteristic behavior	Present state of knowledge	Suggested future work
Role of counterface made of different materials on film formation and graphite	Graphite distribution and debris composition	Variation with counterface of Cu, Al, steel, cast iron	Practically no information available	Relation between extent of film formation and the role of sliding counterface
2. *Extrinsic interactions*				
Effect of chemical nature of environment	Coefficient of friction, wear rate, and extent of chemical reactions	Variation of friction and wear with different gas environments; inert gases N_2, Ar, He: reacting gases O_2, H_2O	Only limited data on a few selected systems. No understanding	Tribological behavior of composites under different environmental conditions, interaction between graphite, matrix, and environments during sliding wear
Effect of atmospheric pressure	Coefficient of friction, wear rate	Variation with pressure	Limited data on only one system. No understanding	Tribological behavior of composites under vacuum and high pressure
Effect of environmental temperature	Coefficient of friction, wear rate, and extent of oxidation	Variation of friction and wear with temperature	Limited data on very few systems. No understanding	Tribological behavior of composites under different temperatures, oxidation layer effect

8.8 The Role of Solid Lubricants

8.8.1 General Considerations

Some key features as explained by Erdemir (2001) on solid lubricants are the following:

1. When there is a sliding interface that is present, the low friction is due to the fact that they can shear much more easily than liquid-type lubricants.
2. They can withstand very high pressures.
3. They are not dependent on temperature compared to liquid-type lubricants which are capable of turning into the solid state at low temperatures and becoming oxidized at high temperatures.
4. They also show some insensitivity toward harsh chemical environments compared to liquids.

However, a major concern about solid lubricants is the fact that they are prone to getting oxidized at high temperatures in an oxygen-rich environment. Once they get oxidized, the chemical structure of the compound gets altered to the point where it may have adverse effects on the friction and wear properties of the material under consideration. Furthermore, this oxidation process can occur gradually over time and thus becomes harder to restore the lubricant. Another disadvantage that is seen when considering a solid lubricant is the fact that they are not very good conductors of heat. Therefore, finding a way for dissipating the heat produced at the sliding interface is a challenge.

In this way, it is seen that solid lubricants can be used for many demanding industrial applications where using liquid-based lubricants may not help. However, the key idea when using solid lubricants is that their properties are significantly affected by surrounding environmental conditions. One particular solid lubricant may work well in a certain instance of temperature and pressure, but may work adversely in other situations. The main point is focusing on exactly what type of solid lubricant needs to be selected, to work in a given setting.

8.8.2 Nanoparticle and Microparticle Lubricants

Recently, there have been advances into the micro and nanotechnology arenas, where nanoparticles have been added to the matrix and/or to the lubricating oil. The primary method is to disperse solid particles within the metal matrix to help in its self-lubricating ability. A good example of this method can be seen in the case of porous bearings in which microparticle lubricants in the form of additives (Erdemir 2001) like hexagonal Born Nitride (h-BN) are incorporated as shown by Pawlak et al. (2009). The sizes of the particles were of the order of 1–2 μm. The results from experimental testing of these self-lubricating bearings with h-BN as additive

showed that there was a definite decrease in overall friction coefficient compared to that of engine oil alone. Their reasoning behind this is that the h-BN lasts for a longer time in the matrix and is "gradually released" to the area of surface interaction. Therefore, it is practical to try to add microparticles into the matrix alloy for greater reduction in friction. An even better approach is to use the nanoparticle-sized h-BN into the composite because that will have an even better chance to propagate itself into the area of surface interaction. These will be more efficient as a solid lubricant than the micron-sized h-BN.

One of the main difficulties as explained by Hernandez-Battez (2010) regarding nanoparticles (Hernandez-Battez 2010) is that they are very hard to synthesize. Despite this fact, there are many applications where the addition of nanoparticles to lubricants or to materials may help greatly in reducing friction and wear.

Rapoport et al. (2005) have used nanoparticles of WS_2 and MoS_2 to create structures that are used as solid lubricants in composite materials. They were found to act as very good solid lubricants especially when under high normal stresses. This obviously had a great advantage over liquid-type lubricants, which would escape out of the rubbing interface and thus have no lubricating effect.

8.8.3 Graphene and Diamond Carbon Additives

Carbon in its various forms, have generated a lot of interest recently among researchers and scientists to see what possible tribological properties they exhibit to help in the reduction of friction coefficients and wear rates. Erdemir (2004) indicates the fact that carbon has many "exotic" structures like fullerenes, nanotubes and the like to provide low friction coefficients. The major type of carbon film that has seen the greatest use and research work done on is the DLC films or the Diamond-like Carbon films. This is basically an amorphous carbon state with different types of carbon–carbon bonds, specifically sp^3 hybridized carbon atom bonds. It possesses the same qualities like diamond in that it is very hard and stiff and at the same time has very low friction coefficient and so is very smooth. It is used in mechanical parts that experience a lot of abrasive wear such as common milling tools, and certain drilling tools as well. It is also used in bearing materials and engine parts to reduce the sliding and rolling wear produced. It also has high chemical inertness and does not corrode easily. Such a material no doubt enjoys many uses in industry today. Graphene is basically graphite at the atomic level, and is composed of sheets that have formed a honey-comb like lattice structure. It is also seeing some use in creating self-lubricating materials or coatings with graphene-based oxides. However, the main difficulty here is that it is very difficult to synthesize and so is seeing limited use in industry.

There are many materials which when used in conjunction with others contribute toward the reduction of the adverse tribological effects associated with friction and wear. The solid lubricants or additives (which may be in the form of a MMC) described above are much superior to their liquid counterparts. In general, the

materials that would assist in this process are those with a layered structure. This is because the materials would easily shear between the moving parts and form a lubricating layer between the two interacting surfaces. This makes graphite a very good example of this type of solid lubricant. As mentioned before the only key point here is the amount of graphite that is needed to be added on to the MMC to enable the part to work efficiently and at the same time not weakening its mechanical properties as a result of the addition. In conclusion, different forms of graphite including graphene, DLC, and possibly nano-sized particles including h-BN are promising additions to the materials that can help reduce overall friction and wear by providing self-lubrication.

8.9 Summary

Although a qualitative picture on friction and wear behavior of metal matrix–graphite particle composites is emerging, the quantitative understanding of their tribological behavior is far from satisfactory. A theoretical basis to predict the tribological behavior of MMCs does not exist; the experimental measurements of friction, wear, and seizure behavior, coupled with macroscopic observations of tribosurface and subsurface have been used to develop tentative mechanistic models. Even the experimental literature suffers from lack of standardization; test conditions used by different investigators are not clearly indicated and are quite different, and only a correlation of results in terms of broad trends is possible. Frequently, the materials characteristics of the composites such as the porosity content, size, and shape of graphite have not been adequately reported making the assessment of results extremely difficult. Despite these problems, the following significant conclusions emerge:

1. The coefficient of friction and wear rate of most of the metal matrix–graphite particle composites investigated to date reduce significantly with increase in the graphite content. The absolute values of friction coefficients and their variation with graphite content depend on the specific matrix composition up to a critical volume level of about 20 vol%. Above 20 vol% of graphite, the values of the coefficient of friction of different MMCs appear to converge to a value around 0.2, which is close to the friction coefficient of pure graphite, regardless of the matrix composition.
2. The variation of wear rate of metal matrix–graphite particle composites with sliding velocity is similar to that of the matrix alloys in composites containing graphite contents below 10 vol%; however, in composites containing above 10 vol% graphite, wear becomes almost insensitive to changes in sliding velocity.
3. The wear rate in metal matrix–graphite particle composites is significantly lower than that in the corresponding matrix alloys under identical load conditions. The wear rate in MMCs with less than 10 vol% graphite increases with normal load.

4. In gray cast iron where graphite precipitates in situ from the liquid phase, the coefficient of friction depends on the matrix, i.e., whether it is ferritic, pearlitic, or martensitic.
5. When the graphite content is below the critical level, the extent of coverage of tribosurface by solid lubricating film increases with the graphite content of the matrix. For composites containing graphite in excess of the critical amount above which the friction coefficient approaches a constant value regardless of the matrix, the sliding surface is completely covered with a graphite solid lubricating film.
6. Once the entire surface is covered by the graphite solid lubricating film, the wear rate does not significantly change with graphite content until the thickness of the graphite film becomes large enough to cause its own wear by delamination.
7. The extent of spread of the graphite film depends on the matrix material and environment, and limited observations with selected composites suggest that the graphite film probably does not form readily under high vacuum, and the friction under these conditions is quite high. Selected metal matrix–graphite particle composites continue to exhibit improved tribological behavior up to 540°C suggesting that the process of graphite film formation is not yet adversely affected.
8. The process of graphite film formation on the tribosurface of a composite containing graphite is still not very clear. The detailed mechanisms are likely to be revealed through a study of wear behavior during the initial transient period during which the graphite film forms. The existence of a critical thickness of the film as predicted by delamination theory may also be verified for composites by direct measurements. The nature of spreading and thickness buildup in the graphite film and its relation to matrix characteristics and alloying should also be investigated in the future for a complete understanding of wear behavior of graphite.
9. The thickness of the graphite film formed on the tribosurface of Al-10 vol% graphite composite is generally of the order of 10–20 nm but at places the film is much thicker. In intercalated graphite, the film is patchy and the thickness is of the order of micrometers. The thickness of the film may depend on the matrix, graphite content, and the test conditions.
10. The gall resistance of aluminum–graphite composite is higher than that of the base alloy. At >2 vol% graphite, the aluminum–graphite composites are able to run under boundary lubrication when they are self-mated, or run against steel.
11. In view of these superior tribological properties of composites containing graphite compared with those in the base alloys, there have already been several applications of these materials. Silver–graphite and copper–graphite composites have been employed in electrical brushes for several years. Iron–graphite composites and cast irons have been used in several mechanical components subjected to wear.
12. Cast aluminum–graphite particle composites have been developed which exhibit reduced friction, wear, and enhanced antiseizing characteristics under boundary lubrication conditions.

Metal matrix–graphite particle composites have been successfully employed by Associated Engineering in racing cars exhibiting reduced wear and friction. These alloys have also been tried as pistons and liners in petrol and diesel engines leading to reduced frictional losses and wear, and enhanced resistance to seizing compared with those observed for standard aluminum alloys or cast iron. The aluminum–-graphite composite has proved to be a better bearing material at lower cost in comparison with phosphor bronzes and leaded bronzes in machine tool and connecting rod bearings.

Part III
Self-Cleaning Materials

Having abandoned attachment, he acts untainted by evil a lotus leaf is not wetted

Bhagavad Gita 5.10

Chapter 9
Thermodynamic Foundations of Wetting and Capillary Phenomena

In the third part of the book, we investigate the phenomenon of self-cleaning and nonadhesive surfaces, i.e., the ability of a surface to repel water, organic liquids, and various types of contaminants, including solid, soft, liquid, and organic, as well as microorganisms. This ability is usually a result of the interplay of surface roughness, coating, micro- and nanostructure, capillary effects, surface energy, and adhesive and chemical properties. The central theme of self-cleaning research is the reduction of adhesion between a liquid and a solid. This involves the reduction of adhesion with the contaminant itself (e.g., with an organic liquid) as well as with water, which washes away contaminants when repelled from a solid surface. Three main approaches to self-cleaning involve (1) the Lotus effect (defined as surface roughness-induced superhydrophobicity and self-cleaning), (2) deposition of a superhydrophilic titanium dioxide (titania) film, and (3) underwater oleophobicity.

In the present chapter, we discuss wetting and capillary phenomena relevant to self-cleaning and introduce fundamental physical equations and laws, which govern wetting and the adhesion of liquid to a solid. This includes the Young equation for the contact angle; the Laplace equation for the pressure drop through a concave or convex interface of a droplet, bubble, or meniscus; and the Kelvin equation for the equilibrium of a liquid with its vapor and the Morse equation for osmotic pressure. We also discuss the formation of capillary menisci, their contribution to the adhesion force, and the effects of surface roughness on the menisci.

In the consequent chapters, we review the physical principles of superhydrophobicity, the biomimetic Lotus effect and titania-based self-cleaning, oleophobic self-cleaning surfaces, and practical methods to manufacture these surfaces using metallic and polymeric composite materials as well as micropatterning, their current and potential applications, and possible methods to increase their robustness and the range of applicability.

M. Nosonovsky and P.K. Rohatgi, *Biomimetics in Materials Science: Self-Healing, Self-Lubricating, and Self-Cleaning Materials*, Springer Series in Materials Science 152,
DOI 10.1007/978-1-4614-0926-7_9,

9.1 The Solid, Liquid, and Vapor Phases of Matter

In order to investigate the interaction of solid surfaces with liquid agents, such as water or organic contaminants, we have to introduce basic concepts related to wetting and capillary effects, as well as phase transformations. It is well-known that any substance can be in one of the three phase states: solid, liquid, and gas (vapor). There also exists the fourth state, plasma; however, plasma is outside the scope of our consideration. Materials in the solid state can have amorphous or crystalline microstructure with atoms or molecules packed closely together and strongly bonded to each other by the covalent, metallic, or ionic bonds. As a result, when solids are examined at the macroscale, they can sustain both compressive and tensile normal stresses and shear stress.

With increasing temperature or decreasing pressure, a solid can melt and transform into the liquid state. In a liquid, polar molecules still have bonds (hydrogen or van der Waals) with each other; however, these bonds are usually weaker than the bonds in a solid, and they can be ruptured easily. At the macroscale, a liquid can sustain only normal isotropic stresses (usually compressive and rarely tensile). When a shear stress is applied, a liquid flows. Typically, molecules of a liquid are packed less closely than those of a solid, so the solid is denser than the liquid. A notorious exception is water, which is at 0°C denser than ice at the same temperature. This property of water is called the "water anomaly." Because of the water anomaly, ice has lower density than water at 0°C and floats at the water surface. The molecules of liquid water are packed almost as dense as the molecules of ice or even denser. Water molecules also have hydrogen bonds of comparable strength with ice molecules; however, the bonds in liquid water usually exist only for very short periods of time.

With further increase of the temperature or decrease of the pressure, a liquid can transform into its vapor, i.e., gas. Gases expand and occupy all available space. The density of a gas is much lower than that of liquid and solid. The distance between gas molecules is large, and it can be assumed in many cases that there is no interaction between the gas molecules, except for the repulsion during their collisions. The physical model of the "ideal gas" is based on this assumption (Rowlinson and Widem 1982; Adamson 1990).

The transitions among solid, liquid, and vapor states are known as the "phase transitions of the first kind," as opposed to the "phase transitions of the second kind." Generally speaking, phase transitions are characterized by an abruptly increased (or decreased) orderliness of the system. The phase transitions of the first kind are characterized also by a significant amount of energy consumed or released during the transition. For example, in order to completely transfer one liter of boiling water at 100°C into vapor, a greater amount of energy is required than what would be needed to heat 1 l of water from 0 to 100°C. The energy is consumed for breaking the bonds between the molecules. An example of phase transitions of the second kind is the transition to the superconductive state or transitions between different magnetic states in a metal, such as the paramagnetic and ferromagnetic phases.

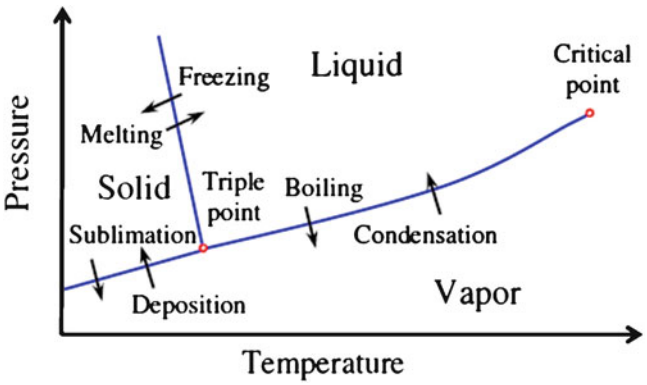

Fig. 9.1 Schematic of phase diagram of water

The transition from solid to liquid is called melting while the opposite transition is called freezing. The transition from liquid to vapor is called evaporation or boiling while the opposite transition is called condensation. The direct transition from solid to vapor (without the liquid-phase stage) is known as sublimation while the opposite transition is called deposition (Rowlinson and Widem 1982; Adamson 1990).

The system reaches a thermodynamic equilibrium at a given temperature (T) and pressure (P) after a sufficient period of time required for the phase transition processes. The state of the system at equilibrium depends only on its temperature and pressure. Therefore, it is convenient to use a phase diagram, which shows the phase state of the substance as a function of temperature and pressure (Fig. 9.1). The boundaries or equilibrium lines among the solid, liquid, and vapor states are shown at the phase diagram as curves, corresponding to pressure as functions of temperature, $P(T)$. Note that for water, the solid–liquid-state equilibrium line has a negative slope, whereas for most other substances the slope is positive. This is due to the water anomaly, the transition from ice to liquid water at a given temperature, which corresponds to increasing pressure (and, therefore, decreasing density).

The unique combination of temperature and pressure at which all three phases can coexist at equilibrium is called the triple point. The liquid–vapor equilibrium line goes from the triple point to another characteristic point at the phase diagram, the critical point. At the critical point, the energy barriers associated with the liquid–vapor phase transition vanish, and the distinct boundary between the two states disappears. Instead, a continuous change of density may lead to the gradual liquid–vapor transformation above the critical point (Rowlinson and Widem 1982; Adamson 1990).

9.2 Phase Equilibrium

When a phase transition line at the phase diagram is crossed, it is normally expected that the substance changes its phase state. However, such a change often requires additional energy input for nucleation of seeds of the new phase. For example, the

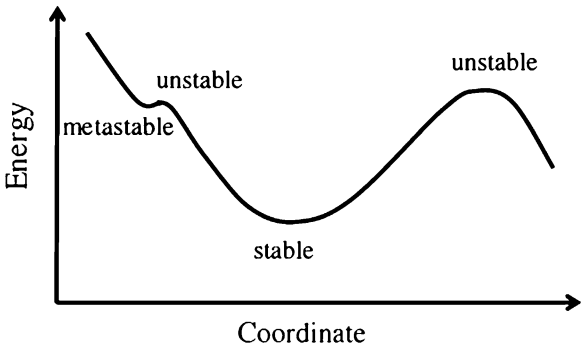

Fig. 9.2 Schematic of an energy profile showing stable, unstable, and metastable equilibriums. The metastable equilibrium is separated by a very small energy barrier

liquid–solid transition requires nucleation of ice crystals while the liquid–vapor transition requires nucleation of vapor bubbles (this process is called cavitation). If special measures are taken to prevent nucleation of the seeds of the new phase, it is possible to postpone the transition to the equilibrium-state phase indefinitely (Trevena 1987). For example, pure water can remain liquid at the temperature below 0°C (supercooled water) or above 100°C (superheated water) if special measures to eliminate nucleation centers are taken. Such states are considered metastable and therefore they are fragile. A small imperfection in the medium, such as a contamination particle, can trigger a catastrophic transition to a stable state, namely, freezing of supercooled water and boiling of superheated water. In general, a metastable equilibrium can be destroyed easily with a small energy input due to a fluctuation. As the stable equilibrium state, the metastable state corresponds to a local energy minimum; however, an energy barrier separating the metastable state from an unstable state is very small (Fig. 9.2).

An interesting and important example of a metastable-phase state is the "stretched" water, i.e., water under tensile stress or negative pressure. When liquid pressure is reduced below the liquid–vapor equilibrium line for a given temperature, it is expected to transform into the vapor state. However, such a transition requires formation of new liquid–vapor interface, usually in the form of vapor bubbles, which needs additional energy input and, therefore, creates energy barriers. As a result, the liquid can remain in a metastable liquid state at low pressure and even when the pressure is negative (Trevena 1987).

There are two factors that act upon a vapor bubble inside a liquid: pressure and interfacial tension. While the negative pressure (tensile stress) is acting to expand the size of the bubble, the interfacial tension is acting to collapse it. For a small bubble, the interfacial stress dominates, however, for a large bubble, the pressure dominates. Therefore, there is a critical radius of the bubble, and a bubble with a radius larger than the critical radius would grow, where as one with a smaller radius would collapse. The value of the critical radius is given by

$$R_c = \frac{2\gamma_{LV}}{P_{sat} - P}, \tag{9.1}$$

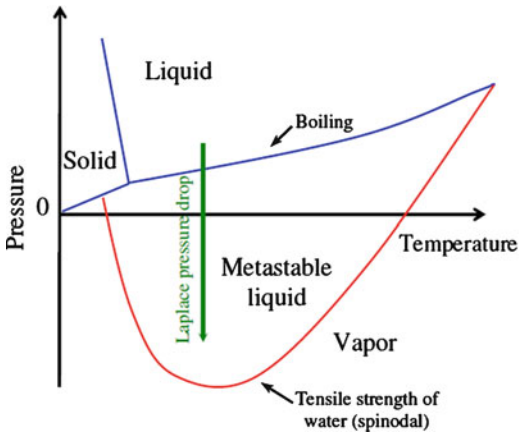

Fig. 9.3 Schematic of phase diagram of water showing the metastable liquid region. While the energy barriers separating the metastable states are small, at the nanoscale these barriers are very significant

where γ_{SL} is the liquid–vapor surface tension, P_{sat} is the saturated vapor pressure, and P is the actual liquid pressure (Herbert and Caupin 2005). The corresponding energy barrier is given by

$$E_b = \frac{16\pi(\gamma_{LV})^3}{3(P_{sat} - P)^2}. \tag{9.2}$$

Cavitation (bubble formation) becomes likely when the thermal fluctuations have energy comparable with E_b.

With the further decrease of pressure in the negative region, the so-called spinodal limit can be reached (Fig. 9.3). At that pressure, the critical cavitation radius becomes of the same order as the thickness of the liquid–vapor interface. In this case, there is a lower energy path of nucleation connecting the liquid to the gas phase by expansion of a smoothly varying density profile (Herbert and Caupin 2005). In the phase diagram, the line that corresponds to the spinodal limit is expected to go all the way to the critical point, although there is an argument among physicists on the exact nature of the spinodal limit due to the lack of reliable experimental data. This critical spinodal pressure at a given temperature effectively constitutes the "tensile strength of liquid water," speaking in terms of mechanics, in other words, the maximum tensile strength water can sustain. Various theoretical considerations, experimental observations, and molecular dynamic simulation results have been used to determine the value of the spinodal limit. At room temperature, the spinodal pressure is between −150 and −250 MPa (Kiselev et al. 1995).

Moderate negative water pressures were obtained in the nineteenth century using a tube sealed with a piston (Trevena 1987). However, it is very difficult to obtain deeply negative pressure at the macroscale because of nucleation. The values that have been reported constitute −19 MPa with the isochoric cooling method (Henderson and Speedy 1980), −17.6 MPa with the modified centrifugal method (Apfel and Smith 1977), and −25 MPa with the acoustic method (Greenspan and

Tschiegg 1967). The situation is different at the micro- and nanoscale. The pressure of −140 MPa in the microscopic aqueous inclusions in quartz crystals was reported (Angell 1988). Tas et al. (2003) showed that water plugs in hydrophilic nanochannels can be at a significant absolute negative pressure due to tensile capillary forces. Yang et al. (2008a, b, c) reported the negative pressure of −160 MPa in liquid capillary bridges, as is discussed below.

An interesting example of negative pressure in nature, which has been discussed recently, is in tall trees, such as the California redwood (*Sequoia sempervirens*) (Fig. 9.4a). Water can climb to the top of the tree due to the capillary effect, and if a tree is tall enough, a negative pressure may be required to supply water to the top (Tyree 2003; Koch et al. 2004). A height difference of more than 10 m would correspond to the pressure difference of more than one atmosphere. Cavitation damage is also a significant technical problem, in particular, for boat propellers, which reduce water pressure due to a high speed (Fig. 9.4b).

The existence of water at tensions as high as 160 MPa requires an explanation. The absolute value of this pressure is larger than the largest positive pressure at which bulk water can be found on the earth's surface, for example the pressure of water at the deepest part of the Marianas Trench in the Pacific Ocean (the deepest point of the Ocean) is about 100 MPa (Zheng et al. 2002). No common van der Waals-bonded liquid can sustain such a large tension. The reason for the existence of such large tension limits lies in the strength of the hydrogen bonds which must be broken in order to form a cavity that is large enough to act as a stable nucleus (Zheng et al. 2002).

9.3 Negative Pressure and Disjoining Pressure in Nanoscale Capillary Bridges

The phase diagram shows phase states of water at equilibrium at a given pressure and temperature. It does not take into account the effects of the interface energy, which may lead to energy barriers and metastable states. However, with decreasing size of a physical system, the surface-to-volume ratio grows and surface and interfacial effects become increasingly important. This is why at the nanoscale the system may be found at a state that is far from the macroscale equilibrium at the given temperature and pressure. Therefore, the water-phase diagram does not always reflect the situation at the nanoscale.

One particularly important example of that, which has a direct relevance to nanoscale friction, is in condensed water capillary bridges (menisci) between very small asperities and, in particular, between an AFM tip (with a radius of the order of 10 nm) and a flat sample (Fig. 9.5). When contact of two solid bodies occurs in air, water tends to condense near the contact spots. This is because a certain amount of vapor is always present in air. Even under low relative humidity (RH), it is not possible to completely eliminate condensation in the form of water capillary

Fig. 9.4 Effect of negative water pressure in everyday life. (**a**) California Redwood (Sequoia) is an example of the tall tree, which needs to develop a negative pressure in order to suck water from the roots up to the top. (**b**) Cavitation damage of a boat propeller. A rapid rotation of the propeller leads to water pressure decrease and cavitation (bubbling) that can damage to propeller over a long period of time (Nosonovsky and Bhushan 2008a)

bridges forming menisci near the contact spots, such as the tips of the asperities of rough solid surfaces (Fisher and Israelachvili 1981; Binggeli and Mate 1994; Bhushan and Sundararajan 1998; Xu et al. 1998; Cappella and Dietler 1999; Bhushan and Dandavate 2000; Szoszkiewicz and Riedo 2005a, b). The menisci are usually concave, or, in other words, they have negative curvature, which can be estimated from the Kelvin equation, as it is explained below. Therefore, the pressure inside the menisci is reduced compared with the pressure outside in

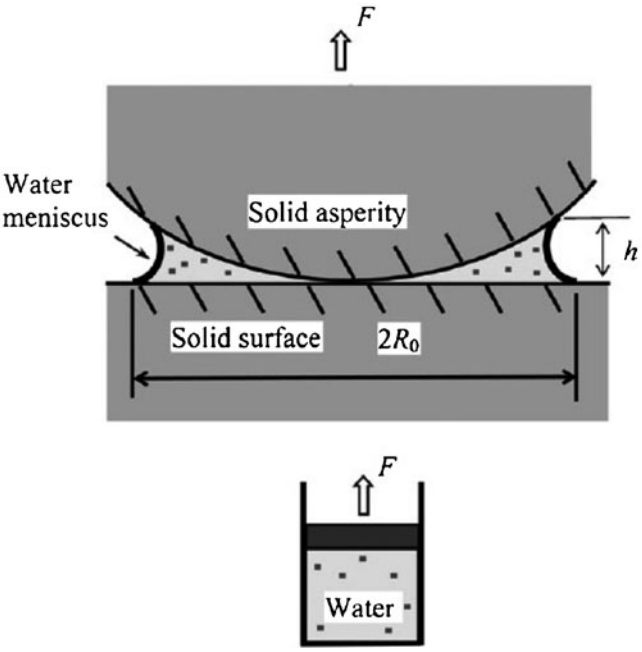

Fig. 9.5 A water capillary bridge between an AFM tip and a flat sample. The Laplace pressure inside the bridge is reduced because the bridge is concave. The bridge is under tension, similarly to water in a sealed tube with a piston with the applied tensile force F

accordance with the Laplace theory. This reduced pressure leads to the attractive meniscus force between the tip and the sample. This meniscus force (or capillary force) is a significant (and often the dominant) part of the adhesion force, and it can be measured with the AFM.

The first group which suggested investigating stretched water in AFM experiments was Yang et al. (2008a, b, c). They noticed that very small values of the AFM tip radius (on the order of 10 nm) correspond to a small size of meniscus (meniscus foundation area on the order of 10^{-16} m^2) and thus even a small force of 10 nN corresponds to huge pressure differences inside and outside the meniscus on the order of 100 MPa or 1,000 atm. This contradicted the conventional wisdom that the pressure inside the menisci is reduced compared to the ambient due to the Laplace pressure drop. An attempt was made to find the values of the pressure inside the bridges in a more accurate way. This is a difficult task since the exact geometrical shape of the capillary bridge is not known. Yang et al. (2008a, b, c) conducted the experiment at different levels of relative humidity and in an ultrahigh vacuum (UHV). They estimated the shape of the meniscus assuming that its curvature is given by the Kelvin equation which relates the meniscus curvature to the relative humidity of air. The results show that the pressure inside these small bridges can be deeply negative, approaching the spinodal pressure (Yang et al. 2007a, b). The negative pressure in the capillary bridges is possible because the size

of the bridges is smaller than the critical cavitation radius given by (9.1) and, therefore, no cavitation occurs.

Caupin et al. (2008) questioned the results by Yang et al. (2008a, b, c), and paid attention to the fact that the Kelvin equation already assumes a certain pressure drop (dependent on the RH) between the meniscus and the ambient, and it is inconsistent to estimate meniscus curvature with the Kelvin equation when the task is to measure experimentally the pressure drop. In addition, they claimed that the capillary bridges correspond to the most stable state and therefore cannot be called "metastable." Caupin et al. (2008) concluded that the results of Yang et al. (2008a, b, c) do not set the "world record" of lowest observed negative pressure in stretched water.

In their response, Yang et al. (2008a) pointed out that their experiments indicate that for significant relative humidity ($>10\%$) there is a good agreement between the experimentally observed values of the adhesion force and those predicted by the Kelvin equations, whereas for low $\mathrm{RH} \leq 10\%$ the Kelvin equation overestimates the pressure drop. Therefore, the calculated values of pressure inside the capillary bridges are within the reasonable error margin (a factor of two) for $\mathrm{RH} > 10\%$, whereas for $1\% \leq \mathrm{RH} \leq 10\%$ the experimental values are three and five times lower than those predicted by the Kelvin theory. This is not unexpected, since the Kelvin theory predicts unboundedly growing pressures for $\mathrm{RH} \to 0\%$, and at some low values of RH it is not applicable.

Regarding the metastability of the bridges, Yang et al. (2008a) noted that "in the AFM context, the bridge is fragile since applying a small external force results in the rupture of the bridge. As soon as the AFM tip starts its motion (but before the bridge fractures), the bridge can become metastable." Their overall conclusion was: "Our objective was not to establish 'the world record' [as Caupin et al. (2008) formulated it], but to attract attention of the community of physicists who investigate the properties of stretched water to AFM experimental data, which have been ignored by that community and which correspond to very low pressures. However, one has to admit that the pressure in AFM nanoscale capillary bridges is lower than in other experiments (with quartz inclusions or with direct measurement), and thus the AFM experiments indeed set a record of very low pressures!"

Several additional studies of capillarity induced negative pressure have been conducted after that. Boyle et al. (2009) investigated the light emission spectrum from a scanning tunneling microscope as a function of RH and showed that it provides a novel and sensitive means for probing the growth and properties of a water meniscus on the nanometer scale. Their modeling indicated a progressive water filling of the tip–sample junction with increasing RH or, more pertinently, of the volume of the localized surface plasmons responsible for light emission; it also accounts for the effect of asymmetry in structuring of the water molecules with respect to the polarity of the applied bias. Choi et al. (2009) performed a molecular dynamic simulation of meniscus growth. Tas et al. (2010) measured capillarity-induced negative pressure of several bars for five different liquids (ethanol, acetone, cyclohexane, aniline, and water). They also investigated the probability of the cavitation using the computational fluid dynamics (CFD) approach.

Another important phenomenon for nanoscale contacts is the so-called disjoining pressure. Atoms or molecules at the surface of a solid or liquid have fewer bonds with neighboring atoms than those in the bulk. The energy is spent for breaking the bonds when a surface is created. As a result, the atoms at the surface have higher energy. This surface energy or surface tension, γ, is measured in N/m, and it is equal to the energy needed to create a surface with the unit area. For a curved surface, the energy depends on the radius of curvature, as, at a convex meniscus surface, atoms have fewer bonds on average than at a flat surface, and therefore it is easier for the water molecules to leave liquid (evaporate). For a concave meniscus, quite oppositely, it is easier for vapor molecules to reach liquid (condense).

A flat water–air interface is in thermodynamic equilibrium with a certain amount of vapor in air, the partial pressure of which is referred to as "the saturated vapor pressure," P_{sat}, so that evaporation and condensation between the flat interface and vapor occur at the same rate. If the partial pressure of vapor in air, P_V, is lower than P_{sat}, evaporation prevails over condensation, whereas in the opposite case ($P_V > P_{sat}$) condensation prevails over the evaporation. The ratio of the two values is referred to as the relative humidity, $RH = P_V/P_{sat}$. For a concave interface, the equilibrium occurs at $P_V/P_{sat} < 1$, whereas for a convex interface it occurs at $P_V/P_{sat} > 1$. The exact value of P_V/P_{sat} for a meniscus of a given curvature is given by the Kelvin equation. The pressure drop of water with density ρ risen for the height h in a capillary tube is $\Delta P = \rho g h$. Using the Laplace equation and the hydrostatic formula for vapor pressure $P = P_0 \exp(-gh/RT)$, where R is the gas constant, P_0 is the pressure at the surface ($h = 0$), and T is the temperature, yields the Kelvin equation

$$\gamma_{LV}\left(\frac{1}{R_1}+\frac{1}{R_2}\right) = \rho RT \ln\frac{P_V}{P_{sat}}, \tag{9.3}$$

where R_1 and R_2 are the principle radii of curvature of the meniscus ($R_k = (1/R_1 + 1/R_2)^{-1}$ is referred to as the Kelvin radius). Equation (9.3) relates the interface curvature at the thermodynamic equilibrium with the ratio of actual and saturated vapor pressure, P_V/P_{sat} (relative humidity). According to the Kelvin model, a concave meniscus with a negative curvature given by (9.3) may form at any relative humidity. An important example of such meniscus is in condensed water capillary bridges at nanocontacts, for example between an AFM tip and a sample.

Another important effect is the so-called disjoining pressure, first investigated by Derjaguin and Churaev (1974). The adhesion force between the solid and water has a certain range x_0 and decreases with the distance x from the interface (Fig. 9.6a). As a result, water in the layer next to the interface is subjected to higher pressure $P = P_0 + \Pi_d(x)$ than the bulk pressure, where $\Pi_d(x)$ is the so-called disjoining pressure. For a thin liquid layer of thickness $H < x_0$, the evaporation/condensation equilibrium is shifted toward condensation, since an additional attractive force acts upon water molecules from the solid surface. As a result, a thin water layer can be in equilibrium with undersaturated vapor, $P_V/P_{sat} < 1$, so the effect of the disjoining

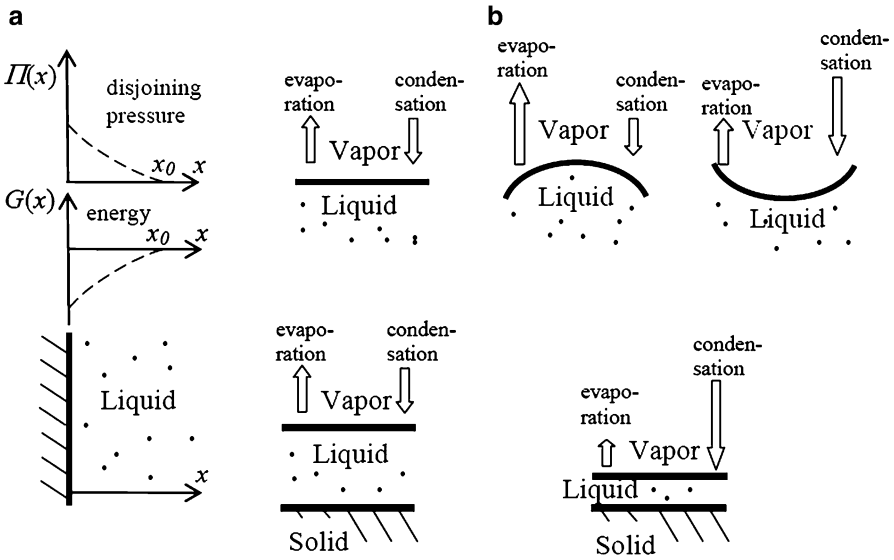

Fig. 9.6 (**a**) Disjoining pressure near a solid surface. (**b**) The effect of meniscus curvature (flat, concave, and convex) and liquid layer thickness on the evaporation–condensation equilibrium

pressure on the thermodynamic equilibrium is similar to the effect of concave meniscus (Asay et al. 2010). The influence of the disjoining pressure and the related wetting films in narrow confinement have to be considered as they may significantly change the meniscus curvature (Fig. 9.6b). A typical effect of nanoscale confinement is the appearance of capillarity-induced negative pressure.

9.4 Water-Phase Diagram at the Nanoscale

Normally, the phase state of water is uniquely characterized by its pressure and temperature. The phase diagram of water shows whether water is in its solid, liquid, or vapor state at a given temperature and pressure. However, at the nanoscale, the situation may be different. Both molecular dynamics (MD) simulations and experimental studies with the atomic force microscope (AFM) and the surface force apparatus (SFA) show that the state of nanoscale volumes of water at a given pressure and temperature is not always the same as prescribed by the macroscale water-phase diagram (Thompson and Robbins 1990; Odelius et al. 1997; Jagla 2002; Braun and Peyrard 2003). In particular, confined small water volumes demonstrate quite unusual properties, such as the melting point depression (Christenson 2001). Several effects that can be detected by AFM are related to this unusual phase behavior of the nanoscale capillary bridges (Herbert and Caupin 2005).

First is the metastability of small volumes of water. When pressure is below the liquid–vapor transition line of the water-phase diagram, vapor is the most stable state. However, the liquid–vapor transition involves energy barriers, and thus a metastable liquid state is possible (Herbert and Caupin 2005). At the macroscale, random fluctuations are normally large enough to overcome the barriers. The metastable states are very fragile, and thus they are not normally observed, except for special circumstances (e.g., superheated water). However, at the nanoscale, the barriers are large compared with the scale of the system, and metastable states can exist for long intervals of time (Herbert and Caupin 2005; Tas et al. 2003; Yang et al. 2008a, b, c).

Second, it has also been suggested that water in the nanoscale capillary bridges may include ice or be a mixture of liquid water with ice (Jinesh and Frenken 2006). Such a mixture would have high viscosity and may act like glue, demonstrating elastic response. The capillary adhesive force, F_{cap}, leads to the component of the friction force, μF_{cap}, that is present even when no external load is applied to the asperity.

There are several ways to estimate the capillary force between an asperity of radius R and a flat substrate. An approximate value is given by

$$F_{\text{cap}} = 4\pi R\gamma_{\text{LV}} \cos\theta, \tag{9.4}$$

where θ is the contact angle between water and the substrate material. Note that the capillary bridges are usually formed between solid asperities only if material of the asperities is hydrophilic, in other words, if $\theta < 90°$, so that $F_{\text{cap}} > 0$. Equation (9.3) is based on the assumption that meniscus radius is small compared to R and that the meniscus has almost cylindrical shape. A more accurate calculation of the capillary force should involve exact calculation of the meniscus shape and pressure inside the capillary bridge.

Equation (9.4) states that F_{cap} is independent of the relative humidity and it provides no information about the pressure inside the capillary bridge. However, it is known from the experiments that F_{cap} depends upon relative humidity (Fig. 9.7). Most experiments show that the capillary force first increases with increasing relative humidity up to approximately 30% and decreases with a further increase of the relative humidity after that (Miranda et al. 1998; Asay and Kim 2006; He et al. 2001). The reasons for this trend are still not completely clear. It has been suggested that water on mica can form a monolayer of an ice-like phase (Hu et al. 1995; Miranda et al. 1998). With decreasing humidity, the ice-like water monolayer breaks into islands and thus the pull-off force decreases. Water often forms adsorbed layers at the surface of many materials. These layers may have ice-like structures (Asay and Kim 2006). The layers are connected to the capillary bridge.

Third is the capillary-induced low-temperature boiling. An important consequence of the water pressure reduction in the capillary bridges is due to the possibility of boiling at temperatures lower than 100°C. If a capillary bridge is large enough so that cavitation occurs, the pressure inside the bridge is reduced compared with the ambient, and the boiling point is depressed by the amount ΔT.

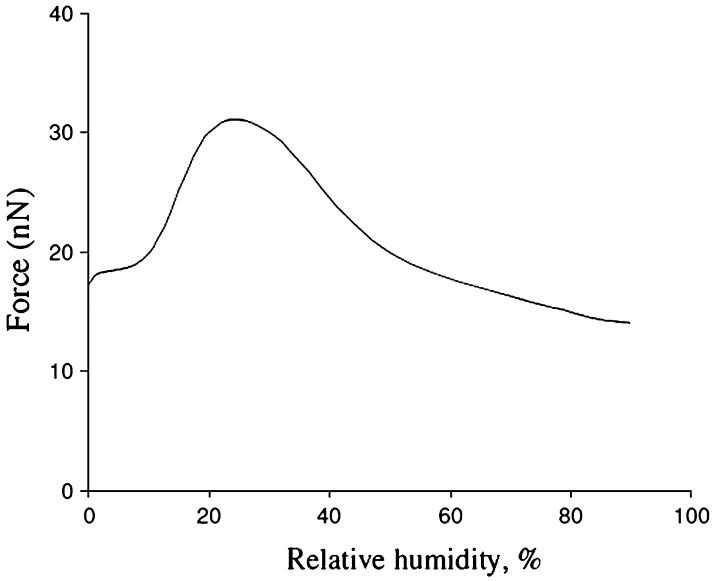

Fig. 9.7 A typical dependence of the pull-off adhesion force between an asperity and a tip upon the relative humidity measured by an AFM (based on He et al. 2001). The dependence has a maximum at the relative humidity close to 30%

The Clausius–Clapeyron equation (Tas et al. 2010) provides the slope of the solid–liquid coexistence curve as

$$\mathrm{d}P/\mathrm{d}T = L/(T\Delta V), \tag{9.5}$$

where L is the latent heat and ΔV is the volume change associated with the phase transition. For the ideal gas approximation, the change of pressure $\Delta P = P_2 - P_1$ is related to the change of the boiling temperature $\Delta T = T_2 - T_1$ as

$$\ln(P_2/P_1) = \Delta h/R(1/T_1 - 1/T_2), \tag{9.6}$$

where Δh is the change of specific enthalpy (Tas et al. 2010).

For example, for a meniscus between an AFM cantilever and a flat surface with a gap between them of 3 μm and the principal radii of curvature of the meniscus $R_1 = R_2 = -2$ μm (Fig. 9.8), we find $R_\mathrm{k} = (1/R_1 + 1/R_1)^{-1} = -1$ μm and the pressure drop, based on the Laplace equation $\Delta P = 72.9$ kPa (or 0.72 atm). Thus, the pressure inside the meniscus is $P = 28.1$ kPa (or 0.28 atm), which corresponds to the boiling point of about 333 K. Yang and coworkers (2007a, b) reported observation of boiling in a meniscus between the cantilever and a flat Si sample under laser irradiation that provided a temperature rise only up to 45°C (Derjaguin and Churaev 1974).

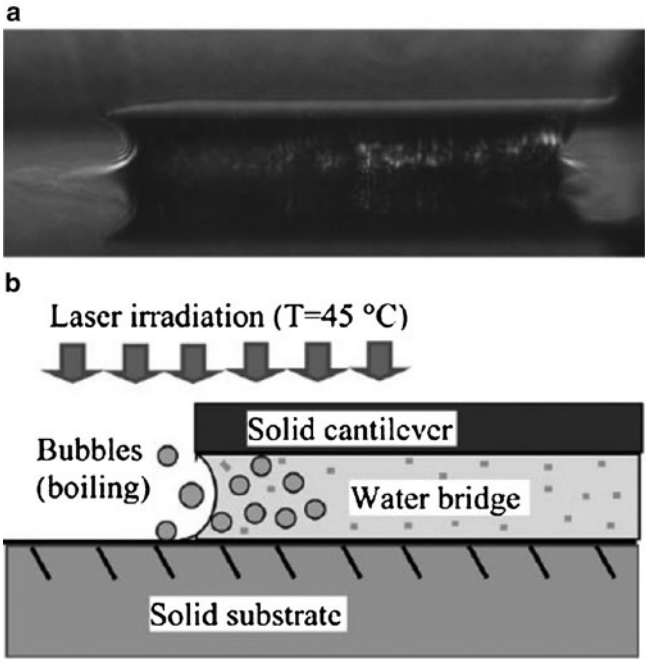

Fig. 9.8 (**a**) Optical image and (**b**) schematic of a water meniscus between a cantilever and a flat surface. The pressure inside the meniscus is reduced and a moderate temperature rise caused by laser irradiation may lead to boiling (Yang et al. 2007a, b)

Szoszkiewicz and Riedo (2005a) investigated the velocity dependence of the nanoscopic friction forces between an AFM tip and a glass sample changing either the sample temperature or the humidity in the experimental chamber. They found that the water gas–liquid-phase diagram is the same at the macroscopic scale as at the nanoscopic tip–sample contact.

We have seen that water at the nanoscale can remain liquid at very low pressures. There are evidences of ice presence at the ambient temperature and pressure in the adsorbed water layers. In addition, the thermal fluctuations can play a significant role at the nanoscale. Therefore, the macroscale phase diagram does not always reflect nanoscale behavior adequately.

9.5 Laplace Equation

Atoms and molecules near the surface have bonds with a smaller number of neighboring atoms and molecules than those in the bulk. As a result, the atoms and molecules at the surface have higher energy. This excess energy is called free surface energy, γ, and it is measured in Joules per area units. Atoms at a curved solid surface have fewer bonds on average than at a flat surface. Therefore, the

energy depends on the radius of curvature. The curvature dependence of the surface energy is characterized by the Tolman's length δ, normally of the molecular scale.

$$\gamma(R) = \gamma_0\left(1 - \frac{2\delta}{R} + \cdots\right), \tag{9.7}$$

where δ is the so-called Tolman's length of the molecular scale and γ_0 is the surface energy for a flat surface (Anisimov 2007). However, this curvature dependence is significant only for very small curvature radii comparable with the molecular length or near the critical point of the phase diagram, so for most practical consideration the surface energy of a flat surface can be taken for calculations, $\gamma = \gamma_0$.

In a similar manner, molecules at the edge have fewer bonds than those at the surface, which leads to excess energy proportional to the line tension τ measured in J m^{-1}. The line tension is related to the Tolman's length, as an edge with a small radius R yields excess energy $\alpha R \times 2\delta\gamma/R$, where α is the angle of the edge. When divided by the circumference length of the edge αR, the line tension is

$$\tau = 2\alpha\delta\gamma. \tag{9.8}$$

Taking into account the contact line effect, for a droplet with radius R is given by

$$\cos\theta = \cos\theta_0 + 2\tau/(R\gamma_{\mathrm{LA}}), \tag{9.9}$$

where τ is the contact line tension and θ_0 is the value given by the Young equation (Boruvka and Neumann 1977).

The free surface energy is defined as the energy needed to create new interface with a unit area and it quantifies the disruption of chemical bonds that occurs when a surface is created. Surfaces are less energetically favorable than the bulk of a material; otherwise, there would be a driving force for surfaces to be created, and surface is all there would be. Cutting a solid body into pieces disrupts its bonds, and therefore consumes energy. For an interface between two materials or phase states of the same material, the interface energy can be defined in a similar manner, e.g., γ_{SL}, γ_{SV}, and γ_{LV} for solid–liquid, solid–vapor, and liquid–vapor free interface energies.

Expanding the interface among solid, liquid, and vapor phases is usually energetically unfavorable. For a vapor bubble of radius R, expanding the size of the bubble for a small amount dR would lead to the surface area change of $8\pi R\mathrm{d}R$ and volume change of $4\pi R^2\mathrm{d}R$. If pressure inside the bubble extends the outside pressure by ΔP, the work of the pressure is given by $\Delta P 4\pi R^2\mathrm{d}R$, whereas the change of the surface energy is given by $\gamma_{\mathrm{LV}} 8\pi R\mathrm{d}R$. It is concluded from the above that the droplet is at equilibrium, if these energy changes are equal, that is, $\Delta P = 2\gamma_{\mathrm{LV}}/R$.

A different (although similar) interpretation of the same result comes if one thinks of a small probing body of cross section S inserted into the droplet (Fig. 9.9). It is energetically profitable for the droplet to decrease its surface area and thus a force pushes the probing body out of the droplet. The advance of the body for a distance δx would result in the decrease of the volume of the droplet by $S\delta x$ and

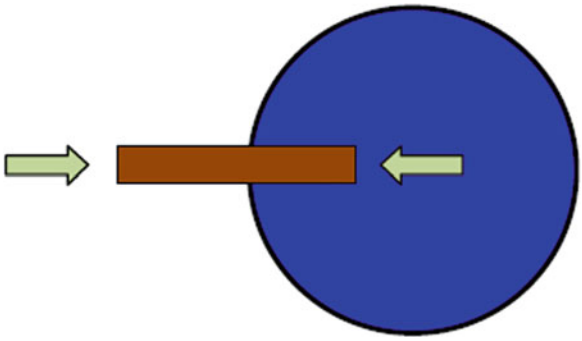

Fig. 9.9 A probing body inserted in a sphere (sphere is trying to decrease surface area)

therefore the decrease of the droplet radius and its surface energy by $\delta R = S\delta x/(4\pi R^2)$ and $\delta E = \gamma_{LV} 8\pi R S\delta x/(4\pi R^2) = 2\gamma_{LV} S\delta x/R$, and thus the pressure is $\Delta P = \delta E/(S\delta x) = 2\gamma_{LV}/R$.

In the general case, the surface is not necessarily spherical, and the pressure change along the curved interface is given by the Laplace equation (sometimes called the Young–Laplace equation, Rowlinson and Widem 1982; Adamson 1990)

$$\Delta P = \gamma_{LV}\left(\frac{1}{R_1} + \frac{1}{R_2}\right), \tag{9.10}$$

where R_1 and R_2 are the principal radii of curvature of the interface at a given point (Rowlinson and Widem 1982; Adamson 1990). It follows immediately from 9.10 that a liquid–vapor interface has the constant mean curvature, $1/R_1 + 1/R_2$, at any point. It also follows that pressure inside a gas bubble or liquid droplet is larger than the pressure outside for the amount given by the Laplace equation. The pressure, calculated from 9.10 is called the Laplace pressure (Rowlinson and Widem 1982).

For some interfaces, the mean curvature is negative. An important example of an interface with a negative mean curvature is the condensed water meniscus between an asperity and a flat surface, which has been discussed earlier in this chapter. The pressure inside such a meniscus is reduced compared to the atmospheric pressure outside, and if the negative mean curvature is low enough, the pressure will be below zero. Taking the typical liquid–air interface energy $\gamma_{LV} = 0.072$ N m^{-1} and the atmospheric pressure $\Delta P = 10^5$ Pa results in the mean curvature radius of 720 nm corresponding to the pressure drop of one atmosphere.

9.6 Young Equation

When a liquid front comes in contact with a flat solid surface under the angle θ (Fig. 9.10), propagation of the liquid front for a small distance dt results in net energy change of $dt(\gamma_{SL} - \gamma_{SV} + \gamma_{LV}\cos\theta)$. Therefore, for the liquid front to be at equilibrium, the Young equation should be satisfied (Rowlinson and Widem 1982)

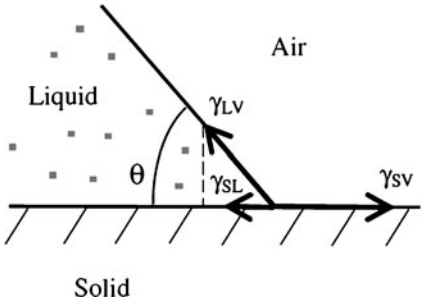

Fig. 9.10 A water vapor surface coming to the solid surface at the contact angle of θ. From the balance of the tension forces, the Young equation should be satisfied, $\gamma_{LV}\cos\theta = \gamma_{SV} - \gamma_{SL}$

$$\gamma_{LV}\cos\theta = \gamma_{SV} - \gamma_{SL}. \tag{9.11}$$

The theory of wetting represented by 9.11 was formulated for the first time by Thomas Young in 1804 in his essay "On the Cohesion of Fluids" (Young 1805). The essay does not contain the formula, but it establishes the contact angle as a parameter characterizing a combination of a solid and liquid, the three "forces'" interfacial tensions (γ_{SL}, γ_{SV}, and γ_{LV}), and it contains a verbal description of 9.11:

> "It is necessary to premise one observation, which appears to be new, and which is equally consistent with the theory and with experiment; that is, that for each combination of a solid and a fluid, there is an appropriate angle of contact between the surfaces of the fluid, exposed to the air, and the solid. We may therefore inquire into the conditions of equilibrium of the three forces acting on the angular particles, one in the direction of the surface of the fluid only, a second in that of the common surface of the solid and fluid, and the third in that of the exposed surface of the solid. Now, supposing the angle of the fluid to be obtuse, the whole superficial cohesion of the fluid being represented by the radius, the part which acts in the direction of the surface of the solid will be proportional to the cosine of the inclination; and this force, added to the force of the solid, will be equal to the force of the common surface of the solid and fluid, or to the differences of their forces . . .. And the same result follows when the angle of the fluid is acute." (Young 1805).

According to the Young equation, a liquid–vapor interface always comes in contact with the solid surface under the same contact angle θ. It is clear from 9.11 that three situations are possible. If $(\gamma_{SV} - \gamma_{SL})/\gamma_{LV} > 1$, the complete wetting takes place with the liquid fully adsorbed by the solid surface ($\theta = 0$). If $(\gamma_{SV} - \gamma_{SL})/\gamma_{LV} < -1$, the complete rejection of the liquid by solid surface takes place ($\theta = 180°$). The most common is the intermediate situation of partial wetting ($-1 < (\gamma_{SV} - \gamma_{SL})/\gamma_{LV} < 1$, $0 < \theta < 180°$). A liquid that has the contact angle $\theta < 90°$ is often referred to as a "wetting liquid" while that with $\theta > 90°$ is "a nonwetting liquid." Corresponding surfaces are called, in the case of water, "hydrophilic" and "hydrophobic," respectively.

An alternative form of the equation for the contact angle θ is given by the so-called Young–Dupré equation which involves the work of cohesion of the solid with liquid, W,

$$\gamma_{LV}(1 + \cos\theta) = W. \tag{9.12}$$

Since W is the work of cohesion and is equal to the energy, required to create a solid–liquid interface of unit area, while the solid–vapor and liquid–vapor interfaces are being destroyed, the work of cohesion is given by

$$W = \gamma_{SV} - \gamma_{SL} + \gamma_{LV}. \tag{9.13}$$

Substituting 9.13 into 9.12 results in 9.11.

The free interface energies can also be viewed as surface tension forces. These forces are applied to the three-phase contact line (the triple line) and directed toward the corresponding interface. The surface tensions are measured in force units per length of the contact line, N m^{-1}, the same units as the interface energy, J m^{-2}. If a section of the triple line of length L moved for the distance of dx in the direction perpendicular to the line, the new surface area Ldx is created, which requires the energy of γLdx. Since the work is equal to the force times the distance, the corresponding surface tension force is given by γL. From this simple consideration, it is seen that the surface tensions and surface free energies are essentially the same. Historically, the Young equation was formulated in early 1800s in terms of forces, after the thermodynamic concept of free energy in general and free surface energy in particular was introduced since the middle and in the second half of the nineteenth century by Helmholtz, Gibbs, and other scientists (Rowlinson and Widem 1982).

The Young's equation was originally formulated for the horizontal component of the tension force. Assuming that three tension forces act upon the triple line from the directions of the three phases (Fig. 9.10), the balance of the horizontal projection of these forces leads to 9.11. As far as the vertical components (y-components) of these forces, their sum is not equal to zero, since the liquid–vapor tension is the only one having the vertical component. While the vertical component is often overlooked, it is balanced by the reaction of the solid substrate. However, the vertical component is significant for understanding the solid–liquid–vapor-phase equilibrium. The droplet acts upon the solid surface and tends to deform (in the case of deformable material) or dissolve (in the case of soluble material, e.g., a water droplet on an icy surface) in such a way that a concave "bed" is formed so that the solid–liquid tension attains a vertical component which tends to balance the vertical component of the liquid–vapor tension. This is a valid assumption for the thermodynamic equilibrium (the quasithermodynamic approximation). If the system is not at equilibrium, the tensile stress, caused by the vertical component, would increase locally the chemical potential of the system so that the material can dissolve and change its shape (Yaminsky 2000; Shanahan and Carré 1995).

The Young equation does not take into account a number of factors, which can significantly affect the contact angle at the micro- and nanoscale. It is emphasized that the contact angle provided by the Young equation is a macroscale parameter, so it is called "the apparent contact angle." The actual angle, under which the liquid–vapor interface comes in contact with the solid surface at the micro- and nanoscale, can be different. There are several reasons for that. First, water molecules tend to form a thin layer upon the surfaces of many materials. This is

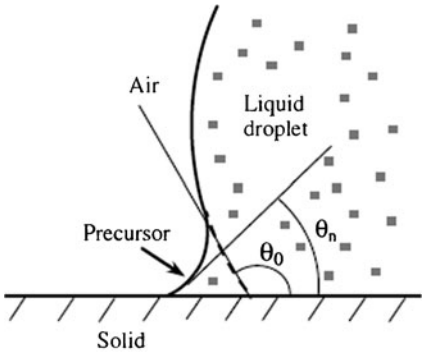

Fig. 9.11 Scale dependence of the contact angle. The apparent contact angle θ_0 is observed at the macroscale while the nanoscale value, θ_n, may be significantly different due to the presence of a precursor or film

because of a long-distance van der Waals adhesion force that creates the so-called disjoining pressure (Derjaguin and Churaev 1974). This pressure is dependent upon the liquid layer thickness and may lead to formation of stable thin films or precursors (Fig. 9.11). In this case, the shape of the droplet near the triple line transforms gradually from the spherical surface into a precursor layer, and thus the nanoscale contact angle is much smaller than the apparent contact angle. In addition, adsorbed water monolayers and multilayers are common for many materials.

Second, even carefully prepared atomically smooth surfaces exhibit certain roughness and chemical heterogeneity. Water tends to cover at first the hydrophilic spots with high surface energy and low contact angle (Checco et al. 2003). The tilt angle due to the roughness can also contribute to the apparent contact angle.

Third, the Young equation provides the value of the so-called static contact angle, that is, it ignores any dynamic effects related to the change of the droplets' shape. The very concept of the static contact angle is not well-defined. For practical purposes, the contact angle, which is formed after a droplet is gently placed upon a surface and stops propagating, is considered the static contact angle. However, depositing the droplet involves adding liquid while leaving it may involve evaporation, so it is difficult to avoid dynamic effects.

Fourth, for small droplet and curved triple lines, the effect of the contact line tension may be significant. Molecules at the surface of a liquid or solid phase have higher energy because they are bonded to fewer molecules than those in the bulk. This leads to the surface tension and surface energy. In a similar manner, molecules at the edge have fewer bonds than those at the surface, which leads to the line tension and the curvature dependence of the surface energy. This effect becomes important when the radius of curvature is comparable with the Tolman's length (Anisimov 2007). However, the triple line at the nanoscale can be bending, and the radius of curvature can be very small so that the line tension effects become important (Pompe et al. 2000). Thus, while the contact angle is a convenient macroscale parameter, wetting is governed by interactions at the micro- and nanoscale, which determine the contact angle hysteresis and other wetting properties.

9.7 Kelvin's Equation

Due to evaporation, a certain amount of water vapor is always present in the air. Evaporation and condensation may have different rates; however, they reach equilibrium at a certain pressure of the vapor. Partial pressure of vapor at which it is at equilibrium with liquid water is called saturation pressure, p_s. The actual partial vapor pressure, p, may be smaller than the saturation pressure. The relative humidity is the ratio of p/p_s. If a liquid–gas interface with negative mean curvature is present, for example, a water meniscus, the Laplace pressure, calculated from 9.10 is reduced as compared to the atmospheric pressure. In this case, the equilibrium of the water in the meniscus and vapor in air can be reached at a much lower pressure than p_s. The relation between the relative humidity and the mean curvature of the meniscus at a given temperature T is given by the Kelvin equation 9.3, which can be presented, for air, in the following form

$$\gamma_{LV}\left(\frac{1}{R_1}+\frac{1}{R_2}\right)=\frac{RT}{V}\ln\left(\frac{p}{p_s}\right), \tag{9.14}$$

where $R = 8.314$ J Kmol^{-1} is the universal gas constant and V is the molar volume of air. At the standard conditions ($T = 273$ K, $P = 10^5$ Pa), $V = 0.023$ m^3 mol^{-1}. The radius of curvature obtained by the Kelvin equation is sometimes called the Kelvin radius, $1/R_k = 1/R_1 + 1/R_2$. The Kelvin equation can also be written as

$$R_k=\frac{\gamma_{LV}V}{RT}\ln\left(\frac{p_s}{p}\right). \tag{9.15}$$

Another way to look at the Kelvin equation is to say that it predicts that for a given relative humidity, p/p_s, as soon as the condensation and evaporation processes reach a thermodynamic equilibrium, a meniscus with the mean curvature R_k given by 9.15 can form. The meniscus should also satisfy the Young equation (9.11) at the triple line. Since the mean curvature of the meniscus is negative, this condition can usually be satisfied at the points where a solid surface is concave, for example, near inside corners of a vessel or at the points of asperity contacts. Therefore, a meniscus forms near asperity contacts with the Laplace pressure drop given by the combination of 9.10 and 9.14

$$\Delta P=\frac{RT}{V}\ln\left(\frac{p}{p_s}\right). \tag{9.16}$$

Equations 9.14–9.16 describe the equilibrium between water molecules leaving the meniscus due to evaporation and vapor molecules approaching the meniscus. In particular, for water at $T = 300$ K, the Kelvin radius in nanometers is $R_k = 0.53/\ln(P_V/P_{sat})$ nm.

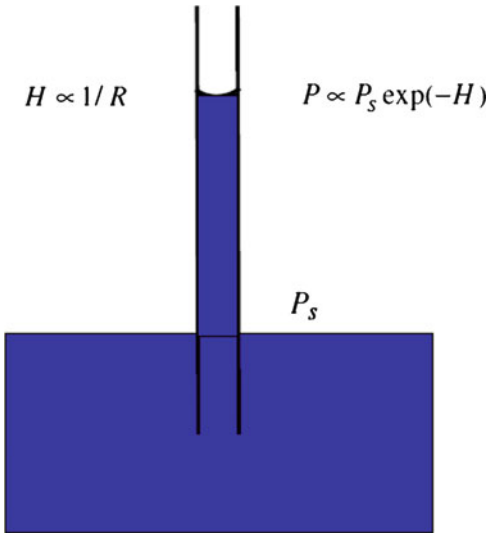

Fig. 9.12 Vapor pressure decreases with height H

In order to derive the Kelvin equation in a rigorous thermodynamic manner, the Gibbs free energy per unit mass should be considered, which is equal to

$$\mathrm{d}G = V\mathrm{d}P - S\mathrm{d}T. \tag{9.17}$$

At constant temperature ($\mathrm{d}T = 0$), the excess free energy above the saturated vapor pressure p_s can be calculated by integration using $PV = nRT$ (the ideal gas law):

$$\Delta G = \int_{p_\mathrm{s}}^{p} V\mathrm{d}P = \int_{p_\mathrm{s}}^{p} \frac{RT}{P}\mathrm{d}P = RT\ln\frac{p}{p_\mathrm{s}}. \tag{9.18}$$

Further assuming that the change of the Gibbs energy in vapor is equated by the change of the pressure in the liquid, $\Delta G = V\Delta P$, immediately yields 9.16.

A less rigorous derivation of the Kelvin equation, which is perhaps easier for visualization is based on the assumption that the vapor pressure decreases with height H in accordance with the hydrostatic formula, i.e., exponentially (Fig. 9.12). At the ground level, the saturated vapor is in equilibrium with a flat liquid interface. Whereas at a capillary tube with height H, vapor at reduced pressure $p = p_0\exp(-H/H_0)$ is still in equilibrium with the concave interface of curvature radius R_k corresponding to the pressure drop $2\gamma/R_\mathrm{k}$, which is proportional to the liquid elevation in the capillary tube. This reasoning leads to the conclusion that $R_\mathrm{k} \propto \ln(p_\mathrm{s}/p)$.

It is observed from 9.16 that the Laplace pressure drop inside the meniscus is expected to grow indefinitely with decreasing relative humidity. The value of the

Laplace capillary force can be calculated by multiplying ΔP by the area of the foundation of the meniscus

$$F_{\text{cap}} = \Delta P \pi {R_0}^2, \tag{9.19}$$

where R_0 is the radius of the foundation of the meniscus. Since the Kelvin radius decreases quickly with decreasing relative humidity, the area of the foundation decreases too. Assuming a conical asperity in contact with a flat surface, there is a linear proportionality of the two radii

$$R_0 \propto R_{\text{k}}. \tag{9.20}$$

Combining 9.16 with 9.19–9.20 yields

$$F_{\text{cap}} \propto -\ln\left(\frac{p}{p_{\text{s}}}\right). \tag{9.21}$$

That is, with reduced relative humidity, the capillary adhesion force is expected to grow. For a more complicated shape of an asperity (e.g., spherical rather than conical), the dependence of R_0 upon R_{k} would be more complicated than 9.20 (Stifter et al 2000); however, it may be expected that 9.21 still provides a general trend.

It is indeed observed from the experiments that the capillary force grows with decreasing relative pressure (Bhushan and Sundararajan 1998; He et al 2001). However, this trend is observed only for the relative humidity greater than 20–30% (Fig. 9.7). At that level of the relative humidity, the Kelvin radius is on the order of nanometers (Stifter et al 2000) and the height of a capillary bridge can constitute only several molecules and is comparable with the thickness of the liquid–vapor interface. In this situation, with the further decrease of the Kelvin radius, there are just not enough molecules to sustain the liquid phase and cause the attractive capillary force, so the Kelvin equation breaks down. As a result, the Laplace force cannot grow unlimitedly with decreasing relative humidity.

9.8 Osmosis and Osmotic Pressure

Osmosis is the movement of water molecules through a semipermeable membrane. Such a membrane allows for water molecules to penetrate through; however, it prevents the penetration of typically large molecules of a solute. Suppose a vessel with a water solution (say, of salt or sugar) divided by such a semipermeable membrane into two section. If solution concentration in one section of the vessel is different from that in the other section, water molecules will tend to diffuse into the section with higher concentration, assuming that the pressures in the two

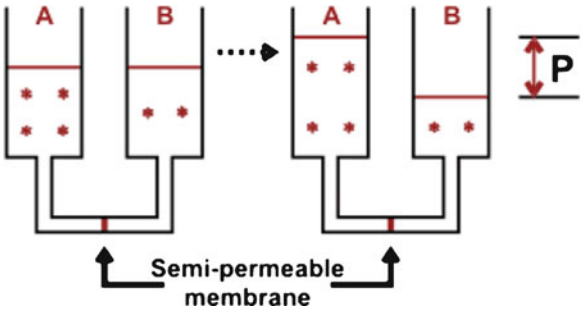

Fig. 9.13 Osmotic pressure

sections are equal (Fig. 9.13). In an idealized model, one can assume that there is no interaction between the molecules of the solute and solvent, neither with each other nor among themselves, similarly to the ideal gas. In that case, in equilibrium, the partial pressures of water (the solvent) in the two sections are equal, whereas the concentration difference of the solute results in pressure on the membrane referred to as "the osmotic pressure."

The process continues until the chemical potentials in the two sections of the vessel become equal. The chemical potentials depend upon both the concentration of the solute and the excess pressure (the osmotic pressure). Assuming that the law of ideal gas, $PV = nRT$, applies to the fluids, the value of the osmotic pressure, π, is given by the Morse equation

$$\pi = iCRT, \tag{9.22}$$

where C is the molar concentration of the solute and i is the dimensionless van 't Hoff factor (the isotonic coefficient). For most nonelectrolytes dissolved in water, the van' t Hoff factor is essentially 1. For most ionic compounds dissolved in water, the van 't Hoff factor is equal to the number of discrete ions in a formula unit of the substance.

Reversed osmosis is commonly used for water desalination and purification. In reverse osmosis, the pressure exceeding the osmotic pressure is applied in order to cause water to penetrate from the section with higher concentration of the solute to the section with lower (or zero) concentration. A typical membrane is a porous medium, usually polymeric. Note that liquid flow q (volume per time per cross-section area) through the porous medium is defined by the Darcy's law as proportional to pressure gradient

$$q = -\frac{k}{\mu}\nabla P, \tag{9.23}$$

where k is the permeability of the medium and μ is the viscosity of the liquid. Darcy's law essentially relates the flow of liquid with the corresponding thermodynamic force (the pressure gradient).

9.9 Capillary Effects During Contacts of Rough Surfaces and Stability Issues

The capillary adhesion force due to condensed water menisci or capillary bridges is the principal contributor to the adhesion force and affects asperity contacts. At the nanoscale, forces between surfaces or adhesion forces are significant and often dominate over forces associated with deformation. The two main models of single-asperity mechanical contact that include the adhesion force were developed in the 1970s, namely, the Johnson–Kendall–Roberts (JKR) and Derjaguin– Muller–Toporov (DMT) models (Johnson et al. 1971a, b; Derjaguin et al. 1975). A significant literature is also devoted to the extension of these models (Tabor 1977; Maugis 1992; Greenwood 1997; Greenwood and Williamson 1966; Johnson 1997; Johnson 1998; Maugis 1999; Adams and Nosonovsky 2000). Several models have also been proposed for multiple-asperity contacts that combine the adhesion force with a rough surface (Fuller and Tabor 1975; Maugis 1996). These models usually consider the adhesion force with the Lennard–Jones potential or with the so-called Maugis–Dugdale simplified potential (Johnson 1997, 1998) and are combined with the models of a rough surface (Greenwood and Williamson 1966). The emergence of AFM in the past two decades has allowed the measurement of very small adhesive forces between samples and AFM tips with radii down to the nanometer scale generating new experimental data available (Carpick et al 1996; Xiaoand and Qian 2000; Sirghi et al. 2000; He et al. 2001; Jones et al. 2002; Szoszkiewicz and Riedo 2005a, b; Jang et al. 2006; Thoreson et al. 2006; Butt et al. 2006; Yang et al. 2007a, b; 2008a, b, c).

The word *adhesion* does not denote a fundamental physical force, but rather it may mean the combination of all attractive forces acting between two bodies. The adhesion force consists of several components, including the relatively weak and long-range van der Waals force, the relatively strong and short-range chemical-bonding force, the electrostatic force, and the capillary forces (Israelachvili 1992). The capillary force is caused by water menisci or capillary bridges, which are formed at the contact spots due to condensation when the contacting materials are hydrophilic. The dominating component of the capillary force is the so-called Laplace force caused by the reduced pressure in the meniscus (the Laplace pressure) compared with the pressure outside (Israelachvili 1992).

Unlike electrostatic, van der Waals, and chemical forces, the capillary force is absent when the contact takes place in vacuum. Therefore, the effect of the capillary force can be estimated by comparing the adhesion force data measured by AFM in air and in UHV. Such measurements indicate that for chemically nonactive surfaces the capillary force dominates over other components of the adhesion force even at small relative humidity. The capillary force normally constitutes 30–90% of the total adhesion force, depending upon material combination, RH, and AFM tip radius (Fisher and Israelachvili 1981; Bhushan and Sundararajan 1998; Xiaoand and Qian 2000; Sirghi et al. 2000; He et al. 2001; Jones et al. 2002; Szoszkiewicz and Riedo 2005a, b; Jang et al. 2006; Thoreson et al 2006; Butt et al. 2006; Yang et al. 2007a, b).

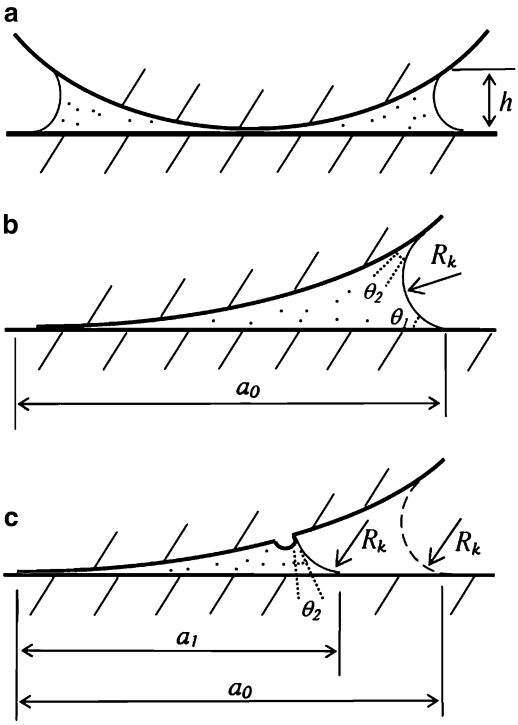

Fig. 9.14 (**a**) Water meniscus with a vertical thickness h between a flat solid and a spherical asperity. (**b**) The contact angle θ between the solids and the water meniscus with radius R_k and foundation radius a_0. (**c**) Small roughness (*a bump*) upon the asperity may result in a big change of the radius of the meniscus, a_0 (Nosonovsky et al. 2011)

Despite the fact that the capillary force dominates adhesion, most contact mechanics models do not consider it and account only for the effect of the van der Waals force and contact force. It has been argued that the Maugis–Dugdale approximation accounts well for the capillary force because it assumes a constant stress acting up to a certain constant distance h, which can be easily identified with the Laplace pressure and meniscus height (Fig. 9.14a) (Johnson 1998; Maugis 1999). While this is true in the case of an ideally smooth surface, in a more realistic case of a rough surface, the meniscus height may be different. A two-dimensional asperity with the radius R is shown in contact with a flat substrate. The meniscus surface, which has a constant Kelvin radius R_k (Rowlinson and Widem 1982), comes in contact with the substrate and asperity under contact angles θ_1 and θ_2, respectively, as shown in Fig. 9.14b. The meniscus foundation radius a_0 can be determined from geometrical considerations, and the capillary force is $F_0 = 2a_0L\Delta P$, where L is the length of the asperity and ΔP is the pressure difference between the meniscus and the ambient. Consider now a very small bump upon the asperity surface (Fig. 9.14c). The meniscus may present a different shape and a different foundation radius a_1 is possible, yielding the force $F_1 = 2a_1L\Delta P$. Thus, a tiny change in the asperity shape can lead to a significant change of the capillary force.

The above shows that a small variation of the surface roughness may result in a large change of the meniscus. Furthermore, in the case of a rough surface, the

meniscus can have multiple configurations. Thus, the capillary force is not a stable function with respect to the surface perturbation or roughness. In addition, a nanoscale meniscus itself can be in a metastable state. This issue has been overlooked by most theories, although due to the instability of the meniscus, conventional contact models that use the Maugis–Dugdale potential do not work well for the capillary force, even though the latter is the most important adhesion force component in applications.

A liquid-mediated mechanical contact involves two types of processes: thermodynamic processes, such as evaporation and condensation, and the mechanical processes of bringing the surfaces together or separating them. These processes may have very different time constants. It has been argued that breaking a water meniscus bridge between two asperities may be a nonequilibrium thermodynamic process (Fisher and Israelachvili 1981; Maeda et al. 2002). On the other hand, in many situations, it may be assumed that mechanical processes are slow compared to the thermodynamic ones, and, therefore, the meniscus is at a thermodynamic equilibrium (Szoszkiewicz and Riedo 2005a, b). With this assumption, we formulate a general expression for the free energy of the liquid meniscus between rough solid surfaces as a function of surface geometry and separation distance between the surfaces. Then, we calculate the force between the two solids as a derivative of the energy with respect to the separation distance, assuming a fast and a slow mechanical process.

9.9.1 Shape of the Meniscus

When two elastic bodies are in contact at the nanoscale, they can often be treated as continuum bodies; however, the attractive adhesion force acting between them should be taken into consideration. Two competing theories of elastic contact with adhesion developed in the early 1970s are the DMT and JKR models. The DMT model assumes that the adhesive forces act outside of the contact area and yields the pull-off force needed to separate a sphere of radius r and a flat surface, $P_{\text{pull-off}} = 2\pi wr$, where w is the work of adhesion. The JKR model assumes that the adhesion forces act inside the contact area and yields the pull-off force of $P_{\text{pull-off}} = 1.5\pi wr$. Analytical results for the transition between DMT and JKR were presented by Maugis (1992) using a simplified model of adhesion based upon the Dugdale crack model (Tabor 1977). Both theories and their extensions are widely used in the literature, especially, after the AFM experimental data on adhesion force measurement have become available since the 1980s (Adams and Nosonovsky 2000). Figure 9.15. shows the number of reference to the original JKR and DMT papers in the Scopus.com online database since 1996 (the database does not provide earlier references). It is seen that the number of references continues to grow and that the two theories have become a standard way of analyzing the single-asperity contact at the nanoscale. Numerous extensions of the DMT and JKR theories, e.g., for the multiasperity contact of randomly rough surfaces, for elastic plastic

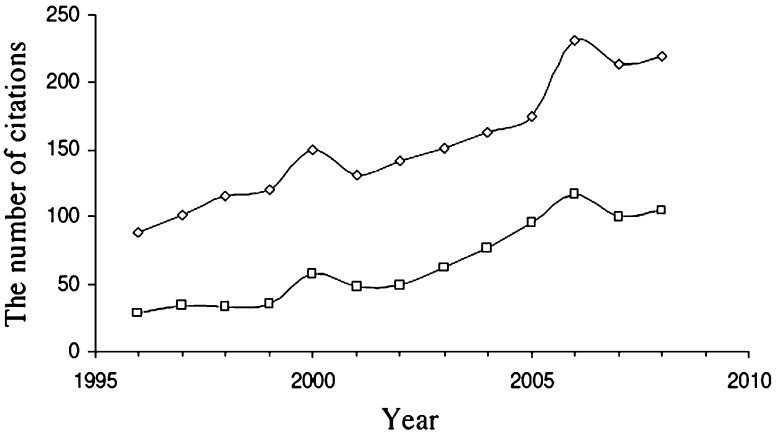

Fig. 9.15 Number of references to the original JKR and DMT publications after 1996 per year in the Scopus database. The data for 2008 (146 and 70 references) are normalized for the 8-month period

materials, and for numerical evaluation of the contact, have been proposed (Adams et al. 2003; Sirghi et al. 2000).

The practical motivation for these studies is in their application to the nanotechnology, micro/nanoelectromechanical systems, and other small devices. The small size of these applications leads to large surface-to-volume ratios and, therefore, a correct evaluation of the surface and adhesion forces is crucial for them. Adhesion is a generic term that involves attractive forces of several natures. Among them is the Van der Waals adhesion force, chemical bonding, electrostatic, and capillary forces. Many experimental data show that the capillary adhesion force is a very significant and often dominant component of the total adhesion force.

The capillary force is caused by condensed water bridges (menisci) at the contact between the two bodies. The water vapor is always present in air, even at low relative humidity, so the processes of evaporation and condensation take place. If the vapor pressure is equal to the saturation value (RH $= 100\%$), the evaporation and condensation of liquid water occur at the same rate, so a liquid layer can be present and it is in thermodynamic equilibrium with vapor. The rate of evaporation and condensation, however, depends on the curvature of the liquid–vapor interface. This is because the surface energy is curvature dependent. A liquid molecule at a concave surface has on average a larger number of neighboring liquid molecules; therefore, its energy is lower than the energy of a molecule at a flat surface and the rate of evaporation is lower. Thus, the evaporation–condensation thermodynamic equilibrium can be reached even at RH $< 100\%$. The exact relation between the meniscus curvature and RH at equilibrium is given by the Kelvin equation (9.14–9.15).

For high-meniscus curvature, the pressure inside the capillary bridges is significantly reduced compared to ambient in accordance with the Laplace equation,

$\Delta P = \gamma/R_m$, and the pressure can drop deeply into the negative region (negative pressure, of course, is nothing else than tensile stress) (Yang et al. 2008b). For example, based on the Kelvin calculation, the value of RH = 30% corresponds to $\Delta P = 162$ MPa (about 1,620 atm) and RH = 10%. The reduced pressure inside the bridges gives a rise to the attractive capillary force equal to the foundation radius of the menisci times ΔP.

Note that the shape of the meniscus should satisfy two types of the boundary condition. First, at the solid–liquid–air contact line, the Young equation (9.11) for the contact angle θ should be satisfied. Second, at the liquid–air interface, the mean curvature is constant and given by the Kelvin equation (9.14). Finding the shape of the meniscus between two solid surfaces with a given topography is a nontrivial and complicated mathematical problem, so no conclusion about the existence or uniqueness of the solution can be made in the general case.

It is an accepted postulate in surface science and tribology that there are no absolutely smooth surfaces. Every nominally flat surface, including even atomically smooth surfaces, has roughness. When a contact model is built, it is often assumed that the contribution of the small-scale roughness can be neglected and surfaces can be modeled as smooth. In most cases, this assumption is justified. However, this is not necessarily so when the capillary effects are investigated, as stability issues may be very important in this case. Consider an elastic sphere with the radius r in contact with the flat surface (contact radius a) with the meniscus near the contact spot of the mean radius R_m (Fig. 9.16a). If the sphere and the flat are smooth, there is a unique position of the meniscus and the unique value of the adhesion pull-off force, corresponding to the foundation radius a_f, as it is assumed by the DMT theory. However, if small-scale roughness with a typical size of a detail $b < R_m$ is introduced, the foundation radius of the meniscus can have a spectrum of values between $b < a < a_f$. While the maximum value of a is close to the foundation radius of the smooth surface (Fig. 9.16b), the minimum radius is comparable with b. Furthermore, with the decreasing size of roughness detail, the average value of b does not reach a_f (Fig. 9.16c)

$$\lim_{b \to 0} (a) \to \frac{a_f}{2} \neq a_f. \tag{9.24}$$

This illustrates that the small-scale roughness cannot be neglected and therefore the contact models that assume a smooth surface can be misleading.

9.9.2 Capillary Force

Let us now assume that the two bodies can move mechanically and separate from each other. Depending on the velocity of the mechanical process, three regimes are possible (Table 9.1). *First*, for a slow mechanical process, there is enough time for the thermodynamic processes of evaporation and condensation to come into

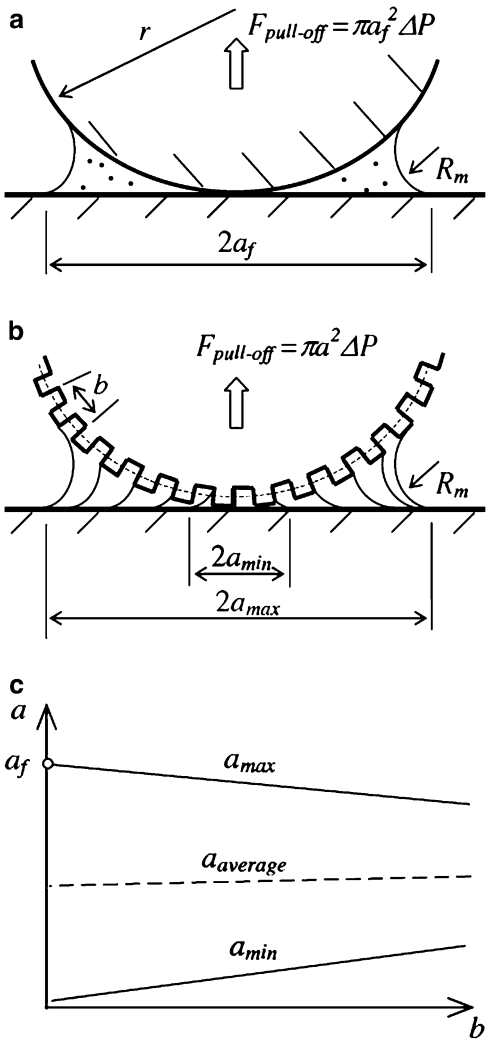

Fig. 9.16 (**a**) Smooth elastic sphere in contact with the flat surface. (**b**) Small-scale roughness detail of typical size b can pin the capillary bridge and change dramatically the size of the meniscus; (**c**) maximum, minimum, and average radius of the capillary bridge as a function of the size of the meniscus

equilibrium, and both the Kelvin's and Young's equations are satisfied. *Second*, for a fast mechanical process, there may not be enough time for the meniscus to come into thermodynamic equilibrium, but it may be assumed that the meniscus is in quasistatic mechanical equilibrium. The meniscus then has a constant pressure inside, which, however, may be different from that predicted by the Kelvin equation, which is valid only for thermodynamic equilibrium. In this case, the liquid–vapor interface still has a constant mean curvature, based on the Laplace equation, and Young's equation is satisfied at the triple line. The volume of the meniscus is constant, as there is not enough time to change the volume by condensation or evaporation. *Third*, for a very fast mechanical process, the meniscus may not be in a quasistatic mechanical equilibrium, and in this case dynamic processes,

Table 9.1 Volume, surface, and the triple line for mechanical process for different relative speeds of the mechanical, thermodynamic, and hydrodynamic processes (T_m, T_n, and T_d are time constants of the corresponding processes)

	Slow mechanical process, $T_m \gg T_n$, $T_m \gg T_d$	Fast mechanical process, $T_n \gg T_m$, $T_m \gg T_d$	Very fast mechanical process, $T_m \ll T_d$, $T_m \ll T_n$
	Thermodynamic and mechanical quasiequilibrium	Mechanical quasistatic equilibrium	Hydrodynamic process
Volume	Not conserved	Conserved	Conserved
Liquid–vapor interface	Kelvin equation	Laplace equation	Dynamic
Triple line	Young's equation	Young's equation	Dynamic

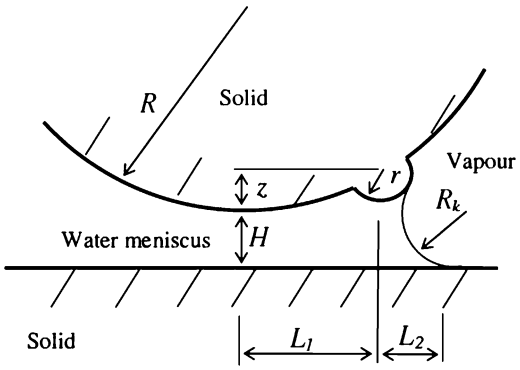

Fig. 9.17 A solid asperity of radius R with a bump of radius r in contact with a flat surface, with a meniscus of radius R_k and contact angle $\theta = 0$

such as interface waves, occur. Then, neither Kelvin's nor Young's equations is satisfied, whereas the volume of the meniscus is still conserved.

Which of the three regimes takes place depends upon the relation of the time constants of the three processes. The meniscus nucleation time, T_n, which obeys an Arrhenius law (Szoszkiewicz and Riedo 2005a, b) governs the thermodynamic process, whereas $T_m = H/v$, which is separation distance (taken as a typical length of the liquid–vapor interface) divided by separation velocity v, is responsible for the mechanical process and $T_d = 2\pi\ (\rho H^3/\gamma_{LV})^{1/2}$ is the period of a capillary wave vibration at a liquid–vapor interface of size H, where ρ is liquid density (Landau and Lifshitz 1959). In many practically important situations, the first regime occurs, since T_n is on the order of 1 ms (Szoszkiewicz and Riedo 2005a, b), T_m is on the order of 0.1 s, and $T_d = 0.75$ ns (calculated for $\rho = 10^3$ kg m^{-3}, $\gamma_{LV} = 70$ mJ m^{-2}, $H = 10$ nm).

We consider as an example a simple case of a two-dimensional rigid cylinder of radius R, with a smaller roughness, represented by a bump of radius r, separated by distance H from a solid flat surface (Fig. 9.17). The meniscus of radius R_k may form between the cylinder and the flat surface.

It is assumed here that the contact angles with water of both the flat substrate and the cylinder are equal to zero. This assumption does not affect significantly the

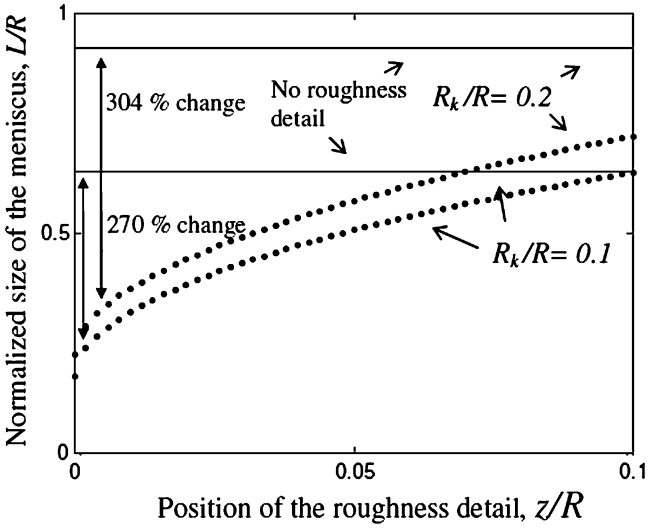

Fig. 9.18 Calculated dependence of the meniscus size upon the position of the small roughness detail. It is observed that introducing the roughness detail and changing its position may lead to a significant change of the meniscus size and, therefore, of the capillary force

qualitative nature of the problem; however, it simplifies the geometry considerably. The width of the meniscus, as defined in Fig. 9.17, is given by

$$L = L_1 + L_2 = \sqrt{(z - H)(2R - z + H)} + \sqrt{r^2 + 2R_k(r + z) - z^2}. \tag{9.25}$$

For the case of small separation between the asperity and the plane, $H \sim 0$, which is a typical case in AFM measurements (Xiaoand and Qian 2000), 9.25 simplifies to

$$L = \sqrt{z(2R - z)} + \sqrt{r^2 + 2R_k(r + z) - z^2}. \tag{9.26}$$

If no rough detail is present, the size of the meniscus is given by

$$L = 2\sqrt{R_k R}. \tag{9.27}$$

Dependencies of L/R upon z/R for different values of $R_k/R = 0.1$ and $R_k/R = 0.2$ are presented in Fig. 9.18 as dotted curves based on 9.26. Corresponding values of L/R, for the case when no roughness is present, are also shown as solid lines. It is observed that introducing the roughness detail and changing its position, z/R, may lead to a significant change in the meniscus size (from $L/R = 0.17$ to $L/R = 0.63$ and from $L/R = 0.22$ to $L/R = 0.89$) and, therefore, in the capillary force. Thus, the meniscus force is very sensitive to the position of the roughness.

Above, the two-dimensional case has been considered. Theoretically, the effect of a small bump upon the meniscus shape is more pronounced for a two-dimensional

profile than for a three-dimensional profile. Nevertheless, a qualitatively similar trend is expected for three-dimensional cases. The following section presents adhesion measurement made for rough surfaces to back up this claim.

Yang et al. (2008a, b, c) measured adhesion force between a spherical glass colloidal probe attached to an AFM cantilever and a silicon sample at different tilt angles. The Kelvin radius of the meniscus is estimated as $R_k = 2$ nm and the mean surface roughness of the colloidal probe $\sigma = 10$ nm for the rough probe and $\sigma = 2$ nm for the smooth probe. The results for the force as a function of the tilt angle are presented in Fig. 9.19a, b. It is observed that a small change of the sample-stage tilt angle greatly affects the measured adhesion force value. Although both the colloidal probe and the sample were not perfectly smooth, statistical fluctuations of their profiles cannot account for such a huge difference in the force. Indeed, as observed from a comparison of Fig. 9.19a, which shows results for a smooth sample, and Fig. 9.19b, which shows results for a much rougher sample, the change of roughness affects the magnitude of the force, but not the relative deviation of the force. Note that the values of the force have high reproducibility (the error bars provided by the AFM are shown in the figure), although they are very sensitive to the tilt angle.

In order to obtain the three-dimensional topography of the colloidal probe, the grating sample is scanned by the colloidal probes. The grating sample has an array of the sharp silicon peaks (this explains the mirror images in the corners) and the given AFM topographies, in Fig. 9.19a, b, are the negative images of the colloidal probes.

Assuming a single-asperity contact, the traditional analysis based upon the DMT model predicts that the pull-off force is given by

$$F = 2\pi w R, \tag{9.28}$$

where $R = 20$ μm is the radius of the colloidal probe and $w = 2\gamma_{LV}\cos\theta$ (Johnson 1998). Taking the typical value for water, $\gamma_{LV} = 70$ mJ m^{-2} (Adamson 1990) and $\cos\theta = 0.5$, $F = 8.8$ mN. The JKR model yields $F = 1.5\pi w R = 6.6$ mN. The theoretically predicted value exceeds the experimentally observed values of $0.1\ \text{mN} < F < 3$ mN for the rough surface, whereas it is within the range of the observed values for the smooth surface, $2\ \text{mN} < F < 55$ mN. The theoretical analysis also does not predict a dependence of the pull-off force upon the tilt angle, which is observed experimentally.

For the multiple-asperity contact, the traditional analysis based upon the Greenwood and Williamson (GW) (1966) methodology states that individual asperity contacts are independent of each other. Thus, the net pull-off force is equal to the sum of pull-off forces at individual asperity junctions. The influence of roughness is characterized by the ratio σ/δ_c, where

$$\delta_c = 0.75(\pi^2 w^2 R/E^{*2})^{1/3}, Z \tag{9.29}$$

where E^* is the composite elastic modulus (Fuller and Tabor 1975; Maugis 1996). Taking $E^* = 44$ GPa, $\delta_c = 0.59$ nm (based on $w = 70$ J m^{-2}, $R = 20$ μm) and

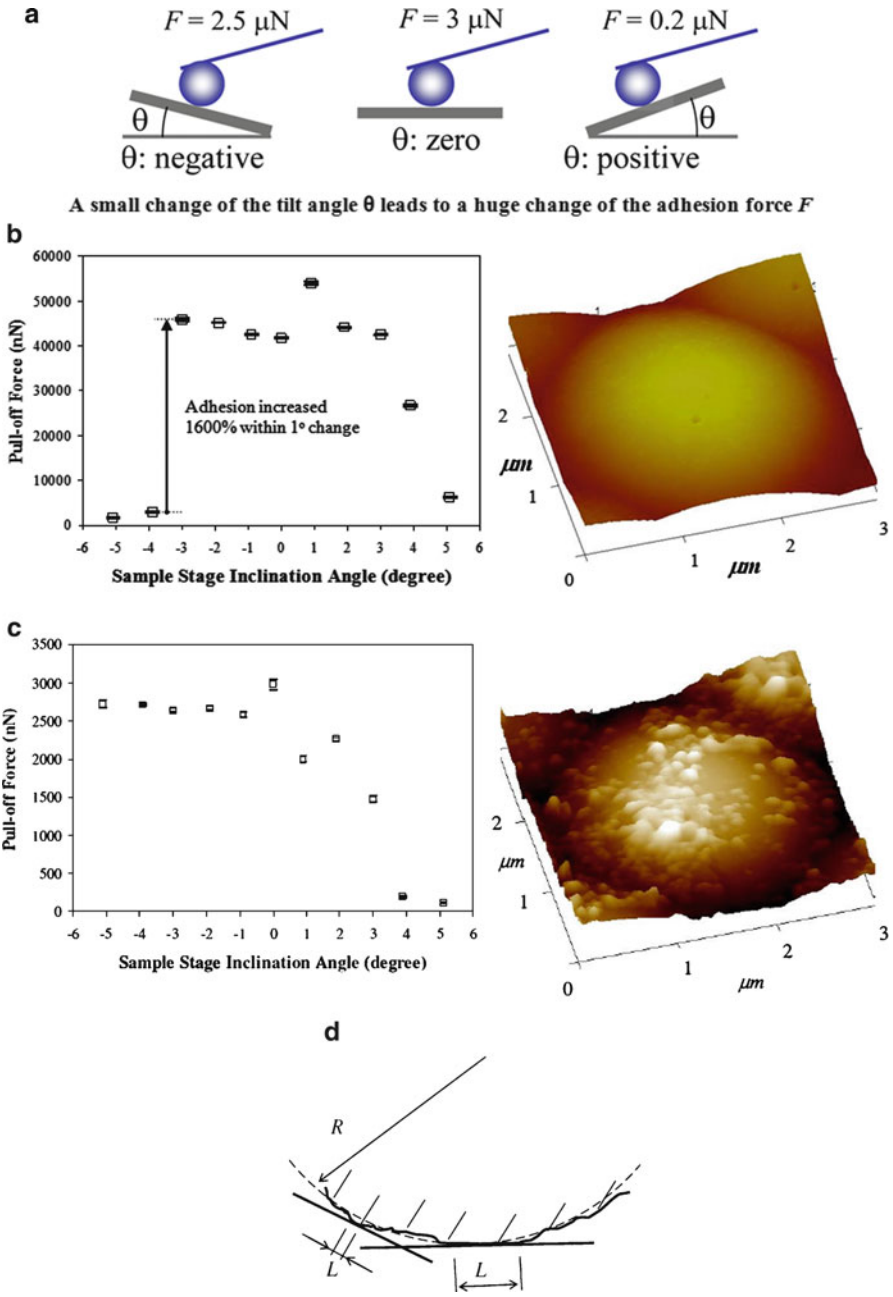

Fig. 9.19 (**a**) Spherical colloidal probe in contact with a flat sample (AFM images represent probe topography). Measured adhesion force as a function of tilt angle of the stage for (**b**) a relatively smooth probe and (**c**) for a rough probe. (**d**) Schematics of a flat surface in contact with a rough sphere. The size of contact L can vary significantly with the change of the tilt angle due to roughness. As a result, the meniscus size and the capillary force would also change significantly

thus $\sigma/\delta_c > 10$. At $\sigma/\delta_c > 2$, the effective adhesion is eliminated (Johnson 1998), so the multiple asperity model also cannot explain the experimental values.

As the sample and colloidal probe separate, capillary bridges at the lower asperities are broken until only one or a few bridges are left. Thus, the pull-off force depends upon the tip radius and shape at a particular asperity, which may vary significantly as shown in Fig. 9.19c. Thus, the experimentally measured pull-off force as a function of the tilt angle is not stable, as has been described in the preceding sections. In order to calculate the meniscus force, an exact shape of the contact spot between the colloidal probe and sample should be known.

The significant role of the capillary force at the nanoscale raises the question of its stability. In classical mechanics, stability analysis of a solution plays a major role both in the statics and in dynamics. It is well-known that in order for solution to exist physically, it should be at a stable equilibrium and correspond to a local minimum of the potential energy. Since the 1960s, it has been recognized that nonequilibrium processes play a very significant role in many physical phenomena, such as the hierarchical and self-organizing structures, and thus the instability and nonstable equilibrium are important to analyze. At the nanoscale, mechanical instabilities are inherent in many processes. For example, mechanical hysteresis of an AFM cantilever is caused by the destabilization of the mechanical equilibrium of the cantilever. Adhesion hysteresis that leads to energy dissipation during the loading–unloading cycle with adhesion is a specific nanoscale example.

Capillary effects constitute another important area of nanomechanics that involve instabilities. The stability of the capillary force with respect to roughness details has not received enough attention from scientists. The classical models of contact with adhesion, such as the JKR and DMT models (Maugis 1999), do not address stability, although experiments show that the capillary force is very sensitive to small changes in roughness. During the multiple-asperity contact of two rough solid surfaces, multiple menisci can form between the bodies. There are only two restrictions upon the geometry of the meniscus at the thermodynamic equilibrium: (1) the curvature of the menisci should satisfy 9.14 and (2) the contact angle should be constant at the triple line (solid–liquid–air contact line). These two requirements may lead to nonunique shapes of the menisci for a given topography of rough surfaces. Furthermore, a slight change of topography may lead to a significant change of the shape of the meniscus and, therefore, of the adhesion force, as it was shown by Nosonovsky (2007a, b, c, d, e) and Yang et al. (2007b). They measured the adhesion force between a rough glass sphere attached to the AFM cantilever and a tilted smooth silicon sample. The response was not stable with respect to the tilt angle, that is, a small change of the tilt angle resulted in a large (sometimes, 300–400%) change in the pull-off adhesion force (Fig. 9.20). While conventional models of contact with adhesion, such as the JKR and DMT, overlook this effect and assume that a meniscus is stable, it has been reported that the pull-off adhesion force between rough surfaces is very sensitive to small changes in roughness. Figure 9.14b, c shows how superimposing a tiny roughness detail upon a 2D asperity can dramatically change the size of the meniscus and, therefore, the capillary force.

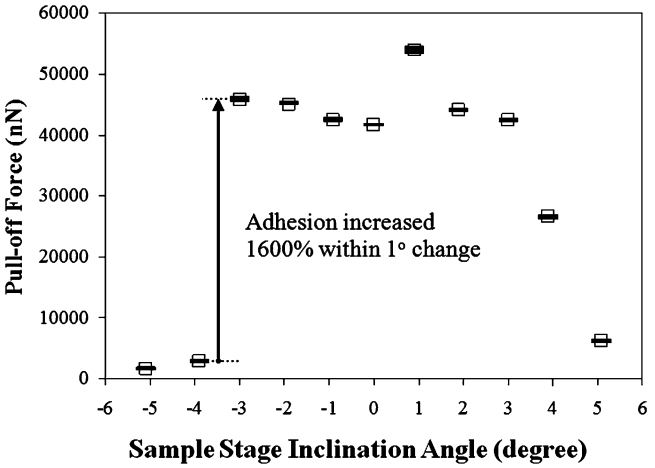

Fig. 9.20 Variation of adhesion force between a rough spherical colloidal probe in contact with a tilted flat sample as a function of tilt angle. Changing the tilt angle results in changing of the contact spot due to roughness and thus leads to a very significant change in the adhesion force (Nosonovsky and Bhushan 2008a)

9.10 Summary

In this chapter, the fundamental equations that govern wetting and capillary effects and wetting have been introduced and discussed: the Laplace, Young, and Kelvin equations. Phase transitions and equilibrium as well as the phase diagrams at the macro and nanoscale have been examined as well. These concepts are important in understanding the phenomena of self cleaning.

Chapter 10
Superhydrophobicity

In the preceding chapter, we have discussed the capillary phenomena related to wetting. Superhydrophobicity or roughness-induced nonwetting is associated with the Lotus effect and currently serves as the main approach to design self-cleaning surfaces. In order to create a robust superhydrophobic surface, two factors are required. First, the surface should be at least slightly hydrophobic initially having water contact angle $>90°$. Second, surface roughness should be applied. Surface roughness plays the dominant role in the superhydrophobicity (in some cases, even an initially hydrophilic surface can become superhydrophobic if proper roughness is applied). It is desirable that the surface roughness is hierarchical or multiscale with submicron scale roughness details imposed on the microscale roughness. The adhesion of water to the solid is reduced significantly if a composite interface with air pockets sitting between the solid and liquid can form.

In this chapter, we review in detail the principles of superhydrophobicity, covering such topics as the effect of roughness on the contact angle and contact angle hysteresis (the difference between a maximum and a minimum possible value of the contact angle for a given surface), transitions between the homogeneous and composite wetting regimes and their stability, the role of hierarchical roughness, the flow of a droplet along an inclined solid surface, the interaction of incoming droplets with a rough solid surface, and other phenomena associated with the superhydrophobicity. We further extend our earlier reviews in Nosonovsky and Bormashenko (2009) and Nosonovsky and Bhushan (2008a, b; 2009; 2010a).

10.1 Contact Angle with a Rough or Heterogeneous Surface

Surface roughness affects wetting of a solid surface and can be applied in such a manner that the surface becomes water-repellent or superhydrophobic.

M. Nosonovsky and P.K. Rohatgi, *Biomimetics in Materials Science: Self-Healing, Self-Lubricating, and Self-Cleaning Materials*, Springer Series in Materials Science 152,
DOI 10.1007/978-1-4614-0926-7_10,

10.1.1 The Wenzel and Cassie Equations

As it was explained in the preceding chapter, the contact angle θ_0 supplied by the Young equation (9.11) is the main parameter, which characterizes wetting of a solid surface. In this chapter, we use it in the following form

$$\cos\theta_0 = \frac{\gamma_{SA} - \gamma_{SL}}{\gamma_{LA}}, \tag{10.1}$$

where indices S, L, and A stand for solid, liquid, and air, respectively. Note that although we use the term "air," the analysis does not change in the case of another gas, such as a liquid vapor. Equation (10.1) was derived by Young using the considerations of the balance of "surface tension" forces, or, more exactly, their horizontal components. It provides the value of the so-called static or most stable contact angle, which is attained by a liquid droplet accurately and slowly placed on a solid surface. The most stable contact angle corresponds to the minimum of net surface energy of the droplet.

However, when a droplet is placed on a rough or chemically heterogeneous surface, the contact angle can attain a different value. The Wenzel (1936) equation, which was derived using the surface force balance and empirical considerations, relates contact angle of a water droplet to a rough solid surface, θ, with that upon a smooth surface, θ_0 (Fig. 10.1a), through the nondimensional surface roughness factor, R_f, equal to the ratio of the surface area to its flat projection (Fig. 10.1b).

$$\cos\theta = R_f \cos\theta_0, \tag{10.2}$$

$$R_f = \frac{A_{SL}}{A_F}. \tag{10.3}$$

Essentially, the Wenzel equation deals with the effective surface energy per unit area.

In a similar manner, for a surface composed of two fractions, one of the fractional area f_1 and the contact angle θ_1 and the other with f_2 and θ_2, respectively (so that $f_1 + f_2 = 1$), the contact angle is given by the Cassie equation

$$\cos\theta = f_1 \cos\theta_1 + f_2 \cos\theta_2. \tag{10.4}$$

For the case of a composite interface (Fig. 10.1c) consisting of the solid–liquid fraction ($f_1 = f_{SL}$, $\theta_1 = \theta_0$) and liquid–vapor fraction ($f_2 = 1 - f_{SL}$, $\cos\theta_2 = -1$), combining (10.2) and (10.4) yields the Cassie–Baxter equation (sometimes it is called the Cassie–Wenzel or Cassie–Baxter–Wenzel equation, since it involves the Wensel roughness factor, R_f)

$$\cos\theta = R_f(1 - f_{LA})\cos\theta_0 - f_{LA}. \tag{10.5}$$

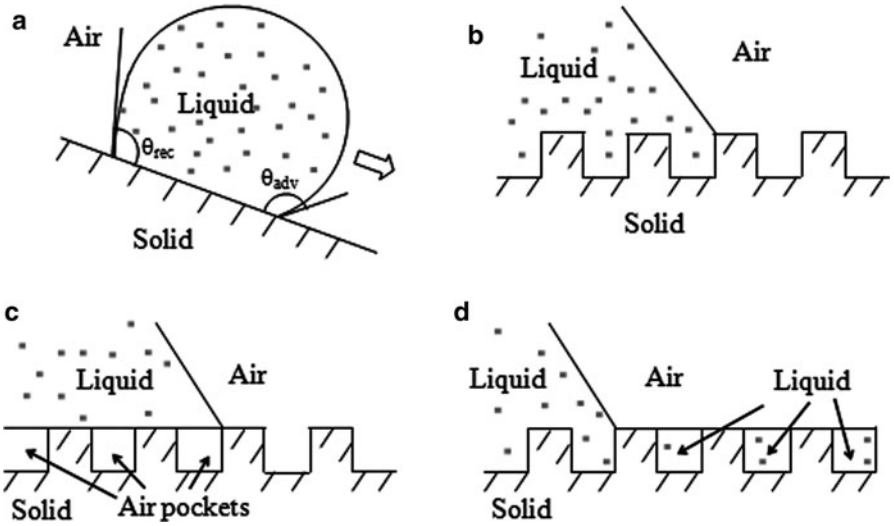

Fig. 10.1 (**a**) Schematics of a droplet on a tilted substrate showing advancing (θ_{adv}) and receding (θ_{rec}) contact angles. The difference between these angles constitutes the contact angle hysteresis. Configurations described by (**b**) the Wenzel equation for the homogeneous interface, (**c**) Cassie–Baxter equation for the composite interface with air pockets, and (**d**) the Cassie equation for the homogeneous interface

The opposite limiting case of $\cos\theta_2 = 1$ ($\theta_2 = 0^o$ corresponds to water-on-water contact) yields

$$\cos\theta = 1 + f_{SL}(\cos\theta_0 - 1) = (1 - f_{LA})\cos\theta_0 + f_{LA}. \tag{10.6}$$

Equation (10.6) is used sometimes (de Gennes et al. 2003) for the homogeneous interface instead of (10.2), if the rough surface is covered by holes filled with water (Fig. 10.1d).

The Wenzel equation predicts that if a surface is already hydrophobic (i.e., $\theta_0 > 90°$), roughness will further enhance the hydrophobicity, while if a surface is hydrophilic ($\theta_0 < 90°$), roughness will increase hydrophilicity. For a hydrophobic surface, a further increase of the roughness factor above $R_f = -1/\cos\theta_0$, according to the Wenzel equation, would yield $\theta = 180°$ and a complete rejection of the liquid by the surface. In practice, this does not happen because air pockets tend to form under the droplet, due to the effect of the droplet weight and other reasons. Similarly, for a hydrophilic surface, an increase of the roughness factor above $R_f = 1/\cos\theta_0$, would yield $\theta = 0°$ and a complete adsorption of the liquid by the surface. This usually does not happen due to the effects of the gas bubbles trapped in the cavities and other reasons.

Two situations in wetting of a rough surface should be distinguished: the homogeneous interface without any air pockets [sometimes called the Wenzel interface, since the contact angle is given by the Wenzel equation or (10.2)] and

the composite interface with air pockets trapped between the rough details [sometimes called the Cassie or Cassie–Baxter interface, since the contact angle is given by (10.9)].

Shuttleworth and Bailey (1964) studied the spreading of a liquid over a rough solid surface and found that the contact angle at the absolute minimum of surface energy corresponds to the values given by (10.2) (for the homogeneous interface) or (10.6) (for composite interface). According to their analysis, spreading of a liquid continues, until both the Young equation is satisfied locally at the triple line, and the minimal surface condition is satisfied over the entire liquid–air interface. The minimal surface condition states that the sum of inversed principal radii of curvature, R_1 and R_2, is constant at any point, and thus governs the shape of the liquid–air interface.

$$\frac{1}{R_1} + \frac{1}{R_2} = \text{const.} \tag{10.7}$$

The curvature of the surface, given by (10.7), remains constant, and its actual value can be obtained from the Kelvin equation (9.3). Mathematically, (10.7) defines a so-called "minimal surface" and its general solution constitutes a challenging problem (Plateau's problem).

Johnson and Dettre (1964) showed that the homogeneous and composite interfaces correspond to the two stable or metastable states of a droplet. Even though it may be geometrically possible for the system to become composite, it may be energetically profitable for the liquid to penetrate into valleys between asperities and to form the homogeneous interface. Marmur (2003) formulated geometrical conditions for a surface, under which the energy of the system has a local minimum and the composite interface may exist. Patankar (2004a, b) pointed out that whether the homogeneous or composite interface exists, depends on the system's history, i.e., whether the droplet was formed at the surface or deposited. However, the above-mentioned analyses do not provide an answer as to which of the two possible configurations, homogeneous or composite, will actually form.

10.1.2 Limits of Applicability of the Wenzel and Cassie Equations

The Cassie equation (10.8) is based on the assumption that the heterogeneous surface is composed of well-separated distinct patches of different material, so that the free surface energy can be averaged. It has been argued also that when the size of the chemical heterogeneities is very small (of atomic or molecular dimensions), the quantity that should be averaged is not the energy, but the dipole moment of a macromolecule (Israelachvili and Gee 1989) and (10.4) may have to be replaced by

$$(1 + \cos\theta)^2 = f_1(1 + \cos\theta_1)^2 + f_2(1 + \cos\theta_2)^2. \tag{10.8}$$

Experimental studies of polymers with different functional groups showed a good agreement with (10.8) and the dependence on the dipole moment is shown only in the case of polymers and may be due to the nature of the polymeric molecular chains (Tretinnikov 2000).

Later investigations put the Wenzel and Cassie equations into a thermodynamic framework; however, they showed also that there is no single value of the contact angle for a rough or heterogeneous surface (Johnson and Dettre 1964; Marmur 2003; Li and Amirfazli 2006). The contact angle can be in a range of values between the so-called receding contact angle, θ_{rec}, and the advancing contact angle, θ_{adv}. The system tends to achieve the receding contact angle when liquid is removed (e.g., at the rear end of a moving droplet), whereas the advancing contact angle is achieved when the liquid is added (e.g., at the front end of a moving droplet). When the liquid is neither added nor removed, the system tends to have a static or "most stable" contact angle, which is given approximately by the Wenzel and Cassie equations. The difference between θ_{adv} and θ_{rec} is known as the "contact angle hysteresis" and it reflects a fundamental asymmetry of wetting and dewetting and the irreversibility of the wetting–dewetting cycle. Although for surfaces with the roughness carefully controlled on the molecular scale, it is possible to achieve contact angle hysteresis as low as $<1^\circ$ (Gupta et al. 2005), it cannot be eliminated completely, since even the atomically smooth surfaces have a certain roughness and heterogeneity. The contact angle hysteresis is a measure of energy dissipation during the flow of a droplet along a solid surface. A water-repellent surface should have a low contact angle hysteresis to allow water to flow easily along the surface.

It is emphasized that the contact angle provided by (10.1)–(10.8) is a macroscale parameter, so it is called sometimes "the apparent contact angle." The actual angle under which the liquid–vapor interface comes in contact with the solid surface at the micro- and nanoscale can be different. There are several reasons for that. First, water molecules tend to forms a thin layer upon the surfaces of many materials. This is because of a long-distance van der Waals adhesion force that creates the so-called disjoining pressure (Derjaguin and Churaev 1974). This pressure is dependent upon the liquid layer thickness and may lead to the formation of stable thin films. In this case, the shape of the droplet near the triple line transforms gradually from the spherical surface into a precursor layer, and thus the nanoscale contact angle is much smaller than the apparent contact angle. In addition, adsorbed water monolayers and multilayers are common for many materials. Second, even carefully prepared atomically smooth surfaces exhibit certain roughness and chemical heterogeneity. Water tends to cover at first the hydrophilic spots with high surface energy and low contact angle (Checco et al. 2003). The tilt angle due to the roughness can also contribute in the apparent contact angle. Third, the very concept of the static contact angle is not well defined. For practical purposes, the contact angle, which is formed after a droplet is gently placed upon a surface and stops propagating, is considered as the static contact angle. However, depositing the droplet involves adding liquid while leaving it may involve evaporation, so it is difficult to avoid dynamic effects. Fourth, for small droplet and curved triple lines, the effect of the contact line tension may be significant. Molecules at the surface of a liquid or

Table 10.1 Wetting of a superhydrophobic surface as a multiscale process

Scale level	Characteristic length	Parameters	Phenomena	Interface
Macroscale	Droplet radius (mm)	Contact angle, droplet radius	Contact angle hysteresis	2D
Microscale	Roughness detail (μm)	Shape of the droplet, position of the liquid–vapor interface (h)	Kinetic effects	3D solid surface, 2D liquid surface
Nanoscale	Molecular heterogeneity (nm)	Molecular description	Thermodynamic and dynamic effects	3D

solid phase have higher energy because they are bonded to fewer molecules, then those in the bulk. This leads to the surface tension and surface energy. In a similar manner, molecules at the edge have fewer bonds than those at the surface, which leads to the line tension and the curvature dependence of the surface energy. This effect becomes important when the radius of curvature is comparable with the so-called Tolman's length, normally of the molecular size (Anisimov 2007). However, the triple line at the nanoscale can be curved so that the line tension effects become important (Pompe et al. 2000). The contact angle with account for the contact line effect for a droplet with radius R is given by $\cos\theta = \cos\theta_0 + 2\tau/(R\gamma_{LV})$, where τ is the contact line tension and is the value given by the Young equation (Boruvka and Neumann 1977). Thus while the contact angle is a convenient macroscale parameter, wetting is governed by interactions at the micro- and nanoscale, which determine the contact angle hysteresis and other wetting properties (Table 10.1).

Gao and McCarthy (2007) showed experimentally that the contact angle of a droplet is defined by the triple line and does not depend upon the roughness under the bulk of the droplet. A similar result for chemically heterogeneous surfaces was obtained by Extrand (2003). Gao and McCarthy (2007) concluded that the Wenzel and Cassie–Baxter equations "should be used with the knowledge of their fault". The question remained, however, under what circumstances the Wenzel and Cassie–Baxter equations can be safely used and under what circumstances do they become irrelevant.

For a liquid front propagating along a rough two-dimensional profile (Fig. 10.2a, b), the derivative of the free surface energy (per liquid front length), W, by the profile length, t, yields the surface tension force $\sigma = dW/dt = \gamma_{SL} - \gamma_{SV}$. The quantity of practical interest is the component of the tension force that corresponds to the advancing of the liquid front in the horizontal direction for dx. This component is given by $dW/dx = (dW/dt)\ (dt/dx) = (\gamma_{SL} - \gamma_{SV})dt/dx$. It is noted that the derivative $R_f = dt/dx$ is equal to Wenzel's roughness factor in the case when the roughness factor is constant throughout the surface. Therefore, the Young equation, which relates the contact angle with solid, liquid, and vapor interface tensions, $\gamma_{LV}\cos\theta = \gamma_{SV} - \gamma_{SL}$, is modified as (Nosonovsky 2007d).

$$\gamma_{LV}\cos\theta = R_f(\gamma_{SV} - \gamma_{SL}). \tag{10.9}$$

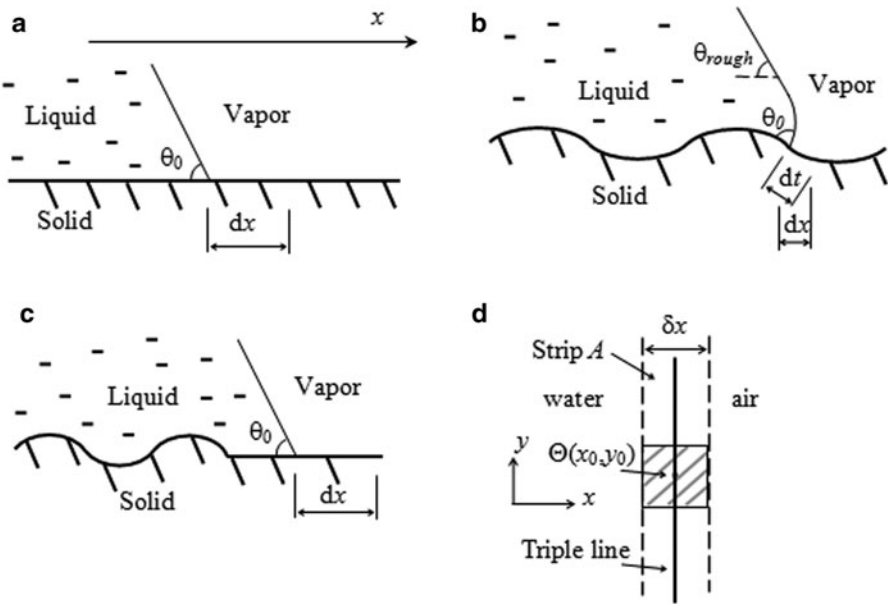

Fig. 10.2 Liquid front in contact with a (**a**) smooth solid surface, (**b**) rough solid surface, propagation for a distance dt along the curved surface corresponds to the distance dx along the horizontal surface. (**c**) Surface roughness under the bulk of the droplet does not affect the contact angle. (**d**) Averaged value of $\Theta(x_0, y_0)$ at the triple is obtained by integration along the square area (*dashed*) with the side δx

Nosonovsky (2007d) showed that for a more complicated case of a nonuniform roughness, given by the profile $z(x)$, the local value of $r(x) = \mathrm{d}t/\mathrm{d}x = (1 + (\mathrm{d}z/\mathrm{d}x)^2)^{1/2}$ matters. In the cases that were studied experimentally by Gao and McCarthy (2007) and Extrand (2003), the roughness was present ($r > 1$) under the bulk of the droplet, but there was no roughness ($r = 0$) at the triple line, and the contact angle was given by (10.9) (Fig. 10.2c). In the general case of a 3D rough surface $z(x, y)$, the roughness factor can be defined as a function of the coordinates $r(x, y) = (1 + (\mathrm{d}z/\mathrm{d}x)^2 + (\mathrm{d}z/\mathrm{d}y)^2)^{1/2}$.

Although (10.9) is valid for uniformly rough surfaces, that is, surfaces with $r = \text{const}$, for nonuniformly rough surfaces, the generalized Wenzel equation is formulated to determine the local contact angle (a function of x and y) with a rough surfaces at the triple line.

$$\cos\theta = r(x, y)\cos\theta_0. \tag{10.10}$$

Equation (10.10) is consistent with the experimental results of the scientists, who showed that roughness beneath the droplet does not affect the contact angle, since it predicts that only roughness at the triple line matters. It is consistent also with the results of the researchers who confirmed the Wenzel equation (for the case of

Table 10.2 Summary of experimental results for uniform and nonuniform rough and chemically heterogeneous surfaces

Experiment	Roughness/ hydrophobicity at the triple line and at the rest of the surface	Roughness at the bulk (under the droplet)	Experimental contact angle (compared with that at the rest of the surface)	Theoretical contact angle, Wenzel–Cassie equations	Theoretical contact angle, generalized Wenzel–Cassie (10.3 and 10.4)
Gao and McCarthy (2007)	Hydrophobic	Hydrophilic	Not changed	Decreased	Not changed
	Rough	Smooth	Not changed	Decreased	Not changed
	Smooth	Rough	Not changed	Increased	Not changed
Extrand (2003)	Hydrophilic	Hydrophobic	Not changed	Increased	Not changed
	Hydrophobic	Hydrophilic	Not changed	Decreased	Not changed
Bhushan and Jung (2007)	Rough	Rough	Increased	Increased	Increased
Barbieri et al. (2007)	Rough	Rough	Increased	Increased	Increased

For nonuniform surfaces, the results shown for droplets larger than the islands of nonuniformity. Detailed quantitative values of the contact angle in various sets of experiments can be found in the referred sources (Nosonovsky 2007d)

the uniform roughness) and of those who reported that only the triple line matters (for nonuniform roughness) (Table 10.2).

The Cassie equation for the composite surface can be generalized in a similar manner introducing the spatial dependence of the local densities, f_1 and f_2 of the solid–liquid interface with the contact angle, as a function of x and y, given by

$$\cos\,\theta_{\text{composite}} = f_1\,(x,\,y)\,\cos\,\theta_1 + f_2(x,y)\cos\,\theta_2, \tag{10.11}$$

where $f_1 + f_2 = 1$, θ_1 and θ_2 are contact angles of the two components (Nosonovsky 2007d).

Another way to view the generalized equations is to consider the transition from two components to a big number of surface components and, in the limit, to the continuously changing local contact angle.

$$\cos\theta_{\text{composite}} = \sum f_n \cos\theta_n = \iint_A \cos\theta\,\mathrm{d}x\mathrm{d}y = \oint_T \Theta(x,y)\,\mathrm{d}t, \tag{10.12}$$

where the first integration is performed by the area A of the strip with the thickness δx along the triple line (Fig. 10.2d), the path integration is performed along the triple line T, and the locally averaged value of $\cos\theta$ is given by

$$\Theta(x_0,y_0) = \int_{x_0-\delta x/2}^{x_0+\delta x/2}\int_{y_0-\delta x/2}^{y_0+\delta x/2} \cos\theta\,\mathrm{d}x\mathrm{d}y. \tag{10.13}$$

If the local value of the cosine is given by $\cos\theta = f_1(x_0, y_0)\cos\theta_1 + f_2(x_0, y_0)\cos\theta_2$, then

$$\Theta(x_0, y_0) = \int_{x_0-\delta x/2}^{x_0+\delta x/2}\int_{y_0-\delta x/2}^{y_0+\delta x/2} f_1(x,y)\,\mathrm{d}x\mathrm{d}y + \cos\theta_2 \int_{x_0-\delta x/2}^{x_0+\delta x/2}\int_{y_0-\delta x/2}^{y_0+\delta x/2} f_2(x,y)\,\mathrm{d}x\mathrm{d}y, \tag{10.14}$$

and (10.12) yield (10.11). Note that the difference between (10.12) and the conventional Cassie equation (10.4) is that only the area A of the strip next to the triple line is considered and not the entire solid–liquid area. It is noted also that the path integration in (10.14) should not necessarily be performed through the entire triple line, but rather through a part of it. The apparent contact angle given by (10.18) can be observed at a large distance from the solid surface, comparing with the length of T, so that the effect of local heterogeneities smoothens. This is possible, for example, if the roughness or heterogeneity has an axisymmetric distribution or constant along the triple line.

The important question remains, what should be the typical size of roughness/heterogeneity details, in order for the generalized Wenzel and Cassie equations (10.10) and (10.11) to be valid. Some scholars have suggested that roughness/heterogeneity details should be comparable with the thickness of the liquid–vapor interface and thus "the roughness would have to be of molecular dimensions to alter the equilibrium conditions" (Bartell and Shepard 1953), whereas others have claimed that roughness/heterogeneity details should be small compared to the linear size of the droplet (Johnson and Dettre 1964; Li and Amirfazli 2006; Bhushan and Jung 2007; Barbieri et al. 2007). The interface in our analysis is an idealized 2D object, which has no thickness. In reality, the triple line zone has two characteristic dimensions: the thickness (of the order of molecular dimensions) and the length (of the order of the droplet size).

The apparent contact angle, given by (10.10) and (10.11), may be viewed as the result of averaging of the local contact angle at the triple line by its length, and thus the size of the roughness/heterogeneity details should be small compared to the length (and not the thickness) of the triple line. A rigorous definition of the generalized equation requires the consideration of several scale lengths. The length $\mathrm{d}x$ needed for averaging of the energy gives the length over which the averaging is performed to obtain $r(x, y)$. This length should be larger than roughness details. However, it is still smaller than the droplet size and the length scale at which the apparent contact angle is observed (at which local variations of the contact angle level out). Since of these three lengths (the roughness size, $\mathrm{d}x$, the droplet size), the first and the last are of practical importance, we conclude that the roughness details should be smaller than the droplet size. When the liquid–vapor interface is studied at the length scale of roughness/heterogeneity details, the local contact angle, θ_0, is given by the Young equation. The liquid–vapor interface at that scale has perturbations, caused by the roughness/heterogeneity, and the scale of the perturbations is the same as the scale of the roughness/heterogeneity details.

However, when the same interface is studied at a larger scale, the effect of the perturbation vanishes, and apparent contact angle is given by (10.10) and (10.11). This apparent contact angle is defined at the scale length, for which the small perturbations of the liquid–vapor interface vanish, and the interface can be treated as a smooth surface. The values of $r(x, y), f_1(x, y), f_2(x, y)$ in (10.10) and (10.11) are average values by area (x, y) with size larger than a typical roughness/heterogeneity detail size. Therefore, the generalized Wenzel and Cassie equations can be used at the scale, at which the effect of the interface perturbations vanish, or, in other words, when the size of the solid surface roughness/heterogeneity details is small compared to the size of the liquid–vapor interface, which is of the same order as the size of the droplet.

We used the surface energy approach to find the domain of validity of the Wenzel and Cassie equations (uniformly rough surfaces) and generalized it for a more complicated case of nonuniform surfaces. The generalized equations explain a wide range of existing experimental data, which could not be explained by the original Wenzel and Cassie equations.

10.2 Contact Angle Hysteresis

Contrary to wide-spread perception, contact angle is not a single number and not the only parameter which characterizes adhesion of water to a solid surface. When contact occurs with a rough or chemically heterogeneous surface (and practically all surfaces are rough or heterogeneous to a certain extent), the contact angle can attain a range of values, demonstrating hysteresis. Contact angle hysteresis is small when the solid–liquid adhesion is small and it is large when the adhesion is large. This makes contact angle hysteresis an important parameter characterizing adhesion, hydrophobicity, and energy dissipation during the droplet flow.

10.2.1 Causes of the Contact Angle Hysteresis

If liquid is added to a sessile droplet, the contact line advances and each time motion ceases, the drop exhibits an advancing contact angle. Alternatively, if liquid is removed from the drop, the contact angle decreases to a receding value before the contact retreats. For a droplet, moving along the solid surface (e.g., if the surface is tilted), there is another definition. The contact angle at the front of the droplet (advancing contact angle) is greater than that at the back of the droplet (receding contact angle), due to roughness, resulting in the contact angle hysteresis (Fig. 10.1a). It is arguable whether the two definitions (for added/removed liquid and for a moving droplet at a tilted surface) are equivalent (Krasovitski and Marmur 2004). However, in many cases, the two definitions have the same meaning (Nosonovsky and Bhushan 2007a).

The contact angle hysteresis is the measure of energy dissipation during the flow of a droplet. The exact reasons for contact angle hysteresis are not known, although it is clear that they are related with surface heterogeneity and roughness at various scales (Johnson and Dettre 1964; Nosonovsky and Bhushan 2007a). The dissipation that leads to contact angle hysteresis may occur either (1) in the bulk volume of the droplet; (2) at the solid–liquid contact area; (3) near the solid–liquid–air contact line (the triple line). While the bulk interactions involving liquid viscosity are eliminated in the quasi-static case (very low flow velocity), both the contact area interactions (due to so-called adhesion hysteresis) and triple line interactions (due to pinning of the triple line by roughness details) remain significant even at the limit of zero flowing velocity. Nosonovsky and Bhushan (2008b) suggested that contact angle hysteresis, as well as the wetting regime transition, involves self-organized criticality. Adding liquid to a droplet is similar to adding grains to a sandpile. The triple line tends to be pinned at the "critical locations," such as the edges of the microstructures, which serve as attractors. After that the triple line suddenly advances to its new location.

10.2.2 Pinning of the Triple Line

A sharp edge can pin the line of contact of the solid, liquid, and air (also known as the "triple line") at a position far from stable equilibrium, i.e., at contact angles different from θ_0 (Eustathopoulos et al. 1999). This effect is illustrated in the bottom sketch of Fig. 10.3, which shows a droplet, propagating along a solid surface with grooves. At the edge point, the contact angle is not defined and can have any value between the values corresponding to the contact with the horizontal and inclined surfaces. For a droplet moving from left to right, the triple line will be pinned at the edge point until it will be able to proceed to the inclined plane. As it is observed from Fig. 10.3, the change of the surface slope (α) at the edge is the reason, which causes the pinning. Because of the pinning, the value of the contact angle at the front of the droplet (dynamic maximum advancing contact angle or $\theta_{adv} = \theta_0 + \alpha$) is greater than θ_0, whereas the value of the contact angle at the back of the droplet (dynamic minimum receding contact angle or $\theta_{rec} = \theta_0 - \alpha$) is smaller than θ_0, This phenomenon is known as the contact angle hysteresis (Johnson and Dettre 1964; Israelachvili 1992; Eustathopoulos et al. 1999). An hysteresis domain of the dynamic contact angle is thus defined by the difference $\theta_{adv} - \theta_{rec}$. The liquid can travel easily along the surface if the contact angle hysteresis is small. It is noted, that the static contact angle lies within the hysteresis domain, therefore, increasing the static contact angle up to the values of a superhydrophobic surface (approaching 180°) will result also in reduction of the contact angle hysteresis. In a similar manner, the contact angle hysteresis also can exist even if the surface slope changes smoothly, without sharp edges.

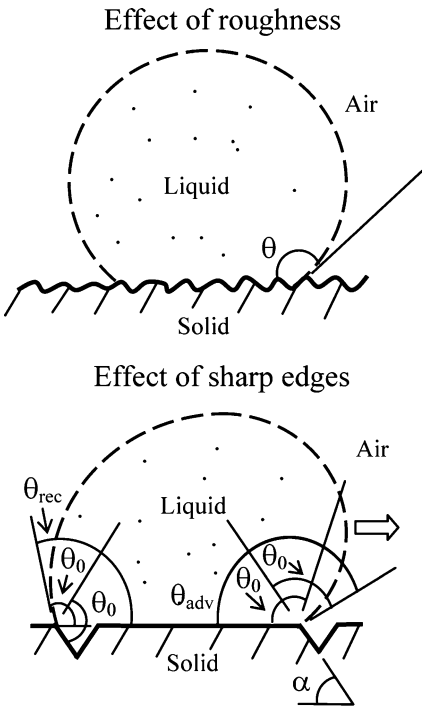

Fig. 10.3 Droplet of liquid in contact with a solid surface–smooth surface, contact angle θ_0; rough surface, contact angle θ; and a surface with sharp edges. For a droplet moving from left to right on a sharp edge (shown by an *open arrow*), the contact angle at a sharp edge may be any value between the contact angle with the horizontal plane and with the inclined plane. This effect results in difference of advancing ($\theta_{adv} = \theta_0 + \alpha$) and receding ($\theta_{rec} = \theta_0 - \alpha$) contact angles (Nosonovsky and Bhushan 2005a, b)

10.2.3 Contact angle Hysteresis and the Adhesion Hysteresis

The contact angle hysteresis is related to the more general phenomenon known as adhesion hysteresis, which is observed also during solid–solid contact (Chen et al. 1991; Yoshizawa et al. 1993). When two solid surfaces come in contact, the energy required to separate them is always greater than the energy gained by bringing them together, and thus the loading–unloading cycle is a thermodynamically irreversible dissipative process (Chen et al. 1991; Yoshizawa et al. 1993; Maeda et al. 2002; Zeng et al. 2006; Ruths and Israelachvili 2007). It was argued that for adhesive dry friction, the frictional shear stress is related to the adhesion hysteresis, rather than the adhesion per se. However, currently, there is no quantitative theory relating the adhesion hysteresis with friction in a manner consistent with the experimental data.

When liquid comes in contact with a solid, the solid–liquid interface is created while solid–vapor and liquid–vapor interfaces are destroyed. The work of adhesion between the liquid and the solid per unit area is given by the Dupré equation

$$W = \gamma_{SV} + \gamma_{LV} - \gamma_{SL} = \gamma_{LV}(1 + \cos\theta). \tag{10.15}$$

As stated earlier, the energy gained for surfaces coming into contact is greater than the energy required for their separation (or the work of adhesion) by the quantity ΔW, which constitutes the adhesion hysteresis. For a smooth surface,

the difference between the two values of the interface energy (measured during loading and unloading) is given by ΔW_0. These two values are related to the advancing contact angle, θ_{adv0}, and receding contact angle, θ_{rec0}, of the smooth surface, assuming that for a smooth surface, the adhesion hysteresis is the main contributor to contact angle hysteresis.

$$\cos\theta_{adv0} - \cos\theta_{rec0} = \frac{\Delta W_0}{\gamma_{LV}}. \tag{10.16}$$

For a composite interface with a micropatterned surface built of flat-top columns ($R_f = 1$), the fraction of the solid–liquid area is given by f_{SL}, so the adhesion hysteresis of a rough surface, ΔW, is related to that of a smooth surface, ΔW_0, as $\Delta W = f_{SL}\Delta W_0$, while the term that includes the surface roughness effect, H_r, should be added. The contact angle hysteresis is then given by

$$\cos\theta_{adv} - \cos\theta_{rec} = \frac{\Delta W}{\gamma_{LV}} + H_r = \frac{f_{SL}\Delta W_0}{\gamma_{LV}} + H_r = f_{SL}(\cos\theta_{adv0} - \cos\theta_{rec0}) + H_r, \tag{10.17}$$

where θ_{adv} and θ_{rec} are the advancing and receding contact angles for a rough surface (Nosonovsky 2007b; Bhushan and Jung 2007). It is assumed that for a rough surface, the contact angle hysteresis involves two terms, ΔW corresponding to the adhesion hysteresis and the roughness parameter H_r, corresponding to the surface roughness. It is observed from (10.17) that small values of f_{SL} provide both a high contact angle and low contact angle hysteresis. Thus, the effect of the adhesion hysteresis is due to the change of the solid–liquid area, f_{SL}. The first term in the right-hand part of (10.17), which corresponds to the inherent contact angle hysteresis of a smooth surface, is proportional to the fraction of the solid–liquid contact area, f_{SL}. The second term, H_r, may be assumed to be proportional to the length density of the pillar edges, or, in other words, to the length density of the triple line (Bhushan and Jung 2007). Thus, (10.17) involves both the term proportional to the solid–liquid interface area and to the triple line length.

Now let us consider the term corresponding to the roughness, H_r. During motion, the droplet passes from one metastable state to another, and these states are separated by energy barriers. For an exact theoretical calculation of the contact angle hysteresis, a thermodynamic analysis of energy barriers for a moving droplet would be required, which is a complicated problem in the case of the three-dimensional geometry. For many practical applications, the case of microfabricated patterned surfaces with small three-dimensional pillars uniformly distributed along the surface is especially important. The main contribution of roughness is expected to be from the sharp edges of the pillars, which may pin a moving droplet. Therefore, the surface roughness term is assumed to be proportional to the density of the edges, which is equal to the perimeter of a pillar, πD, times the number of pillars per unit area, $1/P^2$.

$$H_r \propto \frac{D}{P^2}, \tag{10.18}$$

where D is the diameter of the pillars, P is the pitch distance between them. It is convenient to introduce a nondimensional parameter proportionality constant c, and thus (10.18) is written as

$$H_r = cS_f^2 = (cD)\frac{D}{P^2} \tag{10.19}$$

where $S_f = D/P$ is the nondimensional spacing factor (Nosonovsky and Bhushan 2007a, b).

In the preceding chapters, we studied the solid–solid friction and the effect of the adhesion hysteresis upon it. The solid–solid friction involves two major mechanisms: the adhesion (including adhesion hysteresis) and roughness-dependent mechanisms, such as the deformation. In a somewhat similar manner, the solid–liquid dissipation, characterized by the contact angle hysteresis, involves two mechanisms: the adhesion hysteresis and pinning of the triple line. While the first mechanism is "two-dimensional" in the sense that the dissipation is proportional to the contact area, the second is "one-dimensional" in the sense that the dissipation is proportional to the triple line length. One mechanism involves "rolling" of a droplet while the other one involves its "sliding."

We presented here the theory of roughness-induced superhydrophobicity. The Wenzel and Cassie–Baxter equations provide the contact angle with rough and heterogeneous surfaces. The range of applicability of these equations was discussed. We also discussed the contact angle hysteresis and found that it is governed by two factors: the adhesion hysteresis which is inherently present at any surface due to the nanoscale roughness or heterogeneity and the kinetic effects related to pinning of the triple line. Two wetting regimes are possible: the homogeneous (Wenzel) regime and composite (Cassie) regime with air bubbles trapped between the solid and liquid. For practical applications, the composite regime is required, because it results in a low contact angle hysteresis and, therefore, low rates of dissipation and low adhesion, as well as in high contact angle. The transition between the Cassie and Wenzel regimes for micropatterned superhydrophobic surfaces was discussed. While the exact micro- and nanoscale mechanism of this transition is still not clear, the experimental data suggest that simple microscale geometrical parameters control this transition.

Wetting of a micropatterned surface is a complicated process that involves process at several scale levels. While the macroscale parameters, such as the contact angle and contact angle hysteresis, may be determined approximately by macroscale equations, such as (10.5)–(10.10), these equations do not provide a complete description of the macroscale behavior of system. The contact angle hysteresis is dependent upon micro- and nanoscale effects that control energy dissipation due to the adhesion, kinetic effects, and the fine structure of the triple line. As is shown in the following chapter, the Cassie–Wenzel wetting state transition is also governed by these micro- and nanoscale effects as well as by dynamic effects such as the capillary waves. Furthermore, the very concept of the contact angle is relevant only at the macro- and to some extent, at the microscale,

while at the lower scale such effects are layer and precursor formation, disjoining pressure, surface heterogeneity, contact line tension, and a finite thickness of the liquid–vapor interface dominate. Therefore, despite its apparent simplicity, a droplet upon a rough surface constitutes a multiscale system. In order to control wetting, it is necessary to control parameters at different scale levels. It is not surprising that biological superhydrophobic surfaces have roughness at different scale lengths.

Three types of dissipative process contribute to contact angle hysteresis: interactions in the bulk of the drop, at the solid–liquid contact surface, and at the triple line. While the bulk interactions are a result of liquid viscosity and they can be excluded by considering the quasi-static case (slow motion), the contact surface and triple line interactions remain significant even in the quasi-static limit. The contribution of the contact surface is similar to that of the adhesion hysteresis – the difference in energy required to separate two media (the solid and liquid in this case) and the energy gained by bringing them together. The contribution of the triple line interaction is due to the roughness and pinning of the triple line at rough surface edges. It has been suggested that these two mechanisms are similar to the mechanisms of dry sliding and rolling friction.

10.2.4 Simulation and Semiempirical Models

The task of predicting contact angle hysteresis for a rough surface with a given topography remains a difficult one. A number of simulations have been conducted; however, in most cases they are limited to the 2D topography. Kusumaatmaja and Yeomans (2007) showed that the contact angle hysteresis is sensitive to the details of the surface patterning.

Vedantam and Panchagnula (2007) suggested to use a semiempirical phase field method, which had been used successfully to study various wetting transitions. In this method, the order-parameter $\eta(x, y)$ is selected in such a manner that $\eta = 0$ for the nonwetted regions of the surface and $\eta = 1$ for wetted regions, whereas $0 < \eta < 1$ for partially wetted regions. After that the energy function $f(\eta)$ is constructed in such a manner that the free surface energy can be expressed as

$$E = \int_A f(\eta)\,\mathrm{d}A = \int_{A_{\mathrm{SV}}} f(0)\,\mathrm{d}A + \int_{A_{\mathrm{SL}}} f(1)\,\mathrm{d}A + \int_{A_{(0<\eta<1)}} f(\eta)\,\mathrm{d}A, \tag{10.20}$$

where integration is performed by the area. The function $f(\eta)$ can be built in a somewhat arbitrary manner, however, its minima should correspond to the equilibrium states of the system (e.g., the Wenzel and Cassie states). After that, the energy function is written as

$$L = \int_A \left\{ f(\eta) + \frac{\lambda}{2} |\Delta f(\eta)|^2 \right\} \mathrm{d}A, \tag{10.21}$$

where λ is the gradient coefficient. The function that should be minimized involves the free energy and the gradient of the free energy. The later term is needed to account for the fact that creating an interface between two phases is energetically unprofitable. The kinetic equation is given in the form

$$\beta\eta = -\frac{\mathrm{d}L}{\mathrm{d}\eta} = \lambda\nabla^2\eta - \frac{\partial f}{\partial\eta}, \tag{10.22}$$

where $\beta > 0$ is the kinetic coefficient. In the simplest case, it may be assumed that $\beta = \text{const}$, whereas in the general case a more complicated functional dependence upon η and its derivatives may exist. Vedantam and Panchagnula (2007) showed that in the case of $\beta = \text{const}$ for an axisymmetric drop flowing with the velocity V, (10.22) leads to

$$\cos\theta_{\mathrm{adc}} - \cos\theta_{\mathrm{rec}} = 2\alpha\beta V. \tag{10.23}$$

In other words, assuming that the kinetic coefficient is constant, the contact angle hysteresis is expected to be proportional to the flow velocity. A more complicated form of the kinetic coefficient may lead to a more realistic dependence of the contact angle hysteresis on the velocity.

The phase field method also accounts in a natural way for the contact line tension term and leads to the Boruvka and Neumann (1977) equation

$$\cos\theta = \frac{\gamma_{\mathrm{SV}} - \gamma_{\mathrm{SL}}}{\gamma_{\mathrm{LV}}} - \frac{\tau K}{\gamma_{\mathrm{LV}}}, \tag{10.24}$$

where K is the curvature and τ is the contact line tension. The gradient term in (10.22) implies that the transition between the wetted and unwetted parts of the surface is associated with excess energy, or, in other words, that bending of the phase boundary line at the phase field plane is energetically unprofitable. The contact line term in (10.24) corresponds to this additional contour line energy. As it was already shown, it is important for micrometrically scaled drops only (Pompe et al. 2000). The phase field method seems also promising for the analysis of the Cassie–Wenzel transition.

A semiphenomenological model of the contact angle hysteresis has been proposed recently by Whyman, Bormashenko, and Stein. According to their model, the contact angle hysteresis is given by the equation: $\theta_{\mathrm{adv}} - \theta_{\mathrm{rec}} = (8U/\gamma R_0)^{1/2} h(\theta^*)$ where U is the height of the potential barrier connected with the motion of the triple line along a substrate, R_0 is the initial radius of the spherical drop before deposition on the substrate, $h(\theta^*)$ is the dimensionless function of the apparent contact angle θ^*.

10.3 The Cassie–Wenzel Transition

The homogeneous solid–liquid interface and the composite solid–liquid–air interface correspond to two distinct wetting states called also Wenzel and Cassie states. In the Wenzel state, the contact area between solid and liquid is high, and, therefore,

adhesion can be high. Furthermore, contact angle hysteresis would tend to increase with increasing roughness, since the pinning effect and contact area would tend only to grow. Therefore, the composite Wenzel interface is needed for true superhydrophobicity and measures should be taken to avoid the destabilization of the composite interface or its transition into the Wenzel state.

It has been known from experimental observations of micropatterned surfaces that the transition from the composite to heterogeneous interface is an irreversible event (Lafuma and Quéré 2003; Barbieri et al. 2007; Bhushan and Jung 2007). Whereas such a transition can be induced, for example, by applying pressure or force to the droplet (Lafuma and Quéré 2003), electric voltage (Krupenkin et al. 2004; Bahadur and Garimella 2007), light for a photocatalytic texture (Feng et al 2004), and vibration (Bormashenko et al. 2007b), the opposite transition has never been observed by mechanical impact on the droplet, although there is no apparent reason for that. An exception is the case of reversible superhydrophobicity when surface energy is modified and tuned by an electrical field or another external action.

Several approaches have been proposed for the investigation of the Cassie–Wenzel transition. Lafuma and Quéré (2003) suggested that the transition takes place when the net surface energy of the Wenzel state becomes equal to that of the Cassie state, or, in other words, when the contact angle predicted by the Cassie equation is equal to that predicted by the Wenzel equation. They noticed that in certain case the transition does not occur even when it is energetically profitable and considered such a Cassie state metastable. Extrand (2003) suggested that the weight of the droplet is responsible for the transition and proposed the contact line density model, according to which the transition takes place when the weight exceeds the surface tension force at the triple line. Patankar (2004a, b) suggested that which of the two states is realized might depend upon how the droplet was formed, that is upon the history of the system. Quéré (2005) also suggested that the droplet curvature (which depends upon the pressure difference between inside and outside of the droplet) governs the transition. Nosonovsky and Bhushan (2006a) suggested that the transition is a dynamic process of destabilization and identified possible destabilizing factors. It has been also suggested that curvature of multiscale roughness defines the stability of the Cassie state (Nosonovsky and Bhushan 2007a; Nosonovsky 2007e) and that the transition is a stochastic gradual process (Bhushan and Nosonovsky 2006b; Nosonovsky and Bhushan 2005a, b; Ishino and Okumura 2006; Bormashenko et al. 2007b). Numerous experimental results support many of these approaches, however, it is not clear which particular mechanism prevails.

There is an asymmetry between the wetting and dewetting processes, since droplet nucleation requires less energy than vapor bubbles nucleation (cavitation). During wetting, which involves creation of the solid–liquid interface, less energy is released than the amount required for dewetting or destroying the solid–liquid interface due to the adhesion hysteresis. Adhesion hysteresis is one of the reasons that leads to the contact angle hysteresis and it results also in the hysteresis of the Wenzel–Cassie state transition. Figure 10.4 shows the contact angle of a rough surface as a function of surface roughness (which is measured, for the Wenzel

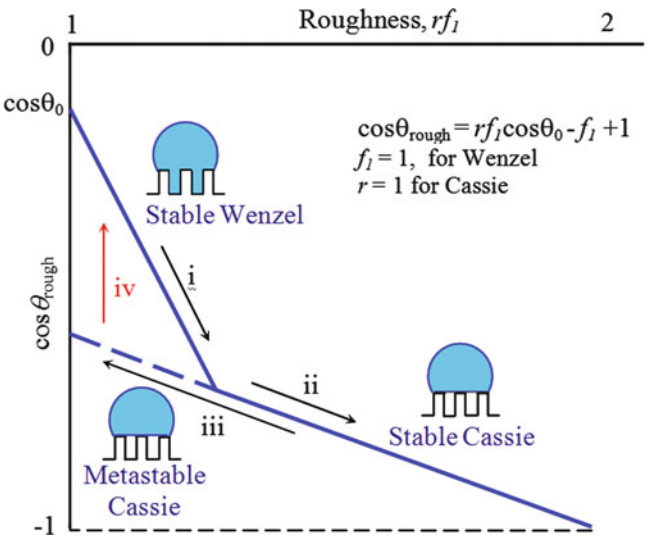

Fig. 10.4 Wetting hysteresis for a superhydrophobic surface. Contact angle as a function of roughness. The stable Wenzel state (i) can transform into the stable Cassie state with increasing roughness (ii). The metastable Cassie state (iii) can abruptly transform (iv) into the stable Wenzel state. The transition (i)–(ii) corresponds to equal Wenzel and Cassie states free energies, whereas the transition (iv) corresponds to a significant energy dissipation and thus it is irreversible (Nosonovsky and Bhushan 2007b)

regime by $r > 1, f_1 = 1$ and for the Cassie regime by $f_1 > 1, r = 1$). It is noted that at a certain point, given by $r = f_1 + (1 - f_1)/\cos\theta_1$, the lines corresponding to the Wenzel and Cassie regimes intersect. This point corresponds to an equal net energy of the Cassie and Wenzel states. For a lower roughness (e.g., larger pitch between the pillars), the Wenzel state is more energetically favorable, whereas for a higher roughness the Cassie state is more energetically favorable.

It is observed from Fig. 10.4 that an increase of roughness may lead to the transition between the Wenzel and Cassie regimes at the intersection point. With decreasing roughness, the system is expected to transit to the Wenzel state. However, experiments show (Bhushan and Jung 2007; Barbieri et al. 2007) that, despite the energy of the Wenzel state being lower than that of the Cassie state, the transition does not necessarily occur and the droplet may remain in the metastable Cassie state. This is because there are energy barriers associated with the transition, which occurs due to destabilization by dynamic effects (such as waves and vibration).

In order to understand the contact angle hysteresis and transition between the Cassie and Wenzel states, the shape of the free surface energy profile can be analyzed. The free surface energy of a droplet upon a smooth surface as a function of the contact angle has a distinct minimum, which corresponds to the most stable contact angle. As shown in Fig. 10.5a, the macroscale profile of the net surface energy allows the determination the contact angle (corresponding to energy minimums), however fails to predict the contact angle hysteresis and Cassie–Wenzel transition,

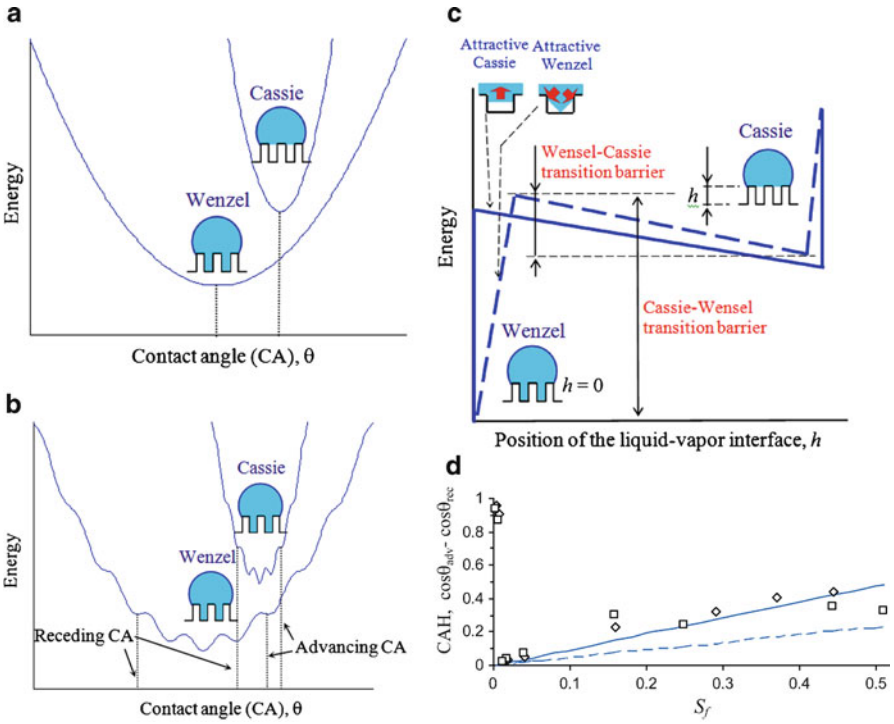

Fig. 10.5 Schematics of net free energy profiles. (**a**) Macroscale description; energy minimums correspond to the Wenzel and Cassie states. (**b**) Microscale description with multiple energy minimums due to surface texture. Largest and smallest values of the energy minimum correspond to the advancing and receding contact angles. (**c**) Origin of the two branches (Wenzel and Cassie) is found when a dependence of energy upon h is considered for the microscale description (*solid line*) and nanoscale imperfectness (*dashed line*), based on (Nosonovsky and Bhushan 2007a, b). When the nanoscale imperfectness is introduced, it is observed that the Wenzel state corresponds to an energy minimum and the energy barrier for the Wenzel–Cassie transition is much smaller than for the opposite transition (**d**) Contact angle hysteresis as a function of S_f for the first (*squares*) and second (*diamonds*) series of the experiments compared with the theoretically predicted values of $\cos\theta_{adv} - \cos\theta_{rec} = (D/P)^2(\pi/4)(\cos\theta_{adv0} - \cos\theta_{rec0}) + c(D/P)^2$, where c is a proportionality constant. It is observed that when only the adhesion hysteresis/interface energy term is considered ($c = 0$), the theoretical values are underestimated by about a half, whereas $c = 0.5$ provides a good fit. Therefore, the contribution of the adhesion hysteresis is of the same order of magnitude as the contribution kinetic effects. (**e**) Droplet radius, R, for the Cassie–Wenzel transition as a function of $P/D = 1/S_f$. It is observed that the transition takes place at a constant value of $RD/P \sim 50$ μm (*dashed line*). This shows that the transition is a linear phenomenon (Nosonovsky and Bhushan 2008a, c). Theoretical (*solid* and *dashed*) and experimental (*squares* for the first series, *diamonds* for the second series) (**f**) contact angle as a function of the spacing factor. (**g**) Advancing contact angle (h), receding contact angle, and values of the contact angle observed after the transition during evaporation (*shaded*) (Nosonovsky and Bhushan 2007a,c)

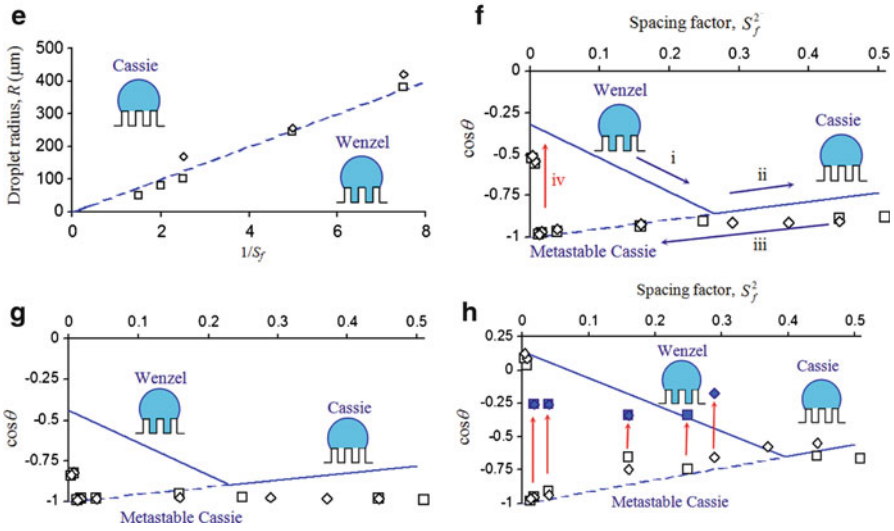

Fig. 10.5 (continued)

which are governed by micro- and nanoscale effects. As soon as the microscale substrate roughness is introduced, the droplet shape can no longer be considered as an ideal truncated sphere, and energy profiles have multiple energy minimums, corresponding to location of the pillars (Fig. 10.5b). The microscale energy profile (solid line) has numerous energy maxima and minima due to the surface micropattern. While exact calculation of the energy profile for a 3D droplet is complicated, a qualitative shape may be obtained by assuming a periodic sinusoidal dependence (Johnson and Dettre 1964), superimposed upon the macroscale profile, as shown in Fig. 10.5b. Thus, the advancing and receding contact angles can be identified as the maximum and the minimum possible contact angles corresponding to energy minimum points. However, the transition between the Wenzel and Cassie branches still cannot be explained. Note also that Fig. 10.5b explains qualitatively the hysteresis due to the kinetic effect of the pillars, but not the inherited adhesion hysteresis, which is characterized by the molecular scale length and cannot be captured by the microscale model.

The energy profile as a function of the contact angle does not provide any information on how the transition between the Cassie and Wenzel states occurs, because these two states correspond to completely isolated branches of the energy profile in Fig. 10.5. However, the energy may depend not only upon the contact angle, but also upon micro/nanoscale parameters, such as, for example, the vertical position of the liquid–vapor interface under the droplet, h (assuming that the interface is a horizontal plane) or similar geometrical parameters (assuming a more complicated shape of the interface). In order to investigate the Wenzel–Cassie transition, the dependence of the energy upon these parameters should be studied. We assume that the liquid–vapor interface under the droplet is a flat horizontal plane.

When such vapor layer thickness or the vertical position of the liquid–vapor interface, h, is introduced, the energy can be studied as a function of droplet's shape, the contact angle, and h (Fig. 10.5c). For an ideal situation, the energy profile has an abrupt minimum at the point corresponding to the Wenzel state, which corresponds to the sudden net energy change due to destroyer solid–vapor and liquid–vapor interfaces [$\gamma_{SL} - \gamma_{SV} - \gamma_{LV} = -\gamma_{LV}(\cos\theta + 1)$ times the interface area] (Fig. 10.5c). In a more realistic case, the liquid–vapor interface cannot be considered horizontal due to nanoscale imperfectness or dynamic effects such as capillary waves (Nosonovsky and Bhushan 2006a). A typical size of the imperfectness is much smaller than the size of details of the surface texture and thus belongs to the molecular scale level. The height of the interface, h, can now be treated as an average height. The energy dependence upon h is now not as abrupt as in the idealized case. For example, the "triangular" shape as shown in Fig. 10.5c, the Wenzel state, may become the second attractor for the system. It is seen that there are two equilibriums, which correspond to the Wenzel and Cassie states, with the Wenzel state corresponding to a much lower energy level. The energy dependence upon h governs the transition between the two states and it is observed that a much larger energy barrier exists for the transition from Wenzel to Cassie than for the opposite transition. This is why the first transition has never been observed experimentally.

We investigated the Cassie–Wenzel wetting regime transition of micropatterned superhydrophobic surfaces by water droplets and found several effects specific for the multiscale character of this process. First, we discussed applicability of the Wenzel and Cassie equations for average surface roughness and heterogeneity. These equations relate the local contact angle with the apparent contact angle of a rough/heterogeneous surface. However, it is not obvious what should be the size of roughness/heterogeneity averaging, since the triple line, at which the contact angle is defined has two very different scale lengths: its width is of molecular size scale while its length is of the order of the size of the droplet (i.e., microns or millimeters). We presented an argument that in order for the averaging to be valid, the roughness details should be small compared to the size of the droplet (and not the molecular size). We showed that while for the uniform roughness/heterogeneity, the Wenzel and Cassie equations can be applied; for a more complicated case of the nonuniform heterogeneity, the generalized equations should be used. The proposed generalized Cassie–Wenzel equations are consistent with a broad range of available experimental data. The generalized equations are valid both in the cases when the classical Wenzel and Cassie equations can be applied as well as in the cases when the later fail.

The macroscale contact angle hysteresis and Cassie–Wenzel transition cannot be determined from the macroscale equations and are governed by micro- and nanoscale effects, so wetting is a multiscale phenomenon. The kinetic effects associated with the contact angle hysteresis should be studied at the microscale, whereas the effects of the adhesion hysteresis and the Cassie–Wenzel transition involve processes at the nanoscale. Theoretical arguments are supported by experimental data on micropatterned surfaces. The experimental study of the contact angle hysteresis demonstrates that two different processes are involved: the changing

solid–liquid area of contact and pinning of the triple line. The latter effect is more significant for the advancing than for the receding contact angle. The transition between wetting states was clearly observed for evaporating microdroplets in ESEM and droplet radius scales with the geometric parameters of the micropattern. These findings provide new insights on the fundamental mechanisms of wetting and can lead to creation of successful nonadhesive surfaces.

The mechanisms that control the Cassie–Wenzel transition for micropatterned surfaces act at various scale levels and thus the transition is a multiscale process. Although the state of the droplet is described by a macroscale parameter, the contact angle, the value of the contact angle depends on the wetting state, and, therefore, is determined by macro-, micro-, and nanoscale processes. We conclude that contact angle hysteresis and the Cassie–Wenzel transition cannot be determined from the macroscale equations and are governed by micro- and nanoscale phenomena. Our theoretical arguments are supported by our experimental data on micropatterned surfaces.

10.4 Effect of the Hierarchical Roughness

Many natural superhydrophobic surfaces have hierarchical or multiscale roughness usually built of submicron-sized details superimposed upon lager scale (usually, microns or dozens of microns) details. Although superhydrophobicity has been observed on single-scale (nonhierarchical) surfaces, it is believed that the hierarchical structure is very essential for robust superhydrophobic surfaces. The reason for that is that wetting is a multiscale phenomenon. The hierarchical (multiscale) roughness is needed to deal with processes at various scale levels and, in particular, to maintain a stable composite interface.

10.4.1 Wetting as a Multiscale Phenomenon

Wetting can be viewed as a multiscale process that involves effects at different scale levels (Nosonovsky and Bhushan 2007a). Unlike many classical systems studied by thermodynamics and statistical physics, a droplet upon a superhydrophobic surface is a multiscale system in the sense that its macroscale properties, such as contact angle and contact angle hysteresis, cannot be determined only from macroscale equations, and thus it cannot be treated as a closed macroscale system. While macroscale thermodynamic analysis allows predictions of the contact angle for both Wenzel and Cassie states, the transition between these two states and the contact angle hysteresis involve processes and instabilities at the micron scale (such as pinning of the triple line) and at the molecular scale (such as the inherent adhesion hysteresis).

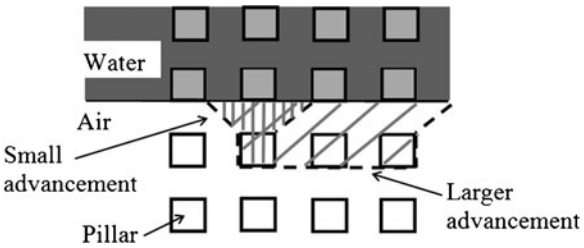

Fig. 10.6 Schematic of liquid advancement upon a micropatterned surface build of square pillars (*top view*). The wetted region is *gray*. The triple line tends to sit at the edges of the pillars (a "critical state"). When the advancement is triggered, the liquid can advance for a small distance or for a large distance, causing an "avalanche" (Nosonovsky and Bhushan 2008a, b)

A truly multiscale approach would be to isolate the effects at each length scale and then incorporate the information at the other scales in some systematic manner.

Additional evidence that the superhydrophobic interface is a multiscale system is the possibility of self-organized behavior. Nosonovsky and Bhushan (2008b) suggested that contact angle hysteresis and the Cassie–Wenzel transition are natural candidates for self-organized criticality (SOC). Adding liquid to a droplet is similar to adding grains to a sandpile. The triple line tends to be pinned at the "critical locations," such as the edges of the microstructures, which serve as attractors (Fig. 10.6). After that the triple line suddenly advances to its new location in an "avalanche-like" behavior, the Cassie–Wenzel transition occurs in a similar manner with water either gradually filling some valleys, or, in an "avalanche" manner filling all values at once. If contact angle hysteresis and the Cassie–Wenzel transition indeed involve SOC, relevant parameters (such as the number of valleys filled in a unit of time) should be related by a "power law" and the "one-over-frequency" noise law should be present. There is evidence that the Cassie–Wenzel transition occurs gradually through consequent filling of valleys, rather than abruptly (Bormashenko et al. 2007a, b) and there is evidence of power-law behavior in the contact angle hysteresis for regular surfaces (di Meglio 1992). However, it still remains to be verified experimentally by investigating the kinetics of the droplet flow and the Cassie–Wenzel transition, in order to determine whether SOC is involved.

Since fractals have been introduced into surface mechanics (Majumdar and Bhushan 1991), arguments continue as to whether the fractal geometry provides an adequate description of physical phenomena and scaling issues (Greenwood and Wu 2001). With advances of nanotechnology, different views on scale effect and scaling laws emerged, as well as on whether the scaling laws are explained by physics of the involved processes, or by pure geometry (Carpinteri and Pugno 2005), including the fractal geometry. Unlike a fractal surface, which is a pure geometrical object and has no characteristic scale length, a hierarchical surface has a set of immanent scale lengths l_N ($l_1 << l_2 << \cdots << l_N$, where N is the number of hierarchy levels), which are related to the physics of relevant processes, rather than to the geometry. In the biomimetic superhydrophobic surfaces, various levels

of hierarchy are related to various physical mechanisms, which act simultaneously and have different characteristic length scales.

Roughness is the central property for biomimetic superhydrophobic surfaces. It is very important to correctly assess the roughness effect on wetting in order to design successful superhydrophobic nonadhesive surfaces. This requires a roughness description that takes into account complicated wetting mechanisms but at the same time is universal enough to include diverse natural and artificial forms. However, traditional roughness parameters, both statistical and fractal, do not fit well to the mechanisms of the superhydrophobicity, such as pinning of the triple line, adhesion hysteresis, composite interface destabilization, and wetting regime transition. Therefore, new parameters are needed. Two simple roughness parameters that have been suggested are the roughness factor that characterizes the density change of surface energy due to the roughness, and the spacing factor for patterned surfaces that characterizes the change of the contact area for the composite interface. These simple parameters are useful; however, a deeper understanding of the effect of roughness on wetting requires an investigation of the multiscale nature of this process. The contact angle hysteresis and the Cassie–Wenzel transition are governed by micro- and nanoscale phenomena that involve a number of length parameters. Roughness descriptions that are based on the hierarchical organization of surfaces and a hierarchy of length scales should be used for the design of superhydrophobic surfaces (Nosonovsky and Bhushan 2008a).

10.4.2 Hierarchical Roughness

Although there is a significant amount of literature about superhydrophobicity and numerous attempts to produce artificial biomimetic roughness-induced hydrophobic surfaces have been made (Yost et al 1995; Shibuichi et al. 1996; Onda et al. 1996; Feng et al. 2006; Erbil et al. 2003; Patankar 2004a, b; Cheng et al. 2005; Sun et al. 2005; Wang et al. 2006), but many details of the mechanism of roughness-induced nonwetting are still not well understood. In particular, it is not clear why the lotus leaf and other natural hydrophobic surfaces have a multiscale (or hierarchical) roughness structure, that is, nanoscale bumps superimposed on microscale asperities. Gao and McCarthy (2006) recently suggested that multiscale roughness affects kinetics of droplet motion and the Laplace pressure at which water intrudes between the bumps. In the present study, we investigate the effect of the multiscale roughness upon stability of the roughness-induced hydrophobic interface.

Wetting of a solid by a liquid is characterized by the contact angle, which is the angle between the solid–air and the liquid–air interfaces. The greater the contact angle, the more hydrophobic is the material. The value of the contact angle is usually greater, when the liquid is added (so-called advancing contact angle), than when it is removed (receding contact angle). The difference between the advancing and receding contact angle constitutes the contact angle hysteresis. The contact angle hysteresis is related to energy barriers, which a liquid droplet should overcome during its flow along a solid

surface, and thus characterizes resistance to the flow. The lower is adhesion of a liquid droplet to the solid; the smaller are the energy barriers and the lower is the value of contact angle hysteresis and the easier it is for the droplet to flow along the surface.

Several mechanisms are responsible for superhydrophobicity of natural surfaces, such as lotus leaves. First, these surfaces are coated with wax, which is hydrophobic itself (with values of contact angle of about 103°, Kamusewitz et al. 1999); second, they have a complicated geometrical structure with bumps or asperities (in the case of plant leaves called *papillae*) on the microscale (for the leaf of lotus the typical size of papillae is of the order of 10 μm) covered with much smaller nanoscale bumps or nanometer-scale structures (Quéré 2005; Cheng et al. 2005). In a similar manner, water strider legs are covered with a large number of oriented tiny hair (microsetae) with fine nanogrooves (Gao and Jiang 2004). Neinhuis and Barthlott (1997) suggested that hierarchical surfaces are less vulnerable against mechanical damage of nanostructures and therefore maintain functionality even after damage. Wagner et al. (2003) showed that hierarchically structured surfaces are more readily able to repel water even if the surfaces tension is drastically reduced as compared to surfaces with only one length scale of roughening. This might be of importance in wetlands or other aquatic habitats where water is often polluted due to decaying plant material and other contaminations reducing surface tension (Wagner et al. 2003). Herminghaus (2000) pointed out that certain self-affine profiles with multiscale roughness may result in superhydrophobic surfaces even for hydrophilic materials. However, theoretical explanation of the predominance of hierarchically structured surfaces in nature remains an important task.

As discussed in the preceding sections, in order to be superhydrophobic, a rough surface should be able to maintain a composite interface with air pockets or bubbles trapped in the valleys between the asperities (Johnson and Dettre 1964; Marmur 2003; Patankar 2004a; Lafuma and Quėrė 2003), as opposed to a homogeneous solid–liquid interface. In many cases, both the composite interface (composite interface) and the homogeneous interface may exist for the same surface, however, only the composite interface provides the required superhydrophobic properties. Furthermore, the composite interface is much less stable than the homogeneous interface, and it may be destroyed by liquid filling the valleys between asperities and form a homogeneous interface, whereas the opposite transition has never been observed (Quéré 2005). The mechanisms of this transition are subject of intensive investigation in recent years (Marmur 2003; Lafuma and Quėrė 2003; Cheng et al. 2005; Nosonovsky and Bhushan 2006a; Nosonovsky 2007e). Among suggested factors, which affect the transition, are the effects of droplet's weight and curvature. For small droplets, surface effects dominate over gravity. The above suggests that stability of a composite interface is a key issue for the design of roughness-induced superhydrophobic surfaces. In this chapter, we formulate a geometrical stability criterion, and then investigate typical two-dimensional and three-dimensional surfaces with roughness at several scale levels. We show that a multiscale (hierarchical) roughness may enhance the stability of a composite interface.

10.4.3 Stability of a Composite Interface and Hierarchical Roughness

Spreading of liquid through porous media with a periodic geometry was studied by several authors (Sharma and Ross 1991; Tsori 2006), however, stability of the composite interface has not been studied in detail in the literature. In this section, a geometrical stability condition for a composite interface will be formulated based on the free energy minimization using Lagrange method of finding a minimum of a function of several variables with constrains. First, we will formulate the extremum criterion and show that it leads to the well-known Young equation, and then a stability criterion will be derived mathematically and its physical meaning will be discussed.

The liquid–air interface is at equilibrium, if the free energy of the solid–liquid–air system reaches its minimum. In order to find local conditional minima of the free surface energy $W = A_{\mathrm{SL}}\gamma_{\mathrm{SL}} + A_{\mathrm{SA}}\gamma_{\mathrm{SA}} + A_{\mathrm{LA}}\gamma_{\mathrm{LA}}$ with the constant volume constraint, $V = V_0$ (this requirement corresponds to the quasi-thermodynamic, i.e., slow evaporation/condensation limit), the Lagrange function is constructed.

$$L(A_{\mathrm{SL}}, A_{\mathrm{SA}}, A_{\mathrm{LA}}, V, \lambda) = A_{\mathrm{SL}}\gamma_{\mathrm{SL}} + A_{\mathrm{SA}}\gamma_{\mathrm{SA}} + A_{\mathrm{LA}}\gamma_{\mathrm{LA}} + p(V - V_0), \qquad (10.25)$$

where A_{SL}, A_{SA}, A_{LA} are areas of the solid–liquid, solid–air, and liquid–air interfaces and γ_{SL}, γ_{SA}, γ_{LA} are corresponding free energies, V_0 is the volume, and p is the Lagrange multiplier (Greenberg 1978), having the dimension of pressure. The corresponding change of L is given by

$$\delta L = \delta A_{\mathrm{SL}}\gamma_{\mathrm{SL}} + \delta A_{\mathrm{SA}}\gamma_{\mathrm{SA}} + \delta A_{\mathrm{LA}}\gamma_{\mathrm{LA}} + \lambda\delta V + \delta p(V - V_0). \qquad (10.26)$$

Note, that the arguments of L are interdependent with $\delta A_{\mathrm{SL}} = -\delta A_{\mathrm{SA}}$, whereas δA_{LA} consists of two terms, $\delta A_{\mathrm{LA}} = \delta A_{\mathrm{LAT}} + \delta A_{\mathrm{LAV}}$. The first term, δA_{LAT}, is due to a change in position of the triple line (line of contact between solid, liquid, and air) and the second, δA_{LAV}, is due to a change of the shape of the liquid–air interface. Furthermore, $\delta A_{\mathrm{LAT}} = \delta A_{\mathrm{SL}} \cos\theta$ from geometrical considerations (Nosonovsky 2007e).

Let us assume that the shape of the liquid–air interface is given parametrically by vector $\vec{r}(u, v)$, where u and v are parameters, which uniquely characterize any point at a surface, and the shape changes slightly.

$$\breve{\vec{r}}(u, v) = \vec{r}(u, v) + \overrightarrow{\delta r}(u, v). \qquad (10.27)$$

The change due to the shape of the liquid–air interface is given by the area of an element of the liquid–air interface $A(u, v)\mathrm{d}u\mathrm{d}v$ times the normal displacement

multiplied by the sum of principal radii of curvature $\vec{n}\overrightarrow{\delta r}\,(1/R_1 + 1/R_2)$, where $\vec{n}$ is the normal vector and R_1, R_2 are the principal radii of curvature.

$$\delta A_{\mathrm{LAV}} = \int_{A_{\mathrm{LA}}} \int \vec{n}\overrightarrow{\delta r}(1/R_1 + 1/R_2) A \,\mathrm{d}u\mathrm{d}v, \tag{10.28}$$

where (Greenberg 1978)

$$A(u,v) = \left[\left(\frac{\partial \vec{r}}{\partial u}\right)^2 \left(\frac{\partial \vec{r}}{\partial v}\right)^2 - \left(\frac{\partial \vec{r}}{\partial u}\,\frac{\partial \vec{r}}{\partial v}\right)^2 \right]^{1/2}. \tag{10.29}$$

The change of volume is given by

$$\delta V = \int_{A_{\mathrm{LA}}} \int \vec{n}\overrightarrow{\delta r} A \,\mathrm{d}u\mathrm{d}v. \tag{10.30}$$

Combining (10.28)–(10.30) and setting $\delta L(\delta A_{\mathrm{SL}}, \delta \boldsymbol{r}, \delta V) = 0$ yield

$$\delta L = \delta A_{\mathrm{SL}} \left[\cos\theta_0 - \frac{\gamma_{\mathrm{SA}} - \gamma_{\mathrm{SL}}}{\gamma_{\mathrm{LA}}} \right] \gamma_{\mathrm{LA}} + \int_{A_{\mathrm{LA}}} \int [\gamma_{\mathrm{LA}}(1/R_1 + 1/R_2) + p]\, \vec{n}\overrightarrow{\delta r} A \,\mathrm{d}u\mathrm{d}v + \lambda \delta V, \tag{10.31}$$

which results in three equations that should be satisfied simultaneously. The first is the Young equation for the contact angle θ_0, which should be satisfied at the points of the triple line, whereas the second equation for the Lagrange multipliers $p = -\gamma_{\mathrm{LA}}(1/R_1 + 1/R_2)$ is satisfied only if the curvature $1/R_1 + 1/R_2$ is a constant independent of u and v throughout the entire liquid–air interface (Nosonovsky 2007e). Physically, of course, this condition reflects Laplace pressure drop through a curved interface The third equation is just the condition of constant volume $V = V_0$ (Nosonovsky 2007e).

In order for the extremum to be a local minimum (rather than maximum) of W, the equilibrium should also satisfy the stability condition $\mathrm{d}^2W > 0$. Differentiating twice $W = A_{\mathrm{SL}}\gamma_{\mathrm{SL}} + A_{\mathrm{SA}}\gamma_{\mathrm{SA}} + A_{\mathrm{LA}}\gamma_{\mathrm{LA}}$ and using $\delta A_{\mathrm{LA}} = \delta A_{\mathrm{SL}} \cos\theta$ yield

$$\mathrm{d}^2W = \mathrm{d}^2A_{\mathrm{SL}} \left[\cos\theta_0 - \frac{\gamma_{\mathrm{SA}} - \gamma_{\mathrm{SL}}}{\gamma_{\mathrm{LA}}} \right] \gamma_{\mathrm{SL}} + \mathrm{d}A_{\mathrm{LA}}\mathrm{d}(\cos\theta) > 0. \tag{10.32}$$

We ignored the effect of changing shape of the liquid–air interface (the term, corresponding to δA_{LAV}), since it is known that $1/R_1 + 1/R_2 = \mathrm{const}$ provides the minimum (rather than maximum) liquid–air interface area condition and only the effect of moving triple line is of interest for us. Using the Young equation,

which is satisfied at the equilibrium, and the fact that $\cos\theta$ decreases monotonically with θ at the domain of our interest, $0 < \theta < 180°$, yields (Nosonovsky 2007e)

$$\mathrm{d}A_{\mathrm{SL}}\mathrm{d}\theta < 0. \tag{10.33}$$

In other words, in order for the interface to be stable, for advancing liquid (increasing A_{SL}) the value of the contact angle should decrease, whereas for receding liquid the contact angle should increase. Note also that for a liquid–air interface coming to the solid surface under the angle θ, an advance of the interface results in the change of energy

$$\begin{aligned}\mathrm{d}W &= \mathrm{d}A_{\mathrm{SL}}(\gamma_{\mathrm{SL}} - \gamma_{\mathrm{SA}}) + \mathrm{d}A_{\mathrm{LA}}\gamma_{\mathrm{LA}} = \mathrm{d}A_{\mathrm{SL}}(\gamma_{\mathrm{SL}} - \gamma_{\mathrm{SA}}) + \mathrm{d}A_{\mathrm{SL}}\gamma_{\mathrm{LA}}\cos\theta \\ &= \mathrm{d}A_{\mathrm{SL}}\gamma_{\mathrm{LA}}\left(-\frac{\gamma_{\mathrm{SA}} - \gamma_{\mathrm{SL}}}{\gamma_{\mathrm{LA}}} + \cos\theta\right) = \mathrm{d}A_{\mathrm{SL}}\gamma_{\mathrm{LA}}(\cos\theta - \cos\theta_0).\end{aligned} \tag{10.34}$$

Thus, if $\theta > \theta_0$, the energy decreases and it is energetically profitable for the liquid to advance, whereas if $\theta < \theta_0$, the liquid would retreat. So, the physical meaning of (10.33) is that for a small advance/retreat of the liquid, it should be more energetically profitable to return to the original position, rather than continue advancing/retreating (Nosonovsky 2007e).

For a two-dimensional surface, since a change of angle $\mathrm{d}\theta$ is equal to the change of slope of the surface, it depends on the sign of curvature of the surface, whether the configuration is stable or not. The convex (bumpy) surface leads to a stable interface, whereas concaved (groovy) surface leads to an unstable interface. The liquid keeps spreading until both the Young equation and (10.33) are satisfied at the triple line and $1/R_1 + 1/R_2 = \text{const}$ at the liquid–air interface, provided the volume of the liquid is conserved. The stability criterion (10.33) can be applied to typical two-dimensional and three-dimensional surfaces with multiscale roughness.

In this section, we consider several surfaces with nanoscale roughness superimposed on larger microscale pillars and investigate the effect of concaved and convex nanoroughness upon the stability of a composite interface. We study the case of an infinitely large reservoir of liquid on top of the pillars. In most applications, liquid droplets of finite size are in contact with a rough surface, however, the size of roughness details is small compared to the size of the droplets and for practical purposes droplet size can be considered infinite.

Consider a two-dimensional structure with rectangular pillars of height h and width a separated by distance b, covered with small semicircular ridges and grooves of radius r (Fig. 10.7a). Since the distance between the pillars is small in comparison with the capillary length, and therefore the effect of gravity is negligible, we can assume that the liquid–air interface is a horizontal plane, and its position is characterized by the vertical coordinate z. The free energy is given by (Nosonovsky 2007e)

$$W = A_{\mathrm{SL}}\gamma_{\mathrm{SL}} + A_{\mathrm{SA}}\gamma_{\mathrm{SA}} + A_{\mathrm{LA}}\gamma_{\mathrm{LA}} = rL\gamma_{\mathrm{LA}}(\sin\alpha - \alpha\cos\theta_0), \quad 0<z<h, \tag{10.35}$$

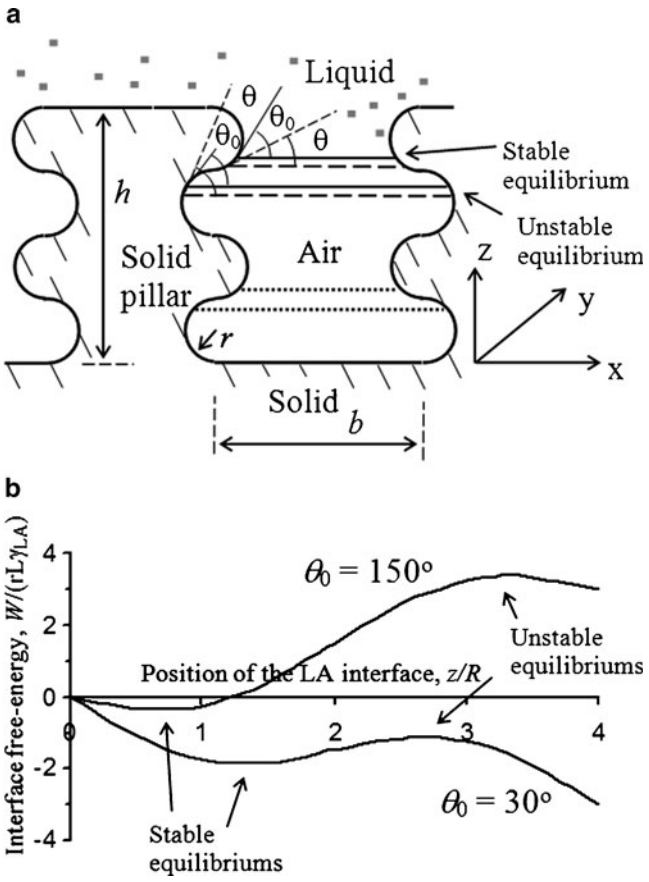

Fig. 10.7 With bumps and grooves for hydrophilic ($\theta_0 = 30°$) and hydrophobic ($\theta_0 = 150°$) materials. Energy (normalized by $Lr\gamma_{LA}$) is shown as a function of vertical position of the interface z (normalized by the radius of bumps/grooves r). Bumps result in stable equilibriums (energy minima), whereas grooves result in unstable equilibriums (energy maxima) (Nosonovsky 2007e)

where $\alpha = a\cos((r - z)/r) + 2\pi N$ is the angle, corresponding to vertical position of the interface z, N is the number of a ridge or groove, and L is the length of the grooves in the y-direction, which is required based on the dimensional considerations. The dependence is presented in Fig. 10.7b, for the cases of hydrophobic ($\theta_0 = 150°$) and hydrophilic ($\theta_0 = 30°$) materials for both the bumpy and the groovy surfaces. It is seen, that for the bumpy surface, there are many states of stable equilibrium (shown in Fig. 10.7a with dotted lines), separated by energy barriers, which correspond to every ridge, whereas for the grooves surface equilibrium states are unstable. Therefore, the ridges can pin the triple line and thus lead to a composite interface. In the case of a hydrophilic surface, each lower position of the equilibrium state corresponds to a lower value of W, therefore, when the liquid advances from one equilibrium state to the next, the total energy decreases and thus

liquid's advance is energetically favorable. When the liquid reaches the bottom of the valley and completely fills the space between the pillars forming a homogeneous interface, the total energy decreases dramatically by the value of

$$\Delta W = bL(\gamma_{SA} + \gamma_{LA} - \gamma_{SL}) = bL\gamma_{LA}(1 + \cos\theta_0).Z \tag{10.36}$$

The opposite transition from an homogeneous interface to composite interface requires high activation energy ΔW and is thus unlikely, making the transition from composite interface to homogeneous interface irreversible. Since the distance between the pillars b is much greater than r, the energy barriers, which separate the equilibrium states, $2\pi rL\gamma_{LA}\cos\theta_0$ are relatively small compared with ΔW, and low activation energy is required for the liquid to spread and propagate from one equilibrium state to the other (Nosonovsky and Bhushan 2007a, b).

Since the change of angle $d\theta$ for a two-dimensional surface is equal to the change of surface slope, based on (10.34), it depends upon the sign of curvature of the surface, whether the configuration is stable or not. The convex (bumpy) surface leads to a stable interface, whereas concaved (groovy) surfaces lead to an unstable interface. The liquid keeps spreading until both (9.10) and (9.12) are satisfied at the triple line and $1/R_1 + 1/R_2 = \text{const}$ at the liquid–air interface, provided the volume of the liquid is conserved, which is the case for a slow thermodynamic process.

Consider now a three-dimensional structure with circular pillars of height h and radius R separated by distance b and distributed hexagonally with the density of $\eta = 2/[\sqrt{3}(2R + b)^2]$ pillars per unit area, covered with small ridges and grooves of radius r (Fig. 10.7a). Similarly to the described in the preceding section, the free energy per area S is given by the circumference of a pillar $2\pi R$ times the number of pillars ηS times $r\gamma_{LA}(\sin\alpha - \alpha\cos\theta_0)$

$$W = 2\pi R\eta S r\gamma_{LA}(\sin\alpha - \alpha\cos\theta_0), \quad 0<z<h, \tag{10.37}$$

The similarity between (10.35) and (10.37) should be noted, both energy profiles are different only in their normalization constant, so the dependence of the free energy upon the position of the interface presented in Fig. 10.7b for the case of two-dimensional pillar, has qualitatively the same profile as for the case of three-dimensional pillars. In a similar manner to the case of two-dimensional pillars, the ridges can pin the triple line (Nosonovsky 2007e).

In the previous sections, we considered two-dimensional nanoscale ridges and grooves superimposed on two- and three-dimensional pillars. Real superhydrophobic surfaces, such as plant leaves, are three-dimensional with three-dimensional nanobumps. For three-dimensional surfaces, the shape of the liquid–air interface may be quite complex and thus the stability of the composite interface is difficult to analyze. In order to consider a three-dimensional configuration which allows for a plane horizontal liquid–air interface, we will investigate the surface, composed of circular pillars of height h and radius R separated by distance b with the density of $\eta = 2/[\sqrt{3}(2R + b)^2]$ pillars per unit area (following the hexagonal distribution pattern shown in Fig. 10.8), which are formed of layers of small spheres of radius r,

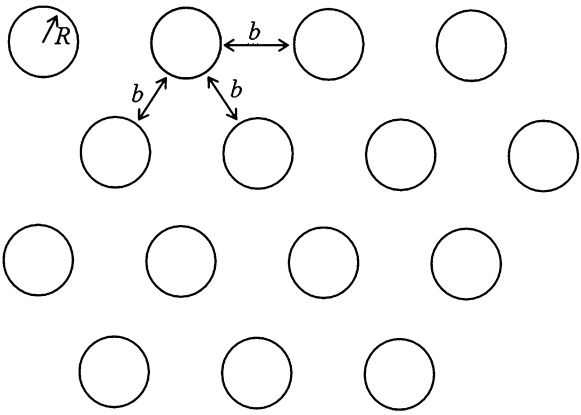

Fig. 10.8 Schematics of spatial distribution of three-dimensional pillars with semicircular bumps/grooves upon a surface (Nosonovsky 2007e)

packed according to the hexagonal pattern (Fig. 10.9). The packing density of the spheres is equal to $1/\left(2\sqrt{3}r^2\right)$ spheres per unit area in every horizontal layer. The liquid–air interface area is now given by the total flat area of the surface, A_0, minus the cross-sectional area of spheres under water. The later is given by A_0 times the pillar density η times the pillar area πR^2 times the packing density of the spheres $1/\left(2\sqrt{3}r^2\right)$ times the cross-sectional area of individual sphere under water, $\pi(r\sin\alpha)^2$, which yields (Nosonovsky 2007e)

$$A_{\mathrm{LA}} = A_0\left(1 - \frac{\eta\pi^2 R^2 \sin^2\alpha}{2\sqrt{3}}\right). \tag{10.38}$$

The solid–liquid interface area is equal to the total surface area of the spheres under water, which is given by the number of spheres $\eta A_0\pi^2R^2/\left(2\sqrt{3}r^2\right)$ times spheres surface area multiplied by the number of layers $4\pi r^2 N$ plus the area of the spheres in the layer, which is only partially under water, $\pi(z^2 + 2z(2r - z))$.

$$A_{\mathrm{SL}} = \frac{\eta A_0\pi^2R^2}{2\sqrt{3}r^2}\left[4r^2N + \left(z^2 + 2z(2r - z)\right)\right]. \tag{10.39}$$

Using $\sin^2\alpha = 1 - \cos^2\alpha = 1 - ((r - z)/r)^2 = 2z/r - (z/r)^2$, the free energy is now given by

$$W = A_{\mathrm{LA}}\gamma_{\mathrm{LA}} + A_{\mathrm{SL}}(\gamma_{\mathrm{LA}} - \gamma_{\mathrm{SA}}) = \gamma_{\mathrm{LA}}(A_{\mathrm{LA}} + A_{\mathrm{SL}}\cos\theta_0)$$
$$= A_0\gamma_{\mathrm{LA}}\left(1 - \frac{\eta\pi^2R^2}{2\sqrt{3}}\left\{2z/r - (z/r)^2 - \left[4\pi N + (z/r)^2 + 2(z/r)(2 - z/r)\right]\cos\theta_0\right\}\right). \tag{10.40}$$

The dependence of the free energy, normalized by $A_0\gamma_{\mathrm{LA}}$, upon the vertical position z is presented in Fig. 10.9 for the cases of hydrophobic ($\theta_0 = 105^{\mathrm{o}}$) and hydrophilic ($\theta_0 = 75^{\mathrm{o}}$) materials (Nosonovsky 2007e).

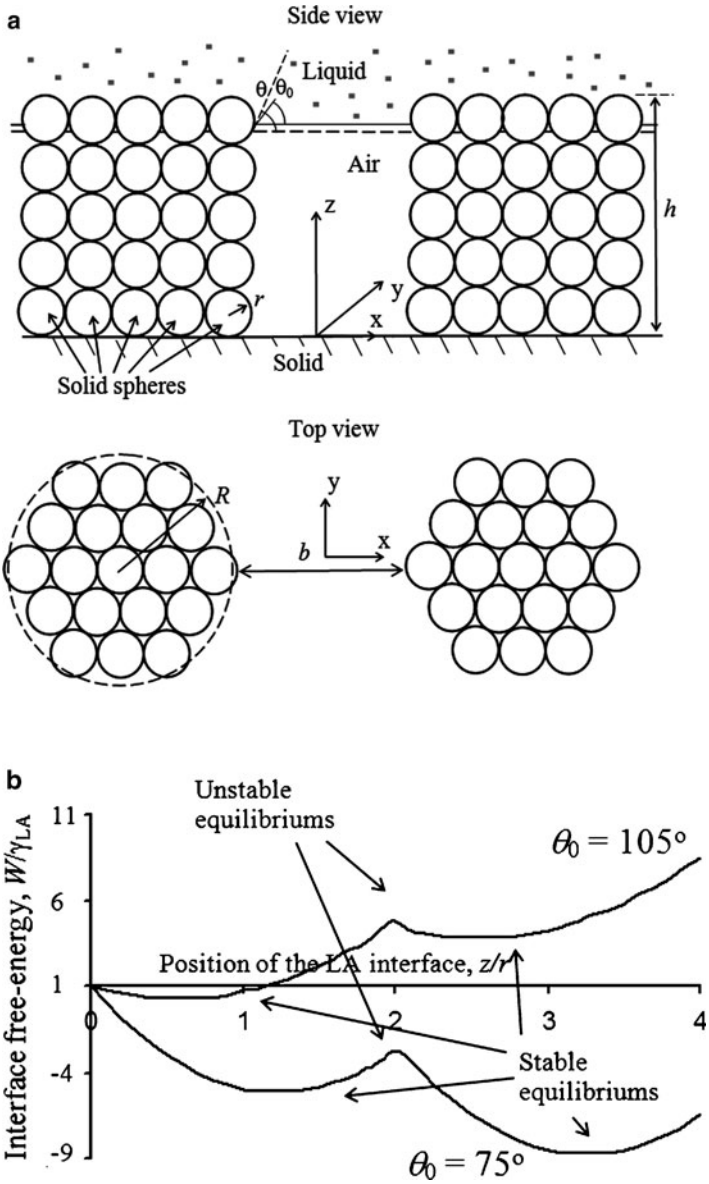

Fig. 10.9 Three-dimensional pillars consisting of *small solid spheres* (**a**) schematics of the structure, (**b**) energy (normalized by $A_0\gamma_{LA}$) as a function of vertical position of the interface z (normalized by the radius of bumps/grooves r) for $\pi^2R^2/(2\sqrt{3}r^2) = 1$ (Nosonovsky 2007e)

To summarize this section, we studied three different surface profiles with large-scale pillars and small-scale roughness superimposed on the pillars. It is observed from Figs. 10.7b and 10.9b that for both the hydrophobic and hydrophilic materials, a convex surface leads to stable equilibriums, whereas a concaved surface

leads to unstable equilibriums. Therefore, a convex small-scale roughness can pin the liquid–air interface even in the case of a hydrophilic material. This may be important for producing reliable superhydrophobic surfaces, since the factors destabilizing the liquid–air interface, such as nanodroplet condensation (Cheng et al. 2005; Oner and McCarthy 2000), chemical surface heterogeneity (Checco et al. 2003), and capillary waves (Nosonovsky and Bhushan 2006a) are scale-dependent and therefore multiscale roughness is required to control the stability.

An experiment, suggesting that the sign of curvature is indeed important for hydrophobicity, was conducted by Sun et al. (2005). They produced both a positive and a negative replica of a lotus leaf surface by nanocasting, using poly(dimethylsiloxane) (PDMS), which has the contact angle with water of about 105°. This value is close to the contact angle of wax, which covers lotus leaves (about 103°, Kamusewitz et al. 1999). The positive and negative replicas have the same roughness factor and thus should produce the same contact angle in the case of a homogeneous interface; however, the values of the surface curvature are opposite. The value of contact angle for the positive replica was found to be 160° (same as for lotus leaf), while for the negative replica it was only 110°. This result suggests that the high contact angle of the lotus leaf is due to the composite, rather than homogeneous interface and that the sign of surface curvature indeed plays a critical role for the formation of the composite interface.

Natural and successful artificial superhydrophobic surfaces exhibit hierarchical multiscale roughness. Thus, the lotus leaf has microscale bumps (papillae) with a typical height and radius of 10–20 μm, which are covered with hydrophobic paraffin wax. Upon these bumps much smaller nanobumps are found, with typical submicron sizes. Artificial biomimetic superhydrophobic surfaces should also have multiscale roughness.

Biomimetic superhydrophobic surfaces should satisfy the following requirements: they should have hydrophobic coating, high roughness factors, providing high contact angle, and the ability to form a composite interface. To achieve a stable composite interface, hierarchical roughness structure with nanoscale bumps upon microscale asperities and valleys is required.

The mechanism of roughness-induced hydrophobicity is complicated and involves effects at various scale ranges. For most superhydrophobic surfaces, it is important that a composite solid–liquid–air interface is formed. A composite interface dramatically decreases the area of contact between liquid and solid and, therefore, decreases adhesion of a liquid droplet to the solid surface and contact angle hysteresis. Formation of a composite interface is also a multiscale phenomenon, which depends upon relative sizes of the liquid droplet and roughness details. The composite interface is fragile, since transition to an homogeneous interface is irreversible. Therefore, stability of a composite interface is crucial for superhydrophobicity and should be addressed for successful development of superhydrophobic surfaces. We have demonstrated that a multiscale roughness can help to resist the destabilization, with convex surfaces pinning the interface and thus leading to stable equilibrium and prevention of filling the gaps between the pillars even in the case of a hydrophilic material. The effect of roughness on wetting is scale-dependent

and mechanisms that lead to destabilization of a composite interface are also scale-dependent. To effectively resist these scale-dependent mechanisms, a multiscale roughness is required. Such multiscale roughness was found in natural and successful artificial superhydrophobic surfaces.

To summarize, it is not enough that the Young and Laplace equations are satisfied at the liquid–vapor interface. The interface should also be stable, so a stability criterion was formulated. In addition, we explored the possibility that the valleys between the asperities are only partially filled with water, that is, the filling of the valleys is a probabilistic process (Nosonovsky and Bhushan 2008a). In the proposed model, filling of the valleys is thermally activated (the probability is proportional to $\exp(kT)$). This may be correct for small (nanoscale) energy barriers between metastable states. For larger energy barriers, the probabilistic law may be different, however, the qualitative picture is expected to be similar. A more detailed discussion of the transition is given in Chap. 8. We studied also a simple three-dimensional surface, which involves both peaks (asperities or pillars) and holes (valley). The three-dimensional surface is different from two-dimensional profiles, for example, in that the holes are isolated (and air pressure may be an issue, although ignored in our simplified analysis). Comparison of the effect of the peaks and valley is interesting, since they constitute a negative replica of each other. In a similar manner, the effect of bubbles and droplets may be compared (it is discussed in more detail in Chap. 9). We discussed also dependence of the meniscus force, which is often the principal component of the friction force, upon roughness. In addition, design optimization considerations have been formulated. The interactions involved in the studied processes act at various scale levels. Making wetting essentially a multiscale process. We also considered the multiscale roughness and its effect upon the stability of the composite interface and found that introduction of small-scale roughness may pin the triple line and thus make the liquid–vapor interface stable even in the case of an initially hydrophilic surface ($\theta_0 < 90^\circ$).

10.5 Reversible Superhydrophobicity

An important area of application of superhydrophobic surfaces is reversible superhydrophobicity; that is, the ability of a surface to switch between the hydrophobic and hydrophilic properties under the influence of the electric potential, ultraviolet or light irradiation, temperature (Feng et al. 2004; Xu et al. 2005; Shirtcliffe et al. 2005; Wang et al. 2007a). This area has emerged in recent years, since 2004, and a number of important findings have been made, including the ability to switch between the Cassie and Wenzel states. Krupenkin et al. (2007) reported that droplet behavior can be reversibly switched between the superhydrophobic Cassie state and the hydrophilic Wenzel state by the application of electrical voltage and current (electrowetting). Krupenkin et al. (2007) with co-workers later suggested the concept of “capillary origami” (Fig. 10.10), a surface

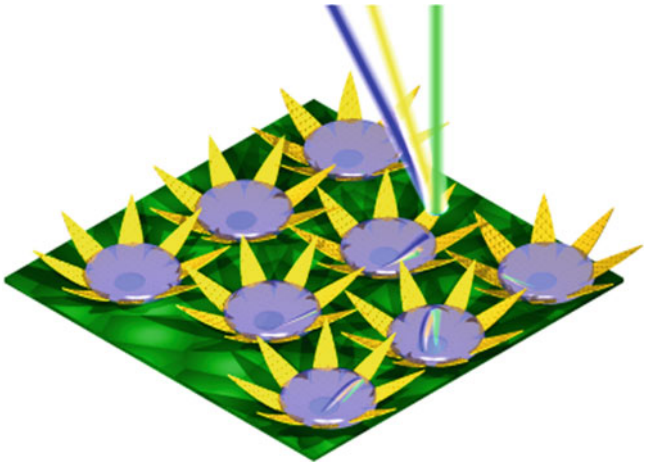

Fig. 10.10 Dynamically tunable microstructures based on capillary origami. The position of flexible platelet petals can be dynamically adjusted, providing a controllable-topography surface. Petal actuation is performed using electrowetting of small liquid droplets (*blue*) by applying a voltage between the droplets and flexible petals. Flexible platelets (*yellow*) can also act as diffraction gratings reflecting incoming light (based on Krupenkin et al. 2007)

with MEMS-controlled topography which can be used for coloration or propulsion. Wang et al. (2007a, b, c) created a surface that can switch between stable superhydrophilic, metastable superhydrophobic, and stable superhydrophobic states. Interestingly, their switchable surface was driven by DNA nanodevices. A number of other approaches to reversible superhydrophobicity have been suggested as well (Ma and Hill 2006).

Recent work by Jiang, Feng with co-workers and other researchers has significantly advanced the field of switchable, reversible, or tunable superhydrophobicity (Liu et al. 2005; Feng and Jiang 2006; Lim et al. 2006, 2007; Wang and Jiang 2007; Wang et al. 2007a, b, c). Lim et al. (2007) reported the fabrication of a rose-like nanostructured vanadium oxide (V_2O_5) film with photoinduced surface wettability switching by carrying out the drop-casting of a suspension of V_2O_5 particles synthesized with the sol-gel method. Although a pure V_2O_5 film was slightly hydrophilic, the addition of alkylamine rendered the nanostructured V_2O_5 film superhydrophobic owing to the intercalation of alkyl chains between the V_2O_5 layers. UV exposure switched the wettability of the V_2O_5 surface to superhydrophilic with a water contact angle of almost 0°, while storage in the darkness reconverted the irradiated surface back to its initial superhydrophobic state. Zhang et al. (2007) reported the preparation and UV-stimulated wettability conversion of superhydrophobic TiO_2 surfaces, as well as the preparation of superhydrophilic–superhydrophobic patterns by the use of UV irradiation through a photomask, using CF_4 plasma to roughen smooth TiO_2 sol-gel films to produce a nanocolumnar morphology, and subsequent hydrophobic modification with octadecylphosphonic acid (ODP).

Gras et al. (2007) categorized switchable surfaces according to the stimuli that trigger changes in surface hydrophobicity, including electrically, electrochemically, thermally, mechanically, photo- and environmentally inducible surfaces, and chemical reactions to modify the properties of switchable surfaces and produce changes in their molecular structure.

Basu and Manasa (2011) synthesized superhydrophobic cobalt hydroxide films with flower-like micro/nanostructures prepared by chemical-bath deposition. The structure changed its wettability from superhydrophobic to superhydrophilic either by immersion in ethyl acetate or by heat treatment at 200°C. The superhydrophobicity was attributed to the combined effect of micro–nano binary surface morphology and the low surface energy of the self-assembled monolayer of stearic acid. Switching to superhydrophilicity was presumably caused by the removal of the adsorbed layer of stearic acid by solvent or heat treatment.

Xia et al. investigated a dual-stimuli-responsive surface with tunable wettability, switching between hydrophilicity and hydrophobicity by fabricating a copolymer thin film on both a flat and an etched silicon substrate. Switching between hydrophilicity and hydrophobicity was found over both a temperature range of about 20°C and over a relatively wide concentration of beta-CD.

Wu et al. (2011) applied precise tuning of surface wettability – by means of curvature-driven reversible switching from the pinned to the roll-down superhydrophobic state. The adhesion force and sliding behaviors of superhydrophobic PDMS pillar arrays showed a strong dependence on surface curvature. Alteration of the curvature of the surface allows a water droplet to be easily adjusted from the "pinned" to the "roll-down" state, which provides the possibility of precise, in situ control of the movements of water droplets.

Cui et al. (2010) demonstrated the ultraviolet (UV) light-induced, reversible wettability behavior for tubular SiC nanostructure film. The film showed the superhydrophilic nature with the water contact angle 152.4° and low sliding angle. The surface transition between superhydrophobicity and superhydrophilicity could be easily achieved by the alternation of UV irradiation and closed thermal heating.

Liu and Jiang (2010) reviewed several techniques that have been developed to switch the adhesion on liquid–solid interfaces, including tuning the surface chemical composition, tailoring the surface morphology, and applying external stimuli. They paid attention to superhydrophobic surfaces with reversible switching between low- and high-adhesion to water droplets in response to external stimuli. The dynamic behavior of water droplets on such surfaces could be controlled ranging from the rolling to pinning state, while maintaining superhydrophobic states. Smart adhesion in oil–water–solid system and platelet–water–solid system was demonstrated, which is of importance for anti-bioadhesion and self-cleaning materials.

Xu et al. (2010) have fabricated superhydrophobic zinc surfaces with reversible transformation between the sliding state and adhesion by a simple hydrothermal method. Uniformly ZnO_2 nanorod was obtained at 120°C. After self-assembling of a film of *n*-octadecanethiol, the surface got the water contact angle of 153°. The surface showed switchable adhesion just upon introducing UV illumination and heating treatment in turn.

Kuo and Gau (2010) investigated superwetting or dewetting properties of a silicon nanowire (SiNW) surfaces grown vertically on SiO_2 or Si substrates by a vapor–liquid–solid process. A sufficiently rough nanowire surface exhibited superhydrophilicity with a contact angle close to 0°. However, the surface could be turned into superhydrophobic by a vacuum treatment, which is a low pressure diffusion process by the vapor from the polydimethylsiloxane material. The superhydrophobicity of the surface can be readily reversed back to superhydrophilicity by annealing at 600°C with nitrogen, and the cycle could be repeated many times.

10.6 A Droplet on an Inclined Surface

For a droplet of radius R moving along the inclined plane with tilt angle α (Fig. 10.11), the energy gain corresponding to the inclined distance l is given by $lmg\sin\alpha$, where mg is the weight of the droplet. The contact angle hysteresis is related to the tilt angle by

$$t\sigma(\cos\theta_{\text{adv}} - \cos\theta_{\text{rec}}) = gm\sin\alpha, \tag{10.41}$$

where σ is the surface tension and t is the length of the triple line (Furmidge 1962). Equation (10.41) was formulated by Macdougall and Ockrent (1942) based on their experimental observations of droplets on inclined surfaces and independently by Frenkel (1948) in his theoretical study of the contact angle hysteresis. Equation (10.41) is based on several assumptions, in particular, that the front edge of the droplet exhibits the advancing and the back end exhibits the receding contact angle and that the droplet foundation is well approximated by the cylindrical or rectangular shape. Marmur (2004) and Krasovitski and Marmur (2004) showed that the droplet on an inclined plane does not necessary exhibit the receding or advancing contact angle, since the former is based on the geometry of the drop, whereas the latter is based on the nature of the solid surface.

We will use the energy balance method to determine the tilt angle. i.e., we will assume that the energy loss due to the adhesion hysteresis is equal to the energy

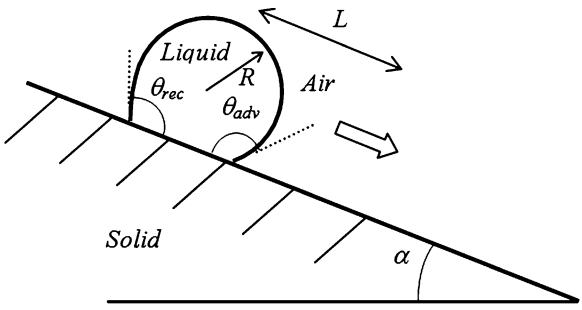

Fig. 10.11 Schematics of a droplet moving along an inclined surface with tilt angle α, advancing contact angle θ_{adv}, and receding contact angle θ_{rec}

gain due to the gravity. The energy loss is given by ΔW times the contact area $lR\sin\theta$. The tilt angle is given by

$$\sin\alpha = \frac{\Delta W_0 f_{\mathrm{SL}} R_{\mathrm{f}} R \sin\theta}{mg}. \tag{10.42}$$

Using the trigonometric relationship

$$\cos\theta_{\mathrm{adv}} - \cos\theta_{\mathrm{rec}} = -2\sin\frac{\theta_{\mathrm{adv}} + \theta_{\mathrm{rec}}}{2}\sin\frac{\theta_{\mathrm{adv}} - \theta_{\mathrm{rec}}}{2}, \tag{10.43}$$

and substituting into (10.42)

$$\sin\left(\frac{\theta_{\mathrm{adv}} - \theta_{\mathrm{rec}}}{2}\right) = -\frac{mg}{2R\gamma_{\mathrm{LA}}\sin\theta\sin(\theta_{\mathrm{adv}} + \theta_{\mathrm{rec}}/2)}\sin\alpha. \tag{10.44}$$

For θ and $(\theta_{\mathrm{adv}} + \theta_{\mathrm{rec}})/2$ close to π, it is found from (10.44) that the tilt angle is proportional to the contact angle hysteresis.

10.7 Bouncing-Off Droplets

Another important phenomenon related to the hydrophobicity is bouncing droplets (Fig. 10.12). When a droplet impacts a superhydrophobic surface with a certain velocity, in some cases it can be bounced off in an almost elastic manner (Hartley and Brunskill 1958; Quéré 2005; Reyssat et al. 2006; Richard et al. 2002). The kinetic energy of the droplet is stored in the surface deformation during the impact. A deformed droplet has higher surface area and therefore higher free surface energy (Nosonovsky and Bhushan 2008a). Therefore, during the impact when the droplet is deformed, it can accommodate the kinetic energy. It was suggested that the effect might be of practical interest for agriculture, in particular, for treating leaves with pesticides (Quéré 2005). Since the leaf is likely to repel the drop, it will not be treated; in addition, the scattering of the droplets contaminates the soil. If small amounts of a polymer soluble in water (such as polyoxyethylene) are added to water (Bergeron et al. 2000), the bulk viscosity of water remains the same, however, the so-called

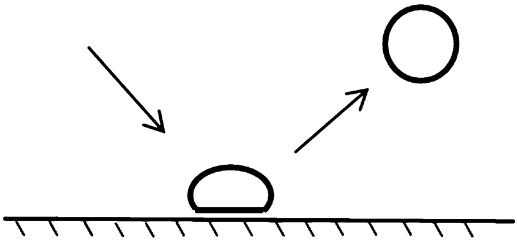

Fig. 10.12 A bouncing droplet impacts a solid hydrophobic surface

elongation viscosity (resistance of the liquid to large extensions) is high. Droplets of such a mixture do not bounce, and it has been used as an agricultural spray (Quéré 2005). On the other hand, the bouncing droplets are useful for waterproof fabrics or concrete that should preserve their dryness under a rain.

The dissipation with the prevention of droplet bouncing is due to viscosity and due to the moving triple line. For the bouncing droplets, the triple lines are small or absent due to the presence of a thin film of compressed air during the impact. It was reported that full rebounding takes place for the surfaces with the contact angles larger than 150°–160° with the ratio of the velocities after and before the impact of 0.9 and higher (Quéré 2005). To estimate the maximum velocities of impact, V, for which the effect takes place, is obtained by the comparison of kinetic and free surface energy. The kinetic energy of a droplet of radius, R_0, and density ρ is given by

$$E_{\text{kin}} = \frac{(4/3)\pi\rho R_0^3 V^2}{2}, \tag{10.45}$$

while the free surface energy is given by

$$E_{\text{surf}} = 4\pi R_0^2 \gamma_{\text{LV}}. \tag{10.46}$$

In order for the surface deformation to accommodate the kinetic energy, the later should be of the same order of magnitude as the former, which yields

$$V^2 = \frac{6\gamma_{\text{LV}}}{\rho R_0}. \tag{10.47}$$

For water ($\gamma_{LV} = 0.072\,\text{N}\,\text{m}^{-1}, \rho = 1,000\,\text{kg}\,\text{m}^{-2}$) droplet of $R_0 = 0.001$, corresponding impact velocity is $V = 0.66$ m s^{-1}. Indeed, with the increasing velocity, the elastic behavior decreases (Richard and Quéré 2000). The ratio of the kinetic and surface energy (or inertial to the capillary forces) is also characterized by the nondimensional Weber number

$$We = \frac{\rho R_0 V^2}{\gamma_{\text{LV}}}. \tag{10.48}$$

Small We corresponds to low kinetic energy in comparison with the free surface energy. Two other important nondimensional numbers are the capillary number

$$Ca = \frac{\mu_{\text{LV}}}{\gamma_{\text{LV}}}, \tag{10.49}$$

that characterizes the ratio of the viscous to capillary forces, and the Reynolds number

$$Re = \frac{\rho V R_0}{\mu_{\text{L}}}, \tag{10.50}$$

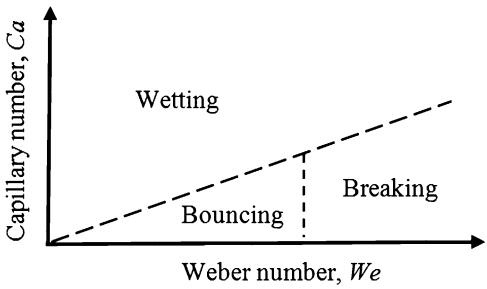

Fig. 10.13 Schematic of various regimes of a droplet impacting a hydrophobic surface. For high *We*, the droplet will break into parts, whereas for high $Re = We/Ca$, the energy will be dissipated due to the viscosity and the droplet can wet the surface

that characterizes the ratio of the inertial to viscous forces (note that $Re = We/Ca$). Bouncing usually requires both small *We*, *Ca*, and *Re*. Big velocity (high *We*) would result in breaking of the droplet into parts, while big viscosity (high *Ca* and *Re*) would result in dissipation and eventual wetting of the surface (Fig. 10.13).

The energy barrier that corresponds to the division of a droplet with the radius R_0 into two droplets with the radius

$$R_1 = 2^{(-1/3)} R_0, \tag{10.51}$$

which provides the same total volume, can be estimated by comparison with the net energy. The energy of the big droplet is given by the sum of the interface energy and the volumetric energy.

$$E_0 = 4\pi R_0^2 \gamma_{\mathrm{LV}} + \frac{4}{3}\rho R_0^3 \frac{2\gamma_{\mathrm{LV}}}{R_0} = \frac{20\pi R_0^2 \gamma_{\mathrm{LV}}}{3}. \tag{10.52}$$

The energy of a smaller droplet is given by

$$E_1 = \frac{20\pi R_1^2 \gamma_{\mathrm{LV}}}{3} = 2^{(-2/3)} \frac{20\pi R_0^2 \gamma_{\mathrm{LV}}}{3}. \tag{10.53}$$

The energy change as a result of the division of the big droplet into two is given by

$$\Delta E = 2E_1 - E_0 = (2^{(1/3)} - 1)\frac{20\pi R_0^2 \gamma_{\mathrm{LV}}}{3} = 1.26 E_0. \tag{10.54}$$

Comparison with the kinetic energy given by (10.51) yields

$$V^2 = \frac{10(2^{(1/3)} - 1)\gamma_{\mathrm{LV}}}{\rho R_0}. \tag{10.55}$$

For water ($\gamma_{\mathrm{LV}} = 0.072\,\mathrm{N\,m^{-1}}, \rho = 1,000\,\mathrm{kg\,m^{-2}}$) droplet of $R_0 = 0.001$, corresponding impact velocity is $V = 0.95\ \mathrm{m\ s^{-1}}$, which provides another estimate

for a maximum velocity. Experimental observations show that small satellite droplets form in certain cases, when the Weber number is of the order of 10 or greater (Quéré 2005). Formation of a small satellite droplet involves smaller energy barriers rather than division of the large droplet into two equal parts (Nosonovsky and Bhushan 2008a).

We can conclude that water droplets can bounce off superhydrophobic surfaces in an elastic manner. The impact velocity should not be very high (small *We* requirement), so that the surface tension can accommodate the kinetic energy. On the other hand, the velocity should not be too low (small *Re* requirement), so that impact time is short, a thin film of compressed air can form, and the dissipation due to the triple line contact and viscosity is small.

Superhydrophobicity is usually defined as the ability to have the static contact angle (CA) with water greater than 150°. In addition, a superhydrophobic surface should have low CA hysteresis, or the difference between the advancing CA (when water is added or the water front advances) and receding CA (when water is removed or the water front recedes). The CA is a measure of adhesion between water and the solid surface, so the greater the contact angle, the lower the adhesion. The CA hysteresis, on the other hand, is a measure of energy dissipation during the wetting–dewetting cycle, or during the flow of a droplet along the solid surface. Interactions in the bulk volume of a droplet at the solid–liquid contact surface and at the triple line (solid–liquid–vapor contact line) affect the dissipation. While the volume interactions due to viscosity can be eliminated in the quasi-static limit of a very slow motion, the surface and line interactions remain even in the case of a low velocity motion.

There is another wetting characteristic, in addition to a high CA and low CA hysteresis, which is of practical importance for water-repellency. This is the behavior of a droplet impacting a surface with a certain velocity. In some cases, it can be bounced off a superhydrophobic surface in an almost elastic manner (Quéré 2005, Bartolo et al. 2006). The kinetic energy of the droplet is stored in the surface deformation during the impact. A deformed droplet has a higher surface area and thus higher surface free energy. Therefore, during the impact when the droplet is deformed, it can accommodate the kinetic energy. It was suggested that the effect might be of practical interest for agriculture, in particular, for treating leaves with pesticides (Quéré 2005).

Since the leaf is likely to repel the droplet, it will not be treated; in addition, the scattering of the droplets contaminates the soil. If small amounts of a polymer soluble in water (such as polyoxyethylene) are added to water (Bergeron et al. 2000), the bulk viscosity of water remains the same; however, the so-called elongation viscosity (resistance of the liquid to large extensions) is high. Droplets of such a mixture do not bounce, and it has been used as an agricultural spray (Quéré 2005). On the other hand, the bouncing droplets are useful for waterproof fabrics or concrete that should preserve their dryness under rain.

The ability of a surface to bounce off droplets constitutes the third property of a superhydrophobic surface, in addition to high CA and low CA hysteresis, that is important for both biological and technical applications. However, this third

property has received relatively little attention. We quantify the bouncing ability of a surface and relate it to the surface roughness using theoretical and experimental considerations.

Jung and Bhushan (2008a, b) studied two series of patterned Si surfaces, covered with a monolayer of hydrophobic tetrahydroperfluorodecyltrichlorosilane (CA with a nominally flat surface, $\theta_0 = 109°$, advancing and receding CA $\theta_{adv0} = 116°$ and $\theta_{rec0} = 82°$), formed by flat-top cylindrical pillars. Series 1 had pillars with the diameter $D = 5$ μm, height $H = 10$ μm, and pitch values $P = (7, 7.5, 10, 12.5, 25, 37.5, 45, 60,$ and $75)$ μm, while series 2 had $D = 14$ μm, $H = 30$ μm, and $P = (21, 23, 26, 35, 70, 105, 126, 168,$ and $210)$ μm. The series were designed in this manner to isolate the effect of the pitch, pitch-to-height, and pitch-to-diameter ratios. The contact angle and contact angle hysteresis of millimeter-sized water droplets upon the samples were measured. In addition, the contact angle and the Wenzel–Cassie transition during evaporation of microdroplets were studied. It was found that for small P the droplets were in the Cassie state sitting on top of the pillars. The droplet radius R at which the transition occurs is linearly proportional to P/D. This is because the area under the droplet is proportional to R^2. The fit (solid line) is shown for

$$RD/P = 50\,\mu\text{m}. \tag{10.56}$$

increasing the value of P, the transition to the Wenzel state occurred. The transition occurs at values of the pitch much greater than the intersection of the energy lines for the two states. Therefore, the droplet was in a metastable Cassie state, separated by an energy barrier from the Wenzel state (corresponding to lower energy) (Nosonovsky and Bhushan 2008a).

For evaporating droplets, the Cassie–Wenzel transition occurred when the droplet radius decreased below a certain critical value. The droplet radius, R, at the Cassie–Wenzel transition was found to be proportional to P/D (or P/H, since the height of the columns was proportional to their diameter). On the other hand, the transition occurs as the vibrational energy of the droplet, E_{vib}, exceeds the energy barrier associated with the transition. The vibrational energy of the droplet (Johnson and Dettre 1964; Li and Amirfazli 2006; Bormashenko et al. 2008) is the energy associated with the vibration of the droplet due to surface waves, thermal vibration, etc. Assuming $E_{vib} = \text{const}$, the proportionality of P/D and R suggests that the barrier $-E$ given by (10.54) is proportional to RD/P or (RH/P). This is indeed true, since the area under the droplet $A_0 = \pi(R\sin\theta)^2$. Substituting $\sin^2\theta = 0.1$, $\cos\theta_0 = \cos 109° = -0.33$, $\gamma_{LV} = 0.072$ J m^{-2} and taking the observed value $RD/P = 50$ μm yields an estimated value of the vibrational energy $E_{vib} = -E = 1.2 \times 10^{-10}$ J (Nosonovsky and Bhushan 2008a).

Jung and Bhushan (2008b) investigated the impact of water droplets with 5 μl volume (about 1 mm radius) upon the same series of surfaces. It was found that droplets impacting the surface with low velocity bounced off the surface, whereas those having high impact velocity stuck to the surface. Sticking was associated with being in the Wenzel state with a large solid–liquid contact area, while the droplets that bounced off the surface were in the Cassie state with an air pocket under them.

Thus, the energy barrier of the Cassie–Wenzel transition can be estimated as the kinetic energy of the droplets. It was found that the dependence is close to linear, however, the series of smaller pillars has larger energies of transition. The value of A_0 is in the range 0.11 mm^2 < A_0 < 0.18 mm^2 for series 1 and 0.05 mm^2 < A_0 < 0.11 mm^2 for series 2, which is of the same order as the actual area under the droplet (Nosonovsky and Bhushan 2008a).

These results suggest that the energy barrier for the Cassie–Wenzel transition is proportional to the area under the droplet. For droplets sitting on the surface or evaporating, the transition takes place when the size of the barrier decreases to the value of the vibrational energy, approximately $E_{\text{vib}} = 10^{-10}$ J, which was estimated from the energy barrier. This may happen because the size of the droplet is decreased or because the pitch between the pillars that cover the surface is increased. A different way to overcome the barrier is to hit the surface with a droplet with a certain kinetic energy (Nosonovsky and Bhushan 2008a).

The vibrational energy E_{vib} also plays a role in overcoming energy barriers that lead to CA hysteresis during liquid flow (Johnson and Dettre 1964). To estimate the effect of the energy barriers on CA hysteresis, we assume that the difference between the advancing and receding CA is given by

$$\cos\theta_{\text{rec}} - \cos\theta_{\text{adv}} = \frac{W}{\gamma_{\text{LV}}}, \tag{10.57}$$

where W corresponds to the energy barrier associated with the wetting–dewetting cycle. Assuming that this energy barrier is of the same order as the vibrational energy per contact area, $W = E_{\text{vib}}/A_0$, and taking $A_0 = 0.1$ mm^2, we end up with $-W = 10^{-3}$ J m^{-2}. For water ($\gamma_{\text{LV}} = 0.072$ J m^{-2}), (10.57) leads to a realistic value of CA hysteresis on a superhydrophobic surface $\cos\theta_{\text{rec}} - \cos\theta_{\text{adv}} = 0.014$. This number provides an estimate for CA hysteresis in the limit of small energy barriers comparable with E_{vib}. The values that provide energy barriers due to so-called adhesion hysteresis and the density of the solid–liquid–vapor contact line that provides additional pinning are dependent upon the solid–liquid contact area. These values for a micropatterned surface were found to be between 0.0144 and 0.440 (Bhushan and Jung 2007), thus showing a good agreement with the value calculated based on E_{vib} as the lower limit. This indicates that the value of U is relevant for both the wetting regime transition and bouncing droplets (Nosonovsky and Bhushan 2008a).

10.8 Summary

In this chapter, we reviewed superhydrophobicity, which constitutes the main approach to self-cleaning. Self-cleaning surfaces repel water, which washes away dirt, and, under certain circumstances, they can also repel liquid organic contaminants.

Superhydrophobicity is a result of interplay of surface roughness with low surface energy (hydrophobicity). In the case of a homogeneous (Wenzel) solid–liquid interface, effective surface energy per unit area is enhanced by roughness in accordance with the roughness factor. In the case of the composite (Cassie–Baxter) interface, the air pockets sitting in the cavities between the solid and liquid decrease the solid–liquid area of contact and adhesion force, making the surface water-repellent. The composite regime is desirable for superhydrophobicity.

The contact angle is a parameter that characterizes wetting and it can be determined from the Wenzel and Cassie–Baxter models. However, the contact angle is not a single number. Instead, it can take a spectrum of values in a certain range. Another important parameter, which characterizes the solid–liquid adhesion, is contact angle hysteresis, i.e., the difference of the advancing (maximum) and receding (minimum) contact angles. Contact angle hysteresis is a result of pinning of the triple line by surface rough details and chemically heterogeneous spots of lower surface energy. Contact angle hysteresis is related to fundamental wetting–dewetting asymmetry. It is also related to the adhesion hysteresis, i.e., the fact that less energy is gained by bringing surfaces together than spent on their separation. As a result, irreversible energy dissipation occurs which can be viewed as a consequence of the Second law of thermodynamics. While the contact angle itself can be well predicted from the Wenzel and Cassie–Baxter models, it is much more difficult to exactly predict quantitatively contact angle hysteresis. In the composite (Cassie–Baxter) regime, contact angle hysteresis is much lower than in the homogeneous (Wenzel) regime.

The transition between the Wenzel and Cassie–Baxter regimes is another phenomenon which is difficult to predict quantitatively from the standard Wenzel and Cassie–Baxter models of wetting. There is an energy barrier between the two regimes, and the composite interface is more fragile, making the transition, which can be viewed as a "phase transition," irreversible and thus another manifestation of the above-mentioned wetting–dewetting asymmetry. Therefore, the fundamental physical causes of the wetting regime transition are similar to those of the contact angle hysteresis.

A robust superhydrophobic surface should also be hierarchical, normally with nanoscale roughness imposed over microscale roughness. The reasons for that are not completely clear. However, it is noted that wetting is a multiscale process, so that it involves interactions with different characteristic scale length. Therefore, different scale sizes of roughness are needed. Part of it may have to do with the mere fact that water droplets can be of different size, ranging from microns (fog) to millimeters. Multiscale roughness may result in stabilizing the composite wetting regime. In addition, it has been argued recently that besides Wenzel and Cassie regimes, hierarchical roughness provides other "mixed" wetting states (e.g., Wenzel for microroughness or Cassie–Baxter for nanoroughness) which are beneficial for superhydrophobicity (Bhushan and Nosonovsky 2010).

Chapter 11
Lotus Effect and Self-Cleaning

Self-cleaning surfaces are capable of repelling contaminants, including solid particles, organic liquids, and biocontaminants. The most common principle of self-cleaning is based on the Lotus effect, which involves the superhydrophobicity induced by surface roughness. The phenomenon of superhydrophobicity and its various implications have been considered in detail in the preceding chapter. The name of the Lotus effect was coined due to the observation that the leaves of Lotus (*Nelumbo*) can emerge clean from dirty water, making lotus a symbol of purity in many Asian cultures. Superhydrophobicity is the core property that leads to the Lotus effect-based self-cleaning, so we discuss in this chapter basic observations on superhydrophobicity in biological surfaces (including, plant leaves, insects, birds, gecko feet, etc.) as well as artificial surfaces.

Another approach to self-cleaning utilizes photocatalytic and superhydrophilic properties of titania (TiO_2). This approach, although opposite to the superhydrophobicity, can be combined with the latter to a certain extent. A different type of self-cleaning materials is related to oleophobicity, i.e., the ability to repel organic contamination, in particular, underwater oleophobicity, which is used for antifouling. In this chapter, we discuss superhydrophobic self-cleaning materials, whereas the underwater oleophobic coatings are reviewed in the consequent chapters.

11.1 Superhydrophobicity in Natural and Biomimetic Surfaces

Superhydrophobicity or extreme water repellency is a remarkable property of many plant leaves of which the most notorious is the Lotus (*Nelumbo nucifera*). The hydrophobicity of the leaves is related to self-cleaning, the ability of the hydrophobic leaves to remain clean after being immersed in dirty water. It is due to its purity the Lotus is considered by many Asian cultures as "sacred." The lotus flower is quoted extensively in Indian and Chinese sacred texts, for example: "*Having abandoned attachment, he acts untainted by evil as a lotus leaf is not wetted*" (Bhagavad Gita 5.10). Not surprisingly, the ability of lotus-like surfaces for

M. Nosonovsky and P.K. Rohatgi, *Biomimetics in Materials Science: Self-Healing, Self-Lubricating, and Self-Cleaning Materials*, Springer Series in Materials Science 152, DOI 10.1007/978-1-4614-0926-7_11,

self-cleaning and water repellency was called the "Lotus effect" (Nosonovsky and Bhushan 2008a). The term was coined in the 1990s, most likely, by German botanist W. Barthlott.

The most important parameter that characterizes wetting is the static contact angle, which is defined as the angle that a liquid makes with a solid. The contact angle depends on the interfacial energies of the solid–liquid, solid–air, and liquid–air interface as well as on several additional factors, such as roughness and the manner of surface preparation, and its cleanliness (Adamson 1990; Israelachvili 1992). If the liquid wets the surface, the value of the static contact angle is $0 \leq \theta \leq 90°$. Such a liquid is called wetting liquid, whereas the surface is called hydrophilic. If the liquid does not wet the surface, the value of the contact angle is $90° < \theta \leq 180°$. Such a liquid is called nonwetting liquid, whereas the surface is called hydrophobic. Surfaces with high energy, formed by polar molecules, tend to be hydrophilic, whereas those with low energy and built of nonpolar molecules tend to by hydrophobic. Surfaces with very high contact angles in the range $150° < \theta \leq 180°$ are called "superhydrophobic". Some scientist argue that certain additional properties besides the high contact angle, such as low contact angle hysteresis, are required for a surface to be called truly superhydrophobic.

The term hydrophobic/philic, which originally applied only to water, since "hydro-" (Ὑδρο-) means "water" in Greek, is used sometimes to describe the contact of a solid surface with any liquid. The term "oleophobic/philic" is used with regard to the wetting by oil or organic liquids. The term lipophobic/philic is used for wetting by fats, lipids, and other nonpolar solvents. Sometimes the term omniphobicity (from Latin "omni" "everything") is used to denote surfaces able to repel every liquid, both water and oil. An alternative term is amphiphobicity/philicity (from the Greek αμφις, "amphis" meaning "both"), which describes a substance possessing both hydrophilic/phobic and lipophilic/phobic properties. Also terms "superphobic/philic" and "ultraphobic/philic" are used sometimes to stress the ability to repel other liquids besides water. The term "icephobicity" is used to denote the ability to repel ice. These terms are summarized in Table 11.1.

It is much more difficult to produce an omniphobic or amphiphilic surface than a hydrophobic surface due to low surface energy typical for organic liquids. This is because water molecules are polar, and therefore, they can form strong polar hydrogen bonds, while most organic liquids such as oils, fats, and lipids are nonpolar. Most nonpolar molecules tend to be "driven out" of water, whereas polar molecules are "driven out" of organic liquids, thus demonstrating the principle "like dissolves like." However, this does not necessarily mean that lipophilic substances are always hydrophobic (and vice versa), since there exist classes of materials, such as silicones and fluorocarbons, which are hydrophobic but not lipophilic.

The effect of roughness on wetting was investigated in the 1930s by Wenzel (1936) who studied experimentally the wetting of textiles and concluded that roughness increases the solid–water area of contact, and as a result the contact angle changes. Later, Cassie and Baxter (1944) suggested that air trapped between a rough surface and a water droplet affects wetting properties of a rough surface. One

Table 11.1 Definitions and requirements for various phobic/philic surfaces and materials

Name	Definition	Requirements
Hydrophobic	Water contact angle $>90°$	Low surface energy
Hydrophilic	Water contact angle $<90°$	High surface energy
Superhydrophobic	Water contact angle $>150°$ and low contact angle hysteresis	Hydrophobic and rough (hierarchical roughness is desirable); composite interface is desirable
Superhydrophilic	Very low water contact angle ~0°	Photocatalytic titania, etc.
Oleophobic	Oil (or nonpolar organic liquid) contact angle $>90°$	Very low surface energy and/or special roughness structure
Underwater oleophobic	Oil-water-solid contact angle $>150°$	Rough and certain requirements for the contact area, composite interface is desirable
Oleophilic	Oil (or nonpolar organic liquid) contact angle $<90°$	High surface energy
Omniphobic	Both superhydrophobic and oleophobic	Very low surface energy and/or special roughness structure
Lipophobic	Does not dissolve fats, lipids and other nonpolar solvents	Polar liquids or oleophobic solids
Lipophilic	Dissolves fats, lipids and other nonpolar solvents	Nonpolar liquids or oleophilic solids
Amphiphobic	Both hydrophobic and lipophobic	
Amphiphilic	Both hydrophilic and lipophilic	Certain surfactants etc.
Icephobic	Ice does not form	Superhydrophobic with certain additional requirements

of the ways to increase the hydrophobic or hydrophilic properties of the surface is to increase surface roughness, so roughness-induced hydrophobicity has become a subject of extensive investigation. Wenzel (1936) found that the contact angle of a liquid with a rough surface is different from that with a smooth surface. Cassie and Baxter (1944) showed that air (or gas) pockets may be trapped in the cavities of a rough surface, resulting in a composite solid–liquid–air interface, as opposed to the homogeneous solid–liquid interface. Shuttleworth and Bailey (1948) studied spreading of a liquid over a rough solid surface and found that the contact angle at the absolute minimum of surface energy corresponds to the values predicted by Wenzel (1936) or Cassie and Baxter (1944). Later, Johnson and Dettre (1964) showed that the homogeneous and composite interfaces correspond to the two equilibrium states of a droplet and paid attention to the fact that the contact angle is not a single parameter, but it depends on whether the liquid advances or recedes. Hysteresis of the contact angle (the difference between the advancing and receding contact angles) is an important measure of energy dissipation and adhesion between the solid surface and liquid.

The original studies by Wenzel (1936) of Cassie and Baxter (1944) used simple considerations of the surface tension force magnified by surface roughness, similar to those of the original paper of T. Young (1805). In addition, Cassie investigated wetting of chemically heterogeneous surfaces, e.g., those build of small patches of different materials, so that the size of a water droplet is much larger than that of the patches. It was clear that there are similarities in wetting of rough and heterogeneous surfaces, as in both cases effective surface energy is averaged through the contact area. Interest in superhydrophobicity has increased since the 1990s as a result of two factors: (1) investigations of the microstructure of plant leaves with Scanning Probe Microscopy revealing the importance of surface roughness for the superhydrophobicity and (2) the ability to produce micro/nanostructured surfaces on different materials, which emerged due to advances in nanotechnology. As a result, theoretical understanding of wetting of rough surfaces advanced quite significantly. In particular, it became clear that wetting of rough surfaces is much more complex that simple Wenzel and Cassie–Baxter models suggest and that it can follow a number of scenarios. The effects of hierarchical surface structures, precursors, instabilities, transition between different wetting regimes, adhesion hysteresis, heterogeneous structure of liquid, and other complex effects have been investigated.

Bico et al. (2002), Marmur (2003, 2004), Lafuma and Quėrė (2003), Patankar (2004a), He et al. (2003), and other authors have investigated recently the metastability of artificial superhydrophobic surfaces and showed that whether the interface is homogeneous or composite may depend on the history of the system (in particular, whether the liquid was applied from the top or from the bottom). Extrand (2002) pointed out that whether the interface is homogeneous or composite depends on droplet size, due to the gravity. It was suggested also that the so-called two-tiered (or double) roughness, composed by superposition of two roughness patterns at different length-scale (Herminghaus 2000; Patankar 2004b; Sun et al. 2005), and fractal roughness (Shibuichi et al. 1996) may lead to superhydrophobicity. Herminghaus (2000) showed that certain self-affine profiles may result in superhydrophobic surfaces even for wetting liquids, in the case the local equilibrium condition for the triple line (line of contact between solid, liquid, and air) is satisfied. Nosonovsky (2007e) pointed out that such configurations, although formally possible, are likely to be unstable. Nosonovsky and Bhushan (2006a, b) proposed a stochastic model for wetting of rough surfaces with a certain probability associated with every equilibrium state. According to their model, the overall contact angle with a two-dimensional rough profile is calculated by assuming that the overall configuration of a droplet is a result of superposition of numerous metastable states. The probability-based concept is consistent with experimental data (Lafuma and Quėrė 2003), which suggests that the transition between the composite and homogeneous interfaces is gradual, rather than instant.

It has been demonstrated experimentally, that roughness indeed affects the contact angle in accordance with the Wenzel model. Yost et al. (1995) found that roughness enhances wetting of a copper surface with Sn–Pb eutectic solder, which has a contact angle of 15–20^{o} for smooth surface. Shibuichi et al. (1996) measured

the contact angle of various liquids (mixtures of water and 1,4-dioxane) on alkylketen dimmer (AKD) substrate (contact angle not larger than 109° for smooth surface). They found that for wetting liquids the contact angle decreases with increasing roughness, whereas for nonwetting liquids it increases. Semal et al. (1999) investigated the effect of surface roughness on contact angle hysteresis by studying a sessile droplet of squalane spreading dynamically on multilayer substrates (behenic acid on glass) and found that an increase in microroughness slows the rate of droplet spreading. Erbil et al. (2003) measured the contact angle of polypropylene (contact angle of 104° for smooth surface) and found that the contact angle increases with increasing roughness.

In the last two decades, material scientists paid attention to natural surfaces, which are extremely hydrophobic. Among them are leaves of water-repellent plants such as *N. nucifera* (lotus) and *Colocasia esculenta*, which have high contact angles with water (Neinhuis and Barthlott 1997; Barthlott and Neinhuis 1997; Wagner et al. 2003). First, the surface of the leaves is usually covered with a range of different waxes made from a mixture of hydrocarbon compounds that have low surface energy, and therefore, they are hydrophobic. Second, the surface is very rough due to so-called papillose epidermal cells, which form asperities or papillae. In addition to the microscale roughness of the leaf due to the papillae, the surface of the papillae is also rough with submicron size of asperities composed of the wax forming hierarchical micro- and nano-sized structures (Wagner et al. 2003). The water droplets on these surfaces readily sit on the apex of nanostructures because air bubbles fill in the valleys of the structure under the droplet. Therefore, these leaves exhibit considerable superhydrophobicity. The water droplets on the leaves remove any contaminant particles from there surfaces when they roll off, leading to self-cleaning ability or referred to as Lotus effect. Other examples of biological surfaces include duck feathers and butterfly wings. Their corrugated surfaces provide air pockets, which prevent water from completely touching the surface.

Strongly water-repellent artificial surfaces can be synthesized by chemically treating surfaces with low-surface-energy substances, such as polytetrafluoroethylene, silicon, or wax, or by fabricating extremely rough hydrophobic surfaces directly (Shibuichi et al. 1996; He et al. 2003; Kijlstra et al. 2002). Sun et al. (2005) studied an artificial poly(dimethylsiloxane) (PDMS) replica of a lotus leaf surface and found the water contact angle of 160° for the rough surface, whereas for the smooth PDMS surface it is about 105°.

Surfaces with the contact angle between 150° and 180° are called superhydrophobic, although some definitions also imply low contact angle hysteresis and, sometimes, the ability to repel incoming water droplets. Contact angle hysteresis is the difference between the advancing and receding contact angles, which are two stable values. If additional liquid is added to a sessile drop, the contact line advances and each time motion ceases, the drop exhibits an advancing contact angle. Alternatively, if liquid is removed from the drop, the contact angle decreases to a receding value before the contact retreats. For a droplet, moving along the solid surface (for example, if the surface is tilted) there is another definition. The contact angle at the front of the droplet (advancing contact angle) is greater than that at the back

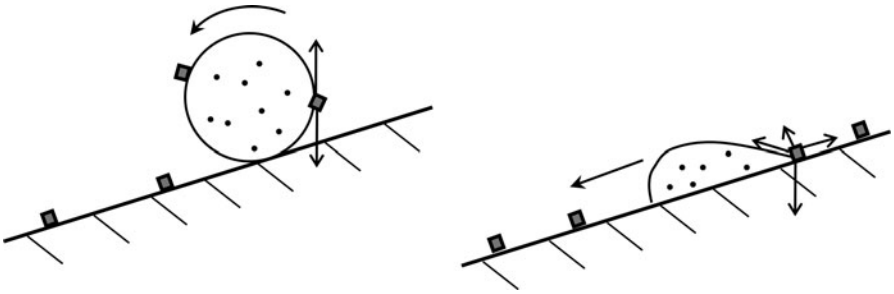

Fig. 11.1 Self-cleaning of a superhydrophobic surface. A drop with a very high contact angle (*left*) washes out contamination particles, while a drop with low contact angle (*right*) does not clean the surface. Forces acting upon a particle are shown

of the droplet (receding contact angle), due to roughness, resulting in the contact angle hysteresis. It has been disputed whether the two definitions are equivalent (Krasovitsky and Marmur 2004); however, in many cases the two definitions have the same meaning. Surfaces with low contact angle hysteresis have a very low water roll-off angle that denotes the angle to which a surface must be tilted for rolling off of water drops (i.e., very low water contact angle hysteresis) (Extrand 2002; Kijlstra et al. 2002).

The interest in superhydrophobicity in the past decade or two is caused by the ability to design, synthesize, and manufacture more sophisticated microstructured surfaces. Numerous micro/nanotribological and micro/nanomechanical application, such as in the microelectromechanical systems (MEMS) require surfaces with low adhesion and stiction. As the size of these devices decreases, the surface forces tend to dominate over the volume forces, and adhesion and stiction constitute a challenging problem for proper operation of these devices. This makes the development of nonadhesive surfaces crucial for many of these emerging applications. It has been suggested that extremely water-repellent (superhydrophobic) surfaces produced by applying a micropatterned roughness combined with hydrophobic coatings may satisfy the need for the nonadhesive surfaces (Nosonovsky and Bhushan 2005a, b, 2006a, b, 2007a, 2008c, e). Wetting may lead to the formation of menisci at the interface between solid bodies during sliding contact, which increases adhesion/friction. As a result of this, the wet friction force is greater than the dry friction force, which is usually undesirable. On the contrary, high adhesion is desirable in some applications, such as adhesive tapes and adhesion of cells to biomaterial surfaces; therefore, enhanced wetting by changing roughness would be desirable in these applications (Nosonovsky and Bhushan 2005a, b, 2006a, 2008c, e).

The lotus effect involves two important properties that are typical for many water-repellent plant leaves: superhydrophobicity and self-cleaning. A surface with the water contact angle greater than 150° and with low contact angle hysteresis is called superhydrophobic. A water droplet rolls along such a surface even when the surface is tilted for a small angle (Fig. 11.1). Self-cleaning is the ability of

many superhydrophobic surfaces to remain clean, since rolling water droplets wash out contamination particles such as dust or dirt. The typical example of a natural superhydrophobic self-cleaning surface is the lotus leaf as well as leaves of many similar water-repellent plants, insect and bird wings, etc. Artificial superhydrophobic surfaces have been introduced in the past decade and a variety of production methods (self-assembly, lithography, sol–gel) and materials (polymers, metals, Si, etc.) have been suggested.

Superhydrophobicity is a result of surface roughness combined with a hydrophobic (low surface energy) coating (e.g., wax or Teflon), with the roughness that magnifies the effect of the coating. The typical size of roughness details in superhydrophobic surfaces is usually of the micron scale. Numerous attempts to mimic the lotus effect for various applications have been made in recent years. These attempts are stimulated, on the one hand, by the development of the technology of micropatterned surfaces (such as lithography), and on the other hand, by the increasing need for nonadhesive (nonsticky) surfaces. Since the surface-to-volume ratio grows with miniaturization, the surface effects are crucial for microdevices such as microelectromechanical systems. In addition to microdevices, the lotus effect finds its application for conventional self-cleaning surfaces (paints, glasses, textiles, etc.), and possible applications for underwater devices, microfluidics, and other areas have been discussed.

11.2 Superhydrophobic Plant Leaves

In this section, superhydrophobic plant leaves, bird feathers, insect wings and legs are discussed. Hydrophobic and water-repellent abilities of many plant leaves have been known for a long time. Scanning electron microscope (SEM) studies of the past 30 years revealed that the hydrophobicity of the leaf surface is related to its microstructure. All primary parts of plants are covered by a cuticle composed of soluble lipids embedded in a polyester matrix, which makes the cuticle hydrophobic in most cases (Barthlott and Neinhuis 1997). The outer single-layered group of cells covering a plant, especially the leaf and young tissues, is called the epidermis. The epidermal cells of leaves produce the protective waxy covering or the cuticle. The cuticle is composed of an insoluble cuticular membrane covered with epicuticular waxes, which are mixtures of hydrophobic aliphatic components, hydrocarbons with chain lengths typically in the range C_{16} to C_{36}, such as paraffins (Baker 1982). The SEM study reveals that the lotus leaf surface is covered by "bumps," more exactly called *papillae* (papillose epidermal cells), which, in turn, are covered by an additional layer of epicuticular waxes (Barthlott and Neinhuis 1997). The wax is hydrophobic with water contact angle of about 95°–110°, whereas the experimental values of the static water contact angle with the lotus leaf were reported as about 160° (Barthlott and Neinhuis 1997). The increase of the contact angle is a result of the surface roughness due to the papillae.

Neinhuis and Barthlott (1997) studied systematically surfaces and wetting properties of about 200 water-repellent plants. They reported several types of epidermal relieves and epicuticular wax crystals, with the papillose epidermal cells as one type of the relief. In leaves having the papillae, either every epidermal cell forms a single papilla or a cell is divided into papillae. The scale of the epidermal relief ranged from 5 μm in multipapillate cells to 100 μm in large epidermal cells. Some surfaces also were convex (rather than having real papillae) and/or had hairs (trichomes). A droplet tends to form a heterogeneous (Wenzel) interface on the surface of a leaf with air pockets trapped between the papillae. This significantly decreases the solid–liquid contact area.

Wagner et al. (2003) also found various types and shapes of wax crystals at the surface. Interestingly, the hairy surfaces without wax, being subjected to rain, exhibited water repellency for short periods (minutes), after which water penetrated under the hairs, whereas waxy trichomes led to strong water repellency. The chemical structure of the epicuticular waxes has been studied extensively by plant scientists and lipid chemists in recent decades (Jetter et al. 2006). The wax crystal surface is very rough, in addition to the roughness created by the papillae. Apparently, roughness plays the dominant role in the lotus effect, since the superhydrophobicity can be achieved independently of type of wax or other hydrophobic coating.

While it is intuitive that water repellency and self-cleaning are related to each other, since the ability to repel water is related to the ability to repel contaminants, it is difficult to quantify self-cleaning. As a result, a quantitative relation of the two properties remains to be established. A qualitative explanation of the self-cleaning was proposed by Barthlott and Neinhuis (1997), who suggested that on a smooth surface contamination particles are mainly redistributed by a water droplet, whereas on a rough surface they adhere to the droplet and are removed from the leaves when the droplet rolls off. A detailed model of this process has not been developed, but, obviously, whether the particle adheres to the droplet depends upon the interactions at the triple line and on whether the magnitude and direction of the surface force allows the particle to be detached from the surface and flown away (Fig. 10.1).

As far as the biological implications of the lotus effect, Barthlott and Neinhuis (1997) suggested that self-cleaning plays an important role in the defence against pathogens, such as spores and conidia of pathogenic microorganisms.

11.3 Rose Petal Effect

Recent experimental findings and theoretical analyses made it clear that the early Wenzel (1936) and Cassie and Baxter (1944) models do not explain the complexity of interactions during wetting of a rough surface, which can follow several different scenarios (Jin et al. 2005; Wang and Jiang 2007; Feng et al. 2008; Xia and Jiang 2008; Gao and McCarthy 2008; McHale 2009; Bhushan and Her 2010; Bhushan and Nosonovsky 2010). As a result, there are several modes of

wetting of a rough surface, and therefore, wetting cannot be characterized by a single number, such as the CA.

Consider now a rough solid surface with the roughness factor $R_f > 1$ equal to the ratio of the solid surface area to its flat projected area. When water comes in contact with such a surface, the effective values of the solid–liquid and solid–air surface energies become $R_f\gamma_{SL}$ and $R_f\gamma_{SA}$. This leads to the Wenzel equation for the CA with a rough surface (Wenzel 1936)

$$\cos\theta = R_f \cos\theta_0. \tag{10.1}$$

If some air is trapped between the rough solid surface and the liquid, then only the fraction $0 < f_{SL} < 1$ constitutes the solid liquid contact interface. The area of the solid–liquid interface is now $R_f f_{SL}$ per unit area, and, in addition, there is $(1 - f_{SL})$ of the liquid–air interface under the droplet. The effective values of the solid–liquid and solid air surface energies become $R_f f_{SL}\gamma_{SL}$ and $R_f f_{SL}\gamma_{SA} + (1 - f_{SL})\gamma_{LA}$. The CA is then given by the Cassie and Baxter (1944) equation

$$\cos\theta = R_f f_{SL} \cos\theta_0 - 1 + f_{SL}. \tag{10.2}$$

If a surface is covered by holes filled (or impregnated) by water, the contact angle is given by

$$\cos\theta = 1 + f_{SL}(\cos\theta_0 - 1). \tag{10.3}$$

This is so-called "impregnating" Cassie wetting regime (Nosonovsky and Bhushan 2008a,c).

In the ideal situation of a perfectly smooth and homogeneous surface, the static CA is a single number which corresponds to the unique equilibrium position of the solid–liquid–air contact line (the triple line). However, when the contact takes place with a rough surface, there may be multiple equilibrium positions which result in an entire spectrum of possible values of the CA. In addition, the value of the surface energy itself exhibits so-called "adhesion hysteresis" and can depend on whether it is measured during the approach of the two bodies or when they are taken apart. As the result, there is always the minimum value of the CA called the receding CA, θ_{rec}, and the maximum value of the CA called the advancing CA, θ_{adv}. The difference between the advancing and receding CA is called CA hysteresis.

The CA is a macroscale parameter characterizing wetting. However, hydrophobicity/philicity is dependent upon the adhesion of water molecules to the solid. On the one hand, a high CA is a sign of low liquid–solid adhesion. On the other hand, low CA hysteresis is a sign of low liquid–solid adhesion as well. There is an argument in the literature as to whether superhydrophobicity is adequately characterized only by a high CA and whether a surface can have a high CA but at the same time strong adhesion. It is now widely believed that a surface can be superhydrophobic and at the same time strongly adhesive to water (e.g., Jin et al. 2005). The so-called "petal effect" is exhibited by a surface that has a high CA,

but also a large CA hysteresis and strong adhesion to water. The phenomenon of the large CA hysteresis and high water adhesion to rose petals (and similar surfaces), as opposed to small CA hysteresis and low adhesion to lotus leaf, was observed by several research groups (Bormashenko et al. 2009; Chang et al. 2009; Bhushan and Her 2010). Bormashenko et al. (2009) reported a transition between wetting regimes, e.g., the penetration of liquid into the micro/nanostructures.

Li and Amirfazli (2007) argued that since "superhydrophobicity" means a strong fear of water or lacking affinity to water, "the claim that a superhydrophobic surface also has a high adhesive force to water is contradictory." Gao and McCarthy (2008) pointed out that the terms "hydrophobic/phillic" should be defined in a more accurate way. They suggested several experiments showing that even Teflon®, which is usually considered very hydrophobic, can be, under certain conditions, considered hydrophilic, i.e., has affinity to water. They argued that the concepts of "shear and tensile hydrophobicity" should be used, so that the wettability of a surface is characterized by two numbers, advancing and receding CAs, and "the words hydrophobic, hydrophilic, and their derivatives can and should only be considered qualitative or relative terms." Instead, "shear and tensile hydrophobicity" should be investigated, which makes wetting (solid–liquid friction) similar to the friction force, as it has been pointed out in the literature earlier (Nosonovsky 2007b). McHale (2009) noted that all solid materials, including Teflon®, are hydrophobic to some extent, if they have Young CA $<180^{\circ}$. Therefore, it is energetically favorable for them to have contact with solid, at least to some extent. Wang and Jiang (2007) suggested five superhydrophobic states (Wenzel's state, Cassie's state, so-called "Lotus" and "Gecko" states, and a transitional state between Wenzel's and Cassie's states). It may be useful also to see the transition between the Wenzel, Cassie, and dry states as a phase transition and to add the ability of a surface to bounce off water droplets to the definition of the superhydrophobicity (Nosonovsky and Bhushan 2008d). In addition, there is an argument on how various definitions of the CA hysteresis are related to each other (Krasovitski and Marmur 2004; Bormashenko et al. 2007a, b, 2009; Chang et al. 2009; Xia and Jiang 2008).

Prof. Bhushan and his coworkers from the Ohio State University investigated the surface roughness of two rose petals measured with an AFM. The data indicates that the low adhesion specimen (Rosa, cv. Showtime) has higher density and height of the bumps, indicating that the penetration of water between the microbumps is less likely. Wetting of a rough surface with a single level of hierarchy of roughness details can follow several scenarios (Table 11.2).

Bhushan and Her (2010) conducted a series of carefully designed experiments to decouple the effects of the micro- and nanostructures. They synthesized microstructured surfaces with pillars out of epoxy resin. The epoxy surfaces were reproduced from model Si templates and were created by a two-step molding process producing a dual replica (first a negative replica and then a positive replica of the original Si template). Surfaces with a pitch (the periodicity of the structure of the pillars) of 23, 105, and 210 μm and with the same diameter (14 μm) and height (30 μm) of the pillars were produced. After that, nanostructures were created on the microstructured sample by self-assembly of the alkane *n*-hexatriacontane

Table 11.2 Wetting regimes of a surface with a single level of hierarchy of roughness

State	Cassie–Baxter	Wenzel	Impregnating Cassie
Cavities	Air	Water under droplet	Water everywhere
CA	High	High	High
CA hysteresis	Low	Can be high	Low

Table 11.3 Different regimes of wetting of a surface with dual roughness

	Air in microstructure	Water under droplet in microstructure	Water impregnating microstructure
Air in nanostructure	Lotus, high CA, low CA hysteresis	Rose, high CA, high CA hysteresis	Rose filled microstructure
Water under droplet in nanostructure	Cassie (air-filled microstructure, water in nanostructure), high CA, low CA hysteresis	Wenzel (water in micro- and nanostructure), high CA, high or low CA hysteresis	Wenzel filled microstructure
Water impregnating nanostructure	Cassie filled nanostructure	Wenzel filled nanostructure	Wenzel filled micro and nanostructure

($CH_3(CH_2)_{34}CH_3$) deposited by a thermal evaporation method. Alkanes of varying chain lengths are common hydrophobic compounds of plant waxes. On smooth surfaces, alkanes can cause a large contact angle and a small contact angle hysteresis for water droplets. To fabricate the nanostructure, various masses of *n*-hexatriacontane were coated on a microstructure. The nanostructure is formed by three-dimensional platelets of *n*-hexatriacontane. Platelets are flat crystals, grown perpendicular to the surface. They are randomly distributed on the surface, and their shapes and sizes show some variation. When different masses of wax are applied, the density of the nanostructure is changed (Bhushan and Nosonovsky 2010).

For a hierarchical structure with small bumps on top of the larger bumps, a larger number of scenarios is available, and they are summarized in Table 11.3 and Fig. 11.2. Water can penetrate either in the micro- or nanostructure, or into both. In addition, the micro- or nanostructure can be impregnated by water or air. The regimes with water penetrating into the microstructure can have high solid–water adhesion and therefore high CA hysteresis (Bhushan and Nosonovsky 2010).

For surfaces with a small pitch of 23 μm, while the mass of *n*-hexatriacontane is changed, there are only small changes in the static contact angle and contact angle hysteresis values, which means that they are always in the "Lotus" wetting regime. On the surface with a 210 μm pitch value, as the mass of *n*-hexatriacontane is increased, the static contact angle is increased, and the reverse trend was found for the contact angle hysteresis. This was interpreted as evidence that the nanostructure is responsible for the CA hysteresis and low adhesion between water and the solid surface. The wetting regimes are shown schematically in Fig. 11.3 as a function of

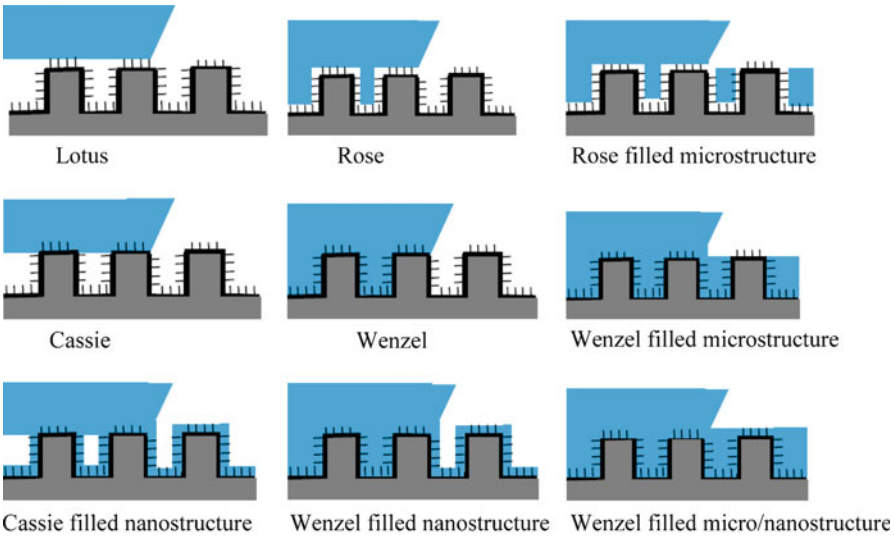

Fig. 11.2 Schematics of nine wetting scenarios for a surface with hierarchical roughness (Bhushan and Nosonovsky 2010)

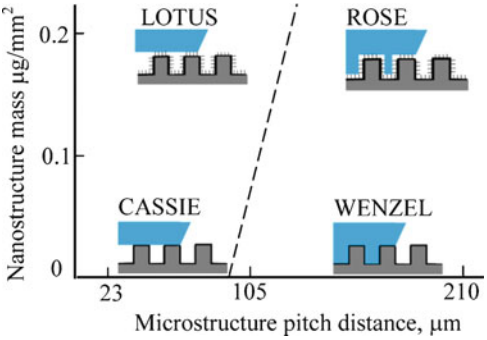

Fig. 11.3 Schematic of a wetting regime map as a function of microstructure pitch and the mass of nanostructure material. The mass of nanostructure material equal to zero corresponds to microstructure only (with the Wenzel and Cassie regimes). Higher mass of the nanostructure material corresponds to higher values of pitch, at which the transition occurs (Bhushan and Nosonovsky 2010)

the pitch of the microstructure and the mass of *n*-hexatriacontane. Small mass of the nanostructure material correspond to the Cassie and Wenzel regimes, whereas high mass of nanostructure corresponds to the Lotus and Rose regimes. The Lotus regime is more likely for larger masses of the nanostructure material (Bhushan and Nosonovsky 2010).

To further verify the effect of wetting states on the surfaces, evaporation experiments with a droplet on a hierarchical structure coated with two different amounts of *n*-hexatriacontane were performed. On the *n*-hexatriacontane

(0.1 μg mm^{-2}) coated surface, an air pocket was not visible at the bottom area of the droplet. However, the droplet on the surface has a high static contact angle (152°) since the droplet still cannot completely impregnate the nanostructure. The footprint size of the droplet on the surface has only small changes from 1,820 to 1,791 μm. During evaporation, the initial contact area between the droplet and hierarchical structured surface does not decrease until the droplet evaporates completely, which means complete wetting between droplet and microstructures. For the *n*-hexatriacontane (0.2 μg mm^{-2}) coated surface, the light passes below the droplet, and air pockets can be seen, so to start with the droplet is in the Cassie–Baxter regime. When the radius of the droplet decreased to 381 μm, the air pockets are not visible anymore. The footprint size of the droplet on the surface is changed from 1,177 to 641 μm, since droplet remained on only a few pillars until the end of the evaporation process (Bhushan and Nosonovsky 2010).

The experimental observations of the two types of rose petals show that hierarchically structured plant surfaces can have both adhesive and nonadhesive properties at the same time with high CA. This is due to the existence of various modes of wetting of a hierarchical surface, so that water can penetrate either into macro- or nanoroughness, or into the both. Water penetration into the microroughness tends to result in high adhesion with the solid surface, whereas the presence of the nanoroughness still provides high CA. As a result, two distinct modes of wetting are observed, one can be called the "lotus" mode with low adhesion and one is the "rose" mode with high adhesion (Bhushan and Nosonovsky 2010) (Table 11.4).

Table 11.4 Typical materials and corresponding techniques to produce micro/nanoroughness

Material	Technique	Contact angle	Notes	Source
Teflon	Plasma	168		Zhang et al. (2004a); Shiu et al. (2004)
Fluorinated block polymer solution	Casting under humid environment	160	Transparent	Yabu and Shimomura (2005)
PFOS	Electro- and chemical polymerization	152	Reversible (electric potential)	Xu et al. (2005)
PDMS	Laser treatment	166		Khorasani et al. (2005)
PS-PDMS, Block copolymer	Electrospinning	>150		Ma et al. (2005)
PS, PC, PMMA	evaporation	>150		Bormashenko et al. (2006)
PS nanofiber	Nanoimprint	156		Lee et al. (2004)
PET	Oxygen plasma etching	>150		Teshima et al. (2005)
Organotriethoxysilanes	Sol–gel	155	Reversible (temperature)	Shirtcliffe et al. (2005)
Al	Chemical etching	>150		Qian and Shen (2005)

(continued)

Table 11.4 (continued)

Material	Technique	Contact angle	Notes	Source
Copper	Electrodeposition	160	Hierarchical	Shirtcliffe et al. (2004)
Si	Photolithography	170		Bhushan and Jung (2007)
Si	E-beam lithography	164		Martines et al. (2005)
Si	X-ray lithography	>166		Furstner et al. (2005)
Si	Casting	158	Plant leaf replica	Sun et al. (2005); Furstner et al. (2005)
Si (Black Si)	Plasma etching	>150	For liquid flow	Jansen et al. (1995)
Silica	Sol-gel	150		Hikita et al. (2005); Shang et al. (2005)
Polyelectrolyte multilayer surface overcoated with silica nanoparticles	Self assembly	168		Zhai et al. (2004)
Nanosilica spheres	Dip coating	105		Klein et al. (2003)
Silica colloidal particles in PDMS	Spin coated	165	Hierarchical	Ming et al. (2005)
Au clusters	Electrochemical deposition	>150		Zhang et al. (2004b)
Carbon nanotubes	CVD	159		Huang et al. (2005)
ZnO, TiO_2, Nanorods	Sol-gel	>150	Reversible (UV irradiation)	Feng et al. (2004)

11.4 Insect and Bird Wings

One of the recently studied biological objects demonstrating pronounced superhydrophobic properties is the dove's feather (Bormashenko et al. 2007a, b), Water-repellent abilities of bird-winds are known from ancient times (Nosonovsky and Bormashenko 2009). The Biblical narrative tells about the patriarch Noah who sent a dove to discover whether the earth had become dry after the Flood (Genesis, 8:8). The bird returned safely to the Ark without suffering from surrounding water. This is due to unusual properties of its feather (pennae). Feathers of birds perform several important functions: they form an insulating layer around the body, they form wing and tail surfaces which are essential for flying, their coloration can provide a bird with a camouflage and, last but not least, they keep a body waterproofed (Nosonovsky and Bormashenko 2009).

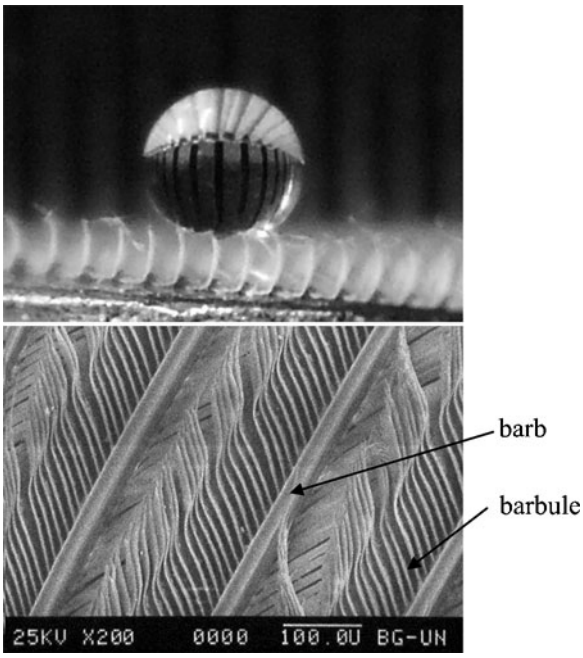

Fig. 11.4 Water drop upon pigeon feather. Microstructure of the feather (Nosonovsky and Bormashenko 2009)

It is generally agreed that water-repelling properties of the outer feathers (pennae) are due to the preen oil (preen wax) spread by the bird under the preening procedure (Damste et al. 2000). However, as discussed by Bormashenko et al. (2007a, b). Doves, unlike for water fowl, have their waterproof abilities at least partially stipulated by the complicated makeup of the feather. The details of the dove's feather morphology, which was investigated by Prof. E. Bormashenko from Ariel University Center (Israel), are depicted in Fig. 11.4 (Nosonovsky and Bormashenko 2009). The network formed by keratin built barbs and barbules can be seen. The water droplets deposited on the thoroughly cleansed feather vanes demonstrated obtuse contact angles as high as 140°–150°. Since contact angle measured on the rachis (or vertebral column) are much smaller, that large contact angles on feather's vane cannot be explained by the increase of the surface underlying the liquid since this can only amplify the wetting (the Wenzel effect). Moreover, measured contact angles follow the prediction of Cassie model discussed below in detail (Bormashenko et al. 2007a, b). The water droplets, supported by a network formed by barbs and barbules, sit partially on air pockets. Small static apparent angle hysteresis also justifies Cassie–Baxter wetting hypothesis. The hierarchical twofold structure of the dove's feather is noteworthy. An importance of hierarchical roughness, promoting water-repellency will be discussed below (Bormashenko et al. 2006). Extremely high contact angles (177°) were also observed recently on some insect (dragonfly) wings. Superhydrophobicity on these objects was also attributed to the Cassie wetting regime (Song et al. 2007).

The hydrophobic abilities of rough surfaces are utilized also by insects that live close to water. A water strider (*Gerris remigis*) has the ability to walk upon the surface of the water without getting wet. Even the impact of rain droplets with a size greater than the strider's size does not immerse the insect. Gao and Jiang (2004) showed that the special hierarchical structure of strider legs, which are covered by large numbers of oriented tiny hairs (microsetae) with fine nanogrooves, might be responsible for the water resistance. According to their measurements, a leg does not pierce the water surface until a dimple of 4.38 mm depth is formed. They found that the maximal supporting force of a single leg is 1.52 mN, or about 15 times the total body weight of the insect. The corresponding volume of water ejected is roughly 300 times that of the leg itself. Gao and Jiang (2004) suggested that superhydrophobicity of the water strider leg is responsible for these abilities. They measured the contact angle of the insect's legs with water and found it equal to 167.6°. Scanning electronic micrographs revealed numerous oriented setae on the legs. The setae are needle-shaped hairs, with diameters ranging from 3 μm down to several hundred nanometers. Most setae are roughly 50 μm in length and arranged at an inclined angle of about 20° from the surface of leg. Many elaborate nanoscale grooves were found on each microseta, and these form a unique hierarchical structure. This hierarchical micro- and nanostructuring on the leg's surface seems to be responsible for its water resistance and the strong supporting force (Nosonovsky and Bormashenko 2009).

Besides plant leaves, insects and birds, the Lotus-effect-based self-cleaning was also found in other living organisms having the hierarchical organization of the surface structure, such as the toes or legs of gecko, which are notorious for their "smart" adhesive properties.

11.5 Lotus-Effect-Based Self-Cleaning

In addition the ability to repelling water, self-cleaning is another important feature associated with the lotus effect. There is a qualitative understanding that water-repellent surfaces also repel other contaminants and that dust can easily be washed from them by flowing water. A number of experimental studies have been conducted. The self-cleaning abilities of patterned surfaces were investigated by Furstner et al. (2005). They studied Si wafer specimens with regular patterns of spikes that were manufactured by X-ray lithography. The specimens were hydrophobized with Au thiol. For comparison, they also studied replicates of plant surfaces, made by a two-component silicon molding mass applied onto the leaf surface. The negative replica is flexible and rubber-like. A melted hydrophobic polyether was applied onto this mold. They also studied several metal foil specimens, hydrophobized by means of a fluorinated agent. In order to investigate the self-cleaning effect, a luminescent and hydrophobic powder was used as a contaminant. Following contamination, the specimens were subjected to an artificial fog and rain (Furstner et al. 2005).

At this point, there has been proposed no quantitative theory of self-cleaning that would relate, for example, the hydrophobic properties of the surface with size or composition of a contaminating particle being washed away. Such a theory perhaps can be build using thermodynamic considerations. The basis for that is the fact that washing away a contaminant increases the "orderliness" of the surface, thus decreasing the entropy of mixing. Therefore, we are dealing here with the situation when microscopically observed orderliness of the system is dependent on the energy dissipated due to the droplet flow.

Droplets of water easily rolled off the Si samples easily with a microstructure consisting of rather slender and sufficiently high spikes; this is attributed to the fact that the Cassie wetting state occurred (Nosonovsky and Bhushan 2008a). These samples could be cleaned after artificial contamination by means of the fog treatment almost completely. The behavior of water drops was different upon surfaces with low spikes and a rather high pitch. The researchers found a considerable decrease of the contact angles and a distinct rise in the sliding angles apparently corresponding to the Wenzel state. Some metal foils and some replicates had two levels of roughness. These specimens did not show a total removal of all contaminating particles when they were subjected to artificial fog, but water drops impinging with sufficient kinetic energy could clean them perfectly. A substrate without structures smaller than 5 μm could not be cleaned by means of fog consisting of water droplets with diameter 8–20 μm because this treatment resulted in a continuous water film on the samples. However, artificial rain removed all the contamination. On the contrary, smooth specimens made of the same material could not be cleaned completely by impinging droplets. This is a clear indication of the different contact phenomena on smooth hydrophobic in contrast to self-cleaning microstructured surfaces. Another interesting observation of this group was that despite the missing structure of the wax crystals, the water contact angle of the Lotus replica was the highest of all the replicates, indicating that the microstructure formed by the papillae alone is already optimized with regard to water repellency (Furstner et al. 2005).

11.6 Titania-Based Superhydrophilic Self-Cleaning

A completely different approach to self-cleaning is based on the use of photocatalytic properties of titania (titanium dioxide, TiO_2). Photolysis is a chemical reaction in which a chemical compound is broken down to its components by light. Fujishima and Honda (1972) found that titania could split water into hydrogen and oxygen when subjected to ultraviolet light. This phenomenon is known as photocatalysis, or the acceleration of a photolysis in the presence of a catalyst. The effect is more pronounced for a thin layer of titania. Thus, a submicron scale layer of titania can split organic compounds into CO_2 and H_2O molecules. This is especially important, since rupturing molecules used by bacteria for attachment can be used for disinfection.

The mechanism of the photocatalysis is a consequence of its semiconductive properties. A photon of ultraviolet (UV) light with a wavelength of about 388 nm can lift an electron into the empty "conduction band," where electrons can flow and carry a current. The negative electron and a positive hole, which form due to this process, can interact with water and oxygen at the surface of the titania, producing superoxide radical anions (O_2^-) and hydroxyl radicals (OH). These are highly reactive chemical species that can then convert organic compounds to carbon dioxide and water (Forbes 2008).

A thin film from of titania particles (prepared by annealing an aqueous suspension) has the property of complete wettability showing water and oil contact angle of zero degrees. The ultraviolet light removes some of the oxygen atoms from the surface, resulting in a patchwork of nanoscale domains where hydroxyl groups become adsorbed, which produced the superhydrophilicity (Forbes 2008). As a result, a water layer spreads at the surface carrying away contamination particles. Such surfaces have antifogging properties, since condensed water vapor forms film on its surface, rather than microscopic droplets (Wang et al. 1997, 1998). The main limitation of this technology is need of UV irradiation, e.g., sunlight. Numerous research has been conducted since the 2000s on using TiO_2 in combination with other self-cleaning technologies as well as in combination with other materials, such as the PVDF membranes (Darmodar et al. 2009), Carbowax Lam et al. (2008) etc., utilizing antibacterial properties.

11.7 Applications of Self-Cleaning Surfaces

A number of products that utilize the lotus effect are already commercially available or being developed. In addition, many patents have been granted for various possible applications of the self-cleaning surfaces. Most applications utilize the self-cleaning effect using superhydrophobicity. Among them are glasses for architectural, automotive, optical, and other applications, tiles for roofs, bathrooms and shower cabins, sprays and paints, which creates clean surface (e.g., graffiti-resistant) have been suggested, as well as water-repellent textiles. Some agricultural applications are also discussed (e.g., pesticide additives that can decrease bouncing off plant surfaces or increase penetration into the soil). Cleaning of windows is an expensive and cumbersome process, especially if the windows are on a skyscraper. The hydrophilic route to self-cleaning windows has been realized by several companies and has been released to market. How far these windows will be a commercial success remains to be seen (Blossey 2003).

The German-based website Lotus-Effekt.de, dedicated to the commercial application of patented self-cleaning superhydrophobic micro-to-nanostructured surfaces, states the following:

"*Lotusan*®, an exterior paint from the firm *Sto* is marketed already with the greatest success since 1999. It is used by professional firms of house painters and is, not yet,

available for the general building trade. Up to the present *Lotusan*® has been used to paint c. 300,000 buildings. In 2004 *Degussa* (daughter company of *Goldschmidt*) has introduced the first spray: *Tegotop*® 105 which can be used to impregnate surfaces. Self-cleaning textiles are being tested at present and will be available commercially from summer 2005. Marquees will probably be the first to receive such treatment. Optical sensors in public high impact areas (for instance, toll bridge sensors on highways) are furnished already throughout Germany with Lotus-*Effect*® glass manufactured by *Ferro AG*. A series of further products is being tested, among these *Aeroxide*® LE of the *Degussa* for plastics. For years self-cleaning glasses have figured in advertisement. Frequently this is about so-called photo catalytic stratification. The firm *Ferro* keeps prototypes of architectural glass with Lotus-*Effect*® in permanent test conditions. In the region of optical sensors (toll bridges) Lotus-*Effect*® glasses are already used successfully. For architectural glass and rear windows of cars applications will probably follow soon. With *Erlus-Lotus*® the first self-cleaning roof in the world came on the market. For demonstrations we employ a spoon with a perfect Lotus-*Effect*® surface. Honey and many other substances roll off without a hint of residue. The spoon is a prototype that is, unfortunately, not for sale. Firms can already order the first spray Tegotop® 105 for testing from the *Degussa-Goldschmidt AG*. The properties of the new-fangled intelligent textiles are astonishing. Not only does water roll off, but ketchup and red wine do likewise. The area of use will hardly lie with suits, ties or shirts, but rather with outdoor clothing, marquees, tents and with tarpaulins for lorries".

In addition to the household and "conventional" products, possible use of roughness- or heterogeneity-induced superhydrophobicity in nano- and biotechnology applications is often discussed: This includes, for example, nonsticky surfaces for the components of micro/nanoelectromechanical systems (NEMS/MEMS). Since adhesion plays an important role for small devices, the so-called "stiction" of two component surfaces is a significant problem in that industry, which may lead to device failure. Making a surface hydrophobic can reduce meniscus force and stiction (Nosonovsky and Bhushan 2008a).

Controlling droplets containing biologically relevant molecules (DNA and proteins) is important in biotechnology. Superhydrophobicity is useful for these applications: the almost fully spherical droplets on a superhydrophobic surface can shrink exactly like a drop in free air. Furthermore, the positioning and shape of water droplets can be controlled by a pattern that combines hydrophilic and hydrophobic elements. Interestingly, some desert beetles capture their drinking water by a hydrophobic/philic structured back (Parker and Lawrence 2001). At a patterned heterogeneous substrate, hydrophilic regions can help to contain small liquid volumes of DNA, which may improve spotting and analyzing DNA and proteins by avoiding wall contact (Gillmor et al. 2000; Blossey 2003).

In micro/nanofluidics, a guided motion of droplets on heterogeneous hydrophobic/philic surfaces gives the opportunity to develop droplet-based microfluidics systems, as opposed to the classical concept based on microfluidic channels. Droplets moving freely on open surfaces and bulk liquids flowing in channels

constitute two extremes, while the patterned heterogeneous hydrophobic/philic surfaces being the intermediate between these two (Drelich et al. 1996). Driving the liquids along the channels and making them merge at predefined locations offers a novel way to mix reactants or steer biochemical reactions, defining the concept of a "liquid microchip" (Gau et al. 1999) or "surface-tension confined microfluidics" (Lam et al. 2002). These open structures have advantages over capillaries, because blocking of the capillary by unforeseen chemical reactions cannot occur. Droplets have very low contact areas with the substrate, they are easy to move by external fields, for example, electrostatic forces or surface capillary waves. Systems that make use of a droplet-based actuation mechanism are also being developed, and their aim is to control droplet positioning and motion on the substrates with as little surface contact as possible, and to turn the droplet-based system into a programmable reactor, by which the liquid positions are prescribed and tuned (Blossey 2003).

The company "Brinker Technology" developed the Platelet Technology as a new and novel method of sealing and locating leaks in pressurized pipelines. It is based on the remote injection of discrete particles known as "Platelets" into a pipeline, which are carried to the leak site due to the flow. When they reach the vicinity of the leak fluid forces entrain them into the leak and hold them against the pipe wall thus facilitating sealing. The technology was first deployed in a 10″ water injection line in BP's Foinaven Field in the UKCS during the Fall of 2004. The Platelet Technology was also applied to seal and locate leaks in small bore subsea umbilical lines. Leaks in these systems are particularly problematic because they are difficult to locate and the eventual external egress of fluid may be some distance from the actual line failure due to the presence of additional outer sheaths. In addition as subsea developments are increasingly involving longer and deeper tie-backs, methods of remote intervention, like this technology, will become more and more important. The fundamental principle behind leak location in these lines is that the creation of a Platelet seal, which is usually an almost instantaneous event, modifies the pressure and flow properties in the line. Through the use of remote pressure and flow monitoring techniques these changes can be detected and used to calculate the location of the leak to a considerable degree of accuracy (within 1% of the line length) (Ryan 2007). Self-cleaning can also be successfully used for concrete pavement to prevent ice formation (Sanchez and Sobolev 2010) as well as for superhydrophobic filters and desalination membranes to prevent the accumulation of contaminants (Bormashenko et al. 2008).

11.8 Deicing and Icephobicity

Ice formation and accretion is undesirable for many systems including airplanes, highway and powerline maintenance, and building construction, water heaters, air conditioners, refrigerators, windmills, ships, and telecommunications equipment. Deicing (the removal of frozen contaminant from a surface) and antiicing (protecting against the formation of frozen contaminant) are significant problems for many applications that have to operate below the water freezing temperature:

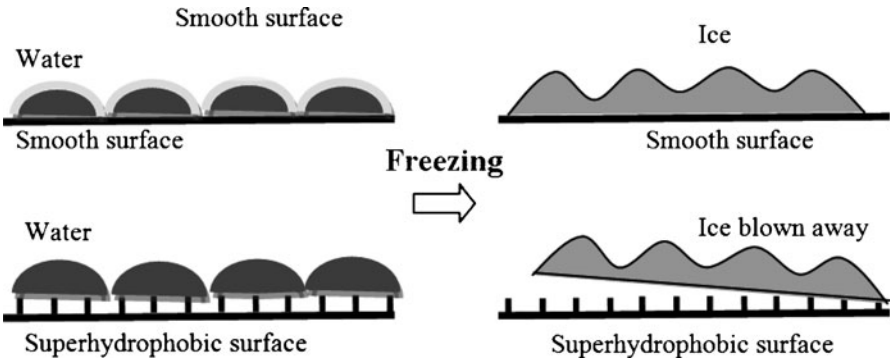

Fig. 11.5 Icephobic microstructure surface. Water is not condensed, so ice layer is not formed

aircrafts, machinery, road and runway pavements, traffic signs and traffic lights, etc. The traditional approaches to deicing include mechanical methods, heating, and the deposition of dry or liquid chemicals that lower the freezing point of water. Antiicing is accomplished by applying a protective layer of a viscous antiice fluid. All antiice fluids offer only limited protection, dependent upon frozen contaminant type and precipitation rate, and it fails when it no longer can absorb the contaminant. In addition to limited efficiency, these deicing fluids, such as propylene glycol or ethylene glycol can be toxic and raise environmental concerns. Antiicing on roadways is used to prevent ice and snow from adhering to the pavement, allowing easier removal by mechanical methods (Fig. 11.5).

Ice formation occurs due to condensation of vapor phase water and further freezing of liquid water. For example, droplets of supercooled water that exist in stratiform and cumulus clouds crystallize into ice when they are struck by the wings of passing airplanes. Ice formation on other surfaces, such as pavements or traffic signs, also occurs via the liquid phase. It is, therefore, suggested that a water repellent surface can also have deicing properties. When such a surface is wetted by water, an air layer or air pockets are usually kept between the solid and the water droplets. After freezing, ice will not adhere to solid due to the presence of air pockets and will be easily washed or blown away.

Despite the pervasiveness of the icing problem, the fundamentals of ice adhesion have received relatively little attention in the scientific literature, and it is not widely understood which attributes must be tuned to systematically design "icephobic" surfaces that are resistant to icing. Most current deicing systems include either physical or chemical removal of ice, both energy and resource-intensive. A more desirable approach would be to prevent ice formation rather than to fight its build-up (Cao et al. 2009).

Under at least some environmental conditions, superhydrophobic surfaces can minimize or even eliminate ice formation by repelling impinging water drops before they can freeze. Subsequent research will build on these results, possibly leading to the fabrication of commercially viable and durable icephobic surfaces that mitigate the icing problem under all environmental conditions (Meuler et al. 2010a, b).

Kulinich and Farzaneh (2009) measured the adhesion strength of artificially created glaze ice (similar to accreted in nature) on rough fluoropolymer-based hydrophobic surfaces with different contact angle (CA) and wetting hysteresis. The direct correlation between ice repellency and CA was found on superhydrophobic surfaces with low wetting hysteresis. Another correlation was found between wetting hysteresis and ice adhesion strength on rough surfaces with similar chemistry. Also they studied ice repellency of rough hydrophobic coatings based on different materials and with different surface topographies were evaluated. The coatings were prepared either from a fluoropolymer incorporated with nanoparticles or by etching aluminum alloy substrate followed by further hydrophobization of the rough surface via an organosilane monolayer adsorbed from solution. This allowed comparing the ice-releasing performance of rough surfaces with high water contact angles (similar to 150°–153°) and different dynamic hydrophobicities and mechanical properties. Artificially created glaze ice, similar to naturally occurring glaze, was accreted on the surfaces by spraying supercooled water microdroplets in a wind tunnel at subzero temperature. The ice adhesion strength was evaluated by spinning the samples in a centrifuge at constantly increasing speeds until ice detachment occurred. Their results showed that after several icing–deicing cycles the more robust surfaces prepared by etching the aluminum substrate maintained their ice-releasing properties better, compared to their counterparts based on nanoparticle-incorporated fluoropolymer. The effect of the dynamic hydrophobicity of the coatings was also examined, clearly demonstrating that the surface with low dynamic hydrophobicity is not ice-repellent, although it demonstrates large values of water contact angle (Kulinich and Farzaneh 2011).

Mishchenko et al. (2010) studied the impact of water droplets on supercooled nano- and microstructured surfaces. They found that highly ordered superhydrophobic materials can be designed to remain entirely ice-free down to ca. −25 to −30°C, due to their ability to repel impacting water before ice nucleation occurs. Ice accumulated below these temperatures can be easily removed. They emphasized the potential of hydrophobic polymeric coatings bearing dosed-cell surface microstructures for their improved mechanical and pressure stability, amenability to facile replication and large-scale fabrication, and opportunities for greater tuning of their material and chemical properties.

He et al. (2010) studied frost formation on superhydrophobic isotactic polypropylene (i-PP) films and found that frost formation is greatly retarded on the superhydrophobic i-PP surface. Meuler et al. (2010a, b) investigated the relationships between advancing/receding water contact angles and the strength of ice adhesion to bare steel and 21 different test coatings (similar to 200–300 nm thick) applied to the nominally smooth steel discs. They argued that any further appreciable reduction in ice adhesion strength will require textured surfaces.

However, superhydrophobicity does not lead directly to the icephobicity and numerous challenges should be resolved to design roughness-induced ice-phobic surfaces. Kulinich et al. (2011) investigated the icephobic performance of various superhydrophobic surfaces under different conditions using glaze ice (similar to that

deposited during "freezing rain"). Their results showed that the ice-repellent properties of the materials deteriorate during icing–deicing cycles, as surface asperities appear to be gradually damaged. Also, the antiicing efficiency of superhydrophobic surfaces is significantly lower in a humid atmosphere, as water condensation both on top of and between surface asperities takes place, leading to significantly larger values of ice adhesion strength. Their conclusion was that superhydrophobic surfaces are not always ice-repellent and their use as antiice materials may, therefore, be limited.

Varanasi et al. (2010) studied frost formation and its impact on icephobic properties of superhydrophobic surfaces with SEM. Frost nucleation occurred indiscriminately on superhydrophobic textures without any particular spatial preference. Ice adhesion measurements on superhydrophobic surfaces susceptible to frost formation showed increased adhesion over smooth surfaces with a strong linear trend with the total surface area. These studies indicate that frost formation significantly compromises the icephobic properties of superhydrophobic surfaces and poses serious limitations to the use of superhydrophobic surfaces as icephobic surface treatments for both on-ground and in-flight applications. Further research of the correlation between the hydrophobicity and icephobicity remain an important task.

11.9 Summary

The Lotus effect provides a mechanism that has been successfully used for self-cleaning. The main limitation of this mechanism is that the micropatterned relief on the surface is vulnerable to even moderate rates of wear, impact, or other damage. To overcome this shortcoming, it may be suggested to use composite materials with the hydrophobic reinforcement embedded in the bulk of the material, rather than at the surface. Another limitation of the Lotus effect-based self-cleaning is that it can be applied only at the three-phase solid–water–air interface, and therefore, it is not available for underwater surfaces in permanent liquid flow. In the consequent chapter, we review the underwater self-cleaning methods and composite materials that are much less vulnerable to wear.

Chapter 12
Self-Cleaning in the Water Flow

In the preceding chapter, we discussed self-cleaning mechanisms that involve the Lotus effect and photocatalysis. These mechanisms imply that contamination can be washed away with the flow of water. Therefore, they require the three-phase system involving solid, water, and air. Some applications, such as water pipes, ship hulls, drainage systems, medical applications, such as heart catheters, have to operate underwater in permanent water flow or in other liquids, such as blood. Therefore, the Lotus effect per se cannot be used for them. However, a similar and related approach of underwater oleophobicity can be used instead, with the three-phase system of solid, water, and oil (or any organic liquid). In this system, the oil or organic liquid is a contaminant; however, it plays the same role as water in the solid–water–air system, whereas water plays the role of air.

Microstructured surfaces able to repel droplets of organic liquids have the potential for antifouling, i.e., the ability to remove biological contamination and film formed by bacteria and microorganisms, since the adhesion of their attachment systems tends to be similar to that of organic contaminants. In addition, the possibility of underwater hydrophobicity has been discussed. It implies that a surface remains water-repellent when immersed in water, at least for a certain period of time. Such a surface may have a thin film of gas upon it, which dramatically decreases the viscous friction and drag. It has been suggested to use microstructured, as well as chemically heterogeneous, surfaces for underwater application for (1) drag reduction due to the slip between the solid and liquid, (2) drag reduction due to the "shark skin effect" (suppression of turbulent modes), and (3) self-cleaning.

In this chapter, we discuss underwater hydrophobicity and oleophobicity. After that, antifouling and oleophobic surfaces are discussed, as well as metallic and polymeric composite materials, which can be used to create heterogeneous hydrophobic and oleophobic surfaces.

M. Nosonovsky and P.K. Rohatgi, *Biomimetics in Materials Science: Self-Healing, Self-Lubricating, and Self-Cleaning Materials*, Springer Series in Materials Science 152,
DOI 10.1007/978-1-4614-0926-7_12,

12.1 Liquid Flow Near a Superhydrophobic Surface

The phenomenon of superhydrophobicity implies the formation of a three-phase solid–water–air interface, which is usually not possible in continuous water flow. However, experimental observations and theoretical analyses suggest that there is a certain correlation between wetting properties of a liquid and surface friction of a water boundary layer (de Gennes 2002; Cottin-Bizonne 2003; Choi and Kim 2006). For liquid flow applications, other parameters than the contact angle and contact angle hysteresis are required to characterize the surface friction of liquid at a solid wall of a channel. The standard boundary condition for the fluid flow along a wall is the "no-slip condition." According to this condition, the tangential fluid velocity at the wall is equal to zero. However, recent observations show that for some hydrophobic surfaces the slip may not be equal to zero.

For continuous macroscale liquid flow near a solid surface, the boundary condition of no-slip (or zero flow velocity at the wall) is usually assumed. However, it has been known on the basis of molecular dynamics simulations and experimental observations that liquid slip can exist over some materials, especially polymers (de Gennes 1997) and surfaces due to a thin film of gas (Zhu and Granick 2001; de Gennes 2002; Cottin-Bizonne 2003). The slip is characterized by the so-called slip length or Navier length (Fig. 12.1), given by

$$l = H\left(\frac{\mu_{\mathrm{L}}}{\mu_{\mathrm{G}}} - 1\right), \tag{12.1}$$

where H is film thickness, μ_{L} and μ_{G} are viscosities of the liquid and gas. The concept of the slip length is based on the idea that the flow velocity grows linearly with an increasing distance from the wall. For the nonslip boundary condition the Navier length is zero, $l = 0$. In the case when there is a thin layer of vapor, air, or another gas between liquid and the solid wall, the gas viscosity is normally much lower than that of the liquid, which results in the effective nonzero slip condition.

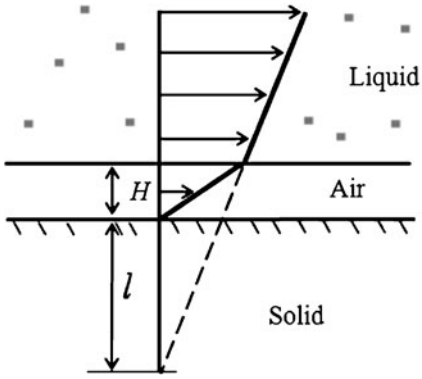

Fig. 12.1 Slip length l for a viscous liquid flow upon a thin gas film

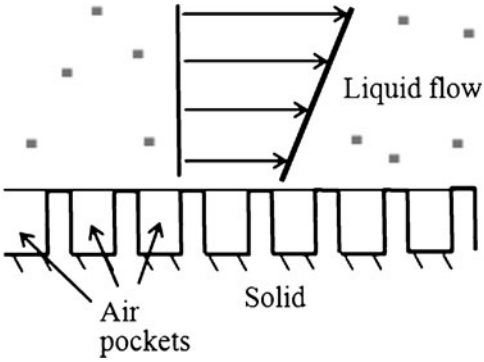

Fig. 12.2 Liquid flow upon a superhydrophobic surface

The possibility of nanobubbles or nanolayers remained controversial for a long time. However, it has been argued that a thin gas layer 5–80 nm can exist at the interface between a hydrophobic solid and water (Zhang et al. 2007). Formation of this layer was attributed to very small bubbles (nanobubbles) that can form at the solid surface and to other effects (Lauga and Brenner 2004). Rough superhydrophobic surfaces can also result in a gas layer trapped at the interface and thus lead to the nonzero slip (Choi and Kim 2006). The effect is very similar to the composite interface between a bubble and a rough surface, which has been considered in detail in the preceding chapters (Fig. 12.2). The conclusions formulated regarding the stability of the composite interface in the case of a droplet upon a superhydrophobic surface are valid also with respect to the liquid flow (Nosonovsky and Bhushan 2008a). Marmur (2006) showed that for a hydrophobic surface made of convex pillars, the underwater superhydrophobicity is, in principle, feasible, and may be thermodynamically stable.

Equation (12.1) is valid for the case of a pure liquid–air interface ($f_{SL} = 0$). For a more realistic case of a composite interface that average slip length is given by averaging over the area of the slip length at the liquid–air interface (fractional area of $1 - f_{SL}$), given by (12.1) and zero slip velocity at the solid–liquid interface (fractional area of f_{SL})

$$l = H\left(\frac{\mu_L}{\mu_G} - 1\right)(1 - f_{SL}). \tag{12.2}$$

Whereas for a pure composite interface, f_{SL} can be calculated from (7.19)–(7.20), for a mixed interface f_{SL} can be calculated using probabilities of liquid filling a valley or air pocket staying there. The thickness of the layer H is assumed to be equal to the pillars height. Based on (9.2), the higher the pillars, the larger is the slip length and, therefore, smaller is the resistance to liquid flow. Note that maximum pressure, which can be supported by the surface, is given by (7.30).

Water pressure and the stability of the composite interface are significant problems for producing successful superhydrophobic surfaces, since the pressure in the liquid flow is significantly higher than that created by the weight of a droplet.

This liquid pressure should be balanced by the surface tension force and by the pressure in the gas. Choi and Kim (2006) showed experimentally that a superhydrophobic "nanoturf" surface made by the black silicon method shows underwater superhydrophobicity. Voronov et al. (2006) used molecular dynamics simulation and found correlation between the slip length and the contact angle.

12.2 Nanobubbles and Hydrophobic Interaction

The possibility of a boundary air layer is closely related to another issue: nanobubbles. Nanobubbles (Fig. 12.3) remained a controversial topic until the early 2000s because there are theoretical arguments against their existence. First, according to the Laplace equation, pressure in a gas bubble at the thermodynamic equilibrium is greater than that in the liquid outside. For bubbles with a very small radius, the pressure difference through the interface may be very big and thus the pressure inside is very high. Such high pressure would result in increasing gas solubility, so that the nanobubbles would rapidly dissolve. Second, the total free energy per unit area of a system in which water is in contact with a hydrophobic surface always increases when a gas layer or nanobubbles are formed, unless the surface is extremely rough, so the existence of the nanobubbles is not energetically favorable. Despite these thermodynamic objections, some experimental studies with the AFM and other equipment have demonstrated the existence of nanobubbles at the solid/water interface (Zhang et al. 2006).

Nanobubbles can play a significant role in a number of processes, such as the long-term hydrophobic attractive force. The hydrophobic interaction is a well-known phenomenon. For example, when one adds small droplets of oil to water, the droplets combine to form a larger droplet. This comes about because water molecules are attracted to each other and are cohesive because they are polar molecules. Oil molecules are nonpolar and thus have no charged regions on them. This means that they are neither repelled nor attracted to each other. The attraction of the water molecules for each other then has the effect of squeezing the oil droplets together to form a larger droplet.

Singh et al. (2006) showed that a long-range hydrophobic interaction can exist underwater due to superhydrophobicity. They found that rough superhydrophobic surfaces experience attractive forces over the separation distance

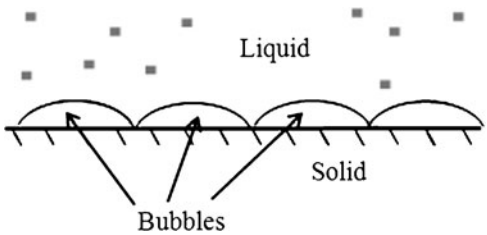

Fig. 12.3 Small gas bubbles form a layer upon a solid wall, which can significantly reduce the friction

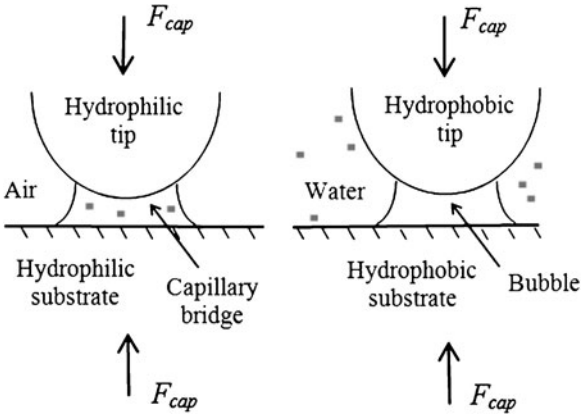

Fig. 12.4 Similarity of the attractive capillary force in the case of a condensed water bridge between hydrophilic surfaces in air and cavitation a bubble between hydrophobic surfaces in water

between the tip and sample of up to 3.5 μm, due to the spontaneous evaporation of the intervening, confined water. The effect was measured with an AFM and it is very similar to the capillary meniscus force. A capillary bridge is formed between a hydrophilic AFM tip and a sample due to condensation of water vapor from air. Let us now assume that the tip and sample are hydrophobic and immersed into water. A gas bubble may form at the contact due to vapor bubble nucleation or due to air dissolved in water. Such a bubble would result in an attractive force the value of which is equal to the pressure difference inside and outside the bubble, ΔP, times the bubble foundation area, $\pi {R_1}^2$

$$F_{\text{cap}} = \pi {R_1}^2 \Delta P = \frac{\pi {R_1}^2 \gamma}{1/R_1 + 1/R_2}. \tag{12.3}$$

In a sense, such a bubble in water formed due to the cavitation between hydrophobic surfaces is a mirror image of a capillary bridge in air between hydrophilic surfaces formed due to the condensation (Fig. 12.4).

12.3 Antifouling

Biofouling is the undesirable accumulation of microorganisms (biofilming), plants and larger organisms (macrofouling) on wetted structures, such as ship hulls (Genzer and Efimenko 2006). Biofouling constitutes a significant problem for various areas of engineering that involve solid surfaces immersed into water, such as ships and submarines, dock and port infrastructure, and applications that deal with water, including pipes, water heaters, meters, etc. According to some estimates, biofouling can reduce a vessel's speed by 10% and increase fuel consumption by up to 40%. Conventional antifouling coating agents, such as tributylin, are toxic and can be harmful for the environment. To help alleviate some of these problems, scientists are paying increased attention to the possibility

of biomimetic antifouling coatings that will mimic the ability of fish to resist fouling in an environmentally friendly manner (Nosonovsky and Bhushan 2008a).

In addition to its importance for applications, the research area of antifouling involves a number of fundamental scientific problems related to wetting of rough surfaces, superhydrophobicity, superoleophobicity and self-cleaning.

12.4 Underwater Oleophobicity

Similarly to the superhydrophobicity, superoleophobicity is defined as the ability of a solid to have a large CA with organic liquids (such as oils). However, the surface tension of organic liquids is much lower than that of water, so it is extremely difficult to create a superoleophobic surface, since it is hard to obtain an initially oleophobic material ($\theta_0 > 90°$). Nosonovsky (2007e) showed that certain curvature parameters define the stability of the composite regime, which can lead to superhydro/oleophobicity even for initially hydro/oleophilic material ($\theta_0 < 90°$). Tuteja et al. (2007, 2008) suggested that such a surface curvature criterion, in conjunction with chemical composition and roughened texture, can be used for liquids with low surface tension, including alkanes such as decane and octane.

The use of lotus-effect type self-cleaning surfaces for antifouling is limited due to the following reasons: *First*, the diversity of marine organisms and their attachment mechanisms make it difficult to design an approach based solidly on a single parameter, such as the surface energy or contact angle that would provide effective antifouling over the entire range of species. *Second*, the lotus effect assumes the formation of a composite solid–air–water interface with air trapped at the cavities. However, air eventually dissolves into the water and thus the method cannot provide a coating that would last for necessary time periods (such as several years).

Surfaces that are both hydrophobic and oleophobic are called "omniphobic" (or amphiphobic). It is understood that the design of an omniphobic surface cannot be governed by a single parameter (such as the Wenzel roughness factor), but it depends upon more complicated characteristics of a surface, involving curvature. Various design strategies and criteria for oleophobic surfaces have been suggested (Tuteja et al. 2007, 2008).

In addition to the oleophobicity in air, underwater oleophobicity is another new research area. Similar to the composite solid–air–water interface of a superhydrophobic surface, a composite solid–water–oil interface can form, under certain conditions, for a rough surface immersed into water, contaminated by oil. Using underwater oleophobicity for antifouling provides a solution to the two main challenges of the use of micropatterned surfaces associated with the Lotus effect, since there is no need for an air film and various types of bioadhesion can be confronted.

Fish scales have a hierarchical structure consisting of sector-like scales with diameters of 4–5 mm covered by "papillae" 100–300 μm in length and 30–40 μm in width. Shark skin, which is a model from nature for a low drag surface, is covered by very small individual tooth-like scales called dermal denticles (little skin teeth), ribbed with longitudinal grooves (aligned parallel to the local flow direction of the water). These grooved scales reduce vortices formation present on a smooth surface, resulting in water moving efficiently over their surface. The water surrounding these complex structures can lead to protection from marine fouling and play a role in the defense against adhesion and growth of marine organisms, e.g., bacteria and algae (Jung and Bhushan 2009a, b, 2010).

In the past, numerous attempts were made to design microstructured antifouling surfaces. However, these attempts had limited success due to a number of challenging problems, related to the roughness-induced antifouling and to the diversity of microorganisms that cause fouling. Different microorganisms tend to adhere to different surfaces (both hydrophobic and hydrophilic) and once the surface is contaminated by one type of organism, further contamination tends to progress. Producing a robust universal oleophobic (omniphobic) surface is a challenging task.

The main difficulty in producing oleophobic surfaces is that organic liquids (such as oils) have low surface energies, and it is difficult to find a solid material with even lower energy, so that $\gamma_{SA} - \gamma_{SW}$ is negative, and the contact angle given by the Young equation exceeds 180°. To overcome this, Nosonovsky (2007e) suggested a geometrical criterion, which was successfully used to produce omniphobic surfaces and has potential for antifouling (Tuteja et al. 2007, 2008). The criterion basically, is curvature based and deals with the fact that a concave surface tends to pin the solid–liquid–vapor interface, whereas a convex surface results in the interface tending to be unstable. As a result, a convex shape can lead to a composite (Cassie) interface even for initially hydrophilic (in the case of wetting by water) or oleophilic (in the case of wetting by organic liquids) materials. However, this approach requires precise control over the details of microroughness.

A different approach uses underwater oleophobicity, that is, the ability of a hydrophobic surface to become oleophobic when immersed in water, due to the forming of the composite solid–water–oil interface (with water playing the same role as air in the composite superhydrophobic interface). If an oil droplet is placed on a solid surface in water, the contact angle of an oil droplet in water, θ_{OW}, is given by Young's equation:

$$\cos\,\theta_{OW} = \frac{\gamma_{OA}\cos\,\theta_O - \gamma_{WA}\cos\,\theta_W}{\gamma_{OW}}, \tag{12.4}$$

where θ_O and θ_W are contact angles of oil and water with the solid surface, γ_{OA}, γ_{WA} and γ_{OW} are interfacial energies for oil–air, water–air, and oil–water interfaces (Jung and Bhushan 2009a, b). As a consequence, a superhydrophobic (in air) surface can become oleophobic when immersed in water, under certain circumstances, which are summarized in Table 12.1.

Table 12.1 Oleophobic and oleophilic interfaces (based on Jung and Bhushan 2009a, b)

Interface					
Solid–air–water	Hydrophobic $\gamma_{SA} > \gamma_{SW}$			Hydrophobic $\gamma_{SA} < \gamma_{SW}$	
Solid–air–oil	Oleophilic if $\gamma_{SA} > \gamma_{SO}$	Oleophobic if $\gamma_{SA} < \gamma_{SO}$		Oleophilic if $\gamma_{SA} > \gamma_{SO}$	Oleophobic if $\gamma_{SA} < \gamma_{SO}$
Solid–water–oil	Oleophilic	Oleophilic if $\gamma_{OA}\cos\theta_0 < \gamma_{WA}\cos\theta_W$	Oleophobic if $\gamma_{OA}\cos\theta_0 > \gamma_{WA}\cos\theta_W$	Oleophilic if $\gamma_{OA}\cos\theta_0 < \gamma_{WA}\cos\theta_W$	Oleophobic if $\gamma_{OA}\cos\theta_0 < \gamma_{WA}\cos\theta_W$

For a rough surface with the roughness factor of R_f the contact angle can be calculated in accordance with the Wenzel model as

$$\cos\theta_{OW} = \frac{\gamma_{OA}\cos\theta_O - \gamma_{WA}\cos\theta_W}{\gamma_{OW}} R_f. \tag{12.5}$$

Furthermore, similarly to the superhydrophobic surfaces, besides the homogeneous solid–oil interface (Wenzel state), a composite solid–oil–water interface (Cassie–Baxter or Cassie state) with water pockets trapped between the solid and the oil droplet can exist. The contact angle is then given by

$$\cos\theta_{OW} = \frac{\gamma_{OA}\cos\theta_O - \gamma_{WA}\cos\theta_W}{\gamma_{OW}} f_{SO} R_f - 1 + f_{SO}, \tag{12.6}$$

where $0 < f_{SO} < 1$ is the fractional solid–oil contact area. The rules of the Cassie–Wenzel wetting regime transition are the same as in the case of superhydrophobic surfaces, as it was discussed in the preceding chapters.

Even a more complex four-phase solid–oil–water–air system can form if both water and air bubbles are present at the composite interface. In this case, there are three fractional areas of contact, so that $f_{SO} + f_{SW} + f_{SA} = 1$, and the contact angle is given by

$$\cos\theta_{OW} = f_{SO}\cos\theta_O + f_{SW}\cos\theta_W - 1 + f_{SO} + f_{SW}, \tag{12.7}$$

or

$$\cos\theta_{OW} = \frac{\gamma_{OA}\cos\theta_O - \gamma_{WA}\cos\theta_W}{\gamma_{ow}} f_{SO} R_f - 1 + f_{SO} + f_{SA}. \tag{12.8}$$

It is expected that with time air will dissolve so that $f_{SA} \to 0$ and (12.8) will yield the same result as (12.6).

It is also noted that successful biological functional surfaces, including antifouling surfaces such as fish scales, have a hierarchical structure, which allows them to adapt to multiple simultaneous processes with different characteristic length scales. We, therefore, propose to investigate underwater oleophobic surfaces with a hierarchical structure and a structure mimicking fish scales.

Jung and Bhushan (2009a, b, 2010) studied experimentally the wetting behavior of water and oil droplets on hydrophobic/philic and oleophobic/philic surfaces in three phase interfaces. Flat and micropatterned surfaces (fish scale replicas, micropatterned polymeric surfaces, and hierarchical surfaces produced using an original method) with varying pitch values were produced by soft lithography. To modify surface energy, they deposited *n*-Pefluoroeicosane ($C_{20}F_{42}$) with low surface energy (6.7 mN m^{-1}) by thermal evaporation to produce superhydrophobic and oleophobic flat and micropatterned surfaces. For water and oil droplets in three phase interfaces, the experimental observations showed that there is a good agreement between the measured contact angle and the predicted values of models. It was also found that the transition can occur for hydrophobic and oleophobic micropatterned surfaces with a larger distance between pillars (Jung and Bhushan 2009a, b, 2010).

In addition, the nano- and hierarchical structures of the Lotus plant surfaces and the shark skin replica as an example of aquatic animal was also investigated for their wetting properties. It was found that the nano- and hierarchical structures with *n*-hexatriacontane were oleophilic as a result of the high surface energy of *n*-hexatriacontane. The structure of the shark skin replica showed a higher propensity for trapped water pocket formation, resulting in a higher contact angle than the theoretical value, whereas the shark skin replica with $C_{20}F_{42}$ had a contact angle of ~0 at the solid–water–oil interface, as predicted by the model. For self-cleaning and antifouling from biological and organic contaminants, an oleophobic surface can be created based on this study (Jung and Bhushan 2009a, b, 2010).

The preliminary results suggest the feasibility of underwater oleophobic surfaces with a hierarchical structure and a structure mimicking fish scales for antifouling and using modern technologies for surface patterning.

The measurements of the contact angle with metal alloys and metal matrix composites (MMC) in the solid–oil–water system were conducted at the University of Wisconsin-Milwaukee. The results show that oleophobicity or oleophilicity of these surfaces depends very significantly on their roughness. Thus, Al-4047 alloy demonstrated a significant increase of roughness when etched by acid for more than 10 s (roughness increased from the initial value of $R_a = 0.2$ μm to $R_a = 0.8$ μm) the solid–oil–water contact angle went up from $\theta = 43^\circ$ to $\theta = 129^\circ$. Such a significant increase apparently indicate that a wetting regime transition from Wenzel to Cassie regime takes occurs, which facilitates the change from oleophilicity to oleophobicity (Fig. 12.5).

Metallic underwater oleophobic materials can be used for various applications in water industry where biofouling and biofilming constitute a problem ranging from water pipes to water meters and heaters, to ship hulls.

12.5 Polymeric Materials, Filters, and Desalination

Biofouling and biofilming is also a significant problem in various applications which use membranes, such as water filters or reverse osmosis desalination. Reverse Osmosis (RO) is a process that forces seawater through a semipermeable membrane

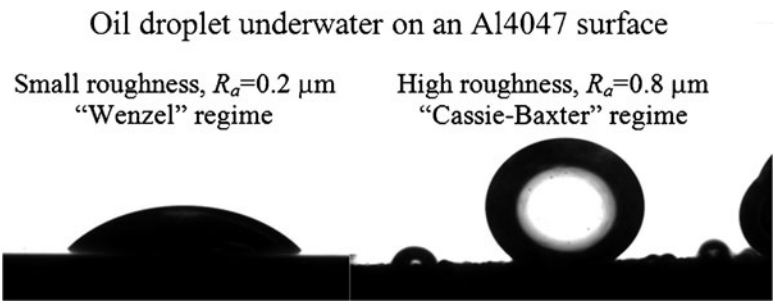

Fig. 12.5 Solid–oil–water system showing a significant contact angle change (from 43° to 141°) when roughness is increased suggests that wetting regime transition occurs

(usually made of some polymeric material) under high pressure, allowing water molecules to pass, while salt and other contaminants are rejected forming a concentrated brine solution (Oldach 2001). This process requires large amounts of electricity to drive the pump for pressurizing the saline solution. The amount of pressure required depends on a number of factors such as the solute concentration, its molecular structure (number of particles generated after ionization of each molecule) and the operating temperature. This pressure (the minimum required for desalination) is referred to as Osmotic pressure, and can be as large as 70 bar for seawater desalination (Hurd et al. 2012).

Osmosis is the transport of a solvent through a semipermeable membrane into a solution of higher solute concentration that tends to equalize the chemical potentials of the solute on either side of the membrane. A semipermeable membrane allows solvent molecules (such as H_2O) to penetrate through while larger solute molecules or ions (such as NaCl) cannot penetrate through the membrane. As a result, when a tube is separated into two sections by a semipermeable membrane isolating solute molecules in one section, water molecules will equilibrate (eventually having the same partial pressure on both sides of the membrane), whereas the solute molecules or ions will create excessive partial pressure upon the membrane, as it is discussed in Chap. 5. This is the osmotic pressure required to maintain equilibrium with no movement of the solvent.

In naturally occurring osmosis, the solvent is generally water and the semipermeable membrane is a membrane of a living cell. This diffusion of molecules is a form of passive transport, in which no applied energy is required. Passive transport occurs due to the molecular internal energy and concentration and is a very important biological processes where water penetrates into living cells through cell membranes and the transport of various substances through blood cells.

The excess hydrostatic pressure, known as osmotic pressure, can be estimated via the Morse Equation

$$\pi = iRTc, \tag{12.7}$$

where π is the osmotic pressure, $R = 8.31\ \mathrm{JK}^{-1}\ \mathrm{mol}^{-1}$ is the universal gas constant, T is absolute temperature (K), and c is the molar concentration of the solute (mol m^{-3}). The variable i, known as the van't Hoff Factor, is defined as the degree of dissociation or association of solute particles in a solution. This is the ratio of the number of moles of solute particles to the number of moles of solute dissolved in a solution (Hurd et al. 2012).

The standard commercial RO filter contains a thin film composite (TFC) membrane spiral wound about a perforated tube and sealed in a pressure vessel. A permeate material is sandwiched between the TFC membrane, which in turn lies between two feed channel spacers. The feed channel spacer allows the feed solution (seawater) to pass through the filter, while creating turbulence to aid in the filtration process. The TFC membrane allows the passage of water molecules which are then absorbed into the permeate material, or membrane. The permeate material is wrapped around a perforated tube at the center of the filter, in which the pure water enters and flows freely.

In efforts to reduce energy consumption and maintenance costs, more specific surface science issues have been related to RO desalination technology. In particular, biofouling or biofilming is a factor that reduces the lifetime of the membranes, increases osmotic pressure, and causes contamination of the output fresh water. To reduce biofouling, self-cleaning antifouling membranes using the principle of the lotus effect (underwater superoleophobicity) have been suggested. The use of self-assembled, superhydrophobic polymeric membranes for reverse osmosis desalination (Bormashenko et al. 2008) has also recently been proposed. Biomimetic membranes based on an array of aligned carbon nanotubes, mimicking biological protein channels by functionalizing the open tips of the nanotubes with a synthetic peptide, are another area of research (Nednoor et al. 2007).

12.6 Summary

Lotus-effect-based self-cleaning cannot be applied directly to underwater applications such as pipes or ship hulls because a three-phase solid–water–air system is required. A thin film of air can remain in the cavities of a superhydrophobic surface immersed in water for a certain time. Such a layer would significantly reduce the viscous water drag and can effectively lead to the violation of the "no-slip" boundary condition, which is beneficial for many applications. However, the water layer would eventually dissolve, the air so this principle cannot be used for sustainable underwater self-cleaning. A different principle implies underwater oleophobicity when the solid–liquid–air system is substituted by the solid–oil–water system. Under certain circumstances, the latter works in the same way as the superhydrophobic surface, and thus, roughness can significantly enhance oleophobic properties, leading to underwater superoleophobicity. Experimental data on metal alloys suggest that with increasing roughness the wetting regime transition (from Wenzel to Cassie–Baxter) can occur.

The principle of underwater oleophobicity can be applied to antifouling, since organic biological contaminants (bacteria etc.) tend to accumulate at the spots where organic contamination (such as oil) is possible. Antifouling surfaces are needed for many applications including water pipes, water equipment, and filters and desalination membranes and ship hulls.

Chapter 13
Artificial Self-Cleaning Surfaces

In this chapter, we discuss some techniques, which are used to produce superhydrophobic self-cleaning surfaces. In recent years, fabrication of superhydrophobic surfaces became an area of active fundamental research. New approaches have been suggested that are discussed in this chapter, and in the near future new technological concepts will emerge. In general, the same techniques that are used for micro- and nanostructure manufacturing, such as the lithography, etching, and deposition, have been utilized for producing superhydrophobic surfaces.

A significant problem which limits the applicability of superhydrophobic surfaces is their durability which is limited because the microstructure can be very easily deteriorated and thus is very vulnerable to wear. The solution can be to use a composite material where a hydrophobic reinforcement is embedded in the bulk of the material and not just at the surface. As a result, when the surface layer is worn, new reinforcement (which was previously in the bulk) will participate in the interfacial contact.

13.1 Techniques to Make a Superhydrophobic Surface

Two main requirements for a superhydrophobic surface are that the surface should be rough and that it should have a hydrophobic (low surface energy) coating. These two requirements lead to two methods of producing a superhydrophobic surface. First, it is possible to make a rough surface from an initially hydrophobic material and, second, to modify an initially rough surface by changing surface chemistry or applying a hydrophobic material upon it. Note that roughness is usually a more critical property than the low surface energy, since both moderately hydrophobic and very hydrophobic materials exhibit similar wetting behavior when roughened (Ma and Hill 2006). This is understandably so, based on the simple Wenzel model, the cosine of the contact angle is given by $R_f \cos \theta_0$, so even small (negative) $\cos\theta_0$ will result in high contact angle when combined with a big roughness factor.

M. Nosonovsky and P.K. Rohatgi, *Biomimetics in Materials Science: Self-Healing, Self-Lubricating, and Self-Cleaning Materials*, Springer Series in Materials Science 152, DOI 10.1007/978-1-4614-0926-7_13,

Table 13.1 Advantages and shortcomings of various fabrication techniques (Nosonovsky and Bhushan 2008a)

Techniques	Advantages	Shortcomings
Lithography	Accuracy, large area	Slow process, high cost
Etching	Fast	Chemical contamination, less control
Deposition	Flexibility, cheap	Can be high temperature, less control

Fabrication of superhydrophobic surfaces has been an area of active research since the mid-1990s. In general, the same techniques that are used for micro- and nanostructure fabrication, such as the lithography, etching, and deposition, have been utilized for producing superhydrophobic surfaces. Advantages and shortcomings of these techniques are summarized in Table 13.1. Among especially interesting development is the creation of switchable surfaces that can be turned from hydrophobic to hydrophilic by applying electric potential, heat or ultraviolet (UV) irradiation, as was discussed in the preceding chapters (Lahann et al. 2003; Sun et al. 2004; Feng et al. 2005; Xu et al. 2005; Ma and Hill 2006). Another important requirement for potential applications for optics and self-cleaning glasses is the creation of transparent superhydrophobic surfaces. In order for the surface to be transparent, roughness details should be smaller than the wavelength of the visible light (about 400–700 nm) (Nakajima et al. 1999).

Two main requirements for a superhydrophobic surface are that the surface should be rough and that it should have a hydrophobic (low surface energy) coating. These two requirements lead to two methods of producing a superhydrophobic surface: first, it is possible to make a rough surface from an initially hydrophobic material and, second, to modify a rough hydrophilic surface by modifying surface chemistry or applying a hydrophobic material upon it. Note that roughness is usually a more critical property than the low surface energy, since both moderately hydrophobic and very hydrophobic materials can exhibit similar wetting behavior when roughened.

13.1.1 Roughening to Create One-level Structure

Lithography is a well-established technique, applied for creating large area of periodic micro/nanopatterns. It includes photo, E-beam, X-ray, and soft lithography. Bhushan and Jung (2007) produced patterned Si using photolithography. To obtain a sample that is hydrophobic, a SAM of 1,1,-2,2,-tetrahydroperfluorodecyltrichlorosilane (PF_3) was deposited on the sample surfaces using vapor phase deposition technique. They obtained a superhydrophobic surface with the contact angle up to 170°. Martines et al. (2005) fabricated ordered arrays of nanopits and nanopillars by using electron beam lithography. They obtained a superhydrophobic surface with the contact angle of 164° and hysteresis of 1° for a surface consisting of tall pillars with cusped tops after a hydrophobization with octadecyltrichlorosilane (OTS). Furstner et al. (2005) created silicon wafers with regular

patterns of spikes by X-ray lithography. The wafer was hydrophobized by sputtering a layer of gold and subsequent immersion in a hexadecanethiol solution.

One well-known and effective way to make rough surfaces is etching using either plasma, laser, chemical, or electrochemical techniques (Ma and Hill 2006). Jansen et al. (1995) etched a silicon wafer using a fluorine-based plasma by utilizing the black silicon method to obtain isotropic, positively and negatively tapered as well as vertical walls with smooth surfaces. Coulson et al. (2000) described an approach in plasma chemical roughening of poly(tetrafluoroethylene) (PTFE) substrates followed by the deposition of low surface energy plasma polymer layers, which give rise to high repellency toward polar and nonpolar probe liquids. A different approach was taken by Shiu et al. (2004), who treated a Teflon film with oxygen plasma and obtained a superhydrophobic surface with contact angle of 168°. Fluorinated materials have a limited solubility, which makes it difficult to roughen them. However, they may be linked or blended with other materials, which are often easier to roughen, in order to make superhydrophobic surfaces. Teshima et al. (2005) obtained a transparent superhydrophobic surface from a poly(ethylene terephthalate) (PET) substrate via selective oxygen plasma etching followed by plasma-enhanced chemical vapor deposition using tetramethylsilane (TMS) as the precursor. Khorasani et al. (2005) produced porous PDMS surfaces with the contact angle of 175° using CO_2-pulsed laser etching method as an excitation source for surface. Qian and Shen (2005) described a simple surface roughening method by dislocation selective chemical etching on polycrystalline metals such as aluminum. After treatment with fluoroalkylsilane, the etched metallic surfaces exhibited superhydrophobicity. Xu et al. (2005) fabricated a reversible superhydrophobic surface with a double-roughened perfluorooctanesulfonate (PFOS)-doped conducting polypyrrole (PPy) film by a combination of electropolymerization and chemical polymerization. The reversibility was achieved by switching between superhydrophobic doped or oxidized states and superhydrophilicity dedoped or neutral states with changing the applied electrochemical potential.

A stretching method can be used to produce a superhydrophobic surface. Zhang et al. (2004a) stretched a Teflon film and converted it into fibrous crystals with a large fraction of void space in the surface, leading to high roughness and the superhydrophobicity.

Deposition methods also make a substrate rougher than the bulk properties of the material and enlarge potential applications of superhydrophobic surfaces. There are several ways to make a rough surface including adsorption, dip coating, electrospinning, anodization, electrochemical, evaporation, chemical vapor deposition (CVD), and plasma. Solidification of wax can be used to produce a superhydrophobic surface. Shibuichi et al. (1996) used alkylketene dimer (AKD) wax on a glass plate to spontaneously form a fractal structure in its surfaces. They obtained the surface with a contact angle larger than 170° without any fluorination treatments. Klein et al. (2003) obtained superhydrophobic surfaces by simply dip-coating a substrate with a slurry containing nanosilica spheres, which adhered to a substrate after a low temperature heat treatment. After reaction of the

surface with a fluoroalkyltrichlorosilane, the hydrophobicity increased with decreasing area fraction of spheres. Ma et al. (2005) produced block copolymer poly(styrene-*b*-dimethylsiloxane) fibers with submicrometer diameters in the range 150–400 nm by electrospinning from solution in tetrahydrofuran and dimethylformamide. They obtained superhydrophobic nonwoven fibrous mats with a contact angle of 163°. Shiu et al. (2004) showed that self-organized close-packed superhydrophobic surfaces can be easily achieved by spin-coating the monodispersed polystyrene beads solution on substrate surfaces. The sizes of beads were reduced by controlling the etching conditions. After plasma treatment, the surfaces were coated with a layer of gold and eventually a layer of octadecanethiol SAM to render hydrophobicity. Abdelsalam et al. (2005) studied the wetting of structured gold surfaces formed by electrodeposition through a template of submicrometer spheres and discussed the role of the pore size and shape in controlling wetting. Bormashenko et al. (2006) used evaporated polymer solutions of polystyrene (PS), polycarbonate (PC), and polymethylmethacrylate (PMMA) dissolved in chlorinated solvents: dichloromethane (CH_2Cl_2) and chloroform ($CHCl_3$) to obtain self-assembled structure with hydrophobic properties. Chemical/physical vapor deposition (CVD/PVD) has been used for the modification of surface chemistry as well. Lau et al. (2003) created superhydrophobic carbon nanotube forests by modifying the surface of vertically aligned nanotubes with plasma enhanced chemical vapor deposition (PECVD). Superhydrophobicity was achieved down to the microscopic level where essentially spherical, micrometer-sized water droplets can be suspended on top of the nanotube forest. Zhu et al. (2005) and Huang et al. (2005) prepared surfaces with two-scale roughness by controlled growth of carbon nanotube (CNT) arrays by CVD. Zhao et al. (2006) also synthesized the vertically aligned multiwalled carbon nanotube (MWCNT) arrays by CVD on Si substrates using thin film of iron (Fe) as catalyst layer and aluminum (Al) film.

Attempts to create superhydrophobic surface by casting and nanoimprint methods have been successful. Yabu and Shimomura (2005) prepared a porous superhydrophobic transparent membrane by casting a fluorinated block polymer solution under a humid environment. The transparency was achieved because the honeycomb-patterned films had sub-wavelength pore sizes. Sun et al. (2005) reported a nanocasting method to make a superhydrophobic PDMS surface. They first made a negative PDMS template using a lotus leaf as an original template and then used the negative template to make a positive PDMS template – a replica of the original lotus leaf. Zhao et al. (2005) prepared a superhydrophobic surface by casting a micellar solution of a copolymer poly(styrene-*b*-dimethylsiloxane) (PS-PDMS) in humid air based on the cooperation of vapor-induced phase separation and surface enrichment of PDMS block. Lee et al. (2004) produced vertically aligned PS nanofibers by using nanoporous anodic aluminum oxide as a replication template in a heat- and pressure-driven nanoimprint pattern transfer process. As the aspect ratio of the polystyrene (PS) nanofibers increased, the nanofibers could not stand upright but formed twisted bundles resulting in a three-dimensionally rough surface with advancing and receding contact angles of 155.8° and 147.6°, respectively.

13.1.2 Coating to Create Hydrophobic Structures

Modifying the surface chemistry with a hydrophobic coating widens the potential applications of superhydrophobic surfaces. There are several ways to modify the chemistry of a surface including sol–gel, dip coating, self-assembly, electrochemical and chemical/physical vapor deposition. Shirtcliffe et al. (2005) prepared porous sol–gel foams from organo-triethoxysilanes which exhibited switching between superhydrophobicity and superhydrophilicity when exposed to different temperatures. The critical switching temperature was between 275°C and 550°C for different materials, and when the foam was heated above the critical temperature, complete rejection of water in the cavities to complete filling of the pores. Hikita et al. (2005) used colloidal silica particles and fluoroalkylsilane as the starting materials and prepared a sol–gel film with superliquid-repellency by hydrolysis and condensation of alkoxysilane compounds. Feng et al. (2004) produced superhydrophobic surfaces using ZnO nanorods by the sol–gel method. They showed that superhydrophobic surfaces can be switched into hydrophilic surfaces by alternation of ultraviolet (UV) irradiation. Shang et al. (2005) did not blend low surface energy materials in the sols, but described a procedure to make transparent superhydrophobic surface by modifying silica-based gel films with a fluorinated silane. In a similar way, Wu et al. (2005) made a microstructured ZnO-based surface via a wet chemical process and obtained the superhydrophobicity after coating the surface with long-chain alkanoic acids.

Zhai et al. (2004) used a layer-by-layer (LBL) self-assembly technique to create a poly(allylamine hydrochloride)/poly(acrylic acid) (PAH/PAA) multilayer which formed a honeycomb-like structure on the surface after an appropriate combination of acidic treatments. After cross-linking the structure, they deposited silica nanoparticles on the surface via alternating dipping of the substrates into an aqueous suspension of the negatively charged nanoparticles and an aqueous PAH solution, followed by a final dipping into the nanoparticle suspension. Superhydrophobicity was obtained after the surface was modified by a CVD of (tridecafluoro-1,1,2,2-tetrahydrooctyl)-1-trichlorosilane followed by a thermal annealing.

Zhang et al. (2004b) showed that the surface covered with dendritic gold clusters, which was formed by electrochemical deposition onto indium tin oxide (ITO) electrode modified with a polyelectrolyte multilayer, showed superhydrophobic properties after further deposition of a *n*-dodecanethiol monolayer. Han et al. (2005) described the fabrication of lotus leaf-like superhydrophobic metal surfaces by using electrochemical reaction of Cu or Cu–Sn alloy plated on steel sheets with sulfur gas, and subsequent perfluorosilane treatment. The chemical bath deposition (CBD) has also been used to make nanostructured surfaces, thus, Hosono et al. (2005) fabricated a nanopin film of brucite-type cobalt hydroxide (BCH) and achieved a contact angle of 178° after further modification of lauric acid (LA). Shi et al. (2006) described the use of galvanic cell reaction as a facile method to chemically deposit Ag nanostructures on the *p*-silicon wafer on a large scale.

When the Ag covered silicon wafer was further modified with a self-assembled monolayer of *n*-dodecanethiol, a superhydrophobic surface was obtained with a contact angle of about 154° and a tilt angle lower than 5°.

13.2 Methods to Create Hierarchical Superhydrophobic Structures

Rough hierarchical structures involving at least two levels (a microstructure and a structure with submicron scale of roughness details) are typical for superhydrophobic surfaces in nature, as was discussed in the preceding chapters. Recently, significant efforts have been devoted to fabricate these hierarchical structures in various ways. Shirtcliffe et al. (2004) prepared a hierarchical copper surface by electrodeposition from an acidic copper sulfate solution onto flat copper and patterning technique of coating with a fluorocarbon hydrophobic layer. Another way to obtain a rough surface for superhydrophobicity is the assembly from colloidal systems. Ming et al. (2005) prepared a hierarchical (double roughened) surface consisting of silica-based raspberry-like particles which were made by covalently grafting amine-functionalized silica particles of 70 nm to epoxy-functionalized silica particles of 700 nm via the reaction between epoxy and amine groups. The surface became superhydrophobic after being modified with PDMS. Northen and Turner (2005) fabricated arrays of flexible silicon dioxide platforms supported by single high aspect ratio silicon pillars down to 1 μm in diameter and with heights up to ~50 μm. When these platforms were coated with polymeric organorods of approximately 2 μm tall and 50–200 nm in diameter, it showed that the surface is highly hydrophobic with a water contact angle of 145°. Chong et al. (2006) showed the combination of the porous anodic alumina (PAA) template with microsphere monolayers to fabricate hierarchically ordered nanowire arrays, which have periodic voids at the microscale and hexagonally packed nanowires at the nanoscale. These were created by selective electrodeposition using nanoporous anodic alumina as a template and a porous gold film as a working electrode that is patterned by microsphere monolayers. Wang et al. (2006) also developed a novel precursor hydrothermal redox method with $Ni(OH)_2$ as the precursor to fabricate a hierarchical structure of nickel hollow microspheres with nickel nanoparticles as the in situ formed building units. The created hierarchical hollow structure exhibited enhanced coercivity and remnant magnetization as compared with hollow nickel submicrometer spheres, hollow nickel nanospheres, bulk nickel, and free Ni nanoparticles. Kim et al. (2007) fabricated a hierarchical structure, which looks like the same structures as lotus leaf. First, the nanoscale porosity was generated by anodic aluminum oxidation and then, the anodized porous alumina surface was replicated by polytetrafluoroethylene. The polymer sticking phenomenon during the replication created the submicrostructures on the negative polytetrafluoroethylene nanostructure replica. The contact angle of the

created hierarchical structure was obtained about 160° and the tilting angle is less than 1°. Del Campo and Greiner (2007) reported that SU-8 hierarchical patterns comprising features with lateral dimensions ranging from 5 to 2 mm and heights from 10 to 500 μm were obtained by photolithography which comprises a step of layer-by-layer exposure in soft contact printed shadow masks which are embedded into the SU-8 multilayer.

13.3 MMC-Based Sustainable Superhydrophobic Surfaces

The range of actual and potential application of self-cleaning surfaces is diverse including optical (e.g., self-cleaning lenses), building and architecture (windows, exterior paints, roof tiles), textiles, solar panels, microdevices (where the reduction of adhesion is crucial), applications requiring antifouling from biological and organic contaminants, etc. (Nosonovsky and Bhushan 2009). Since the 1990s, when new technologies emerged to produce microstructured surfaces, a huge amount of research work was done on design, fabrication, and characterization of superhydrophobic surfaces from various materials, ranging from polymers and ceramics to textiles, etc. A significant limitation on the practical application of the Lotus effect for self-cleaning is the sustainability of superhydrophobic microstructured coatings, which is often extremely vulnerable even to small wear rates and contamination.

It is much more difficult to produce a superhydrophobic metallic material than a polymer- or ceramic-based one, because metals tend to have higher surface energies (Kietzig et al. 2009; Tadmor et al. 2009; Bormashenko et al. 2006). In the area of metallic superhydrophobic materials a number of advances have been made. Yet in the 1950s, Bikerman investigated wetting of stainless steel plates with different finishes with the contact angles around 90° and proposed that the surface roughness provides resistance for the sliding of water droplets. Since then, few studies of nonwetting metallic materials have been conducted. Qian et al. (2005) studied the effect of the surface roughness induced by the chemical etching on metallic composites superhydrophobicity. They used Al, Cu, and Zn specimens immersed into an etchant (a mixture of HCl, H_2O, and HF) at room temperature for time periods from 5 to 15 s. Shirtcliffe et al. (2005) studied the wettability of Cu-base superhydrophobic surfaces. They used Cu to form the base material and a coating to hydrophobize it. The removal or addition of material roughened the surface to control wetting by combining roughness with surface patterning. Sommers and Jacobi (2006) achieved anisotropic wettability on an Al surface by controlling its surface microtopography.

Metal matrix composites (MMCs) are composite materials which have a metallic matrix and a reinforcement of another metallic or non-metallic (ceramics, polymer, etc.) material. MMCs with hydrophobic reinforcement can provide much broader opportunities than pure metals for design and fabrication of composite surfaces and readily supply the reinforcement hydrophobic fraction and surface

roughness due to the reinforcement. However, superhydrophobic MMCs have not yet been explored in the literature. Furthermore, in a composite material the hydrophobic reinforcement is in the bulk of the material rather than at the surface and thus wear does not necessarily lead to the deterioration of the hydrophobic coatings making these materials appropriate to the situations where traditional Lotus-effect coatings cannot be used. The use of composite materials with hydrophobic reinforcement in the bulk has already been suggested for concretes to prevent water penetration (Sobolev and Ferrada- Gutiérrez 2005). In this chapter, we investigate wetting of MMCs with the potential for various applications where self-cleaning sustainable surfaces are needed ranging from antifouling for water industry to magnetic tape-head interfaces (Mortazavi and Nosonovsky 2011a).

13.3.1 Modeling of Wetting of Composite Materials

For a composite interface built of two fractions with the fractional areas of f_1 and f_2 (so that $f_1 + f_2 = 1$) the contact angle is given by the Cassie equation

$$\cos\,\theta = f_1\,\cos\,\theta_1 + f_2\,\cos\,\theta_2, \tag{13.1}$$

where θ_1 and θ_2 are the contact angles of the fractions. If a composite material has a matrix and reinforcement with the volume fractions of f_m and f_r (so that $f_\mathrm{m} + f_\mathrm{r} = 1$) forming a rough surface the contact angle is then given by

$$\cos\,\theta = R_\mathrm{fm}(1 - f_\mathrm{r})\cos\,\theta_\mathrm{m} + R_\mathrm{fr} f_\mathrm{r}\,\cos\,\theta_\mathrm{r}, \tag{13.2}$$

where θ_m and θ_r are the contact angles for the matrix and reinforcement materials, and R_fm and R_fr are corresponding roughness factors. Note that for spherical reinforcement particles the roughness factor is equal to the ratio of half of the sphere's area $2\pi R^2$ to the cross-sectional area πR^2 or $R_\mathrm{fr} = 2$. Solving for the reinforcement fraction yields the volume of the reinforcement fraction providing the desired contact angle θ

$$f_\mathrm{r} = \frac{\cos\,\theta - R_\mathrm{fm}\,\cos\,\theta_\mathrm{m}}{R_\mathrm{fr}\,\cos\,\theta_\mathrm{r} - R_\mathrm{fm}\,\cos\,\theta_\mathrm{m}}. \tag{13.3}$$

Further assuming $R_\mathrm{fr} = 2$, $R_\mathrm{fm} = 1$ (no roughness expect from the reinforcement particles), and $\theta = 180^\circ$ (the superhydrophobic limit) yields

$$f_\mathrm{r} = \frac{-1 - \cos\,\theta_\mathrm{m}}{2\,\cos\,\theta_\mathrm{r} - \cos\,\theta_\mathrm{m}}, \tag{13.4}$$

which has a solution ($f_\mathrm{r} < 1$) if $\theta_\mathrm{r} > 120^\circ$. Thus, it is difficult to produce a composite interface by only using the reinforcement roughness.

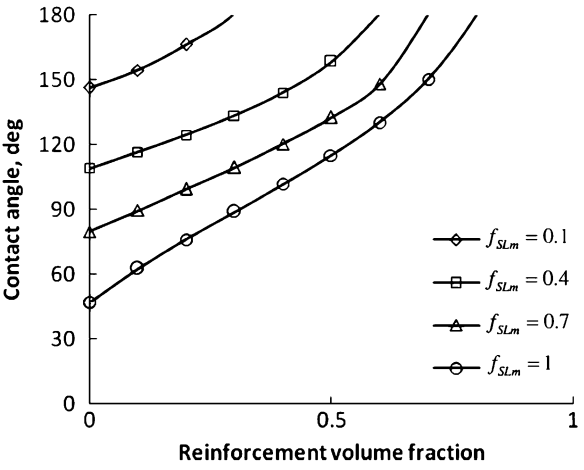

Fig. 13.1 The water contact angle as a function of graphite fiber reinforcement volume fraction (Cassie–Baxter regime) for different values of f_{SLm}

If water forms partial contact with the solid (composite or Cassie–Baxter) interface with the fractional solid–liquid contact areas f_{SLm} and f_{SLr}, the contact angle is given by

$$\begin{aligned}\cos\,\theta =& R_{\mathrm{fm}}\,(1-f_{\mathrm{r}})f_{\mathrm{SLm}}\,\cos\,\theta_{\mathrm{m}} + R_{\mathrm{ft}}f_{\mathrm{t}}f_{\mathrm{SLr}}\,\cos\,\theta_{r} - 1 + f_{\mathrm{t}}f_{\mathrm{SLr}} \\ &+ (1-f_{\mathrm{r}})f_{\mathrm{SLm}}.\end{aligned} \tag{13.5}$$

Solving for the reinforcement fraction yields the volume of the reinforcement fraction providing the desired contact angle θ

$$f_{\mathrm{r}} = \frac{\cos\,\theta - R_{\mathrm{fm}}f_{\mathrm{SLm}}\,\cos\,\theta_{\mathrm{m}} + 1 - f_{\mathrm{SLm}}}{R_{\mathrm{fr}}f_{\mathrm{SLr}}\,\cos\,\theta_{\mathrm{r}} - R_{\mathrm{fm}}f_{\mathrm{SLm}}\,\cos\,\theta_{\mathrm{m}} + f_{\mathrm{SLr}} - f_{\mathrm{SLm}}}. \tag{13.6}$$

Making the assumptions of $R_{\mathrm{fr}} = 2$, $R_{\mathrm{fm}} = 1$, $f_{\mathrm{SLr}} = 1$, and $\theta = 180^{\circ}$ yields

$$f_{\mathrm{r}} = \frac{-f_{\mathrm{SLm}} - f_{\mathrm{SLm}}\,\cos\,\theta_{\mathrm{m}}}{2\,\cos\,\theta_{\mathrm{r}} - f_{\mathrm{SLm}}\,\cos\,\theta_{\mathrm{m}} + 1 - f_{\mathrm{SLm}}}. \tag{13.7}$$

Let us apply (13.1)–(13.7) to the metallic (aluminum or copper) matrix with graphite reinforcement. For that end, we need to substitute material properties of these materials. We measured the water contact angle with graphite, aluminum, and copper, which were used to produce MMC samples at the UWM Center for Composite materials, using the Ramé-Hart Model 250 goniometer/tensiometer. We found the values of the contact angle equal to 140°, and 47.2°, and 47.7°, respectively. These results are close to those available in the literature (Mortazavi and Nosonovsky 2011b). Figure 13.1 shows the variation of the contact angle of water droplet on surface of metal matrix composite reinforced by graphite particles vs. reinforcement volume fraction, as obtained from (13.8) for various values of

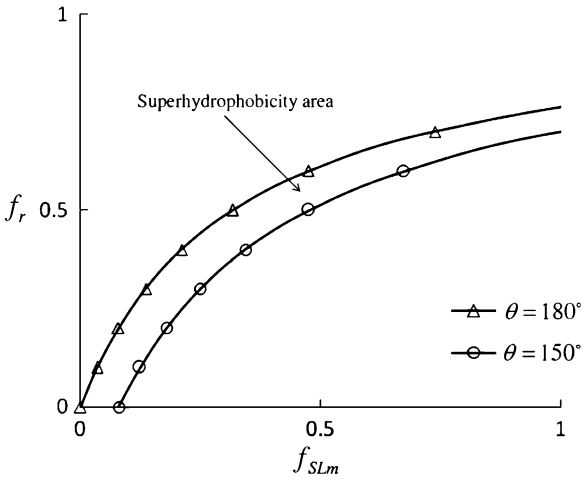

Fig. 13.2 The variation of f_{SLm} vs. reinforcement volume fraction, f_r

f_{SLm}. As it is seen in this figure, the contact angle increases with increasing the reinforcement volume fraction. Figure 13.2 shows the variation of f_{SLm} vs. the reinforcement volume fraction, f_r as obtained from (13.7).

Effect of wear on a composite material is twofold. First, the matrix roughness factor, R_{fm}, can be changed due to material removal and evolve to a certain "equilibrium value" (Wang et al. 2005). This can affect the solid–liquid fractional area, f_{SLm}. Second, the reinforcement particles can be removed as matrix surface layers are removed due to the deterioration. However, new particles come in contact so it is expected that the values of R_{fr} and f_{SLr} do not change significantly. To decouple the effect of reinforcement and matrix roughness we investigated experimentally wetting of composite materials with initially smooth surface and with the matrix roughness by etching, as described in the next section.

13.3.2 Experimental

In order to verify experimentally the models presented in the preceding section, we prepared eight samples of MMCs, four with a relatively smooth surfaces and four roughened by etching, and measured their roughness and contact angles. The four samples of Al- and Cu-based alloys and their graphite composites were sectioned to 2.0 cm × 1.5 cm × 0.2 cm pieces. Table 13.2 presents the chemical composition of the samples.

The samples were ground and polished to create a smooth surface before the etching process. The grinding involved successive steps with 400, 600, and 1,200 grit SiC paper. Polishing was done with a soft cloth impregnated with 1 μm alumina. The scanning electron microscope (SEM) images of the polished samples are as shown in Fig. 13.3.

Table 13.2 Chemical composition of the samples

Sample material	Composition
Copper base alloy	Cu (79.0–82.0%), Sn (2.5–3.5%), Pb (6.3–7.7%), Zn (7.0–10%), P (0.02%), Al (0.05%), Si (0.005%)
Copper–graphite composite	Cu (81%), Ni (5%), Fe (4%), Al (9%), Mn (1%), 60 vol% of graphite
Al base alloy	Al (88%), Si (12%)
Al–graphite composite	Al (35%), Si (5%), 60 vol% of graphite

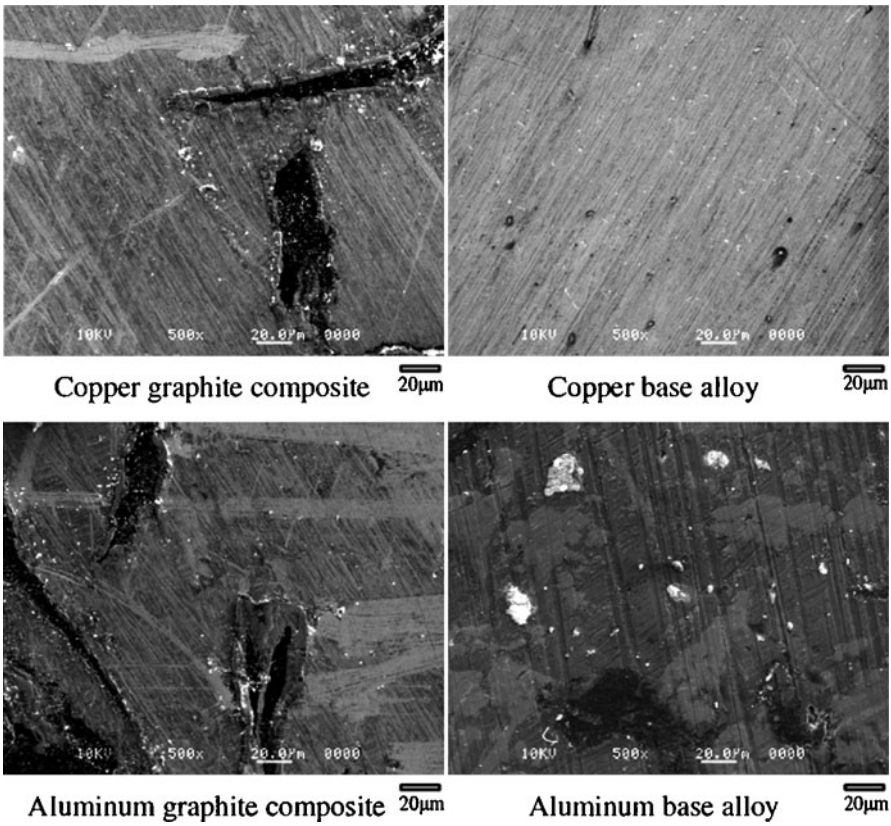

Fig. 13.3 SEM images of polished samples

After that four samples were etched. The reagents used in the selective dislocation etching are as follows (Qian et al. 2005). For the aluminum base alloy and the aluminum–graphite composite, the etchant consisted of 40 mL of 37 wt% HCl, 12.5 mL of H_2O, and 2.0 mL of 48 wt% of HF. The etching time was set for 20 s, for a two cycle test. On the other hand, the etchants used for the copper-based alloy and

Table 13.3 Measured and calculated surface roughness and contact angles (Nosonovsky et al. 2011)

	Measured			Calculated		
Sample	Etching time	R_a (μm)	Measured contact angle	R_{fm}	Contact angle (Wenzel, $f_{SLm} = 1$)	Contact angle (Cassie-Baxter, $f_{SLm} = 0$)
Al–graphite composite	0	0.2	59.1°	1	93°	117°
Cu–graphite composite	0	0.2	86.7°	1	93°	117°
Al base alloy	20 s	0.8	82.5°	1.89	0°	80°
Cu base alloy	20 h	0.4	91.1°	1.28	29°	97°
Al–graphite composite	20 s	0.7	136.8°	1.72	82°	105°
Cu–graphite composite	20 h	0.4	99.2°	1.28	89°	112°

the copper–graphite composite was 0.1 molar concentration of 37 wt% HCl. The etching time was 20 h for both sample types.

The surface roughness of the samples was measured before and after the etching process using a surface profilometer (Mitutoyo Surftest. 402). The roughness of the samples was measured again after the etching. The roughness parameter measured in the above cases is the average roughness value, R_a, defined as the arithmetic average of the absolute values of the roughness profile ordinates.

After that, the contact angles were measured. These measurements were done using the model 250 Rame Hart Goniometer. The measured contact angles showed that none of the surfaces were hydrophobic, though surfaces of the composites had a higher contact angle with water (Table 13.3). This can be attributed to the graphite particles which has an effect on the surface roughness of the composites when compared to the base alloys. Figure 13.4 shows the contact angle profiles of these samples before etching.

It is observed that all etched samples except Al base alloy became hydrophobic, i.e., have the contact angle larger than 90°. The contact angle profiles for Al and Cu samples that were etched for 20 s and 20 h, respectively are as shown in Fig. 13.5.

To compare the experimental results with the model and determine whether the homogeneous or composite interface is realized, the contact angle was calculated for the Wenzel (13.2) and Cassie–Baxter wetting regimes (13.5). For that end, it was assumed that nonetched sample have smooth matrix ($R_{fm} = 1$) and the surfaces roughness is caused by spherical reinforcement particles ($R_{fr} = 2$). For etched samples, the matrix roughness is significant in comparison with the reinforcement roughness, although the exact values of R_{fm} cannot be calculated from the measured R_a. However, it can be estimated as

$$R_{fm} = \sqrt{1 + \left(\frac{R_a}{L}\right)^2}, \tag{13.8}$$

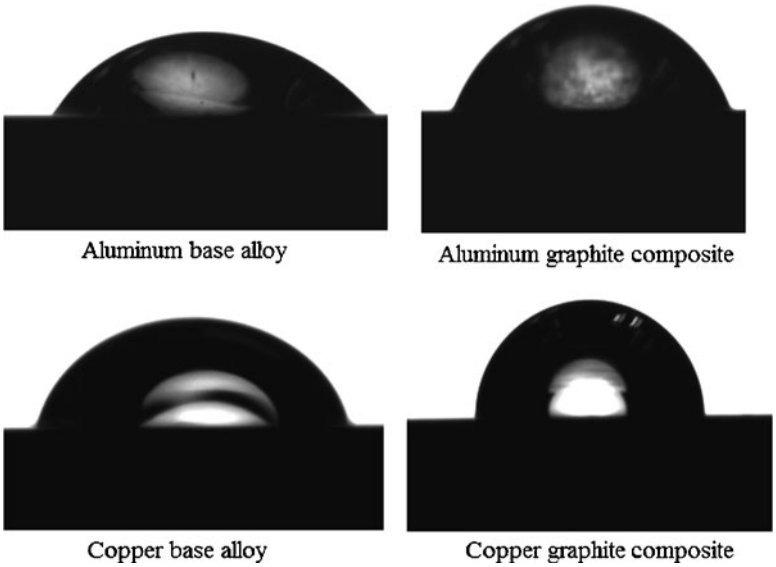

Fig. 13.4 Images of water droplet on nonetched samples

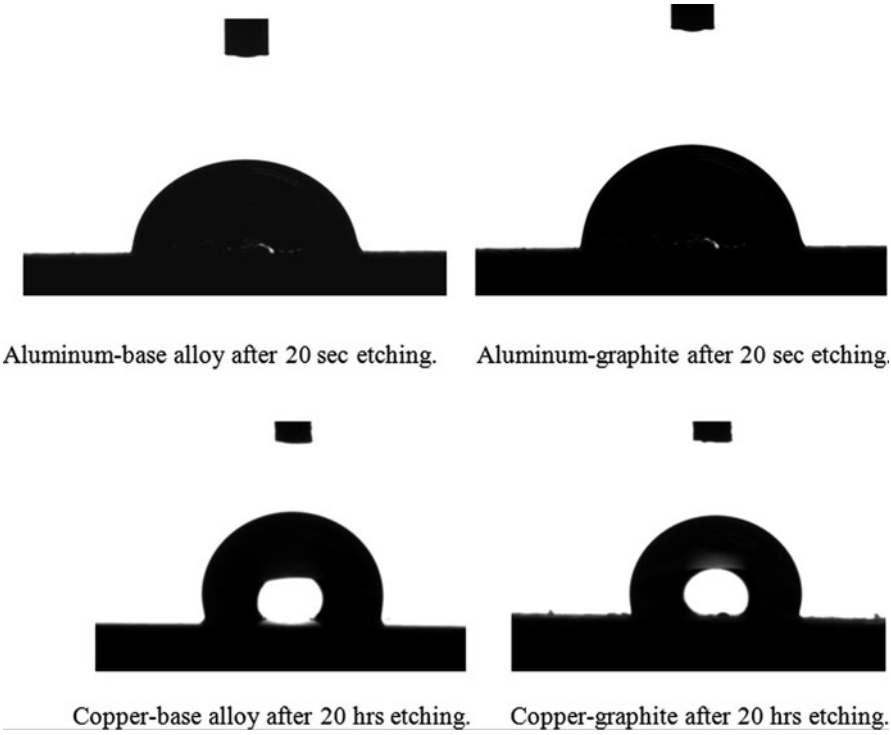

Fig. 13.5 Images of water droplet on etched samples

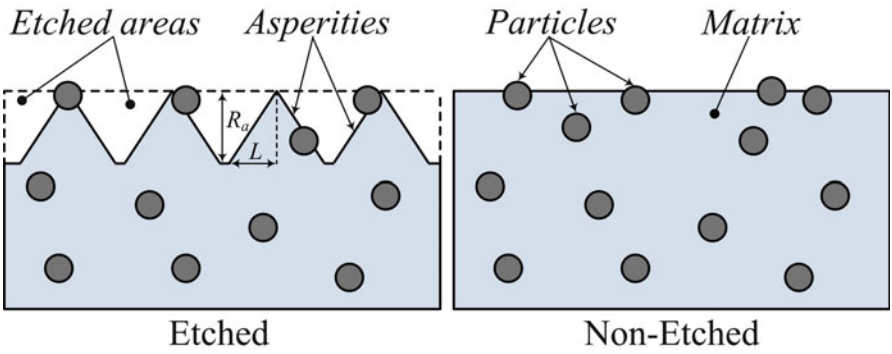

Fig. 13.6 The schematic of surface before and after etching for a matrix reinforced with particles

where L is a typical length of an asperity(Fig. 13.6). For the Cassie–Baxter model, we assumed $f_{\mathrm{SLm}} = 0$ (no matrix in contact with water) and $f_{\mathrm{SLr}} = 1$ (entire reinforcement area is covered by water). Assuming $L = 0.5$ μm, the roughness factors and the contact angles were further calculated (Table 13.3).

It is observed from Table 13.3 that for smoother samples (no etching) the Wenzel model predicts more accurate results, whereas for the etched samples the Cassie–Baxter model is better. The experimental data show that, for all samples, the contact angle increased with increasing roughness. The contact angle of the Al–graphite sample was larger than that for Cu–graphite. The main reason for this is the difference in their average roughness values, R_{a}. Since the average roughness values of samples are different for Al– and Cu–graphite composites, respectively, so each sample follows the different behavior.

The standard method of creating a superhydrophobic surface implies roughening the surface and placing some low-energy (hydrophobic) material on it. Instead, we suggested here to place low-energy reinforcement into the matrix of the composite material. We presented a model for the overall contact angle of such a composite material and for the reinforcement volume fraction needed to make the material superhydrophobic. We also conducted experiment with low-energy graphite-reinforced aluminum and copper-based composites and showed that the contact angle can be determined from the model with certain reasonable assumptions about the roughness factors and solid–liquid fractional contact areas. In order to decouple the effects of reinforcement and roughness, the experiments were conducted for initially smooth and etched matrix and composite materials. The composite materials can be used to produce sustainable (wear-resistant) superhydrophobic surfaces.

13.4 Polymeric Superhydrophobic Surfaces

Several processes which are used to create superhydrophobic polymeric surfaces were reviewied by Mortazavi and Nosonovsky (2012). Electrospinning is a process in which a high-electrical field is used to fabricate fibers with diameters ranging

from a few nanometers to tens of micrometers from liquid polymeric solutions. A composition of solvents can be used as well. The process of electrospinning was invented in 1902 by J.F. Cooley and W.J. Morton. A number of further developments were made after that in the 1930–1960s by A. Formhals, G.I. Taylor, N.D. Rozenblum, I.V. Petryanov-Sokolov, and others. Since the early 1990s the technique was used for many polymers and the term "electrospinning" was popularized, being coined from "electrostatic spinning" and now is widely used in literature.

The process is suitable for a wide variety of polymers and can be conducted at room temperature. The morphology, surface texture, and wetting properties of the fabricated fibrous mat can be controlled by changing the solution characteristics or electrospinning parameters. The solution concentration, viscosity, applied voltage, ambient relative humidity, and temperature are the most important parameters which control this process (Mortazavi and Nosonovsky 2012).

Electrospinning was first used for fabrication of superhydrophobic surfaces by Jiang et al. (2004). Solutions of polystyrene (PS) in dimethylformamide (DMF) at different polymer concentrations were prepared and the effect of concentration on the morphology of the resultant surfaces was investigated. Polystyrene (PS) is a hydrophobic polymer with a water contact angle of 95°. Nanofibrous structure with WCA of 139° was formed from a concentrated solution. Porous microparticles with WCA as high as 162°, but with low structural stability were formed from a highly concentrated solution. A porous microsphere/nanofiber composite coating with WCA of 160° and good stability was obtained from a medium concentrated solution. No information about contact angle hysteresis was reported in this study (Mortazavi and Nosonovsky 2012).

Injection molding is a widely used polymer process in which molten plastic is forced under high pressure to flow into a mold cavity where it is held until it cools and hardens to the shape of the mold. Injection molding can be used to fabricate materials with nanopatterned surfaces. AAO nanotemplates can be mounted into the mold to transfer the nanopatterns to the molten polymer. Puukilainen et al. (Esa Puukilainen 2006) fabricated two AAO templates with various pore nanostructures by altering the voltage used in the electrochemical reaction. The lower voltage resulted in the higher order structure. The fabricated AAO templates were used to make nanopatterns on the surface of two polyethylene (PE) and one polypropylene (PP) samples by injection molding. Well-ordered nanostructures comparable to those of the AAO templates were formed. The wettability property of the surface was investigated by static contact angle measurements of the nanostructured and flat surfaces. The WCA was increased due to the enhanced surface roughness. More increase was observed for the surfaces made by using higher order templates (Mortazavi and Nosonovsky 2012).

Many surfaces in nature such as lotus leaves and wings of some insects are superhydrophobic exhibiting WCA larger than 150° (Neinhuis 1997; Wagner et al. 1996). The water repellency property is mostly considered to be the effect of micro and nanoscale roughness on these surfaces. A simple approach for fabrication of superhydrophobic surfaces is the replication of the surface structure of natural

surfaces with polymeric materials using various methods (Mortazavi and Nosonovsky 2012).

Silica nanoparticles can be used to introduce nanoscale roughness into the superhydrophobic surfaces. Since silica nanoparticles are hydrophobic, a surface modification is needed in order to show a water repellency property. Hou and Wang (2007) fabricated transparent coatings ranging from superhydrophilic to superhydrophobic through the casting of polystyrene (PS)–SiO_2 nanoparticle mixtures at different concentration and different drying temperatures. The change in the PS/SiO_2 nanoparticle compositions and drying temperatures resulted in the formation of coating with various surface roughness and surface chemistry. The changes were believed to be due to the presence of either more hydrophobic PS groups or hydrophilic SiO_2 functional groups at the most outer surface of the coating (Mortazavi and Nosonovsky 2012).

Carbon nanotubes are allotropes of carbon in which graphite sheets have been rolled up to form hollow cylinders with diameter of a few nanometers and length up to a few centimeters. Nanotubes with their special structure have attracted a lot of interest in many application fields, such as nanotechnology, electronics, and optics in recent years. Nanotubes have been added to various polymer matrices for different physical and mechanical properties enhancements. They can also be used to make nanosized roughness very similar to those of lotus leaves due to their nanosized diameter and high aspect ratio (surface/area ratio). The combination of micro- and nanotexture of the nanotubes, and the hydrophobic nature of them can be applied to fabricate nature-inspired superhydrophobic surfaces (Mortazavi and Nosonovsky 2012).

13.5 Summary

Various techniques can be applied to make microstructured superhydrophobic surfaces (Table 13.4). These techniques involve coating and roughening as well as methods to make hierarchical surfaces out of nanoparticles, and other approaches. A particularly promising approach is to use metal matrix composites and other composite materials with the reinforcement in the bulk of the materials rather than at the surface, since this can lead to wear resistant sustainable superhydrophobicity and oleophobicity.

Table 13.4 Various techniques to produce polymeric superhydrophobic surfaces (Mortazavi and Nosonovsky 2012)

Polymer	Technique	Contact angle (°)	Note	Source
PDMS	Laser treatment		–	Khorasani et al. (2005)
	Plasma treatment		–	
	Sol–gel	162	SiO_2 nanoparticles	Peng et al. (2005)
	Nanocomposite	164	$CaCO_3/SiO_2$ particles	Yang et al. (2009)
	Polymer casting			Lee et al. (2007)
	CVD + nanocomposite		Plant leaf replica	Ghosh (2009)
	Replica molding + CVD	160	Oil-repellent performance	Rahmawan et al. (2010)
Cotton	Assembly of CNT	>150	Special textile	Liu et al. (2007)
	CNT treatment	154	CNT treatment	Li et al. (2010)
	Nanocomposite	130	Silica nanoparticles	
	Electrospinning	160	Coating with PVDF/FSM	Sarkar et al. (2010)
	Nanocomposite	170	Functionalized SiO_2	Ch Xue (2009)
	Sol–gel	163	SiO_2 nanoparticles	Xuea et al. (2008)
UV curable	Nanoimprint lithography		Plant leaf replica	Lee and Kwon (2006)
	Nanoparticle + ozone treatment	160	Al_2O_3 nanoparticles	Choi et al. (2008)
	Nanoimprint lithography	132	Cicada wing replica	Hong et al. (2009)
Polyurethane	Nanocomposite		Plant leaf replica	Feng et al. (2009)
	Electrospinning		–	Wu et al. (2009)
	Electrospinning + nanocomposite		SiO_2 nanoparticles	
	Nanocomposite		PS nanoparticles	Jilin Zhang (2006)
PE	Nano–microreplication + blending		–	Puukilainen et al. (2006)
	Plasma treatment		–	
	Nano–microreplication			Sheng and Zhang (2009)
	Ultrasonic nano–microreplication			Lee et al. (2004)
	Solution method	153	High stability	Yuan et al. (2008)
	Solution method	173	Good stability	Lu et al. (2004)
	Solution method	160		Yuan et al. (2009)

(continued)

Table 13.4 (continued)

Polymer	Technique	Contact angle (°)	Note	Source
PP	Nano–microreplication + blending			Puukilainen et al. (2006)
	Nano–microreplication		Using AAO membrane	Yoo et al. (2009)
	Solution method		Anticoagulation property	Hou et al. (2010)
PMMA	Plasma treatment	152	Transparent	Vourdas et al. (2007)
	Nano–micromolding		Nanomicrofluidic systems	
	Solution casting	140	Different nanoparticles	
	Spray coating	154	PMMA–SiO_2 solution	
	Seeding polymerization		PMMA core/PDMS shell	Xiaobo Deng and Cao (2007)
Carbon fiber	Chemical vapor deposition	169	CNT decoration	Hsieh et al. (2008)
	Chemical-wet impregnation		SiO_2 particles on CF	Hsieh et al. (2008)
Epoxy resin	Replication + self assembly			Bhushan et al. (2008) (×7)
	Spray coating	165	Micro/nano-SiO_2	
PS	Spin coating	124	PS micro/nanospheres	Yan et al. (2007)
	Vertical deposition		PS nanospheres	Ge et al. (2006)
	Spin coating		PS nanoparticles	Shiu et al. (2004)
	Spray coating	160	PS-CNT nanocpmposite	Yang et al. (2009)
	Reactive-ion etching (RIE)	180	SiO_2 surface treatment	Park et al. (2010)
	Replication		Nanoporous templates	Lee et al. (2004)
	Solution casting		PS/SiO_2 nanocomposite	Hou and Wang (2007)
	Sol–gel		PS/SiO_2 nanocomposite	
	Polymer imprinting technique		Fabrication of AAO	
	Spin coating			
	Molding	>150	Alumina porous template	Cheng et al. (2010)
	Electrospinning	<160		J. Zheng (2006)
	Electrospinning	159	THF/DMF/PS solution	
	Electrospinning	154	DMF/PS solution	Kang et al. (2008)
	Electrospinning	178	TiO_2 + graphene	
	Electrospinning	150	High tensile strength	

	Spray coating	155		
	Copolymerization			
	Solution method	156		Yuan et al. (2007)
	Replication	158		Yuan et al. (2007)
PVFD	Solution casting + molding			Bormashenko et al. (2006)
	Electrospinning	>150	Fluorinated silane PVDF	
	Chemical vapor deposition	155		Zheng et al. (2009)
	Chemical bath deposition	157	Grafting by DTS/DDS	Zheng et al. (2010)
	Solution casting	155		Peng et al. (2005)
PTFE	Electrospinning		Teflon sheath/PCL core	Han and Steckl (2009)
	Nanocomposite	165	PTFE nanoparticles	Hong and Pan (2010)
	Radio frequency sputtering	164		Sarkar et al. (2008)
	Molding		Filter paper as template	Hou and Wang (2009)
	Physical vapor deposition	165	Surface treatment of Al	Weibel et al. (2010)
	Nanocomposite	160	CNT/PFTE nanoparticles	Li et al. (2010)
	Pulse electron deposition	166		Gupta et al. (2009)
	Molding	165	Extending a PTFE type	Jilin Zhang et al. (2004a, b)
	Spray coating	156	Oil–water separation	
PVP	Electrospinning		Titana/PVP core–shell	
	Electrospinning	169		J. Jabal (2009)
PC	Solution casting	160		Zhang et al. (2008)
	Solvent induced crystallization			Zhao et al. (2006)
PET	Nanocomposite	158		Bae et al. (2010)
	Plasma treatment + CVD	>150		K. Teshima et al. (2005)
	Nanocomposite	158	Au nanoparticles	Bae et al. (2009)
PCL	Electrospinning + CVD	175		Ma et al. (2005)
	Electrospinning	172		Yoon et al. (2010)

(continued)

Table 13.4 (continued)

Polymer	Technique	Contact angle (°)	Note	Source
PVC	Solution method	155	Good stability	Yongmei Ma (2006)
	Solution method	154		Chen et al. (2009)
PI	Polymerization	156	Porous alumina molding	
	Nanocomposite	160	Layer–layer assembly	Van Zhao (2008)
PLA	Nanocomposites	150	Modified nanosilica	Geun Yeol Bae (2010)
	Solution method	150		Jun Shi (2008)

Chapter 14
Outlook

In this book, we discussed theoretical foundations and practical principles of design of novel materials with the ability for self-organization, namely, self-healing, self-lubricating, and self-cleaning materials. These materials are biomimetic, i.e., they are inspired by materials in living nature. In the theoretical analysis, our emphasis was on thermodynamic description of these materials, since nonequilibrium thermodynamic has provided a basis for the study of pattern formation and self-organization. Our purpose was to develop theoretical models, which could be useful for better understanding of structure–property relationships in these smart materials and could serve as a guide for their design and, in a sense, to bridge the gap between the theories of self-organization, which have been developed decades ago, and current experiment-driven research of modern materials. In the practical realization, our focus was on the metallic and, in particular, metal matrix composite materials.

The area of self-healing materials has become quite significant in recent years. Biannual international conferences of self-healing materials took place in 2007 (Delft, the Netherlands), 2009 (Chicago, USA), and 2011 (Bath, the UK). Most advances in self-healing materials are related to the polymeric-based materials and composites. While there is general consensus among material scientists that the field of self-healing is biomimetic in the sense that living nature serves as a source of inspiration for these materials, it is hardly possible currently to borrow concepts from biology directly into materials science. This is because living nature uses much more sophisticated mechanisms, than those currently available to engineers. However, certain design concepts still can be emphasized, and among them is the hierarchical organization of material in living nature, which provides natural organisms with their remarkable abilities. The area of bone growth and regeneration can be particularly interesting for the development of self-healing materials.

In the field of metallic self-healing materials, most research efforts are related to three approaches. First, the use of supersaturated solid solution (e.g., underaged alloys), which provides a readily available mechanism of precipitation of the solute

M. Nosonovsky and P.K. Rohatgi, *Biomimetics in Materials Science: Self-Healing, Self-Lubricating, and Self-Cleaning Materials*, Springer Series in Materials Science 152, DOI 10.1007/978-1-4614-0926-7_14,

at micro-voids, which serve as sources of nucleation of the precipitated phase. Only very small (nanoscale) voids can be healed in this way. Second is the embedding of a healing agent into the matrix of a composite material. This may require either diffusion barriers (microcapsules) or a low melting temperature alloy embedded into the matrix. The specimen should be heated above the melting temperature of the healing alloy in order to initiate healing, so self-healing is non-autonomous. Numerous issues should be resolved, such as the capillary action, volume restoration, and whether the crack path allows for healing. The third approach, also non-autonomous, is embedding shape memory alloy fibers. Currently, only specimens with limited ability to heal cracks and restore original mechanical properties can be produced.

From the thermodynamic point of view, we considered self-healing systems as systems that are away from equilibrium and tend to restore the equilibrium state. The healing is driven by the same thermodynamic force, which tends to restore equilibrium in the system. For example, in the case of the precipitation mechanism, material transport to the voids is caused by the non-equilibrium state of the system, and it is the same mechanism that heals the voids. In the case of a healing agent embedded into the matrix, the transport of the agent is caused by the nonequilibrium and it also heals the crack. For SMA-fiber reinforced materials, nonequilibrium causes the fibers to attain their original shape and thus to close the crack. Therefore, by relating quantitatively these processes to material microstructure, one can obtain desired structure–property relationships for the design of these materials. Furthermore, from the thermodynamic point of view, multiscale organization of the material plays a key role, as healing is achieved at the expense of deterioration at the lower length scale (microcapsules are irreversibly fractured to heal cracks, etc.).

Self-lubricating materials constitute another important field. While there is no common definition of what is a "self-lubricating material," typically, those materials that can operate with low friction and wear without any external supply of lubricant are considered self-lubricating. This includes materials with hard coating (to reduce wear) and low surface energy (to reduce adhesion), as well as materials capable of forming certain protective structures, such as tribofilms, at the interface dynamically during the sliding. Apparently this reflects the general tendency of nonequilibrium systems to tune themselves to the state of minimum entropy production, and, in particular, minimum energy dissipation due to friction and minimum material deterioration due to wear.

Friction and wear reflect the tendencies of energy to irreversibly dissipate (heat, generated by friction) and material to deteriorate (wear) in accordance with the Second law of thermodynamics. It is therefore reasonable to quantitatively explain various mechanisms of friction and wear using the thermodynamic concept of entropy production and thus to relate material microstructure to its tribological properties. Furthermore, this may be the only appropriate general explanation of the origin of friction and wear, which is common for various friction mechanisms, since it is based on the physical origin of friction. However, so far the thermodynamic approach had limited success for tribological applications.

It may be much more promising to use nonequilibrium thermodynamic concepts, rather than the current approach. In particular, two concepts from the field of nonequilibrium thermodynamics are especially significant in tribology. First is, the linear Onsager relationships governing kinetics of the processes close to equilibrium, which state that flows (and velocities) are linearly related to thermodynamic forces. This principle can be directly linked to the linear empirical laws of friction (the Coulomb law) and wear (the Archard law). In addition, this approach provides coupling between energy (heat) flow and mass transport (diffusion) thus providing a basis to link friction and wear together, supporting the observation of D. Tabor who considered these two phenomena as two sides of the same process. Friction itself can be viewed as a process occurring at the 2D interface and thus the laws of friction should be deduced by an asymptotic decomposition of constitutive laws in the bulk 3D material.

The second concept is Prigogine's principle of minimum entropy production, which states that a nonequilibrium system tends to reach a stationary state of minimum entropy production. This can explain why most tribosystems tend to evolve to the state of lower friction and wear (e.g., the stationary state after the so-called running-in) and why self-organized structures can form at the frictional interface. A stability criterion can be formulated for the stationary state indicating whether the transition to a self-organized state is likely to occur and relating it to materials microstructure. In this manner, various types of self-organization are related to a general stability criterion. These types include friction-induced vibrations due to dynamic instabilities as a result of coupling of friction to the thermal expansion, wear, and other effects. It also includes tribofilm formation at the interface and surface roughness evolution during the running-in stage. More exotic mechanisms of self-organization, such as self-organized criticality and reaction-diffusion (Turing) systems have been considered as well. The theory is able, in principle, to supply recommendation on desirable composition of a material in order to facilitate the effect of self-lubrication. Speaking of the practical realization, we reviewed tribological properties of metal matrix composite materials.

The third type of materials of interest to us was self-cleaning materials. Most of the self-cleaning materials use the so-called Lotus effect or surface roughness-induced superhydrophobicity and self-cleaning. Superhydrophobicity was discovered decades ago; however, it became an area of very intensive research in the past 20 years due to the advent of scanning probe microscopy and various techniques to produce micro- and nanostructured functional surface. Many insights into the interaction of roughness with wetting were obtained using the thermodynamic approach, such as the surface free energy. In particular, it is clear now that many wetting regimes are possible and that wetting cannot be characterized by a single parameter, the contact angle. Robust superhydrophobic surfaces should have hierarchical organization. The very latest advances in superhydrophobicity are related to the design of tunable surfaces (with controlled surface energy and wettability) and to the development of surfaces capable of repelling organic liquids (i.e., oleophobic surfaces).

Besides the Lotus effect, self-cleaning surfaces can be obtained with the photocatalytic effect using titania and some other materials. Underwater self-cleaning is a separate but related field involving oleophobicity and omniphobicity, which can be utilized for anti-fouling. The main challenge for the microstructure superhydrophobic surfaces is their vulnerability to even small or moderate wear. The surface layer involving microstructure deteriorates easily. Composite materials and, in particular, the MMCs and nanocomposites, can solve this problem if they have hydrophobic reinforcement in the bulk of the material rather than at the surface.

To summarize, thermodynamic methods can be very useful to the development of novel smart and biomimetic materials capable for self-organization. MMCs and nanocomposites constitute a class of materials with the potential for self-healing, self-lubrication, and self-cleaning.

About the Authors

Dr. Michael Nosonovsky is an Assistant Professor at the University of Wisconsin, Milwaukee (UWM). He is a coauthor of one monograph, ten book chapters, and more than 50 research articles. For his work on the Lotus effect and biomimetic surfaces, he was honored with the 2008 Burt L. Newkirk Award by ASME.

Dr. Pradeep Kumar Rohatgi is Wisconsin Distinguished Professor and Director of the UWM Center for Composites. He is a pioneer in the field of composite materials, particularly metal matrix composites. Rohatgi has coauthored and edited 11 books and over 400 scientific papers, and holds 20 US patents. In 2006, he was honored with the "Rohatgi Honorary Symposium" on Solidification Processing of Metal Matrix Composites by The Minerals, Metals, and Materials Society.

M. Nosonovsky and P.K. Rohatgi, *Biomimetics in Materials Science: Self-Healing, Self-Lubricating, and Self-Cleaning Materials*, Springer Series in Materials Science 152,
DOI 10.1007/978-1-4614-0926-7,

References

Abdel-Aal, H.A.: Wear and irreversible entropy generation in dry sliding. Annals Dundarea de Jos of Galati (Tribology). **VIV**, 115–123 (2006)

Abdelsalam, M.E., Bartlett, P.N., Kelf, T., Baumberg, J.: Wetting of regularly structured gold surfaces. Langmuir. **21**, 1753–1757 (2005)

Abrahamson, E.P., Jahanmir, S., Suh, N.P.: The effect of surface finish on the wear of sliding surfaces. CIRP Ann. **24**, 513 (1975)

Adams, G.G.: Self-excited oscillations of the two elastic half-spaces sliding with a constant coefficyient of friction. ASME J. Appl. Mech. **62**, 867–872 (1995)

Adams, G.G.: Steady sliding of two elastic half-spaces with friction reduction due to interface stick–slip. Trans. ASME, J. Appl. Mech. **65**, 470–475 (1998). doi:10.1115/1.2789077

Adams, G.G., Nosonovsky, M.: Contact modeling – forces. Tribol Int. **33**, 441–442 (2000)

Adams, G.G., Barber, J.R., Ciavarella, M., Rice, J.R.: A paradox in sliding contact with friction. ASME J. Appl. Mech. **72**, 450–452 (2005)

Adams, G.G., Muftu, S., Mohd Azhar, N.: A scale-dependent model for multiasperity contact and friction, ASME J. Tribol. **125** 700–708 (2003)

Adamson, A.V.: Physical chemistry of surfaces. Wiley, New York (1990)

Adler, M., Ferrante, J., Schilowitz, A., Yablon, D., Zypman, F.: Self-organized criticality in nanotribology. Mater. Res. Soc. **782**, 111 (2004)

Aizawa, A., Mitsuo, A., Yamamoto, S., Sumitomo, T., Muraishic, S.: Self-lubrication mechanism via the in situ formed lubricious oxide tribofilm. Wear. **259**, 708–718 (2005)

Akhadejdamrong, T., Aizawa, T., Yoshitake, M., et al.: Self-lubrication mechanism of chlorine implanted TiN coatings. Wear. **254**, 668–679 (2003)

Alexandridou, S., Kiparissides, C., Fransaer, J., et al.: On the synthesis of oil-containing microcapsules and their electrolytic codeposition. Surf. Coating Technol. **71**, 267–276 (1995)

Alexeev, N., Jahanmir, S.: Mechanics of friction in self-lubricating composite materials. Wear. **166**, 41–48 (1993)

Amiri, M., Khonsari, M.M.: On the thermodynamics of friction and wear – a review. Entropy **12**, 1021–1049 (2010)

Anderson, H.M., Keller, M.W., Moore, J.S., Sottos, H.R., White, S.R.: Self-healing polymers and composites. In: van der Zwaag, S. (ed.) Self healing materials – an alternative approach to 20 centuries of materials science, pp. 19–44. Springer, Dordrecht, The Netherlands (2007)

Angell, C.A.: Approaching the limits. Nature **331**, 206 (1988)

Anisimov, M.A.: Thermodynamics at the meso- and nanoscale. Dekker Encyclopedia of Nanoscience and Technology, pp. 3893–3904 (2004)

Anisimov, M.A.: Divergence of Tolman's length for a droplet near the critical point. Phys. Rev. Lett. **98**, 035702 (2007)

Apfel, R., Smith, M.: The tensile strength of di-ethyl ether using Briggs's method. J. Appl. Phys. **48**, 2077–2078 (1977)

Archard, J.F.: Elastic deformation and the laws of friction. Proc. R. Soc. Lond. A **243**, 190–205 (1957)

Asay, D.B., Kim, S.H.: Effects of adsorbed water layer structure on adhesion force of silicon oxide nanoasperity contact with humid ambient. J. Chem. Phys. **124**, 174712 (2006)

Asay, D.B., de Boer, M.P., Kim, S.H.: Equilibrium vapor adsorption and capillary force: exact Laplace-Young equation solution and circular approximation approaches. J Adhes Sci Technol. **24**, 2363–2382 (2010)

Badia, F.A.: pp. 1–14. North American Die Casting Association Trans., Oak Ridge, TN (1989)

Badia, F.A., Rohatgi, P.K.: SAE Trans. **77**, 1280 (1969)

Bae, Y.W., Lee, W.Y., Besmann, T.M., et al.: Preparation and friction characteristics of self-lubricating TiN-MoS2 composite coatings. Mater. Sci. Eng. A **209**, 372–376 (1996)

Bae, G.Y., Min, B.G., Jeong, Y.G., Lee, S.C., Jang, J.H., Koo, G.H.: Superhydrophobicity of cotton fabrics treated with silica nanoparticles and water-repellent agent. J. Colloid Interface Sci. **337**, 170–175 (2009)

Bae, G.Y., Jeong, Y.G., Min, B.G.: Superhydrophobic PET fabrics achieved by silica nanoparticles and water-repellent agent. Fiber Polym. **11**, 976–981 (2010)

Bahadur, V., Garimella, S.V.: Electrowetting-based control of static droplet states on rough surfaces. Langmuir **23**, 4918–4924 (2007)

Bak, P.: How nature works: the science of self-organized criticality. Springer, New York (1996)

Baker, E.A.: Chemistry and morphology of plant epicuticular waxes. In: Cutler, D.F., Alvin, K.L., Price, C.E. (eds.) The plant cuticle, pp. 139–165. Academic, London (1982)

Baker, R.M., Hewitt, G.W.: Brush wear in hydrogen and in air. J. Electr. (Lond.) **33**, 287 (1936)

Balazs, A.C.: Modeling self-healing materials. Mater Today **10**, 18–23 (2007)

Barber, J.R.: Thermoelastic instabilities in the sliding of conforming solids. Proc. R Soc. Lond. A. **312**, 381–394 (1969)

Barbieri, L., Wagner, E., Hoffmann, P.: Water wetting transition parameters of perfluorinated substrates with periodically distributed flat-top microscale obstavles. Langmuir **23**, 1723–1734 (2007)

Bar-Cohen, Y. (ed.): Biomimetics: biologically inspired technologies. Taylor and Francis, Boca Raton (2005)

Barry, H.F., Binkelman, J.P.: MoS2 lubrication of various metals. Lubr. Eng. **22**, 139 (1966)

Bartell, F.E., Shepard, J.W.: Surface roughness as related to hysteresis of contact angles. J. Phys. Chem. **57**, 455–458 (1953)

Barthlott, W., Neinhuis, C.: Purity of the sacred lotus, or escape from contamination in biological surfaces. Planta **202**, 1–8 (1997)

Bartolo, D., Bouamrirene, F., Verneuil, E., Buguin, A., Silberzan, P., Moulinet, S.: Bouncing or sticky droplets: impalement transitions on superhydrophobic micropatterned surfaces. Europhys. Lett. **74**, 299–305 (2006)

Basu, B.J., Manasa, J.: Reversible switching of nanostructured cobalt hydroxide films from superhydrophobic to superhydrophilic state. Appl Phys. A **103**, 343–348 (2011)

Bejan, A., Marden, J.H.: The constructal unification of biological and geophysical design. Phys. Life Rev. 6 (2009)

Belko, V.O., Bondarenko, P.N., Emelyanov, O.A.: The dynamic characteristics of self-healing processes in metal film capacitors. Russ Electr Eng **78**, 138–142 (2007)

Bender, M., Olson, G.B.: Computational thermodynamics-based design of nanodispersion-strengthened shape memory alloys. SMST-2007: Proceedings of International Conference on Shape Memory and Superelastic Technol., pp. 115–122 (2008)

Bercovici, D.: Generation of plate tectonics from lithosphere-mantle flow and void-volatile self-lubrication. Earth Planet Sci Lett **154**, 139–151 (1998)

Bergeron, V., Bonn, D., Martin, J.Y., Vovelle, L.: Controlling droplet deposition with polymer additives. Nature **405**, 772–775 (2000)

Bershadski, L.I.B.I.: Kostetski and the general concept in tribology. Trenie I Iznos (Russ Frict Wear) **14**, 6–18 (1993)
Bershadsky, L.I.: On self-organization and wear resistance in tribo-systems. Trenie i Iznos **13**, 1077–1094 (1992) (in Russian)
Bershadsky, L.I.: B. I. Kostetsky and the general concept in tribology. Trenie i Iznos (Russian Friction and Wear) **14**, 6–18 (1993)
Bhushan, B.: Principles and applications of tribology. Wiley, NY (1999)
Bhushan, B.: Introduction to tribology. Wiley, NY (2002)
Bhushan, B., Dandavate, C.: Thin-film friction and adhesion studies using atomic force microscopy. J. Appl. Phys. **87**, 1201–1210 (2000)
Bhushan, B., Her, E.K.: Fabrication of superhydrophobic surfaces with high and low adhesion inspired from rose petal. Langmuir **26**, 8207–8217 (2010)
Bhushan, B., Jung, Y.C.: Wetting study of patterned surfaces for superhydrophobicity. Ultramicroscopy **107**, 1033–1041 (2007)
Bhushan, B., Nosonovsky, M.: Scale effects in friction using strain gradient plasticity and dislocation-assisted sliding (microslip). Acta Mater. **51**, 4331–4340 (2003)
Bhushan, B., Nosonovsky, M.: Comprehensive model for scale effects in friction due to adhesion and two- and three-body deformation (plowing). Acta Mater. **52**, 2461–2474 (2004a)
Bhushan, B., Nosonovsky, M.: Scale effects in dry and wet friction, wear, and interface temperature. Nonotechnology. **15**, 749–761 (2004b)
Bhushan, B., Nosonovsky, M.: The rose petal effect and the modes of superhydrophobicity. Phil Trans Royal. Soc. A. **368**, 4713–4728 (2010)
Bhushan, B., Sundararajan, S.: Micro/nanoscale friction and wear mechanisms of thin films using atomic force and friction force microscopy. Acta Mater. **46**, 3793–3804 (1998)
Bhushan, B., Gupta, B.K., Vancleef, G.W., et al.: Fullerene (C-60) films for solid lubrication. Tribol Trans **36**, 573–580 (1993)
Bhushan, B., Koch, K., Jung, Y.C.: Nanostructures for superhydrophobicity and low adhesion. Soft Matter **4**, 1799–1804 (2008)
Bico, J., Thiele, U., Quéré, D.: Wetting of textured surfaces. Colloid Surf. A **206**, 41–46 (2002)
Binggeli, M., Mate, C.M.: Influence of capillary condensation of water on nanotribology studied by force microscopy. Appl. Phys. Lett. **65**, 415–417 (1994)
Biswas, S.K., Pramila Bai, B.N.: Dry wear of al-graphite particle composites. Wear **68**, 347 (1981)
Biswas, S., Rohatgi, P.K.: Tribological properties of cast graphite aluminum composites. Tribology International, (UK), vol. 16 **N2**, 89–102 (1983)
Blanchet, T.A., Peng, Y.L.: Wear resistant irradiated FEP unirradiated PTFE composites. Wear **214**, 186–191 (1998)
Blau, P.J.: Friction and wear transitions of materials: break-in, Run-in, wear-in. Noyes, Park Ridge, NJ, USA (1989)
Blau, P.J., Dumont, B., Braski, D.N., et al.: Reciprocating friction and wear behavior of a ceramic-matrix graphite composite for possible use in diesel engine valve guides. Wear **225**, 1338–1349 (1999)
Blossey, R.: Self-cleaning surfaces – virtual realities. Nat. Mater. **2**, 301–306 (2003)
Bond, I.P., Trask, R.S., Williams, H.R., Williams, J.R.: Self-healing fiber-reinforced polymer composites: an overview. In: van der Zwaag, S. (ed.) Self healing materials – an alternative approach to 20 centuries of materials science, pp. 115–138. Springer, Dordrecht, The Netherlands (2007)
Bormashenko, E., Stein, T., Whyman, G., Bormashenko, Y., Pogreb, E.: Wetting properties of the multiscaled nanostructured polymer and metallic superhydrophobic surfaces. Langmuir **22**, 9982–9985 (2006)
Bormashenko, E., Bormashenko, Y., Stein, T., Whyman, G., Pogreb, R., Barkay, Z.: Environmental scanning electron microscope study of the fine structure of the triple line and Cassie-Wenzel wetting transition for sessile drops deposited on rough polymer substrates. Langmuir **23**, 4378–4382 (2007a)

Bormashenko, E., Pogreb, R., Whyman, G., Erlich, M.: Cassie-Wenzel wetting transition in vibrated drops deposited on the rough surfaces: is dynamic Cassie-Wenzel transition 2D or 1D affair? Langmuir **23**, 6501–6503 (2007b)
Bormashenko, E., et al.: Micrometer-scale honeycomb polymer films and their properties. Macromol. Mater. Eng. **293**, 872–877 (2008)
Bormashenko, E., Stein, T., Pogreb, R., Aurbach, D.: "Petal effect" on surfaces based on lycopodium: high-stick surfaces demonstrating high apparent contact angles. J. Phys. Chem. C **113**, 5568–5572 (2009)
Boruvka, L., Neumann, A.W.: Generalization of the classical theory of capillarity. J. Chem. Phys. **66**, 5464–5476 (1977)
Bowden, P.H.: Mach. Des. **7**, 195 (1963)
Bowden, F.P., Tabor, D.: J. Appl. Phys. **14**, 141 (1945)
Bowden, F.P., Tabor, D.: The friction and lubrication of solids. Oxford/Clarendon, New York (1950)
Boyle, M.G., Mitra, J., Dawson, P.: The tip-sample water bridge and light emission from scanning tunnelling microscopy. Nanotechnology **20**, 335202 (2009)
Bragg, W.L.: Introduction to crystal analysis. Bell, London (1928)
Braun, O.M., Peyrard, M.: Dynamics and melting of a thin confined film. Phys. Rev. E **68**, 011506 (2003)
Bridgman, P.W.: Proc. Am. Acad. Arts Sci. **71**, 387 (1936)
Brinson, L.C.: 1D constitutive behavior of shape memory alloys: thermomechanical derivation with non-constant materials functions and redefined martensite internal variable. J. Intelligent Mater Sys. Struct. **4**, 229–242 (1993)
Bruck, H.A., Evans, J.J., Peterson, M.L.: The role of mechanics in biological and biologically-inspired materials. Exp Mech **42**, 361–371 (2002)
Bruni, L., Higuera, P.: A new silicon-graphite-aluminium alloys for cylinder lines. Automotive Eng. **3**, 29 (1978)
Bryant, M.D.: Entropy and dissipative processes of friction and wear. FME Trans **37**, 55–60 (2009)
Bryant, P.J., Gutshall, R.L., Taylor, L.H.: A study of mechanisms of graphite friction and wear. Wear **7**, 118–126 (1964)
Bryant, M.D., Khonsari, M.M., Ling, F.F.: On the thermodynamics of degradation. Proc. R. Soc. Lond. A **464**, 2001–2014 (2008)
Buha, J., Lumley, R.N., Crosky, A.J., Hono, K.: Secondary precipitation in an Al-Mg-Si-Cu alloy. Acta Mater. **55**, 3015–3024 (2007)
Buldyrev, J., Ferrante, F., Zypman, F.: Dry friction avalanches: experiment and theory. Phys. Rev. E **74**, 066110 (2006)
Burgess, S.C.: Reliability and safety strategies in living organisms: potential for biomimicking. J. Proc Inst. Mech Eng E **216**, 1–13 (2002)
Burton, D.S., Gao, X., Brinson, L.C.: Finite element simulation of a self-healing shape memory alloy composite. Mech. Mater. **38**, 525–537 (2006)
Bushe, N., Gershman, I.S.: Compatibility of tribosystems. In: Fox-Rabinovich, G.S., Totten, G.E. (eds.) Self-organization during friction advanced surface-engineered materials and systems design, pp. 59–80. CRC Taylor & Francis, Boca Raton, FL (2006)
Butt, H.-J., Farshchi-Tabrizi, M., Kappl, M.: Using capillary forces to determine geometry of nanocontacts. J. Appl. Phys. **100**, 024312 (2006)
Callister, W.D.: Materials science and engineering: an introduction. Wiley, New York, NY (2003)
Campbell, C.S., Cleary, P.W., Hopkins, M.: Large-scale landslide simulations-global deformation, velocities and basal friction. J. Geophys. Res. Solid Earth **100**, 8267–8283 (1995)
Cao, L., et al.: Anti-icing superhydrophobic coatings. Langmuir **25**, 12444 (2009)
Cappella, B., Dietler, G.: Force-distance curves by atomic force microscopy. Surf. Sci. Rep. **34**, 1–104 (1999)
Carpick, R.W., Agrait, N., Ogletree, D.F., Salmeron, M.: Variation of the interfacial shear strength and adhesion of a nanometer-sized contact. Langmuir **12**, 3334–3340 (1996)

Carpinteri, A., Paggi, M.: Size-scale effect on the friction coefficient. Int. J. Solids Struct. **42**, 2901–2910 (2005)
Cassie, A., Baxter, S.: Wettability of porous surfaces. Trans. Faraday Soc. **40**, 546–551 (1944)
Casstevens, J.M., Rylander, H.G., Eliezer, Z.: Friction and wear properties of two types of copper – graphite brushes under severe sliding conditions. Wear **48**, 121 (1978a)
Casstevens, J.M., Rylander, H.G., Eliezer, Z.: Influence of high velocities and high current densities on the friction and wear behavior of copper-graphite brushes. Wear **48**, 409 (1978b)
Casstevens, J.M., Rylander, H.G., Eliezer, Z.: Friction and wear characteristics of powder metallurgy copper-graphite brushes at high sliding speeds. Wear **50**, 371 (1978c)
Caupin, F., Herbert, E., Balibar, S., Cole, M.W.: Comment on Nanoscale water capillary bridges under deeply negative pressure. Phys. Chem. Lett. **463**, 283–285 (2008)
Chang, W.R., Etzion, I., Bogy, D.B.: An elastic-plastic model for the contact of rough surfaces. J Tribol. **109**, 257–263 (1987)
Chang, F.M., Hong, S.J., Sheng, Y.J., Tsao, H.K.: High contact angle hysteresis of superhydrophobic surfaces: hydrophobic defects. Appl. Phys. Lett. **95**, 064102 (2009)
Checco, A., Guenoun, P., Daillant, J.: Nonlinear dependence of the contact angle of nanodroplets on contact line curvatures. Phys. Rev. Lett. **91**, 186101 (2003)
Chen, J.D., Ju, C.P.: Low energy tribological behavior of carbon-carbon composites. Carbon **3**, 7–62 (1995)
Chen, Y.L., Helm, C.A., Israelachvili, J.: Molecular mechanisms associated with adhesion and contact-angle hysteresis of monolayer surfaces. J. Phys. Chem. **95**, 10736–10747 (1991)
Chen, L.M., Lengauer, W., Dreyer, K.: Advances in modern nitrogen-containing hard-metals and cermets. Int. J. Refract. Metals Hard Mater. **18**, 153–161 (2000)
Chen, X., Dam, M.A., Ono, K., Mal, A.K., Shen, H., Nutt, S.R., Wudl, F.: A thermally remendable crosslinked polymeric material. Science **295**, 1698–1702 (2002)
Chen, Q., Amano, R.S., Xin, M.: Experimental and computational study of R134A condensation heat transfer inside the micro-FIN tubes. Int. J. Heat Mass Transfer **41**, 785–791 (2005)
Chen, H., Yuan, Z., Zhang, J., Liu, Y., Li, K., Zhao, D., Li, S., Shi, P., Tang, J.: Preparation, characterization and wettability of porous superhydrophobic poly (vinyl chloride) surface. J. Porous Mater. **16**, 447–451 (2009)
Cheng, Y.T., Rodak, D.E., Angelopoulos, A., Gacek, T.: Microscopic observations of condensation of water on lotus leaves. Appl. Phys. Lett. **87**, 194112 (2005)
Cheng, Z., Gao, J., Jiang, L.: Tip geometry controls adhesive states of superhydrophobic surfaces. Langmuir **26**, 8233–8238 (2010)
Choi, C.-H., Kim, C.-J.: Large slip of aqueous liquid flow over a nanoengineered superhydrophobic surface. Phys. Rev. Lett. **96**, 066001 (2006)
Choi, S.J., Suh, K.Y., Lee, H.H.: A geometry controllable approach for the fabrication of biomimetic hierarchical structure and its superhydrophobicity with near-zero sliding angle. Nanotechnology **19**, 1–5 (2008)
Choi, H.J., Kim, J.Y., Hong, S.D., Ha, M.Y., Jang, J.: Molecular simulation of the nanoscale water confined between an atomic force microscope tip and a surface. J. Phys. Chem. B **113**(14), 4688–4697 (2009)
Chong, M.A.S., Zheng, Y.B., Gao, H., Tan, L.K.: Combinational template-assisted fabrication of hierarchically ordered nanowire arrays on substrates for device applications. Appl. Phys. Lett. **89**, 233104 (2006)
Choo, W.K., Hong, C.H.: J. Korean Inst. Met. **17**, 474 (1979)
Christenson, H.K.: Confinment effects on freezing and melting. J. Phys. Condens. Matt. **13**, R95–R133 (2001)
Clauss, F.J.: Solid lubricants and self-lubricating solids. Academic, New York (1972)
Conrad, H., Narayan, J.: On the grain size softening in nanocrystalline materials. Scripta Mater **42**, 1025–1030 (2000)
Cordier, P., Tournhilac, F., Soulie-Ziakovic, C., Leibler, L.: Self-healing and thermoreversible rubber from supramolecular assembly. Nature **451**, 977–980 (2008)
Cornie, J.A., Moon, H.K., Flemings, M.C.: In: Masounave, J., Hamel, F.G. (eds.) Fabrication of particulates reinforced metal composites, p. 63. ASM International, Materials Park, OH (1990)

Cottin-Bizonne, C., Barrat, J.-L., Bocquet, L., Charlaix, E.: Low-friction flows of liquid at nanopatterned interfaces. Nat. Mater. **2**, 237–240 (2003)
Coulson, S.R., Woodward, I., Badyal, J.P.S., Brewer, S.A., Willis, C.: Super-repellent composite fluoropolymer surfaces. J. Phys. Chem. B **104**, 8836–8840 (2000)
Craig, N.: Entropy analysis: an introduction to chemical thermodynamics. VCH, New York (1992)
Cui, H., et al.: Reversible ultraviolet light-manipulated superhydrophobic-to-superhydrophilic transition on a tubular SiC nanostructure film. Appl. Phys. Lett. **97**, 183112 (2010)
Dai, Z., Yang, S., Xue, Q.: Thermodynamic model of fretting wear. J. Nanjing Univ. Aeronaut. Astronaut. **32**, 125–131 (2000)
Damste, J.S.S., Dekker, M., van Dongen, B.E., Schouten, S., Piersma, T.: Structural identification of the diester preen-gland waxes of the red knot (*calidris canutus*). J. Nat. Prod. **63**, 381–384 (2000)
Darmodar, R.A., You, S.J., Chou, H.H.: Study of self-cleaning, antibacterial, and photocatalitic properties of TiO_2 entrapped PVDF membranes. J. Hazerdous Mater. **172**, 1321–1328 (2009)
Das, S., Prasad, S.V.: Microstructure and wear of cast (Al-Si alloy)-graphite composites. Wear **133**, 136 (1989)
de Gennes, P.G.: Soft interfaces. Cambridge University Press, Cambridge (1997)
de Gennes, P.G.: On fluid/wall slippage. Langmuir **18**, 3413–3414 (2002)
de Gennes, P.G., Brochard-Wyart, F., Quėrė, D.: Capillarity and wetting phenomena. Springer, Berlin (2003)
De Groot, S.R., Mazur, P.: Non-equilibrium thermodynamics. Interscience, NY (1962)
Deacon, R.F., Goodman, J.F.: Proc. R. Soc. **A243**, 464 (1958)
del Campo, A., Greiner, C.: SU-8: a photoresist for high-aspect-ratio and 3D submicron lithography. J. Micromech. Microeng. **17**, R81–R95 (2007)
Dellacorte, C., Sliney, H.E.: Tribological properties of PM212 – a high temperature, self-lubricating, powder-metallurgy composite. Lubric Eng **47**, 298–303 (1991)
Deng, J.X., Cao, T.K.: Self-lubricating mechanisms via the in situ formed tribofilm of sintered ceramics with CaF2 additions when sliding against hardened steel. Int. J. Refract. Metals Hard Mater. **25**, 189–197 (2007)
Derjaguin, B.V., Churaev, N.V.: Structural component of disjoining pressure. J. Colloid Interface Sci. **49**, 249–255 (1974)
Derjaguin, B.V., Muller, V.M., Toporov, Yu.P.: Effect of contact deformation on the adhesion of particles. J. Colloid Interface Sci. **53**, 314–326 (1975)
di Meglio, L.M.: Contact angle hysteresis and interacting surface defects. Europhys. Lett. **17**, 607–612 (1992)
Dienwiebel, M., Verhoeven, G.S., Namboodiri, P., Frenken, J.W.M., Heimberg, J.A., Zandbergen, H.W.: Superlubricity of graphite. Phys. Rev. Lett. **92**, 126101 (2004)
Dilich, S., Kuhlmann-Wilsdorf, D.: Mater. Sci. Eng. **57**, 213 (1983)
Djugum, R., Lumley, R.N., Polmear I.J.: Healing and crack closure in an Al-Cu by remedial heat treatment.2nd International Conference on Self Healing Materials. Chicago, Illinois USA (2009)
Doelling, K.L., Ling, F.F., Bryant, M.D., Heilman, B.P.: An experimental study of the correlation between wear and entropy flow in machinery components. J. Appl. Phys. **88**, 2999–3003 (2000)
Dowson, D.: History of tribology, 2nd edn. Wiley, New York (1998)
Drelich, J., Wilbur, J.L., Miller, J.D., Whitesides, G.M.: Contact angles for liquid drops at a model heterogeneous surface consisting of alternating and parallel hydrophobic/hydrophilic strips. Langmuir **12**, 1913–1922 (1996)
Dry, C.: Matrix cracking repair and filling using active and passive modes for smart timed release of chemicals from fibers into cement matrices. Smart Mater. Struct **3**, 118–123 (1994)
Dufiet, V., Boissonade, J.: Conventional and nonconventional turing patterns. J. Chem. Phys. **96**, 664–673 (1991)
Dufiet, V., Boissonade, J.: Numerical studies of turing patterns selection in a two-dimensional system. Phsica A **188**, 158–171 (1992)

Dutta, L., Pan, D., Jadhav, S.: Impression creep testing and microstructurally adaptive creep modeling of lead free solder interconnects. In: Proceedings of the 6th International Conference on Thermal, Mechanical and Multi-Physics Simulation and Experiments in Micro-Electronics and Micro-Systems – EuroSimE 2005. 18–20 April 2005

Dutta, I., et al.: Role of Shape-memory Alloy Reinforcements on Strain Evolution in Lead-free Solder Joints. Journal of Electronic Materials, 35, 1902–1913 (2006)

Erbil, H.Y., McHale, G., Newton, M.I.: Drop evaporation on solid surfaces: constant contact angle mode. Langmuir **18**, 2636–2641 (2002)

Erbil, H.Y., Demirel, A.L., Avci, Y.: Transformation of a simple plastic into a superhydrophobic surface. Science **299**, 1377–1380 (2003)

Erdemir, A.: Tribological properties of boric-acid and boricacid-forming surfaces. Lubr Eng **47**, 168–173 (1991)

Erdemir, A.: In Modern tribology handbook; Bhushan, B, (ed.): CRC Press: Boca Raton, FL, vol. II. (2001)

Erdemir, A.: Design criteria for superlubricity in carbon films and related microstructures. Tribol Int **37**, 577–583 (2004)

Erdemir, A., Fenske, G.R., Erik, R.A.: A study of the formation and self-lubrication mechanisms of Boric-acid films on boric oxide coatings. Surf Coating Tech **43–4**, 588–596 (1990)

Erdemir, A., Erck, R.A., Robles, J.: Relationship of Hertzian contact pressure to friction behavior of selflubricating boric acid films. Surf Coat Tech. **49**, 435–438 (1991)

Erdemir, A., Bindal, C., Zuiker, C., Savrun, E.: Tribology of naturally occurring boric acid films on boron carbides. Surf Coat Tech. **86–87**, 507–510 (1996a)

Erdemir, A., Bindal, C., Fenske, G.R.: Formation of ultralow friction surface films on boron carbide. Appl. Phys. Lett. **68**, 1637–1639 (1996b)

Eustathopoulos, N., Nicholas, M.G., Drevet, B.: Wettability at high temparatures. Pergamon, Amsterdam (1999)

Extrand, C.W.: Model for contact angle and hysteresis on rough and ultraphobic surfaces. Langmuir **18**, 7991–7999 (2002)

Extrand, C.W.: Contact angle hysteresis on surfaces with chemically heterogeneous islands. Langmuir **19**, 3793–3796 (2003)

Extrand, C.W.: Criteria for ultralyophobic surfaces. Langmuir **20**, 5013–5018 (2004)

Favret, E., Fuentas, N.O. (eds.): Functional Properties of Bio-inspired Surfaces: Characterization and Technological Applications. World Scientific, Singapore (2009)

Feng, X.J., Jiang, L.: Design and creation of superwetting/antiwetting surfaces. Adv. Mater. **18**, 3063–3078 (2006)

Feng, Q.L., Cui, F.Z., Pu, G., Wang, R.Z., Li, H.D.: Crystal orientation, toughening mechanisms and a mimic of nacre. Mater. Sci. Eng. C **11**, 19–25 (2000)

Feng, X.L., Feng, L., Jin, M.H., Zhai, J., Jiang, L., Zhu, D.B.: Reversible super-hydrophobicity to super-hydrophilicity transition of aligned ZnO nanorod films. J. Am. Chem. Soc. **126**, 62–63 (2004)

Feng, L., Zhang, Y., Xi, J., Zhu, Y., Wang, N., Xia, F., Jiang, L.: Petal effect: a superhydrophobic state with high adhesive force. Langmuir **24**, 4114–4119 (2008)

Feng, J., Huang, B., Zhong, M.: Fabrication of superhydrophobic and heat-insulating antimony doped tin oxide/polyurethane films by cast replica micromolding. J. Colloid Interface Sci. **336**, 268–272 (2009)

Files, B., Olson, G.: Terminator 3: biomimetic self-healing alloy composite in SMST. In: Proceedings of Second International Conference on Shape Memory and Superelastic Technology, pp. 281–286. Pacific Grove, CA (1997)

Fisher, R.L., Israelachvili, J.N.: Direct measurement of the effect of meniscus forces on adhesion: a study of the applicability of macroscopic thermodynamics to microscopic liquid interfaces. Colloids Surf **3**, 303–319 (1981)

Flemings, M.C.: Solidification processing. McGraw-Hill College, New York (1974)

Fleurquin, P., Fort, H., Kornbluth, M., Sandler, R., Segall, M., Zypman, F.: Negentropy generation and fractality in dry friction of polished surfaces. Entropy **12**, 480–489 (2010)
Forbes, P.: Self-cleaning materials: lotus leaf-inspired nanotechnology. Sci. Am. Mag. **8** (2008)
Fox-Rabinovich, G.S., Totten, G.E. (eds.): Self-organization during friction: advance surface engineered materials and systems design. CRC Taylor and Francis, Boca Raton, FL (2006)
Fox-Rabinovich, G.S., Veldhuis, S.C., Kovalev, A.I., Wainstein, D.L., Gershman, I.S., Korshunov, S., Shuster, L.S., Endrino, J.L.: Features of self-organization in ion modified nanocrystalline plasma vapor deposited AlTiN coatings under severe tribological conditions. J. Appl. Phys. **102**, 074305 (2007)
Frenkel, Y.I.: On the behavior of liquid drops on a solid surface. 1. The sliding of drops on an inclined surface. J. Exp. Theor. Phys. (USSR) **18**, 659 (1948)
Friedman, L.H., Chrzan, D.C.: Scaling theory of the Hall-Petch relation for multilayers. Phys. Rev. Lett. **81**, 2715–2718 (1998)
Friedman, H., Eidelman, O., Feldman, Y., et al.: Fabrication of self-lubricating cobalt coatings on metal surfaces. Nanotechnology **18**, 115703 (2007)
Fujishima, A., Honda, K.: Electrochemical photolysis of water at a semiconductor electrode. Nature **238**, 37–38 (1972)
Fuller, K.N.G., Tabor, D.: The effect of surface roughness on the adhesion of elastic solids. Proc. R. Soc. Lond. **A324**, 327–342 (1975)
Furmidge, C.G.L.: Studies at phase interfaces. I. The sliding of liquid drops on solid surfaces and a theory for spray retention. J. Colloid Sci. **17**, 309–324 (1962)
Furstner, R., Barthlott, W., Neinhuis, C., Walzel, P.: Wetting and self-cleaning properties of artificial superhydrophobic surfaces. Langmuir **21**, 956–961 (2005)
Gao, X.F., Jiang, L.: Biophysics: water-repellent legs of water striders. Nature **432**, 36 (2004)
Gao, L., McCarthy, T.J.: The lotus effect explained: two reasons why two length scales of topography are important. Langmuir **22**, 2966–2967 (2006)
Gao, L., McCarthy, T.J.: How Wenzel and Cassie were wrong. Langmuir **23**, 3762–3765 (2007)
Gao, L., McCarthy, T.J.: Teflon is hydrophilic. Comments on definitions of hydrophobic, shear versus tensile hydrophobicity, and wettability characterization. Langmuir **24**, 9184–9188 (2008)
Garkunov, D.N.: Triboengineering (wear and non-deterioration). Moscow Agricultural Academy Press, Moscow (2000) (in Russian)
Garkunov, D.N.: Scientific discoveries in tribotechnology. MSHA, Moscow (2004) (in Russian)
Garkunov, D.N.: The selective transfer effect at points of friction, Moscow, in Russian (1985)
Gau, H., Herminghaus, S., Lenz, P., Lipowsky, R.: Liquid morphologies on structured surfaces: from microchannels to microchips. Science **283**, 46–49 (1999)
Ge, H., Song, Y., Jiang, L., Zhu, D.: One-step preparation of polystyrene colloidal crystal films with structural colors and high hydrophobicity. Thin Solid Films **515**, 1539–1543 (2006)
Gebeshuber, I.C., Drack, M., Scherge, M.: Tribology in biology. Tribol Surf Mater Interfaces **2**(4), 200–212 (2008)
Genzer, J., Efimenko, K.: Recent developments in superhydrophobic surfaces and their relevance to marine fouling: a review. Biofouling **22**, 339–360 (2006)
Gerde, E., Marder, M.: Friction and fracture. Nature **413**, 285–288 (2001)
Gershman, I.S.: Formation of secondary structures and self-organization process of tribosystems during friction with the collection of electric current. In: Fox-Rabinovich, G.S., Totten, G.E. (eds.) Self-organization during friction: advanced surface-engineered materials and systems design, pp. 197–230. CRC Taylor & Francis, Boca Raton, FL (2006)
Ghosh, S.K. (ed.): Self-healing materials: fundamentals, design strategies, and applications. Wiley WCH, Weinheim (2009)
Ghosh, P.K., Ray, S., Rohatgi, P.K.: Incorporation of alumina particles in aluminum-magnesium alloy by stirring the melt. Trans Jn. Inst. Metals. **25**, 440–444 (1984)
Gibson, P.R., Clegg, A.J., Das, A.A.: Wear **95**, 193 (1984)

Gillmor, S.D., Thiel, A.J., Strother, T.C., Smith, L.M., Lagally, M.G.: Hydrophilic/hydrophobic patterned surfaces as templates for DNA arrays. Langmuir **16**, 7223–7228 (2000)
Gorb, S.: Fundamental surfaces in biology: mechanisms and applications. In: Bar-Cohen, Y. (ed.) Biomimetics: biologically inspired technologies, pp. 381–397. Taylor and Francis, Boca Raton (2005)
Gorbunov, V., Parshin, V.D., Panin, U.V.: Russ. Cast. Prod. **8**, 348 (1974)
Gras, S.L., et al.: Intelligent control of surface hydrophobicity. Chem. Phys. Chem. **8**, 2036–2050 (2007)
Greenberg, M.D.: Foundation of applied mathematics. Prentice-Hall, Englewood Cliffs, NJ (1978)
Greenspan, M., Tschiegg, C.: Radiation-induced acoustic cavitation: apparatus and some results. J. Res. Natl. Bur. Stand. Sect. C **71**, 299–312 (1967)
Greenwood, J.A.: Adhesion of elastic spheres. Proc. R. Soc. Lond. **A453**, 1277–1297 (1997)
Greenwood, J.A.: Personal communication, July (2009)
Greenwood, J.A., Williamson, J.B.P.: Contact of nominally flat surfaces. Proc. R Soc. Lond. **A295**, 300–319 (1966)
Greenwood, J.A., Wu, J.J.: Surface roughness and contact: an apology. Meccanica **36**, 617–630 (2001)
Guoand, M.L.T., Tsao, C.Y.A.: Tribological behavior of self-lubricating aluminium/SiC/graphite hybrid composites synthesized by the semi-solid powder-densification method. Comp Sci Technol. **60**, 65–74 (2000)
Gupta, P., Ulman, A., Fanfan, F., Korniakov, A., Loos, K.: Mixed self-assembled monolayer of alkanethiolates on ultrasmooth gold do not exhibit contact angle hysteresis. J. Am. Chem. Soc. **127**, 4–5 (2005)
Gupta, S., Arjunan, A.C., Deshpande, S., Seal, S., Singh, D., Singh, R.K.: Superhydrophobic polytetrafluoroethylene thin films with hierarchical roughness deposited using a single step vapor phase technique. Thin Solid Films **517**, 4555–4559 (2009)
Haken, H.: Synergetics: an introduction. Nonequilibrium phase transitions in physics, chemistry and biology, 3rd edn. Springer, New York (1983)
Haken, H.: Advanced synergetics: instability hierarchies of self-organizing systems and devices. Springer-Verlag, New York (1993)
Hall, E.O.: Proc. Phys. Soc. B **64**, 747–753 (1951)
Han, D., Steckl, A.J.: Superhydrophobic and oleophobic fibers by coaxial electrospinning. Langmuir **25**, 9454–9462 (2009)
Han, J.T., Jang, Y., Lee, D.Y., Park, J.H., Song, S.H., Ban, D.Y., Cho, K.: Fabrication of a bionic superhydrophobic metal surface by sulfur-induced morphological development. J. Mater. Chem. **15**, 3089–3092 (2005)
Hartley, G.S., Brunskill, R.T.: Reflection of water drops from surfaces. In: Danielli, J.F. (ed.) Surface phenomena in chemistry and biology, pp. 214–223. Pergamon, London (1958)
Hautakangas, S.: Positron Annihilation Spectroscopy as a Tool to Develop Self Healing in Aluminium Alloys. In Proceedings of 14th International Conference on Positron Annihilation, ICPA 14, July 23–28, 2006
Hautakangas, S., Schut, H., van der Zwaag, S., Rivera Diaz del Castillo, P.E.J., van Dijk, N.H.: Positron annihilation spectroscopy as a tool to develop self-healing in aluminum alloys. Phys. Status. Solid. **4**, 3469–3472 (2007a)
Hautakangas, S., Schut, H., van der Zwaag, S., del Castillo, R.D., van Dijk, N.H.: The role of the aging temperature in the self-healing kinetics in an underaged AA2024 aluminum alloy. Proceedings of 1st International Conference on Self-Healing Materials, Noordwijk aan Zee, The Netherlands, 18–20 April 2007
Hautakangas, S., Schut, H., van Dijk, N.H.: Self-healing of deformation damage in underaged Al-Cu-Mg alloys. Scripta Mater. **58**, 719–722 (2008)
Hayes, S.A., Zhang, W., Branthwaite, M., Jones, F.R.: Self-healing of damage in fibre reinforced polymer-matrix composites. J. R. Soc. Interface **4**, 381–386 (2007)

He, G., Robbins, M.O.: Scale effects and the molecular origins of tribological behavior. In: Hsu, S. H., Ying, Z.C. (eds.) Nanotribology: critical assessment and research needs, pp. 29–44. Kluwer, Dordrecht (2003)
He, M., Blum, A.S., Aston, D.E., Buenviaje, C., Overney, R.M., Luginbühl, R.: Critical phenomena of water bridges in nanoasperity contacts. J. Chem. Phys. **114**, 1355–1360 (2001)
He, B., Patankar, N.A., Lee, J.: Multiple equilibrium droplet shapes and design criterion for rough hydrophobic surfaces. Langmuir **19**, 4999–5003 (2003)
He, S.M., van Dijk, N.H., Schut, H., van der Zwaag, S.: Self healing in Fe-Cu and Fe-Cu-B-N-Ce alloys studied by positron annihilation spectroscopy. In Proceedings of 2nd International Conference on Self-healing Materials, Chicago, 2009
He, M., et al.: Super-hydrophobic film retards frost formation. Soft Matter. **6**, 2396–2399 (2010)
He, S.M., et al.: Thermally activated precipitation at deformation-induced defects in Fe-Cu and Fe-Cu-B-N alloys studied by positron annihilation spectroscopy, Phys. Rev. **B 81**, 094103, (2010a)
He, S.M., et al.: In situ determination of aging precipitation in deformed Fe-Cu and Fe-Cu-B-N alloys by time-resolved small-angle neutron scattering, Phys. Rev. **B 82**, 174111, (2010b)
Heine, H.J.: Foundry Manage. Technol. **116**(7), 25 (1988)
Henderson, H.J., Speedy, R.J.: A Berthelot-Bourdon tube method for studying water under tension. J. Phys. E **13**, 778–782 (1980)
Herbert, E., Caupin, F.: The limit of metastability of water under tension: theories and experiments. J. Phys. Condens. Matter **17**, S3597–S3602 (2005)
Herminghaus, S.: Roughness-induced non-wetting. Europhys. Lett. **52**, 165–170 (2000)
Hernandez-Battez, A., et al.: Friction reduction properties of a CuO nanolubricant used as lubricant for a NiCrBSi coating. Wear **268**, 325–328 (2010)
Hikita, M., Tanaka, K., Nakamura, T., Kajiyama, T., Takahara, A.: Superliquid-repellent surfaces prepared by colloidal silica nanoparticles covered with fluoroalkyl groups. Langmuir **21**, 7299–7302 (2005)
Hokao, M., Hironaka, S., Suda, Y., et al.: Friction and wear properties of graphite/glassy carbon composites. Wear **237**, 54–62 (2000)
Holm, R.H.: Electrical contacts, 4th edn. Springer, New York (1967)
Hong, L., Pan, T.: Photopatternable superhydrophobic nanocomposites for microfabrication. J. Microelectromech. Syst. **19**, 246–253 (2010)
Hong, S.H., Hwang, J., Lee, H.: Replication of cicada wing's nano-patterns by hot embossing and UV nanoimprinting. Nanotechnology **20**, 1–5 (2009)
Hosono, E., Fujihara, S., Honma, I., Zhou, H.: Superhydrophobic perpendicular nanopin film by the bottom-up process. J. Am. Chem. Soc. **127**, 13458–13459 (2005)
Hou, W., Wang, Q.: Wetting behavior of a SiO2-polystyrene nanocomposite surface. J. Colloid Interface Sci. **316**, 206–209 (2007)
Hou, W., Wang, Q.: Stable polytetrafluoroethylene superhydrophobic surface with lotus-leaf structure. J. Colloid Interface Sci. **333**, 400–403 (2009)
Hou, X., Wanga, X., Zhua, Q., Baoa, J., Mao, C., Jianga, L., Shena, J.: Preparation of polypropylene superhydrophobic surface and its blood compatibility. Colloids Surf. B Biointerfaces **80**, 247–250 (2010)
Hsieh, C.T., Chen, W.Y., Wu, F.L.: Fabrication and superhydrophobicity of fluorinated carbon fabrics with micro/nanoscaled two-tier roughness. Carbon **46**, 1218–1224 (2008)
Hu, J., Xiao, X.-D., Ogletree, D.F., Salmeron, M.: Imaging the condensation and evaporation of molecularly thin films of water with nanometer resolution. Science **268**, 267–269 (1995)
Huang, L., Lau, S.P., Yang, H.Y., Leong, E.S.P., Yu, S.F.: Stable superhydrophobic surface via carbon nanotubes coated with a ZnO thin film. J. Phys. Chem. **109**, 7746–7748 (2005)
Humphreys, F.J., Hatherly, M.: Recrystallization and related annealing phenomena. Pergamon, Oxford (1995)

Hurd, T.G., Beyhaghi, S., Nosonovsky, M.: Ecological aspects of water desalination improving surface properties of reverse osmosis membranes. In: Nosonovsky M., Bhushan B. (eds.) Green Tribology Biomimetics, Energy Conservation, and Sustainability, Springer (2012, in press)
Hutchinson, J.W.: Int. J. Solid. Struct. **37**, 225–238 (2000)
Ilie, F., Tita, C.: Investigation of layers formed through selective transfer with atomic force microscopy. Proceedings of 10th International Conference on Tribology ROTRIB '07, Bucharest, Romania (2007)
Ishino, C., Okumura, K.: Nucleation scenarios for wetting transition on textured surfaces: the effect of contact angle hysteresis. Europhys. Lett. **76**, 464–470 (2006)
Israelachvili, J.N.: Intermolecular and surface forces, 2nd edn. Academic, London (1992)
Israelachvili, J.N., Gee, M.L.: Contact angles on chemically heterogeneous surfaces. Langmuir **5**, 288–289 (1989)
Jagla, E.A.: Boundary lubrication properties of materials with expansive freezing. Phys. Rev. Lett. **88**, 245504 (2002)
Jahanmir, S., Suh, N.P., Abrahamson, E.P.: Wear **32**, 33 (1975)
Jang, J., Ratner, M.A., Schatz, G.C.: Atomic-scale roughness effect on capillary force in atomic force microscopy. J Phys. Chem. B. Lett **110**, 659–662 (2006)
Jansen, H., de Boer, M., Legtenberg, R., Elwenspoek, M.: The black silicon method: a universal method for determining the parameter setting of a fluorine-based reactive ion etcher in deep silicon trench etching with profile control. J. Micromech. Microeng. **5**, 115–120 (1995)
Jetter, R., Kunst, L., Samuels, A.L.: Composition of plant cuticular waxes. In: Riederer, M., Müller, C. (eds.) Biology of the plant cuticle, pp. 145–181. Blackwell, Oxford (2006)
Jha, A.K., Rohatgi, P.K.: Aluminum alloy solid lubricant talc particle composites. J. Mater. Sci. **21**, 3681–3685 (1986)
Jha, A.K., Prasad, S.V., Upadhyaya, G.S.: Sintered 6061 aluminium alloy – solid lubricant particle composites: sliding wear and mechanism of lubrication. Wear **133**, 163 (1989)
Jiang, L., Zhao, Y., Zhai, J.: Angew. Chem. Int. Ed. **43**, 4338–4341 (2004)
Jin, M.H., Feng, X.J., Xi, J.M., Zhai, J., Cho, K.W., Feng, L., Jiang, L.: Superhydrophobic PDMS surface with ultra-low adhesive force. Macromol. Rapid Commun. **26**, 1805–1809 (2005)
Jinesh, K.B., Frenken, J.W.M.: Capillary condensation in atomic scale friction: how water acts like a glue. Phys. Rev. Lett. **96**, 166103 (2006)
Jinesh, K.B., Yu Krylov, S., Valk, H., Dienwiebel, M., Frenken, J.W.M.: Thermolubricity in atomic-scale friction. Phys. Rev. B **78**, 155440 (2008)
Johnson, K.L.: Adhesion and friction between a smooth elastic spherical asperity and a plane surface. Proc. R Soc. Lond. **A453**, 163–179 (1997)
Johnson, J.L.: Mechanics of adhesion. Tribol. Int. **31**, 413–418 (1998)
Johnson, R.E., Dettre, R.H.: Contact angle hysteresis. In: Fowkes, F.M. (ed.) Contact angle, wettability, and adhesion. Adv. Chem. Ser, vol. 43, pp. 112–135. American Chemical Society, Washington, DC (1964)
Johnson, L.B., Kuhlmann-Wilsdorf, D.: Mater. Sci. Eng. **58**, 4 (1983a)
Johnson, L.B., Kuhlmann-Wilsdorf, D.: Mater. Sci. Eng. **58**, 21 (1983b)
Johnson, J.L., Schreurs, J.: Wear **78**, 219 (1982)
Johnson, J.L., Taylor, O.S.: IEEE Trans., CHMT-3, 31 (1980)
Johnson, J.L., Moberly, L.E.: Proceedings of Conference on 'Electrical contacts', p. 109. Illinois Institute of Technology, Chicago, IL (1967)
Johnson, J.L., Mckinney, J.K.: Proceedings of Conference on 'Electrical contacts', p. 155. Illinois Institute of Technology, Chicago, IL, (1970)
Johnson, K.L., Kendall, K., Roberts, A.D.: Surface energy and the contact of elastic solids. Proc R. Soc. Lond. A **324**, 301–313 (1971)
Jones, L.: The physic of electrical contacts. Oxford, Clarendon Press (1957)
Jones, R., Pollock, H.M., Cleaver, J.A.S., Hodges, C.S.: Adhesion forces between glass and silicon surfaces in air studied by AFM. Langmuir **18**, 8045–8055 (2002)

Jones, F.R., Zhang, W., Hayes, S.A.: Thermally induced self-healing of thermosetting resins and matrices of smart composites. In: van der Zwaag, S. (ed.) Self healing materials – an alternative approach to 20 centuries of materials science. Springer, Dordrecht, The Netherlands (2007)

Jonkers, H.M.: Self healing concrete: a biological approach. In: van der Zwaag, S. (ed.) Self healing materials – an alternative approach to 20 centuries of materials science, pp. 195–204. Springer, New York (2007)

Jonkers, H.M., Schlangen, E.: Towards a sustainable bacterially-mediated self healing concrete. Proceedings of 2nd International Conference on Self-Healing Materials, Chicago (2009)

Jun, Q., Linan, A., Blau, P.J.: Sliding friction and wear characteristics of Al_2O_3-Al nanocomposites. STLE/ASME International Joint Tribology Conference, IJTC 2006, Ser. 2006, ASME, New York (2006)

Jung, Y.C., Bhushan, B.: Wetting behavior during evaporation and condensation of water microdroplets on superhydrophobic patterned surfaces. J Micros. **229**, 127–180 (2008a)

Jung, Y.C., Bhushan, B.: Dynamic effects of bouncing water droplets on superhydrophobic surfaces. Langmuir **24**, 6262–6269 (2008b)

Jung, Y.C., Bhushan, B.: Wetting behavior of water and oil droplets in three-phase interfaces for hydrophobicity/philicity and oleophobicity/philicity. Langmuir **25**, 14165–14173 (2009a)

Jung, Y.C., Bhushan, B.: Mechanically durable carbon nanotube-composite hierarchical structures with superhydrophobicity, self-cleaning and low drag. ACS Nano **3**, 4155–4163 (2009b)

Jung, Y.C., Bhushan, B.: Biomimetic structures for fluid drag reduction in laminar and turbulent flows. J. Phys. Condens. Matt. **22**, 035104 (2010)

Kagan, E.: Turing systems, entropy, and kinetic models for self-healing surfaces. Entropy **12**, 554–569 (2010)

Kalra, A., Garde, S., Hummer, G.: Osmotic water transport through carbon nanotube membranes. Proc. Natl. Acad. Sci. U.S.A. **100**, 10175–10180 (2003)

Kamusewitz, H., Possart, W., Paul, D.: The relation between Young's equilibrium contact angle and the hysteresis on rough paraffin wax surfaces. Colloids Surf. A Physicochem. Eng. Asp. **156**, 271–279 (1999)

Kanga, M., Junga, R., Kima, H.S., Jinb, H.J.: Preparation of superhydrophobic polystyrene membranes by electrospinning. Colloids Surf. A Physicochem. Eng. Asp. **313–314**, 411–414 (2008)

Kauffman, H.N.: Szari, A.Z. (ed.) Tribology-friction-lubrication and wear. Hemisphere, New York (1980)

Kawamoto, M., Okabayashi, K.: Study of dry sliding wear of cast iron as a function of surface temperature. Wear **58**, 59–95 (1980)

Kawamoto, M., Adach, M., Ando, S., Okabayashi, K.: Imono (J. JpnFoundrymen's Soc.) **50**, 32 (1978)

Kerr, C., Barker, D., Walsh, F., et al.: The electrodeposition of composite coatings based on metal matrix-included particle deposits. Trans. Inst. Metal Finishing **78**, 171–178 (2000)

Kessler, D.A.: Surface physics: a new crack on friction. Nature **413**, 260–261 (2001)

Khorasani, M.T., Mirzadeh, H., Kermani, Z.: Wettability of porous polydimethylsiloxane surface: morphology study. Appl. Surf. Sci. **242**, 339–345 (2005)

Kietzig, A.M., Hatzikiriakos, S.G., Englezos, P.: Patterned superhydrophobic metallic surfaces. Langmuir **25**, 4821–4827 (2009)

Kijlstra, J., Reihs, K., Klami, A.: Roughness and topology of ultra-hydrophobic surfaces. Colloids Surf. A Physicochem. Eng. Asp. **206**, 521–529 (2002)

Kim, S., Lorente, S., Bejan, A.: Vascularized materials: tree-shaped flow architectures matched canopy to canopy. J. Appl. Phys. **100**, 063525 (2006)

Kim, D., Hwang, W., Park, H.C., Lee, K.L.: Superhydrophobic micro- and nanostructures based on polymer sticking. Key Eng. Mat. **334–335**, 897–900 (2007)

Kincaid, N.M., O'Reilly, O.M., Papadopoulos, P.: Automotive disc brake squeal. J. Sound Vib **267**, 105–166 (2003)

Kirshnan, B.P., Raman, N., Narayanaswamy, K., Rohatgi, P.K.: Wear **60**, 205 (1981)

Kirshnan, B.P., Raman, N., Narayanaswamy, K., Rohatgi, P.K.: Tribol. Int. **16**, 239 (1983)

Kiselev, S.B., Levelt-Sengers, J.M.H., Zheng, Q.: Physical limit to the stability of superheated and stretched water. In: White, H.J., et al. (eds.) Proceedings of the 12th International Conference on the Properties of Water and Steam, pp. 378–385. Begell House, Orlando, FL (1995)
Klamecki, B.E.: Wear – an entropy production model. Wear **58**, 325–330 (1980a)
Klamecki, B.E.: A thermodynamic model of friction. Wear **63**, 113–120 (1980b)
Klamecki, B.E.: Energy dissipation in sliding. Wear **77**, 115–128 (1982)
Klamecki, B.E.: An entropy-based model of plastic deformation energy dissipation in sliding. Wear **96**, 319–329 (1984)
Klein, R.J., Biesheuvel, P.M., Yu, B.C., Meinhart, C.D., Lange, F.F.: Producing super-hydrophobic surfaces with nano-silica spheres. Z. Metallkd. **94**, 377–380 (2003)
Koch, G.W., Sillet, S.C., Jennings, G.W., Davis, S.D.: The limits of tree height. Nature **428**, 851 (2004)
Koch, K., Dommisse, A., Barthlott, W.: Chemistry and crystal growth of plant wax tubules of lotus (Nelumbo nucifera) and nasturtium (Tropaeolum majus) leaves on technical substrates. Crystl. Growth Des. **6**, 2571–2578 (2006)
Koch, K., Bhushan, B., Ensikat, H.J., Barthlott, W.: Self-healing of voids in the wax coating on plant surfaces. Phil. Trans. R. Soc. A **367**, 1673–1688 (2009)
Kogut, L., Etsion, I.: A static friction model for elastic-plastic contacting rough surfaces. J. Tribol. **126**, 34–40 (2004)
Krasovitski, B., Marmur, A.: Drops down the hill: theoretical study of limiting contact angles and the hysteresis range on a tilted plane. Langmuir **21**, 3881–3885 (2004)
Krupenkin, T.N., Taylor, J.A., Schneider, T.M., Yang, S.: From rolling ball to complete wetting: the dynamic tuning of liquids on nanostructured surfaces. Langmuir **20**, 3824–3827 (2004)
Krupenkin, T.N., Taylor, J.A., Wang, E.N., Kolodner, P., Hodes, M., Salamon, T.R.: Reversible wetting-dewetting transitions on delectrically tunable superhydrophobic nanostructured surfaces. Langmuir **23**, 9128–9133 (2007)
Kuhlmann-Wilsdorf, D.: Temperatures at interfacial contact spots: dependence on velocity and on role reversal of two materials in sliding contact. J Tribology **109**, 321–329 (1987)
Kuhlmann-Wilsdorf, D., Makel, D.D., Sondergaard, N.., Maribo, D.W.: Proceedings of 14th International Conference on Electrical Contacts, Paris, IEEE, p. 1, (1988)
Kuhlmann-Wilsdorf, D., Makel, D.D., Sondergaard, N.A., Maribo, D.W.: In: Fishman, S.G., Dhingra, A.K. (eds.) 'Cast reinforced metal composites', p. 347. ASM International, Materials Park, OH (1988)
Kulinich, S.A., Farzaneh, M.: How wetting hysteresis influences ice adhesion strength on superhydrophobic surfaces. Langmuir **25**, 8854–8856 (2009)
Kulinich, S.A., Farzaneh, M.: On ice-repelling properties of rough hydrophibic surfaces. Cold Regions Sci Technol. **65**, 60–64 (2011)
Kulinich, S.A., Farhadi, S., Nose, K., Du, X.W.: Superhydrophobic surfaces: are they really ice-repellent? Langmuir **27**, 25–29 (2011)
Kuo, C.Y., Gau, C.: Control of superhydrophilicity and superhydrophobicity of a superwetting silicon nanowire surface. J. Electrochem. Soc. **157**, K201–K205 (2010)
Kusumaatmaja, H., Yeomans, J.M.: Modeling contact angle hysteresis on chemically patterned and superhydrophobic surfaces. Langmuir **23**, 6019–6032 (2007)
Lafuma, A., Quėrė, D.: Superhydrophobic states. Nat. Mater. **2**, 457–460 (2003)
Laha, K., Kyono, J., Sasaki, T., Kishimoto, S., Shinya, N.: Improved creep strength and creep ductility of type 347 austenitic stainless steel through the self-healing effect of boron for creep cavitation. Metal. Mater. Trans. **36A**, 399–409 (2005)
Laha, K., Kyono, J., Shinya, N.: Some chemical and microstructural factors influencing creep cavitation resistance of austenitic stainless steels. Phil. Mag. **87**, 2483–2505 (2007a)
Laha, K., Kyono, J., Shinya, N.: An advanced creep cavitation resistance Cu-containing 18Cr-12Ni-Nb austenitic stainless steels. Scripta Mater. **56**, 915–918 (2007b)
Lahann, J., Mitragotri, S., Tran, T., Kaido, H., Sundaram, J., Choi, L.S., Hoffer, S., Somorjai, G.A., Langer, R.: A reversibly switching surface. Science **299**, 371–374 (2003)

Lam, P., Wynne, K.J., Wnek, G.E.: Surface-tension-confined microfluidics. Langmuir **18**, 948–951 (2002)
Lam, S.W., Gan, W.Y., Chiang, K., Amal, R.: Ti2 semoconductor – a smart self-cleaning material. J. Aust Ceram Soc. **44**, 6–11 (2008)
Lancaster, J.K.: In: Loomis, W.R. (ed.) New Directions in Lubrication, Materials, Wear and Surface Interaction – Tribology in the 80's, p. 320. Noyes, New Jersey (1983)
Landau, L., Lifshitz, E.: Fluid mechanics. Pergamon, London (1959)
Landauer, R.: Inadequancy of entropy and entropy derivatives in characterizing the steady state. Phys. Rev. A **12**, 636 (1975)
Lau, K.K.S., Bico, J., Teo, K.B.K., Chhowalla, M., Amaratunga, G.A.J., Milne, W.I., McKinley, G.H., Gleason, K.K.: Superhydrophobic carbon nanotube forests. Nano Lett. **3**, 1701–1705 (2003)
Lauga, E., Brenner, M.P.: Dynamic mechanisms for apparent slip on hydrophobic surfaces. Phys. Rev. E **70**, 026311 (2004)
Lavernia, E.J.: The evolution of microstructure during spray atomization and deposition. Int J. Rapid Solid. **5**, 47–85 (1989)
Lee, P.K., Johnson, J.L.: High current brushes. IEEE Trans. CHMT-l, 40 (1978)
Lee, S.M., Kwon, T.H.: Mass-producible replication of highly hydrophobic surfaces from plant leaves. Nanotechnology **17**, 3189–3196 (2006)
Lee, W., Jin, M.K., Yoo, W.C., Lee, J.K.: Nanostructuring of a polymeric substrate with well-defined nanometer-scale topography and tailored surface wettability. Langmuir **20**, 7665–7669 (2004)
Lee, E.-K., Amano, R.S., Rohatgi, P.K.: Metal matrix composite solidification in the presence of cooled fibers: numerical simulation and experimental observation. Heat Mass Transfer **43**, 741–748 (2007)
Lee, L., Kim, S., Lorente, S., Bejan, A.: Vascularization with trees matched canopy to canopy: diagonal channels with multiple sizes. Int. J. Heat Mass Transfer **51**, 2029–2040 (2008)
Leppänen, T.: Computational studies of pattern formation in turing systems. Dissertation for the degree of Doctor of Science in Technology, Helsinki University of Technology (2004)
Li, W., Amirfazli, A.: A thermodynamic approach for determining the contact angle hysteresis for superhydrophobic surfaces. J. Colloid Interface Sci. **292**, 195–201 (2006)
Li, W., Amirfazli, A.: Superhydrophobic surfaces: adhesive strongly to water? Adv. Mater. **19**, 3421–3422 (2007)
Li, W., Amirfazli, A.: Superhydrophobic surfaces: adhesive strongly to water? Adv. Mater. 19, 3421–3422 (2007)
Li, J.L., Xiong, D.S.: Tribological properties of nickel-based self-lubricating composite at elevated temperature and counterface material selection. Wear **265**, 533–539 (2008)
Li, V.C., Lim, Y.M., Chan, Y.-W.: Feasability study of a passive smart self-healing cementions composite. Composites B **29**, 819–827 (1998)
Li, Y., Ruoff, R.S., Chang, R.P.H.: Boric acid nanotubes, nanotips, nanorods, microtubes, and microtips. Chem. Mater. **15**, 3276–3285 (2003)
Li, K., Xiang, D.H., Lei, X.Y.: Green and self-lubricating polyoxymethylene composites filled with low-density polyethylene and rice husk flour. J. Appl. Polym. Sci. **108**, 2778–2786 (2008)
Li, X., Du, X., He, J.: Self-cleaning antireflective coatings assembled from peculiar mesoporous silica nanoparticles. Langmuir **26**, 13528–13534 (2010)
Lim, H.S., et al.: Photoreversibly switchable superhydrophobic surface with erasable and rewritable pattern. J. Am. Chem. Soc. **128**, 14458–14459 (2006)
Lim, H.S., et al.: UV-driven reversible switching of a roselike vanadium oxide film between superhydrophobicity and superhydrophilicity. J. Am. Chem. Soc. **129**, 4128 (2007)
Lin, J.F., Chu, H.Y.: Analysis of the Bénard Cell-Like Worn Surface Type Occurred During Oil-Lubricated Sliding Contact. Proceedings of ASME/STLE 2009 International Joint Tribology Conference, IJTC2009, Memphis, Tennessee, USA (2009)

Liu, M.J., Jiang, L.: Switchable adhesion on liquid/solid interfaces. Adv. Funct. Mater. **20**, 3753–3764 (2010)
Liu, H.W., Xue, Q.J.: The tribological properties of TZP-graphite self-lubricating ceramics. Wear **198**, 143–149 (1996)
Liu, Y.: PhD thesis, University of Wisconsin-Milwaukee (1990)
Liu, Y., Nath, D., Lopez, H.F., Rohatgi, P.K.: Powder Metall. Int. **22**, 16 (1990)
Liu, Z.W., Bando, Y., Mitome, M., Zhan, J.: Unusual freezing and melting of gallium encapsulated in carbon nanotubes. Phys. Rev. Lett. **93**, 095504 (2004)
Liu, Y., Mu, L., Liu, B.H., Kong, J.L.: Controlled switchable surfaces. Chem Euro J. **11**, 2622–2631 (2005)
Liu, Y., Tang, J., Wang, R., Lu, H., Li, L., Kong, Y., Qi, K., Xin, J.H.: Artificial lotus leaf structures from assembling carbon nanotubes and their applications in hydrophobic textiles. J. Mater. Chem. **17**, 1071–1078 (2007)
Livshits, A.I., Shluger, A.L.: Self-lubrication in scanning-force-microscope image formation on ionic surfaces. Phys Rev. B **56**, 12482–12489 (1997)
Lovell, M.R., Kabir, M.A., Menezes, P.L., Higgs III, C.F.: Influence of boric acid additive size on green lubricant performance. Phil. Trans. R. Soc. A **368**, 4851–4868 (2010)
Lu, X., Zhang, C., Han, Y.: Low-density polyethylene superhydrophobic surface by control of its crystallization behavior. Macromol. Rapid Commun. **25**, 1606–1610 (2004)
Lucci, J.M., Amano, R., Rohatgi, P.K.: Computational analysis of self-healing in a polymer matrix with microvascular networks. Proceedings of ASME Design Engineering Technical Conference 2008DETC, ASME, NY (2008)
Lucci, J.M., Amano, R., Rohatgi, P.K., Schultz, B.: Experimental and computational analysis of self-healing in an aluminum alloy. Proceedings of Mechanical Congress and Exhibition, IMECE2008-68304 (2008a)
Lucci, J.M., Amano, R.S., Rohatgi, P.K., Schultz, B.: Self-healing in an aluminum alloy reinforced with microtubes. Proceedings of Energy Nano08 ASME Turbo Expo, ENIC2008-53011 (2008b)
Lucci, J.M., Amano, R.S., Rohatgi, P.K., Schultz, B.: Computational analysis of self-healing in a polymer matrix with microvascular networks. Proceedings of ASME Design Engineering Technical Conference, DETC2008-50148 (2008c)
Lucci, J.O.M., Amano, R.S., Rohatgi, P.K., Schultz, B.: Self-healing in an aluminum alloy reinforced with carbon fiber microtubes. Proceedings on Conference of AIAA, Orlando, USA, 3–6 Jan 2009
Lugscheider, E., Barwulf, S., Barimani, C.: Properties of tungsten and vanadium oxides deposited by MSIP-PVD process for self-lubricating applications. Surf Coating Technol. **120**, 458–464 (1999)
Lumley, R.: Advances in self healing of metals. In: van der Zwaag, S. (ed.) Self healing materials: an alternative approach to 20 centuries of materials science. Springer series in materials science, vol. 100, pp. 219–254. Springer, Dordrecht (2007)
Lumley, R.M., Schaffer, G.B.: Precipitation induced densification in a sintered Al-Zn-Mg-Cu alloy. Scripta Mater. **55**, 207–210 (2006)
Lumley, R.N., Morton, A.J., Polmear, L.J.: Enhanced creep performance in an Al-Cu-Mg-Ag alloy through underageing. Acta Mater. **50**, 3597–3608 (2002)
Lumley, R.N., Polmear, L.J., Morton, A.J.: Interrupted aging and secondary precipitation in aluminum alloys. Mater. Sci. Technol. **19**, 1483–1490 (2003)
Ma, M., Hill, R.M.: Superhydrophobic surfaces. Curr Opin Colloid Interface Sci **11**, 193–202 (2006)
Ma, M., Hill, R.M., Lowery, J.L., Fridrikh, S.V., Rutledge, G.C.: Electrospun poly(styrene-block-dimethylsiloxane) block copolymer fibers exhibiting superhydrophobicity. Langmuir **21**, 5549–5554 (2005)

Ma, Y., Wang, F., Li, X., Chen, G., Feng, L., Zhao, H., Jiang, L.: Preparation of a superhydrophobic poly(vinyl chloride) surface via solvent-nonsolvent coating. Polymer **47**, 506–509 (2006)
Ma, S.L., Ma, D.Y., Guo, Y., et al.: Synthesis and characterization of super hard, self-lubricating Ti-Si-C-N nanocomposite coatings. Acta Mater. **55**, 6350–6355 (2007)
Macdougall, G., Ockrent, C.: Surface energy relations in liquid solid systems. Proc. R. Soc. London **180**, 0151–0173 (1942)
Maeda, N., Chen, N., Tirrell, M., Israelachvili, J.N.: Adhesion and friction mechanisms of polymer-on-polymer surfaces. Science **297**, 379–382 (2002)
Maegawa, S., Nakano, K.: Mechanism of stick-slip associated with Schallamach waves. Wear **268**, 924–930 (2010)
Majumdar, A., Bhushan, B.: Fractal model of elastic-plastic contact between rough surfaces. J Tribol. **113**, 1–11 (1991)
Mandelbrot, B.: The fractal geometry of nature. Freeman, New York (1983)
Manuel, M.V.: Principles of self-healing in metals and alloys: an introduction. In: Ghosh, S.K. (ed.) Self-healing materials: fundamentals, design strategies, and applications, pp. 251–266. Wiley, Weinheim/New York (2009)
Manuel, M.V.: Design of a biomimetic self healing alloy composite. PhD thesis, Northwestern University (2007)
Manuel, M.V., Olson, G.B.: Biomimetic self-healing metals. Proceedings of 1st International Conference on Self-Healing Materials, Noordwijik aan Zee, The Netherlands, 18–20 April 2007
Manuel, M., Olson, G.B.: Biologically inspired self-healing metals. Proceednigs of 2nd International Conference on Self-healing Materials, Chicago, 2009
Marmur, A.: Wetting on hydrophobic rough surfaces: to be heterogeneous or not to be? Langmuir **19**, 8343–8348 (2003)
Marmur, A.: The lotus effect: superhydrophobicity and metastability. Langmuir **20**, 3517–3519 (2004)
Marmur, A.: Underwater superhydrophobicity: theoretical feasibility. Langmuir **22**(4), 1400–1402 (2006)
Marshall, R.A.: The mechanism of current transfer in brushes. IEEE Trans. **PAS-85**(11), 1177 (1966)
Martines, E., Seunarine, K., Morgan, H., Gadegaard, N., Wilkinson, C.D.W., Riehle, M.O.: Superhydrophobicity and superhydrophilicity of regular nanopatterns. Nano Lett. **5**, 2097–2103 (2005)
Martinez Lucci, J.O.: Heat transfer and fluid flow analysis of self-healing in metal matrix composites. PhD Thesis, University of Wisconsin-Milwaukee (2011)
Martins, J.A.C., Guimaraes, J., Faria, L.O.: Dynamic surface solutions in linear elasticity and viscoelasticity with frictional boundary conditions. J Vib Acoust **117**, 445–451 (1995)
Maugis, D.: Adhesion of spheres: the JKR-DMT transition using a Dugdale model. J. Colloid Interface Sci. **150**, 243–269 (1992)
Maugis, D.: On the contact and adhesion of rough surfaces. J Adhes Sci. Technol. **10**, 161–175 (1996)
Maugis, D.: Contact adhesion and rupture of elastic solids. Springer, Berlin (1999)
Mayrhofer, P.H., Mitterer, C., Wen, J.G., Greene, J.E., Petrov, I.: Self-organized nanocolumnar structure in superhard TiB2 thin films. Applied Physics Letters, **86**(13), 131909-131909-3 (2005)
Mayrhofer, P.H., Mitterera, C., Hultmanb, L., Clemensa, H.: Microstructural design of hard coatings. Prog. Mater. Sci. **51**(8), 1032–1114 (2006)
McHale, G.: All solids, including Teflon, Are hydrophilic (to some extent), but some have roughness induced hydrophobic tendencies. Langmuir **25**, 7185–7187 (2009)
McHale, G., Aqil, S., Shirtcliffe, N.J., Newton, M.L., Erbil, H.Y.: Analysis of droplet evaporation on a superhydrophobic surface. Langmuir **21**, 11053–11060 (2005)
Menezes, P.L., Kishore, Kailas, S.V.: Studies on friction and transfer layer using inclined scratch. Tribol Int **39**, 175–183 (2006)

Meuler, A.J., McKinley, G.H., Gareth, G., Cohen, R.E.: Exploiting topographical texture to impart icephobicity. ACS Nano **4**, 7048–7052 (2010a)
Meuler, A.J., Smith, J.D., Varanasi, K.K., Mabry, J.M., McKiney, G.H., Cohen, R.E.: Relationships between water wettability and ice adhesion. ACS Appl. Mater. Interfaces **2**, 3100–3110 (2010b)
Ming, W., Wu, D., van Benthem, R., de With, G.: Superhydrophobic films from raspberry-like particles. Nano Lett. **5**, 2298–2301 (2005)
Miranda, P.B., Xu, L., Shen, Y.R., Salmeron, M.: Icelike water monolayer adsorbed on mica at room temperature. Phys. Rev. Lett. **81**, 5876–5879 (1998)
Mishchenko, L., Hatton, B., Bahadur, V., Taylor, J.A., Krupenkin, T., Aizenberg, J.: Design of ice-free nanostructured surfaces based on repulsion of impacting water droplets. ACS Nano **4**, 7699–7707 (2010)
Mohan, S., Agarwala, V., Ray, S.: The effect of lead content on the wear characteristics of a stir-cast Al-Pb alloy. Wear **140**, 83–92 (1990)
Mollart, T.P., Haupt, J., Gilmore, R., et al.: Tribological behaviour of homogeneous Ti-B-N, Ti-B-N-C and TiN/h-BN/TiB2 multilayer coatings. Surf. Coating Technol. **86**, 231–236 (1996)
Momoun, M.M.: At design engineering and show. NY, ASME (1975)
Morks, M.F., Tsunekawa, Y., Okumiya, M., et al.: Microstructure of plasma-sprayed cast iron splats with different particle sizes. Mater. Trans. **44**, 743–748 (2003)
Mortazavi, V., Nosonovsky, M.: Friction-induced pattern-formation and turing systems. Langmuir **29**, 4772–4779 (2011a)
Mortazavi, V., Nosonovsky, M.: Wear-induced microtopography evolution and wetting properties of self-cleaning, lubricating and healing surfaces. J. Adhesion Sci. Technol. **25**(12), 1337–1359 (2011b)
Mortazavi, M., Nosonovsky, M.: Polymer adhesion and biomimetic materials. In: Green Tribology Biomimetics, Energy Conservation, and Sustainability. Springer, Heidelberg (2012)
Mulligan, C.P., Gall, D.: CrN-Ag self-lubricating hard coatings. Surf Coating Technol. **200**, 1495–1500 (2005)
Muran, M., Srnanek, M.: Kovove Mater. **23**, 107 (1985)
Murray, J.D.: Mathematical Biology II: Spatial Models and Biomedical Applications, Third Edition. Springer (1989)
Nakajima, A., Fujishima, A., Hashimoto, K., Watanabe, T.: Preparation of transparent superhydrophobic boehmite and silica films by sublimation of aluminum acetylacetonate. Adv. Mater. **11**, 1365–1368 (1999)
Nakao, W., Mori, S., Nakamura, J., Takahashi, K., Ando, K.: Self-crack-healing behavior of mullite/SiC particle/SiC whisker multi–composite and potential use for ceramic springs. J. Am. Ceramic Soc. **89**, 1352–1357 (2006)
Nakao, W., Takahashi, K., Ando, K.: Self-healing of surface cracks in structural ceramics. In: Ghosh, S.K. (ed.) Self-healing materials: fundamentals, design strategies, and applications, pp. 183–218. Wiley WCH, Weinheim (2009)
Nednoor, P., Gavalas, V.G., Chopra, N., Hinds, B.J., Bachas, L.G.: Carbon nanotube based biomimetic membranes: mimicking protein channels regulated by phosphorylation. J. Mater. Chem. **17**, 1755–1757 (2007)
Neerinck, D., Persoone, P., Sercu, M., et al.: Diamond-like nanocomposite coatings for low-wear and low-friction applications in humid environments. Thin Solid Films **317**, 402–404 (1998)
Neinhuis, C., Barthlott, W.: Characterization and distribution of water-repellent, self-cleaning plant surfaces. Ann. Bot. **79**, 667–677 (1997)
Nguyen, Q.S.: Instability and friction. Comptes Rendus Mechanique **331**, 99–112 (2003)
Nicolis, G., Prigogine, I.: Self-organization in nonequilibrium systems. Wiley, New York (1977)
Nix, W.D., Gao, H.: Indentation size effects in crystalline materials: a law for strain-gradient plasticity. J Mech. Phys. Solids **46**, 411–425 (1998)
Northen, M.T., Turner, K.L.: A batch fabricated biomimetic dry adhesive. Nanotechnology **16**, 1159–1166 (2005)

Nosonovsky, M.: Oil as a lubricant in ancient Middle East. JAST Tribology Online **2**, 44–49 (2007a)
Nosonovsky, M.: Model for solid-liquid and solid-solid friction for rough surfaces with adhesion hysteresis. J. Chem. Phys. **126**, 224701 (2007b)
Nosonovsky, M.: Modeling size, load, and velocity-dependence on friction at micro/nanoscale. Int. J. Surf. Sci. Eng. **1**, 22–37 (2007c)
Nosonovsky, M.: On the range of applicability of the Wenzel and Cassie equations. Langmuir **23**, 9919–9920 (2007d)
Nosonovsky, M.: Multiscale roughness and stability of superhydrophobic biomimetic interfaces. Langmuir **23**, 3157–3161 (2007e)
Nosonovsky, M., Adams, G.G.: Dilatational and shear waves induced by the frictional sliding of two elastic half-spaces. Int. J. Eng Sci. **39**, 1257–1269 (2001)
Nosonovsky, M., Adams, G.G.: Vibration and stability of frictional sliding of two elastic bodies with a wavy contact interface. ASME J. Appl. Mech. **71**, 154–300 (2004)
Nosonovsky, M., Bhushan, B.: Scale effects on dry friction during multiple asperity contact. ASME J Tribol **127**, 37–46 (2005a)
Nosonovsky, M., Bhushan, B.: Roughness optimization for biomimetic superhydrophobic surfaces. Microsys. Technol. **11**, 535–549 (2005b)
Nosonovsky, M., Bhushan, B.: Wetting of rough three-dimensional superhydrophobic surfaces. Microsys. Technol. **12**, 273–281 (2006a)
Nosonovsky, M., Bhushan, B.: Stochastic model for metastable wetting of roughness-induced superhydrophobic surfaces. Microsys. Technol. **12**, 231–237 (2006b)
Nosonovsky, M., Bhushan, B.: Multiscale friction mechanisms and hierarchical surfaces in nano- and bio-tribology. Mater. Sci. Eng. R **58**, 162–193 (2007a)
Nosonovsky, M., Bhushan, B.: Biomimetic superhydrophobic surfaces: multiscale approach. Nano Lett. **7**, 2633–2637 (2007b)
Nosonovsky, M., Bhushan, B.: Non-adhesive patterned surfaces: superhydrophobicity and wetting regime transitions. Langmuir **24**, 1525–1533 (2008a)
Nosonovsky, M., Bhushan, B.: Energy transitions in superhydrophobicity: low adhesion, easy flow and bouncing. J Phys Condens. Matt. **20**, 395005 (2008b)
Nosonovsky, M., Bhushan, B.: Biologically-inspired surfaces: broadening the scope of roughness. Adv. Func. Mater. **18**, 843–855 (2008c)
Nosonovsky, M., Bhushan, B.: Multiscale dissipative mechanisms and hierarchical surfaces: friction, superhydrophobicity, and biomimetics. Springer-Verlag, Heidelberg, Germany (2008d)
Nosonovsky, M., Bhushan, B.: Do hierarchical mechanisms of superhydrophobic lead to self-organized criticality? Scripta Mater. **59**, 941–944 (2008e)
Nosonovsky, M., Bhushan, B.: Superhydrophobic surfaces and emerging applications: non-adhesion, energy, green engineering. Curr. Opin. Colloid Interface Sci. **14**, 270–280 (2009)
Nosonovsky, M., Bhushan, B.: Thermodynamics of surface degradation, self-organization and self-healing for biomimetic surfaces. Phil. Trans. R. Soc. Lond A **367**, 1607–1627 (2009).
Nosonovsky, M., Bhushan, B.: Surface self-organization: from wear to self-healing in biological and technical surfaces. Appl. Surf. Sci. **256**, 3982–3987 (2010a)
Nosonovsky, M., Bhushan, B.: Introduction to green tribology: principles, research areas, and challenges. Phil. Trans. R. Soc. A (2010b)
Nosonovsky, M., Bormashenko, E.: Lotus effect: superhydrophobicity and self-cleaning. In: Favret, E., Fuentes, N. (eds.) Functional properties of biological surfaces: characterization and technological applications, pp. 43–78. World Scientific, Singapore (2009)
Nosonovsky, M., Esche, S.K.: A Paradox of decreasing entropy in multiscale Monte Carlo grain growth simulation. Entropy **10**, 49–54 (2008a)
Nosonovsky, M., Esche, S.K.: Multiscale effects in crystal grain growth and physical properties of metals. Phys. Chem. Chem. Phys. **10**, 5192–5195 (2008b)

Nosonovsky, M., Bhushan, B.: Do hierarchical mechanisms of superhydrophobicity lead to self-organized criticality? Scripta Mater. **59** (2008b)
Nosonovsky, M., Amano, R., Lucci, J.M., Rohatgi, P.K.: Physical chemistry of selforganization and self-healing in metals. Phys. Chem. Chem. Phys. **11**, 9530–9536 (2009a). doi:10.1039/b912433k
Nosonovsky, M.: From wear to self-healing in nanostructured biological and technical surfaces. Proceedings of ASME/STLE International Joint Tribology Conference IJTC2009, Memphis, ASME (2009)
Nosonovsky, M., Yang, S.-H., Zhang, H.: On the sensitivity of the capillary adhesion force to the surface roughness. In: Bhushan, B., (ed.), Scanning probe microscopy in nanoscience and nanotechnology springer series in Nanoscience and technology, (2011) vol. 2, 573–588
Nosonovsky M. Self-organization at the frictional interface for green tribology. Phil. Trans. R. Soc. A (2010b)
Odelius, M., Bernasconi, M., Parrinello, M.: Two-dimensional ice adsorbed on mica surface. Phys. Rev. Lett. **78**, 2855–2858 (1997)
Okumoto, T., Sasaki, T., Yamada, T.: Imono (J. JpnFoundrymen's Soc.) 46, 913 (1974)
Oldach, R.: Matching renewable energy with desalination plants (Muscat, Sultanate of Oman: The Middle East Desalination Research Center, MEDRC). MEDRC Series of R&D Reports, MEDRC Project: 97-AS-006a (2001)
Olson, G.B.: Computational design of hierarchically structured materials. Science **277**, 1237–1242 (1997)
Olson, G.B., Hartman, H.: Martensite and life-displacive transformations as biological processes. Journal De Physique **43**, 855–865 (1982)
Olson, G., Zhang, S., Manuel, M.: Self-healing metals: perspective from the Chicago school. In Proceedings of 2nd International Conference on Self-healing Materials, Chicago (2009)
Onda, T., Shibuichi, S., Satoh, N., Tsujii, K.: Super-water-repellent fractal surfaces. Langmuir **12**, 2125–2127 (1996)
Oner, D., McCarthy, T.J.: Ultrahydrophobic surfaces. Effects of topography length scales on wettability. Langmuir **16**, 7777–7778 (2000)
Onions, R.A., Archard, J.F.: The contact of surfaces having a random structure. J. Phys. D: **6**, 289–304 (1973)
Owen, K.C., Wang, M.J., Persad, C., Eliwzer, Z.: Wear **120**, 117 (1987)
Pai, B.C., Rohatgi, P.K.: Trans. Indian Inst. Met. **27**, 97 (1974)
Painlevé, P.: Sur le lois du frottement de glissement. C. R. Acad. Sci. Paris **121**, 112–115 (1895)
Pardee, R.P.: IEEE Trans. 1967, PAS-86, 616 (1967)
Park, S.G., Moon, J.H., Lee, S.K., Shim, J., Yang, S.M.: Bioinspired holographically featured superhydrophobic and supersticky nanostructured materials. Langmuir **26**, 1468–1472 (2010)
Parker, A.R., Lawrence, C.R.: Water capture by a desert beetle. Nature **414**, 33–34 (2001)
Patankar, N.A.: Transition between superhydrophobic states on rough surfaces. Langmuir **20**, 7097–7102 (2004a)
Patankar, N.A.: Mimicking the lotus effect: influence of double roughness structures and slender pillars. Langmuir **20**, 8209–8213 (2004b)
Pawlak, Z., et al.: A comparative study on the tribologicalbehaviour of hexagonal boron nitride (h-BN) as lubricating micro-particles – an additive in porous sliding bearings for a car clutch. Wear **267**, 1198–1202 (2009)
Pei, Y.T., Galvan, D., De Hosson, J.T.M.: Nanostructure and properties of TiC/a-C: H composite coatings. Acta Mater. **53**, 505–4521 (2005)
Pei, Y.T., Huizenga, P., Galvan, D., et al.: Breakdown of the Coulomb friction law in TiC/a-C: H nanocomposite coatings. J. Appl. Phys. **100**, 114309 (2006)
Peng, M., Li, H., Wu, L., Zheng, Q., Chen, Y., Gu, W.: Porous poly(vinylidene fluoride) membrane with highly hydrophobic surface. J. Appl. Polym. Sci. **98**, 1358–1363 (2005)
Perkins, J.: Ti-Ni and Ti-Ni-X shape memory alloys. Metals Forum **4**, 153–163 (1981a)

Perkins, J.: Shape memory behavior and thermoelastic martensitic transformations. Mater. Sci. Eng. **51**, 181–192 (1981b)
Polcar, T., Evaristo, M., Cavaleiro, A.: Comparative study of the tribological behavior of self-lubricating W-S-C and Mo-Se-C sputtered coatings. Wear **266**, 388–392 (2009)
Pompe, T., Fery, A., Herminghaus, S.: Measurement of contact line tension by analysis of the three-phase boundary with nanometer resolution. In: Drelich, J., Laskowski, J.S., Mittal, K.L. (eds.) Apparent and microscopic contact angles, pp. 3–12. VSP, Utrecht (2000)
Poole, C.P., Owens, F.J.: Introduction to nanotechnology. Wiley, New York (2003)
Prasad, S.V., Rohatgi, P.K.: Tribological properties of Al alloy particle composites. J. Met. **39**(11), 22–26 (1987)
Prigogine, I.: Introduction to thermodynamics of irreversible processes, 2nd edn. Interscience, New York, NY (1961)
Prigogine, I.: Introduction to Thermodynamics of irreversible processes. New york, NY, Wiley (1968)
Prigogine, I.: From being to becoming. Freeman, San Francisco, CA (1980)
Prigogine, I., Nicolis, G.: Self-organization in non-equilibrium systems. Wiley, NY (1977)
Prigogine, I., Stengers, I.: Order out of chaos. Bantam, NY (1984)
Puukilainen, E., Koponen, H.K., Xiao, Z., Suvanto, S., Pakkanen, T.A.: Nanostructured and chemically modified hydrophobic polyolefin surfaces. Colloid Surf. A Physicochem. Eng. Asp. **287**, 175–181 (2006)
Qian, B., Shen, Z.: Fabrication of superhydrophobic surfaces by dislocation-selective chemical etching on aluminum, copper, and zinc substrates. Langmuir **21**, 9007–9009 (2005)
Quere, D.: Surface wetting model droplets. Nat. Mater. **3**, 79–80 (2004)
Quere, D.: Non-sticking drops. Rep. Prog. Phys. **68**, 2495–2535 (2005)
Quintelier, J., Samyn, P., De Doncker, L., et al.: Self-lubricating and self-protecting properties of polymer composites for wear and friction applications. Polym Comp **30**, 932–940 (2009)
Raabe, D.: Scaling Monte Carlo kinetics of the Potts model using rate theory. Acta Mater. **48**, 1617–1628 (2000)
Raabe, D.: Cellular automata in materials science with particular reference to recrystallization simulation. Ann Rev Mater Res **32**, 53–76 (2002)
Rabinowicz, E.: Friction and wear of materials. Wiley, New York (1966)
Rack, H.J.: Fabrication of high-performance powder metallurgy aluminum matrix composites. Adv. Mater. Manuf Proc. **3**, 327–358 (1988)
Rahmawan, Y., Moon, M.W., Kim, K.S., Lee, K.R., Suh, K.Y.: Wrinkled, dual-scale structures of diamond-like carbon (DLC) for superhydrophobicity. Langmuir **26**, 484–491 (2010)
Ran, S., Winnubst, L., Blank, D.H.A., et al.: Effect of microstructure on the tribological and mechanical properties of CuO-Doped 3Y-TZP ceramics. J Am. Ceramic Soc. **90**, 2747–2752 (2007)
Ranjith, K., Rice, J.R.: Slip dynamics at a dissimilar material interface. J. Mech. Phys. Solids **49**, 341–361 (2001)
Rapoport, L., Fleischer, N., Tenne, R.: Fullerene-like WS2 nanoparticles: Superior lubricants for harsh conditions. Adv. Mater. **15**, I651–I655 (2003)
Rapoport, L., Fleischer, N., Tenne, R.: Applications of WS2 (MoS2) inorganic nanotubes and fullerene-like nanoparticles for solid lubrication and for structural nanocomposites. J. Mater. Chem. **15**, 1782–1788 (2005)
Ray, S.: Indian J. Technol. **28**, 368 (1990)
Reihs, K., Duparré, A., Notni, G.: Substrate with a reduced light-scattering, ultraphobic surface and a method for the production of the same. World patent 01/92179 (2001)
Remmers, J.J.C., de Borst, R.: Numerical modeling of self-healing mechanisms. In: van der Zwaag, S. (ed.) Self healing materials – an alternative approach to 20 centuries of materials science, pp. 365–380. Springer, Dordrecht, The Netherlands (2007)
Reyssat, M., Pepin, A., Marty, F., Chen, Y., Quere, D.: Bouncing transitions on microtextured materials. Europhys. Lett. **74**, 306–312 (2006)

Rice, J.: Dislocation nucleation from a crack tip: an analysis based on the Pierls concept. J. Mech. Phys. Solids **40**, 239–271 (1991)
Richard, D., Quéré, D.: Bouncing water drops. Europhys. Lett. **50**, 769–775 (2000)
Richard, D., Clanet, C., Quere, D.: Contact time of a bouncing drop. Nature **417**, 811 (2002)
Rigney, D.A., Chen, L.H., Taylor, M.G.S., Rosenfield, A.R.: Wear processes in sliding systems. Wear **100**, 195 (1984)
Rohatgi, P.K.: Tribological properties of Al alloy and aluminium matrix composites for automotive applications. J. Minerals Metals Mater. Soc. **43**, 10 (1991)
Rohatgi, P.K., Pal, B.C.: Wear **59**, 323 (1980)
Rohatgi, P.K., Pal, B.C.: J. Tribology (Trans. ASME) **101**, 367 (1979)
Rohatgi, P.K., Pai, B.C., Panda, S.C.: Preparation of cast aluminum-silica particulate composites. J. Mater. Sci. **14**, 2277–2283 (1979)
Rohatgi, P.K., Asthana, R., Das, S.: Solidification, structures, and properties of cast metal – ceramic particle composites. Int Metals Rev **31**, 115–139 (1986)
Rohatgi, P.K., Liu, Y., Yin, M., Barr, T.L.: Mater. Sci. Eng. **A123**, 213 (1990a)
Rohatgi, P.K., Liu, Y., Barr, T.L.: In: Rohatgi, P.K., et al. (eds.) Tribology of Composite Materials, p. 113. ASM International, Materials Park, OH (1990)
Rohatgi, P.K., Liu, Y., Aathana, R. In: Rohatgi, P.K., et al. (eds.) Tribology of Composite Materials, p. 69. ASM International, Materials Park, OH (1990)
Rohatgi, P.K., Ray, S., Liu, Y.: In: Rohatgi, P.K., et al. (eds.) Tribology of Composite Materials, p. 1. ASM International, Materials Park, OH (1990)
Rohatgi, P.K., Liu, Y., Barr, T.L.: Metall. Trans. **22A**, 1435 (1991)
Rohatgi, P.K., Ray, S., Liu, Y.: Tribological properties of metal matrix-graphiteparticle compositesInt. Mater. Rev. **37**, 129–149 (1992)
Rowlinson, J.S., Widem, B.: Molecular theory of capillarity. Clarendon, Oxford (1982)
Ruff, A.W., Peterson, M.B.: In: Rohatgi, P.K., et al. (eds.) Tribology of Composite Materials, p. 43. ASM International, Materials Park, OH (1990)
Ruths, M., Israelachvili, J.N.: Surface forces and nanorheology of molecularly thin films. In: Bhushan, B. (ed.) Springer handbook of nanontechnology, 2nd edn, pp. 859–924. Springer, Berlin (2007)
Ruzek, A.C.: Synthesis and characterization of metallic systems with potential for self-healing. M. Sc. Thesis, University of Wisconsin-Milwaukee (2009)
Ryan, N.J.: Using platelet technology to seal and locate leaks in subsea umbilical lines. Offshore Technology Conference held in Houston, OTC-18882-PP, 30 April–3 May 2007
Ryan, N.J.: Using platelet technology to seal and locate leaks in subsea umbilical lines. OTC-18882-PP, Offshore Technology Conference, Houston, Texas, USA, 30 April–3 May (2007b)
Rybakova, L.M., Kuksenova, L.I.: Sov. Eng. Res. **5**, 9 (1985)
Sadowski, J.: Untersuchungen zur maximalen Verschleibetafestigkeit fester korper (Research into the maximum wear resistance of solids). Tribologie und Schmierungstechnik **37**, 171–174 (1990)
Sadowski, J.: Energie-und Verschleissverteilung zwischen den Festkorpern wahrend der Reibung (Energy and wear division into solids during friction process). Tribologie und Schmierungstechnik **42**, 131–134 (1995)
Sanchez, F., Sobolev, K.: Nanotechnology in concrete – a review. Constr Build Mater **24**(11), 2060–2071 (2010)
Sarikaya, M., Aksay, I.A.: Biomimetics: design and processing of materials. AIP Series in polymers and complex materials. AIP, Woodbury, N.Y (1995)
Sarkar, D.K., Farzaneh, M., Paynter, R.W.: Superhydrophobic properties of ultrathin rf-sputtered Teflon films coated etched aluminum surfaces. Mater. Lett. **62**, 1226–1229 (2008)
Sarkar, M.K., He, F., Fan, J.: Differential superhydrophobicity and hydrophilicity on a thin cellulose layer. Thin Solid Films **518**, 5033–5039 (2010)

Sasada, T.: In: Proceedings of Conference on Tribology, Japanese Society of Lubrication Engineers, p. 623 (1985)
Savage, R.H.: Graphite lubrication. J. Appl. Phys. **19**, 1 (1948)
Savage, R.H., Schaffer, D.L.: Vapor lubrication of graphite sliding contacts. J. Appl. Phys. **27**, 136 (1956)
Scharf, T.W., Neira, A., Hwang, J.Y.: Self-lubricating carbon nanotube reinforced nickel matrix composites. J. Appl. Phys. **106**, 013508 (2009)
Semal, S., Blake, T.D., Geskin, V., de Ruijter, M.L., Castelein, G., De Coninck, J.: Influence of surface roughness on wetting dynamics. Langmuir **15**, 8765–8770 (1999)
Sen, R., Govindaraj, A., Rao, C.N.R.: Metal-filled and hollow carbon nanotubes obtained by the decomposition of metal-containing free precursor molecules. Chem. Mater. **9**, 2078–2081 (1997)
Shanahan, M.E.R., Carré, A.: Viscoelastic dissipation in wetting and adhesion phenomena. Langmuir **11**, 1396–1402 (1995)
Shang, H.M., Wang, Y., Limmer, S.J., Chou, T.P., Takahashi, K., Cao, G.Z.: Optically transparent superhydrophobic silica-based films. Thin Solid Films **472**, 37–43 (2005)
Sharma, R., Ross, D.S.: Kinetics of liquid penetration into periodically constrained capillaries. J Chem. Soc. Faraday Trans. **87**, 619–624 (1991)
Sharma, A., Soni, P.R., Rajan, T.V.: Met. Powder Rep. **43**, 25 (1988)
Sheng, X., Zhang, J.: Superhydrophobic behaviors of polymeric surfaces with aligned nanofibers. Langmuir **25**, 6916–6922 (2009)
Shi, F., Song, Y., Niu, J., Xia, X., Wang, Z., Zhang, X.: Facile method to fabricate a large-scale superhydrophobic surface by galvanic cell reaction. Chem. Mater. **18**, 1365–1368 (2006)
Shi, J., Alves, N.M., Mano, J.F.: Towards bioinspired superhydrophobic poly(L-lactic acid) surfaces using phase inversion-based methods. Bioinspir. Biomim. **3**, 034003 (2008) (6 pp.)
Shibuichi, S., Onda, T., Satoh, N., Tsujii, K.: Super-water-repellent surfaces resulting from fractal structure. J. Phys. Chem. **100**, 19512–19517 (1996)
Shinya, N., Kyono, J., Laha, K.: Self-healing effect of boron nitride precipitation in austenitic stainless steel. J. Intell Mater Syst. Struct. **17**, 1127–1133 (2006)
Shirtcliffe, N.J., McHale, G., Newton, M.I., Chabrol, G., Perry, C.C.: Dual-scale roughness produces unusually water-repellent surfaces. Adv. Mater. **16**, 1929–1932 (2004)
Shirtcliffe, N.J., McHale, G., Newton, M.I., Perry, C.C., Roach, P.: Porous materials show superhydrophobic to superhydrophilic switching. Chem. Commun. 3135–3137 (2005)
Shiu, J., Kuo, C., Chen, P., Mou, C.: Fabrication of tunable superhydrophobic surfaces by nanosphere lithography. Chem. Mater. **16**, 561–564 (2004)
Shuttleworth, R., Bailey, G.L.J.: The spreading of liquid over a rigid solid. Discuss. Faraday Soc. **3**, 16–22 (1948)
Singer, I.L., Dvorak, S.D., Wahl, K.J., Scharf, T.W.: Role of third bodies in friction and wear of protective coatings. J. Vac. Sci. Technol. A **21**, 232–240 (2003)
Singh, S., Houston, J., van Swol, F., Brinker, C.J.: Superhydrophobicity: drying transition of confined water. Nature **442**, 526 (2006)
Sirghi, L., Nakagiri, N., Sugisaki, K., Sugimura, H., Takai, O.: Effect of sample topography on adhesive force in atomic force microscopy in air. Langmuir **16**, 7796–7800 (2000)
Skarvelis, P., Papadimitriou, G.D.: Plasma transferred arc composite coatings with self lubricating properties, based on Fe and Ti sulfides: microstructure and tribological behavior. Surf. Coating Technol. **203**, 1384–1394 (2009)
Skeldon, P., Wang, H.W., Thompson, G.E.: Formation and characterization of self-lubricating MoS2 precursor films on anodized aluminium. Wear **206**, 187–196 (1997)
Sloof, W.G.: Self healing in coatings at high temperatures. In: van der Zwaag, S. (ed.) Self healing materials – an alternative approach to 20 centuries of materials science, pp. 309–321. Springer, Dordrecht, The Netherlands (2007)
Sloof, W.G.: Self-healing mechanism in materials for high temperatureapplications. In: Proceedings of 2nd International Conference on Self-Healing Materials, Chicago (2009)

Slowik, M.A.: Research: Self-Healing Materials Using Electro-hydrodynamics. http://www.princeton.edu/~cml/html/research/self_healing.html (2009). Accessed 31 Oct 2009
Smith, J.M., Smith, R.M.: Aluminum engines design for modern fabrication. SAE Trans. **67**, 295–311 (1959)
Sobolev, K., Ferrada-Gutiérrez, M.: How nanotechnology can change the concrete world: part 2. Am. Ceram. Soc. Bull. **11**, 16–19 (2005)
Sokoloff, J.B.: Theory of the effects of multiscale surface roughness and stiffness on static friction. Phys Rev. B **73**, 016104 (2006)
Sommers, A.D., Jacobi, A.M.: Creating micro-scale surface topology to achive anisotropic wettability on an aluminum surface. J. Micromech. Microeng. **16**, 1571–1578 (2006)
Song, F., Xiao, K.W., Bai, K., Bai, Y.L.: Microstructure and nanomechanical properties of the wing membrane of dragonfly. Mater. Sci. Eng. A **457**, 254–260 (2007)
Sosnovskiy, L.A., Sherbakov, S.S.: Surprizes of tribo-fatigue. Magic Book, Minsk (2009)
Stewart, D.E.: Finite dimensional contact mechanics. Phil Trans. R. Soc. Lond. A **359**, 2467–2482 (2001)
Stifter, T., Marti, O., Bhushan, B.: Theoretical investigation of the distance dependence of capillary and van der Waals forces in scanning force microscopy. Phys Rev. B **62**, 13667–13673 (2000)
Strnad, G., Biro, D., Bolos, V., et al.: Researches on nanocomposite self-lubricating coatings. Metallurgia Int. **14**, 121–124 (2009)
Sugishita, J., Fujiyoshi, S.: The effect of cast iron graphites on friction and wear performance. I. Wear **68**, 7 (1981a)
Sugishita, J., Fujiyoshi, S.: The effect of cast iron graphites on friction and wear performance. II. Wear **66**, 209 (1981b)
Suh, N.P.: Wear **44**, 1 (1977)
Suh, N.P.: Tribophysics. Prentice-Hall, New Jersey (1986)
Suh, M.S., Chae, Y.H., Kim, S.S.: Friction and wear behavior of structural ceramics sliding against zirconia. Wear **264**, 800–806 (2008)
Sun, M., Luo, C., Xu, L., Ji, H., Ouyang, Q., Yu, D., Chen, Y.: Artificial lotus leaf by nanocasting. Langmuir **21**, 8978–8981 (2005)
Suwa, M.: Hitachi graphite-dispersed cast alloy – Gradia Internal Report. Hitachi, Japan (1986)
Suwa, M., Komuro, K., Soeno, K.: J. Jpn. Inst. Met. **42**, 1034 (1978)
Suwa, M., Komuro, K., Soeno, K.: J. Jpn Inst. Met. **40**, 1074 (1976)
Szoszkiewicz, R., Riedo, E.: Nanoscopic friction as a probe of local phase transitions. Appl. Phys. Lett. **87**, 033105 (2005a)
Szoszkiewicz, R., Riedo, E.: Nucleation time of nanoscale water bridges. Phys. Rev. Lett. **95**, 135502 (2005b)
Szoszkiewicz, R., Bhushan, B., Huey, B.D., Kulik, A.J., Gremaud, G.: Correlations between adhesion hysteresis and friction at molecular acales. J. Chem. Phys. **122**, 144708 (2005)
Tabor, D.: Surface forces and surface interactions. J. Colloid Interface Sci. **58**, 2–13 (1977)
Tadmor, R., et al.: Measurement of lateral adhesion forces at the interface between a liquid drop and a substrate. Phys. Rev. Lett. **103**, 266101 (2009)
Takahashi, K., Ando, K., Nakao, W., Tsutagawa, Y.: Effect of SiC nano-sizing on self-crack-healing during service. Proceedings of 1st International Conference on Self-Healing Materials, Noordwijk aan Zee, The Netherlands, 18–20 April 2007
Tas, N.R., Mela, P., Kramer, T., Berenschot, J.W., Van der Berg, A.: Capillarity induced negative pressure of water plugs in nanochannels. Nano Lett. **3**, 1537 (2003)
Tas, N.R., Escalante, M., van Honschoten, J.W.: Capillary negative pressure measured by nanochannel collapse. Langmuir **26**, 1473–1476 (2010)
Teraoka, T.: Wear of arc resistant sintered copper alloy for pantograph, Technical Report, p. 5. Railway Technical Research Institute, Japan (1983)

Teshima, K., Sugimura, H., Inoue, Y., Takai, O., Takano, A.: Transparent ultra water-repellent poly(ethylene terephthalate) substrates fabricated by oxygen plasma treatment and subsequent hydrophobic coating. Appl. Surf. Sci. **244**, 619–622 (2005)
Therriault, D., White, S.R., Lewis, J.A.: Chaotic mixing in threedimensional microvascular networks fabricated by direct-write assembly. Nat. Mater. **2**, 265–271 (2003)
Thomas, T.R.: Rough surfaces. Longman, New York (1982)
Thompson, P.A., Robbins, M.O.: Origin of stick-slip motion in boundary lubrication. Science **250**, 792–794 (1990)
Thoreson, E.J., Martin, J., Burnham, N.A.: The role of few-asperity contacts in adhesion. J. Collolid. Interface Sci. **298**, 94–101 (2006)
Tocha, E., Pasaribu, H.R., Schipper, D.J., et al.: Low friction in CuO-doped yttria-stabilized tetragonal zirconia ceramics: a complementary macro- and nanotribology study. J. Am. Ceramic Soc. **91**, 1646–1652 (2008)
Tokisue, H., Abbaschian, G.J.: Friction and wear properties of aluminum-particulate graphite composites. Mater. Sci. Eng. **34**, 75–78 (1978)
Tolstoi, D.M.: Significance of the normal degree of freedom and natural normal vibrations in contact friction. Wear **10**, 199–213 (1967)
Toohey, K.S., Sottos, N.R., Lewis, J.A., Moore, J.S., White, S.R.: Self-healing materials with microvascular netweorks. Nat. Mater. **6**, 581–585 (2007)
Trask, R.S., Bond, I.P.: Biomimetic self-healing of advanced composite structures using hollow glass fibers. Smart Mater. Struct. **15**, 704–710 (2006)
Trask, R.S., Williams, G.J., Bond, I.: Bioinspired self-healing of advanced composite structures using hollow glass fibers. J. R. Soc. Interface **4**, 363–373 (2007)
Tretinnikov, O.N.: Wettability and microstructure of polymer surfaces: stereochemical and conformational aspects. In: Drelich, J., Laskowski, J.S., Mittal, K.L. (eds.) Apparent and microscopic contact angle, pp. 111–128. VSP, Utrecht (2000)
Trevena, D.H.: Cavitation and tension in liquids. Adams Hilger, Bristol (1987)
Tsori, Y.: Discontinuous liquid rise in capillaries with varying cross-sections. Langmuir **22**, 8860–8863 (2006)
Tsuya, Y., Takagi, R.: Lubrication properties of lead filns on copper. Wear **7**, 131–143 (1964)
Tsuya, Y.: J. Jpn Inst. Compos. **11**, 127 (1985)
Tu, J.P., Jiang, C.X., Guo, S.Y., et al.: Micro-friction characteristics of aligned carbon nanotube film on an anodic aluminum oxide template. Mater. Lett. **58**, 1646–1649 (2004)
Turcotte, D.L.: Self-organized criticality. Rep. Prog. Phys. **62**, 1377–1429 (1999)
Turing, A.M.: The chemical basis of morphogenesis. Phil Trans. R. Soc. B **237**, 37–72 (1952)
Tuteja, A., Choi, W., Ma, M., Mabry, J.M., Mazzella, S.A., Rutledge, G.C., McKinley, G.H., Cohen, R.E.: Designing superoleophobic surfaces. Science **318**, 1618–1622 (2007)
Tuteja, A., Choi, W., Mabri, J.M., McKinley, G.H., Cohen, R.E.: Robust omniphobic surfaces. Proc. Natl. Acad. Sci. U.S.A. **105**, 18200–18205 (2008)
Tyree, M.T.: Accent of water. Nature **423**, 923 (2003)
Umeda, J., Kondoh, K., Imai, H.: Friction and wear behavior of sintered magnesium composite reinforced with CNT-Mg2Si/MgO. Mater. Sci. Eng. A **504**, 157–162 (2009)
Urbakh, M., Klafter, J., Gourdon, D., Israelachvili, J.: The nonlinear nature of friction. Nature **430**, 525–528 (2004)
Van Brunt, C., Savage, R.H.: Carbon brush contact films. General Electric. Rev. **47**, 16–91 (1944)
van der Zwaag, S. (ed.): Self healing materials – an alternative approach to 20 centuries of materials science. Springer, Dordrecht, The Netherlands (2007)
van der Zwaag, S.: Self-healing behaviour in man-made engineering materials: bioinspired but taking into account their intrinsic character. Phil. Trans. R. Soc. A **367**, 1689–1704 (2009)
Varanasi, K.K., Deng, T., Smith, J.D., Hsu, M., Bhate, N.: Frost formation and ice adhesion on superhydrophobic surfaces. Appl. Phys. Lett. **97**, 234102 (2010)
Vedantam, S., Panchagnula, M.V.: Phase field modeling of hysteresis in sessile drops. Phys. Rev. Lett. **99**, 176102 (2007)

Vermolen, F.J., Van Rossum, W.G., Javierre, E., Adam, J.A.: Modeling of self-healing of skin tissue. In: van der Zwaag, S. (ed.) Self healing materials – an alternative approach to 20 centuries of materials science, pp. 337–364. Springer, Dordrecht, The Netherlands (2007)
Vilar, R.: Laser cladding. J. Laser Appl. **11**, 64–79 (1999)
Vincent, J.F.V., Bogatyreva, O.A., Bogatyrev, N.R., Bowyer, A., Pahl, A.K.: Biomimetics: its practice and theory. J. R. Soc. Interface **3**, 471–482 (2006)
Voevodin, A.A., Capano, M.A., Laube, S.J.P., Donley, M.S., Zabinski, J.S.: Design of a Ti/TiC/DLC functionally gradient coating based on studies of structural transitions in Ti-C thin films. Thin Solid Films **298**, 107–115 (1997)
Voronov, R.S., Papavassiliou, D.V., Li, L.L.: Boundary slip and wetting properties of interfaces: correlation of the contact angle with the slip length. J. Chem. Phys. **124**, 204701 (2006)
Vourdas, N., Tserepi, A., Gogolides, E.: Nanotextured super-hydrophobic transparent poly(methyl methacrylate) surfaces using high-density plasma processing. Nanotechnology **18**, 1–7 (2007)
Wagner, T., Neinhuis, C., Barthlott, W.: Wettability and contaminability of insect wings as a function of their surface sculptures. Acta. Zoolog. **77**, 213–225 (1996)
Wagner, P., Furstner, R., Barthlott, W., Neinhuis, C.: Quantitative assessment to the structural basis of water repellency in natural and technical surfaces. J. Exper. Botany **54**, 1295–1303 (2003)
Wang, S., Jiang, L.: Definition of superhydrophobic states. Adv. Mater. **19**, 3423–3424 (2007)
Wang, R., et al.: Light-induced amphiphilic surfaces. Nature **388**, 431–432 (1997)
Wang, R., et al.: Photogeneration of highly amphiphilic TiO_2 surfaces. Adv. Mater. **10**, 135 (1998)
Wang, L.Y., Tu, J.P., Chen, W.X., et al.: Friction and wear behavior of electroless Ni-based CNT composite coatings. Wear **254**, 1289–1293 (2003)
Wang, Z.X., Dutta, I., Majumdar, B.S.: Thermomechanical response of a lead-free solder reinforced with a shape-memory alloy. Scripta Mater. **54**, 627–632 (2005)
Wang, Y., Zhu, Q., Zhang, H.: Fabrication and magnetic properties of hierarchical porous hollow nickel microspheres. J. Mater. Chem. **16**, 1212–1214 (2006)
Wang, S., Liu, H., Liu, D., Ma, X., Fang, X., Jiang, L.: Enthalpy driven three state switching of a superhydrophilic/superhydrphobic surfaces. Angew. Chem. Int. Ed. **46**, 3915–3917 (2007a)
Wang, H., Huang, P., Li, Z.: Crack and void healing in metals. In: van der Zwaag, S. (ed.) Self healing materials – an alternative approach to 20 centuries of materials science, pp. 255–277. Springer, Dordrecht, The Netherlands (2007b)
Wang, S.T., et al.: Enthalpy-driven three-state switching of a superhydrophilic/superhydrophobic surface. Angewandte Chem. **46**, 3915–3917 (2007c)
Wang, A.H., Zhang, X.L., Zhang, X.F., et al.: Ni-based alloy/submicron WS2 self-lubricating composite coating synthesized by Nd: YAG laser cladding. Mater. Sci. Eng. A **475**, 312–318 (2008)
Weibel, D.E., Michels, A.F., Feil, A.F., Amaral, L., Teixeira, S.R., Horowitz, F.: Adjustable hydrophobicity of Al substrates by chemical surface functionalization of nano/microstructures. J. Phys. Chem. C **114**, 13219–13225 (2010)
Wenzel, R.N.: Resistance of solid surfaces to wetting by water. Indust. Eng. Chem. **28**, 988–994 (1936)
White, S.R., Sottos, N.R., Geubelle, P.H., Moore, J.S., Kessler, M.R., Sriram, S.R., Brown, E.N., Viswanathan, S.: Autonomic healing of polymer composites. Nature **409**, 794–797 (2001)
Williams, G.J., Trask, R.S., Bond, I.P.: Self-healing functionality for CFRP. Proceedings of 1st International Conference on Self-Healing Materials, Noordwijik aan Zee, The Netherlands, 18–20 April 2007
Wool, R.P.: Self-healing materials: a review. Soft Matter **4**, 400–418 (2008)
Wu,G., Gao, F., Kaltchev, M., Gutow, J., Mowlem, J.K., Schramm, W.C., Kotvis, P.V., Tysoe, W.T.: An investigation of the tribological properties of thin KCl films on iron in ultrahigh vacuum: modeling the extreme-pressure lubricating interface. Wear 252 595–606 (2002)
Wu, X., Zheng, L., Wu, D.: Fabrication of superhydrophobic surfaces from microstructured ZnO-based surfaces via a wet-chemical route. Langmuir **21**, 2665–2667 (2005)

Wu, X.H., Qin, W., Guo, Y., et al.: Self-lubricative coating grown by micro-plasma oxidation on aluminum alloys in the solution of aluminate-graphite. Appl. Surf. Sci. **254**, 6395–6399 (2008)
Wu, W., Zhu, Q., Qing, F., Han, C.C.: Water repellency on a fluorine-containing polyurethane surface: toward understanding the surface self-cleaning effect. Langmuir **25**, 17–20 (2009)
Wu, D., et al.: Curvature-driven reversible in situ switching between pinned and roll-down superhydrophobic states for water droplet transportation. Adv. Mater. **23**, 545 (2011)
Xia, F., Jiang, L.: Bio-inspired, smart, multiscale interfacial materials. Adv. Mater. **20**, 2842–2858 (2008)
Xia, H.W., et al.: Tuning surface wettability through supramolecular interactions. Soft Matter. **7**, 1638–1640 (2011)
Xiao, Y., Amano, R.S.: Aluminized composite solid propellant particle path in combustion chamber of solid rocket motor. Advances in fluid mechanics, pp. 153–164. WIT, UK (2006)
Xiaoand, X., Qian, L.: Investigation of humidity-dependent capillary force. Langmuir **16**, 8153–8158 (2000)
Xu, L., Lio, A., Hu, J., Ogletree, D.F., Salmeron, M.: Wetting and capillary phenomena of water on mica. J. Phys. Chem. B **102**, 540–548 (1998)
Xu, L., Chen, W., Mulchandani, A., Yan, Y.: Reversible conversion of conducting polymer films from superhydrophobic to superhydrophilic. Angew. Chem. Int. Ed. **44**, 6009–6012 (2005)
Xu, X.H., et al.: Switchable adhesion of superhydrophobic ZnO nanorod film. J. Macromol Sci A **47**, 1091–1095 (2010)
Xue, C.H., Jia, S.T., Zhang, J., Tian, L.Q.: Superhydrophobic surfaces on cotton textiles by complex coating of silica nanoparticles and hydrophobization. Thin Solid Films **517**, 4593–4598 (2009)
Yabu, H., Shimomura, M.: Single-step fabrication of transparent superhydrophobic porous polymer films. Chem. Mater. **17**, 5231–5234 (2005)
Yaminsky, V.: Molecular mechanisms of hydrophobic transitions. In: Drelich, J., Laskowski, J.S., Mittal, K.L. (eds.) Apparent and microscopic contact angles, pp. 47–95s. VSP, Utrecht (2000)
Yan, L., Wang, K., Wu, J., Ye, L.: Hydrophobicity of model surfaces with closely packed nano- and micro-spheres. Colloid Surf. A Physicochem. Eng. Asp. **296**, 123–131 (2007)
Yang, S.-H., Zhang, H., Hsu, S.M.: Correction of random surface roughness on colloidal probes in measuring adhesion. Langmuir **23**, 1195–1202 (2007a)
Yang, S.-H., Gates, R., Nosonovsky, M., Cook, R.: (National Institute of Standards and Technology), private communication (2007)
Yang, S.-H., Zhang, H., Nosonovsky, M., Chung, K.H.: The effect of contact geometry upon the pull-off force measurement with a colloidal probe. Langmuir **24**, 743–748 (2008a)
Yang, S.H., Nosonovsky, M., Zhang, H., Chung, K.-H.: Nanoscale water capillary bridges under deeply negative pressure. Chem. Phys. Lett. **451**, 88–92 (2008b)
Yang, S.-H., Nosonovsky, M., Zhang, H., Chung, K.-H.: Response to the comment on 'Nanoscale water capillary bridges under deeply negative pressure' by Caupin et al. Chemical Physics Letters **463**, 286–287 (2008c)
Yang, J., Zhang, Z., Men, X., Xu, X.: Fabrication of stable, transparent and superhydrophobic nanocomposite films withpolystyrene functionalized carbon nanotubes. Appl. Surf. Sci. **255**, 9244–9247 (2009)
Yasa, E., Morooka, T., Hayama, F.: J. Jpn Inst. Met. **50**, 1032 (1986)
Ying, Z.C., Hsu, S.M.: First observation of elastic plowing in nanofriction. In: Proceedings of the World Tribology Congress III, pp. 339–340 (2005)
Yoo, Y.E., Kim, T.H., Choi, D.S., Hyun, S.M., Lee, H.J., Lee, K.H., Kim, S.K., Kim, B.H., Seo, Y. H., Lee, H.G., Lee, J.S.: Injection molding of a nanostructured plate and measurement of its surface properties. Curr. Appl. Phys. **9**, e12–e18 (2009)
Yoon, H., Park, J.H.: G.H Kim, a superhydrophobic surface fabricated by an electrostatic process. Macromol. Rapid Commun. **31**, 1435–1439 (2010)
Yoshizawa, H., Chen, Y.L., Israelachvili, J.: Fundamental mechanisms of interfacial friction – relation between adhesion and friction. J. Phys. Chem. **97**, 4128–4140 (1993)
Yost, F.G., Michael, J.R., Eisenmann, E.T.: Extensive wetting due to roughness. Acta Metall. Mater. **45**, 299–305 (1995)

Young, T.: An essay on cohesion of fluids. Phil. Trans. R. Soc. **95**, 65–87 (1805)
Yu, Q., Nosonovsky, M., Esche, S.K.: On the accuracy of Monte Carlo Potts models for grain growth. J Comp. Meth. Sci. Eng. **8**, 227–243 (2008)
Yuan, Z., Chen, H., Tang, J., Gong, H., Liu, Y., Wang, Z., Shi, P., Zhang, J., Chen, X.: A novel preparation of polystyrene film with a superhydrophobic surface using a template method. J. Phys. D: Appl. Phys. **40**, 3485–3489 (2007)
Yuan, Z., Chen, H., Zhang, J., Zhao, D., Liu, Y., Zhou, X., Li, S., Shi, P., Tang, J., Chen, X.: Preparation and characterization of self-cleaning stable superhydrophobic linear low-density polyethylene. Sci. Technol. Adv. Mater. **9**, 1–5 (2008)
Yuan, Z., Chen, H., Tang, J., Zhao, D.: A stable porous superhydrophobic high-density polyethylene surface prepared by adding ethanol in humid atmosphere. J. Appl. Polym. Sci. **113**, 1626–1632 (2009)
Zeng, H.B., Tirrel, M., Israelachvili, J.: Limit cycles in dynamic adhesion and friction prpcesses: a discussion. J. Adhes. **82**, 933–943 (2006)
Zhai, L., Cebeci, F.C., Cohen, R.E., Rubner, M.F.: Stable superhydrophobic coatings from polyelectrolyte multilayers. Nano Lett. **4**, 1349–1353 (2004)
Zhang, Z.: In: Fishman, S.G., Dhingra, A. (eds.) Cast Reinforced Metal Composites, p. 93. ASM International, Materials Park, OH (1988)
Zhang, J.L., Li, J.A., Han, Y.C.: Superhydrophobic PTFE surfaces by extension. Macromol. Rapid Commun. **25**, 1105–1108 (2004a)
Zhang, X., Feng, S., Yu, X., Liu, H., Fu, Y., Wang, Z., Jiang, L., Li, X.: Polyelectrolyte multilayer as matrix for electrochemical deposition of gold clusters: toward super-hydrophobic surface. J. Am. Chem. Soc. **126**, 3064–3065 (2004b)
Zhang, X., Tan, S., Zhao, N., Guo, X., Zhang, X., Zhang, Y., Xu, J.: Evaporation of sessile water droplets on superhydrophobic natural lotus and biomimetic polymer surfaces. Chem Phys Chem **7**, 2067–2070 (2006)
Zhang, X.T., et al.: Superhydrophobic TiO_2 surfaces: preparation, photocatalytic wettability conversion, and superhydrophobic−superhydrophilic patterning. J. Phys. Chem. C **111**, 14521–14529 (2007)
Zhang, Y., Wang, H., Yan, B., Zhang, Y., Yin, P., Shen, G., Yu, R.: A rapid and efficient strategy for creating super-hydrophobic coatings on various material substrates. J. Mater. Chem. **18**, 4442–4449 (2008)
Zhang, W.J., Zhang, D., Le, Y.K., et al.: Fabrication of surface self-lubricating composites of aluminum alloy. Appl. Surf. Sci. **255**, 2671–2674 (2008b)
Zhang, M.Q., Rong, M.Z., Yin, T.: Self-healing polymers and polymer composites. In: Ghosh, S. K. (ed.) Self-healing materials: fundamentals, design strategies, and applications, pp. 29–72. Wiley WCH, Weinheim (2009)
Zhao, N., Xie, Q.D., Weng, L.H., Wang, S.Q., Zhang, X.Y., Xu, J.: Superhydrophobic surface from vapor-induced phase separation of copolymer micellar solution. Macromolecules **38**, 8996–8999 (2005)
Zhao, N., Weng, L., Zhang, X., Xie, Q., Zhang, X., Xu, J.: Lotus-leaf-like superhydrophobic surface prepared by solvent-induced crystallization. Chemphyschem **7**, 824–827 (2006)
Zhao, V., Lu, Q., Chen, D., Wei, Y.: Superhydrophobic modification of polyimide films based on gold-coated porous silver nanostructures and self-assembled monolayers. J. Mater. Chem. **16**, 4504–4509 (2006)
Zheludkevich, M.: Self-healing anti-corrosion coatings. In: Ghosh, S.K. (ed.) Self-healing materials: fundamentals, design strategies, and applications, pp. 101–140. Wiley WCH, Weinheim (2009)
Zheng, W.T., Sun, C.Q.: Electronic process of nitriding: mechanism and applications. Prog Solid State Chem. **34**, 1–20 (2006)
Zheng, Q., Green, J., Kieffer, J., Poole, P.H., Shao, J., Wolf, G.H., Angell, A.C.: Limiting tensions for liquids and glasses from laboratory and MD studies. In: Imre, A.R., et al. (eds.) Liquids under negative pressure, pp. 33–46. Kluwer, Dorchester (2002)

Zheng, Z., Gu, Z., Huo, R., Ye, Y.: Superhydrophobicity of polyvinylidene fluoride membrane fabricated by chemical vapor deposition from solution. Appl. Surf. Sci. **255**, 7263–7267 (2009)
Zheng, Z., Gu, Z., Huo, R., Luo, Z.: Superhydrophobic poly(vinylidene fluoride) film fabricated by alkali treatment enhancing chemical bath deposition. Appl. Surf. Sci. **256**, 2061–2065 (2010)
Zhou, B.L.: Bio-inspired study of structural materials. Mater. Sci. Eng. C **11**, 13–18 (2000)
Zhou, S.M., Zhang, X.B., Ding, Z.P., et al.: Fabrication and tribological properties of carbon nanotubes reinforced Al composites prepared by pressureless infiltration technique. Composites A Appl Sci Manufact. **38**, 301–306 (2007)
Zhu, Y., Granick, S.: Limits of the hydrodynamic No-slip boundary condition. Phys. Rev. Lett. **88**, 106102 (2002)
Zhu, A.W., Chen, J., Starke, E.A.: Precipitation strengthening in stress-aged Al-XCu alloys. Acta Mater. **48**, 2239–2246 (2000)
Zhu, L., Xiu, Y., Xu, J., Tamirisa, P.A., Hess, D.W., Wong, C.: Superhydrophobicity on two-tier rough surfaces fabricated by controlled growth of aligned carbon nanotube arrays coated with fluorocarbon. Langmuir **21**, 11208–11212 (2005)
Zmitrowicz, A.: A thermodynamical model of contact, friction, and wear. Wear **114**, 135–221 (1987)
Zucchelli, A., Minak, G., Lotti, F.: Self-repairing vitreous enamel coating for metal substrate. In Proceedings of 2nd International Conference on Self-Healing Materials, Chicago (2009)
Zypman, F., Ferrante, J., Jansen, M., Scanlon, K., Abel, P.: Evidence of self-organized criticality in dry sliding friction. J. Phys. Condens. Matt. Lett. **15**, 191 (2003)

Index